9-9-91
E6161

NASA Conference Publication 3121

# Space Photovoltaic Research and Technology 1991

*Proceedings of a conference held at*
*NASA Lewis Research Center*
*Cleveland, Ohio*
*May 7–9, 1991*

NASA

*NASA Conference Publication 3121*

# Space Photovoltaic Research and Technology 1991

*NASA Lewis Research Center*
*Cleveland, Ohio*

Proceedings of a conference held at
NASA Lewis Research Center
Cleveland, Ohio
May 7–9, 1991

NASA
National Aeronautics and
Space Administration
Office of Management
Scientific and Technical
Information Program
**1991**

# Contents

*Foreword*
Dennis Flood, Chief, Photovoltaic Branch, NASA Lewis Research Center ..... ix

## Session 1 - Experimental InP Solar Cell Results

*Tunnel Junctions for InP-on-Si Solar Cells*
C. Keavney, S. Vernon, and V. Haven ..... 1-1

*Fabrication and Performance Analysis of 4-cm$^2$ Indium Tin Oxide/InP Photovoltaic Solar Cells*
T.A. Gessert, X. Li, P.W. Phelps, T.J. Coutts, and N. Tzafaras ..... 2-1

*A Comparative Study of $p^+n$ and $n^+p$ InP Solar Cells Made by a Closed Ampoule Diffusion*
M. Faur, M. Faur, D.J. Flood, I. Weinberg, D.J. Brinker, C. Goradia, N.S. Fatemi, M. Goradia, and W. Thesling ..... 3-1

*Improvements in Contact Resistivity and Thermal Stability of Au-Contacted InP Solar Cells*
N.S. Fatemi and V.G. Weizer ..... 4-1

*Grooved Surfaces on InP*
S.G. Bailey, N.S. Fatemi, G.A. Landis, and P. Jenkins ..... 5-1

*Effect of Dislocations on Properties of Heteroepitaxial InP Solar Cells*
I. Weinberg, C.K. Swartz, H.B. Curtis, D.J. Brinker, P. Jenkins, and M. Faur ..... 6-1

*High Resolution Electrolyte for Thinning InP by Anodic Dissolution and Its Applications to EC-V Profiling, Defect Revealing and Surface Passivation*
M. Faur, M. Faur, I. Weinberg, M. Goradia, and C. Vargas ..... 7-1

## Session 2 - GaAs Solar Cell Studies

*Recent Advances in GaAs/Ge Solar Cells*
C.L. Chu, P.A. Iles, W. Patterson ..... 8-1

*Production Status of GaAs/Ge Solar Cells and Panels*
B. Smith, M. Gillanders, P. Vijayakumar, D. Lillington, H. Yang, and R. Rolph ..... 9-1

*Photoreflectance and DLTS Evaluation of Plasma-Induced Damage in GaAs and InP Prior to Solar Cell Fabrication*
L. He and W.A. Anderson ..... 10-1

*Calculation of Gallium-Metal-Arsenic Phase Diagrams*
J.D. Scofield, J.E. Davison, A.E. Ray, and S.R. Smith ..... 11-1

## Session 3 - Multijunction Solar Cell Results

*$GaInP_2$ /GaAs Tandem Cells for Space Applications*
J.M. Olson, S.R. Kurtz, A.E. Kibbler, K.A. Bertness, and D.J. Friedman ..... 12-1

*Two-Terminal Monolithic InP-Based Tandem Solar Cells With Tunneling Intercell Ohmic Connections*
C.C. Shen, P.T. Chang, and K.A. Emery ..... 13-1

*GaAs(AlGaAs)/$CuInSe_2$ Tandem Solar Cells-- Technology Status and Future Directions*
N.P. Kim, R.M. Burgess, R.P. Gale, and R.W. McClelland ..... 14-1

*Development of n/p AlGaAs Free-Standing Top Solar Cells for Tandem Applications*
G.H. Negley, L.C. DiNetta, J.R. Cummings, M.H. Hannon, P.E. Sims, and A.M. Barnett ..... 15-1

*Monolithic InP/$Ga_{0.47}In_{0.53}As$ Tandem Solar Cells for Space*
M.W. Wanlass, J.S. Ward, T.J. Coutts, K.A. Emery, T.A. Gessert, and C.R. Osterwald ..... 16-1

*Recent Advancements in Monolithic AlGaAs/GaAs Solar Cells for Space Applications*
K.R. Wickham, B-C. Chung, M. Klausmeier-Brown, M.S. Kuryla, M. Ladle Ristow, G.F. Virshup, and J.G. Werthen ..... 17-1

## Session 4 - Array and Solar Cell Development

*Direct Glass Bonded High Specific Power Silicon Solar Cells for Space Applications*
L.C. DiNetta, J.A. Rand, J.R. Cummings, S.M. Lampo, K.P. Shreve, A.M. Barnett ..... 18-1

*Flexible Copper-Indium-Diselenide Films and Devices for Space Applications*
J.H. Armstrong, C.O. Pistole, M.S. Misra, V.K. Kapur, and B.M. Basol ..... 19-1

*Key Results of the Mini-Dome Fresnel Lens Concentrator Array Development Program Under Recently Completed NASA & SDIO SBIR Projects*
M.J. O'Neill, M.F. Piszczor, L.M. Fraas ..... 20-1

*The Status of Lightweight Photovoltaic Space Array Technology Based on Amorphous Silicon Solar Cells*
J.J. Hanak and J. Kaschmitter ..... 21-1

*Reverse Bias Voltage Testing of 8 cm x 8 cm Silicon Solar Cells*
T. Woike, S. Stotlar, and C. Lungu ..... 22-1

*Mass Properties Survey of Solar Array Technologies*
R. Kraus ..... 23-1

## Session 5 - Photovoltaics for Conversion of Laser Radiation

*Space Power by Laser Illumination of PV Arrays*
G.A. Landis ..... 24-1

*Potential Converter for Laser-Power Beaming Using Diode Lasers*
G.H. Walker, M.D. Williams, G.L. Schuster, and P.A. Iles ..... 25-1

*GaAs Solar Cells for Laser Power Beaming*
L.C. Olsen, G. Dunham, D.A. Huber, F.W. Addis, N. Anheier, and E.P. Coomes ..... 26-1

## Session 6 - Experimental and Modeling Results of InP Solar Cells

*High-Efficiency Heteroepitaxial InP Solar Cells*
M.W. Wanlass, T.J. Coutts, J.S. Ward, and K.A. Emery ..... 27-1

*InP Concentrator Solar Cells for Space Applications*
J.S. Ward, M.W. Wanlass, T.J. Coutts, and K.A. Emery ..... 28-1

*Comparative Modeling of InP Solar Cell Structures*
R.K. Jain, I. Weinberg, and D.J. Flood ..... 29-1

*A Theoretical Comparison of the Near-Optimum Design and Predicted Performance of n/p and p/n Indium Phosphide Homojunction Solar Cells*
C. Goradia, W. Thesling, and I. Weinberg ..... 30-1

*Fiesta ROC: A New Finite Element Analysis Program for Solar Cell Simulation*
R.O. Clark ..... 31-1

## Session 7 - Space Environmental Effects on Solar Cells

*Significant Reduction In Arc Frequency of Negatively Biased Solar Cells: Observations, Diagnostics, and Mitigation Technique(s)*
B.L. Upschulte, G.M. Weyl, W.J. Marinelli, E. Aifer, D. Hastings, and D. Snyder ..... 32-1

*Measurement of High-Voltage and Radiation-Damage Limitations to Advanced Solar Array Performance*
D.A. Guidice, P.S. Severance, and K.C. Reinhardt ..... 33-1

*LEO Micrometerorite/Debris Impact Damage*
P.M. Stella ..... 34-1

*The Effects of Lunar Dust Accumulation on the Performance of Photovoltaic Arrays*
C.M. Katzan, D.J. Brinker, and R. Kress ..... 35-1

*Rapid Thermal Cycling of Solar Array Blanket Coupons for Space Station Freedom*
D.A. Scheiman and B.K. Smith ..... 36-1

## Session 8 - Radiation Damage of Solar Cells by Electrons and Protons

*Radiation Resistance of Ge, $Ge_{0.93}Si_{0.07}$, GaAs, and $Al_{0.08}Ga_{0.92}As$ Solar Cells*
M.L. Timmons, R. Venkatasubramanian, P.A. Iles, and C.L. Chu ..... 37-1

*Gallium Arsenide Solar Cell Radiation Damage Experiment*
R.H. Maurer, J.D. Kinnison, G.A. Herbert, and A. Meulenberg ..... 38-1

*I-V Analysis of Irradiated Gallium Arsenide Solar Cells*
A. Meulenberg, R.H. Mauer, and J.D. Kinnison ..... 39-1

*Radiation Hardness of $Ga_{0.5}In_{0.5}P/GaAs$ Tandem Solar Cells*
S.R. Kurtz, J.M. Olson, K.A. Bertness, D.J. Friedman, A. Kibbler, B.T. Cavicchi, and D.D. Krut ..... 40-1

*The Effects of Electron and Proton Radiation on GaSb Infrared Solar Cells*
P.E. Gruenbaum, J.E. Avery, and L.M. Fraas ..... 41-1

*Temperature Coefficients and Radiation Induced DLTS Spectra of MOCVD Grown $n^+p$ InP Solar Cells*
R.J. Walters, R.L. Statler, and G.P. Summers ..... 42-1

*Annealing Characteristics of Amorphous Silicon Alloy Solar Cells Irradiated With 1.00 MeV Protons*
S.S. Abdulaziz and J.R. Woodyard ..... 43-1

*The Advanced Solar Cell Orbital Test*
D.C. Marvin and M. Gates ..... 44-1

## Invited Papers

*Low Earth Orbital Atomic Oxygen, Micrometeoroid, and Debris Interactions With Photovoltaic Arrays*
B.A. Banks, S.K. Rutledge, and K.K. de Groh ..... 45-1

*The Space Radiation Environment for Electronics*
E.G. Stassinopoulos and J.P. Raymond ..... 46-1

*LEO Space Plasma Interactions*
D.C. Ferguson ..... 47-1

## Workshop Summaries

*Thin Film Cell Development Workshop Report*
J.R. Woodyard ..... 48-1

*III-V Cell Development Workshop*
R.W. Statler and R.P. Gale ..... 49-1

*Workshop Summary - Space Environmental Effects*
A. Meulenberg and B.E. Anspaugh ..... 50-1

## Program Reviews

*Journey Into Tomorrow - NASA's Future Space Power Requirements*
G.L. Bennett ..... 51-1

*The Survivable Power Subsystem Demonstration Program (SUPER)*
J.W. Geis ..... 52-1

*Overview - Air Force and SDIO Photovoltaics*
W.T. Cooley ..... 53-1

# Foreword

Dennis Flood
Chief, Photovoltaic Branch
Lewis Research Center

The Eleventh Space Photovoltaic Research and Technology Conference is the largest yet held in the series, both in terms of attendance and in the number of papers presented. There are several noteworthy observations that can be made as a result. It would appear possible, for example, to conclude that GaAs space solar cells have become a mature technology. The evidence for that is the fact that only four papers on GaAs cells were presented, two of which were manufacturing status reports, and two of which were radiation damage studies related to potential actual flight usage. A second conclusion, based on the fact that 25% of the papers presented were in this area, is that interest in InP solar cells has grown. Rapid progress is being made on achieving high efficiency in a variety of alternate InP cell structures, and in understanding the radiation resistance of this material. If we add to the above the additional papers on multijunction cell development using indium and phosphorus based compounds, it becomes very evident that InP and related compounds have become very important for future improvements in space solar cells.

This conference can also be characterized by the breadth of its content, which ranged from Space Station Freedom 8 cm x 8 cm silicon solar cell test results to flexible, thin film solar cell blanket development, to solid progress on multijunction solar cells. Results were presented on the latter topic from a variety of approaches, all directed toward achieving or exceeding 30% AM0 in planar and/or concentrator devices. Rapid progress in all these areas seems assured, given adequate funding.

The size and content of the Eleventh SPRAT make it a challenge to organize. The fact that it went so smoothly is a tribute to the dedication of the organizing committee. Donald Chubb served as General Chairman , Sheila Bailey as Logistics Chairman, and David Wilt as Publication Chairman. Their persistence and hard work were very much appreciated by all who attended.

# TUNNEL JUNCTIONS FOR InP-on-SI SOLAR CELLS [1]

C. Keavney, S. Vernon, V. Haven
Spire Corporation
Bedford, Mass. 01730-2396

We have succeeded in growing, by metalorganic chemical vapor deposition, a tunnel junction which makes possible an ohmic back contact in an n-on-p InP solar cell on a silicon substrate. The junction between heavily doped layers of p-type InGaAs and n-type InP shows resistance low enough not to affect the performance of these cells. InP solar cells made on n-type Si substrates with this structure were measured with an efficiency of 9.9% (AM0, 1- sun). Controls using p-type GaAs substrates showed no significant difference in cell performance, indicating that the resistance associated with the tunnel junction is less than about 0.1 ohm-cm$^2$.

## INTRODUCTION

Growth of InP solar cells on silicon substrates is one promising approach to achieving the high efficiency and radiation resistance of InP solar cells (refs. 1,2) without the high cost of InP wafers. Research into InP on Si has been motivated by the favorable results achieved with GaAs cells on silicon substrates (refs. 3-6). Dislocation densities as low as 2 x $10^6$ cm$^{-2}$ (ref. 4) and efficiencies over 18% AM0 have been reported (ref. 5). Since a recent theoretical study (ref. 7) projected achievable efficiencies of 18% with InP if dislocation density of $10^6$ cm$^{-2}$ or less could be achieved, these results make InP on silicon solar cells a promising avenue of research.

Considerable progress has been made in the related area of InP growth on GaAs substrates. In reference 8 a cell with 13.7% efficiency at one sun and 19% at concentration is reported on a GaAs substrate.

However, growth of n-on-p InP cells on silicon substrates has proved difficult because the first III-V layer grown on the silicon is always n-type; this makes an ohmic contact to the back of the cell problematic. (ref. 9) In previous work, researchers have circumvented this problem by using a p-on-n cell structure (ref. 10), by arranging to contact the base from the front of the structure, or by providing current paths outside of the active area of the cell (ref. 9). The p-on-n cells currently have somewhat lower efficiency than n-on-p, and the other techniques limit the size of the cells and detract from the available active area, which is expected to complicate the assembly of practical arrays.

The use of a tunnel junction between the substrate and the cell has been proposed as a solution to this difficulty (ref. 9). Here we report success in using such a tunnel junction, leading to InP-on-Si efficiencies of 9.8% AM0.

## THEORY

The tunnel junction consists of two heavily-doped semiconductor layers of opposite types. The doping in each layer must be degenerate (Fermi level outside of the band gap), and the width of the depletion region must be narrow enough for quantum-mechanical tunneling to occur across the triangular barrier formed by the depletion

[1] This work was supported by the NASA Lewis Research Center under contract # NAS3-25798.

region (fig. 1). Under these conditions, electrons can tunnel between states in the valence band of the n-type material and states of the same energy in the conduction band of the p-type material.

Specifically, as shown in references 11 and 12, the effective conductance of the tunnel junction is given roughly by:

$$S = \frac{q^2}{4\pi^3\hbar^2 W}(2mE_g)^{1/2} \exp\left[-\frac{4W}{3}\frac{(2mE_g)^{1/2}}{\hbar}\frac{E_g}{qV_b}\right] \tag{1}$$

where W, the depletion width, is given by:

$$W = \left[\frac{2\epsilon E_g(N_A+N_D)}{q^2 N_A N_D}\right]^{1/2} \tag{2}$$

In these equations, $S$ is the tunnel junction conductance (which has the units of $A/cm^2V$), $q$ the elementary charge, $E_g$ the band gap energy, $V_b$ the built-in voltage (slightly larger than $E_g$), $m$ the effective mass of electron (the tunneling current for holes is generally less than that for electrons), $\hbar$ (Plank's constant $h/2\pi$, $\varepsilon$ the dielectric permittivity ($12.2\varepsilon_0$ for InP), and $N_A$ and $N_D$ the dopant concentrations.

In practice, useful values of current density for solar cells require W to be less than 20 nm, which in turn means that the doping density in each of the two regions must be approximately $10^{19}$ or greater. From experience with the materials involved and from the results of reference 13, we concluded that the most appropriate choice for the tunnel junction was a combination of p-type $In_{0.53}Ga_{0.47}As$ and n-type InP, since doping levels of this order can easily be achieved in those materials, and the combination has a good lattice match. Figure 2 shows the calculated tunneling resistance for this combination as a function of the doping densities.

## EXPERIMENT

Figure 3 shows the experimental structure used in this work. All the layers described here were grown by metalorganic chemical vapor deposition. On a an n-type silicon substrate, a layer of GaAs is grown, following procedures developed earlier (ref. 14). Then a layer of $In_xGa_{1-x}As$ is grown, with a graded composition varying from close to x=0 to x=0.53, which is the lattice-matched composition to InP. All these layers are n-type. After the graded layer, a thin layer of n+ InP is deposited, followed by a thin layer of p+ $In_{0.53}Ga_{0.47}As$ to form the tunnel junction. Measurements indicated a dopant density of about $1.2 \times 10^{19}$ $cm^{-3}$ in the p-type layer and $3 \times 10^{19}$ $cm^{-3}$ in the n-type layer. This is followed by the solar cell structure, which consists of a p+ BSF, p-type base, thin n+ emitter, and n-type $In_{0.53}Ga_{0.47}As$ cap. (The solar cell structure is described in more detail in reference 1.)

Control cells were made using a p-type GaAs substrate with a graded layer which was similar but p-type. The same cell structure was used for the controls, but no tunnel junction.

The material was characterized by transmission electron microscopy and photoluminescence decay as well as solar cell measurements.

After the growth of the structure was complete, solar cells were made using established metallization, etching, and antireflection coating procedures (ref. 1,2). Solar cell areas were 1.00 and 0.25 $cm^2$. The efficiency of the cells was measured under a Spectrolab X25 solar simulator at AM0 intensity, calibrated with a GaAs reference cell. Internal quantum efficiency and dark I-V characteristics were also measured, and the series resistance extracted.

## RESULTS

TEM examination of InP films grown uncer the same conditions revealed a defect density in the range of $10^8$ $cm^{-2}$. This is only slightly lower than that measured on InP films grown on GaAs or silicon without such a graded layer, and considerably more than reported in reference 8. Figure 4 shows a cross-sectional TEM image of the graded layer; it can be seen that the distribution of defects in the graded layer is uneven. Further work on graded layers is in progress. Photoluminescence decay measurements showed lifetime of 0.7 ns.

Results of the solar cell efficiency measurements are given in table I. It is interesting to note that the results of wafer #2 are essentially equivalent to those of wafer #3, the GaAs control. This indicates that the low efficiency is due primarily to the high defect density, and not to the formation of a barrier at the back surface.

Figure 5 shows the measured I-V characteristics for representative 1.00 $cm^2$ cells from wafers 2 and 3. The similarity of the curves shows that the use of the silicon substrate has not resulted in additional series resistance. The total series resistance, obtained from dark I-V and $V_{oc}$-$I_{sc}$ curves, is 1.17 ohms for an 0.25 $cm^2$ cell on the silicon substrate (#2), and 1.16 ohms for a similar control cell (#3).

## CONCLUSIONS

We have made n-on-p InP solar cells on silicon substrates using a tunnel junction to make ohmic contact to the back of the cell. Measurements indicate that the tunnel junction has a resistance which is negligible, at least for one-sun applications (less than 0.1 ohm-$cm^2$).

This result, in addition to yielding the highest InP-on-Si solar cell efficiency so far published, is important because it indicates that InP structures of either polarity can be grown on silicon substrates without suffering a penalty due to the back contact. Using this technique, we expect that any efficiency which can be achieved in InP with GaAs substrates can be duplicated with silicon substrates.

## REFERENCES


1. Keavney, C.J.; Haven, V.E.; Vernon, S.M.: "Emitter structures in MOCVD InP solar cells," Proc. of the 21st IEEE Photovoltaic Specialists Conference, Orlando, May 1990, p. 141.

2. Keavney, C.J.; and Spitzer, M.B.: "Indium Phosphide Solar Cells Made by Ion Implantation," Appl. Phys. Lett. 52, 1439 (1988).

3. Yamaguchi, M.; Amano, C.; Itoh, Y.; Hane, K.; Ahrenkiel, R.K.; Al-Jassim, M.M.: "Analysis for High-Efficiency GaAs Solar Cells on Si Substrates," Proc. of the 20th IEEE Photovoltaic Specialists Conference, Las Vegas, Sept. 1988 p. 749.

4. Itoh, Y.; Nishioka, T.; Yamamoto, A.; and Yamaguchi, M.: "GaAs Heteroepitaxial Growth on Si for Solar Cells," Appl. Phys. Lett. 52, 1617 (1988).

5. Okamoto, H.; Kadota, Y.; Watanabe, Y.; Fukuda, Y.; O'hara, T.; Ohmachi, Y.: "High Efficiency GaAs Solar Cells Fabricated on Si Substrates," Proc. of the 20th IEEE Photovoltaic Specialists Conference, Las Vegas, Sept. 1988, p. 475.

6. Vernon, S.M.; Tobin, S.P.; Haven, V.E.; Bajgar, C.; Al-Jassim, M.; Ahrenkiel, R.K.: "Efficiency Improvements in GaAs-on-Si Solar Cells," Proc. of the 20th IEEE Photovoltaic Specialists Conference, Las Vegas, Sept. 1988, p. 481.

7. Yamaguchi, M.; Yamamoto, A.; Uchide, N. and Uemura, C.: "A New Approach for Thin Film InP Solar Cells," Solar Cells, 19, 85 (1986).

8. Wanlass, M.W.; Coutts, T.J.; Ward, J.S.; and Emery, K.A.: "High-Efficiency Heteroepitaxial InP Solar Cells," This Conference (1991).

9. Keavney, C.J.; Vernon, S.M.; Haven, V.E.; Wojtczuk, S.J. and Al-Jassim, M.M.: "Fabrication of n+/p InP Solar Cells on Silicon Substrates," Appl. Phys. Lett. 54, 1139 (1989).

10. Yamaguchi, M.; Yamamoto, A.; Itoh, Y. and Nishioka, T.: "High Efficiency GaAs and InP Thin-Film Solar Cells Fabricated on Si Substrates," 19th IEEE Photovoltaic Specialists Conference, May 1987.

11. Moll, J.L.: "Physics of Semiconductors," McGraw-Hill (1960).

12. Sze, S.M.: "Physics of Semiconductor Devices," John Wiley & Sons (1981).

13. Shen, C.C.; Chang, P.T. and Choi, K.Y.: "An $In_{0.53}Ga_{0.47}As$ Tunnel Diode for Monolithic Multijunction Solar Cell Application," Proc. of the 20th IEEE Photovoltaic Specialists Conference, Las Vegas, Sept. 1988, p. 771.

14. Vernon, S.M.; Haven, V.E.; Tobin, S.P. and Wolfson, R.G.: "Metalorganic Chemical Vapor Deposition of GaAs on Si for Solar Cell Applications," J. Crystal Growth 77, 530 (1986).

Table I. Solar Cell Results.
(AM0, 25°C)

| Wafer # | Substrate Structure | $V_{oc}$ (mV) | $J_{sc}$ (mA/cm$^2$) | Fill Factor | Efficiency (%) |
|---|---|---|---|---|---|
| 2 (avg.) | n-GaAs/n-Si | 679 | 27.24 | 0.710 | 9.6 |
| 2 (std.) | | 2 | 0.43 | 0.009 | 0.2 |
| 2 (best) | | 682 | 28.07 | 0.706 | 9.9 |
| 3 (avg.) | p-GaAs | 689 | 26.62 | 0.706 | 9.4 |
| 3 (std.) | | 3 | 0.41 | 0.022 | 0.3 |
| 3 (best) | | 689 | 27.66 | 0.699 | 9.7 |

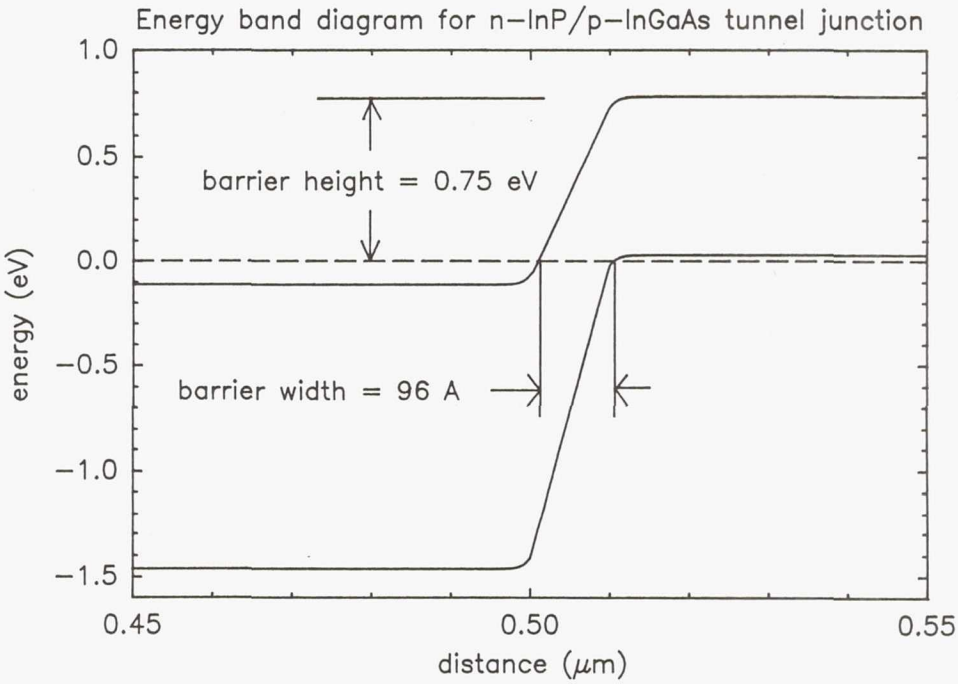


Figure 1. Band diagram of an n-InP/p-InGaAs tunnel junction. Tunneling takes place between filled states in the valence band of the n-type material and empty states of the same energy in the p-type material.

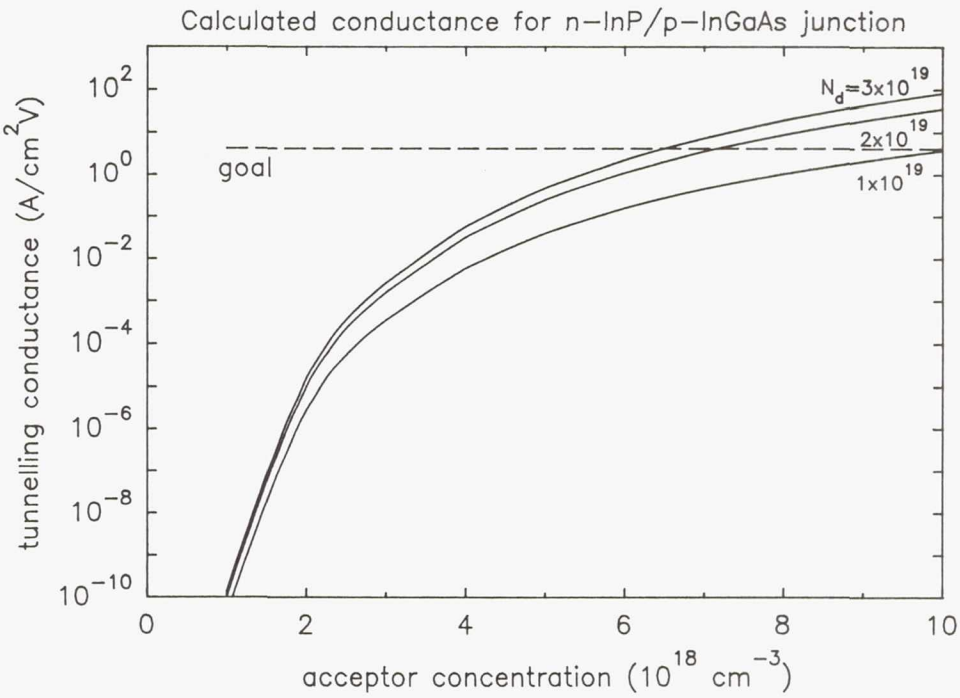


Figure 2. Calculated resistance of the tunnel junction as a function of the doping densities (note log scale).

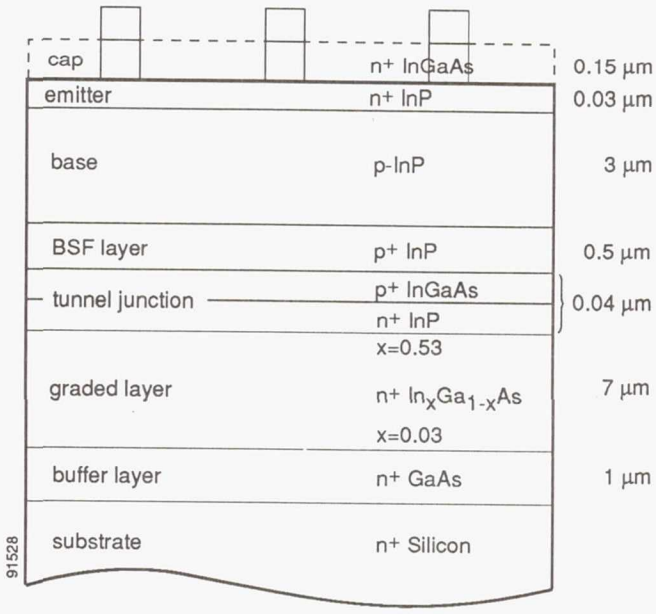


Figure 3. Cell structure used in this work. The graded InGaAs layer reduces the defect density and the tunnel junction provides an ohmic interconnection between the p-InP layer and the substrate.

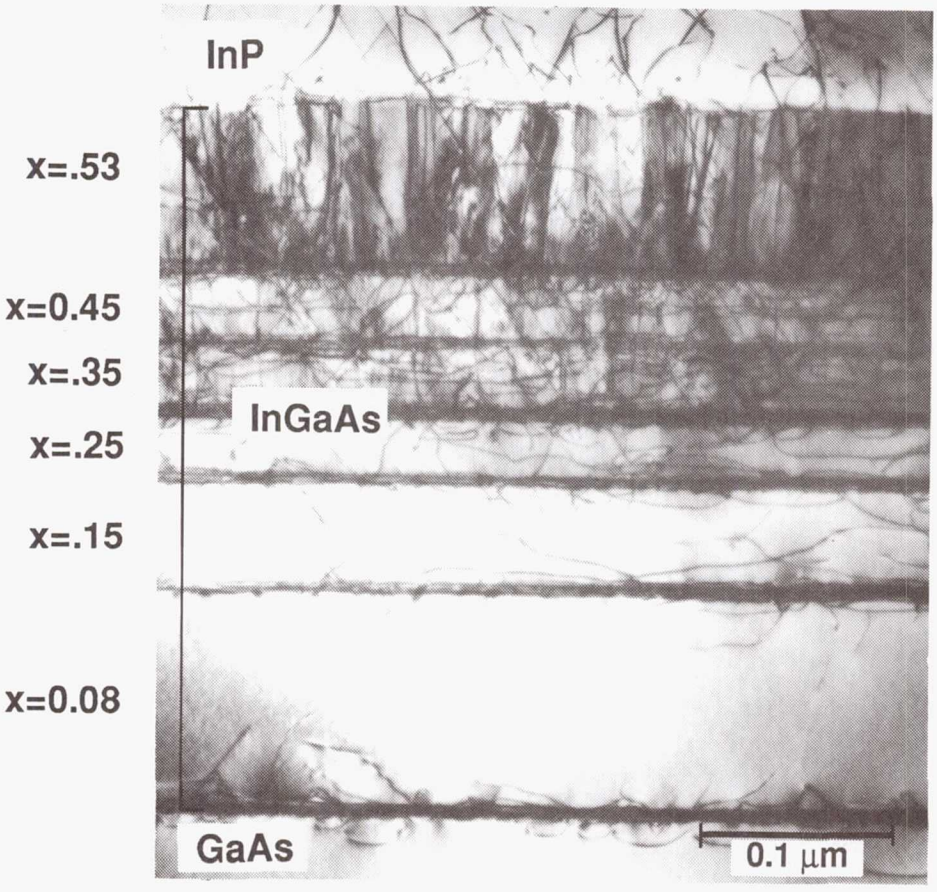


Figure 4. Cross-sectional TEM image of the cell structure. High defect density results from lattice mismatch at the intermediate interfaces.

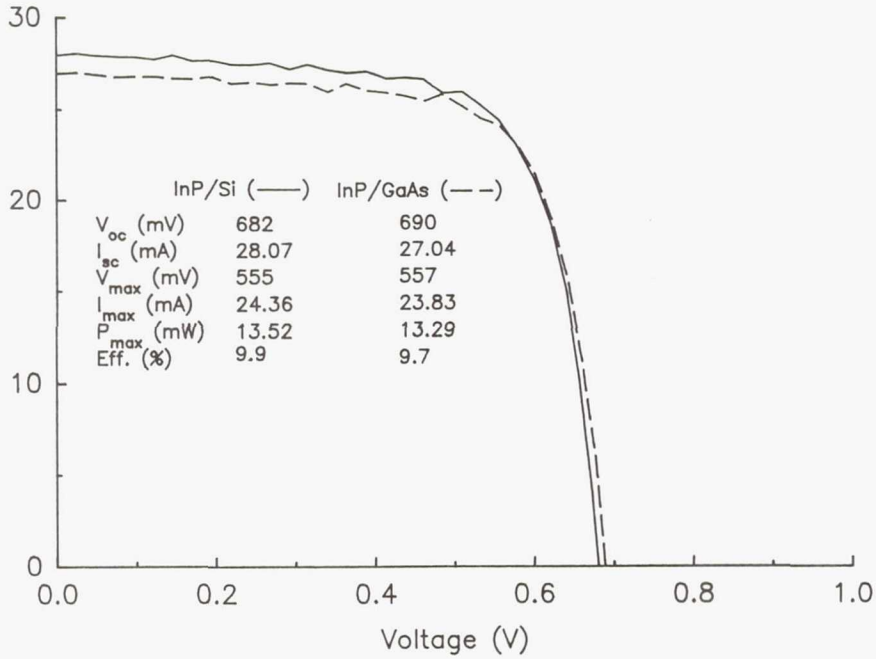


Figure 5. I-V characteristics of an InP-on-Si cell and an InP-on- GaAs control. The cells on silicon substrates show slightly lower voltages but higher currents than the controls.

# Fabrication and Performance Analysis of 4-cm$^2$ Indium Tin Oxide/InP Photovoltaic Solar Cells*

T.A. Gessert, X. Li, P.W. Phelps and T.J. Coutts
Solar Energy Research Institute
Golden, Colorado

and

N. Tzafaras
AT&T Microelectronics
Reading, Pennsylvania

## Introduction

Large-area photovoltaic solar cells based on direct current (dc) magnetron sputter deposition of indium tin oxide (ITO) onto single-crystal p-InP substrates have demonstrated both the radiation hardness and high performance necessary for extraterrestrial applications. (**ref. 1**) Recently, ITO/InP cells with a total area of 4 cm$^2$ have been delivered to NASA for flight and experimental analysis on the UoSAT-F satellite, attesting to the advancing maturity of this technology. Although only a small number of these 4-cm$^2$ ITO/InP cells (approximately 10 cells total) were fabricated for this experiment, the efficiency of the best cell (15.7% at air mass zero [AM0], NASA measurement) compares favorably with the best result reported from a larger production of ~1300 2-cm$^2$ cells, in which the junction was fabricated through a closed-ampoule diffusion process (16.6% AM0, NASA measurement). **(ref. 2)**

Because the results mentioned above indicate that the ITO/InP technology is quickly nearing practicality, a small-scale production project has been initiated in which approximately 50 ITO/InP cells are being produced. Through this project, not only is a more representative assessment of the performance of large-area ITO/InP cells being established, but the heretofore assumed advantages of production scale-up are also being tested. This larger volume of cells has also created the opportunity to gain a better understanding of the effect of fabrication procedures on cell performance and has allowed several recently developed process improvements to be further optimized. These improvements include two-gun sputtering, pre-metallization plasma cleaning, and grid/metallization optimization. Performance improvements have been achieved through these changes, resulting in cells with AM0 efficiencies of 16.1% (SERI measurement).

This paper presents and discusses the procedures used in this small-scale production of 4-cm$^2$ ITO/InP cells. The discussion includes analyses of the performance range of all available production cells, and device performance data of the best cell thus far produced. Additionally, processing experience gained from the production of these cells is discussed, indicating other issues that may be encountered when larger-scale productions are begun.

## Experimental

The materials and processes used for this small-scale production of ITO/InP cells have been developed over many years of research and are discussed in detail elsewhere. **(ref. 3 & 4)** However, some important process parameters are outlined here. The single-crystal InP substrates were supplied by AT&T Microelectronics (Reading, PA) in two different carrier concentrations of 0.5-2.0 x1 $0^{16}$ and 1-2 x $10^{17}$ cm$^{-3}$ [Zn-doped, (100) orientation]. The substrates were supplied polished on the front side and chemically etched on the back side. Except for cleaning the surfaces in organics, no additional surface preparation was performed before back-contact metallization or ITO deposition (i.e., junction formation). Photoluminescence measurements of these as-received substrates indicated bulk lifetimes very similar to those of other ~2 x $10^{16}$ (Zn-doped) materials used in previous research, demonstrating up to ~10 nsec on unpassivated surfaces.

Prior to junction formation, back-contact metallization was performed using a multistep process involving the vacuum deposition of 120 nm of AuBe (1 weight % Be), annealing, chemical etching, and electrochemical Au plating (1.5 μm). **(ref. 5)** The ITO deposition was performed in an ULTEK vacuum system using 2-inch planar US Guns in a sputter-up orientation. The ITO targets were 91 molar % $In_2O_3$ and 9 molar % $SnO_2$. Earlier studies indicated that adding a small amount of $H_2$ to the Ar sputtering environment during ITO deposition substantially increased the open-

* This work was supported by NASA Lewis Research Center under Interagency Order No.C-3000-K and by the U.S. Department of Energy under Contract No. DE-AC02-83CH10093.

circuit voltage ($V_{OC}$) and fill factor (FF) of the resultant solar cell. **[3]** However, continued sputtering in this $H_2$-rich atmosphere progressively altered the target material, resulting in a poor control of the optical and electrical properties of the ITO. Thus, to provide greater compositional control of the ITO film(s), two US Guns have been incorporated into the vacuum system for this production. The first gun deposits ITO in an $Ar/H_2$ atmosphere at a very slow deposition rate (~0.01 nm $sec^{-1}$). Because the optical transmission of this $H_2$-rich ITO is poor, the thickness of this layer is limited to 5 nm. The remaining 50 nm of ITO is deposited with a second US Gun source. This layer reduces the emitter sheet resistance and completes the necessary thickness for the first layer of a two-layer ITO/$MgF_2$ antireflection coating (ARC). For this second ITO deposition, an $Ar/O_2/H_2$ ambient is used ("$O_2$-rich" ITO); the $O_2$ and $H_2$ partial pressures are adjusted to yield optimum electrical and optical properties. Both the $H_2$-rich and the $O_2$-rich depositions are performed without breaking vacuum. Following deposition, ellipsometry and four-point probe measurement are used to determine the ITO thickness and sheet resistance, respectively. If the sheet resistance is found to be excessively high (1000-40,000 Ω/□), the ITO-coated cell is placed in a Technics Planar Etch II plasma etching system and exposed to a pure-$H_2$ plasma. This procedure reduces the sheet resistance of the ITO to ~600-800 Ω/□ while still maintaining optical clarity. It is believed that this process removes excess $O_2$ for the ITO, thereby creating vacancy-generated carriers. **(ref. 6)**

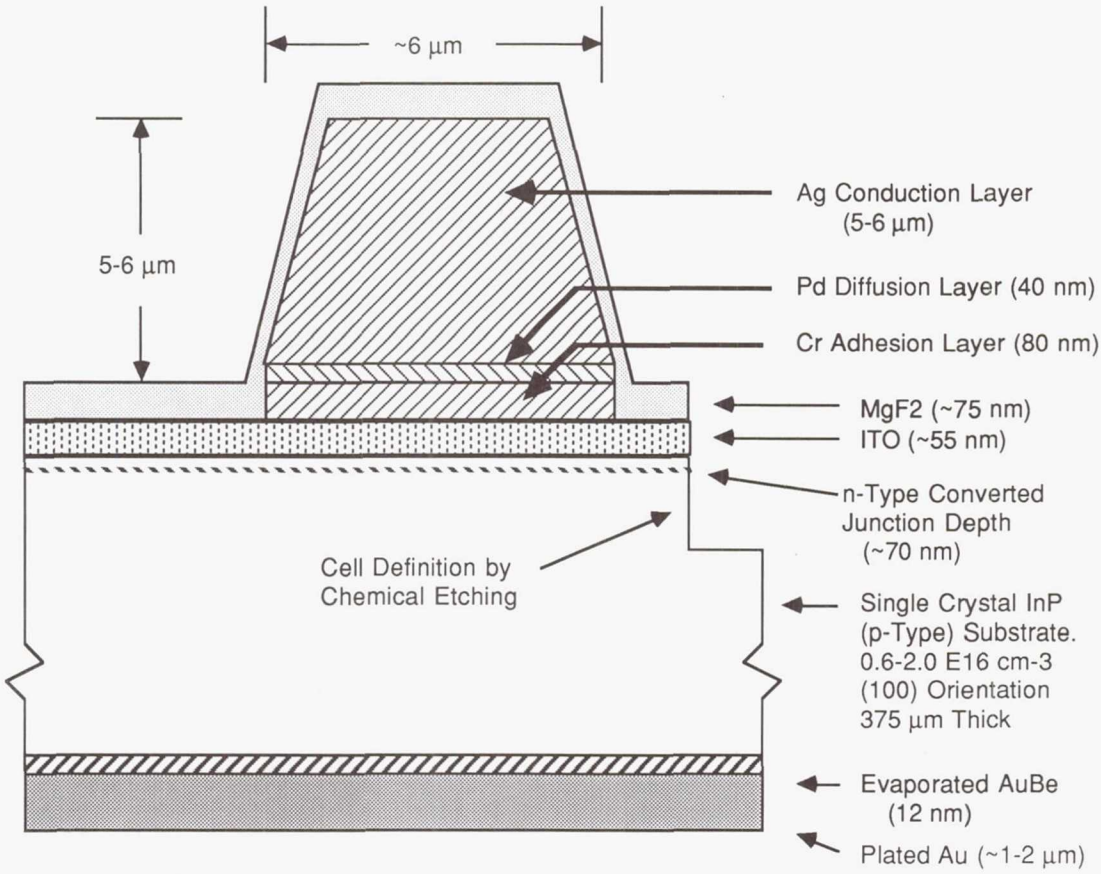


**Figure 1.** Cross-sectonal view of ITO/InP solar cell showing metallization and antireflection coatings. Note high aspect ratio of grid line made possible by the photolithographic lift-off techniques used.

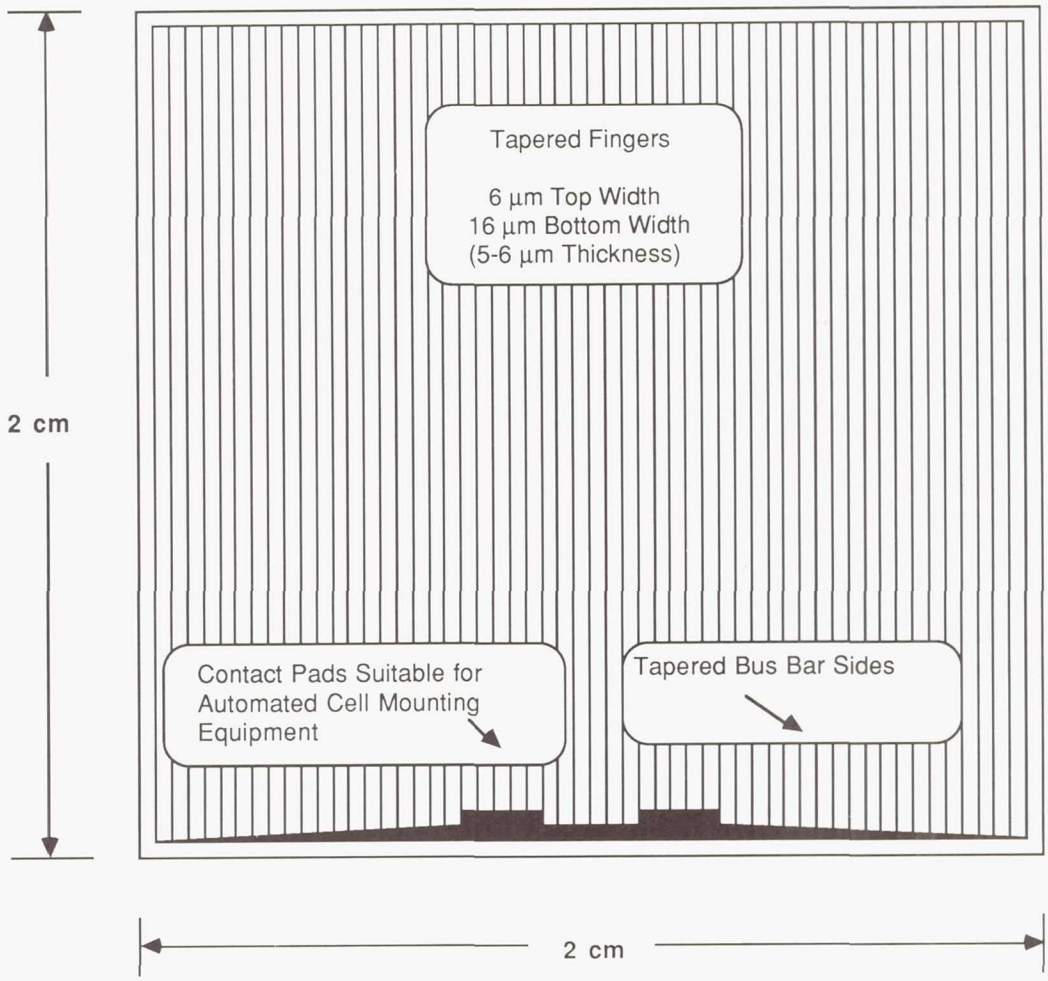


**Figure 2**. Plan view of grid design used on 4 $cm^2$ ITO/InP solar cells. The (modeled) losses of this grid are: Resistance ~2.8% and Shadowing ~3.3%, yielding a total grid losses ~6.1%.

After ITO deposition, top grid electrical contacts were patterned using an additive lift-off procedure involving chlorobenzene. **(ref. 7 & 8)** Following photolithography, but prior to metallization, the cells were plasma cleaned in Ar using the same Technics Planar Etch II system already mentioned. This promoted the adhesion of the the subsequent metallization. Metallization (See **Figure 1**) was performed in an electron-beam vacuum system with Cr/Pd/Ag layers of 80 nm, 40 nm, and 5 μm, respectively. **(ref. 9)** The top grid contact is an optimum design which, in addition to very high aspect-ratio grid lines, utilizes tapered bus bars and fingers (**See Figure 2**). The grid also included two relatively large contact pads and an interconnect between the pads, a design conforming to the requirements of semi-automatic mounting equipment currently used in the space industry. After metallization lift off, the active cell area was defined using photolithography and HCl chemical etching. Following cell definition, the second layer of the ARC was formed using resistively evaporated $MgF_2$.

As a final process step before cell measurement, a post-deposition heat treatment (PDHT) at 125°C for 30 min was performed. This treatment increased the short-circuit current ($J_{SC}$) of the cells by ~2% without adversely affecting other device parameters. This PDHT was necessary because the photolithographic processes used for this production are of lower temperature (<100°C) than those used in previous research (~120°C). Thus, PDHT occurs *automatically* if the photolithographic processing involves typically used temperatures. Although the PDHT does add an additional step to the process, it also yields the opportunity to isolate and study an aspect of the ITO/InP cell fabrication that has not been previously observed. After fabrication, the cells were characterized using quantum efficiency measurements and light and dark current-voltage measurements using standardized methods. **(ref. 10)**

## Results and Discussion

The project began with 38 1-in.$^2$ InP substrates of the low doping density range (low $10^{16}$ cm$^{-3}$), and 20 substrates of the higher doping range (low $10^{17}$ cm$^{-3}$). At this time, all of the $10^{16}$ cm$^{-3}$ substrates have been fabricated into solar cells, but only one cell has been fabricated for the $10^{17}$ cm$^{-3}$ material. Thus, most of the results presented here involve performance characteristics of cells made on the $10^{16}$ cm$^{-3}$ material, although some preliminary, yet insightful results from the cell made on the higher-doped material will also be discussed. Of the 38 ($10^{16}$ cm$^{-3}$) substrates, four were broken or damaged during back contacting procedures, one was broken during chemical etching, and one suffered grid adhesion loss. Shown in **Figure 3 and Figure 4** is the range of demonstrated AM0 performance for the remaining 32 cells. From these data, the average cell efficiency is determined to be 15.5%, with a standard deviation of 0.35%. The highest cell performance obtained is 16.1% AM0 (SERI measurement). Dark I-V data analysis indicates that the cells demonstrate near-ideal characteristics, with a diode-ideality factor and reverse-saturation current density of 1.02 and 1.1 x $10^{-12}$ mAcm$^{-2}$, respectively.

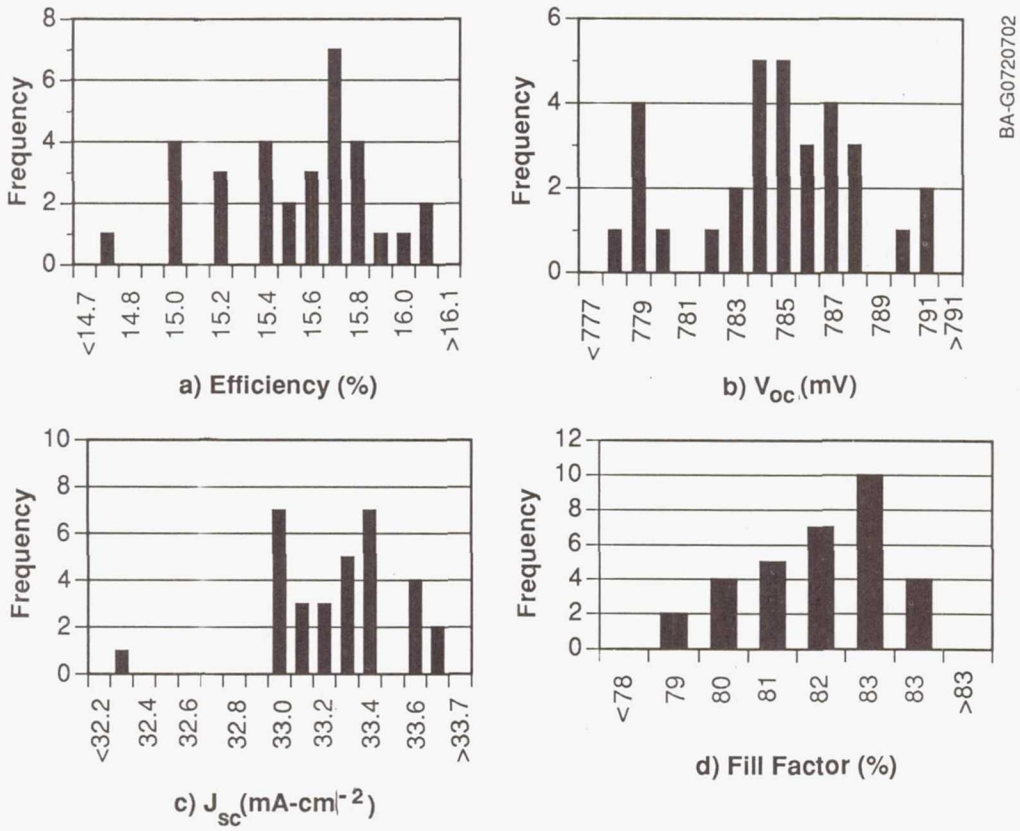


**Figure 3.** Histograms illustrating the AM0 (1367 Wm$^{-2}$) performance parameters of the 32 4-cm$^2$ ITO/InP solar cells fabricated during the small-scale production. a) Efficiency. b) Open-circuit voltage. c) Short-circuit current density. d) Fill factor.

As mentioned previously, the PDHT was found to increase the $J_{SC}$ of the cells. However, as indicated by quantum efficiency analysis shown in **Figure 5**, the effect of the PDHT is not completely beneficial. Indeed, although during PDHT the central and short-wavelength response is enhanced, the long-wavelength response is noticeably reduced. A plausible explanation for this is that the PDHT tends to reduce the extent of type-conversion throughout the junction region, with the overall effect being to shift the effective depth of the sputter-formed junction nearer the surface. This is consistent with earlier observations, in which higher-temperature heat treatments (200°C) resulted not only in increased current density but severely reduced $V_{OC}$. **(ref. 11)** However, in this earlier work, a reduction in the long-wavelength QE was not observed, probably because the substrates and processes used at that time resulted in much poorer long-wavelength response.

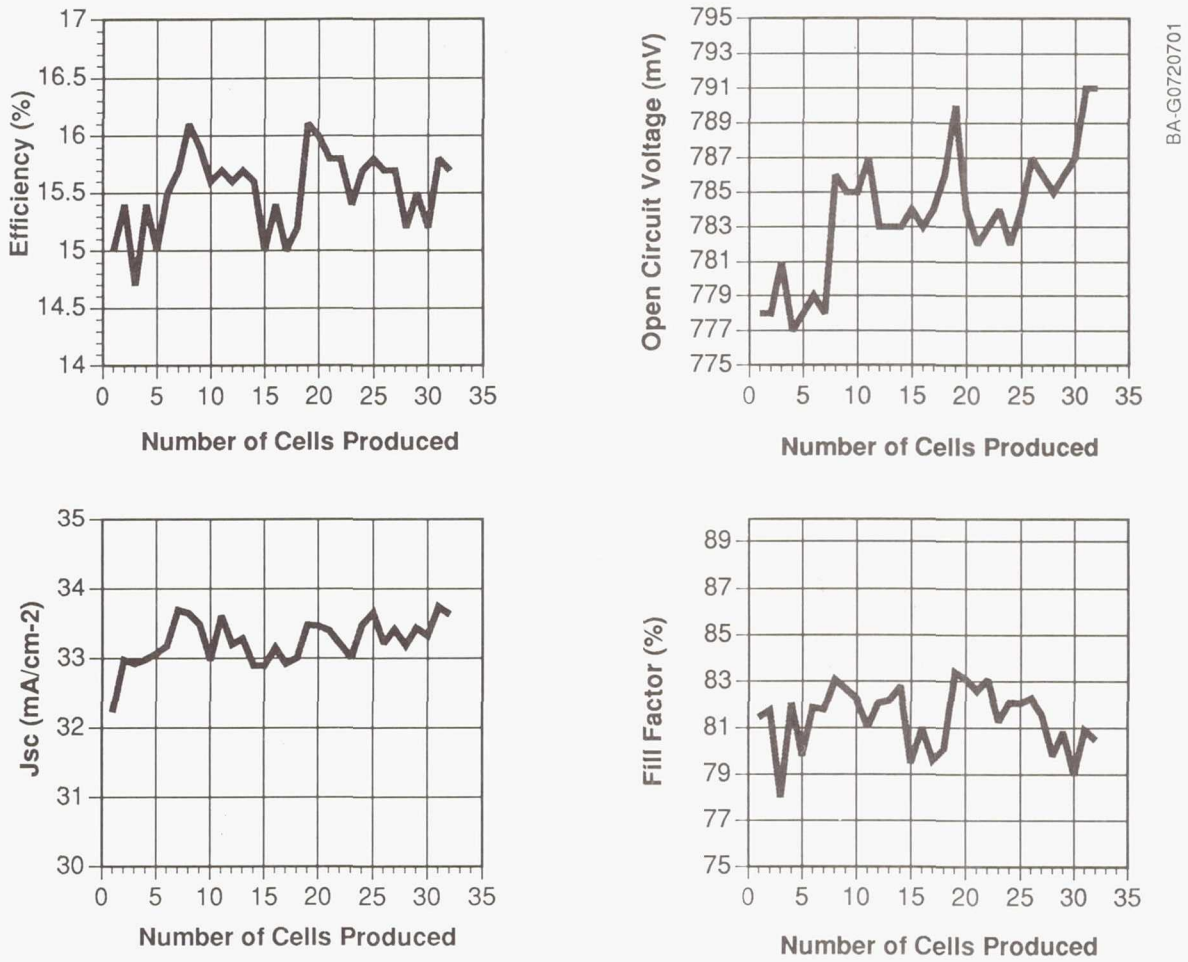


**Figure 4**. AM0 performance characteristics of the 32 4-$cm^2$ ITO/InP solar cells as a function of fabrication experience. Note that the only performance parameter that indicates a slight progressive improvement is the $V_{oc}$.

Shown in **Figure 6** is the light current-voltage characteristics of one of the two best 4-$cm^2$ cells made on the $10^{16}$ $cm^{-3}$ material, demonstrating an AM0 efficiency of 16.1% (SERI measurement). By comparing these data with those taken from the best small-area cell produced (16.5% AM0, 0.1 $cm^2$, SERI measurement), **(ref. 3)** one notes that the $J_{sc}$ and the FF values are nearly identical. This not only suggests that the junction-formation mechanism is spatially very uniform, but also that the grid design/metallization are nearly optimal for this 4-$cm^2$ cell. Only $V_{oc}$ is lower (by ~10-20 mV) than that previously measured on best smaller ITO/InP cells made from previously used bulk material. At present, the reason for this is not apparent. Past observations from these ITO/InP cells have indicated a trend of *decreasing* $V_{oc}$ with *increasing* substrate doping (i.e., increasing $N_A$). **(ref. 3 & 12)** However, the recent results from the cell fabricated on the$10^{17}$ $cm^{-3}$ substrate, as discussed below, indicate that the substrates and processes used for this production demonstrate the opposite (but more classical) behavior of increasing $V_{oc}$ with increasing substrate doping.

Although the efficiency spread of the cells made on the $10^{16}$ $cm^{-3}$ substrates is quite small, it should be noted that several process-related aspects strongly affected the measured performance of the individual cells. Perhaps the most important of these is the amount of time during which the cell is exposed to air between ITO and $MgF_2$ deposition. Indeed, a cell will degrade by up to ~5 mV per week if it is not capped with $MgF_2$. A possible explanation for this is that the sputtered ITO is believed to be relatively porous, allowing $O_2$ diffusion and subsequent reaction at the emitter/ITO interface. Here, the $O_2$ may neutralize the passivating effect of the $H_2$. The evaporated $MgF_2$, however, may be much less porous, reducing $O_2$ diffusion. Other parameters that were initially difficult to control were the sheet resistance, transparency, and thickness of the ITO. As observed in earlier work, care must be taken to maintain an optimum combination of electrical and optical properties of the ITO as the sputtering source erodes.

Although this can be accomplished through small adjustments in the $O_2/H_2$ ratio of the sputtering ambient of the $O_2$-rich ITO layer, considerable variation is still observed. Luckily, the effects of this problem (FF reduction) were virtually eliminated once the post-deposition $H_2$ plasma exposure procedure was developed and implemented. The final area of noted weakness in device fabrication was the back contacting procedure. It was during this part of cell production that the majority of cell breakage occurred. The underlying reason for this appears to be that, although the two-step back metallization procedure gives a reliably low-resistance ohmic contact, it involves many steps in which the substrate is physically handled (e.g., during wax mounting, chemical etching, annealing, etc.). Because most of this handling results from the requirement to remove the BeO that forms during sintering, **(ref. 5)** it has been suggested that other contacting procedures could be developed that would make use of either different metals and/or entirely in-vacuo process techniques.

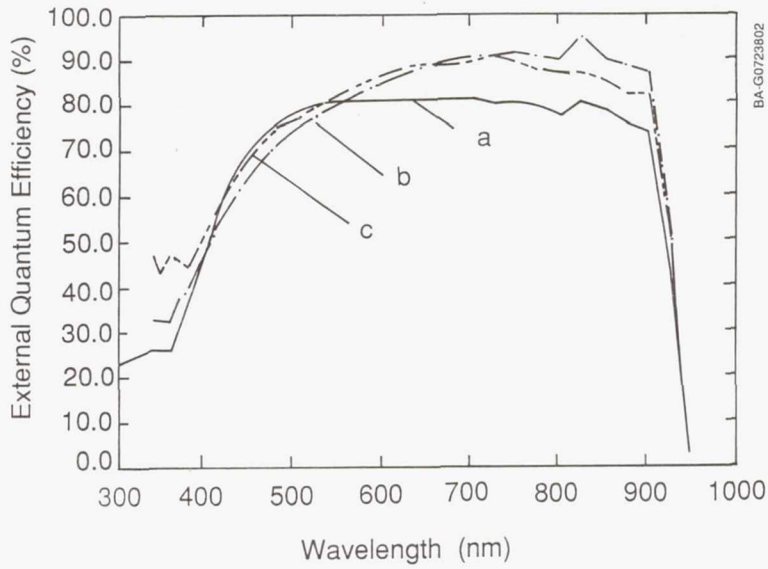


**Figure 5.** External quantum efficiency of a 4-$cm^2$ ITO/InP cell produced on $10^{16}$ $cm^{-3}$ substrate material. a) ITO only. b) ITO/$MgF_2$. c) ITO/$MgF_2$ after post-deposition heat treatment.

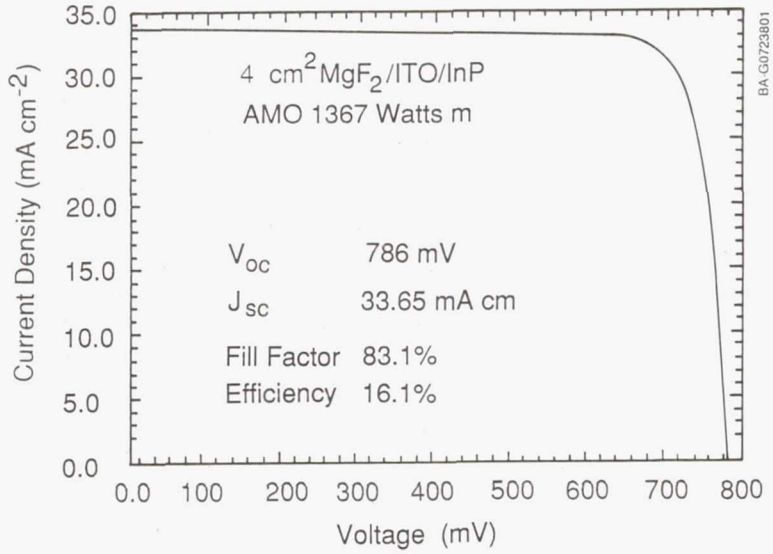


**Figure 6.** Light I-V characteristics of one of the best 4-$cm^2$ ITO/InP cell produced from $10^{16}$ $cm^{-3}$ substrate material.

As mentioned previously, 20 substrates with a higher doping density of 1-2 x $10^{17}$ $cm^{-3}$ were supplied by AT&T Microelectronics. Because earlier research had indicated that the best cell performance has always been achieved on $10^{16}$ $cm^{-3}$ material, only a single device has thus far been fabricated on the $10^{17}$ $cm^{-3}$ material. Although it was thought that the performance of this device would, as in the past, be much poorer than that of the$10^{16}$ $cm^{-3}$ material (due to reduced $V_{OC}$ and $J_{SC}$), **Figure 7** shows the surprising result that an efficiency of 15.8% AM0 (SERI measurement) was achieved. Perhaps the most noteworthy fetaure of this result is that, instead of a reduced $V_{OC}$, as was always observed in past research, the $V_{OC}$ is 12 mV higher than than that from the best of the 32 cells made from the $10^{16}$ $cm^{-3}$ material (nearly 20 mV greater than the average $V_{OC}$ measured for the 32 cells). However, because the long-wavelength portion of the QE is reduced, the $J_{SC}$ of this cell is ~3% lower than that of cells made on the $10^{16}$ $cm^{-3}$ material. Presently, studies are ongoing to determine if the grid design can be modified to function without the benefits of the ITO (lower sheet and contact resistance). If this can be done, better optical matching of the ARC may be possible. For example, if a material such as ZnS replaces the ITO, modeling studies indicate that the $J_{SC}$ of these ($10^{17}$ $cm^{-3}$) cells would increase to ~33.8 $mAcm^{-2}$. If this can be done while maintaining current values of FF and $V_{OC}$, than the efficiency would increase from 15.8% to 16.3% AM0. In addition, because the ZnS is less absorbing than the ITO, modeling results also suggest that $J_{SC}$ values up to 36.5 $mAcm^{-2}$ may be possible (assuming 4% shadow loss); this would result in a cell with an efficiency of ~17.7% AM0. Finally, because these large-area cell results indicate that the junction formation is relatively insensitive to surface irregularities, investigations are ongoing in collaboration with researchers at NASA Lewis Research Center to determine what effects deliberate surface texturing (V-Groove) may have on the junction parameters (**ref. 13**). If these parameters are insensitive to texturing, further increases in current collection may be possible.

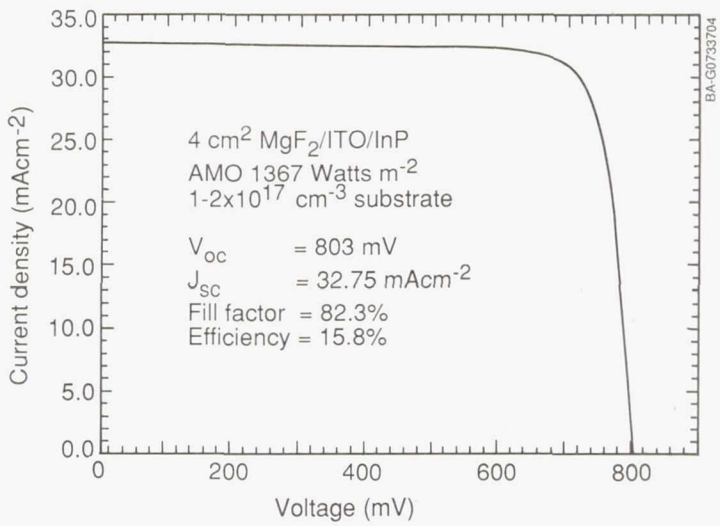


**Figure 7**. Light I-V characteristics of a 4-$cm^2$ ITO/InP cell produced from $10^{17}$ $cm^{-3}$ substrate material. Note that the $V_{OC}$ is higher than for the $10^{16}$ $cm^{-3}$ material but that the $J_{SC}$ is slightly reduced.

## Conclusions

This project has demonstrated that the sputtering process used to form small-area ITO/InP solar cells can readily be scaled to produce large-area (4-$cm^2$) devices. These large-area cells demonstrate nearly identical performance to similar small-area cells, suggesting that the spatial independence of the junction-formation mechanism may be exploited further to productions involving larger batches. These results also suggest that this method of junction fabrication is not as sensitive to the same predeposition surface irregularities, which tend to have devastating effects in other solar cell technologies. The highest resultant solar cell efficiency from the 32 cells produced on substrate material doped 0.5-2.0 x $10^{16}$ $cm^{-3}$ is 16.1% AM0 (SERI measurement), which is comparable to the highest efficiency reported from another *production* method using closed-ampoule diffusion. Additionally, because the sputter-deposition technology can be configured for in-line (rather than only batch) production modes, this process may possess additional economic advantages. Finally, since the substrates used for this production were acquired from a US supplier, this technique represents a completely US-based technology for manufacturing radiation-hard solar cells.

## References


1. Weinberg, I., C.K. Swartz, R.E. Hart, Jr., and T.J. Coutts. 1988. Radiation Resistance and Comparative Performance of ITO/InP and N/P InP Homojunction Solar Cells. Proc. 20th IEEE Photovoltaic Specialists Conf., Las Vegas, NV. Sept. 26-30 (IEEE, New York, 1988) 893-897.
2. Yamaguchi, M., T. Hayashi, A. Ushirokawa, Y. Takahashi, M. Koubata, M. Hashimoto, H. Okazaki, T. Takamoto, M. Ura, M. Ohmori, S. Ikegami, H. Arai, and T. Orii. First Flight of InP Solar Cells. 1990. Proc. 21st IEEE Photovoltaic Specialists Conf., Kissimimee, FL, May 21-25 (IEEE, New York, 1990) 1198-1202.
3. Gessert, T.A., X. Li, M.W. Wanlass, A.J. Nelson, and T.J. Coutts. Investigation of Buried Homojunctions in p-InP Formed During Sputter Deposition of Both Indium Tin Oxide and Indium Oxide. 1990. J. Vac. Sci. Technol. A, **8** (3) 1912-1916.
4. Gessert, T.A., X. Li, M.W. Wanlass, and T.J. Coutts. 1990. Progress in the ITO/InP Solar Cell. Proc. Second Int. Conf. on InP and Related Mat., Denver, CO. April 23-25, 1990, IEEE Cat. No. 90CH2895 (IEEE, New York,1990) 260-264.
5. Gessert, T.A., X. Li, T.J. Coutts, M.W. Wanlass, and A.B. Franz. 1989. Aspects of Processing Indium Tin Oxide/InP Solar Cells. Proc. First Int. Conf. on Indium Phosphide and Related Mat. for Adv. Electronic and Optical Devices, Norman, OK, March 20-22, 1989, SPIE Proceedings Vol. 1144 (SPIE, Bellingham, WA, 1989) 476-487.
6. Gessert, T.A., D.L. Williamson, T.J. Coutts, A.J. Nelson, K.M. Jones, R.G. Dhere, H. Ahoroni, and P. Zurcher. 1987. The Dependence of the Electrical Properties of Ion-Beam Sputtered Indium Tin Oxide on it Composition and Structure. J. Vac. Sci. Technol. A, **5** (4) 1314 -1315.
7. Gessert, T.A., X. Li, and T.J. Coutts, presented at the 10th PVAR&D Meeting, Lakewood, CO, Oct. 23-25, 1990, to be published in Solar Cells.
8. Hatzakis, M., B.J. Canavello, and J.M. Shaw. 1980. Single-Step Optical Lift-Off Process. IBM J. Res. Develop., **24** (4) 452-460.
9. Gessert, T.A., and T.J. Coutts. 1990. Requirements of Electrical Contacts to Photovoltaic Solar Cells. MRS Proc. Vol. 181 (MRS, Pittsburgh, PA, 1990) 301-312.
10. "Standard Test Methods for Electrical Performance of Non-Concentrator Photovoltaic Cells Using Reference Cells," ASTM Standard E948.
11. Coutts, T.J., X. Wu, T. A. Gessert, and X. Li. 1988. Direct-Current Magnetron Fabrication of Indium Tin Oxide/InP Solar Cells. J. Vac. Sci. Technol. A. **6** (3) 1722-1726.
12. Coutts, T.J., and S. Naseem. 1985. High Efficiency Indium Tin Oxide/Indium Phosphide Solar Cells. Appl. Phys. Lett., **46** (2) 164-166.
13. Bailey, S., N. Fatemi, G.A. Landis, D. Brinker, M. Faur, and M. Faur. 1990. Application of V-Groove Technology to InP Solar Cells. Proc. Second Int. Conf. on InP and Related Mat., Denver, CO. April 23-25, 1990, IEEE Cat. No. 90CH2895 (IEEE, New York,1990) 73-79.

# A Comparative Study of $p^+n$ and $n^+p$ InP Solar Cells Made by a Closed Ampoule Diffusion

M. Faur, M. Faur, D. J. Flood*, I. Weinberg*, D. J. Brinker*, C. Goradia, N. Fatemi**, M. Goradia and W. Thesling

Space Photovoltaic Research Center***, Electrical Engineering Dept.
Cleveland State University, Cleveland, Ohio 44115

*NASA Lewis Research Center, Cleveland, Ohio 44135

**Sverdrup Technology, Inc., Cleveland, Ohio 44135

## ABSTRACT

The purpose of this study was to demonstrate the possibility of fabricating thermally diffused $p^+n$ InP solar cells having high open-circuit voltage without sacrificing the short circuit current. The $p^+n$ junctions were formed by closed-ampoule diffusion of Cd through a 3-5 nm thick anodic or chemical phosphorus-rich oxide cap layer grown on n-InP:S($N_D$ = 3 x $10^{16}$ and 5 x $10^{17}$ $cm^{-3}$) Czochralski LEC grown substrates. After thinning the emitter from its initial thickness of 1 to 2.5 μm to 0.06 - 0.15 μm, the maximum efficiency was found when the emitter was 0.2 to 0.3 μm thick. Typical AMO, 25° C values of 854-860 mV were achieved for $V_{oc}$. $J_{sc}$ values were from 27.5 to 29.1 mA/$cm^2$ using only the P-rich passivating layer left after the thinning process as an anti-reflection coating.

For solar cells made by thermal diffusion we expect the $p^+n$ configuration to have a higher efficiency than the $n^+p$ configuration. Based on this study we predict that the AMO, BOL efficiencies approaching 19% should be readily achieved providing that good ohmic front contacts could be realized on the $p^+$ emitters of thickness lower than 1 μm. If, as we expect, the $p^+n$ structures prove to be at least as radiation tolerant as $n^+p$ structures, then $p^+n$ InP solar cells made by thermal diffusion can become attractive for space applications, due to a relatively low fabrication cost, for this method of fabrication.

## INTRODUCTION

Owing to its potential low cost, reduced complexity and adaptability to large scale batch processing thermal diffusion is a desirable technique for $p^+n$ or $n^+p$ InP junction formation.

---

***Funded by NASA Lewis Research Center

Most research on InP solar cells, so far has concentrated on the $n^+p$ configuration. However, there is no apriori reason why the $n^+p$ configuration should yield higher BOL efficiency and/or higher radiation tolerance than the $p^+n$ configuration.

$n^+p$ InP solar cells made either by closed ampoule diffusion of sulfur into InP:Zn [1] or InP:Cd [2] substrates or by open tube diffusion [3] have been extensively studied. Good quality $p^+n$ InP solar cells on the other hand, have been fabricated only by epitaxial techniques [4,5]. This may be so because of the difficulty of 1) fabricating thin $p^+$ emitters in a controlled manner, 2) forming good ohmic contacts to $p^+$ surfaces and 3) passivating $p^+$ surfaces.

The results we report here are part of a larger experimental effort undertaken in an attempt to optimize the processing of InP homojunction solar cells made by thermal diffusion, so as to achieve high-efficiency low cost InP solar cells by this method of junction formation.

We have previously reported on limitations of $n^+p$ InP solar cells made by closed ampoule diffusion [2,6]. Therefore, most emphasis here is on the $p^+n$ configuration. Specifically, the objective of this preliminary work was to demonstrate the possibility of fabricating thermally diffused $p^+n$ InP solar cells having high open-circuit voltage ($V_{oc}$) without sacrificing the short circuit current ($I_{sc}$).

In developing high-efficiency, radiation resistant $p^+n$ InP solar cells made by thermal diffusion our short-term effort, still in progress, consists of:

1. Investigate the effects of i) various surface preparation procedures including chemical treatments and anodic or chemical oxidation, ii) choosing between Zn and Cd diffusants, in elemental form or as $Zn_3P_2$ and $Cd_3P_2$. and iii) diffusion through bare and capped surfaces, on the characteristics, reproducibility and quality of $p^+n$ InP structures made by closed ampoule thermal diffusion of Zn or Cd into Czochralski LEC grown n-InP:S substrates;

2. Design optimum front contact grid pattern and form good ohmic contacts on the emitters of thickness lower than 1 μm;

3. Choose from among the following processes for thinning the $p^+$ InP emitter and optimize the processing parameters:
   a) anodic dissolution;
   b) anodic oxidation-removal cycles;
   c) chemical etching,

   so that the residual oxide left as a result of thinning i) is stable, ii) has good passivating properties at the $p^+$/oxide interface, and iii) can possibly be used as a first layer AR coating.

4. Find an appropriate second layer AR coating.

5. Radiation tolerance measurements.

Based on previous reports on $n^+p$ InP solar cells made by closed-ampoule diffusion [1, 2, 6] and this work, we evaluate the limitations of the $n^+p$ and $p^+n$ configurations in order to choose the structure and the fabrication procedure of solar cells made by thermal diffusion with efficiencies approaching those of epitaxially grown structures [5, 7].

## EXPERIMENTAL

Cd and Zn diffusions into n-InP:S ($N_D$ = 3.5 x $10^{16}$ and 4.5 x $10^{17}$ $cm^{-3}$) were performed by a closed ampoule technique, using high purity Cd and Zn or $Cd_3P_2$ and $Zn_3P_2$ [8]. Diffusion temperatures were from 480 to 550° C in the case of Zn and from 550 to 600° C in the case of Cd diffusion. Diffusion times were from 5 to 75 minutes. The substrates were Czochralski LEC grown with EPDs from 3 x $10^4$ to 7 x $10^4 cm^{-2}$.

Diffusions were performed through bare surfaces or by using cap layers of: i) resistively evaporated $SiO_2$ (50-100Å thick) [9]; ii) phosphorus rich anodic [10] and chemical [11] oxides (35-50Å thick).

The quality of $p^+n$ InP structures was investigated from:

1. Inspection of the post-diffused surface topography using Nomarski and SEM microscopy;

2. Revealing the surface and deep precipitates after thinning down the $p^+$ layer to different depths by anodic dissolution using the FAP electrolyte, and SEM inspection [12].

3. Investigation of surface and deep etch pit density revealed electrochemically using the FAP electrolyte at high current densities (1-3 $mA/cm^2$) under illumination [12].

4. Electrochemical C-V; $1/C^2$-V, G-V and I-V characteristics by using a Polaron PN4200 profiler.

5. Performance parameters of $p^+n$ InP solar cells fabricated on selected $p^+n$ structures.

## RESULTS AND DISCUSSION

### $p^+n$ InP JUNCTION FORMATION

Using elemental Zn and Cd as diffusants, the $p^+$ surfaces were seriously pitted even when phosphorus-rich oxide capping was employed.

Using high purity $Zn_3P_2$ and $Cd_3P_2$ sources, significant improvements in the surface and $p^+n$ diode quality were achieved. Due to space limitation we are going to refer here only to diffusions using the compound sources.

Diffusion through bare surfaces has led to unacceptable levels of surface defect densities, e.g., as high as $10^9 cm^{-2}$ in the case of Zn-diffusion and of up to about 5 x $10^7 cm^{-2}$ in the case of Cd-diffusion.

The surface quality could be improved by diffusion through resistively evaporated $SiO_2$ cap layers. In the case of Cd-diffusion EPDs values as low as $8 \times 10^5 cm^{-2}$ were recorded, after removing the $SiO_2$ cap layer and the contaminated front emitter layer (about 100Å) from the surface using the FAP electrolyte [12]. However, from electrochemical C-V, $1/C^2$-V, G-V and I-V characteristics, in this case, it was found that relatively good diode characteristics were obtained only after removing the front 0.2-0.3 μm layer from the surface.

Using phosphorus-rich anodic and chemical oxide cap layers, the quality of $p^+n$ structures was dramatically improved.

Anodic oxides were grown in $o\text{-}H_3PO_4:H_2O:ACN$ (1:200:300) under strong illumination (≈ 100 $mWcm^{-2}$) at a constant current density of 0.6 $mA/cm^{-2}$ [10]. Prior to diffusion the front In-rich oxide was removed by a short dip in dilute HF (5%) solution, and the thickness of P-rich interfacial oxide layer used as a cap was varied from about 25 to 50Å (cell voltage: 30 to 40 V).

Chemical oxides were grown using a newly developed etchant, called "PNP" [11] with general formula: $(o\text{-}H_3PO_4)_u:(HNO_3)_v:(H_2O_2)_t:(H_2O)_{100-(u+v+t)}$, which grows an interfacial layer rich in $In(PO_3)_3$ of thickness which is proportional to the etching time and depends on the composition of the etchant.

Zn diffusion due to its higher diffusivity as compared to Cd diffusion is hard to control. Furthermore, not only do the surface precipitates have a high density but these precipitates extend deep into the $p^+$ emitters. The surface precipitates have a density ranging from $5 \times 10^4$ to about $5 \times 10^8 cm^{-2}$ depending on the diffusion temperature, amount of evaporating material and temperature gradient between the end of the quartz ampoule containing the source and the substrates region, and the P-rich diffusion cap being used. We observed that keeping the source region at a lower temperature (about 10° C below the substrate region) improves the diode quality by reducing the surface precipitates.

In the case of Cd diffusion the precipitates which had a density ranging from $4 \times 10^2$ to $6 \times 10^7 cm^{-2}$, depending on the diffusion conditions, appear to be superficial. After removal of about 50Å from the surface (below the oxide layer), no deep precipitates could be revealed.

Figure 1 shows a typical view of $p^+$ surface topography for Cd and Zn diffusion through capped and uncapped surfaces. As seen, specular surfaces are obtained in the case of Cd diffusion through the thin P-rich oxide cap layer.

Surface dislocation densities as seen in Figure 2 revealed either electrochemically using the FAP electrolyte [12] at a high current density or chemically using the Hubert etchant, have shown that extremely low EPDs are achieved in the case of Cd diffusion using P-rich anodic or chemical cap layers. The lowest EPD of 400-800 $cm^{-2}$ in this case was obtained at a diffusion temperature of 560°C with a temperature gradient between the source and substrates of about 15°C. EPDs were about one order of magnitude higher if no temperature gradient was used (see Figure

2B) and as high as $10^9$ $cm^{-2}$ in the case of Zn diffusion through bare surfaces (Figure 2C).

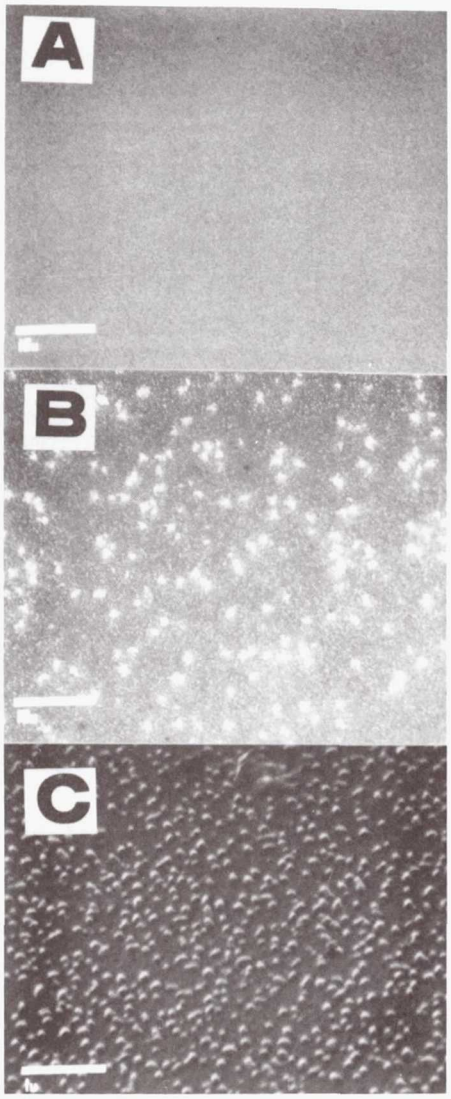


**Figure 1.** SEM view of surface topography of $p^+n$ InP structures made by diffusion of Cd at 560°C (A & B) and Zn at 540°C for 30 min (C) through about 35 Å thick chemical oxide cap layer (A & B) and bare surface (C). Temperature gradient between the surface and the substrates: A) 15°C; B) 0°C; C) 15°C.

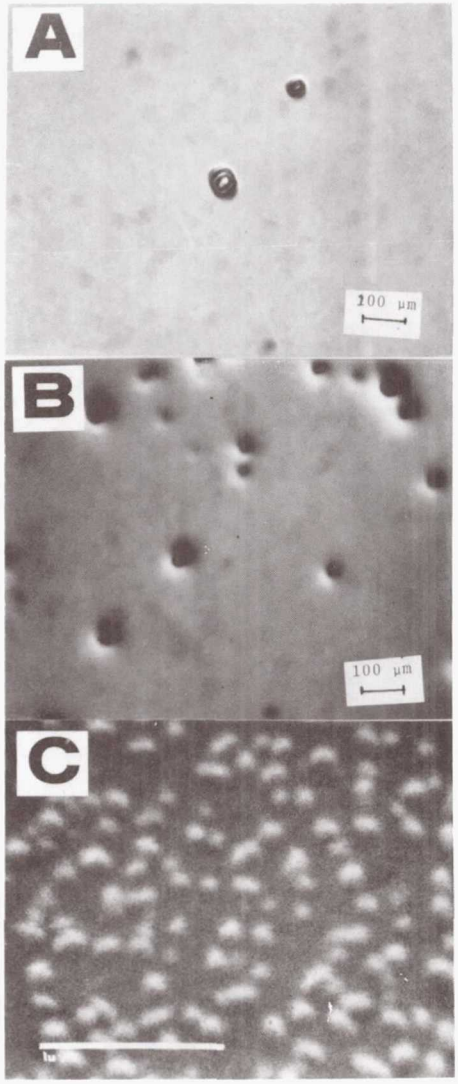


**Figure 2.** EPD's revealed electrochemically (A & B) using the FAP electrolyte at 2 $mA/cm^2$ under illumination and C) chemically using HBr:o-$H_3PO_4$ (1:2) for structures in Figure 1.

From electrochemical C-V, $1/C^2$-V, G-V, and dark and illuminated I-V characteristics, which were done for all $p^+n$ structures, the diode quality was found to be the best for Cd diffusion through the P-rich oxide cap layers. An example of these characteristics after removing about 0.03 µm is shown in Figure 3. As seen quasi-ideal characteristics are obtained in this case even at a diffusion temperature of 600° C. The diode characteristics in this case were found to be near perfect even after removing just the front oxide layer, implying an absence of a front dead layer, which proves that the P-rich oxide is a very good choice as a diffusion cap layer.

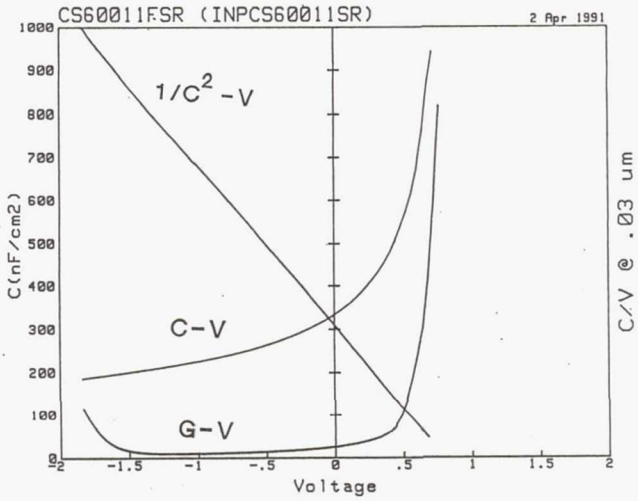


**Figure 3.** Electrochemical C-V, $1/C^2$-V and G-V characteristics using the FAP electrolyte [12] for a $p^+n$ InP structure, Cd diffused at 600°C for 10 min, after removing 0.03 µm from the surface.

After Zn-diffusion, in the best case (diffusion at 540°C) reasonably good diode characteristics were obtained only after the removal of about 0.4 to 0.5 µm from the surface.

Electrochemical C-V (EC-V) profilings performed using the FAP electrolyte [12] have shown that the net acceptor concentration, $(N_A-N_D)$, at the surface, in the case of Cd-diffusion for diffusion temperatures of 550 to 600°C, was from 9 x $10^{17}$ to 2 x $10^{18}$ $cm^{-3}$, depending on the diffusion conditions. In Figure 4 are shown two EC-V profiles after Cd diffusion through about 40Å P-rich chemical oxide cap layer into InP:S of two doping levels. As expected the diffusivity of Cd into the highly doped substrate appears lower than in the low doping substrate.

## $p^+n$ InP SOLAR CELL PERFORMANCES

Small area (0.48 $cm^2$) $p^+n$ InP solar cells were fabricated on structures diffused at 560°C, the diffusion temperature at which the surface dislocation density is minimum.

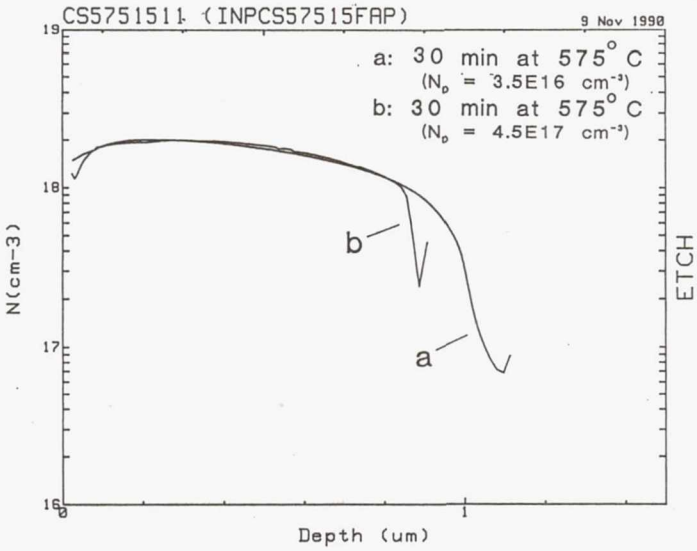


**Figure 4.** EC-V profiles of two $p^+n$ InP structures made by Cd diffusion into n-InP:S through a $In(PO_3)_3$-rich chemical oxide cap layer (~40 Å thick).

Since Au-Zn-Au front contacts melt as far deep as 2 µm into InP during sintering at 430°C, $p^+n$ structures with thick emitters were fabricated. Therefore, after front contact sintering at temperatures from 390°C to 430°C, the emitters had to be thinned down over the uncontacted areas. Anodic oxidation-removal cycles and chemical etching were considered. Since none of the etchants known to us could be used, a new etchant which we call the "PNP" etchant wad developed [11]. Resulting surfaces using this etchant are very smooth as seen in Figure 5 and a P-rich oxide grows during the dissolution process. Performance parameters were recorded at CSU after each thinning

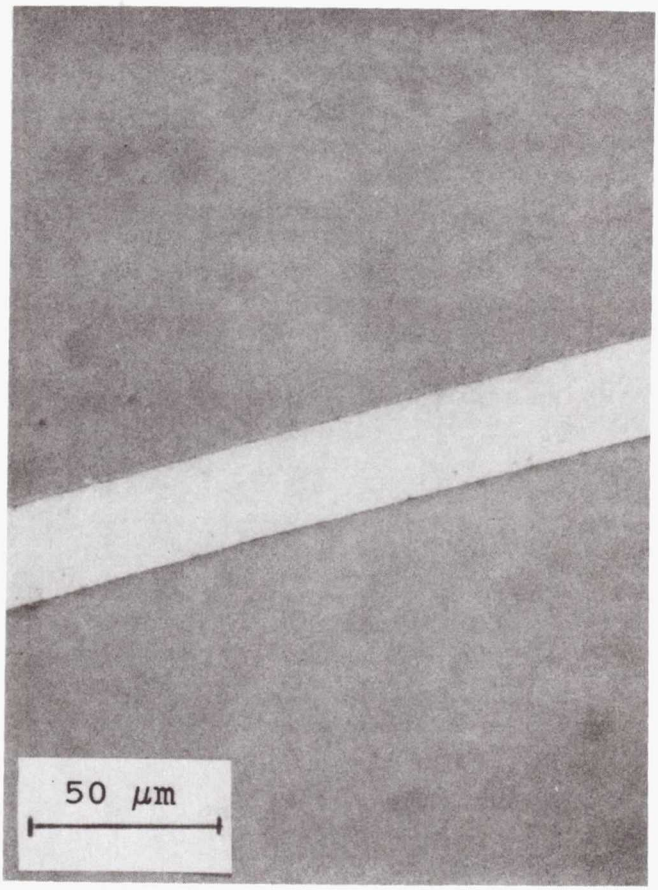


**Figure 5.** Nomarski micrograph of a surface after thinning the $p^+$ layer from ~2.5 µm to ~0.1 µm using the "PNP" etchant, (u = 15, v = 45, t = 1) [11].

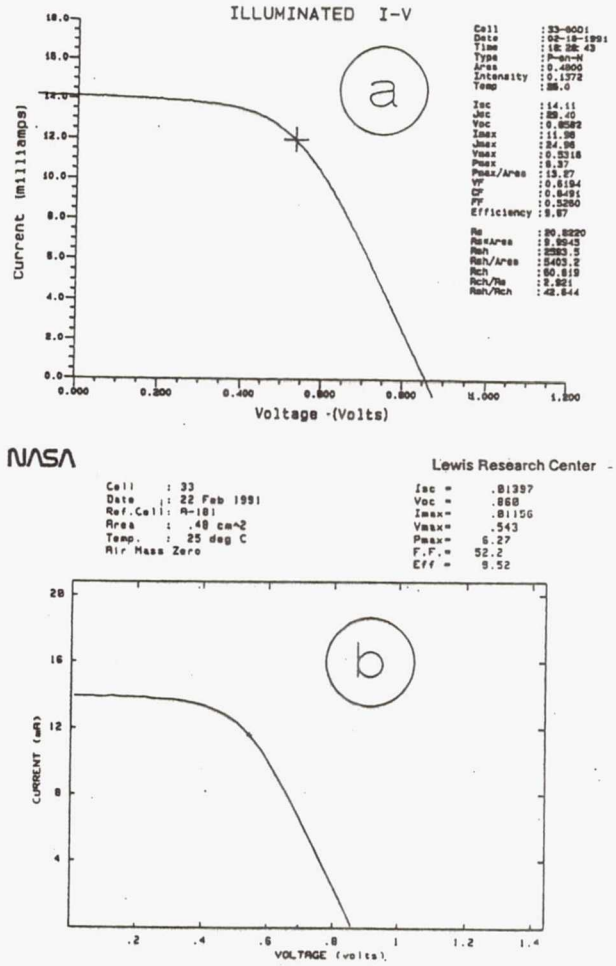


**Figure 6.** Illuminated I-V characteristics of cell #33 using a) an ELH lamp and b) under AMO, 25°C conditions.

step (see figure 6a). Up to 150 steps were used in the case of chemical thinning in order to find the optimal emitter thickness. For selected cells, illuminated I-V (see Figure 6b) dark I-V, $I_{sc}$-$V_{oc}$ and spectral response measurements were done under AMO conditions at NASA-LeRC.

Dark I-V, $I_{sc}$-$V_{oc}$ characteristics, have shown that the diode quality factor calculated at the maximum power point was from 1.03 to 1.08 and the dark saturation current density from $8 \times 10^{-17}$ to $2 \times 10^{-16}$ A/cm$^2$.

As seen in Figure 7, $I_{sc}$ values increase with decreasing emitter thickness and reaches a maximum at 0.15 to 0.25 µm. $\eta_{max}$ was found for emitter thickness of 0.2 to 0.3 µm. This means that most of the current comes from the low defect density emitter and space charge regions. The low FF values are due to the large values of $R_s$ due to an inappropriate front grid design. The decrease of FF as a result of thinning the emitter is directly related to an increase in $R_s$ due to a large increase in sheet resistance once the surface concentration goes below $9 \times 10^{17}$cm$^{-3}$.

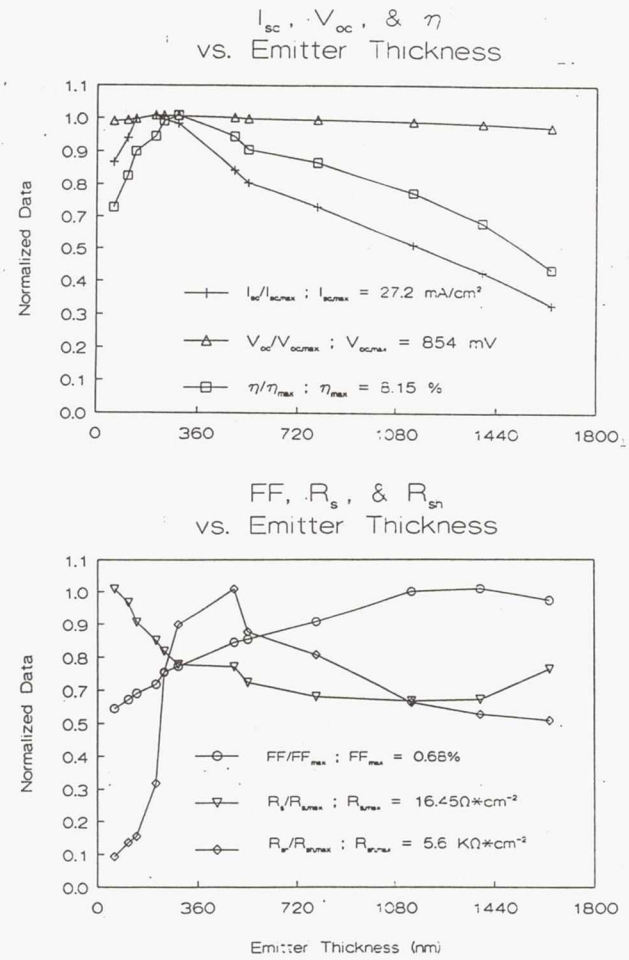


**Figure 7.** Relative variations of $I_{sc}$, $V_{oc}$, FF, $\eta$, $R_s$ and $R_{sh}$ as functions of junction depth of a $p^+n$ InP solar cell (#17).

Table 1 shows the variation of the short circuit current density $J_{sc}$ and the open circuit voltage $V_{oc}$ for several $p^+n$ InP solar cells fabricated by closed ampoule diffusion of Cd into InP:S substrates after thinning the emitter from about 2.5 µm to 0.06-0.15 µm by anodic and chemical oxidation, as a function of the oxide type and thickness. As seen, by using the PNP-2 etchant [11] the largest $J_{sc}$ and $V_{oc}$ values have been obtained. The high $V_{oc}$ values for these thermally diffused $p^+n$ InP solar cells correlate well with the low surface state density minimum $N_{ss,min}$ of 3 x $10^{10}cm^{-2}$ $eV^{-1}$ recorded after dissolution of a $p^+n$ InP structure using the PNP-2 etchant, from 2 µm down to ≈ 0.25 µm. The oxide thickness in this case was ≈ 120 nm. The $N_{ss}$ values were calculated from the conductance-voltage (G-V) data at different frequencies using a Polaron PN 4200.

In-rich surface layers have previously been identified to be a possible cause of the high density of interface states [13]. From the large enchancement of Photoluminescence Intensity as a result of removing the In-rich surface oxide layer [14], it will appear that this is the case. This might explain the data in Table 1 which show an increase in $V_{oc}$ of anodic oxide covered solar cells after

**Table 1.** $J_{sc}$ and $V_{oc}$ of selected $p^+n$ InP Solar cells after thinning the $p^+$ emitter by anodic oxidation-removal and chemical etching with PNP etchant [11].

| Cell # * | Oxide type | Approx. oxide thickness (nm) | Before removing the front oxide layer (b) $J_{sc}$ (b) (mA/cm$_2$) | $V_{oc}$ (b) (mV) | After removing the front oxide layer (a) $J_{sc}$ (a) (mA/cm$_2$) | $V_{oc}$ (a) (mV) | $J_{sc}$(b)/$J_{sc}$(a) ( % ) |
|---|---|---|---|---|---|---|---|
| 20(c) | anodic | 120 | 25.69 | 849 | 23.33 | 854 | 90.8 |
| 22(d) | chemical | 850 | 27.00 | 859 | 22.43 | 852 | 83.1 |
| 23(e) | chemical | 150 | 27.65 | 859 | 22.33 | 850 | 80.0 |
| 26(f) | anodic | 130 | 20.80 | 846 | 21.22 | 851 | 102.0 |
| 27(g) | chemical | 400 | 27.96 | 859 | 23.04 | 853 | 82.4 |
| 33(h) | chemical | 120 | 29.10 | 860 | - | - | - |

* Illuminated I-V characteristics measured at NASA LeRC, under AM0, 25°C conditions; (c) grown in 3% citric acid in ethylene glycol (1:3) buffered to pH7 with 20% $NH_4OH$ solution; (d),(e) and (g) grown in PNP-1 etchant; (d):(u=0, v=60, t=1); (e):(u=15, v=45, t=1); (g):(u=5, v=60, t=1); (f) grown in o-$H_3PO_4$:$H_2O$:ACN (1:200:300) [10]; (h) using PNP-2 etchant:(u=10, v=30, t=1); where the PNP etchant is: [ $(o\text{-}H_3PO_4)_u$ : $(HNO_3)_v$ : $(H_2O_2)_t$ : $(H_2O)_{100-(u+v+t)}$ ]

removing the front In-rich oxide layer. As seen, after removing the front oxide layers, the solar cell performance parameters are comparable for the cells made using the two thinning processes, namely, the PNP-1 etchant and anodic oxidation. However, the cell performance parameters are even better using the PNP-2 etchant. Since the anodic oxidation-removal process is very laborious and hard to control [10] as compared to a simple chemical etching process, the latter seems to be the best answer.

The above $V_{oc}$ values, measured at NASA LeRC under the AMO, 25° C conditions, are higher than any previously reported $V_{oc}$ values for InP solar cells made by thermal diffusion.

**Table 2. Measured or Predicted AM0, 25°C p/n or n/p InP Solar Cell Performances**

| Structure | Junction formation technique | Dopant | Approx. Junction depth (μm) | Voc (mV) | Jsc mA/cm² | FF (%) | η (%) | References |
|---|---|---|---|---|---|---|---|---|
| $p^+$-i-n | LPE | Mg/S | 0.6 | 823.7 | 37.6 (active area) | 75.4 | 17.2 (active area) | Itoh et al., NTT [4] (Measured) |
| $p^+$(InGaAs)/ $p^+$(InP)/n(InP)/ $n^+$(InP) | LPE | Zn/S | 0.7 | 866 | 29.25 | 81 | 15 | Shen, et al. [5] Arizona State Univ. |
| | MOCVD | | | 864 | 32.84 | 76.7 | 15.9 | (Measured) |
| $n^+$-p | Closed Ampoule | S/Zn | 0.2-0.3 | 828 | 33.7 | 81.6 | 16.6 | Okazaki et al., NTT [1] (Measured) |
| $n^+$-p | Closed Ampoule | S/Cd | 0.15 | 806 | 30.5 | 80.1 | 14.35 | Faur, et al., CSU [2] (Measured) |
| | | | 0.08-0.1 | 840 | 36.5 | 84 | 18.8 | (Predicted) |
| $p^+$-n (Cell 33) | Closed Ampoule | Cd/S | 0.25 | 860 | 29.1 | 52.2 | 9.52 | Faur, et al., CSU, (Measured) This work. |
| | | | 0.25 | 880 | 34.5 | 83 | 18.36 | (Predicted) |
| | | | 0.25-0.3 | 890 | 37.4 | 84 | 20.4 | (Predicted) |

Radiation tolerance scale: $p^+$-n = $n^+$-p-$p^+$ > $n^+$-p > $p^+$-i-n (after Okazaki, et al., NTT ) [1]

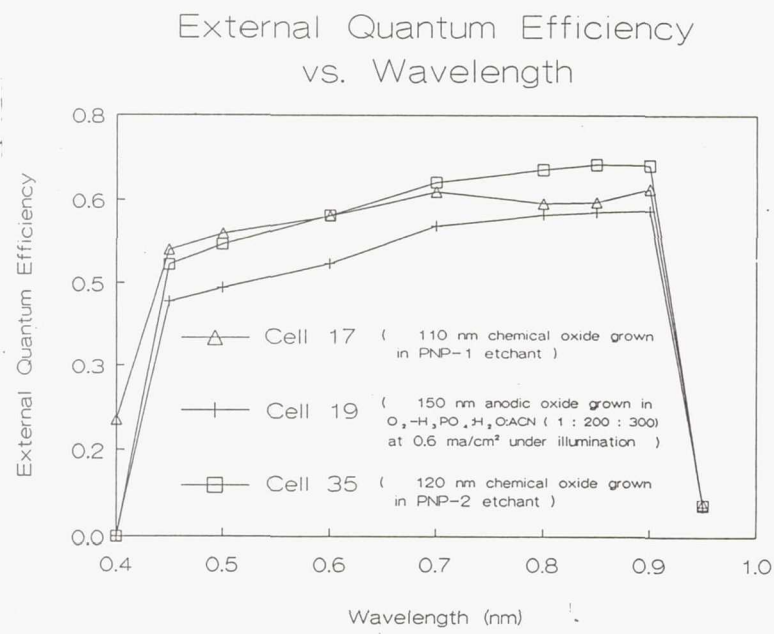


In Table 2 is shown a review of performances of $p^+n$ InP solar cells including those measured and predicted for our high performance $p^+n$ junctions. For comparison, performances of $n^+p$ InP solar cells made by closed-ampoule sulfur diffusion into Zn and Cd doped substrates are also given in this table.

One can see that our measured $V_{oc}$ and $I_{sc}$ values are higher or very close to

**Figure 8.** External Quantum Efficiency plots of selected $p^+n$ InP solar cells measured under AMO, 25°C conditions at NASA LeRC.

previously reported values of epitaxially grown $p^+$-i-n [4] or $p^+$(InGaAs)/$p^+$ InP/n(InP)/$n^+$ InP [5] solar cells.

From the external quantum efficiency plots, seen in Figure 8, an increase of 15 to 25% in $I_{sc}$ can be expected by optimizing the passivating layer and using a second layer AR coating. From the $I_{sc}$-$V_{oc}$ characteristics such an increase in $I_{sc}$ will produce an increase of about 10 mV in $V_{oc}$. By further optimizing the diffusion process we estimate that a $V_{oc}$ value of 880 mV is readily achievable using these high performance thermally diffused $p^+n$ InP structures. Assuming that by reducing $R_s$, FF values of 83% can be achieved, a simple computation based on presently measured $V_{oc}$ and $I_{sc}$ values indicates that AMO efficiencies of over 18% are readily achievable. By further reducing the external losses (i.e. 4% grid coverage and below 5% overall reflexivity), using better quality substrates (i.e. defect density below $10^4 cm^{-2}$), optimizing base doping, further optimizing the diffusion process and the quality of the passivating layer, AMO, 25° C $V_{oc}$ values as high as 890 mV for solar cells fabricated by this method of junction formation should be possible. The $J_{sc,max}$ in this case is of about 37.4 $mA/cm^2$. Assuming a FF of 84%, the expected maximum AMO efficiency is of 20.4%.

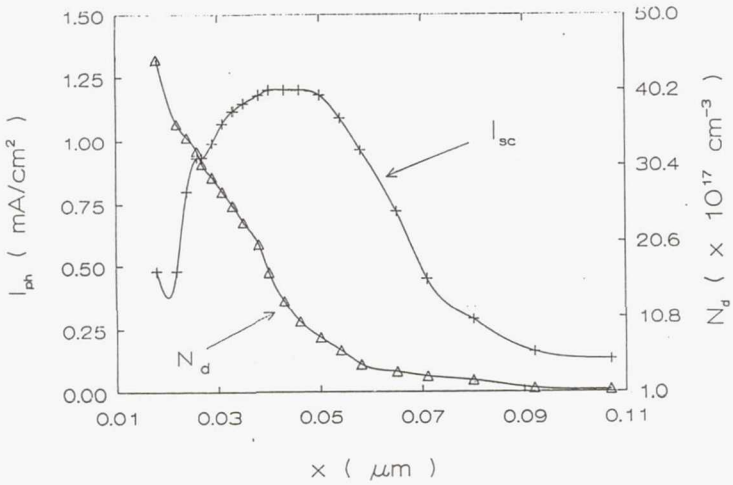


**Figure 9.** Variation of $I_{ph}$ and majority carrier concentration ($N_D$) as function of depth after photoanodic dissolution using the FAP electrolyte [12] of an $n^+p$ InP structure made by thermal diffusion [2].

By comparison, the maximum reported AMO efficiency for an $n^+p$ InP solar cell made by thermal diffusion is 16.6% [1]. $V_{oc}$ in this case is the principal limiting parameter. Based on our thorough investigation on $n^+p$ InP thermally diffused structures [2, 6 ] we estimate that the maximum achievable $V_{oc}$ is about 840 mV which is in close agreement with previously predicted values [1]. The maximum $J_{sc}$ in this case is limited to 36.5 $mA/cm^2$. Assuming a similar FF value of 84%, the maximum AMO efficiency in this case is of about 18.8%. These values were calculated for an $n^+p$ InP solar cell with similar minimal external losses as described above, for a stucture fabricated by sulfur diffusion into Cd-doped InP substrates, using a thin $In(PO_3)_3$ diffusion cap layer and removing the phosphorus depleted dead layer from the surface ( 400Å).

As seen in Figure 9 which plots the variation of $I_{sc}$ at the FAP electrolyte/$n^+$ InP interface and $N_d$ as a function of the dissolution depth, however the highest $I_{sc}$ value is found after removal of about 400Å from the surface, which corresponds to a surface concentration $N_d$ of about 2 x $10^{18} cm^{-3}$. The dislocation density minimum at this level was about 6 x $10^5 cm^{-2}$, as revealed electrochemically. This explains the relatively low $V_{oc}$ and $I_{sc}$ predicted values. However, by further thinning the emitter, $I_{sc}$ and $V_{oc}$ both increase and reach a maximum at about 500Å. Due

to the graded nature of the diffusion profile [6], in this case the $R_s$ drastically increases due to an increase in sheet resistance. Because of this the maximum efficiency in this case was found for emitter thickness of 800 to 1000Å, which offers an explanation of why the $V_{oc,max}$ is only 840 mV, and the $J_{sc}$ is below than that expected from a well designed $p^+n$ InP solar cell.

Very few and contradictory comparative radiation resistance measurements of the two $n^+p$ and $p^+n$ InP configurations have been reported [1,15]. While Okazaki, et al. [1] assume the radiation tolerance scale for InP solar cells of different configurations to be: $p^+$-n = $n^+$-p-$p^+$ > $n^+$-p > $p^+$-i-n, Weinberg, et al. [15] on the contrary predict the $n^+p$ configuration to be more radiation resistant than the $p^+n$ configuration. An explanation of this is that radiation tolerance evaluations were not done on structures fabricated under similar conditions. Therefore more insight in this area is necessary. We plan to do radiation resistance measurements on $p^+n$ InP solar cells but only after the external losses are drastically reduced, i.e. an AMO efficiency greater than 16%.

## CONCLUSIONS

From our preliminary investigation it appears that optimal conditions for high quality thermally diffused $p^+n$ structures are: i) $Cd_3P_2$ as source; no added phosphorus; ii) diffusion through thin (25-40Å thick) $In(PO_3)_3$-rich chemical oxide; iii) diffusion temperature: 560° C and iv) about 15°C temperature gradient between the source and substrates.

For solar cells made by thermal diffusion we expect the $p^+n$ configuration to have higher efficiency than the $n^+p$ configuration, due especially, to an increased $V_{oc}$.

Based on this study we predict that $p^+n$ InP solar cells with AMO, BOL efficiencies approaching 19% should be readily achievable providing that good ohmic front contacts could be realized on the $p^+$ emitters of thickness lower than 1 μm. The maximum expected AMO efficiencies for the $p^+n$ configuration is about 20.4%, while for the $n^+p$ configuration, it is about 18.8%.

If, as we expect, the $p^+n$ structures prove to be at least as radiation tolerant as the $n^+p$ structures, then $p^+n$ InP solar cells made by thermal diffusion can become very attractive for space applications due to a potential low cost, reduced complexity and adaptability to large scale batch processing.

## REFERENCES


[1] H. Okazaki, T. Tokamoto, H. Takamura, T. Kamei, M. Ura, A. Yamamoto and M. Yamaguchi, 20th PVSC, 886 (1988).

[2] M. Faur, M. Faur, C. Goradia, M. Goradia, N. Fatemi, D. J. Brinker and R. D. Thomas, Proceedings of the 1st Int. Conference on InP and Related Materials, Norman, OK, 459 (1989).

[3] K. K. Parat and S. K. Ghandhi, Solid-State Electronics, 31(6),1053 (1988).

[4] Y. Itoh, M. Yamaguchi and C. Uemura, IEEE Electron Device Lett., EDL-7(2),127 (1986).

[5] K. Y. Choi, C. C. Shen and B. I. Miller, 19th IEEE PVSC, 255 (1987).

[6] M. Faur, M. Faur, C. Goradia, R. D. Thomas, D. J. Brinker, N. Fatemi and F. Honecy, 10th SPRAT Conference, 332 (1989).

[7] C. J. Keavney, V. E. Haven and S. M. Vernon, 2nd. Int. Conf. on InP and Related Materials, 435 (1990).

[8] M. Faur, M. Faur, C. Goradia, M. Goradia and I. Weinberg, To appear in Proceedings of the 3rd Int. Conf. on InP and Related Materials, Cardiff, Wales, U.K., April 8-11 (1991).

[9] C. B. Wheeler, R. J. Roedel, R. W. Nelson, S. N. Schauer and P. Williams, J. Appl. Phys. 68(3),969 (1990).

[10] M. Faur, M. Faur, J. T. Jayne, M. Goradia and C. Goradia, Surface and Interface Analysis, 15,641 (1990).

[11] M. Faur, M. Faur, S. Bailey, D. J. Brinker, M. Goradia, I. Weinberg and N. Fatemi, to be presented at the 22nd IEEE PVSC, Las Vegas, October (1991).

[12] M. Faur, M. Faur, C. Vargas and M. Goradia, this conference.

[13] G. Hollinger, J. Joseph, Y. Robach, E. Bergignat, B. Commere, P. Viktorovich and M. Froment, J. Vac. Sci. Technol. B5(4), 1108 (1987).

[14] M. Faur, M. Faur, P. Jenkins, M. Goradia, S. Bailey, D. T. Jayne, I. Weinberg and C. Goradia, Surface and Interface Analysis, 15(745) (1990).

[15] I. Weinberg, C. K. Swartz, R. E. Hart, Jr. and R. L. Statler, Proc. 19th IEEE PVSC, 548 (1987).

# IMPROVEMENTS IN CONTACT RESISTIVITY AND THERMAL STABILITY OF Au-CONTACTED InP SOLAR CELLS

*Navid S. Fatemi* † *and Victor G. Weizer* ‡
†Sverdrup Technology, Inc., Brook Park, Ohio 44142
‡NASA Lewis Research Center, Cleveland, Ohio 44135

Specific contact resistivities for as-fabricated Au contacts on n/p InP solar cells are typically in the $10^{-3}$ Ω-cm$^2$ range, but contact resistivities in the $10^{-6}$ Ω-cm$^2$ range can be obtained if the cells are heat treated at 400°C for a few minutes. This heat treatment, however, results in a dramatic drop in the open circuit voltage of the cell due to excessive dissolution of the emitter into the metallization. We have found that low values of contact resistivity can be secured without the accompanying drop in the open circuit voltage by adding Ga and In in the Au metallization. We will show that Au contacts containing as little as 1% atomic Ga can suppress the reaction that takes place at the metal-InP interface during heat treatment, while exhibiting contact resistivity values in the low $10^{-5}$ Ω-cm$^2$ range. Similarly, we have found that the deposition of the alloy $Au_9In_4$ on InP can inhibit all the metallurgical reactions which take place at the metal-InP interface even when heat treated at 400°C for many hours. We will present detailed explanations for the observed superior thermal stability of these contacts when compared to Au-only contacts. In addition, we will show that the very low contact resistivities observed with Au on n-InP when heat treated at 400°C is due the formation of the compound $Au_2P_3$ at the metal-InP interface.

## INTRODUCTION

Ohmic contacts to III-V solar cells have not traditionally met all of the requirements expected of them. Ideally, these contacts should show negligibly low contact resistance, react minimally with the semiconductor substrate yet remain adherent, and be stable with aging at operating temperatures. These requirements are more stringent for the front emitter contacts than for the back base metallization.

For the front emitter contacts of III-V cells to have a negligible contribution to the series resistance, the contact resistivity $\rho_c$, should be in the low $10^{-3}$ Ω-cm$^2$ range for one sun and in the low $10^{-5}$ Ω-cm$^2$ range for 100X operations (ref. 1,2,3). $\rho_c$ values two orders of magnitude higher than those for the front contacts are normally adequate for the back base contacts (ref. 2). Post-fabrication high temperature contact heat treatment or prefabrication semiconductor surface ion damage methods are normally used to obtain low resistance ohmic contacts (ref. 4 to 7). Both of these techniques, however, can be destructive for devices with shallow emitters such as n/p InP homojunction solar cells.

Ideally, a contact system should exhibit low contact resistance as-fabricated and also should be able to withstand thermal stress, such as high operating temperatures or radiation damage annealing, without compromising emitter integrity. Traditionally used Au and Au-based contact systems can not adequately satisfy either of the above criteria. However, we have found that the addition of small amounts of Ga or In to Au contacts not only lowers the as-fabricated $\rho_c$ by an order of magnitude compared to Au-only contacts, but it also suppresses the metal-InP solid state interactions that normally occur at elevated temperatures. Our investigation of the Au-InP system and the mechanisms involved in contact formation (ref. 8 to 11), have enabled us to explain the superior thermal stability of these contacts as compared to Au-only contacts.

We will present the results of our study on Au-Ga and Au-In contact systems to n-InP and will also

provide an explanation for the observed two-to-three order of magnitude drop in contact resistivity of Au on n-InP at 400°C.

## EXPERIMENTAL

Epitaxially grown n/p InP diodes used in our study were obtained from the Spire Corporation. n-type emitters were 0.2 μm thick with a doping density of $1.7 \times 10^{18}$ $cm^{-3}$ (Si). The p-type (100) substrates were Zn doped to about $8 \times 10^{16}$ $cm^{-3}$. The Transmission Line Method (TLM) (ref. 12) was used to measure specific contact resistivity of the contacts on n/p diodes, and the Cox & Strack (C&S) method (ref. 13) was used to measure contact resistivity of the contacts made to bulk n-InP (100) substrates doped to about 5E18 $cm^{-3}$ (S).

Contact deposition was by *e*-beam evaporation at a pressure in the $10^{-6}$ Torr range. Au-Ga contacts were made by sandwiching 20Å (1% atomic) and 200Å (9% atomic) Ga layers between two 900Å layers of Au. The Au-In deposition technique has been described elsewhere (ref. 9). The metallization thickness for all Au and Au-In contacts was 2000Å. Also contacts referred to as as-fabricated have undergone mild heat treatments (110°C, 30 min.) during photolithographic processing. Also, The diodes were contacted on the base with ohmic Au-Zn metallization.

In order to monitor the degree of emitter dissolution/perforation caused by the heat treatment process, we observed the n/p diode current-voltage (I-V) characteristics. As a measure of I-V quality, we arbitrarily defined a diode conduction voltage $V_1$, as the voltage at which the forward current through the TLM patterned diode with an area of $5.6 \times 10^{-3}$ was 1 mA. A good n/p junction should exhibit a $V_1$ of about 900 mV. Lower values of $V_1$ indicate a degraded emitter.

All heat treatments were performed in a rapid thermal annealing (RTA) furnace in a forming gas ambient. The compositional depth profile analysis of the contacts was performed via x-ray photoelectron spectroscopy (XPS), that was specifically calibrated for use with the Au-In binary system (ref.14).

## RESULTS

### I. *Au-Ga CONTACTS*

The motivation to add Ga to Au was provided by the phosphorus release studies of Mojzes *et al.* (ref. 15), where it was shown that adding Ga to Au contacts on InP was effective in suppressing the release of P during heat treatment. We know from our previous studies of the Au-InP system (ref. 8 to 10) that the interaction of Au with InP is always initiated by the dissolution of In into Au followed by the release of P. Therefore, suppressing the release of P through Ga addition to Au was an indication that the dissolution of In was also suppressed. Fig. 1 shows XPS depth profiles of Au-only and Au-1%Ga contacts on InP heat treated simultaneously at 355°C for 40 minutes. As shown, addition of only 1% Ga to Au can suppress the metal-InP interaction significantly.

Fig. 1 also shows that Ga addition to Au eliminates the characteristic In peak at the free surface of the metal observed in Au-InP couples even at room temperature (ref. 11, 16, 17), replacing it with a Ga peak. The absence of this In peak indicates that Ga is somehow preventing In from diffusing dissociatively, i.e. interstitially, in the Au lattice (ref. 8). The presence of a Ga peak, on the other hand indicates that Ga is itself being transported dissociatively in Au. Therefore, it is apparent that Ga, by saturating the interstitial sites in Au prevents In from entering the interstitial pool, thus suppressing the metal-InP interaction. In fact, the presence of Ga in Au suppresses all the solid state phase transitions in the Au-InP system (three stages) which involve the formation and diffusion of the In interstitial (ref. 18).

Fig. 2 illustrates the effectiveness of adding 9%Ga to Au in preserving the emitter integrity of a n/p

diode during heat treatment. As shown, the diode with Au-only metallization begins to fail at about 370°C, whereas minimal degradation is observed for the Au-9%Ga contacted diode up to 440°C. It should be noted that addition of 9% Ga to Au is more effective in suppressing the metal-InP interaction than is the addition of 1% Ga to Au. This is due to the fact that some Ga interstitials take substitutional positions in the Au lattice during heat treatment, thereby losing their ability to prevent In interstitials to enter the lattice. However, if sufficient amount of Ga is added to Au (i.e., 9%) so that some Ga atoms can remain in their interstitial positions during heat treatment, the In interstitial entry into the Au lattice can still be prevented.

In addition to the desirable reaction suppressing effects of Ga addition to Au, we have found that Ga addition improves the contact resistance of Au contacts. As shown in Fig. 3, Au-9%Ga contact shows a one to two order of magnitude lower contact resistivity than the Au-only contact up to 400° C. A minimum $\rho_c$ value of 3.2 X $10^{-5}$ $\Omega$-cm$^2$ is observed with Au-9%Ga contacts at the 270-280°C range. The contact resistivity values of Au-1%Ga contacts are very similar to those of Au-9%Ga contacts.

Since Ga causes the In entry rate into Au to slow down, P atoms released at the metal-InP interface have time to dissipate. It has been shown that a decrease in the amount of accumulated P at the metal-InP interface can result in lower contact resistivity values (ref.18). This may explain the lower $\rho_c$ values observed with Au-Ga contacts as compared to Au-only contacts.

II. *Au-In CONTACTS*

Another method to inhibit In entry into the Au lattice, and thus improve $\rho_c$, is to introduce In into the metallization in place of Ga. But since the addition of In to Au in amounts less than 10% atomic (the saturated solid solution of In in Au) can not suppress the metal-InP interactions, we deposited Au-In mixtures ranging from 12 to 35% In. Fig. 4 shows the effect of adding In (and Ga) to Au for as-fabricated contacts on n-InP. As shown, Au-In and Au-Ga as-fabricated contacts have about an order of magnitude lower contact resistivity than Au-only contacts.

To examine the thermal stability of Au-In contacts at elevated temperatures, we subjected Au contacts containing 23, 35, and 30% ($Au_9In_4$) In to isothermal annealing at 400°C. The compound $Au_9In_4$ was specifically chosen because it is the end product of the third stage of a series of solid state interactions in the Au-InP system (ref. 10), and therefore, was expected to withstand thermal stress at elevated temperatures. Indeed, as shown in Fig. 5, n/p diodes contacted with $Au_9In_4$ showed no degradation at 400°C for at least 12 hours. Also evident from the figure is the fact that although the 23% and 35% In-Au contacts are not as stable as $Au_9In_4$, they are far superior than Au-only contacts.

In addition to their metallurgical stability, Au-In contacts show stable contact resistivities at 400°C. As shown in Fig. 6, $\rho_c$ values in the low $10^{-5}$ to low $10^{-4}$ $\Omega$-cm$^2$ range are obtainable with these contacts. Here again, $Au_9In_4$ is more stable than other Au-In contacts.

III. *Au CONTACTS*

Looking back, in Fig. 3, it is seen that although Au-only contacts show higher $\rho_c$ values than the Au-Ga contacts at lower temperatures, at 400°C a two-to-three order of magnitude drop in contact resistivity is observed. We were able to correlate this resistivity drop with a phase transition (stage II) in the Au-InP system where the contact metallization is transformed to the pink colored compound $Au_3In$ (ref. 9). This is illustrated in Fig. 7 where Au-contacted InP was heat treated at 353°C. As shown, $\rho_c$ reaches a plateau in the low $10^{-6}$ $\Omega$-cm$^2$ range as the entire metal is converted to $Au_3In$.

The stage II phase transition, which is apparently responsible for this resistivity drop, is accompanied by three prominent physical changes in the Au-InP system. First is the conversion of the contact to the stable alloy $Au_3In$. Second, the compound $Au_2P_3$ is formed at the metal-InP interface concurrent with the appearance of $Au_3In$, and finally the surface of InP beneath the contact becomes pitted (ref. 9).

In order to determine which of the above changes are responsible for the resistance drop, we designed the following experiment where various stage II products were selectively removed and replaced. To facilitate alignment and remasking of the contacts, we prepared five samples each having Au discs of various sizes on bulk n-type InP for contact resistivity measurement via the C&S technique. The contacts were heat treated at 390°C for 3 minutes to induce stage II phase transition. As shown in Fig. 8, all five samples exhibited ~two order of magnitude drop in $\rho_c$ (note that here overall $\rho_c$ values are lower than samples used for TLM measurements since the InP doping density is higher by ~factor of 3) (ref.19).

We then removed $Au_3In$ and $Au_2P_3$ from three samples (dark circles in Fig. 8), leaving a pitted InP surface, and only $Au_3In$ from the remaining two samples (light circles) leaving $Au_2P_3$ on the InP surface. As shown in the figure, $\rho_c$ values for samples with $Au_2P_3$ remained essentially the same after $Au_3In$ removal. We then remasked all samples and redeposited a 2000Å layer of Au over original patterns. Again as seen in the figure, $\rho_c$ values for samples with $Au_2P_3$ did not change, but samples without $Au_2P_3$ showed resistivity values nearly as high as their original as-fabricated values (note that pitted InP surface, having a larger area than the smooth surface, measures a lower $\rho_c$ value than its true value).

From the above results, we can conclude that the observed large drop in contact resistance is due neither to the changes in the InP surface geometry nor to the presence of the $Au_3In$ alloy, but in fact it is due to the formation of $Au_2P_3$ at the metal-InP interface.

## SUMMARY

We have investigated Au-Ga and Au-In contact systems as front emitter metallization for use on n/p InP solar cells. Our major findings are as follows:

1). When Ga is added to Au, it precludes the entry of other species such as In and Au into the Au lattice.

2). Because In interstitial formation and migration are involved in all three stages of the Au-InP interaction, all aspects of the reaction of Au with InP are suppressed if sufficient interstitial Ga is present in the Au lattice.

3). The addition of as little as 1% atomic Ga into Au on n-InP reduces the as-fabricated contact resistivity by an order of magnitude.

4). Addition of various amounts of In to Au on n-InP can show as-fabricated contact resistivity values in the high $10^{-5}$ $\Omega$-cm$^2$ range.

5). The alloy $Au_9In_4$ deposited on n-InP is metallurgically and electrically stable for many hours of heat treatment at 400°C.

6). The two-to-three order of magnitude drop in contact resistivity observed with Au on n-InP when heat treated at 400°C is the result of the formation of the compound $Au_2P_3$ at the metal-semiconductor interface.

7). Finally, we have shown that Au-Ga and Au-In contact systems have lower contact resistivity and superior thermal stability than Au-only contacts to n-InP, and they are suitable candidates for use as the front emitter ohmic contacts to n/p InP solar cells for one sun or concentrator applications.

## REFERENCES


1. N. S. Fatemi, "Study of Ohmic Contacts to GaAs for Solar Cell Applications," MS Thesis, Cleveland State University, August 1987.

2. D. K. Schroder and D. L. Meier, IEEE Trans. Elec. Dev., vol. ED-31, no. 5, May 1984, pp. 637-647.

3. T. A. Gessert and T. J. Coutts, *Advanced Metallizations in Microelectronics*, Materials Research Soc. (MRS) Symp. Proc. vol. 181, 1990, pp. 301-312.

4. W. C. Dautremont-Smith, P. A. Barnes, and J. W. Stayt, J. Vac. Sci. Tech. vol. B2, 1984, p. 620.

5. R. Kaumans, N. Grote, H-G. Bach, and F. Fidorra, Inst. Phys. Conf. Ser. vol. 91, 1987, p. 501.

6. A. Katz, W. C. Dautremont-Smith, S. N. G. Chu, S. J. Pearton, M. Geva, B. E. Weir, P. M. Thomas, and L. C. Kimerling, Mat. Res. Soc. Symp. Proc. vol. 181, 1990, p. 401.

7. A. Applebaum, M. Robbins, and F. Schrey, IEEE Trans. Elec. Dev., vol. ED-34, 1987, p. 1026.

8. N. S. Fatemi and V. G. Weizer, J. Appl. Phys. vol. 65, 1989, p. 2111.

9. N. S. Fatemi and V. G. Weizer, J. Appl. Phys. vol. 67, 1990, p. 1934.

10. V. G. Weizer and N. S. Fatemi, J. Appl. Phys. vol. 68, 1990, p. 2275.

11. N. S. Fatemi and V. G. Weizer, Appl. Phys. Lett. vol. 57, 1990, p. 500.

12. H. H. Berger, Solid State Elect. vol. 15, 1972, p. 145.

13. R. H. Cox and H. Strack, Solid State Elect. vol. 10, 1967, p. 1213.

14. D. T. Jayne, N. S. Fatemi, and V. G. Weizer, Proc. 37th American Vacuum Soc. (AVS) Symp., Toronto, 1990; also NASA TM 103659.

15. I. Mojzes, D. Szigethy, and R. Veresegyhazy, Electron. Lett. vol. 19, 1983, p. 117.

16. A. Hiraki, S. Kim, W. Kammura, and M. Iwami, Surf. Sci., vol. 86, 1979. p. 706.

17. A. Hiraki, K. Shuto, S. Kim, W. Kammura, and M. Iwami, Appl. Phys. Lett. vol. 31, 1977, p. 611.

18. V. G. Weizer and N. S. Fatemi, J. Appl. Phys. June 15, 1991.

19. C. Y. Chang, Y. K. Fang, and S. M. Sze, Solid State Elect. vol. 14, 1971, p. 541.

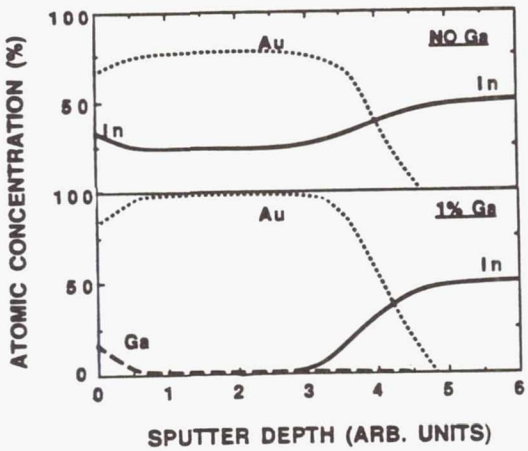


Fig. 1 XPS Compositional depth profiles for Au-only (upper) & Au-1%Ga (lower) contacts heat treated at 355°C for 40 minutes.

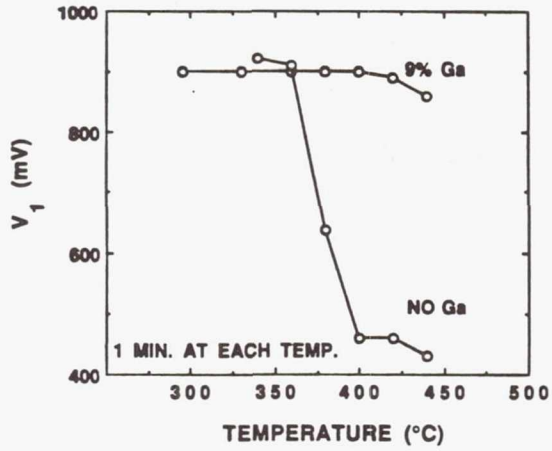


Fig. 2 The n/p diode conduction voltage Vs. temperature for Au-only & Au-9%Ga contacts.

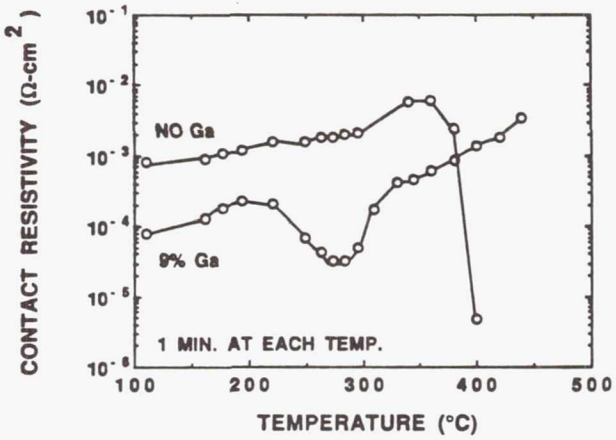


Fig. 3 The specific contact resistivity Vs. temperature for Au-only & Au-9%Ga contacts on n-InP.

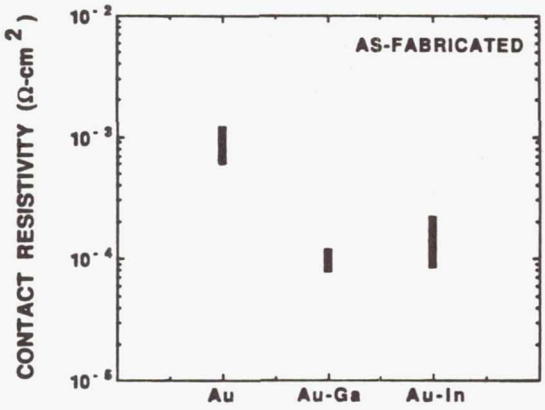


Fig. 4 As-fabricated contact resistivities for Au-only, Au-Ga, & Au-In contacts on n-InP.

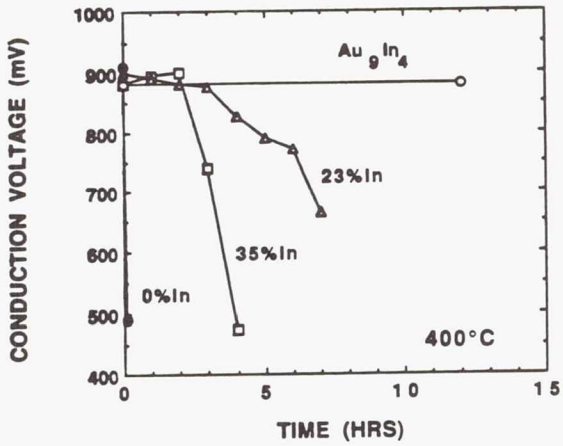


Fig. 5 The variation of the n/p diode conduction voltage with time for Au contacts containing various amounts of In at 400°C.

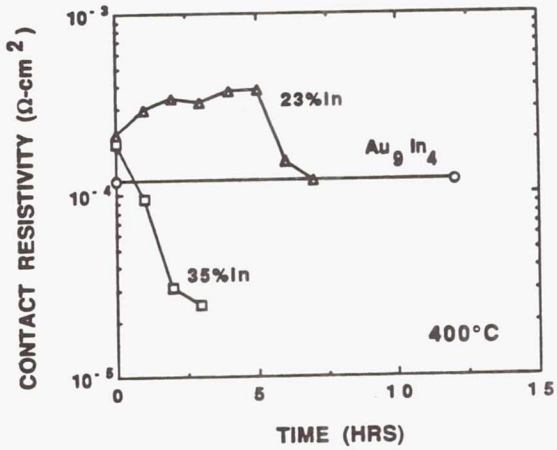


Fig. 6 The variation of contact resistivity with time for Au contacts containing various amounts of In at 400°C.

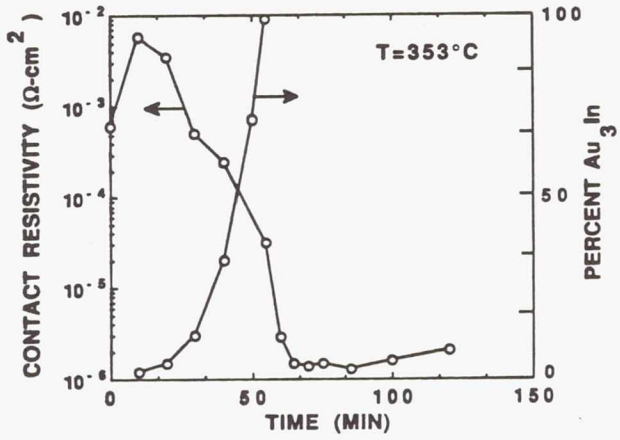


Fig. 7 Contact resistivity and percent Au(In)-to-$Au_3In$ conversion for Au-only contacts as a function of time at 353°C on n-InP.

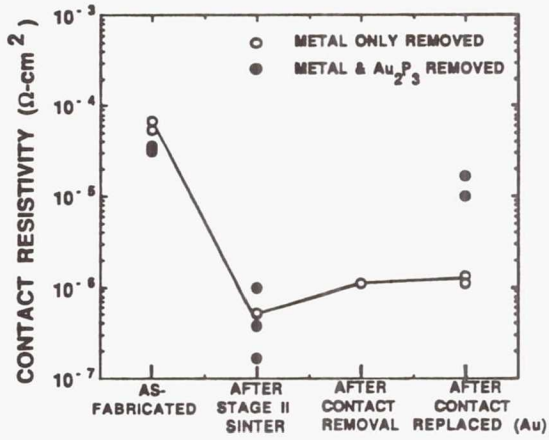


Fig. 8 The effect of contact removal & replacement on the specific contact resistivity.

# GROOVED SURFACES ON InP

Sheila G. Bailey
NASA Lewis Research Center, Cleveland, Ohio, 44142

Navid S. Fatemi and Geoffrey A. Landis,
Sverdrup Technology, Inc., Brookpark, Ohio, 44135

Phillip P. Jenkins
Cleveland State University, Space Photovoltaic Research Center,
Cleveland, Ohio

## INTRODUCTION

Formation of a textured or grooved front surface on a solar cell can increase the efficiency in several ways, including enhanced absorption and light trapping. Anisotropic etching techniques have been little used on indium phosphide (InP), principally because anisotropic etching in the III-Vs is more complicated than on silicon. In III-V materials the (111) plane is chemically different from the $(\bar{1}\bar{1}\bar{1})$ plane, and both etching and epitaxial deposition behave differently on these surfaces [Ref. 1]. This paper summarizes the current state of profile etching in InP and includes data on novel geometries attainable as a function of etchant temperature and composition, substrate orientation and carrier concentration, and the oxide thickness between the substrate and the photoresist. Depending on dopant concentration, the same etchant can produce either anisotropic or isotropic grooves. V-grooved solar cells have been manufactured on InP, and the improved optical absorption demonstrated [Ref. 2]. Preferred parameters for various applications are listed and discussed.

## ANISOTROPIC ETCHING

Reduction of surface reflection, as shown in figure 1, can be achieved by use of a grooved surface. The groove walls are (111) In crystal planes. The grooves are defined by a photoresist pattern, and an anisotropic etchant is used to etch the groove profile through the open stripes in the photoresist. Reflection is minimum when the groove top and bottom surfaces are sharp, with minimum or no flat area. For the (111) grooves on a (100) InP wafer, the photoresist stripes must be aligned along the $[01\bar{1}]$ direction. (As discussed, alignment in the perpendicular direction will produce other groove shapes.) Figure 2 shows the flat orientation for a (100) InP wafer. Note that the Japanese and European standard for the primary and secondary flat is different from the SEMI standard.

An etchant composed of 10:1:1 proportions of HBr, $H_2O_2$, and HCl, respectively, will produce V-grooves on InP. Each component is precooled to -20°C prior to mixing and carefully maintained at -20°C during the required etching time to achieve the desired geometry. This time varies with the chosen geometry and the substrate doping concentration. For doping concentrations less than 1E18 $cm^{-3}$, a complete sawtooth structure of 8 micron periodicity takes approximately six minutes, when the photoresist is applied over a native oxide layer.

The effect of the etchant used can be seen in Figures 3 and 4, which are views of InP wafers that have been cleaved after etching but before removal of the photoresist stripes to show the cross section of the grooves produced. The photoresist is visible at the top of the grooves. Figure 3 shows an InP wafer etched in HCl. The HCl etchant reveals low-angle (311) planes. Figure 4 shows an identical wafer etched with the HBr:$H_2O_2$:HCl etchant discussed above. The planes revealed by the etching are (111) surfaces. It should be noted that the etching shown here was done in ambient "room light," and is believed to be unenhanced by photoetching [Ref. 3].

We have found that producing the desired sharp groove-tops is dependant on the surface treatment of the InP wafer. Initial oxidation has been found to be rapid in InP [Ref. 4]. A "native" oxide layer formed in room air of

variable humidity can be expected to be approximately 3 nm thick. Removal of this oxide layer prior to photoresist application has a dramatic effect on the lateral etch rate, as can be seen by comparing Figures 5 and 6. Nearly sharp groove peaks are produced by undercutting on InP wafers with an oxide layer, while almost no undercutting, resulting in flat groove tops, is produced on InP wafers where the oxide layer has been stripped. Deliberate growth of anodic oxides was found to slightly increase the rate of lateral etching, but yielded the same final structure. Previous authors have found differences in etch rates and profiles using $SiO_2$ and standard photoresist [Ref. 5].

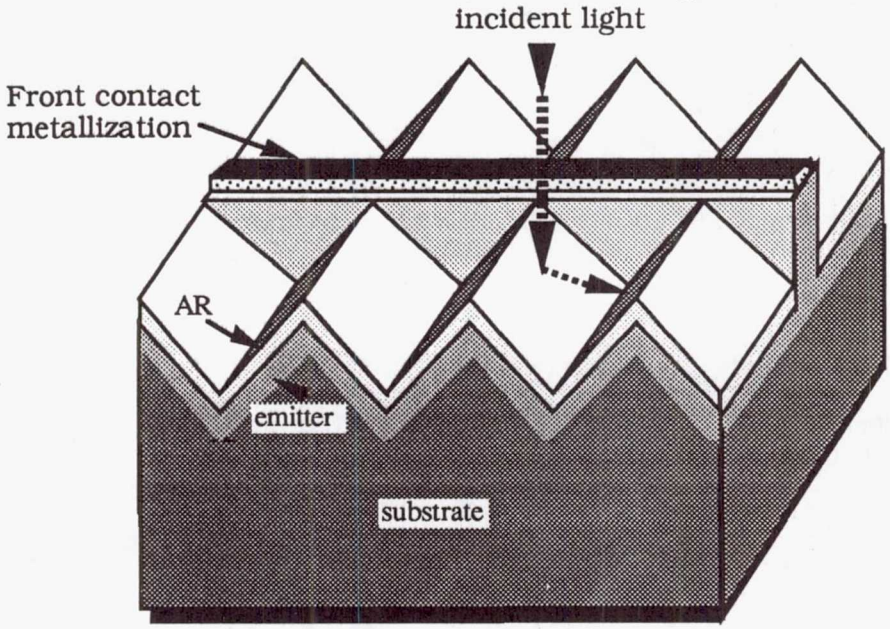


Figure 1. V-Grooved InP Solar Cell.

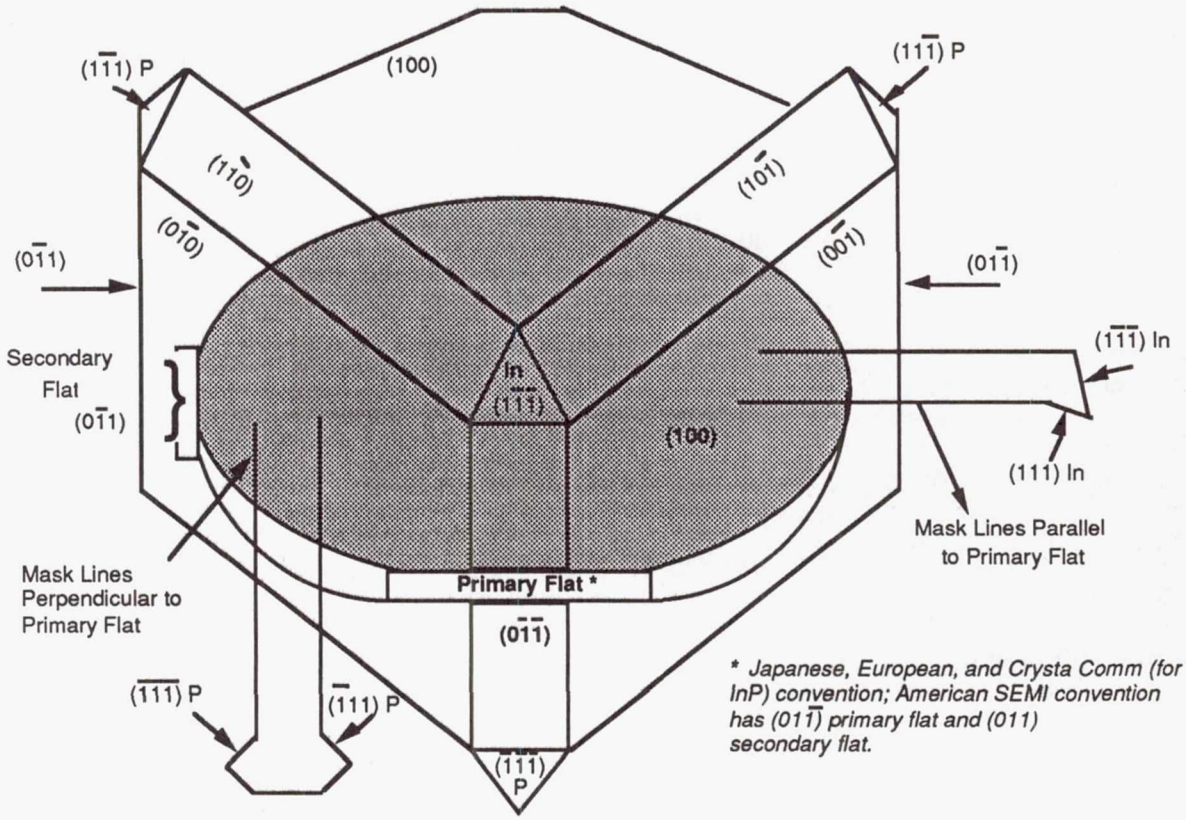


Figure 2. Orientation of InP wafer and mask lines for desired geometries

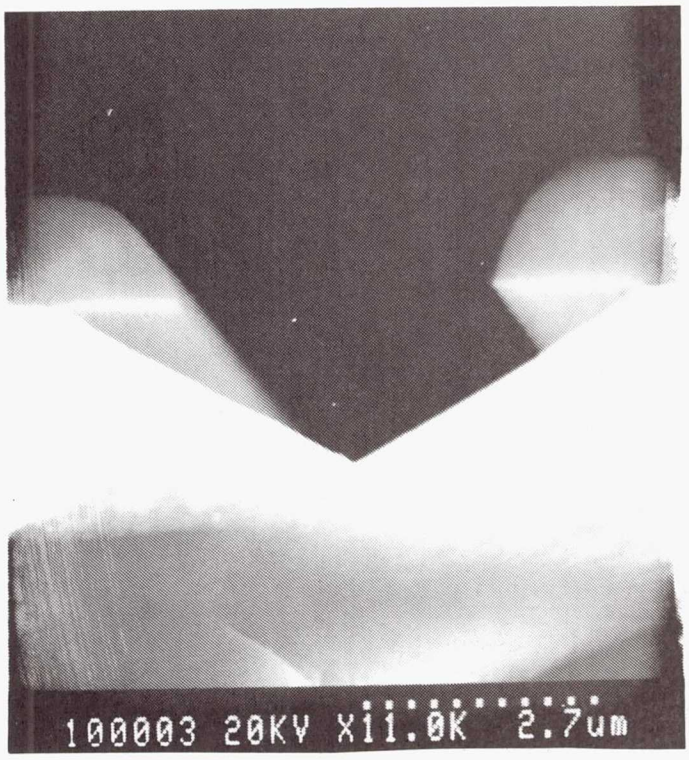


Figure 3. InP (Zn: 2E16 $cm^{-3}$) etched in HCl

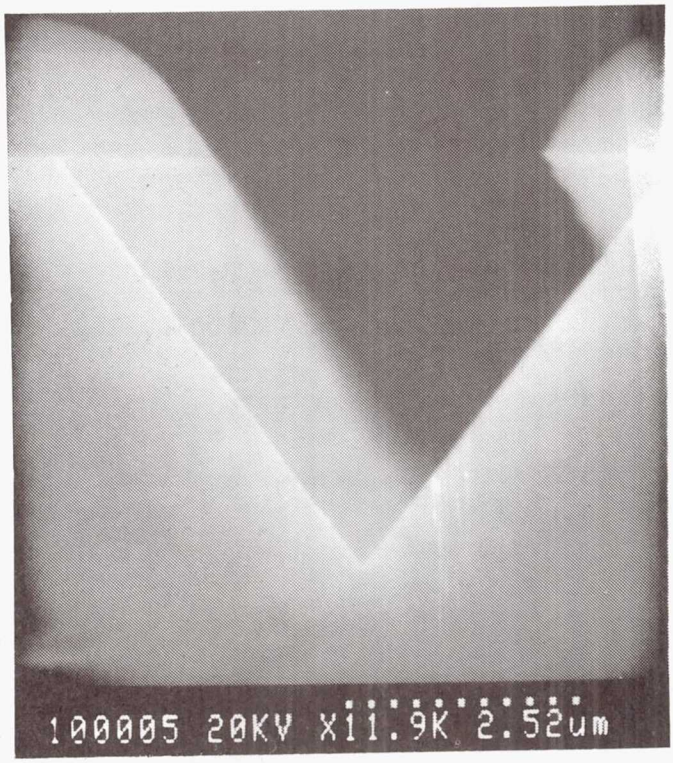


Figure 4. InP (Zn: 2E16 $cm^{-3}$) etched in $10HBr:1H_2O_2:1HCl$

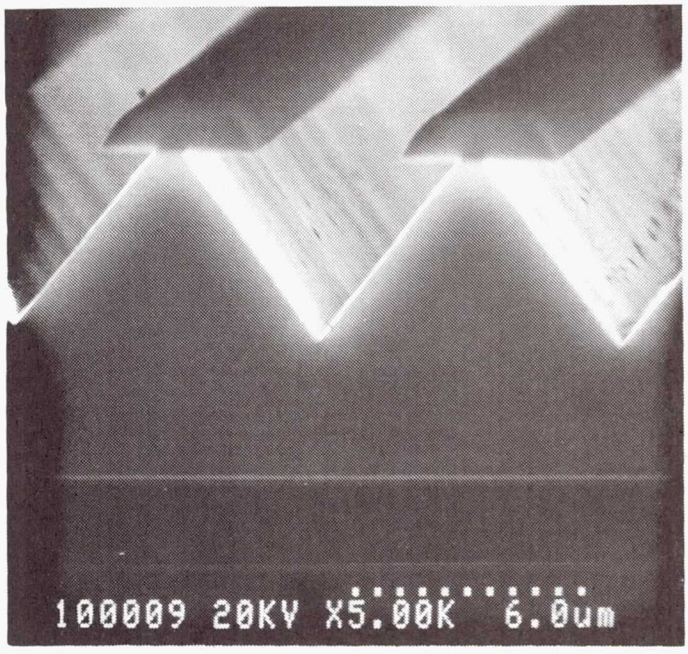


Figure 5. InP (Zn: 2E16 $cm^{-3}$) with native oxide; etched 6 minutes

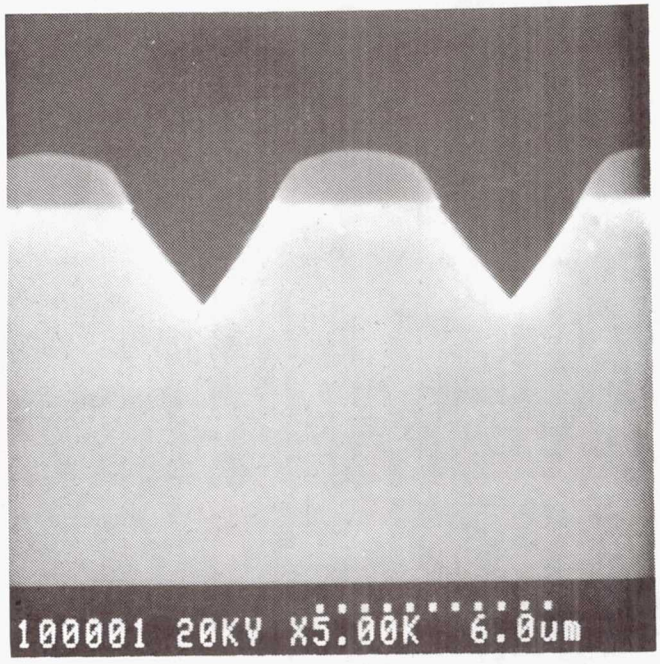


Figure 6. InP (Zn: 2E16 $cm^{-3}$) without oxide; etched 10 minutes

## EFFECT OF CARRIER CONCENTRATION

The etching results are also influenced by the carrier concentration, as is shown in Figures 7 and 8. Anisotropic etching can be achieved for all substrates with carrier concentrations lower than 1E18 $cm^{-3}$. Substrates with carrier densities greater than 1E18 $cm^{-3}$ etch anisotropically at the initial stage of etching, but rapidly become isotropic. The mask lines in this case parallel the primary flat illustrated in Figure 2.

The orientation of the photoresist stripes is also important. When the mask lines are perpendicular to the primary flat, the resulting geometries are shown in Figures 9 and 10. Again, the etching changes from isotropic to anisotropic when the carrier concentration increases, however, as expected, in neither case is a V-grooved profile obtained.

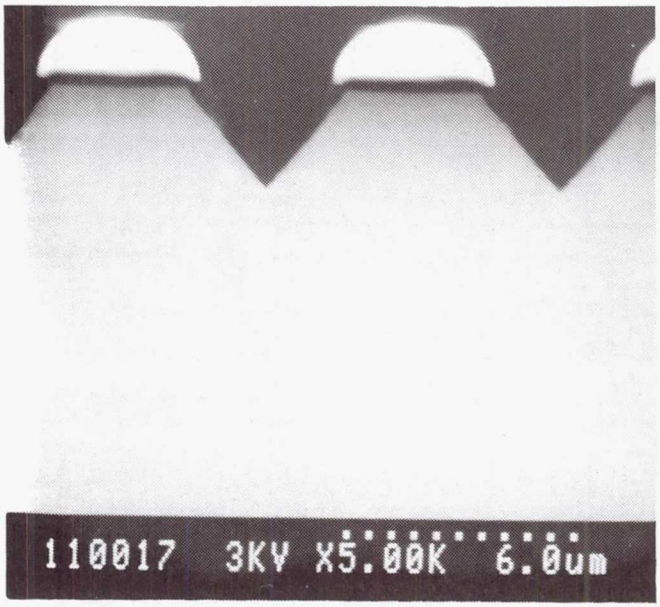


Figure 7. $[011\bar{1}]$ direction; Zn: 4E17 $cm^{-3}$ etched 1 minute

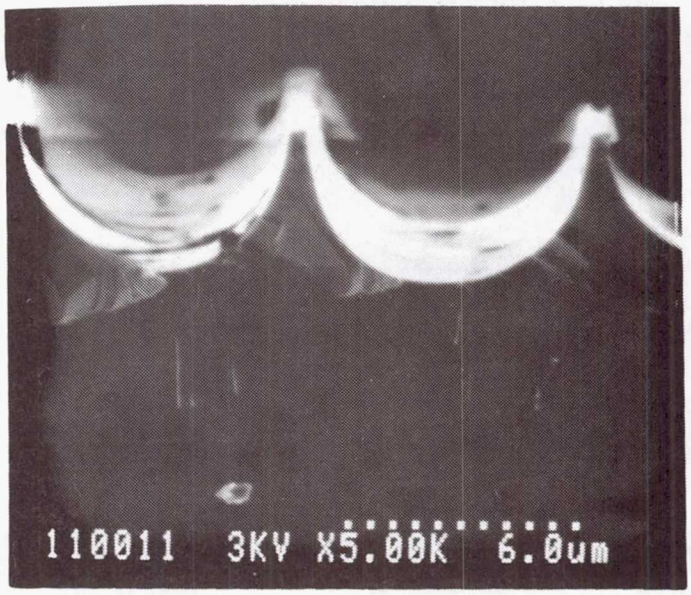


Figure 8. $[0\bar{1}\bar{1}]$ direction; Zn:1.5E18$cm^{-3}$ etched 1 minute

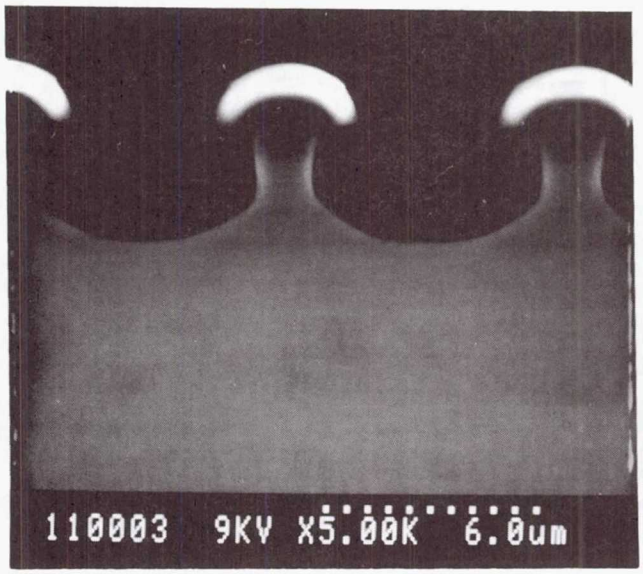


Figure 9. $[01\bar{1}]$ direction; Zn: 4E17$cm^{-3}$; etched 1.5 minutes

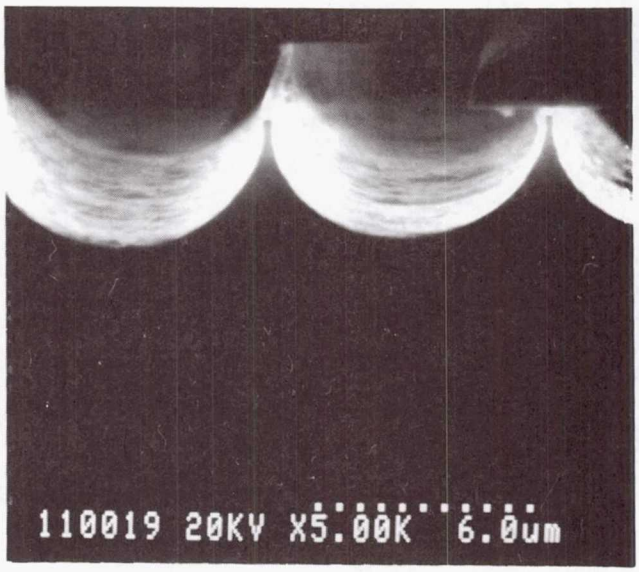


Figure 10. $[0\bar{1}\bar{1}]$ direction; Zn: 1.5E18$cm^{-3}$; etched 1.5 minutes

The etching time has a dramatic effect on the surface geometry of samples with carrier concentrations greater than 1E18 $cm^{-3}$. The rate of lateral versus vertical etching can be controlled on samples with lower concentrations to produce a complete saw tooth, with the vertical depth of etching controlled by the mask line widths and spacing. However, in the case of samples with higher concentrations, the effect of etching time is marked by a change from anisotropic to isotropic etching. This is shown in Figures 11 and 12.

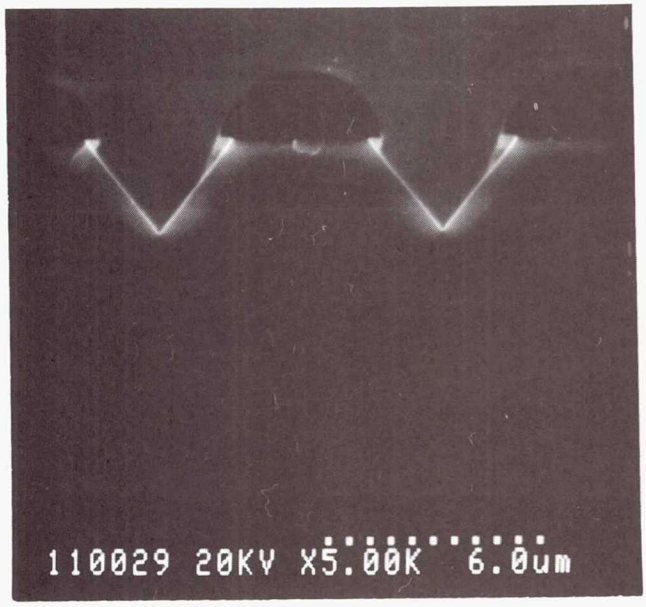


Figure 11. $[01\bar{1}]$direction; Zn: 1.5E18$cm^{-3}$; etched 30 seconds

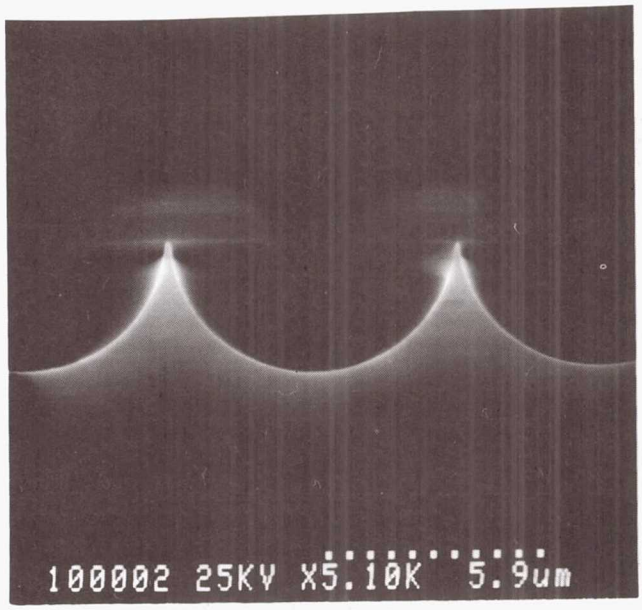


Figure 12. $[0\bar{1}\bar{1}]$ direction; Zn: 1.5E18$cm^{-3}$; etched 60 seconds

## UNMASKED V-GROOVES

It is also possible to produce low-angle V-grooves on InP without a photoresist mask [Ref. 6]. The low-angle groove process uses concentrated HCl (assay 37%) as an etchant at 17°C in room light. The grooved surface produced by this process is shown in Figure 13. Approximately 100 microns of InP are removed before grooves of approximately 2.4 μm cover the entire surface. This effect is not dependent on the carrier concentration or type. These grooves are approximately 23.2° with respect to the (100) plane which is typical of the (311) plane which is preferentially exposed by an HCl etchant.

These low-angle V-grooves can also be used to decrease the surface reflectivity in solar cells which include a glass cover. This effect is achieved by the use of total internal reflection at the air/coverglass interface [Ref. 6].

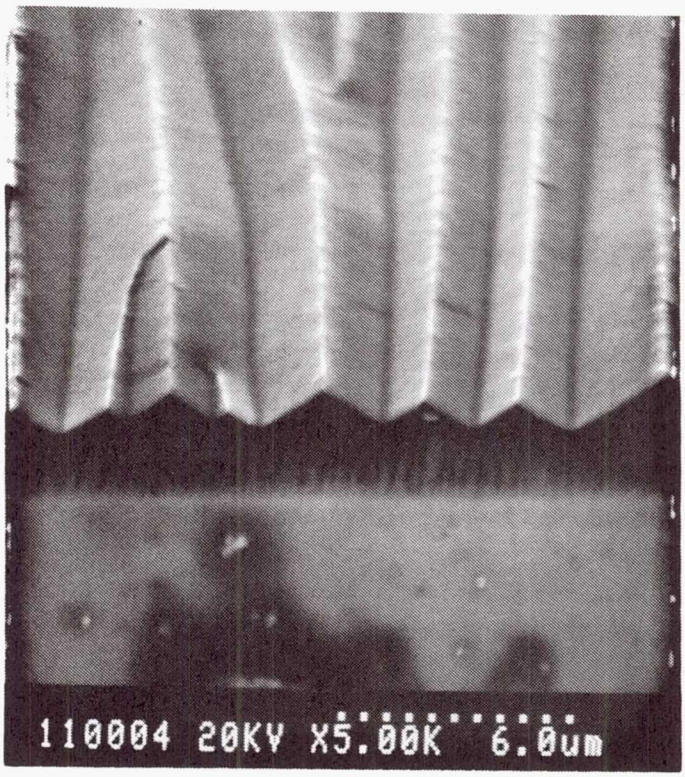


Figure 12. SEM image of low-angle V-grooves formed after etching InP in concentrated HCl

## CONCLUSIONS

Geometric etching can be controlled in InP by an appropriate choice of etchant and mask orientation. The conditions required for a given geometry are dependent on the dopant concentration and oxide thickness between photoresist and substrate. There is a transition from anisotropic to isotropic etching when substrate carrier concentrations exceed $10^{18}/cm^3$. Recent work has indicated that isotopic profiles are possible in InP when a diffusion-controlled reaction dominates [Ref. 5]. The lateral etch rate was found to be strongly dependent on the surface conditions. The desired sharp-topped (111) V-grooves are most readily achieved with an etchant of 10HBr:1 $H_2O_2$:1 HCl at -20°C. An alternative maskless process in HCl can be used to produce low-angle (311) grooves.

## REFERENCES

1. S. G. Bailey, G. A. Landis, and D. M. Wilt, *J. Electrochem. Soc.*, Vol 136, No. 11, Nov. 1989, pp. 3444-3449.

2. S. G. Bailey, N. S. Fatemi, G. A. Landis, D. J. Brinker, *Proceedings of the Second International Conference on Indium Phosphide and Related Materials*, 1990, pp. 73-79.

3. T. D. Lowes and D. T. Cassidy, *J. Appl. Phys.* **68** (2), July, 1990, pp. 814-819.

4. J. van de Ven, J. J. M. Binsma, and N. M. A. de Wild, *J. Appl. Phys.* **67** (12), June, 1990, pp. 7568-7571.

5. P. H. L. Notten, *J. Electrochem. Soc.*, Vol. 138, No. 1, January, 199l, pp. 243-249.

6. P. Jenkins and G.A. Landis, *3rd Int. Conf. on InP and Related Compounds,* Cardiff, Wales, Apr. 1991.

# EFFECT OF DISLOCATIONS ON PROPERTIES OF HETEROEPITAXIAL InP SOLAR CELLS

I. Weinberg, C. K. Swartz, H. B. Curtis and D. J. Brinker
NASA Lewis Research Center
Cleveland, Ohio

P. Jenkins and M. Faur
Cleveland State University
Cleveland, Ohio

## ABSTRACT

The apparently unrelated phenomena of temperature dependency, carrier removal and photoluminescence are shown to be affected by the high dislocation densities present in heteroepitaxial InP solar cells. Using homoepitaxial InP cells as a baseline, it is found that the relatively high dislocation densities present in heteroepitaxial InP/GaAs cells leads to increased values of dVoc/dt and carrier removal rate and substantial decreases in photoluminescence spectral intensities. With respect to dVoc/dt, the observed effect is attributed to the tendency of dislocations to reduce Voc. Although the basic cause for the observed increased in carrier removal rate is unclear, it is speculated that the decreased photoluminescence intensity is attributable to defect levels introduced by dislocations in the heteroepitaxial cells.

## INTRODUCTION

Several research programs, now underway, are aimed at producing InP solar cells from thin layers of InP epitaxially deposited on cheaper, more durable substrates (refs. 1,2,3). The motivation for this research lies in the high cost and relative fragility of InP. Efforts to date have focused on the use of Si and GaAs substrates. Although intervening lattice matching layers have been used , the lattice constant mismatch between InP and these foreign substrates introduces dislocations which tend to adversely affect cell performance. It is anticipated that the adverse effect of dislocations will eventually be minimized. However, in the present state of the art, dislocations are a dominant factor in adversely affecting cell performance and in contributing to increased radiation resistance (refs. 1,3,4). Although information exists concerning the effects of dislocations on cell performance and radiation resistance, little or nothing is known concerning their effects on such cell properties as temperature dependence, carrier removal and photoluminescence spectral intensities. The present paper is concerned with our initial results concerning the effects of dislocations on these properties.

## EXPERIMENTAL DETAILS

The cells were produced by organo-metallic vapor phase epitaxy (OMVPE) at the Spire Corporation under contract to NASA Lewis. Both homoepitaxial and heteroepitaxial n+p+ cells were processed, the latter consisting of InP cells on GaAs substrates. Etch pit densities, determined by electrochemical etching, were $4X10^7$ $cm^{-2}$ for the heteroepitaxial cells

and $4X10^3$ $cm^{-2}$ for the homoepitaxial cells. Performance parameters of both cell types are listed in table I. Temperature dependencies were determined over a range from 25 to 75°C. Over this temperature range, a pulsed Xenon arc solar simulator was used to determine cell performance. Carrier concentrations were determined by capacitance-voltage (C-V) measurements after irradiation by 10 MeV protons in the Lewis cyclotron. Photoluminescence (PL) spectra were obtained at 11 and 298K. The PL spectrometer covered the wavelength range from 850 to 3000 nm while the excitation wavelength was 514 nm.

## RESULTS AND DISCUSSION

### Temperature Dependencies

The temperature dependency of Voc, from 25 to 75°C is shown in fig.1. With the exception of Isc (fig.2) all of the parameters shown in table I were linear over this temperature range. The non-linear behavior of Isc is consistent with our previous data obtained over a much wider temperature range (ref. 5). A summary of temperature dependencies at 328 K is shown in table II. This temperature was chosen to avoid the non linearity in Isc. In addition, it falls within the temperature range of several space orbits of interest. As seen from the table, the temperature dependencies of all parameters, except Voc, are equal within the standard deviations. Clearly, dVoc/dT is greater for the heteroepitaxial cell.

The temperature dependency of Voc can be discussed using the relation (ref. 6),

$$dVoc/dT = ((Voc-Eg(T))/T) - 3k/q - \alpha\, T(T+2\beta)/(T+\beta)^2 + (kT/qIsc)(dIsc/dT) \quad (1)$$

where Eg(T) is the bandgap at temperature T, k is the Boltzmann constant, while $\alpha$ and $\beta$ are constants in the expression

$$Eg(T) = Eg(0) - \alpha\, T^2/(T+\beta) \quad (2)$$

Eg(0) is the bandgap at 0 K (1.421 eV) and $\alpha = 6.63X10^{-4}$ ev/K with $\beta$ = 552 K (ref. 5). Values calculated for dVoc/dT, at 328 K, are shown in table III where it is seen that the measured and calculated values differ by 9.7 and 13% for the homoepitaxial and heteroepitaxial cells respectively. Despite this, equation 3 is useful in correlating values of Voc with its temperature coefficient. Detailed calculations indicate that the first term in equation 3 is dominant. Hence cells with higher values of Voc should have smaller values for dVoc/dT. The data of table III is in agreement with this prediction. Furthermore, since increased dislocation densities result in smaller values of Voc (ref.7) the data, and equation 1, tend to support the conclusion that increased dislocation densities result in higher values of dVoc/dT.

### Carrier Removal

Carrier removal, after 10 MeV proton irradiations, is shown in fig.3. The carrier removal rate is obtained using the relation,

$$\Delta p = R_c \phi \quad (3)$$

where the $\Delta p$ are carriers removed at the fluence $\phi$ and Rc is the carrier removal rate. From (3) a slope of one is indicated for the plot shown in the figure. Since this is indeed the case, Rc can be determined from points on the straight lines of fig.3. The results shown in table IV indicate that the cell with the highest dislocation density has the highest carrier removal rate. Although the increased carrier removal is correlated with the increased dislocation density, the basic mechanism responsible for this effect is unclear at present.

Photoluminescence

The photoluminescence spectrum of an unirradiated InP/GaAs cell, at 11 K, is shown in fig.4. The peaks at 1.382 eV and 1.419 eV are attributed to the conduction band to acceptor and interband radiative transitions respectively. The remaining peak is the so called phonon replica of the conduction band-acceptor peak. Except for additional structure in the interband peak, the peak positions and slope of the homoepitaxial cell are similar to those shown in fig.4. The relative intensities, at 11 K, for each spectral component, except the phonon replica, are shown in fig.5. It is readily seen that the intensities for each component of the heteroepitaxial cell are at least an order of magnitude less than the spectral intensities for the homoepitaxial cell. The room temperature peaks of fig.6 confirm the tendency for the cell with greatly increased dislocation density to exhibit a considerably reduced photoluminescence intensity. The decreased intensity for the heteroepitaxial cell can be attributed to the presence of additional transitions outside the range of the spectrometer and/or to additional non-radiative transitions, both effects attributed to the effects of dislocations. In either case, it is assumed that the undetectable transitions are to defects caused by the increased presence of dislocations in the heteroepitaxial cells. It is noted that we have been unable to find evidence, in the literature, for the presence of additional defects,due to dislocations in p-type InP. However, for n-type InP, DLTS measurements indicate the presence of defects attributable to the presence of dislocations (refs. 8,9). Lacking such evidence for the p-type base of the InP/GaAs cell we tentatively assume the presence of additional defects due to the high dislocation density in this cell.

## CONCLUSION

The present data indicates that large differences in dislocation density lead to increased values of dVoc/dT and carrier removal rate together with a drastic decrease in photoluminescence intensity. Considering the limited data set, it is perhaps premature to overgeneralize concerning the effects of dislocations on these quantities. On the other hand, the present data set tends to indicate that the increased value of dVoc/dT is due to the tendency of dislocations to reduce minority carrier diffusion length and thus Voc. Considering photoluminescence, it is speculated that the decreased intensity in the heteroepitaxial cells is due primarily to defects associated with the increased dislocation density. However, the basic cause of the increased carrier removal rate is relatively unclear at present.

## REFERENCES


1. C. Keavney, S. Vernon and V. Haven, "Tunnel Junctions for InP-on -Si Solar Cells," Proceedings 11th Space Photovoltaic Research and Technology Conf., NASA Lewis Research Center, May 7-9,1991, to be Published.

2. M. W. Wanlass, T. J. Coutts, S. S. Ward, K. A. Emery and G. S. Horner, "High Efficiency, Thin-Film InP Concentrator Cells," Proceedings 3rd Int'l Conf. on InP and Related Materials, Cardiff, Wales, April 8-11, 1991, IEEE to be Published.

3. T. J. Coutts, M. W. Wanlass, T. A. Gessert, X. Li and J. S. Ward, "Progress in InP-Based Solar Cells," Ibid 1991.

4. I. Weinberg, C. K. Swartz, D. J. Brinker and D. M. Wilt, "Effects of Radiation on InP Cells Epitaxially Grown on Si and GaAs Substrates," Proceedings 21st IEEE Photovoltaic Specialists Conf., p 1235, 1990.

5. I. Weinberg, C. K. Swartz, R. Hart, Jr., and R. L. Statler,"Radiation and Temperature effects in Gallium Arsenide, Indium Phosphide and Silicon Solar Cells," Proceedings 19th IEEE Photovoltaic Spec. Conf.,p548, 1987.

6. J. C. C. Fan, "Theoretical Temperature Dependence of Solar Cell Parameters," Solar Cells 17, p309, 1986.

7. M. Yamaguchi, A. Yamamoto, N. Uchida and C. Uemura "A New Approach for Thin Film InP Solar Cells," Solar Cells 19 p 85, 1986-1987.

8. A. Zozime and W. Schroter, "Deep Levels Associated with and Dislocations in p-Type InP," Appl. Phys. Lett. 57, p1326, 1990.

9. M. Sugo, Y. Takanashi M. M. Al-jassim and M. Yamaguchi, "Heteroepitaxial Growth and Characterization of InP on Si Substrates," J. Appl. Phys. 68, p 540, 1990.

**TABLE I. CELL PARAMETERS AT 298K**

| CELL TYPE | NUMBER OF CELLS | Jsc $mA/cm^2$ | Voc (mV) | FF (%) | EFFICIENCY % |
|---|---|---|---|---|---|
| InP/InP | 4 | 32.3±0.1 | 0.874±.001 | 83.3±1.4 | 17.1±0.3 |
| InP/GaAs | 4 | 28±0.2 | 0.7±.006 | 69.8±3.9 | 10±0.6 |

**TABLE II. CELL TEMPERATURE COEFFICIENTS AT 328K**

| CELL | $dP_M/dT$ $mW/cm^2K$ | dVoc/dT mV/K | dIsc/dT $mA/cm^2K$ | dFF/dT %/K |
|---|---|---|---|---|
| InP/InP | $-(5.46\pm.21)X10^{-2}$ | -2.07±.02 | $+(2.21\pm.4)X10^{-2}$ | $-5.43\pm1.56$ $X10^{-2}$ |
| InP/GaAs | $-(5.63\pm.25)X10^{-2}$ | -2.51±.01 | $+(1.99\pm.11)X10^{-2}$ | $-7.5\pm1.97$ $X10^{-2}$ |

**TABLE III. CALCULATED AND MEASURED VALUES OF dVOC/dT**

| CELL | EPD $cm^{-2}$ | Voc mV | Voc/dT(mv/K) MEASURED | CALCULATED |
|---|---|---|---|---|
| InP/InP | $4 X 10^3$ | 874±1 | -2.07±.02 | -2.27±.01 |
| InP/GaAs | $4 X 10^7$ | 700±6 | -2.51±.02 | -2.84±03 |

**TABLE IV. CARRIER REMOVAL RATES AFTER 10 MeV PROTON IRRADIATION**

| CELL | REMOVAL RATE $cm^{-1}$ | EPD $cm^{-2}$ |
|---|---|---|
| InP/GaAs | $8.8 \times 10^2$ | $4 \times 10^7$ |
| InP/InP | $5 \times 10^2$ | $4 \times 10^3$ |

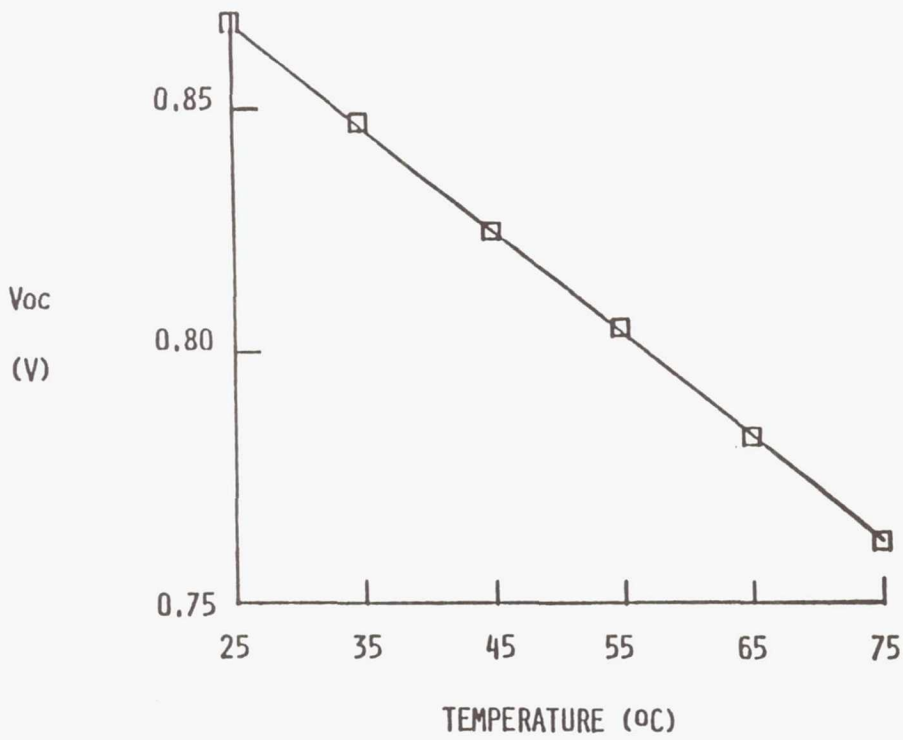


FIGURE 1 - TEMPERATURE DEPENDENCE OF OPEN CIRCUIT VOLTAGE (InP/InP CELL)

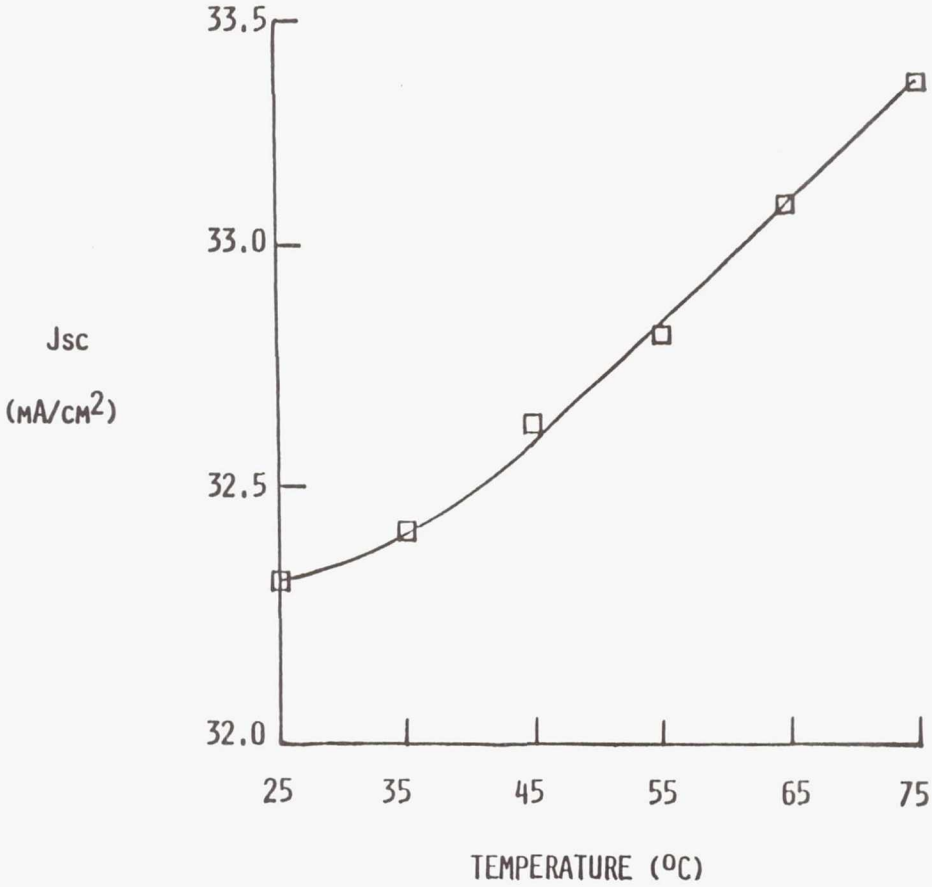


FIGURE 2 - TEMPERATURE DEPENDENCE OF SHORT CIRCUIT CURRENT (InP/InP CELL)

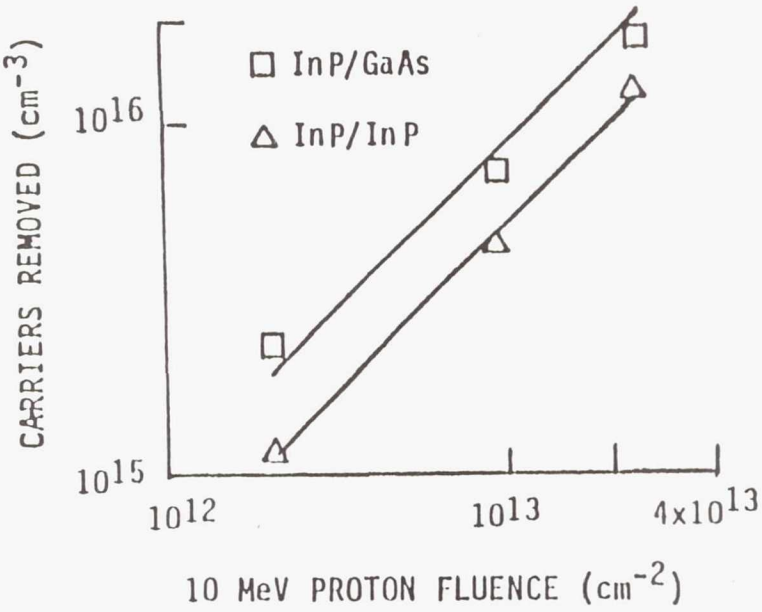


FIGURE 3 - CARRIER REMOVAL BY 10 MeV PROTONS

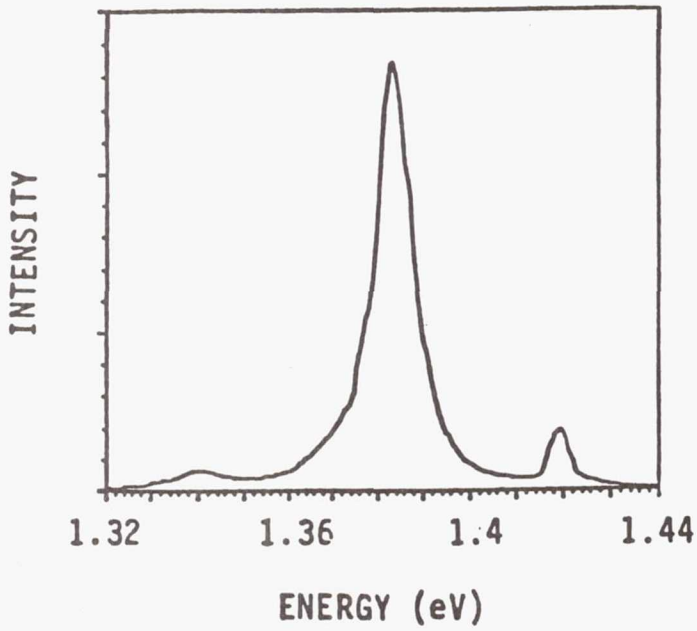


FIGURE 4 - PHOTOLUMINESCENCE AT 11 K
(InP/GaAs CELL)

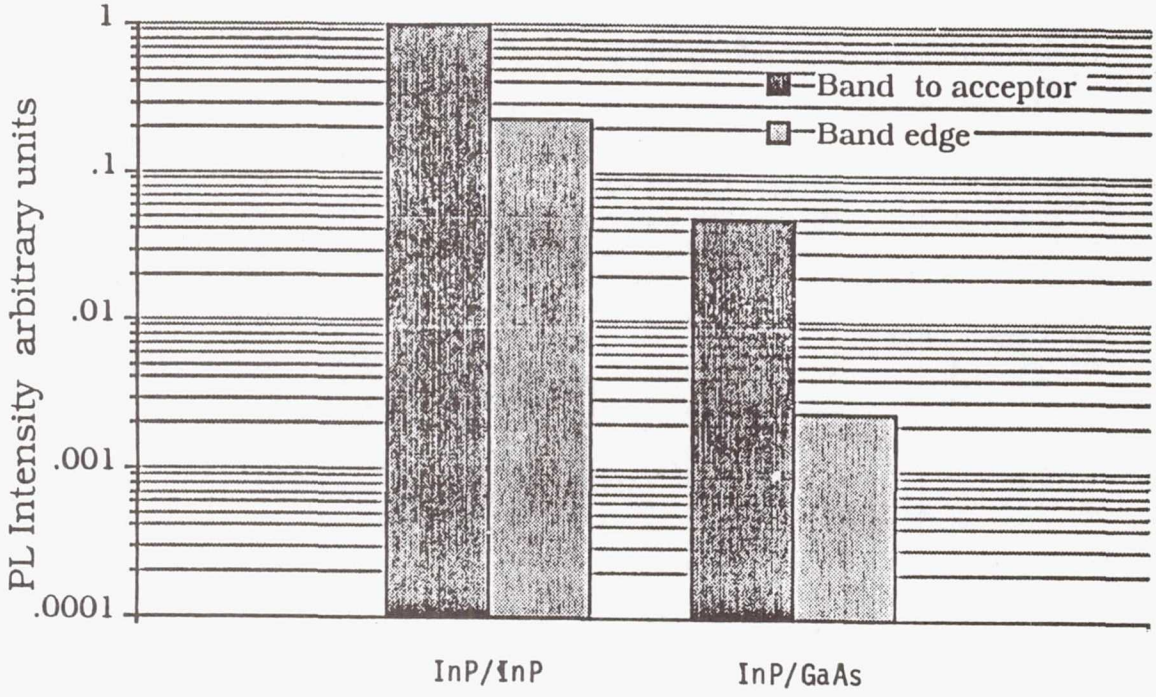


FIGURE 5 - RELATIVE INTENSITIES AT 11 K

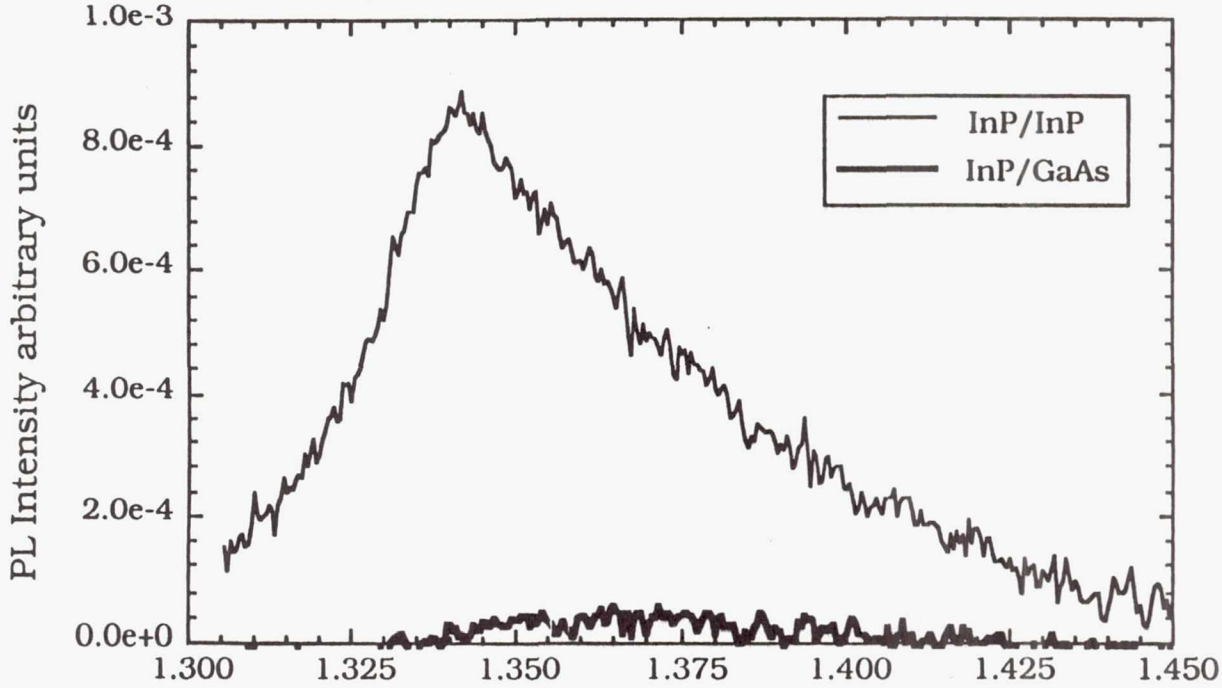


FIGURE 6 - ROOM TEMPERATURE PHOTOLUMINESCENCE

# High Resolution Electrolyte for Thinning InP by Anodic Dissolution and its Applications to EC-V Profiling, Defect Revealing and Surface Passivation

Maria Faur, Mircea Faur, Irving Weinberg*,
Manju Goradia and Carlos Vargas**

Space Photovoltaic Research Center***, Electrical Engineering Department
Cleveland State University, Cleveland, Ohio 44115

*NASA Lewis Research Center, Cleveland, Ohio 44135
**Kent State University, Kent, Ohio 44242

## ABSTRACT

An extensive experimental study was conducted using various electrolytes based on HCl, o-$H_3PO_4$, $H_2SO_4$, $HIO_3$, $HNO_3$, HF, $CH_3COOH$, $H_2O_2$ and $NH_4OH$ in an effort to find an appropriate electrolyte for anodic dissolution of InP. From the analysis of electrochemical C-V, $1/C^2$-V, G-V, I-V characteristics in the dark and under different illumination levels, X-ray Photoelectron Spectroscopy and SEM/Nomarski inspection of the surfaces, we have determined that the anodic dissolution of InP front surface layers by FAP electrolyte is a very good choice for rendering smooth surfaces, free of oxide and contaminants and with good electrical characteristics.

After experimentation with a fairly large number of p, n, $p^+$, $n^+$ Czochralski LEC/VGF grown InP substrates and $n^+p$ and $p^+n$ InP structures made either by thermal diffusion or epitaxy, the FAP electrolyte based on HF, $CH_3COOH$ and $H_2O_2$ appears to be inherently superior to previously reported electrolytes (i.e., 0.5M HCl and the pear etch) for performing accurate EC-V profiling of InP at current densities of up to 0.3 $mA/cm^2$. It can also be used for accurate electrochemical revealing of either precipitates or dislocation density with applications to EPD mapping as a function of depth, and for defect revealing of multilayer InP structures at any depth and/or at the interfaces. Owing to its inherent qualities, the FAP electrolyte can also be used, with good results, for surface passivation of InP prior to deposition of an insulator or antireflective coating.

## INTRODUCTION

One of the major problems yet to be solved in InP device technology is to remove, in a controlled manner, the contaminated and/or damaged surface layers due to processing steps such as masking, doping and annealing, in such a way that smooth surfaces with good electrical characteristics are obtained.

***Funded by NASA Lewis Research Center

For most semiconductors, including InP, simple chemical etching does not yield smooth surfaces with good electrical characteristics. Thinning the damaged surface layers of InP by plasma etching so as to obtain smooth surfaces is also not easily achieved due to preferential sputtering at the defect areas.

Anodic dissolution [1] can be successfully used for controlled thinning of surface layers, providing that a proper electrolyte and processing parameters are selected. For InP, none of the previously reported electrolytes such as 0.5M HCl [2] and the pear etch [3] seem to satisfy the criteria of an ideal electrolyte. They either dissolve InP preferentially at the defect areas, and/or form insoluble products on the surface. This makes the thinning process dependent on the surface chemistry and, therefore hard to control.

Thinning InP surfaces by anodic dissolution occurs via an anodic oxidation-dissolution process. The choice of the electrolyte is therefore crucial if smooth surfaces, free of contaminants and oxide, and with good electrical characteristics are desired. The electrolyte should contain both an oxidizing and a reducing component, chosen such that both elemental species of InP are nearly equal during dissolution. In other words, it should not promote preferential oxidation at the dislocation areas [4] or form stable oxide species on the surface [1].

From a fairly large number of new electrolytes we have tried in this study we have selected the so called "FAP" electrolyte [5], which proved to be inherently superior to previously reported electrolytes know to us, for thinning the heavily damaged $n^+$ and $p^+$ front layers of thermally diffused $n^+p$ and $p^+n$ InP structures [6]. In this study we investigated the use of this new electrolyte for other applications where smooth surfaces are required (e.g. electrochemical C-V (EC-V) profiling and surface passivation of InP), as well as for exposing the structural defects (precipitates and etch pit densities) at a given depth of front $n^+$- or $p^+$-InP layers.

Other studies using the FAP electrolyte, presently still under investigation include:

1. Photocapacitance spectroscopy.

2. Determination of surface state density of InP.

3. The use of this and/or related electrolytes for material characterization and/or processing of other III-V compounds.

## EXPERIMENTAL

We have conducted an extensive experimental study using various electrolytic solutions based on HCl, o-$H_3PO_4$, $H_2SO_4$, $HIO_3$, $HNO_3$, HF, $CH_3COOH$, $H_2O_2$ and $NH_4OH$ in an effort to find an appropriate electrolyte for anodic dissolution of InP.

The experimental study was performed using a large number of:

(a) n, p, $n^+$ and $p^+$ Czochralski LEC grown InP substrates from Crystacomm, Inc. and Nippon Mining Co.;

(b) p-InP substrates grown by the VGF method, from AT & T;

(c) thermallly diffused $n^+p$ and $p^+n$ InP structures fabricated by us at the Cleveland State University.

(d) high quality epitaxially grown $n^+p$ InP structures from SPIRE Corporation.

The dissolution process and the quality of the surfaces after dissolution to different depths were characterized by:

(a) an analysis of C-V, $1/C^2$-V, G-V and I-V characteristics using a Polaron Model PN4200 profiler with an exposed area of 0.009 or 0.1025 $cm^2$;

(b) inspection of surface topography using Nomarski and SEM microscopy;

(c) Dektak inspection of the craters;

(d) and, on selected samples, X-ray Photoelectron Spectroscopy (XPS) study of the surface contaminants and oxidation stage after dissolution in different electrolytes.

## RESULTS AND DISCUSSION

As a result of this study, a new electrolyte, which we call the FAP electrolyte was developed for controlled thinning of InP resulting in smooth surfaces with good electrical characteristics and free of oxide and contaminants. The FAP electrolyte has successfully been used for accurate EC-V profiling, defect revealing and surface passivation of InP prior to growing deposition of the insulator or anti-reflective (AR) coating layers.

## ANODIC DISSOLUTION

Most of the processing steps used in fabrication of InP devices such as masking, diffusion and annealing, leave contaminated and/or damaged surface layers which are not desired if good quality devices are to be fabricated.

To limit our discussion we are going to refer here only to InP structures made by thermal diffusion used for fabrication of homojunction $n^+p$ or $p^+n$ InP solar cells. It is known that $n^+p$ or $p^+n$ InP structures made either by thermal diffusion or ion implantation have the surface stoichiometry destroyed. As an example, in the case of $n^+p$ InP structures made by closed-ampoule diffusion of sulfur into p-InP substrates, we have previously found that the phosphorus depleted dead layer can extend up to several hundred angstroms below the surface [7] and it strongly affects the solar cell performance parameters [8]. Therefore, an

important step in the fabrication of high performance InP solar cells or other devices using thermal diffusion or ion implantation consists of removing, in a controlled manner, the destroyed surface layer.

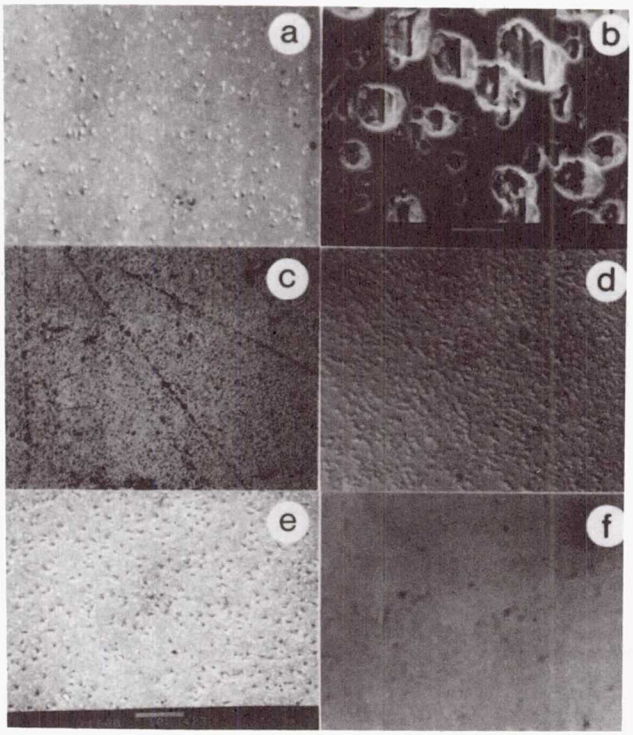


**Figure 1.** Nomarski and SEM micrographs of $n^+p$ InP surfaces: a) initial (x1,100), and after photoanodic dissolution to a depth of 0.3 µm using: b) 0.5 M HCl; c) 0.5 M $H_2SO_4$ (x1,100); d) 1MHF (x1,100); e) 1 M HF:0.5M HCl (1:1); and FAP electrolyte (x1,100) [1].

By using different electrolytes it has been reported [9, 10] that during anodic dissolution of InP or GaAs, reactive intermediates capable of injecting electrons into the conduction band expose crystal planes other than those initially found at the surface. Usually, smooth surfaces can be obtained only if both elemental species of the InP are nearly equal. Also, surface defects generally inhibit anodic dissolution of the semiconductors by enhancing the recombination rate of photogenerated holes.

In an effort to find a well suited electrolyte for anodic dissolution of high defect density $n^+p$ InP made by thermal diffusion [1], we have previously found that from a large number of possible combinations of oxidizing and reducing agents, the FAP electrolyte was the best answer [1]. As an example the micrographs presented in Figures 1 show the surface topography of the bottom of the craters after anodic dissolution to a constant depth of 0.3µm of high defect density $n^+p$ InP structures using selected electrolytes. The polarization was maintained in the dissolution region (anodically relative to $V_{fb}$) so as to yield an anodic current density of 0.3mA/cm$^2$. As seen, the smoothest surface is obtained using the FAP electrolyte. From the C-V and I-V characteristics, and XPS inspection it was also found that the resulting surfaces are free of oxides and contaminants.

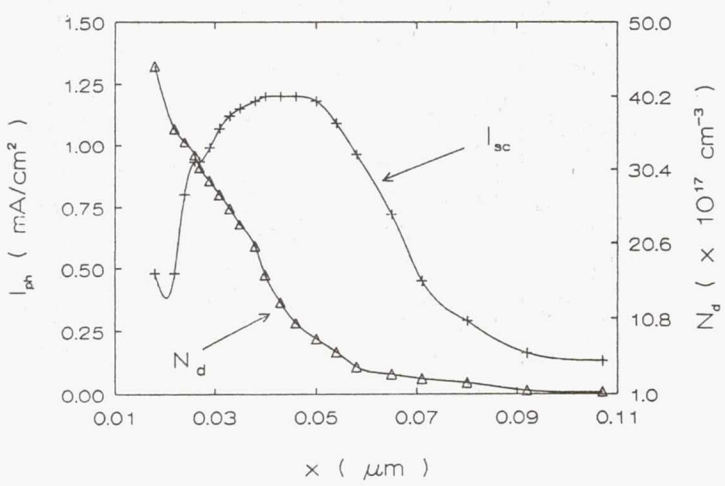


**Figure 2.** Variation of $I_{ph}$ and majority carrier concentration ($N_D$) as a function of dissolution depth after photoanodic dissolution at 0.2V bias voltage of the $n^+$ layer of structure in Figure 1a, using the FAP electrolyte.

For similar $n^+p$ InP structures as those used in connection with Figure 1, the effect of removing the highly damaged front $n^+$ layer using this electrolyte on

the quality of the emitter is evident in Figure 2 by the variation of the photoelectrochemical short circuit current at the FAP electrolyte InP liquid junction under a constant low level illumination. The Isc reaches a maximum after removal of about 400Å from the surface corresponding to a surface carrier concentration of about 2 x $10^{18}cm^{-3}$. Interestingly enough, AES profiling have shown in this case that the phosphorus depleted dead layer also extends to about 400Å below the surface [7].

## EC-V PROFILING

Electrochemical C-V (EC-V) profiling of semiconductors is probably the most used and convenient method for accurate determination of thermal equilibrium majority carrier concentration depth profiles. The accuracy of EC-V profiles of III-V compounds in general and InP in particular, is strongly dependent on the surface chemistry, structural defect density, electrolyte type, current density and illumination level. For a given InP structure the electrolyte plays an essential role. In choosing the electrolyte, several criteria should be met, such as:

1. It should make good rectifying contact to both p- and n-InP surfaces;

2. The electron number for p-and n-InP should be constant;

3. The chemical etch rate should be much smaller than the anodic dissolution rate;

4. The crater must have a smooth bottom, free of oxide, with straight walls and no rounding at the crater rim.

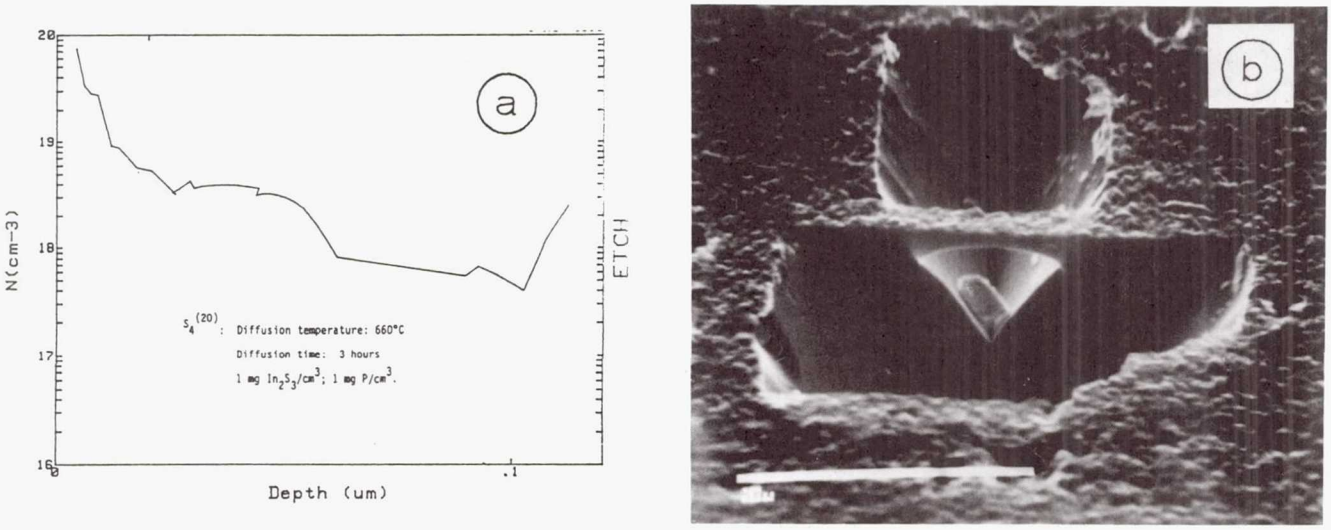


**Figure 3.** a) EC-V profile of a high defect density n⁺p InP structure using 0.5 M HCl; b) close-up view of the bottom of the crater.

EC-V profiling utilizes an electrolyte-semiconductor liquid junction for the C-V measurements where the electrolyte is also an anodic etchant for the material being profiled [11]. The depth profiling is accomplished by alternately dissolving the surface of the semiconductor

to some depth, thereby creating a crater-like etch profile, and then performing a low reverse bias C-V measurement.

None of the previously reported electrolytes, recommended for EC-V profiling of InP, such as 0.5M HCl [2] and the Pear etch [3] seem to satisfy the criteria of an ideal electrolyte because of one or more drawbacks such as: dissolving InP preferentially at the defect areas, forming insoluble products on the surfaces, producing rounding at the crater rim, introducing parasitic capacitance components at the electrolyte/semiconductor interface, etc., which result in inaccurate profiles.

This study was promoted by the necessity to record accurate EC-V depth profiles of high defect density $n^+p$ InP structures. Using the 0.5M HCl electrolyte, a typical EC-V profile of these $n^+p$ InP strucures is shown in Figure 3a. HCl based electroytes dissolve InP ppreferentially at the dislocation areas and since with this electrolyte the dissolution rate in dark for p-type InP is much higher than that of n-type InP, several micron deep pits are etched along the (111) planes before the thin (about 0.15 μm thick) $n^+$ layer is completely removed, as seen in Figure 3b. The large differences between the geometric and effective areas explain why the apparent carrier concentration values are over one order of magnitude higher than expected.

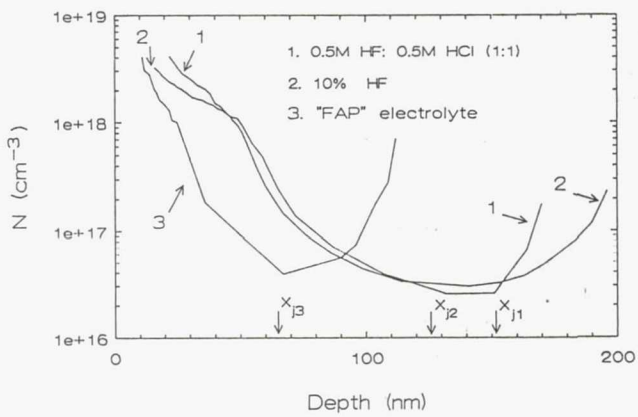


**Figure 4.** Comparison of EC-V profiles of an $n^+p$ InP structure using three different electrolytes.

The accuracy of all carrier concentration profiles derived from measurements of Mott-Schottky capacitances are critically dependent on the area of the semiconductor contact and its edge definition. Due to the square low dependence of $|N_D-N_A|$ on the barrier area, small differences between the geometric and effective areas due to i) rough bottoms or ii) rounding at the crater rim, as is the case with 0.5M HCl aqueous solutions, will give rise to large errors in calculated carrier concentration depth profiles such as that shown in Figure 3a.

Using 0.5M HF:0.5M HCl (curve 1) or 10% HF (curve 2) electrolytes, as seen in Figure 4, we observe an improvement in the quality of the EC-V profiles of $n^+p$ InP structures similar to the ones discussed in Figure 3a. The apparent junction depths ($x_{j1}$ and $x_{j2}$) were still about twice than the expected value since these electrolytes still dissolve InP preferentially at the dislocation areas. Using the FAP electrolyte (curve 3), we claim the EC-V profile to be very close to the real one since all the requirements of good EC-V profiling mentioned before, are met.

Figure 5 shows the view of the craters after EC-V profiling of thermally diffused $p^+n$ InP structures with low dislocation density [12]

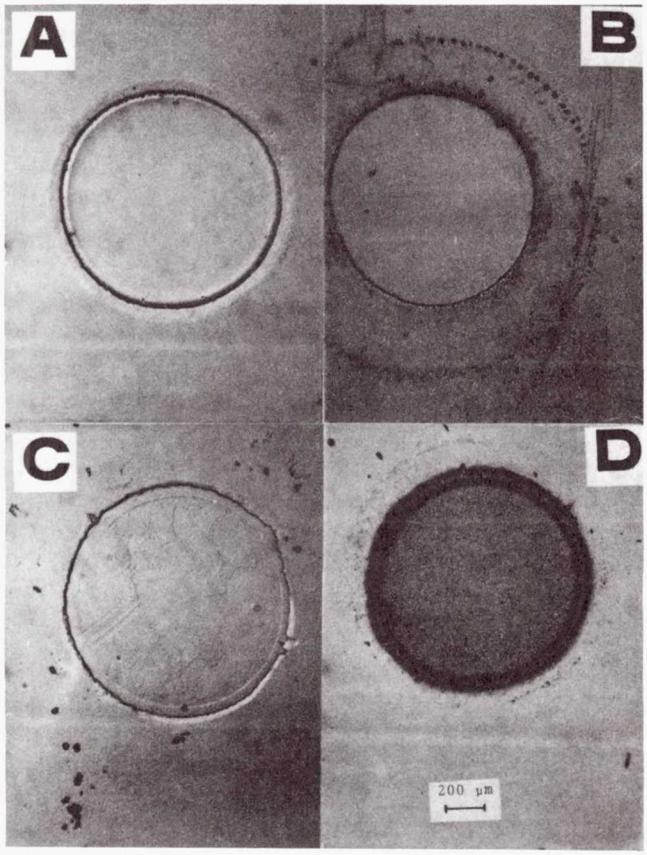


**Figure 5.** Nomarski view of the craters formed in good quality p⁺n InP structures after EC-V profiling using: (A) the FAP electrolyte; (B) 0.5M HCl; (C) the Pear etch (in $H_2O$); (D) the Pear etch (in $CH_3OH$).

made by Cd diffusion into n-InP:S ($N_D = 3.5 \times 10^{16} cm^{-3}$) using four different electrolytes. We have also done a SEM inspection of the bottom of craters and verified that the smoothest surface is obtained by using the FAP electrolyte as seen in Figure 5A. Dektak profiles of the craters of Figure 5 shown in Figure 6 indicate that using the FAP electrolyte, the crater walls are straight with no rounding at the crater rim (as is seen to be the case for 0.5M HCl solution) and the crater bottom is flat. This, associated with very low parasitic capacitance components, explains the excellent agreement between the depth obtained by a dektak measurement and that calculated from the integrated current density of anodic dissolution using the FAP electrolyte.

In choosing a good electrolyte for the EC-V profiling, the C-V characteristics of the semiconductor-electrolyte interface must approximate a Schottky barrier over a reasonable voltage range such that the overall interface capacitance, C, is given by the well-known equation [11]:

$$1/C^2 = 2(V_{fb}-V-kT/q)/q\varepsilon\varepsilon_o|N_D-N_A| \quad (1)$$

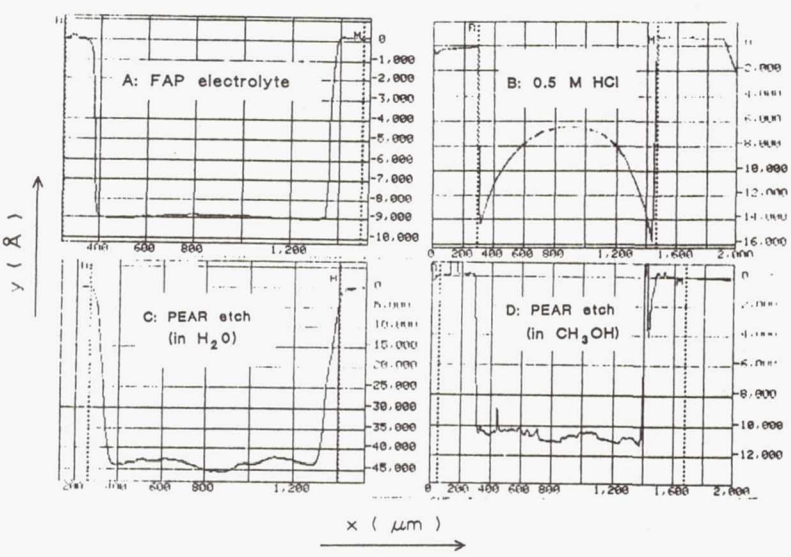


**Figure 6.** Dektak profiles of craters shown in Figure 5.

i.e. effects due to electrolyte, surface oxide layer, or surface states on the capacitance should be negligible. This is the case for the FAP electrolyte as shown in Figure 7 which shows C-V, $1/C^2$-V, G-V and I-V characteristics of a good quality p⁺n InP structure [12]. The characteristics of Figure 7 were done after removal of the front oxide layer (≈ 30Å). One can see from Figure 7 that the FAP electrolyte is a very good choice for EC-V profiling of InP as compared to 0.5M

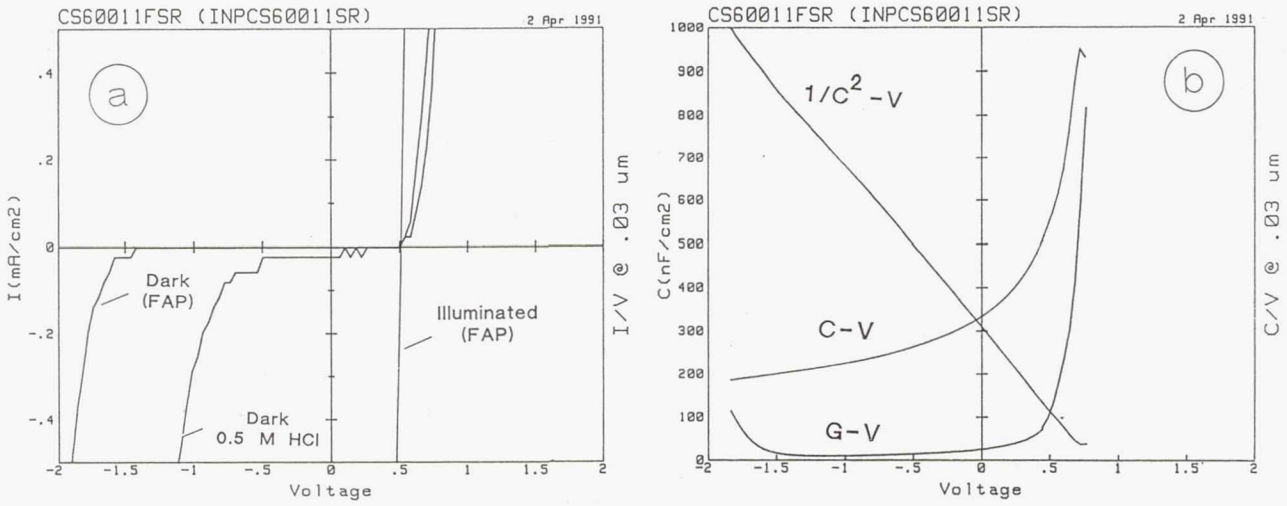


**Figure 7.** a) I-V characteristics of a good quality $p^+n$ InP structure using the FAP and 0.5 M HCl electrolytes; b) Electrochemical C-V, $1/C^2$-V and C-V characteristics at a frequency of 3 kHz using the FAP electrolyte after removal of 0.03 μm from the surface.

HCl solution. Although not shown here, in all cases studied, we found that the contribution of the parasitic capacitances to the overall interface capacitance was insignificant in the case of the FAP electrolyte as compared to previously recommended electrolytes.

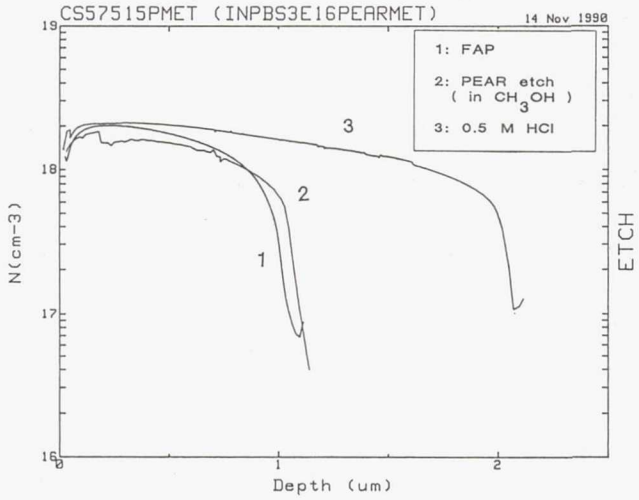


**Figure 8.** Comparison of EC-V depth profiles of good quality $p^+n$ InP structures using different electrolytes.

EC-V profiling of good quality p, n and $p^+n$ InP have shown that of all the previously reported electrolytes, the Pear etch (in methanol) is a reasonably good choice. However, even in this case the FAP electrolyte appears to be the best answer. In Figure 8 is presented a comparison of EC-V profiles in the case of a good quality $p^+n$ InP structure [12] using the FAP electrolyte, the 0.5M HCl and the Pear etch (in methanol). The large deviation of EC-V profile performed using the 0.5M HCl solution is mainly due to the rounding at the crater rim, while the fluctuations in the EC-V profile using the Pear etch is mainly due to fluctuations in the thickness of the residual surface oxide layer.

Using the FAP electrolyte after experimentation with fairly good quality p, n, $p^+$ and $n^+$ InP we found that the electron number for n- or p-InP is constant (n = 6). The relatively high anodic dissolution rate (i.e. of about 0.3 μm/h at 0.2 mA/cm$^2$) is much higher than the chemical etch rate which for p-InP, in the dark, is below 5Å/h. The best results for p-type surfaces were obtained in the dark at a current density of 0.1 to 0.3 mA/cm$^2$ and for n-InP under low illumination at 0.05 to 0.25 mA/cm$^2$.

The low values refer to high defect density surfaces. The resulting surfaces in these cases were very smooth, free of oxide and contaminants, and with excellent electrical characteristics.

## DEFECT REVEALING

Chemical etching (i.e. the Hubert etch, e.g. $H_3PO_4$:HBr(2:1)) is generally used for defect revealing of InP. The drawbacks are:

(a) High chemical etch rate (over 1μm/min. in most cases),

(b) The larger pits meld with the nearby smaller ones, thereby making the EPD appear smaller than it is in reality,

(c) It is not possible to perform defect density mapping as a function of depth, to reveal the defect density at the interfaces, etc.

In our experience the Hubert etch can be used for relativey accurate revealing of InP substrates or diffused structures of up to $10^5$ EPD/cm$^2$. For higher defect density the larger pits meld with the nearby smaller ones, which makes the EPD appear to be much smaller than it really is [13].

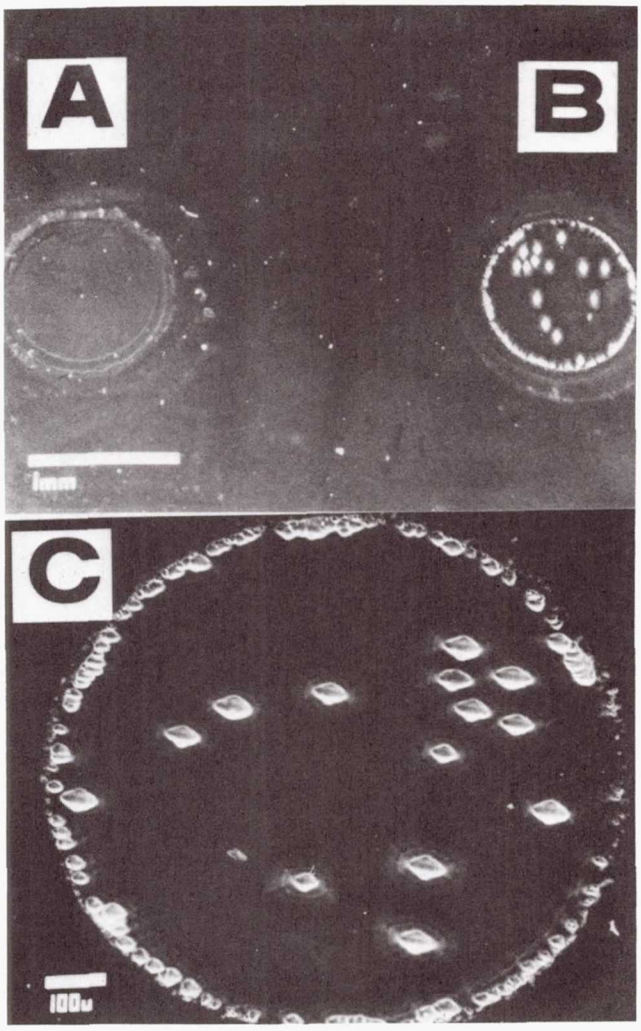


Using higher resolution etching solutions such as HBr:$HNO_3$(3:1), which produce sharp pits on both p- or n-InP [14], accurate defect revealing of up to 5 x $10^6$ EPD/cm$^2$ is possible, but due to a relatively large overall etch rate it is not possible to perform EPD revealing inside one given layer of a thin multilayer structure or at the interfaces.

Electrochemical revealing techniques can be made a lot more accurate than chemical revealing techniques, providing that the electrolyte and working conditions are carefully chosen.

The parameters that affect the width and the depth of the etch spots include the electrolyte type, dissolution time, current density and illumination level.

**Figure 9.** Defect revealing of a $p^+n$ InP (Cd:S) structure ($X_j \approx 2$ μm) diffused at 575°C [12] after removing about 1 μm from the surface using the FAP electrolyte. SEM view of the bottom of the craters at a current density ($J_e$): (A) $J_e$ = 0.3 mA/cm$^2$, in the dark; (B) $J_e$ = 2mA/cm$^2$, under illumination; (C) close-up view of B.

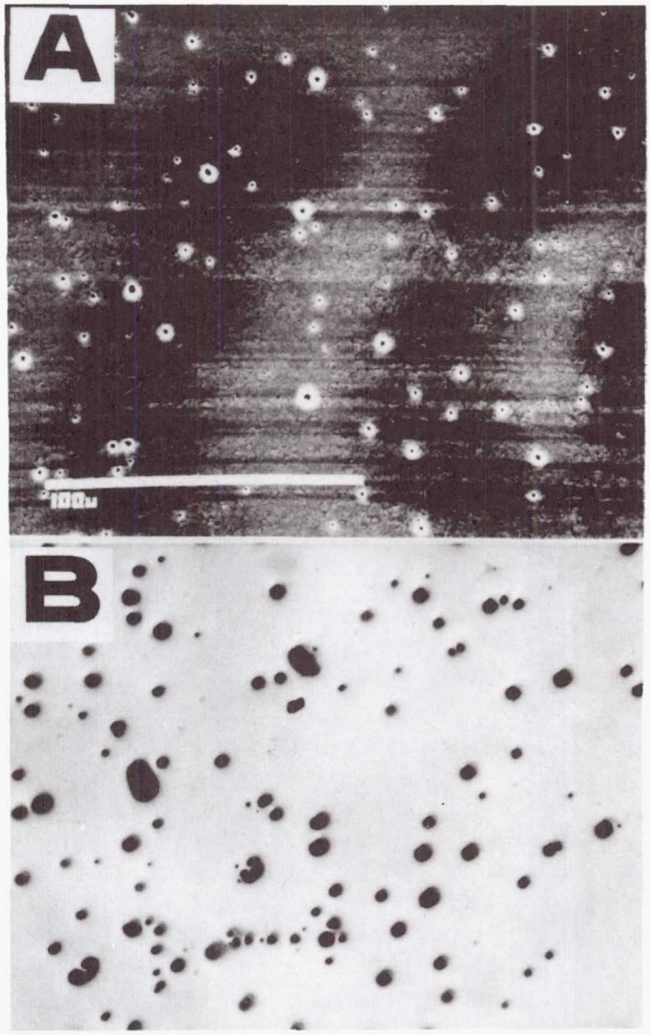


**Figure 10.** Deep precipitates and EPD revealed using the FAP electrolyte of (A) high defect density $n^+p$ InP (S:Zn) structure ($X_j \approx 150$nm), after removing ~ 50 nm from the surface at $J_e$ = 0.2 mA/cm²; (B) EPD and deep precipitates revealed after first removing ~ 100nm from the surface ($J_e$ = 0.2 mA/cm²) of a good quality epitaxially grown $n^+p$ InP (Si:Zn) structure ($X_j \approx 0.2$ µm) at $J_e$ = 1.5 mA/cm². (X440)

As a by-product of this study we show that 0.5M HF:1M HCl(1:1) and 0.5M o-$H_3PO_4$:0.5M HF(1:1) electrolytes, due to a high aspect ratio (depth/width) of the etch pits, are good candidates for accurate defect revealing of high dislocation density $n^+p$ InP surfaces [13]. However, as in the case of chemical revealing techniques, these electrolytes can be used for defect revealing at a given depth only for fairly homogeneous substrates.

The choice of the FAP electrolyte for defect revealing was done having in mind i) mapping of dislocation density as a function of depth and ii) defect revealing of thin multilayer InP structures. In this case the InP structure is dissolved first to the required depth as described in the first paragraph (i.e. current density of up to 0.3 mA/cm², see Figure 9a, in the dark for a good quality $p^+$-InP) and then by changing the working conditions (i.e. 1-3 mA/cm², under illumination for $p^+$-InP) preferential dissolution at the dislocation areas occur. (See Figures 9b and c). The high aspect ratio (of up to 3 recorded) after removal of only about 100Å from the surface, allows accurate mapping of dislocation density as a function of depth and/or at the interfaces. However, for each depth one needs a different spot to be used which imply that the structure should be very uniform over the area.

The FAP electrolyte was used for revealing deep precipitates in the case of $n^+p$ InP stuctures made by closed-ampoule sulfur diffusion into Zn-doped InP substrates. The white spots seen in Figure 10a, revealed after removal of about 500Å from the surface were identified to be ZnS conglomerates.

Figure 10b shows the defect density EPDs and deep precipitates revealed after removal of about 1000Å of a good quality epitaxially grown $n^+p$ InP structure (emitter thickness 0.2µm).

## SURFACE PASSIVATION

In our experience [15] most of the chemical etching solutions used for surface passivation of InP leave a thin (at least 15Å thick) oxide layer on the surface, with a large content of contaminants, which are in part responsible for i) instabilities of devices such as MISFET's and ii) high SRV values in the case of InP solar cells.

In order to form clean, well-ordered InP surfaces, an alternative approach to chemical etching is anodic dissolution using a non-defect revealing electrolyte. This technique exploits the good inherent characteristics of the FAP electrolyte described in the previous paragraphs. After anodic dissolution using the FAP electrolyte of both p- and n-InP at current densities of up to 0.3 $mA/cm^2$, the resulting surfaces are very smooth, free of oxide and contaminants and with excellent electrical characteristics. This makes this technique desirable for surface passivation prior to growing or deposition of an insulator or a first layer AR coating. As an example, after removal of about 300Å from the surface using the FAP electrolyte, and further removal of about 1μm by chemical etching using a newly developed etchant [16] of a good quality $p^+n$ InP structure [13] (initial thickness 2.5μm), we have recorded a surface state density minima $N_{ss,min}$ as low as $3 \times 10^{10} cm^{-2} eV^{-1}$ at the $p^+$InP/P-rich oxide interface. The newly developed so called "PNP" etchant, has the general composition $(o\text{-}H_3PO_4)_u:(HNO_3)_v:(H_2O_2)_t:(H_2O)_{1-(u+v+t)}$. The residual oxide layer left after using fuming $HNO_3$ is homogeneous with depth and rich in $In(PO_3)_3$. Due to its good passivating and optoelectronic properties [16] we do propose it to be used as a first layer AR coating in fabrication of high voltage $p^+n$ InP solar cells made by thermal diffusion [17].

## CONCLUSIONS

We have developed a new electrolyte which we have called the "FAP" electrolyte. We have tested it for anodic dissolution of InP surfaces, and have found the following:

1) Using the FAP electrolyte we have been able to remove heavily damaged InP surface layers and the resulting surfaces were very smooth, free of oxides and contaminants and with excellent electrical characteristics.

2) Based on our experience, we have found the FAP electrolyte to be the best choice for performing accurate electrochemical C-V (EC-V) profiling of InP, at current densities ($J_c$) of up to 0.3 $mA/cm^2$.

The experimental study of EC-V profiling of InP which was conducted using a large number of p, n, $p^+$, $n^+$ InP substrates and $n^+p$ and $p^+n$ InP structures seems to indicate:

(a) 0.5M HCl solution cannot be used for accurate profiling of InP even in the case of high quality substrates;

(b) The Pear etch (in the methanol system) could be used with

reasonably good results for high quality p-InP substrates. It gives relatively poor results on n-InP substrates and $p^+n$ InP structures and the profiles are highly questionable for large front dislocation density $n^+p$ InP structures;

(c) Due to its inherent qualities, the FAP electrolyte is, in our opinion, the best choice for performing accurate EC-V profiling of InP.

We have tested the new electrolyte with very good results for other applications, such as:

a) Revealing surface and deep dislocation defects in InP at higher current densities of 1-3 $mA/cm^2$, and

b) Removing the damaged and/or contaminated surface layer prior to extrinsic surface passivation, or deposition (growing) of the first layer AR coating.

## REFERENCES


[1] M. Faur, M. Faur, M. Goradia and S. Bailey, Proceedings of the 2nd Int. Conf. on InP and Related Materials, IEEE Catalog #90CH 2859-7, p. 242 (1990).

[2] T. Ambridge and D. J. Ashen, Electron Lett. 15,674 (1979).

[3] R. T. Green, D. K. Walker and C. M. Wolfe, J. Electrochem. Soc. 133(11), 2278 (1986).

[4] M. Faur, M. Faur, D. T. Jayne, M. Goradia and C. Goradia, Surface and Interface Analysis, 15,641 (1990).

[5] M. Faur and M. Faur, "High Resolution Electrolyte for Thinning InP and Applications", Submitted for patenting, Sept. 1990.

[6] M. Faur M. Faur, C. Vargas and M. Goradia, To appear in Proceedings of the 3rd Int. Conf. on InP and Related Materials, Cardiff, Wales, U.K., April 8-11 (1991).

[7] M. Faur, M. Faur, M. Goradia, C. Goradia, D. Jayne, F. Honecy and I. Weinberg, Proceedings of the 1st Int. Conf. on InP and Related Materials, SPIE Vol. 1144,501 (1989).

[8] M. Faur, M. Faur, C. Goradia, M. Goradia, N. Fatemi, D. Brinker and R. Thomas, Ibid, 459 (1989).

[9] P. A. Kohl, C. Wollowodiuk and F. W. Ostermayer, Jr., J. Electrochem. Soc., 130,2288 (1983).

[10] D. W. Shaw, Ibid, 128,874 (1981).

[11] T. Ambridge and M. M. Faktor, J. Appl. Electrochem., 5,319 (1975).

[12] M. Faur, M. Faur, C. Goradia, M. Goradia and I. Weinberg, To appear in Proceedings of the 3rd. Int. Conf. on InP and Related Materials, Cardiff, Wales, U.K., April 8-11 (1991).

[13] M. Faur, I. Weinberg, M. Faur, C. Goradia and R. Clark, Proceedings of the 2nd. Int. Conf. on InP and Related Materials, IEEE Catalog #90CH2859-7,397 (1990).

[14] S. N. Chu, C. M. Jodlauk and A. A. Ballman, J. Electrochem. Soc., 129,352 (1982).

[15] M. Faur, M. Faur, P. Jenkins, M. Goradia, S. Bailey, D. Jayne, I. Weinberg and C. Goradia, Surface and Interface Analysis, 15,745 (1990).

[16] M. Faur, M. Faur, S. Bailey, D. Brinker, M. Goradia, I. Weinberg, and N. Fatemi, To be presented at the 22nd. PVSC, Las Vegas, 1991.

[17] M. Faur, M. Faur, D. J. Flood, I. Weinberg, D. J. Brinker, C. Goradia, N. Fatemi, M. Goradia and W. Thesling, This conference.

# RECENT ADVANCES IN GaAs/Ge SOLAR CELLS

C. L. Chu, P. A. Iles
Applied Solar Energy Corporation
City of Industry, CA

W. Patterson
MANTECH Directorate
Wright Laboratories, Ohio

## 1.0 BACKGROUND

GaAs solar cells have several advantages for space use including high efficiency, radiation resistance and lower power fall-off at elevated operating temperatures. In the latter part of the 1980's, GaAs cells delivering 50 KW of space power were manufactured at ASEC.

By growing the GaAs cell on a Ge substrate, the advantages of GaAs cells can be retained and the higher mechanical strength of the Ge makes larger, thinner GaAs cells possible.

To conform to immediate user requirements, ASEC modified GaAs growth conditions to eliminate the additional PV output at the GaAs/Ge interface. GaAs cells on inactive Ge substrates have demonstrated efficiencies over 20% (AMO), for areas up to 6 x 6 $cm^2$, and cell thicknesses down to 3.5 mils (lower thicknesses are possible). Those cells had all the other advantages of GaAs/GaAs cells.

An unexpected bonus was the much reduced degradation observed after exposure to high reverse currents, thus increasing survivability of partially shadowed panels in space applications.

## 2.0 MANUFACTURING TECHNOLOGY

To demonstrate acceptable cell manufacturing technology, the major areas in cell manufacture were analyzed and developed, and effectively combined. Also the cells were successfully assembled on current lightweight arrays. The main areas of effort are discussed next.

### 2.1 Ge Substrates

We continued to specify square substrates (4.5 x 4.5 $cm^2$), 8 mils thick. Because of the inactive Ge design, we could relax the electrical requirements, specifying only the crystallographic and surface quality. We evaluated three Ge suppliers, who used either Czochralski or Horizontal Bridgman techniques to grow the Ge crystals. Table 1 shows the results of those tests.

**Table 1 Comparison of Ge Substrates**

| Ge Ingot Growth | Vendor | Wafer Size ($cm^2$ - mil) | Elec. Yield ($\geq$17%) | Process Lot |
|---|---|---|---|---|
| Czochralski | Laser Diode<br>Eagle Picher | 4.5x4.5--3.5<br>4.5x4.5--3.5 | 96.2%<br>95.2% | M111<br>M84,M86 |
| Horizontal Bridgman | Crystal Specialties | 4.5x4.5--3.5 | 82.6% | M79<br>M81<br>M82 |

Note: The mechanical yield of the 4.5 x 4.5 $cm^2$ thin cell is around >70%.
The results of 6.0 x 6.0 $cm^2$ thin cells are also close.

Low dislocation density or lineage were not serious requirements. Some crystals contained "linear defects" and these defects often caused cracking because they etched perpendically during the thinning process and the resultant thin Ge layer was more easily cracked. Figure 1 shows some of these defects. These defects were problems even when substrates as thin as 5 mils were thinned. We are working with the Ge suppliers to eliminate these defects.

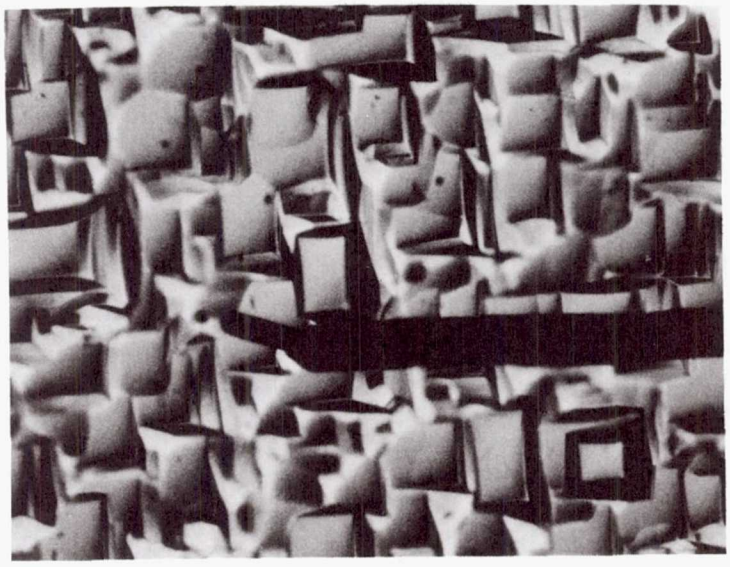

**Figure 1 Linear defect (revealed in Ge Substrate Thinning) (X400)**

## 2.2 MOCVD Growth

All our layers were grown on one of five production reactors operating continuously. The overall MOCVD growth conditions have been optimized and generally give high electrical yields. In a few runs, poor surface morphology or unwanted impurities can lead to reduced electrical performance. For runs with very poor morphology, repolishing the wafers for re-use is cost-effective, and can provide good cells with reasonable yields.

To show the effectiveness of the process, we present Figure 2 which shows electrical yields for 40 successive runs. These cells were 8 $cm^2$ area, 8 mils thick, but similar results were obtained for thin, larger area cells.

| Lot # | Voc (mV) | Isc (mA) | Eff (%) @ 825 mV 4x2 cm | Projected Eff (%) at Pmax 2x4 cm |
|---|---|---|---|---|
| 1 | 1008.0 | 246.5 | 17.6 | 18.7 |
| 2 | 1008.0 | 248.5 | 17.9 | 19.0 |
| 3 | 1005.0 | 245.8 | 17.5 | 18.6 |
| 4 | 1007.0 | 247.3 | 17.5 | 18.6 |
| 5 | 1012.0 | 245.3 | 17.8 | 18.9 |
| 6 | 1009.0 | 245.5 | 17.7 | 18.8 |
| 7 | 1002.0 | 245.1 | 17.4 | 18.5 |
| 8 | 1007.0 | 248.8 | 17.8 | 18.9 |
| 9 | 1005.0 | 246.6 | 17.7 | 18.8 |
| 10 | 1008.0 | 244.0 | 17.5 | 18.6 |
| 11 | 1008.0 | 246.5 | 17.8 | 18.9 |
| 12 | 1006.0 | 249.0 | 17.6 | 18.7 |
| 13 | 1006.0 | 244.3 | 17.6 | 18.7 |
| 14 | 1009.0 | 245.0 | 17.8 | 18.9 |
| 15 | 1010.0 | 246.7 | 17.8 | 18.9 |
| 16 | 992.0 | 246.7 | 17.2 | 18.3 |
| 17 | 992.0 | 246.7 | 17.2 | 18.3 |
| 18 | 1005.0 | 246.9 | 17.6 | 18.7 |
| 19 | 1007.0 | 247.4 | 17.7 | 18.8 |
| 20 | 998.0 | 248.2 | 17.6 | 18.7 |
| 21 | 1013.7 | 246.1 | 17.2 | 18.3 |
| 22 | 995.7 | 246.5 | 17.2 | 18.3 |
| 23 | 1002.0 | 243.3 | 17.3 | 18.4 |
| 24 | 1001.0 | 248.2 | 17.4 | 18.5 |
| 25 | 999.0 | 245.0 | 17.2 | 18.3 |
| 26 | 1004.0 | 244.4 | 17.6 | 18.7 |
| 27 | 1010.0 | 245.8 | 17.8 | 19.0 |
| 28 | 1006.0 | 244.8 | 17.4 | 18.5 |
| 29 | 1006.0 | 247.9 | 17.6 | 18.7 |
| 30 | 1009.0 | 244.7 | 17.6 | 18.7 |
| 31 | 1009.0 | 246.1 | 17.8 | 18.9 |
| 32 | 1008.0 | 246.1 | 17.7 | 18.9 |
| 33 | 1009.0 | 244.5 | 17.6 | 18.7 |
| 34 | 998.0 | 248.2 | 17.3 | 18.4 |
| 35 | 1013.0 | 247.6 | 18.0 | 19.2 |
| 36 | 1009.0 | 248.5 | 17.8 | 18.9 |
| 37 | 1012.0 | 248.7 | 18.1 | 19.2 |
| 38 | 1008.0 | 246.7 | 17.8 | 19.0 |
| 39 | 1009.0 | 241.7 | 17.5 | 18.6 |
| 40 | 1012.0 | 247.9 | 18.1 | 19.2 |
| Average | 1006.3 | 246.4 | 17.6 | 18.7 |

**Figure 2** **Lot Average Data for GaAs/Gei Solar Cells (8 $cm^2$) at AMO Condition, 28 Deg. C for 40 Consecutive Lots, 1991**

## 2.3 Cell Processing

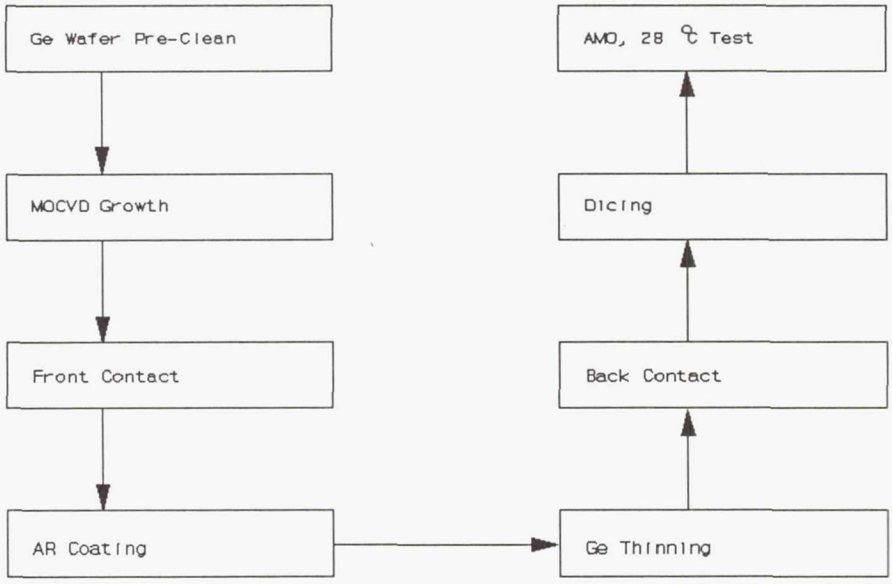


Figure 3 Flow Chart of GaAs/Ge Thin Cell Process

We have adapted standard production processes to apply front surface contacts and Al coatings to the grown layers. We have slightly modified the processing sequence and methods along with the testing to reduce breakage in the thinning process.

## 2.4 Thinning the Ge Substrates

A protective layer is applied to the front surface, and the Ge substrate is thinned (from 8 to <4 mils) by wet-etching. We are continuing evaluation of dry etching and other wet processes to see if the preferential attack on linear defects is reduced.

# 3.0 CELL PERFORMANCE

## 3.1 Electrical Output

For cells up to 6 x 6 $cm^2$, 3.5 mils thick, efficiencies over 20% have been obtained.

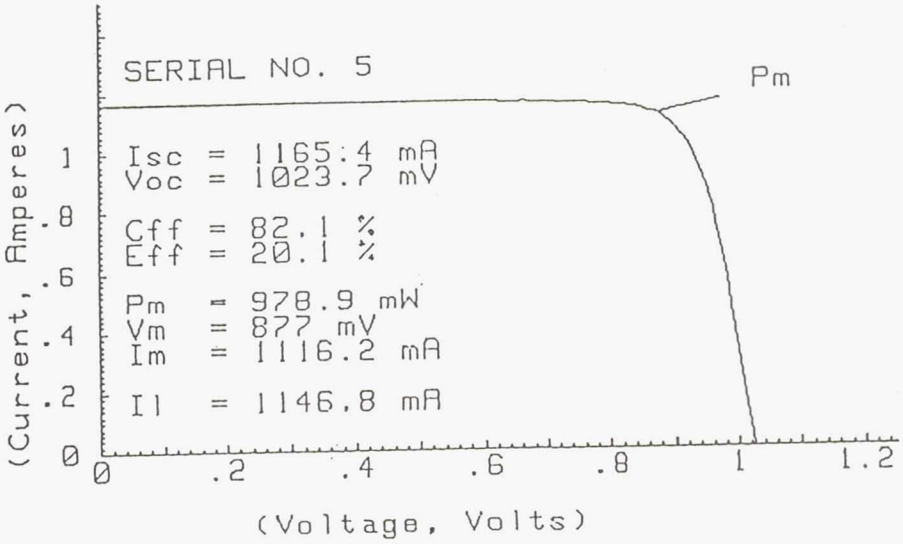


**Figure 4 I-V Curve 6 x 6 cm² Thin Cell**

Average lot efficiencies have exceeded 18% (4 x 4 cm², 3.5 mil thick).

**Table 2 Electrical Testing Results of GaAs/Ge 4 x 4 cm² Thin Cells**

Description: GAAS/GE THIN 4X4 M155
Test: Baseline — Date: 4 Dec 1990
Lot number: M155 — Time: 11:48:23
Load Voltage: .825

| Cell # | Voc mV | Isc mA | IL mA | Vm mV | Im mA | Pm mW | Cff % | Eff % |
|---|---|---|---|---|---|---|---|---|
| 1 | 1016 | 495 | 485 | 882 | 466 | 411 | 81.7 | 19.0 |
| 2 | 1012 | 495 | 480 | 866 | 464 | 402 | 80.2 | 18.6 |
| 3 | 1010 | 488 | 475 | 867 | 460 | 399 | 80.9 | 18.4 |
| 4 | 1011 | 495 | 452 | 846 | 440 | 372 | 74.4 | 17.2 |
| 5 | 1010 | 496 | 486 | 877 | 470 | 412 | 82.3 | 19.0 |
| 6 | 1011 | 492 | 460 | 862 | 434 | 374 | 75.2 | 17.3 |
| 7 | 1012 | 495 | 482 | 874 | 465 | 406 | 81.1 | 18.8 |
| 8 | 1010 | 499 | 488 | 870 | 473 | 412 | 81.7 | 19.0 |
| 9 | 1018 | 492 | 482 | 871 | 467 | 407 | 81.2 | 18.8 |
| 10 | 1019 | 501 | 491 | 874 | 476 | 416 | 81.5 | 19.2 |
| 11 | 1004 | 497 | 485 | 867 | 470 | 407 | 81.7 | 18.8 |
| 12 | 1012 | 490 | 475 | 868 | 460 | 399 | 80.5 | 18.4 |
| 13 | 1016 | 499 | 489 | 875 | 474 | 415 | 81.8 | 19.2 |
| 14 | 1011 | 495 | 476 | 861 | 462 | 398 | 79.5 | 18.4 |
| 15 | 1016 | 505 | 495 | 871 | 480 | 418 | 81.5 | 19.3 |
| 16 | 1009 | 496 | 405 | 855 | 394 | 337 | 67.3 | 15.6 |
| 17 | 1014 | 501 | 493 | 873 | 478 | 417 | 82.1 | 19.3 |
| 18 | 980 | 494 | 482 | 871 | 466 | 406 | 83.8 | 18.8 |
| 19 | 1016 | 505 | 493 | 869 | 477 | 415 | 80.8 | 19.2 |
| 20 | 1015 | 505 | 496 | 873 | 480 | 419 | 81.8 | 19.4 |
| 21 | 1013 | 496 | 478 | 857 | 464 | 398 | 79.1 | 18.4 |
| 22 | 1011 | 504 | 489 | 867 | 474 | 411 | 80.7 | 19.0 |
| 23 | 1016 | 499 | 488 | 871 | 474 | 413 | 81.4 | 19.1 |
| 24 | 1013 | 500 | 490 | 872 | 475 | 414 | 81.8 | 19.1 |
| 25 | 1014 | 495 | 484 | 875 | 469 | 410 | 81.8 | 18.9 |
| 26 | 1003 | 494 | 355 | 843 | 347 | 293 | 59.0 | 13.5 |
| 27 | 1012 | 493 | 483 | 876 | 465 | 407 | 81.6 | 18.8 |
| 28 | 1018 | 498 | 487 | 875 | 470 | 411 | 81.1 | 19.0 |
| 29 | 1013 | 504 | 488 | 863 | 473 | 408 | 80.0 | 18.8 |
| 30 | 1015 | 497 | 486 | 876 | 470 | 412 | 81.6 | 19.0 |
| 31 | 1014 | 497 | 486 | 872 | 470 | 410 | 81.3 | 18.9 |
| 32 | 1014 | 496 | 484 | 877 | 466 | 409 | 81.3 | 18.9 |
| 33 | 1015 | 507 | 496 | 868 | 481 | 418 | 81.1 | 19.3 |
| 34 | 1011 | 497 | 486 | 875 | 469 | 410 | 81.7 | 18.9 |
| 35 | 1005 | 490 | 479 | 862 | 465 | 401 | 81.4 | 18.5 |
| 36 | 1017 | 507 | 497 | 877 | 480 | 421 | 81.6 | 19.4 |
| 37 | 1015 | 497 | 486 | 874 | 471 | 412 | 81.6 | 19.0 |
| 38 | 1014 | 495 | 471 | 862 | 455 | 392 | 78.1 | 18.1 |
| Average | 1012 | 497 | 479 | 869 | 463 | 402 | 79.9 | 18.6 |
| Standard Dev | 6 | 5 | 26 | 8 | 25 | 24 | 4.5 | 1.1 |

The cell efficiency has been retained when cells are mounted on panels (see 3.6).

### 3.2 Temperature Coefficients, Radiation Resistance

Similar values to those requested for GaAs/GaAs cells are obtained.

### 3.3 Contact Pull Strength

High pull strengths and satisfactory bonding onto arrays were obtained for thin cells using both soldered and welded interconnects with only slight adjustment in normal bonding schedules.

**Table 3 Pull Strength of GaAs/Ge Cells**

| No. of Joints | Interconnected Area ($mil^2$) | Pull Strength (Gram) | |
|---|---|---|---|
| | | Front | Back |
| 34 | Soldered Joints | 1173 | -- |
| 55 | 35 x 75 | 758 | -- |
| 43 | | -- | 1130 |
| | Welded Joints | | |
| 11 | 50 x 75 | 464 | -- |
| 54 | | -- | 810 |
| 10 | 25 x 45 | 358 | -- |

The efficiency of the cells used for the test is 17% - 18%.

### 3.4 Resistance to Reverse Current Stressing

After exposure to reverse currents 20 to 30% above the Isc (AMO) value, the degradation of GaAs/Ge cells was very low, a significant improvement over results obtained for GaAs/GaAs cells.

### 3.5 Contact Modifications

#### 3.5.1 Coplanar Back Contacts

To adapt to flexible array interconnections, 6 x 6 cm, 8 mil cells with coplanar contacts (wraparound or wrapthrough) have been made with efficiencies up to 18%. Present work is directed at improved consistency in the process sequence.

### 3.5.2 High Temperature Stability

We have modified the contact structure to withstand exposure to high temperatures. With minimum process modification (addition of a barrier layer), cells can withstand exposure to 500-550°C. With additional process steps, we have shown the feasibility of no degradation (from 18%) after 600°C for 5 minutes and less than 5% degradation after heating at 600°C for 30 minutes. Present work is aimed at simplification of structures and processes to increase the yields of cells which are stable after high temperature exposure.

## 3.6 Panel Performance

These large area, thin GaAs/Ge cells have been successfully assembled on lightweight rigid panels. Panels 1 ft x 1 ft, containing forty-nine 4 x 4 $cm^2$ cells were made with both welded and soldered interconnects. The panel efficiencies were 17.7%.

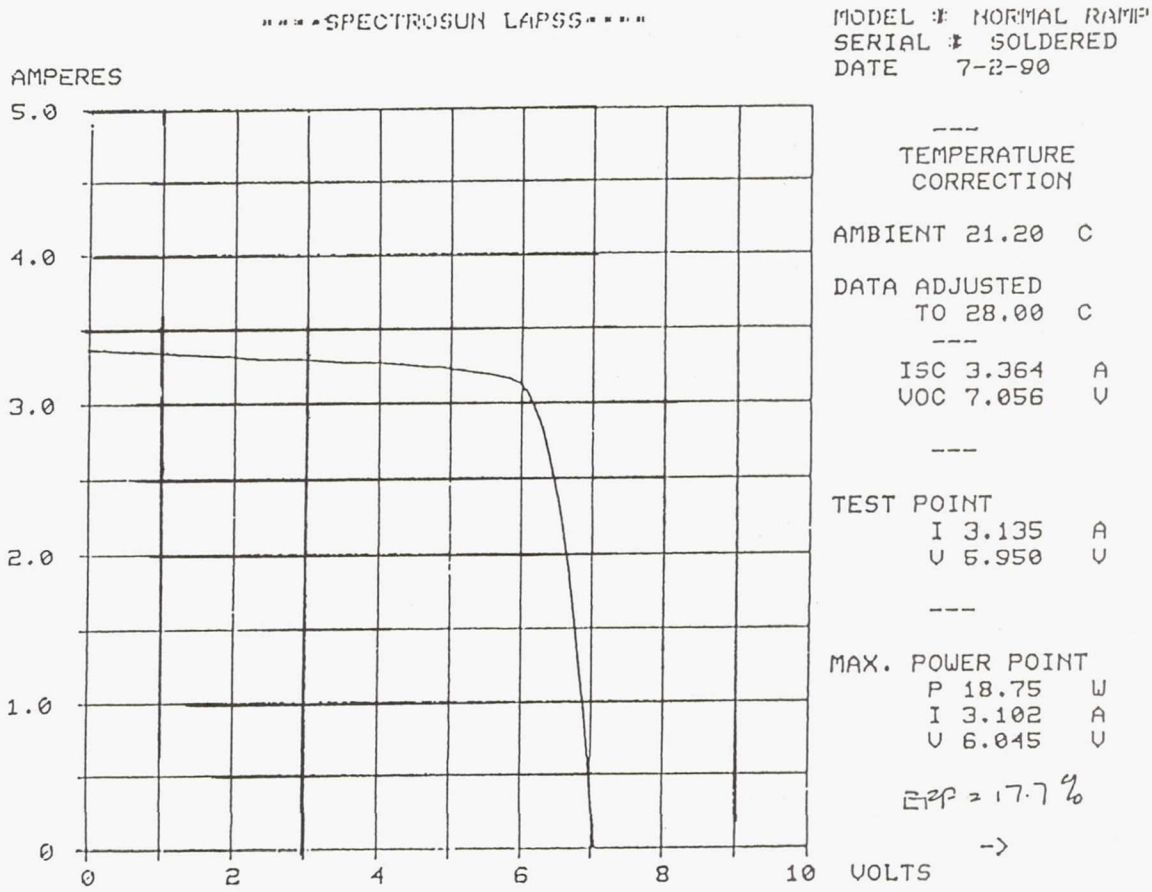


**Figure 5 I-V Curve of Soldered 4 x 4 $cm^2$, Thin Cell Panel (7P, 7S)**

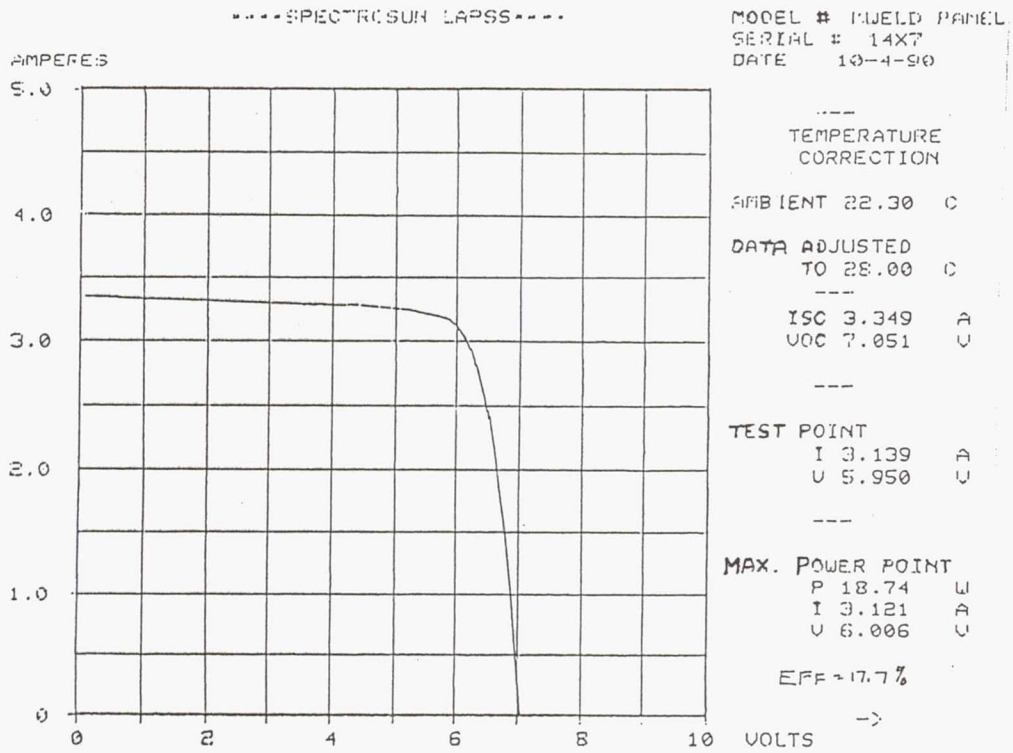


**Figure 6 I-V Curve of Welded 2 x 2 cm$^2$ Thin Cell Panel (7P, 7S)**

A small panel (2S, 2P 4 x 4 cm$^2$ cells) had efficiency 19.4%.

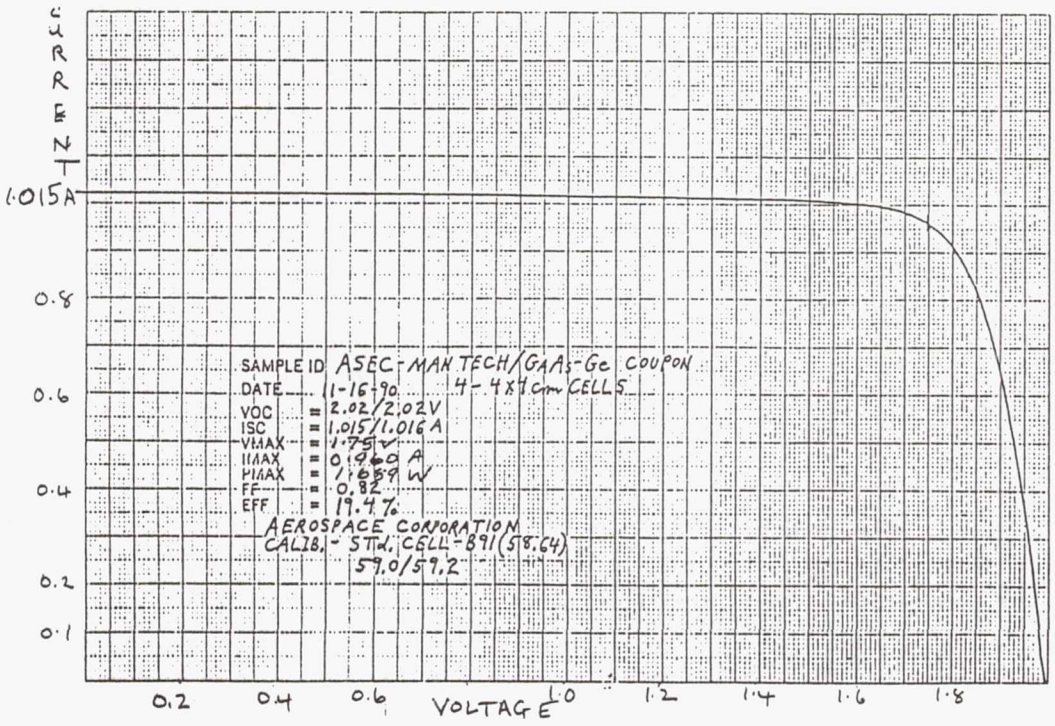


**Figure 7 I-V Curve of 4 x 4 cm$^2$, Thin Cell Coupon (2P, 2S) After 5,000 Thermal Cycles**

A small panel (3S, 3P, 6 x 6 $cm^2$ cells) had efficiency 18.8%

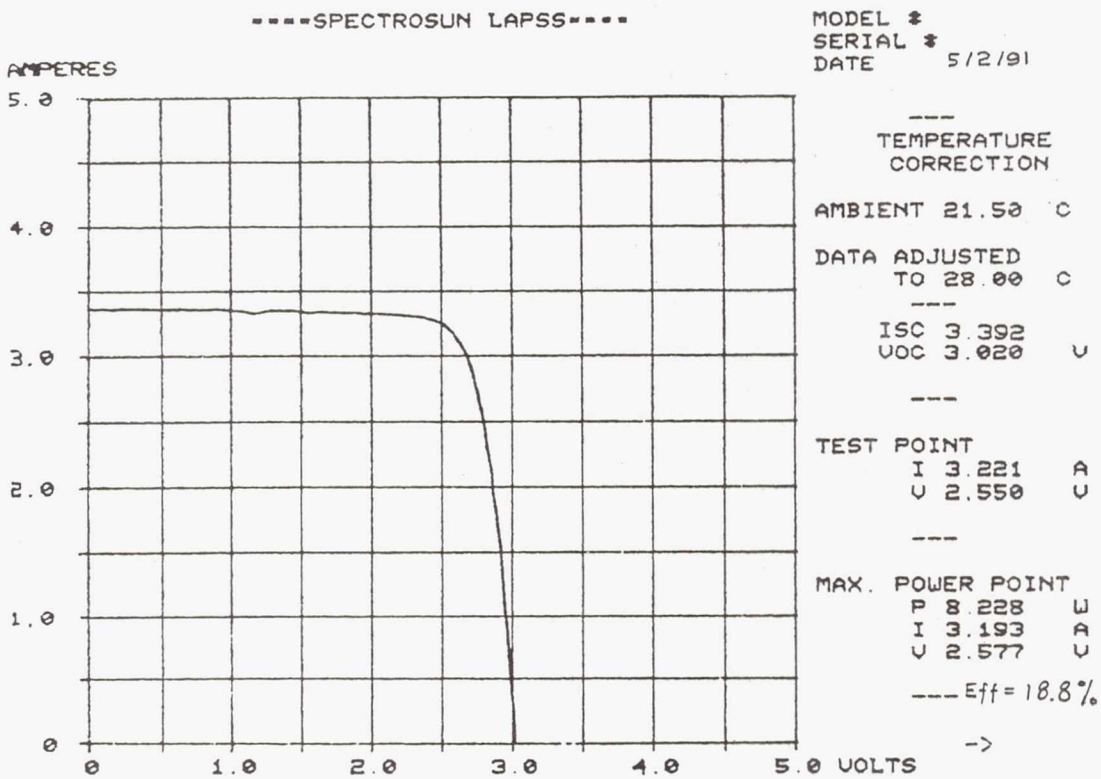


**Figure 8 I-V Curve of 6 x 6 $cm^2$ Thin Cells (3S, 3 P Panel)**

These panels have withstood standard space qualification testing conditions.

Other users have successfully mounted these thin, large area cells on lightweight flexible cells as well as other lightweight rigid panels.

### 3.7 Costs

Although costs depend on cell specification and quantities, we have demonstrated that the reduced material costs and higher mechanical yields have resulted in a significant reduction in costs of GaAs cells grown on Ge substrates.

## 4.0 CONCLUSIONS

We have demonstrated the advantages of using Ge substrates for supplying large area, lightweight, highly efficient GaAs cells. These cells and panels made from them, have passed typical qualification tests. These results have provided the foundation for firm estimates of controlled yields and lower costs for high production rates, and have helped to increase the demand for these cells for a variety of space missions, both military and commercial.


## Acknowledgment

Part of this work reported was suggested by the MANTECH Directorate of the Air Force.

# PRODUCTION STATUS OF GaAs/Ge SOLAR CELLS AND PANELS

B. Smith, M. Gillanders, P. Vijayakumar, D. Lillington
Spectrolab, Inc.
Sylmar, CA

and

H. Yang, and R. Rolph
Hughes Aircraft Company
Torrance, CA

GaAs/Ge solar cells with lot average efficiencies in excess of 18.0% have been produced by MOCVD growth techniques. A description of the cell, its performance and the production facility are given. Production GaAs/Ge cells of this type were recently assembled into circuits and bonded to aluminum honeycomb panels to be used as the solar array for the British UOSAT-F program.

## INTRODUCTION

GaAs/Ge solar cells are in demand for applications involving spacecraft solar arrays which require increasingly higher power outputs per unit area but have no capacity for growth due to limitations on the array envelope. GaAs is grown onto a germanium wafer by metallo-organic chemical vapor deposition (MOCVD) techniques. The use of germanium as a growth substrate instead of gallium arsenide, enables solar cells to be manufactured which are robust enough to survive the assembly processes and handling required to produce solar arrays.

To meet this demand for high efficiency, rugged GaAs/Ge solar cells, Spectrolab has recently commissioned a new production facility which is able to fabricate solar cells in excess of 18.0% efficiency in a range of sizes varying from 2cm x 2cm to 6cm x 6cm. To date this facility has processed over 2000 4.5cm x 4.5cm wafers and produced material from which single junction GaAs/Ge, wrapthrough GaAs/Ge and dual junction GaAs/Ge solar cells have been fabricated. These cell types are presently being integrated into solar cell circuits for use on military and scientific research programs.

Earlier this year single junction GaAs/Ge cells of dimension 2cm x 4cm were produced and assembled into the UOSAT-F solar array. This effort is noteworthy on many counts. The program was completed in an extremely short time frame - 3 months; the bare cell lot average efficiency was 18.3% with a maximum of 19.7% the delivered solar array had an average circuit efficiency of 18.2% with a maximum of 18.6%.

In the following sections, a description of the solar cell design is given, including some unique features devised to increase cell stability at high temperatures. The new Spectrolab facility is described with its projected capacity for mass production of GaAs/Ge solar cells. Cell performance distributions from different programs are shown and finally, a description of the design and build of the UOSAT-F solar array is given including acceptance test performance data of the completed array.

## MOCVD MANUFACTURING FACILITY

Spectrolab has established a high volume MOCVD manufacturing facility, currently occupying 7000 sq. ft. with room for expansion to 30,000 sq. ft. This area presently houses 3 MOCVD barrel reactors, each of which has produced GaAs solar cells of over 20% at AM0, 28$^{o}$C efficiency.

Currently, the problem with large scale barrel MOCVD reactors is that gas depletion, which occurs as the source gases traverse the wafer, results in large variations in layer thickness and doping uniformity which ultimately translate to reduced yield and radiation hardness.

Based on this fact, and the need for improved uniformity to meet the more stringent needs of advanced solar cells such as $GaInP_2$/GaAs or AlGaAs/GaAs tandem cells, our strategy has been to pursue the development of improved, MOCVD systems to replace the conventional barrel design. Delivery of the first reactor is scheduled for delivery in the second quarter of 1992 with commissioning completed by the third quarter of 1992. Additional systems will be added to meet the needs of the market as it matures.

Our MOCVD strategy is also driven by the need for substantial cost reduction and the ability to provide an enabling technology for larger area GaAs/Ge solar cells up to 8cm x 8cm in size. The reactor is therefore being designed with 4" diameter wafer capability to provide a growth option for Air Force programs currently utilizing large area silicon cells or as a possible growth option for Space Station Freedom. Alternatively up to six 2cm x 4cm cells can be laser scribed from a 4" wafer, substantially reducing the cost of smaller area cells below current levels. Further cost reduction will also be possible through a three-fold reduction in cycle time thus substantially increasing the reactor throughput.

## CELL DESCRIPTION

The cross section of the GaAs/Ge cell is shown in Figure 1.

The starting wafer upon which the active GaAs layers are grown is 7 mils thick, 4.5cm x 4.5cm n-type Ge, chem-mechanically polished on the front side and chemically etched on the backside. The wafer is doped to 5E17 $cm^{-3}$ with Sb and oriented several degrees off <100> toward the nearest <111> plane.

MOCVD growth of GaAs is performed at low pressure. Growth conditions have been optimized to ensure electrical performance uniformity of $\pm$ 3% between the top and bottom rows.

The n-type GaAs buffer is between 2 to 6 microns thick and is doped to 5E18 $cm^{-3}$ with Si. It is grown using a specific nucleation/growth procedure designed to minimize the diffusion of Ga into the wafer, thus assuring the elimination of an active Ge junction.

The base is typically 2 to 3 microns thick and is doped to nominally 2E17 $cm^{-3}$ with Si.

The p-type emitter is doped to between 2 and 4E18 $cm^{-3}$ with Zn and is typically 0.5 microns thick. The thickness is controlled using SPC to ensure radiation hardness which is known to be a strong function of emitter thickness.

An $Al_{0.85}Ga_{0.15}As$ window serves to passivate the surface of the emitter by providing an optically transparent heteroface at the cell surface. It is typically 500 A thick and is heavily doped to 2E18 $cm^{-3}$ with Zn.

The dual antireflection (AR) coating used is $Ta_2O_5/Al_2O_3$. The window surface is specially treated prior to AR coating to guarantee subsequent environmental stability.

A noteworthy feature of the cell design is the front contact GaAs cap structure. This provides a very effective barrier against metal diffusion into the sensitive junction region. Cells manufactured at Spectrolab with this type of contact have shown thermal stability up to 550$^{o}$C for several minutes duration and for over 500 hours at 350$^{o}$C. The GaAs cap is typically 0.3 to 0.5 microns thick and is heavily doped (>1E19 $cm^{-3}$) with Zn to allow good ohmic contact to be achieved between the grid and the front of the cell. It also allows higher efficiencies to be achieved, compared to other designs, since it reduces the recombination velocity beneath the contact, allowing higher Voc to be achieved.

Both front and back silver contact layers are typically 5 microns thick and are weldable using Ag or Ag/Kovar interconnects without degrading cell performance.

## CELL PERFORMANCE

Spectrolab has processed approximately 2000 Ge wafers on its manufacturing line into cell sizes from 2cm x 2cm, up to 6cm x 6cm. AM0 efficiencies exceeding 18% have been achieved for each cell type.

In Figure 2 we show the efficiency distribution of approximately 640 weldable 2cm x 4cm GaAs/Ge cells fabricated for the UOSAT-F flight program. The average efficiency was 18.3%. Representative cells, flown on the NASA Lewis Research Center Learjet under near ideal AM0 conditions confirmed the inactivity of the Ge wafer.**

In Table 1 we also show the efficiencies of thirty two 4cm x 4cm cells recently fabricated. The average AM0, 28$^{o}$C efficiency was 18.3% with a best efficiency of 19.2%.

A limited number of 6cm x 6cm prototypes have also been made from 6.5cm x 6.5cm wafers. The IV curve of the best cell with an AM0 efficiency of 18.2% is shown in Figure 3. Further improvements in efficiency are expected by increasing the grid height to over 12 microns.

** The authors would like to thank David Brinker of NASA LeRC for assistance in performing the learjet measurement.

## UOSAT-F

The UOSAT series of micro-satellites are built by the University of Surrey. Their primary goal is to provide a vehicle for research into satellite engineering topics at low cost. UOSAT-F is the fifth in the series and will fly an RAE Solar Cell Technology experiment, including indium phosphide and cleft GaAs cells for NASA-Lewis. The payload also includes a CCD Earth imaging camera.

The solar arrays are body mounted and fairly small area. To maximize power, therefore, GaAs is the material of choice for the array solar cells. The UOSAT-3 and -4 arrays were made by Mitsubishi and FIAR/CISE/EEV respectively. UOSAT-F provided an opportunity to fly an American GaAs/Ge solar array for the first time on an European satellite. Specifically it enabled Spectrolab to combine its skills as cell manufacturer and panel assembler to design build and test the array in an extremely short timeframe. UOSAT-F is scheduled for ARIANE launch in early May 1991.

## UOSAT-F SOLAR PANEL ASSEMBLY

Cells taken from the distribution shown in Figure 2 were interconnected by means of welded silver-plated Kovar interconnects. Welding was chosen as the method of interconnection since earlier panel assembly experience had shown that solder wets GaAs and sometimes wicks under the interconnect and over the cell edge, thus shorting out the GaAs cell junction just below the surface. Attrition through the welding line was, as a result, less than 1%.

The cells were covered with 6 mil ceria doped microsheet and then interconnected into circuits of 42 cells series, 2 parallel.

The array consisted of three panels, each panel having two circuits bonded to it with CV 2568 silicone adhesive.

Each circuit was wired with 24 awg redundant wiring which were later connected directly into the spacecraft power system since the panels were body mounted.

The six circuits were tested on a LAPSS and found to have efficiencies varying from 17.9% to 18.6%.

The panel outputs at maximum power varied from 32.6 watts to 33.9 watts at 38 volts. The I-V curve for the latter is shown in Figure 4. The three completed panels are shown in Figure 5.

## CONCLUSION

Spectrolab's MOCVD GaAs/Ge solar cells are now available in lot average efficiencies in excess of 18.0% in dimensions varying from 2cm x 2cm to 6.5cm x 6.5cm. Production capability is to be significantly increased with commissioning of a new, improved design reactor which will allow production of 8cm x 8cm cells.

Spectrolab's capability for integrating these cells into solar panels has been proven by the fabrication of the UOSAT array with circuit efficiencies as high as 18.6%.

Table 1 PERFORMANCE DISTRIBUTION OF 4cm x 4cm GaAs/Ge CELLS

| Voc (mV) | Isc (mA) | Vmp (mV) | Imp (mA) | Pmp (mW) | Cff (%) | Eff (%) |
|---|---|---|---|---|---|---|
| 1019 | 488 | 870 | 455 | 396 | 79.6 | 18.3 |
| 1013 | 474 | 874 | 444 | 389 | 80.9 | 18.0 |
| 1022 | 484 | 893 | 450 | 402 | 81.4 | 18.6 |
| 1018 | 468 | 873 | 444 | 387 | 81.3 | 17.9 |
| 1020 | 466 | 883 | 439 | 388 | 81.7 | 17.9 |
| 1025 | 468 | 896 | 444 | 398 | 83.0 | 18.4 |
| 1029 | 485 | 890 | 458 | 407 | 81.5 | 18.8 |
| 1020 | 465 | 888 | 435 | 386 | 81.5 | 17.8 |
| 1031 | 483 | 910 | 456 | 415 | 83.3 | 19.2 |
| 1025 | 455 | 893 | 438 | 391 | 83.9 | 18.1 |
| 1032 | 481 | 900 | 456 | 410 | 82.7 | 19.0 |
| 1031 | 484 | 894 | 443 | 396 | 79.4 | 18.3 |
| 1028 | 482 | 888 | 448 | 398 | 80.3 | 18.4 |
| 1031 | 490 | 892 | 463 | 413 | 81.7 | 19.1 |
| 1022 | 469 | 872 | 435 | 379 | 79.1 | 17.5 |
| 1026 | 469 | 886 | 433 | 384 | 79.7 | 17.7 |
| 1025 | 485 | 878 | 438 | 385 | 77.3 | 17.8 |
| 1027 | 478 | 894 | 444 | 397 | 80.9 | 18.3 |
| 1025 | 469 | 886 | 430 | 381 | 79.2 | 17.6 |
| 1028 | 475 | 902 | 449 | 405 | 83.0 | 18.7 |
| 1029 | 480 | 892 | 449 | 401 | 81.1 | 18.5 |
| 1031 | 488 | 892 | 467 | 417 | 82.8 | 19.2 |
| 1027 | 476 | 890 | 440 | 392 | 80.1 | 18.1 |
| 1031 | 468 | 904 | 447 | 404 | 83.7 | 18.7 |
| 1018 | 459 | 886 | 427 | 378 | 80.9 | 17.5 |
| 1023 | 478 | 900 | 448 | 403 | 82.5 | 18.6 |
| 1021 | 472 | 900 | 442 | 398 | 82.5 | 18.4 |
| 1023 | 471 | 898 | 439 | 394 | 81.9 | 18.2 |
| 1026 | 474 | 898 | 449 | 403 | 82.9 | 18.6 |
| 1026 | 483 | 891 | 444 | 396 | 80.0 | 18.3 |
| 1028 | 477 | 908 | 449 | 408 | 83.1 | 18.8 |
| 1025 | 470 | 900 | 436 | 392 | 81.5 | 18.1 |

**Average Effy = 18.3**

* AM0, 28 C

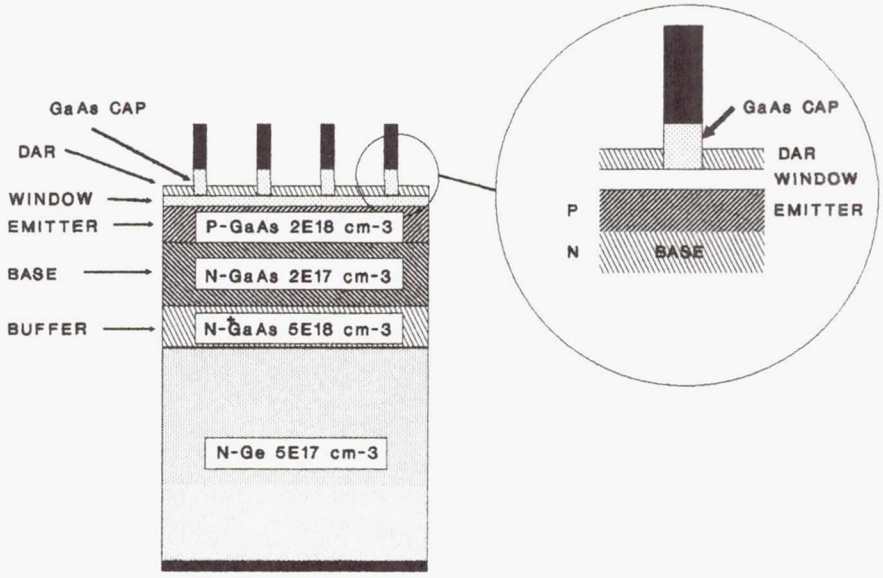


Figure 1 GaAs/Ge CELL CROSS-SECTION

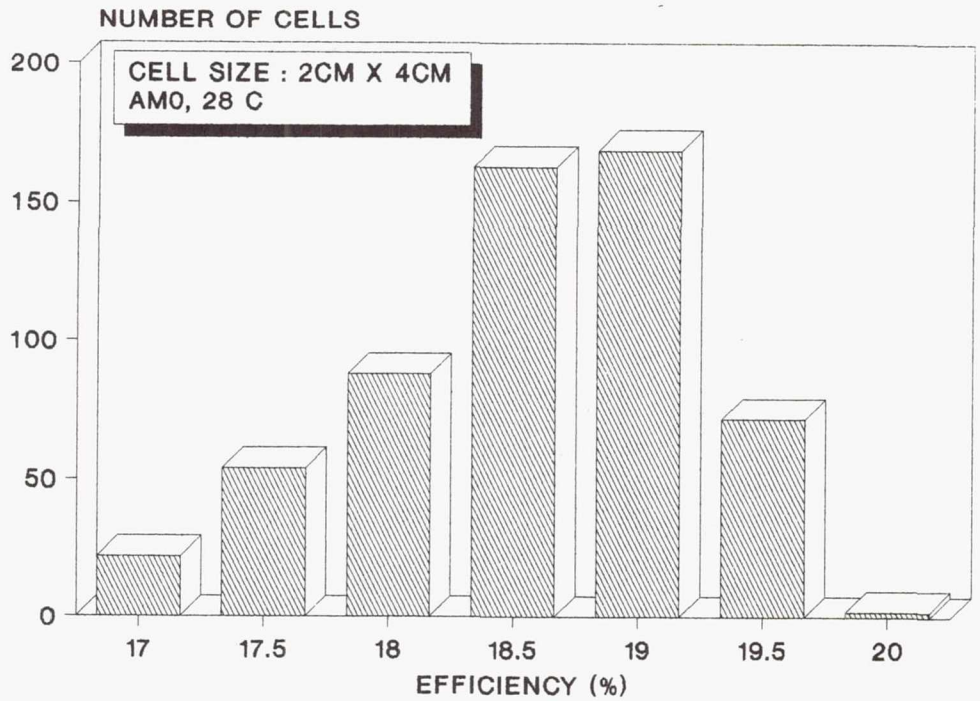


640 CELLS > 16.5% (18.30% AVG)

Figure 2 EFFICIENCY DISTRIBUTION FOR UOSAT CELLS

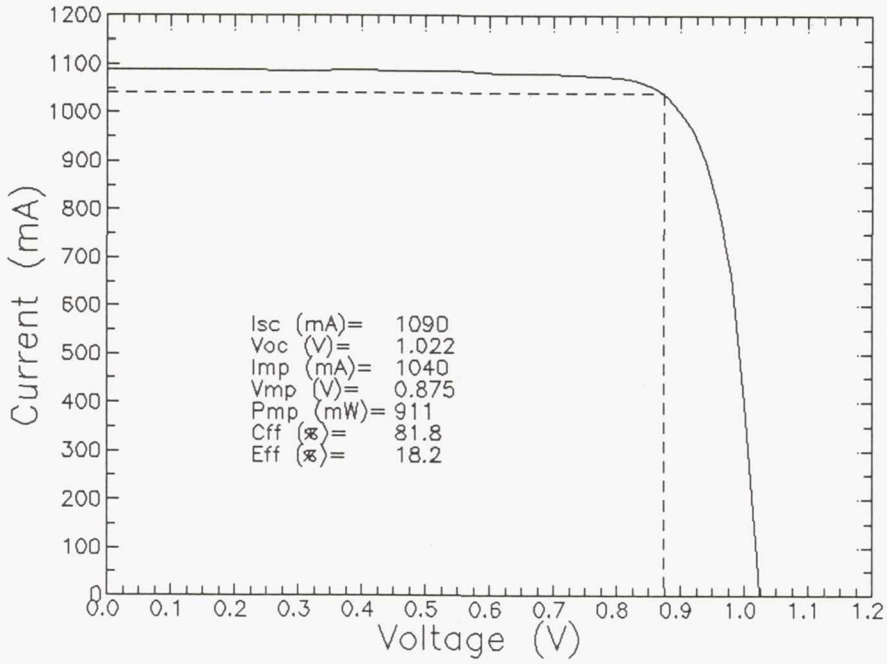


Figure 3 IV CURVE FOR 6.5cm x 6.5cm GaAs/Ge SOLAR CELL

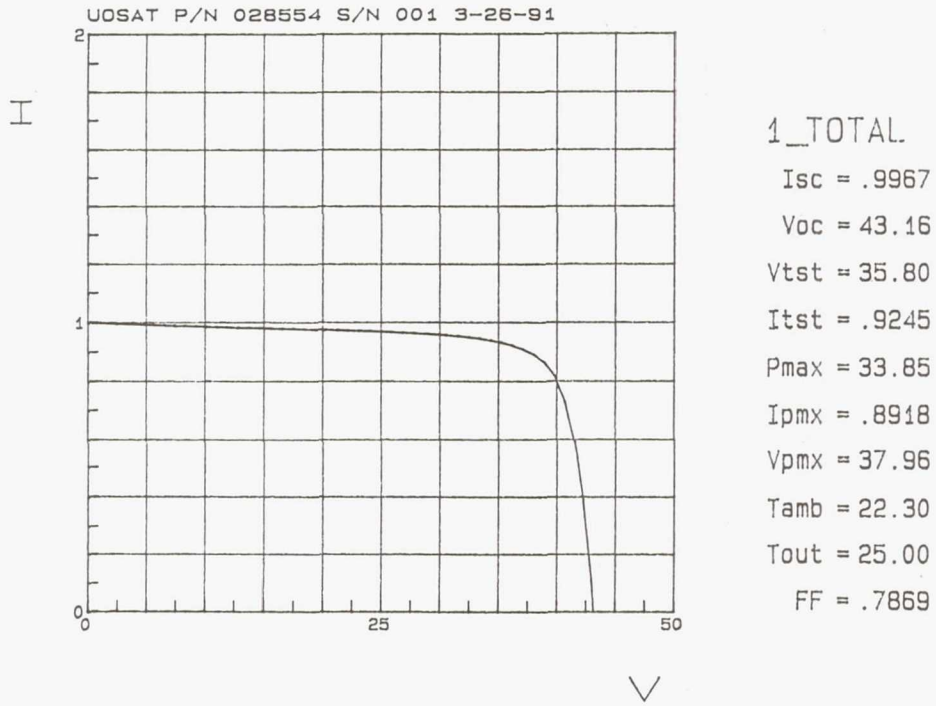


Figure 4 UOSAT PANEL POWER OUTPUT

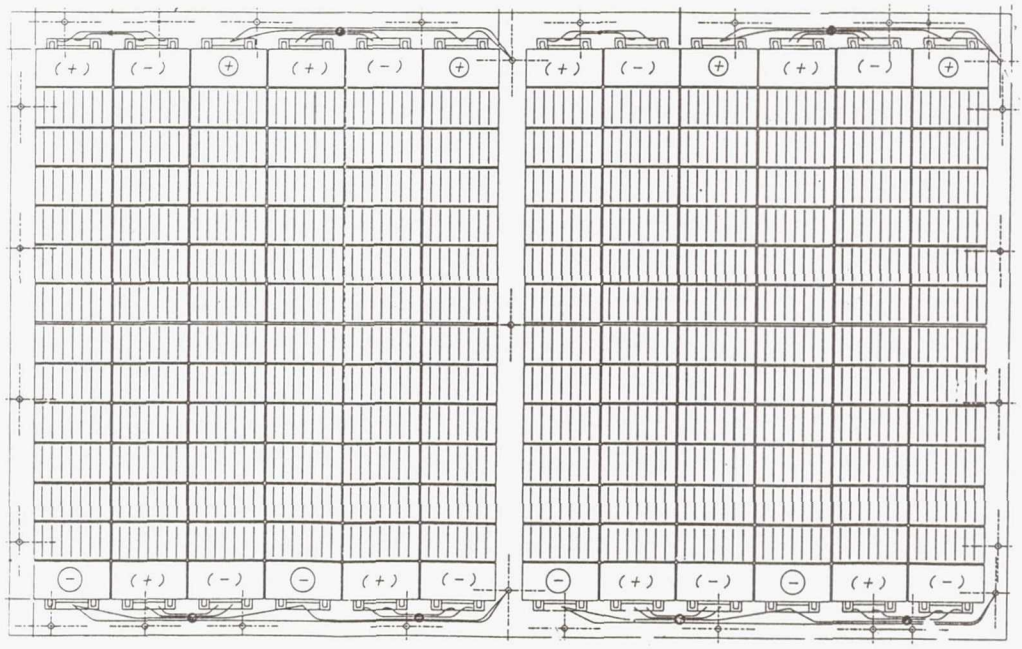


Figure 5 SCHEMATIC OF UOSAT PANEL LAYOUT

# PHOTOREFLECTANCE AND DLTS EVALUATION OF PLASMA-INDUCED DAMAGE IN GaAs AND InP PRIOR TO SOLAR CELL FABRICATION

L. He and W.A. Anderson
State University of New York at Buffalo
Center for Electronic and Electro-optic Materials
Department of Electrical and Computer Engineering
Bonner Hall, Amherst, NY 14260

## ABSTRACT

This study considers the effect of plasma etching on both GaAs and InP followed by damage removal using rapid thermal annealing (RTA). Effects of these processes were studied by photoreflectance spectroscopy (PR) and deep level transient spectroscopy (DLTS). These techniques are useful in evaluation of wafers prior to and effects of plasma processing during solar cell fabrication.

Wafers examined in this study included GaAs with $N_D = 5x10^{17}cm^{-3}$, undoped (u) InP with $n = 5x10^{15}cm^{-3}$, InP with $N_D = 4x10^{17}cm^{-3}$ and InP with $N_A = 1x10^{16}cm^{-3}$. Samples were taken from these wafers for an initial study of PR and DLTS using Au- Schottky contacts. Some samples were then plasma etched in $CF_4$ gas using conditions of 50-150W and a pressure of 10-100 m Torr. Some of these were processed by RTA at 450°C for 10s to remove plasma damage. PR data showed energy gap (Eg) to decrease by 0.006 eV after plasma etching for n-GaAs and u-InP. Eg recovered completely after plasma etching. PR also showed the appearance of defect-related extraneous signals after plasma etching which were removed by RTA. DLTS revealed the addition of new defects after plasma etching which were later removed by RTA. For example, defects in n-GaAs with activation energy of 0.38 eV, 0.57 eV and 0.67 eV were proven to be surface related by the shift in DLTS signal with fill pulse height. These signals disappeared completely following RTA.

## INTRODUCTION

Plasma etching is widely used in semiconductor technology to form fine surface structures. It has the advantages of selectivity, precision and versatility. In photovoltaic devices, plasma etching may permit selective diffusion or ion implantation, perhaps for the region underneath grid lines. It may also be used to form openings in passivation layers such that fine grid contacts may be formed. This study considers the effect of plasma etching on both GaAs and InP followed by damage removal using rapid thermal annealing (RTA). Effects of these processes were studied by photoreflectance spectroscopy (PR) and deep level transient spectroscopy (DLTS). PR is proven to be an effective non- destructive tool in evaluating processed wafers prior to final solar cell fabrication.

Plasma dry etching is used for fabrication of GaAs-based electronic and photonic devices and their integration (refs. 1-2). Its advantages in high resolution, anisotropic processing and controllability have been clearly demonstrated. Plasma etching inherently induces damage, which may affect various surface properties of the substrate. Contamination originating from polymer formation during etching or materials sputtered from the etching chamber can also influence device performance. A number of reports have been made on the investigation of different cases of plasma induced damage (refs. 3-8). Damage has been observed and compared in GaAs by sputter etching and ion beam etching. The characterization techniques most widely used include deep level transient spectroscopy (DLTS) and more recently, photoluminescence (PL). The removal of plasma induced damage has also been discussed by some authors. In this paper we report the study of reactive ion etching in $CF_4$ performed in a parallel plate reactor for GaAs, particularly in terms of chamber pressure and power. Photoreflectance spectroscopy (PR) was used to evaluate the sample surface electrical and optical properties in a nondestructive manner (refs. 10-13). Rapid thermal annealing (RTA) was conducted for a study of the plasma induced damage removal. The effect of plasma etching on device characteristics was studied by evaluating Schottky diodes fabricated on the plasma etched material surfaces. Deep level transient spectroscopy (DLTS) was used to detect and characterize trap centers.

Much less work has been conducted on InP. Our work is also of a preliminary nature but includes both PR and DLTS data for studies of the initial wafer, effects of plasma etching and the healing produced by RTA.

## EXPERIMENTAL

The samples used in this work were (100) n-GaAs with doping ($N_d$) of about $2.5 \times 10^{17}/cm^3$. Chemical etching in $H_3PO_4$:$H_2O_2$:$H_2O$ = 3:1:100 for 8 seconds and HCl:$H_2O$ = 1:1 for 1 minute were performed to remove an initial damaged surface and native oxide layer. Ohmic contacts were first applied to the back of the wafers by AuGe/Ni evaporation. A 450°C, 10 seconds RTA was conducted for the ohmic contact formation. After RTA treatment, the starting wafer was sectioned. One of the pieces was directly taken for PR measurement. The others were plasma etched with the process under study. The plasma etched samples were labeled as G1, G2 and G3 following in sequences of 10mTorr/50W, 50mTorr/100W and 100mTorr/150W plasma etching conditions. Each separately etched wafer was then cut into halves. One half was immediately loaded into a vacuum chamber for Schottky Au deposition. Another half was first taken for PR testing followed by a 450°C/10s RTA treatment to remove plasma induced damage. Finally, Schottky metal was deposited as in the other samples. Correspondingly, after RTA removal of plasma induced damage, 3 samples were labeled as GR1,GR2 and GR3, respectively. Measurement was also conducted on a starting wafer which was labeled G0.

Undoped InP($n = 5 \times 10^{15}/cm^3$), n-type doped InP($N_D = 4 \times 10^{17}/cm^3$), and p-type doped InP($N_A = 1 \times 10^{16}/cm^3$) wafers were also used in this study. In the plasma etching, a $CF_4$ gas was used with an etching time of 2 minutes. Plasma etching was conducted in a Varian RF-diode sputtering system. RTA was conducted with a commercial RTA HEATPULSE 210 in a nitrogen atmosphere at 360°C for 10s. A standard arrangment of PR apparatus was used to measure PR on the starting wafer, after plasma etching and after RTA. A detailed description of the PR set-up was presented elsewhere (ref. 11).

## RESULTS AND DISCUSSION

### A. Gallium Arsenide

According to Aspnes' theory (ref. 12), the parameters of the GaAs layer used in this study would have the PR spectra near bandedge in the high field limit. Thus, the PR signal is an expression of the product of Airy functions and their derivatives which shows the asymptotic form:

$$\Delta R/R \sim \cos\{(2/3)[(\hbar\omega - E_g)/\hbar\Omega]^{3/2} - \pi(d-1)/4\} \quad (1)$$

where $\hbar\omega$ is the energy of the probe beam, $E_g$ is the energy of the bandgap, $\hbar\Omega$ is the characteristic energy of a quantum mechanical particle of interband reduced mass $\mu$ being accelerated by the electric field, $F_s$

$$\hbar\Omega = (e^2 F_s^2 \hbar^2 / 8\mu)^{1/3} \quad (2)$$

Here, d is the dimensionality of the critical point. For a direct transition on GaAs, d = 3 (ref.13).

Figure 1 shows the PR spectra from the starting GaAs wafer and plasma etched samples. Significant PR spectra inflection was observed from plasma etched samples. The large features around the bandgap energy region arise from excitonic effects in the surface space charge region(SCR) (ref. 13). FKO was clearly shown in most samples which are related to the surface electric field as mentioned above. In Fig. 1 (b), (c) and (d) are plotted the PR spectra immediately after plasma etching with chamber pressures of 10mTorr, 50mTorr and 100mTorr. The starting wafer G0, shown in Fig.1 (a), has the strongest PR signal which implies good crystal structure perfection (ref. 14). From the FKO period, a $F_s$ of $2.25 \times 10^5$ V/cm was obtained from G0. The PR spectrum from G1 is shown in Fig.1 (b). PR signal amplitude was decreased about 60% and FKO could not be seen. Both phenomena showed the introduction of crystal imperfection by plasma etching. Displayed in Fig.1 (c) is the PR of G2 where FKO were observed and a $F_s$ of $1.29 \times 10^5$ V/cm was calculated. Fig.1(d) shows the PR from sample G3. Figs.1(c) and (d) showed decreased PR signal amplitude compared with the starting wafer Fig.1(a). Several features at energy lower than bandgap energy position(labeled as T1, T2) were clearly shown. We consider these features to come from plasma etching-induced damage.

Fig. 2 shows the PR spectra of the samples GR1, GR2 and GR3 which were G1, G2 and G3 after RTA treatment, respectively. It is obvious that RTA treatment eliminated or reduced plasma induced damage. The PR signal amplitudes were increased for all samples and the spectra shapes became similar to those for the starting wafer. In particular, Figs.2 (b) and (c) are almost exact copies of Fig.1 (a). FKO were observed in all three RTA treated samples giving $F_s$ values of $1.63 \times 10^5$ V/cm, $1.76 \times 10^5$ V/cm and $2.43 \times 10^5$ V/cm for GR1, GR2 and GR3, respectively.

### B. DLTS analysis

Figure 3 shows the DLTS spectra from the starting wafer G0 (solid line) and for comparison purpose, from one of the plasma etched sample G3 (dashed line). Two traps were

detected in the starting wafer. One labeled E1 with activation energy $E_a = 0.83eV$, capture cross section $\sigma = 2.1\text{-}2.8 \times 10^{-13}$ $cm^2$ and trap concentration $N_t = 3\text{-}4 \times 10^{14}/cm^3$ at bias voltage $V_r = 2V$, and FPH = 0.5V. We consider this trap to be the well known residual defect in bulk GaAs material as EL2 (ref. 15). Another trap labeled E2 was found with $E_a = 0.16\text{-}0.17eV$, $\sigma = 1.25\text{-}2.25 \times 10^{-16}$ $cm^2$, and $N_t = 3\text{-}4 \times 10^{14}/cm^3$. By changing bias and FPH amplitude, the DLTS peak position did not show an apparent shift which indicated these traps in G0 to be in the bulk arising from the material growth process. A plasma induced trap peak in G3 is also shown in Fig. 3 which is more than one order higher in trap concentration compared with those traps found in G0.

Figure 4 is a typical DLTS spectra from sample G2. The detected trap was clearly observed in all 6 different rate windows. Figure 5 shows DLTS spectra from plasma etched samples G1, G2 and G3 under the same testing conditions. One trap peak in a temperature range between $320^oK$ and $360^oK$ was detected in every sample. In the spectra shown, this plasma-induced trap peak was dominant since it has a much higher trap concentration than those in the starting wafer. Values of $E_a$, $\sigma$, and $N_t$ were calculated and are summarized in Table 1. For 10mTorr/50W plasma etching of sample G1, a trap with $E_a = 0.38eV$, $\sigma = 1.25 \times 10^{-17}$ $cm^2$ and $N_t = 1.6 \times 10^{16}/cm^3$ was found under 2V bias and 0.5V FPH. For the same DLTS condition, a trap with $E_a = 0.57eV$, $\sigma = 4.65 \times 10^{-15}$ $cm^2$, and $N_t = 1.2 \times 10^{16}/cm^3$, and with $E_a = 0.67eV$, $\sigma = 2.03 \times 10^{-13}$ $cm^2$ $N_t = 5.4 \times 10^{15}/cm^3$ were detected for the 50mTorr/100W (G2) and 100mTorr/150W (G3) plasma etching conditions, respectively. Conditions used for sample G3 are obviously preferred. Figure 6 shows DLTS spectra from sample G2 under different conditions of fill pulse height(FPH). The trap peak shifting can be clearly seen. As the FPH value increased, the peak position shifted to the lower temperature side. Similar results were obtained from G1 and G3. This shows these plasma induced traps to be interface traps.

The activation energies of induced traps are related to plasma etching pressure and power. Data showed the activation energy to increase with the pressure and power during the plasma etching. This suggests that the higher pressure and power, which increases the plasma particle density participating in collision with the substrate, creates deeper trap levels. The detailed mechanism of the activation energy deviation is under investigation. Arrhenius plots of the thermal emission rates of the deep electron levels found in plasma etched GaAs are presented in Figure 7. The reduction of induced deep levels by RTA annealing was effective. Only one trap, E2, in the starting wafer, was observed in GR1. All plasma induced trap levels disappeared after RTA treatment.

B. Indium Phosphide

Very pronounced FKO was observed in p-type doped InP after plasma etching and RTA as shown in Fig. 8. The PR from the starting wafer is given in Fig. 8(a) where the PR signal was quite weak and FKO was absent. After plasma etching, a pronounced FKO was achieved and the PR signal became very strong. The weak PR signal in the starting wafer may come from an initial oxidation layer which was effectively removed after plasma etching. A $F_s$ of $2.74 \times 10^4$ V/cm was obtained. After RTA treatment at $360^oC/10s$, good FKO were still observed and the shape of the PR was similar to that before RTA. The bandgap transition shifted to the higher energy side and a higher surface electric field $F_s$ of $4.13 \times 10^4$ was obtained.

Figure 9 shows the PR spectra of an n-type doped InP sample. No obvious FKO was observed here. The PR modulation in the near bandgap region was obtained from every spectrum which permits the bandgap energy to be determined by Aspnes' method. A lower energy side peak labeled To, with energy position at 1.210 eV, was observed in all PR spectra which may come from impurity or structral defect modulation. Other authors concluded the low energy side peak to be associated with doping inhomogeneities in the samples (ref. 17). Another PR maximum peak occurred on the higher energy side labeled $O_1$ in Figure 9 with energy position at 1.417 eV. After the plasma treatment, the higher energy peak disappeared which implied that $O_1$ came from a kind of surface oxidation layer which could be removed by the plasma etching. A new peak with energy position at 1.280 eV, labeled $T_1$, appeared after plasma etching which should come from the plasma damage. The current RTA treatment on n-type InP ($360^{o}C/10s$) could not remove both To and $T_1$. But, the PR signal became stronger after RTA which indicated the partial recovery of the crystal structure damage (ref. 18). It was found that the higher energy side peak $O_1$ reoccurred after RTA which may be attributed to a newly grown oxidation layer.

Figure 10 shows the PR spectra of undoped(n-type) InP material. An extra peak at energy below bandgap with position at 1.258 eV, labeled To, was observed in all PR spectra which may arise from impurity or defect modulation as found in the n-type doped InP. Another peak, labeled $T_1$, occurred in the plasma treated sample with energy position at 1.305 eV which was introduced by the plasma etching. Different RTA conditions were used for undoped InP which include: $360^{o}C/10s$, $390^{o}C/10s$, $390^{o}C/20s$, and $420^{o}C/10s$. After the $390^{o}C/20s$ RTA treatment, $E_g$ shifted back to 1.344 eV and the $T_1$ peak diminished which showed this annealing condition to effectively recover the crystal imperfection and damage due to the plasma. The energy peak To kept occurring in all PR spectra, at the same position and intensity, which shows that it could not be influenced by plasma and RTA. We also noticed that the PR signal became weaker after plasma treatment which showed that the plasma processing did introduce a disordered region and affected crystal perfection.

## CONCLUSIONS

Both photoreflectance (PR) and deep level transient spectroscopy (DLTS) are effective in evaluating quality of starting wafers and defects introduced by plasma etching. Photoreflectance is particularly valuable because of the non-destructive nature of the test. Both PR and DLTS reveal damage signals after plasma etch with DLTS giving traps having activation energy dependent on plasma condition. Studies on GaAs reveal an almost complete healing of plasma-induced defects after RTA at $450^{o}C$ for 10s. The degree of damage induced by plasma etch may be controlled by variation of the power and pressure during plasma etching. Thus, an optimum condition may be achieved.

Similar studies on InP revealed a much greater sensitivity to plasma etching such that samples could not be tested by DLTS after plasma etching although a PR signal could be seen. Complete recovery after RTA was not observed. InP also exhibited extraneous PR signals both above and below $E_g$ indicating inherent defects as well as plasma induced ones. Similar defects have been seen by others but have not been clearly identified.

## REFERENCES


1. L.A. Coldren, K. Iga, B. I. Miller and J.A. Rentschler, Appl. Phys. Lett., 37, 681 (1980).
2. S. Semmra, T. Ohta, T. Kwroda and H. Nakashima, Jpn. J. Appl. Phys., 24, L463 (1985).
3. K. Asakawa and S. Sugata, J. Vac. Sci. Tech., B3, 402 (1985).
4. S.W. Pang, J. Electrochem. Soc.: Solid-State Sci. & Technol., 133, 784 (1980).
5. S.W. Pang, G.A. Lincoln, R.W. McClelland, P.d. DeGraff, M.W. Geis and W.J. Piacentini, J. Vac. Sci. & Technol., B1, 1334 (1983).
6. Y. Yuba, T. Ishida, K. Gamo and S. Namba, J. Vac. Sci. & Technol., B6, 253 (1988).
7. J.Z. Yu, N. Masui, Y. Yuba, T. Hara, M. Hamagaki, Y. Aoyagi, K. Gamo and S. Namba, Jpn.J. Appl. Phys., 28, 2391 (1989).
8. S. Sugata and K. Asakawa, J. Vac. Sci & Technol., B6, 876 (1988).
9. F.H. Pollak and H. Shen, J. Elect. Mat., 19, 399 (1990).
10. H. Shen, F.H. Pollak and J.M. Woodall, J. Vac. Sci. Technol. B8, 413 (1990).
11. L.He and W. A. Anderson, J. Elect. Mat., 20, 359 (1991).
12. D.E. Aspnes, Proc. 1st Int. Conf. on Modulation Spectroscopy,1972, [surf. Sci. 37, 418 (1973)].
13. M. Sydor, N. Jahren, W.C. Mitchel, W.V. Lampert, T.W. Haas, M. Y. Yen, S.M. Mudare and D.H. Tomich, J. Appl. Phys., 67, 7423 (1990).
14. N. Bottka, D.K. Gaskill, R.S. Sillmon, R. Henry and R. Glosser, J. Elect. Mat., 17, 161 (1988).
15. D.W.E. Allsopp, Solid State Phenomena, 1 & 2, 211 (1988).
16. K. Yamasaki, M. Yoshida and T. Sugano, Jpn. J Appl. Phys., 18, 113 (1979).
17. M. Gal, R. Shi and J. Tann, J. Appl. Phys., 66, 6196 (1989).
18. S.K. Brierley and D. S. Lehr, J. Appl. Phys., 67, 3878 (1990).


**Table 1 Data from DLTS Studies of GaAs**

**(@ Vr = -2V, FPH = 0.5V)**

| Sample | Activation Energy $E_a$(eV) | Capture Cross-Section $\sigma$(cm$^2$) | Trap Density $N_t$(cm$^{-3}$) |
|---|---|---|---|
| G0 | 0.83 | $2.80 \times 10^{-13}$ | $3.0 \times 10^{14}$ |
| | 0.16 | $1.25 \times 10^{-16}$ | 4.0x1014 |
| G1 | 0.38 | $1.25 \times 10^{-17}$ | $1.6 \times 10^{16}$ |
| G2 | 0.57 | $4.65 \times 10^{-15}$ | $1.2 \times 10^{16}$ |
| G3 | 0.67 | $2.03 \times 10^{-13}$ | $5.4 \times 10^{15}$ |

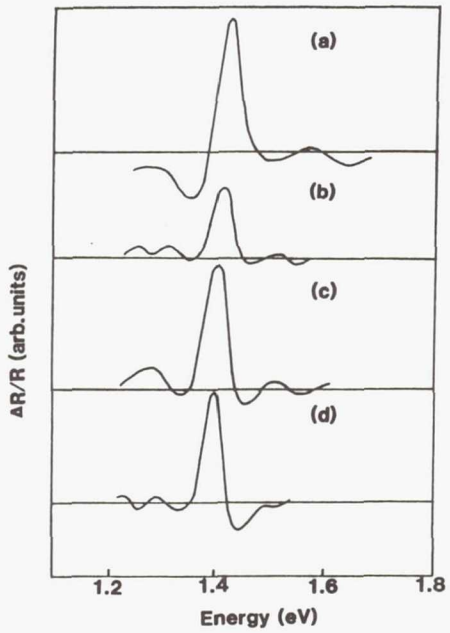


Fig. 1 The PR spectra of (a) starting wafer, and after plasma etching at (b) 10m Torr/50W, (c) 50mTorr/100W, (d) 100mTorr/150W.

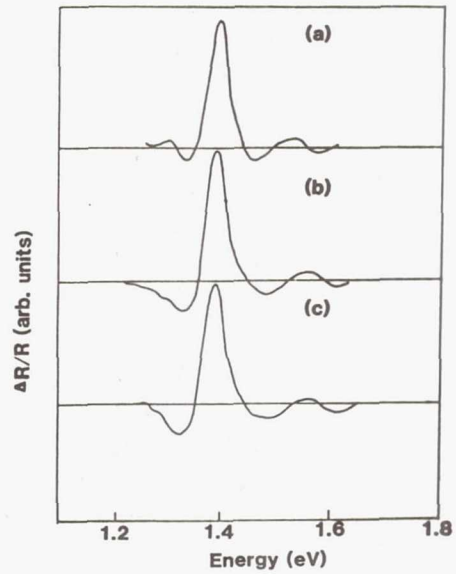


Fig. 2 The PR spectra from plasma etched samples (a) 10mTorr/50W, (b) 50mTorr /100W and (c) 100mTorr/150W, all after RTA treatment at 450°C, 10 seconds.

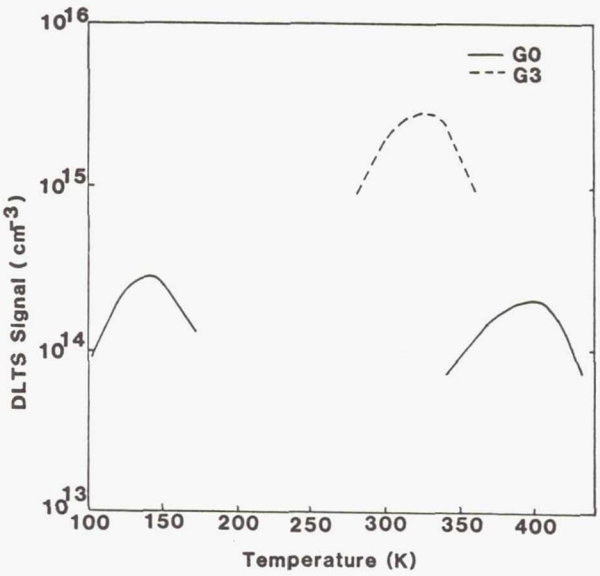


Fig. 3 DLTS spctra for the starting GaAs wafer G0 (solid line) and plasma etched sample G3 where the dashed line shows the added signal.

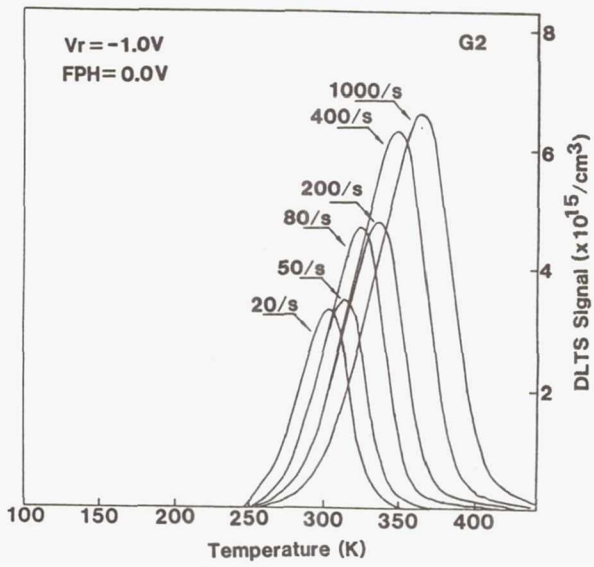


Fig. 4 A typical DLTS spectra of sample G2 (50mTorr/100W plasma etched) for different rate windows.

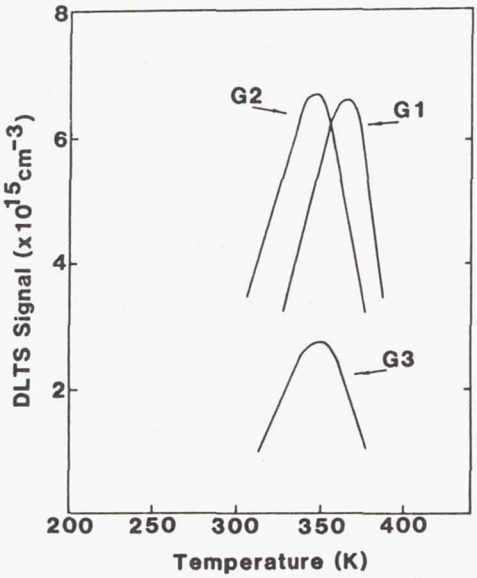


Fig. 5 The DLTS spectra from samples G1, G2 and G3 under the same testing conditions.

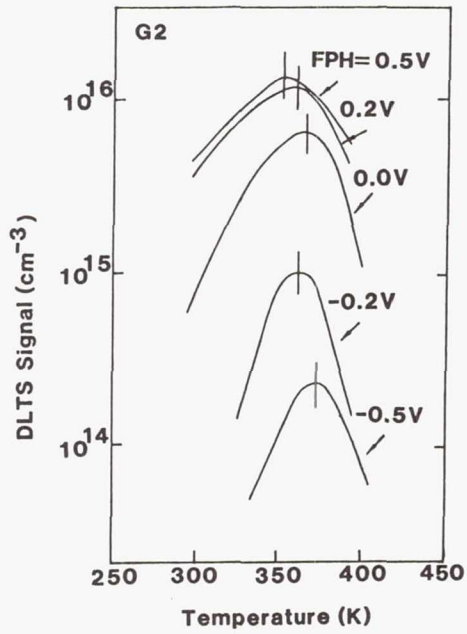


Fig. 6 The DLTS spectra from sample G2 under different fill pulse height (FPH).

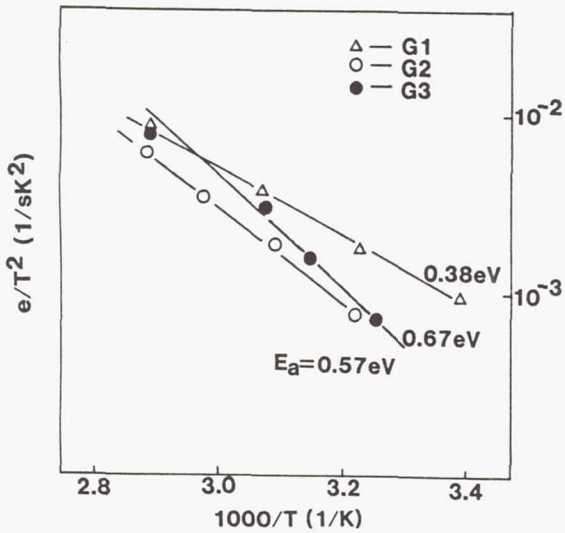


Fig. 7 Arrhenius plots of the thermal emission rates of the electron traps found in plasma etched GaAs samples G1, G2 and G3.

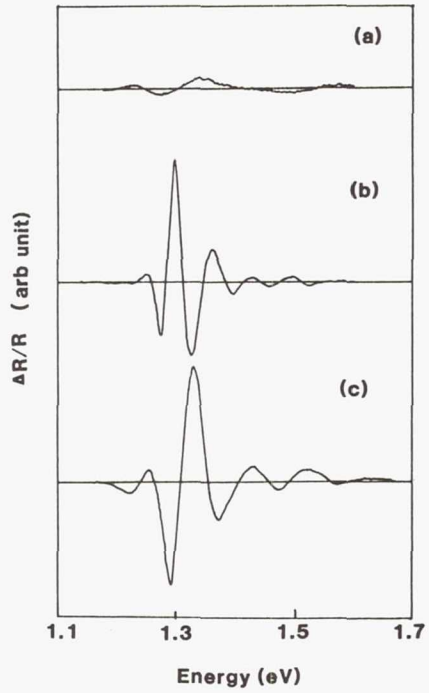


Fig. 8 PR spectra from a p-type InP from (a) starting wafer and the wafer after: (b) plasma etching, (c) RTA.

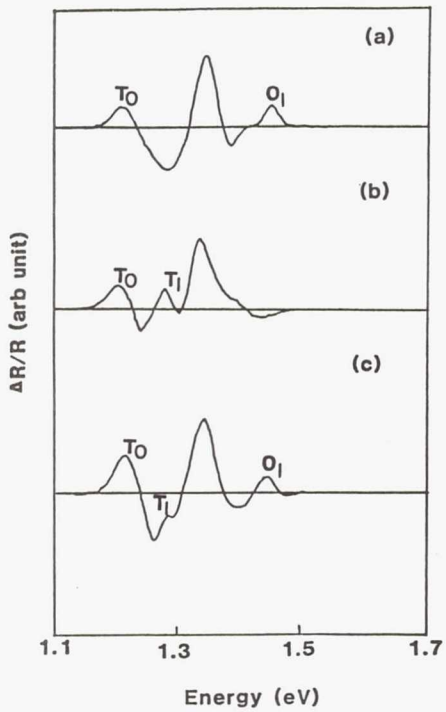


Fig. 9 PR spectra of n-type doped InP.
(a) starting wafer (b) plasma etched and (c) RTA treated wafer.

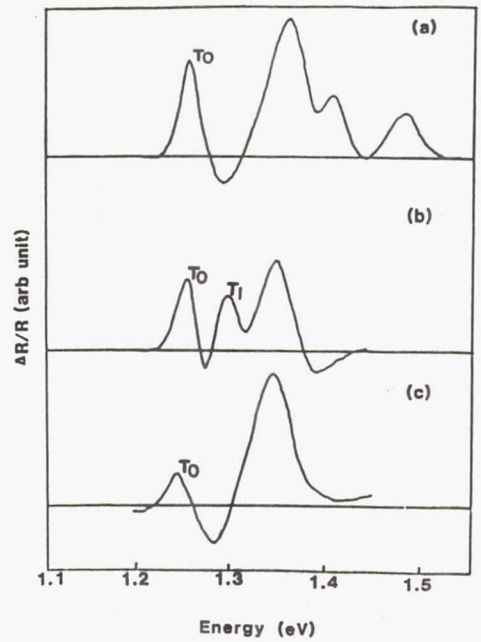


Fig.10 PR spectra of undoped InP.
(a) starting wafer (b) plasma etched and (c) RTA treated wafer.

# CALCULATION OF GALLIUM-METAL-ARSENIC PHASE DIAGRAMS

**J. D. Scofield**
**Wright Laboratory**
**WPAFB OH**

**J. E. Davison, A. E. Ray and S. R. Smith**
**University of Dayton, Research Institute**
**Dayton OH**

## ABSTRACT

Electrical contacts and metallizations to GaAs solar cells, intended for satellite array and other space-based applications, must survive at high temperatures for several minutes under specific mission scenarios. The determination of which metallizations or alloy systems that are able to withstand extreme thermal excursions with minimal degradation to solar cell performance can be predicted by properly calculated temperature constitution phase diagrams. Alternately, the thermodynamic behavior of metal-GaAs systems could only be accomplished by performing hundreds of controlled reactions and experimentally determining compound formation, diffusion couples, eutectic points, and finally, electrical/mechanical performance degradation. A method for calculating a ternary diagram and its three constituent binary phase diagrams is briefly outlined and ternary phase diagrams for three Ga-As-X alloy systems are presented. Free energy functions of the liquid and solid phases are approximated by the regular solution theory. The three binary systems comprising the boundaries of a ternary phase diagram are utilized to calculate the binary regular solution parameters. The free energy functions for the ternary system liquid and solid phases are then written as a combination of the binary regular solution parameters. Liquidus and solidus boundaries, as functions of temperature and composition, for the ternary diagrams are calculated from these free energy functions. Phase diagrams calculated using this method are presented for the Ga-As-Ge and Ga-As-Ag systems.

## INTRODUCTION

This research effort was initiated to determine an alloy system which is chemically stable when exposed to extreme temperature excursions, exceeding 873 K, while functioning as electrical contact metallization to GaAs. The theoretical portion of this investigation has been the calculation and utilization of temperature constitution phase diagrams to determine suitable alloy compositions, which will be in equilibrium with the (p) or (n)GaAs solar cell emitter when the device is thermally stressed. Large

numbers of binary phase diagrams have been determined experimentally and are readily available in the open literature [1-4]. However, only a few of the possible ternary alloy systems have been experimentally investigated. The vast numbers of possible ternary alloys, and the extensive experimental effort that would be required to satisfactorily determine a ternary phase diagram, prompted us to utilize computational methods to calculate the equilibrium phase boundaries for selected alloy systems. Mathematical representations for the liquidus and solidus phase boundaries were derived through an application of the heterogeneous phase equilibrium principle [5-6] to ternary alloy systems. The analytical expressions were developed with the following assumptions made: (a) the liquid and solid phases can be described by the theory of a regular solution [6], (b) the regular solution parameter is a linear function of the absolute temperature, (c) the free energy function of the ternary phases can be represented by a linear combination of the binary regular solution parameters [7], (d) the binary compounds have a fixed composition and have no solubility for any of the elemental constituents, and (e) the Neumann-Kopp rule is obeyed [8].

## BINARY ALLOY SYSTEMS

The development of an expression representing the thermodynamic equilibrium in a binary alloy system was accomplished for two distinct phase boundary conditions. The first representation describes the equilibrium between a binary liquid phase and a terminal solid solubility phase. The second case treats the equilibrium between a binary liquid phase and an intermediate binary compound. The equations describing these two cases are utilized in conjunction with the experimentally determined elemental and binary alloy data to calculate the values for the binary regular solution parameters. In order to obtain a quantitative measure as to the correctness of the computational method, the calculated values for the regular solution parameters were used to generate the boundaries for the liquidus and solidus phases of binary systems and then compared to the experimentally obtained values for the phase equilibrium boundaries.

## EQUILIBRIUM BETWEEN A BINARY LIQUID PHASE AND A BINARY TERMINAL SOLID SOLUBILITY PHASE

In developing the mathematical relations to express the thermodynamic equilibrium between a binary liquid phase and a terminal solid solubility phase the following procedure and principles were utilized:

1. Apply the principle of heterogeneous phase equilibrium.

2. Represent the partial molal free energy terms of each of the elemental components as functions of the standard state free energies of the pure elements, the activity coefficients, the

mole fractions of the components, and the absolute temperature.

3. The difference between the standard state free energies of the liquid and solid states of each of the elements is expressed in terms of their heats of fusion and melting temperatures. The difference between the heat capacities of the liquid and solid phases is assumed to be zero.

4. Use the regular solution model of alloying behavior to obtain expressions for the activity coefficients of the elemental components.

A straightforward application of these steps results in the expressions for the boundaries of the phase diagram.

The analytical representation for the thermodynamic equilibrium between a binary liquid phase and a terminal solid solubility phase is given by the two simultaneous equations:

$$\Delta HF_1 \times (1 - T/T_1) = R \times T \times \ln(N_{1S}/N_{1L}) + S12 \times N_{2S}^2 - L12 \times N_{2L}^2 \qquad (1a),$$

and

$$\Delta HF_2 \times (1 - T/T_2) = R \times T \times \ln(N_{2S}/N_{2L}) + S12 \times N_{1S}^2 - L12 \times N_{1L}^2 \qquad (1b),$$

where $HF_1$ and $HF_2$ are the heats of fusion for element 1 and element 2 respectively; L12 is the liquid phase regular solution parameter for alloy 1-2; S12 is the solid phase regular solution parameter for alloy 1-2; $N_{1L}$, $N_{2L}$, $N_{1S}$, and $N_{2S}$ are the mole fractions of element 1 and element 2 in the liquid and solid phases; R is the gas constant; T is the system temperature; and $T_1$ and $T_2$ are the melting temperatures of the two component elements.

The regular solution parameters, L12 and S12, are assumed to be linear functions of the absolute temperature as shown below:

$$L12 = \alpha + \beta T \qquad (2a)$$

and

$$S12 = \chi + \delta T \qquad (2a),$$

where the slope and intercept constants are determined from a fit of the data to a linear function of the absolute temperature.

## EQUILIBRIUM BETWEEN A BINARY LIQUID PHASE AND A BINARY COMPOUND PHASE

The relationship developed for describing composition of the liquid boundary which is in equilibrium with an intermediate binary compound was developed by following the following steps:

1. The molal free energy of the compound is expressed in terms of the compound composition and the partial free energies of its solid elemental components.

2. Heterogeneous phase equilibrium principles are used to describe the partial molal free energies in terms of the elemental components of the liquid phase which are in equilibrium with the compound.

3. The molal free energy of the compound is expressed in terms of the absolute temperature, standard state free energies, mole fractions, and the activity coefficients of the components in the liquid phase.

4. The molal free energy of the liquid phase, which has the same composition as that of the compound, is described using the same variables as in Step 3 above.

5. The heat capacity differences between the compound and the liquid are assumed to be zero. The molal free energy differences of the compound and the liquid phase are expressed in terms of the heat of fusion and temperature of the compound. The free energy difference between the liquid and solid phases at the equilibrium melting temperature is zero.

6. Regular solution theory is used to define the relations for the activity coefficients of each component of the liquid phase.

The resulting equation which describes the equilibrium between the binary liquid phase and the binary compound is given by the relation [9],

$$\begin{aligned}\Delta H_C \times (1 - T/T_C) &= R \times T \times (N_{1C} \times \ln(N_{1C}) + N_{2C} \times \ln(N_{2C})) \\ &- R \times T \times (N_{1C} \times \ln(N_{1L}) + N_{2C} \times \ln(N_{2L})) \\ &+ N_{1C} \times L12 \times N_{2C}^2 + N_{2C} \times L12 \times N_{1C}^2 \\ &- N_{1C} \times L12 \times N_{2L}^2 - N_{2C} \times L12 \times N_{1L}^2 .\end{aligned} \tag{3}$$

## RESULTS FOR BINARY ALLOY SYSTEMS

### Gallium-Germanium

To demonstrate the validity of this computational method of

calculating equilibrium phase diagrams, the gallium-germanium (Ga-Ge) system is discussed in detail as an example and compared to empirical data from the literature. Equations (1a) and (1b) were utilized to obtain the binary regular solution parameters. Elemental values for the melting temperatures and the heats of fusion were taken from the compilation of Hultgren [10] and are listed in Table 1. Temperature and composition values for the liquidus and solidus boundaries, required for these calculations, are from the experimental efforts of Keck and Broder [11], Greiner and Breidt [12], and Thurmond and Kowalchik [13].

**Table 1**

Values for the Heats of Fusion and Melting Points of Selected Elements

| Element | Heat of Fusion (Cal/gm-at) | Melting Point (K) |
|---|---|---|
| Silver (Ag) | 2700 | 1234 |
| Arsenic (As) | 2600 | 1090 |
| Gallium (Ga) | 1335 | 303 |
| Germanium (Ge) | 8100 | 1210 |

At several temperatures the values for the regular solution parameters were calculated. These data points were fit to a linear function of the temperature by the method of least squares. Calculated values for the slope and intercept for the Ge-Ga and other selected binary systems are shown in Table 2. As a check on the computations, phase boundaries for the Ge-Ga binary system were calculated and compared to experimental values from Hansen [14]. Figure 1 shows the liquidus and solidus boundaries calculated for the Ga-Ge system. Ge solubility in Ga is very small and the region of terminal solubility is almost coincident with pure Ga. The composition calculated for the eutectic of Ga-Ge is located close to the melting point of pure Ga, which is in agreement with experimental results. The calculated and experimental liquidus boundary difference is less than 1 atomic percent over the complete composition and temperature range. Ge solidus boundary calculations also show the same retrograde solubility characteristic that has been experimentally observed. Maximum Ga solubility in solid Ge occurs near 650°C for both calculated and experimental boundaries.

## GaAs Liquidus Boundary

Experimental values are available for only a few compounds of interest [8,9], therefore two sets of computations were completed. In the first set, values for the heat of fusion, melting point, and composition of GaAs, and the composition and temperature of the liquid phase that is in equilibrium with the compound were used to calculate the regular solution parameter for the liquid phase.

Experimental values for GaAs were taken from References [14,15,19]. The regular solution parameter calculated from these values using Equation 3 is shown in Table 2.

**Table 2**

Calculated Binary Regular Solution Parameters

| System | Liquid Intercept | Liquid Slope | Solid Intercept | Solid Slope | Ref. |
|---|---|---|---|---|---|
| Ag-As | -9256.9 | .12305 | 134.12 | -4.1037 | [16] |
| Ag-Ga | -28,269 | 18.887 | -25,839 | 15.932 | [17] |
| As-Ga* | 10,455 | -11.608 | --- | --- | [14,15] |
| As-Ga** | 19,264 | -11.233 | --- | --- | [14,15] |
| As-Ge | -6200.4 | 4.688 | 16,816 | -6.0467 | [18] |
| Ga-Ge | 210.23 | -.54553 | 5945.4 | -2.0719 | [11-13] |

* Calculated with the heat of fusion = 10,758 cal/gm-at.
**Calculated with the heat of fusion = 3,613 cal/gm-at.

The second set of computations involved using the same values for the melting point and composition of GaAs and the same liquidus boundary to determine values for the heat of fusion of GaAs and the regular solution parameter of the liquid phase. The GaAs heat of fusion calculation, in addition to those for other binary compounds, are listed in Table 3. The slope and intercept values are listed in Table 2.

**Table 3**

Heat of Fusion of Selected Binary Compounds

| Compound | $H_f$ Calculated | $H_f$ Experimental |
|---|---|---|
| AsGa | 3613 | 10,578 |
| $As_2Ge$ | 7789 | --- |
| AsGe | 8087 | --- |

The heat of fusion value difference between the calculated and experimental results is considerable. Similarly, the values obtained for the regular solution parameter shows a significant disparity. In order to determine accuracy of subsequent calculations using these values, the liquidus boundaries were computed using the values obtained in the two sets of calculations. The resulting Ga-As phase diagram showing the comparison between the two sets of calculations are shown in Figure 2. Statistical analysis of the results shows that the maximum deviation between the computed and experimental boundaries is less than five atomic

percent arsenic. While the thermodynamic values are significantly different between the two approaches, the resulting liquidus boundaries for the calculated and experimental values are in satisfactory agreement.

## TERNARY ALLOY SYSTEMS

Expressions describing the equilibrium in ternary systems were developed for two situations. First, the equilibrium between a ternary liquid phase and a ternary terminal solid solubility phase is represented by three simultaneous equations. Secondly, the expression for the equilibrium between a ternary liquid phase and a binary compound was formulated. The thermodynamic behavior is approximated by the binary regular solution parameters in both instances.

## EQUILIBRIUM BETWEEN A TERNARY LIQUID AND A TERNARY SOLID SOLUBILITY PHASE

The assumptions and procedures for developing the relations describing the binary equivalent to this case were applied and the following three simultaneous equations were generated.

$$\Delta H_{f1}\times(1 - T/T_1) = R\times T\times\ln(N_{1S}/N_{1L}) + L12\times N_{2L}\times(1 - N_{1L}) + L13\times N_{3L}\times(1 - N_{1L}) - L23\times N_{2L}\times N_{3L} - S12\times N_{1S}\times(1 - N_{2S}) - S23\times N_{3S}\times(1 - N_{2S}) + S13\times N_{1S}\times N_{3S}, \quad (4a)$$

$$\Delta H_{f2}\times(1 - T/T_2) = R\times T\times\ln(N_{2S})/N_{2L} + L12\times N_{1L}\times(1 - N_{2L}) + L23\times N_{3L}\times(1 - N_{2L}) - L13\times N_{1L}\times N_{3L} - S12\times N_{1S}\times(1 - N_{2S}) - S23N_{3S}\times(1 - N_{2S}) + S13\times N_{1S}\times N_{3S}, \quad (4b)$$

and

$$\Delta H_{f3}\times(1 - T/T_3) = R\times T\times\ln(N_{3S}/N_{3L}) + L13\times N_{1L}\times(1 - N_{3L}) + L23\times N_{2L}\times(1 - N_{3L}) - L12\times N_{1L}\times N_{2L} - S13\times N_{1S}\times(1 - N_{3S}) - S23\times N_{2S}\times(1 - N_{3S}) + S12\times N_{1S}\times N_{2S}. \quad (4c)$$

Equations (4a)-(4c) were solved to yield a solution, as a function of temperature, for the ternary Ga-As-Ge liquidus boundary which is in equilibrium with the Ge solid solubility phase. The binary regular solution parameters, which are used to estimate the alloying behavior of the ternary alloys, are those listed in Table 2. A 1000K isothermal section of the resulting ternary diagram is shown in Figure 3a and includes several tie-lines which connect the compositions on the liquidus boundary which are in equilibrium with the composition on the Ge solidus boundary. These calculations were repeated for the Ag-Ga-As system and an 800K isothermal plot of the liquidus and solidus boundaries is shown in Figure 3b.

## EQUILIBRIUM BETWEEN A TERNARY LIQUID AND A BINARY INTERMEDIATE COMPOUND PHASE

An expression describing the equilibrium between a ternary liquid and a binary compound relates the heat of fusion and melting temperature of the binary compound, and the regular solution parameters, composition, and temperature of the ternary liquid phase. Following the steps outlined for the equivalent binary case given above, the following equation results.

$$\begin{aligned}\Delta H_C \times (1 - T/T_C) = {} & R \times T \times (N_{1C} \times \ln(N_{1C}) + N_{2C} \times \ln(N_{2C})) - R \times T \times (N_{1C} \times \ln(N_{1L} + N_{2C} \times \ln(N_{2L})) \\ & + N_{1C} \times N_{2C} \times L12 - N_{1C} \times (L12 \times N_{2L} \times (1 - N_{1L}) + L13 \times N_{3L} \times (1 - N_{1L}) \\ & - L23 \times N_{2L} \times N_{3L}) - N_{2C} \times (L12 \times N_{1L} \times (1 - N_{2L}) + L23 \times N_{3L} \times (1 - N_{2L}) \\ & - L13 \times N_{1L} \times N_{3L}) . \end{aligned} \tag{5}$$

Equation (5) was solved as a function of temperature to yield the compositions of the Ga-As-Ge liquidus boundary which are in equilibrium with the compound GaAs. Figure (4a) shows the resulting diagram and the calculated liquidus boundary, which is the dominant liquid surface for this ternary system.

This liquidus surface has two intersections with the previously calculated ternary liquid boundary, which is in equilibrium with the Ge solid solubility phase, at a temperature of 873K. These two intersections define the compositional endpoints for which the liquid phase will be present. Figure 5a is a plot of the 1000K isothermal section and shows the liquid and solid boundaries with tie-lines connecting the liquid and solid phases at the two intersection endpoints mentioned above. Ternary compositions which fall between these two points will result in the presence of only two solid phases at equilibrium, the GaAs compound and the Ge alloy. There is however, a ternary eutectic involving GaAs, GeAs, and the Ge solid solubility phase and will act to lower the limit of the As-rich Ge solid solubility phase that is in equilibrium with GaAs.

These calculations were also performed for the Ag-Ga-As ternary system. The results of the previous section for the 800K computation, which determined the boundary between a ternary liquid phase that is in equilibrium with GaAs, is shown in Figure 4b. The results of this section were combined with the calculations reflected in Figure 4b and the resulting complete 800K Ag-Ga-As ternary diagram, showing liquidus and solidus boundaries with compositional tie-lines is presented in Figure 5b.

## TERNARY EUTECTICS OF THE Ag-Ga-As SYSTEM

A eutectic point involving the ternary liquid phase, GaAs, GeAs, and a primary Ge solid alloy phase was calculated from the intersection of the three relevant ternary liquidus phase boundaries. These three boundaries are related to the equilibrium

between the ternary liquid phase and the GaAs compound, the GeAs compound, and the solid Ge alloy phase. The ternary liquid phase composition and temperature of the eutectic point and the composition of the solid Ge alloy phase in equilibrium with the GaAs and GeAs at this temperature is listed in Table 4. Of the three solid phases in this eutectic reaction the Ge solid solubility phase contains 99.78 atomic percent Ge, 0.16 atomic percent As, and 0.06 atomic percent Ga. Ge compositions on the solidus boundary containing a higher percentage of As will be in equilibrium with the GeAs compound.

The composition and temperature of the ternary liquid phase in equilibrium with the three compounds GaAs, GeAs, and $GeAs_2$ at the eutectic was determined from the intersection of the three liquidus surface boundaries described above but with the solid Ge alloy phase replaced by the compound $GeAs_2$ as the third liquidus boundary. These compositional values and eutectic temperature are also listed in Table 4.

**Table 4**

| Solid Phases | Temp. (K) | Liquidus Atomic % Ga | As | Balance |
|---|---|---|---|---|
| GaAs, GeAs, Ge | 1002 | 41.8 | 1.7 | Ge |
| GaAs, GeAs, $GeAs_2$ | 1000 | 60.9 | 0.6 | Ge |

Calculated Eutectic Compositions for the As-Ga-Ge System

Presented in Figure 6 is a representation of the complete As-Ga-Ge ternary phase diagram, including the three component binary diagrams which comprise the complete system. Visualization of the two eutectic points is enhanced by this representation. It is located by two distinct valleys which would form when the entire liquidus surface connecting the boundaries between the three binary diagrams is generated.

## SUMMARY

Germanium and silver alloys compositions which are in equilibrium with gallium arsenide were determined from the appropriate ternary phase diagrams. The procedure for calculating these compositions consists of:

1. Modeling the free energy functions of the binary and ternary phases by an application of the theory of a regular solution.

2. Generating the representations for the binary and ternary liquid and solid boundaries from the calculated free energy functions.

3. Binary regular solution parameters are calculated from the melting temperatures, and heats of fusion elemental values and the experimental values for the binary liquidus and solidus boundaries.

4. Approximating the ternary liquid and solid regular solution parameters as a sum of the component binary systems.

5. The compositions of the ternary liquid and solid boundaries are calculated as a function of temperature.

6. Calculating the compositions at the intersections of the ternary liquidus boundaries as a function of temperature. These compositions are the limiting values for which the liquid phase will be present. Between these limits only the solid phases will be present.

7. Using the tie-lines between the liquid and solid phases to obtain the compositions on the ternary solidus surface that are in equilibrium with the ternary liquid phase at the intersection points.

8. The solid compositions resulting from Step 7 are the endpoints for which only two solid phases, GaAs and the terminal solid solubility phase will coexist.

Ternary eutectic involving the ternary terminal solid solubility will limit the compositional range of solid alloys that will be in equilibrium with GaAs. A ternary eutectic point involving the three solid phases was obtained from the intersection of the ternary liquidus surfaces whose compositions are in equilibrium with each of the three solid phases.

Experimental verification of the correctness of the ternary phase equilibrium model is currently being undertaken. Differential scanning calorimetry is the primary technique being utilized to verify the equilibrium reactions predicted. Additional analysis to determine composition and compound formation is to include TEM and SIMS techniques but have yet to be initiated. Initial calorimetry results would seem to indicate that the non-equilibrium solid state reactions will have equal importance in the development of a suitable alloy system for high temperature metallizations to GaAs.

REFERENCES

1. M. Hansen, Constitution of Binary Alloys, (McGraw-Hill Book Co., New York, 1958).
2. R. Elliott, Constitution of Binary Alloys, (McGraw-Hill Book Co., New York, 1965).
3. F. Shunk, Constitution of Binary Alloys, (McGraw-Hill Book Co., New York, 1969).
4. W. Moffat, Handbook of Binary Phase Diagrams, General Electric Co., Schenectady NY, 1984).

5. O. Kubachewski, Journal of the Institute of Metals 93, 329-38, (1965).
6. A. Prince, Alloy Phase Equilibria, (American Elsevier Publishing Co., 1966).
7. M. Hoch, Trans. of the Metallurgical Society of AIME, 224 379-82, (1962).
8. O. Kubachewski and E. Evans, Metallurgical Thermochemistry, 3rd Ed., (Pergammon Press, Ny, 1958).
9. L. Vieland, Acta Metallurgica, 11, 137-42 (1963).
10. R. Hultgren, Selected Values of Thermodynamic Properties of Metals and Alloys, (John Wiley, 1963).
11. P. Keck and J. Broder, Phys Rev. 60, 521-2, (1953).
12. E. Greiner and P. Breidt, Trans. AIME 203, 187, (1955).
13. C. Thurmond and M. Kowalchik, Bell System Tech. J. 39, 169, (1960).
14. R. Hall, J. Electrochem. Soc. 46, 385, (1955).
15. W. Koester and B. Thoma, Z. Metallk. 46, 291, (1959).
16. G. Eade and W. Hume-Rothery, Z. Metallk. 50, 123, (1959).
17. W. Hume-Rothery and K. Andrews, J Inst. Metals 68, 133, (1942).
18. B. Gather and R. Blachnik, Z. Metallk. 3, 168, (1976).
19. M. Tmar, et.al.,J. Crystal Growth 60, 421, (1984).2

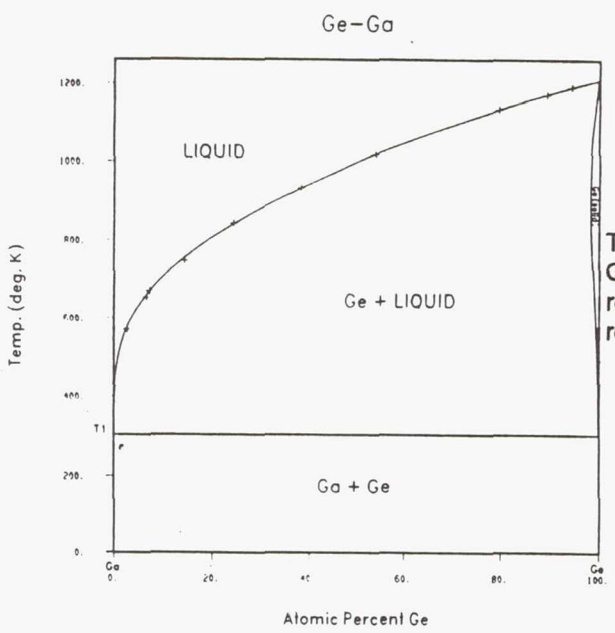


FIGURE 1

The temperature - constitution phase diagram for the Ga-Ge system. The calculated boundaries are represented by the solid lines and the experimentally reported results are shown as "+" symbols.

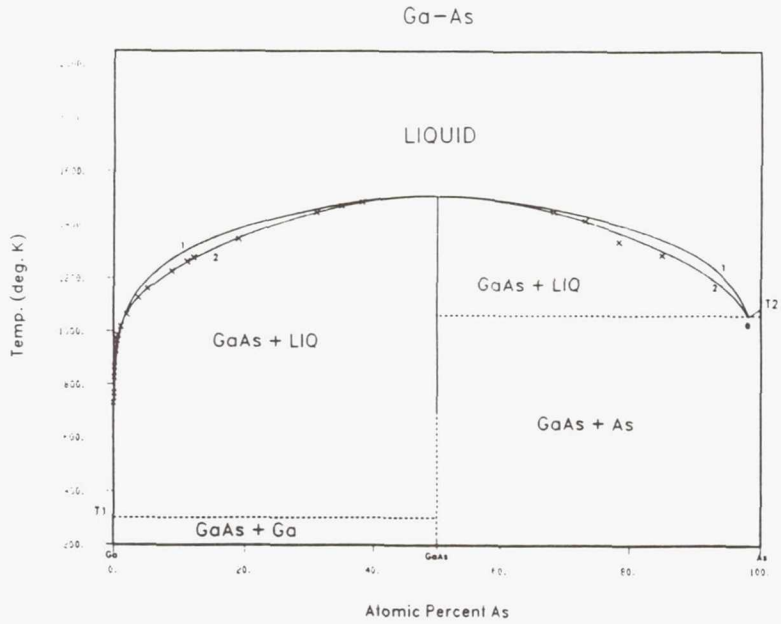


FIGURE 2

Temperature constitution phase diagram for the Ga-As system. Curve 1 is the calculated liquidus boundary and curve 2 the experimental boundary.

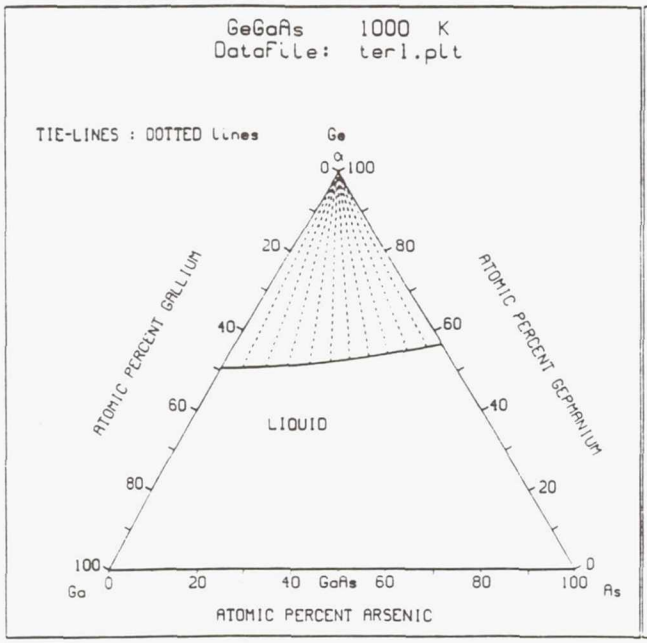


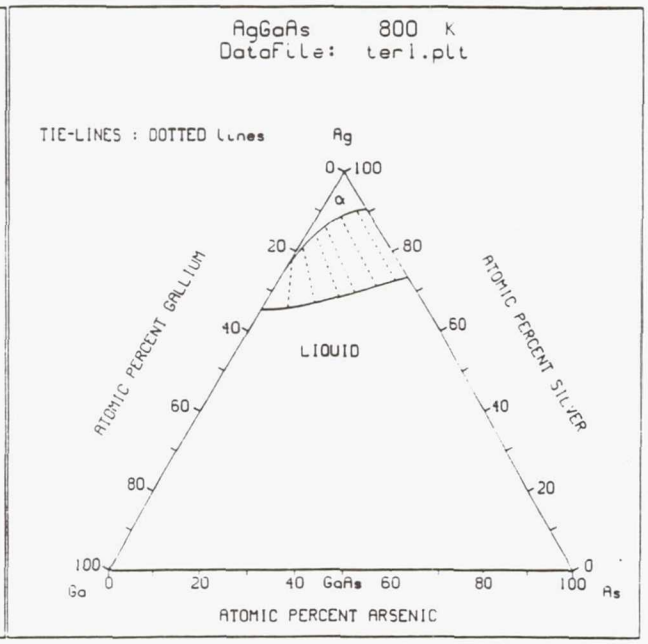


FIGURE 3a

FIGURE 3b

The Ge and Ag rich corners of their respective ternary phase diagrams. Tie-lines shown connect the liquid and solid compositions which are in equilibrium.

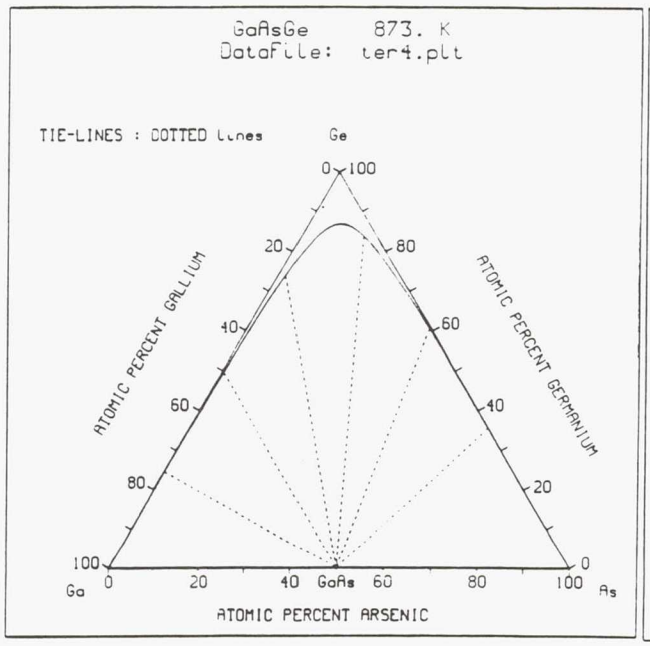


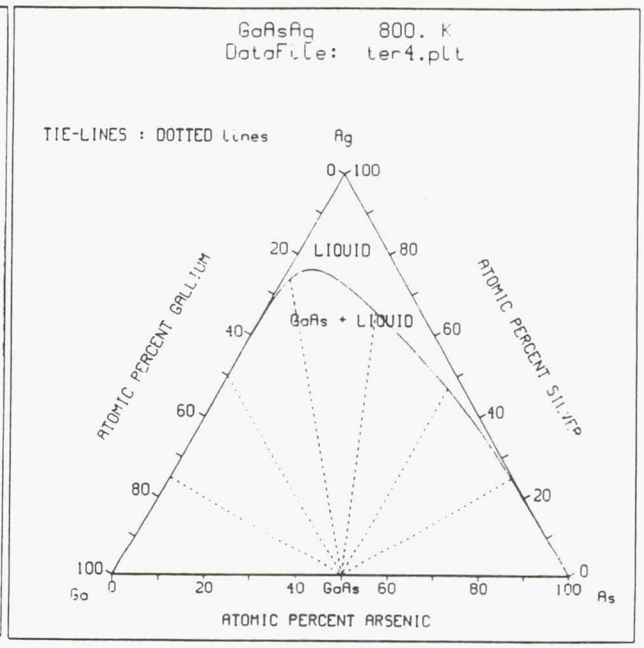


FIGURE 4a

FIGURE 4b

Ga-As-Ge and Ga-As-Ag phase diagrams showing the ternary liquid composition which are in equilibrium with GaAs.

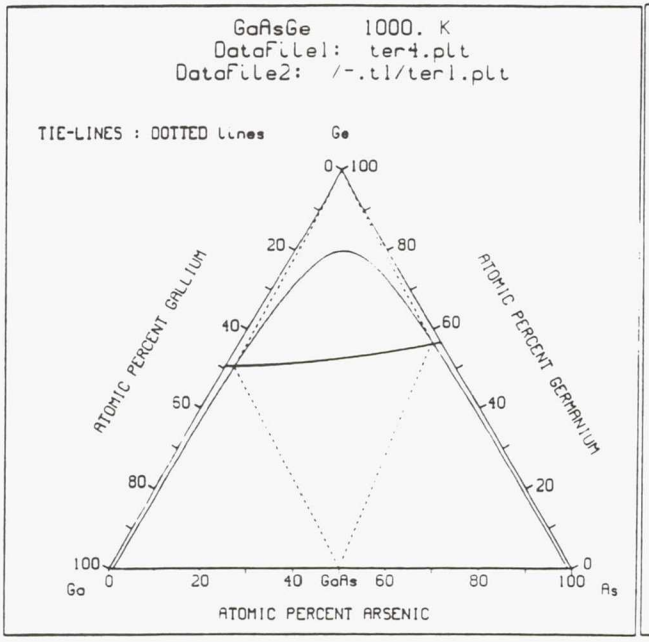


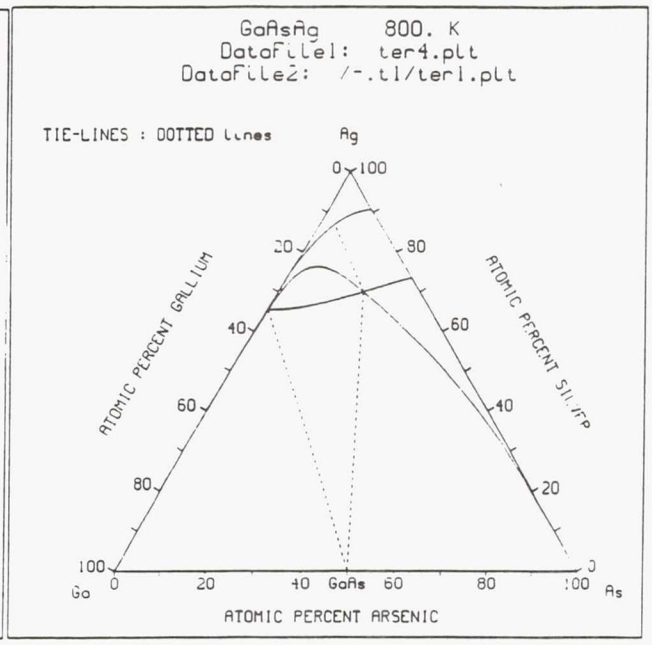


FIGURE 5a

FIGURE 5b

Plots for the two liquid boundary intersections of the Ga-As-Ge and Ga-As-Ag ternary systems. Tie-lines show the liquid and solid compostions in equilibrium.

## REPRESENTATION OF THE Ga-As-Ge SYSTEM

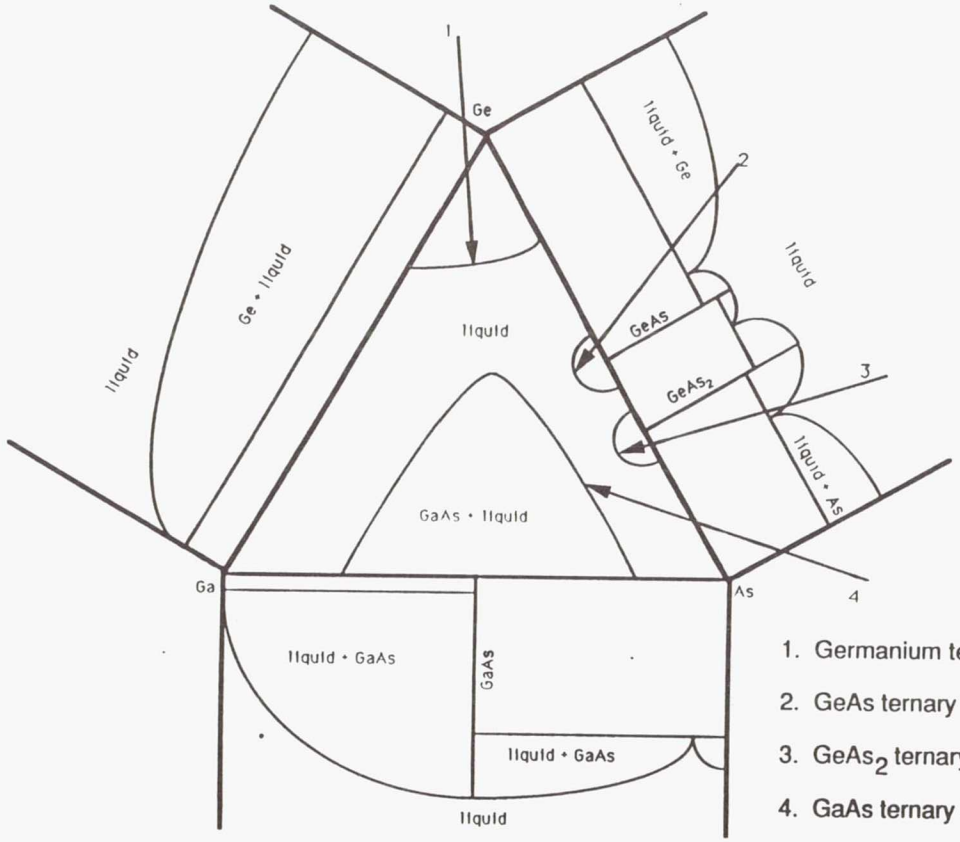


1. Germanium ternary liquidus boundary.
2. GeAs ternary liquidus boundary.
3. $GeAs_2$ ternary liquidus boundary.
4. GaAs ternary liquidus boundary.

FIGURE 6

Ternary Ga-As-Ge phase diagram showing the 3 component binary diagrams.

# $GaInP_2$/GaAs TANDEM CELLS FOR SPACE APPLICATIONS

J.M. Olson, S.R. Kurtz, A.E. Kibbler, K.A. Bertness, and
D.J. Friedman
Solar Energy Research Institute
Golden, CO 80401

The monolithic, tunnel-junction-interconnected tandem combination of a $GaInP_2$ top cell and a GaAs bottom cell has achieved a one-sun, AM1.5 efficiency of 27.3%. With proper design of the top cell, air mass zero (AM0) efficiencies greater than 25% are possible. A description and the advantages of this device for space applications are presented and discussed. The advantages include high-voltage, low-current, two-terminal operation for simple panel fabrication, and high conversion efficiency with low-temperature coefficient. Also, because the active regions of the device are aluminum-free, the growth of high efficiency devices is not affected by trace levels of $O_2$ or $H_2O$ in the metal organic chemical vapor deposition (MOCVD) growth system. While this study focuses on material grown on GaAs substrates, the device is probably adaptable to growth on Ge substrates. Encouraging preliminary radiation resistance data are presented in a companion paper.

## INTRODUCTION

The basic requirements for space solar cells are high efficiency at elevated temperatures, high power-to-weight ratio, and resistance to the damaging effects of low orbit radiation. The $GaInP_2$/GaAs monolithic, two-terminal tandem solar cell, invented and developed at SERI (Olson, 1985), has a good chance of meeting these requirements. In the following sections, we briefly review the previous work in this area, describe the design of an AM0 version of the $GaInP_2$/GaAs tandem cell, examine some of the advantages and disadvantages of the device, and give a brief overview of the tunnel junction interconnect.

## $GaInP_2$/GaAs TANDEM SOLAR CELL

A schematic diagram of the $GaInP_2$/GaAs monolithic cascade cell is shown in Fig. 1. The structure was grown in a vertical, air-cooled reactor at one atmosphere using MOCVD, the detailed aspects of which are described elsewhere (Olson, 1986; Olson, 1987). The Group III source gases were trimethyl indium, trimethyl gallium, and trimethyl aluminum; the Group V source gases were arsine and phosphine. The dopant sources were diethyl zinc (DEZ) and hydrogen selenide. The arsine and phosphine were purified on line by passing them over a gettering compound supplied by Advanced Technology Materials, Inc. The optoelectronic properties (Kurtz, 1988) and photovoltaic quality (Olson, 1987) of the materials listed above are complex and coupled functions of the growth temperature ($T_g$), V/III ratio, composition, dopant type and concentration, and substrate quality. Generally, however, the cascade device was grown at $T_g$ = 700 °C. The phosphides were grown with V/III = 30 and growth rate = 80-100 nm/min; the arsenides, with V/III = 35 and growth rate = 120-150 nm/min, except that the GaAs tunnel diode was grown at a rate of 40 nm/min.

The absorbers of both subcells were doped with Zn to a level of 1-4 x $10^{17}$ $cm^{-3}$. The emitters and window layers were doped with Se at about $10^{18}$ $cm^{-3}$. Both layers of the GaAs tunnel diode were heavily doped at concentrations approaching $10^{19}$ $cm^{-3}$.

The post-growth processing of these devices is very similar to that used for single-junction GaAs cells. The front and back contacts to all the devices reported here were electroplated with gold. Because of the high dopant concentration in both the GaAs substrate and the top GaAs contacting layer (not shown in Fig. 1), no thermal annealing of either contact was required. The front contact was defined by photolithography and obscured approximately 5% of the total cell area. The cell perimeter was also defined by photolithography and a mesa etch that uses a sequential combination of concentrated hydrochloric acid and a dilute ammonia:peroxide:water solution. The ammonia/peroxide solution was also used to remove the GaAs contacting layer between the gold grid fingers. The antireflection coating was a double layer of evaporated ZnS and $MgF_2$, with thicknesses of 65 and 120 nm, respectively.

The cell efficiency was measured using the multisource simulator method of Glatfelter and Burdick (1987). The simulated solar spectrum was adjusted using two reference cells. One reference cell was a $GaInP_2$ top cell; the other was a GaAs cell coated with the GaAs tunnel junction and a layer of $GaInP_2$ to simulate the optical transmission to the GaAs bottom cell in the actual tandem device. The spectrum of the simulator was adjusted with filters until both reference cells produced the correct (ASTM) standard E892-87 global, short-circuit current at 1000 $W/cm^2$. Using this spectrum, the current of the cascade cell was then measured.

The best efficiency (at one sun, AM 1.5) measured to date for this device is 27.3% (Olson, 1990). The light IV curve of this device is shown in Fig. 2. The short-circuit current density ($J_{sc}$), open circuit voltage, ($V_{oc}$), and fill factor (FF), are 13.6 $mAcm^{-2}$, 2.29 V, and 0.87, respectively. The area of this device is 0.25 $cm^2$, and the band gap of the top cell is 1.85 eV. This is the highest efficiency reported for a two-terminal, tunnel-junction-interconnected tandem photovoltaic device, and it represents a significant improvement with respect to our previously reported work (Olson, 1985; Olson, 1987). Chung et al. (1989) have reported a 27.6% efficient monolithic AlGaAs/GaAs solar cell. This device has a metal (as opposed to a tunnel-junction) interconnect and includes a prismatic cover slip to eliminate the photocurrent loss associated with grid shadowing. In our case, the prismatic cover slip would boost the efficiency from 27.3% to 28.7%.

Numerous factors affect the efficiency of these multijunction solar cells. They include the electronic quality of the top and bottom cell materials, the band gap and thickness of the top cell, the design of the anti-reflection coating (ARC), the tunnel junction interconnect, and the thickness and passivating properties of the window layers.

The $GaInP_2$/GaAs tandem cell just described had a thin $GaInP_2$ top cell designed for current-matched, optimum performance under a AM 1.5 global spectrum. Under an AM0 spectrum (and for all series connected tandem cells in general), a significant potential loss mechanism is associated with current matching between the top and bottom cells. The top and bottom cell currents ($J_T$ and $J_B$) are determined primarily by the band gaps of the top and bottom cell materials. It was assumed in previous treatments of this problem that the subcells were infinitely thick and that quantum efficiencies were equal to 100%. With these assumptions, for a bottom-cell band gap of 1.42 eV, the optimum top-cell band gap for an AM0 solar spectrum is 2 eV. Because the nominal band gap of $GaInP_2$ is 1.9 eV, we expect that $J_T > J_B$ for a thick, high-quality $GaInP_2$ top cell on a GaAs bottom cell. Furthermore, the band gap of MOCVD-grown $GaInP_2$ can be as low as 1.82 eV, depending on growth conditions (Kurtz, 1990), exacerbating this problem. This anomalous change in band gap appears to be related to changes in the short- or long-range site order of Ga and In on the Group III sublattice. For top-cell material with a low band gap, the solution to this problem is to reduce the thickness of the top cell. A calculation of the expected effect is shown graphically in Fig. 3 (Kurtz, 1990). Plotted in Fig. 3a are the efficiencies of a series-connected tandem cell with infinite and optimized top-cell thicknesses as a function of the band gap of the top cell for a GaAs (1.423 eV) bottom cell. In Fig. 3b, we plot the optimum top cell thickness as a function of the top-cell band gap. All of these calculations assume no external losses and unity internal quantum efficiencies. For top-cell band gaps greater than 2 eV, $J_T < J_B$ and current matching is not achievable. For top cell band gaps from 1.84 to 1.9 eV, the current-matched top-cell thickness varies from 500 to 700 nm and the AM0 efficiency varies from 30.8% to 31.5%. For a top-cell band gap of 2 eV, the maximum efficiency is 32.4%. Therefore, it is apparent that substantial changes in the top-cell band gap can be accommodated with only minimal loss in the tandem cell efficiency.

## ADVANTAGES

The $GaInP_2$/GaAs tandem cell has several advantages for space applications as compared to GaAs and InP single-junction cells and AlGaAs/GaAs, GaAs/Ge, InP/GaInAs, and GaAs/GaSb tandems. Table 1 lists the present AM0 efficiency of a nonoptimized $GaInP_2$/GaAs tandem cell with the predicted efficiency of an optimized tandem cell. The predicted beginning of life (BOL) efficiency is 26.1%. The present AM0 performance is from cell parameters all taken from one device that was not current matched for AM0. The largest deficiency between present and predicted performance are for the parameters $V_{oc}$ and $J_{sc}$. The $V_{oc}$ for the present device is low because of losses associated with a high interface recombination velocity at the back of the $GaInP_2$ top cell (80-100 meV) and an anomalous loss of voltage for bottom cells coated with a tunnel junction and a $GaInP_2$ top cell. Both of these problems have recently been solved and the combined $V_{oc}$ of separate top and coated bottom cells is now 2.41 V. Another 20 mV is expected with further improvements in the top cell. The predicted $J_{sc}$ is one-half of 34 mA/cm$^2$ (an extrapolation of the AM1.5 $J_{sc}$ predicted by Tobin, et al. (1990), less 0.3 mA/cm$^2$ for absorption losses associated with the GaAs tunnel junction interconnect (vide infra). The predicted BOL efficiency of 26.1% is a 15% improvement over a comparable single-junction GaAs cell with a $J_{sc}$ of about 34 mA/cm$^2$ and a predicted efficiency of 22.7%. It would appear at this time that the achievement of 26.1% does not require any major technological breakthroughs or advances.

Besides efficiency, the $GaInP_2$/GaAs tandem cell has numerous advantages over the other multijunction devices. With a tunnel-junction interconnect, it is a true monolithic, two-terminal device that does not require a prismatic cover slip to compensate for the excess obscuration of a metal interconnect. As a two-terminal device, it should also be easier to assemble into modules than the three- and four-terminal devices. Using a tunnel-junction interconnect also makes post-growth processing of the device similar to that of a single-junction device and considerably easier than that of a three- or four-terminal device.

The choice of top and bottom cell band gaps also has a major effect on the efficiency, temperature coefficient, and $I^2R$ losses in the cell. The efficiency of the $GaInP_2$/GaAs tandem cell has a temperature coefficient similar to that of the bottom GaAs cell and not much different than that of a four-terminal $GaInP_2$/GaAs tandem structure, as shown in Fig. 4. For these calculations, band gaps of 1.424 and 1.9 eV were used for the GaAs and $GaInP_2$, respectively. Except for the AlGaAs/GaAs tandem cell, all of the other tandem cells listed here have a low-band-gap bottom cell and, hence, a much larger temperature coefficient. The cell current is determined by the top-cell band gap. The cell current will be a factor of two lower, and the associated $I^2R$ losses (for a given cell resistance) will be a factor of four lower, than those of InP/GaInAs or GaAs/GaSb tandem cells. These factors are particularly important for concentrator applications, where the cell is run at elevated current and temperature.

It would appear from preliminary experiments that the $GaInP_2$/GaAs tandem cell, like GaAs, can be grown on germanium substrates. It should also be compatible with the (CLEFT) technology. These technologies can significantly increase the power-to-weight ratio of this device as compared to the other tandem cell structures.

Compared to the AlGaAs/GaAs tandem cell, the $GaInP_2$/GaAs tandem cell contains no Al in the active regions of the device. (Aluminum is used in window layers where material quality is less critical.) Because of the strong affinity between Al and $O_2$ and $H_2O$, growing high-quality AlGaAs is difficult if not impossible in most systems. This is very important from the standpoint of yield and manufacturability. It also means that one can generally use lower growth temperatures than those used for AlGaAs. On the other hand, $GaInP_2$ has been viewed as a material that is also difficult to grow. Its composition must be precisely controlled; there are anomalous changes in its band gap with growth conditions; and there difficulties associated with the chemistry of trimethyl indium and $PH_3$. However, all of these problems are manageable and well understood, and numerous laboratories around the world have abandoned 1.9 eV AlGaAs and are growing $GaInP_2$ laser and LED devices with MOCVD.

Finally, it appears that because of the thin top cell (and other phenomena that are not well understood) the $GaInP_2$/GaAs tandem cell can be designed to be relatively radiation resistant, with an end-of-life efficiency ($10^{15}$ 1 MeV electrons/$cm^2$) close to 21%. This aspect of the problem is discussed further in a companion paper in this volume (Kurtz, 1991).

## TUNNEL JUNCTION INTERCONNECTS

The main issues for tunnel-junction interconnects are (1) absorption losses of light destined for the bottom cell, (2) the series resistance and peak tunneling current, and (3) effects associated with the required heavy doping. There are two ways to minimize absorption losses: (1) fabricate the tunnel junction in a semiconductor with a band gap that is greater than or equal to that of the top cell (this may not always work because of incomplete absorption of all super-band-gap light in the top cell and/or sub-band-gap absorption of light in the degenerately doped tunnel junction), or (2) reduce the thickness of the tunnel junction. The peak tunneling current is an exponential function of the band gap of the material. Therefore, for tandem cells with high-band-gap top cells like $GaInP_2$, it is better to employ the second approach and use, in our case, a thin GaAs tunnel junction for the interconnect. From calculations similar to those of Kurtz, et al. (1990), modeling the absorption of light in degenerately doped GaAs, we have shown that the current loss to the bottom GaAs cell per unit thickness of the GaAs tunnel junction is about 0.01 mA/$cm^2$/nm. A 30-nm-thick GaAs tunnel junction will reduce the tandem cell current by less than 2%.

The series resistance and peak tunneling current are complex functions of the dopant type and concentration, interdiffusion, memory effects, and homogeneous and heterogeneous reaction chemistry. Contrary to the popular lore, an adequate tunnel junction can be fabricated in GaAs with the dopants Zn and Se. A solar concentration of 1000x requires a peak tunneling current of greater than 14 A/$cm^2$. Peak tunneling currents of 60 A/$cm^2$ have been achieved with Se and Zn, albeit with low yield, at a growth temperature of 600°C. The yield increases significantly at a growth temperature of 650°C with a peak tunneling current of 42 A/$cm^2$. The major problem with these devices is the spillover of the dopants into top cell. This problem is caused mainly by the large memory effects that are normally associated with these dopants. Silicon from $Si_2H_6$ and C from $CCl_4$ were studied as alternatives for Se and Zn, respectively. Both of these dopant sources are known to exhibit negligible memory effects. When C is substituted for Zn, peak tunneling currents in excess of 100 A/$cm^2$ were achieved after optimization, still the memory problems with Se persist. When Si and C are substituted for Se and Zn, there are no memory problems, but the best tunnel junctions made so far, while suitable for one-sun operation, will dominate the series resistance of the device for concentrations around 500x. In the course of this work, we also discovered that C appears to form a deep level (in addition to a shallow acceptor) in $GaInP_2$ and would therefore not be a suitable dopant for the base layer of the top cell (Kibbler, 1991). More work must be done to fully optimize these tunnel junctions.

## SUMMARY

In summary, we have reviewed the previous work in designing and operating $GaInP_2$/GaAs tandem solar cells for terrestrial systems. We show that this device technology is easily adaptable to space PV applications and has numerous advantages over other single-junction and multijunction solar cells. These advantages include a projected AM0 efficiency close to 26% with a low cell current, a low temperature coefficient, and a relatively high tolerance to the effects of radiation. The materials are generally well understood, and their growth is compatible with large-scale deposition on lightweight substrates such as germanium.

## REFERENCES


Chung, B.-C., G.F. Virshup, S. Hikido, and N.R. Kaminar. 1989. Appl. Phys. Lett. 55:1741.

Glatfelter, Troy, and Joseph Burdick. 1987. Proceedings of the 19th IEEE Photovoltaic Specialists Conference (IEEE, New York) p. 1187.

Kibbler, A.E., Sarah R. Kurtz, and J.M. Olson. 1991. Carbon Doping and Etching of MOCVD-Grown GaAs, InP, and Related Ternaries Using $CCl_4$. J. Cryst. Growth 109:258-263.

Kurtz, S.R., J.M. Olson, and A. Kibbler. 1988. Solar Cells. 24:307.

Kurtz, Sarah R., P. Faine, and J.M. Olson. 1990. Modeling of Two-Junction, Series-Connected Tandem Solar Cells Using Top-Cell Thickness as an Adjustable Parameter. J. Appl. Phys. 68:1890.

Kurtz, Sarah R., J.M. Olson, and A. Kibbler. 1990. Effect of Growth Rate on the Band Gap of $Ga_{0.5}In_{0.5}P$. Appl. Phys. Lett. 57:1922-1924.

Olson, J.M., T. Gessert, and M.M. Al-Jassim. 1985. Proceedings of the Eighteenth IEEE Photovoltaic Specialists Conference (IEEE, New York) p. 552.

Olson, J.M., and A. Kibbler. 1986. J. Cryst. Growth. 77:182.

Olson, J.M., A.E. Kibbler, and S.R. Kurtz. 1987. Proceedings of the 19th IEEE Photovoltaic Specialists Conference (IEEE, New York), p. 285.

Olson, J.M., Sarah R. Kurtz, and A.E. Kibbler. 1990. Proceedings of the 21st Photovoltaic Specialists Conference, (IEEE, New York).

Olson, J.M., S.R. Kurtz, A.E. Kibbler, and P. Faine. 1990. A 27.3% Efficient $Ga_{0.5}In_{0.5}P$/GaAs Tandem Solar Cell. Appl. Phys. Lett. 56:623-625.

Tobin, S.P., S.M. Vernon, S.J. Wojtczuk, C. Bajgar, M.M. Sanfacon, and T.M. Dixon. 1990. Advances in High-Efficiency GaAs Solar Cells. Proceedings of the 21st IEEE Photovoltaic Specialists Conference (IEEE, New York), pp. 158-162.

Table 1. Present and Predicted AM0 Performance of $GaInP_2/GaAs$ Cells

| **Cell Parameters** | **Present** | **Predicted** |
|---|---|---|
| $V_{oc}$ [V] | 2.3 | 2.43 |
| $J_{sc}$ [mA/cm$^2$] | 16.1 | 16.7 |
| ff | 0.87 | 0.88 |
| AM0 Efficiency [%] | 23.6 | 26.1 |

| | t (micron) | |
|---|---|---|
| $MgF_2$ | 0.12 | COATING |
| ZnS | 0.065 | |
| n - $AlInP_2$ | 0.04 | TOP CELL |
| n - $GaInP_2$ | 0.1 | |
| p - $GaInP_2$ | 0.8 | |
| p+ - GaAs | 0.02 | TUNNEL DIODE |
| n+ - GaAs | 0.02 | |
| n - AlGaAs | 0.2 | BOTTOM CELL |
| n - GaAs | 0.1 | |
| p - GaAs | 3.5 | |
| p+ - GaAs | substrate | |

Fig. 1. A schematic cross-section of the $GaInP_2$/GaAs tandem cell. A GaAs contacting layer, antireflection coating, and metallization are not shown.

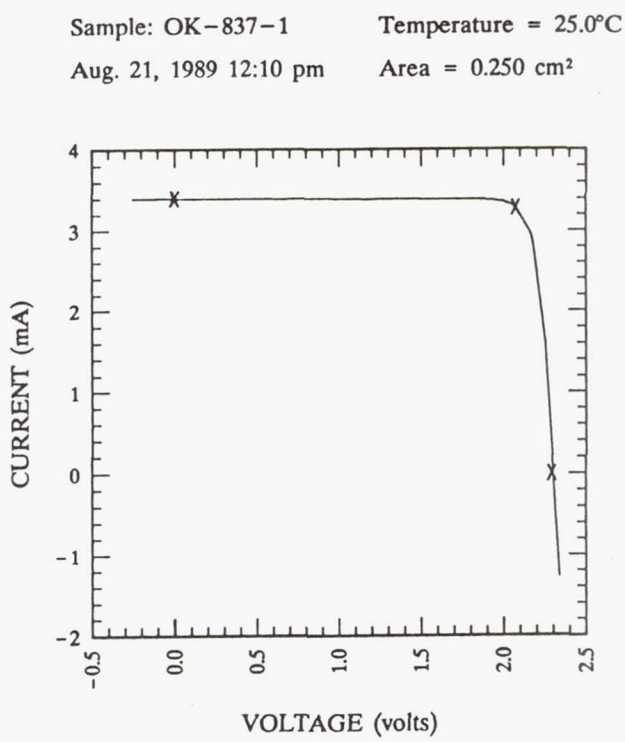


Fig. 2. Light IV curve of a 27.3%-efficient (AM1.5), two-terminal $GaInP_2$/GaAs tandem solar cell.

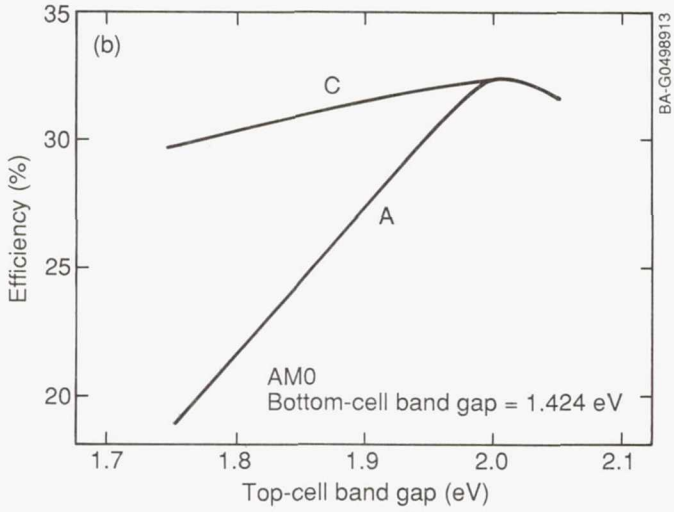


Fig. 3a. Modeled AM0 tandem-cell efficiency, assuming no losses, as a function of the top cell band gap with a thick (Curve A) and optimally thin top cell (Curve C). The efficiency for Curve C assumes zero recombination velocity at the interface between the top cell and the tunnel-junction interconnect.

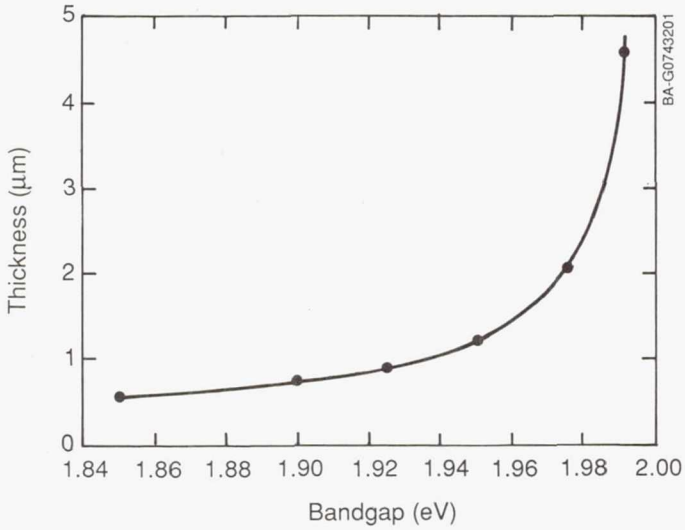


Fig. 3b. Optimal top cell thickness as a function of top cell band gap. The bottom cell is GaAs with a band gap of 1.424 eV.

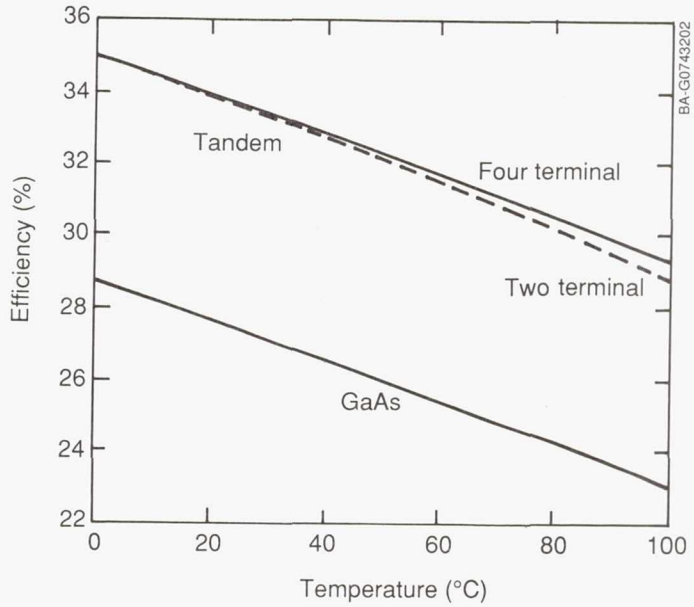


Fig. 4. Modeled cell efficiency (AM0) as a function of cell temperature for a single-junction GaAs cell and series- and separately connected $GaInP_2$/GaAs tandem cells. These are ideal efficiencies with no losses.

# Two-terminal Monolithic InP-based Tandem Solar Cells with Tunneling Intercell Ohmic Connections

C. C. Shen and P. T. Chang
Center for Solid State Electronics Research
Arizona State Unversity, Tempe, AZ 85287

K. A. Emery
Solar Energy Research Institute, Golden, CO. 80401

## SUMMARY

We have successfully fabricated a monolithic two-terminal InP/InGaAsP tandem solar cell. This tandem solar cell consists of a p/n InP homojunction top subcell and a 0.95 eV p/n InGaAsP homojunction bottom subcell. A patterned 0.95 eV $n^+/p^+$ InGaAsP tunnel diode was employed as intercell ohmic connection. The solar cell structure was prepared by two-step liquid phase epitaxial growth. Under one sun, AM1.5 global illumination, our best tandem cell delivered a conversion efficiency of 14.8%.

## INTRODUCTION

Although multijunction solar cells have exhibited higher conversion efficiency than single junction solar cells in recent years, its full potential is far from being realized. Most of the R & D work on III-V tandem solar cells is based on GaAs and its related ternary compound semiconductors. The highest conversion efficiency reported for a monolithic two-terminal tandem solar cell under one-sun, AM1.5 global illumination is about 27% [1][2]. InP-based multijunction tandem solar cells have not received much attention until recently. InP and its related ternary and quaternary compound semiconductors such as InGaAs and InGaAsP offer desirable combinations of energy bandgap values and show great promises for multijunction tandem solar cell applications; especially for tandem solar cells which consist of three subcells.

One of the key components for a two-terminal monolithic mulitijunction tandem solar cell is a low-loss, highly conductive intercell ohmic contacts (IOCs) for the series connection of individual subcells. Two types of IOCs are considered to be feasible for monolithic tandem solar cells. They are tunnel junctions and metal interconnects (MICs). Both tunnel junctions and metal interconnects have been used as IOCs for GaAs-based multijunction tandem cells [1] [2] [3]. For InP-based mutijunction solar cells, only MICs have been used recently as IOCs for the InP/InGaAs tandem solar cells developed by M. Wanlass and coworkers at SERI [4]. In this work, we have developed a 0.95 eV $n^+/p^+$ InGaAsP tunnel diode and successfully employed it as IOCs for a monolithic two-terminal InP/InGaAsP tandem solar cell. Details of the device structure, device fabrication procedures and device performance are discussed in following sections.

## DEVICE STRUCTURE, EPITAXIAL GROWTH AND DEVICE FABRICATION

A schematic cross section of a two-terminal monolithic InP/InGaAsP tandem solar cell is shown in Fig. 1. The entire tandem cell structure was grown on a (100) oriented n-type InP substrate by using two-step liquid-phase epitaxial (LPE) growth. The two subcells are connected with a patterned 0.95 eV $n^+/p^+$ InGaAsP tunnel junction. The patterned $n^+/p^+$ InGaAsP tunnel junction covers about 12.5% of the total surface area. The patterning of the tunnel junction was accomplished by using photolithography and selective wet chemical etching. A p-InP layer was grown on top of the InGaAsP lower cell and used as an etch-stop layer to facilitate the patterning processes. A patterned $p^+$-InGaAs layer was employed as the contacting layer for the front grid contacts. The front contacts cover about 12.5% of the surface area. The complete solar cells are of mesa type, with a total surface area of 4 $mm^2$. Single layer of $Sb_2O_3$ was used as antireflection coating.

In the early stage of this work, $n^+/p^+$ $In_{0.53}Ga_{0.47}As$ tunnel junctions were considered for IOCs for the series connection of the InP subcell and the InGaAsP subcell. $In_{0.53}Ga_{0.47}As$ has a direct energy bandgap of 0.75 eV and is lattice matched to InP, which makes it an attractive material for tunnel junctions. In our previous work [5], we have investigated the electrical properties of $p^+/n^+$ $In_{0.53}Ga_{0.47}As$ tunnel junctions prepared by LPE. Since then, we have made better $p^+/n^+$ $In_{0.53}Ga_{0.47}As$ tunnel junctions with higher conductivities and larger peak current densities. We have also developed 0.95 eV $p^+/n^+$ InGaAsP tunnel junctions by LPE. Their electrical properties are listed in Table 1, along with several different type of tunnel junctions which have been used as IOCs for GaAs-based tandem solar cells. Although $In_{0.53}Ga_{0.47}As$ tunnel junctions offer the highest peak current densities as well as the largest conductivities, we found that it was difficult to incorporate them into our tandem solar cell structures by LPE, since melt-back problem during LPE growth forbids the direct growth of InP on $In_{0.53}Ga_{0.47}As$. As a result, we switched to InGaAsP tunnel junctions and were successful in using them as IOCs.

The thickness and doping concentration of individual epitaxial layer for the first and second LPE growth are listed in Table 2. The LPE growth procedures for the p/n InP upper cell and the p/n InGaAsP lower cell were similar to what we reported previously [6] [7]. Typical growth temperatures for the first and second growth are $630^0C$-$625^0C$ and $580^0C$-$550^0C$, respectively. In order to simplify the InP growth processes for the InP/InGaAsP tandem structure, the p-InP region and the p-InGaAsP region were not grown epitaxially as we did for the single-junction InP and InGaAsP solar cells but were created by in-diffusion of p-type impurities (Zn) during the growth period. Consequently, both subcells are essentially of diffused junction type rather than grown junction type. The depth of both p/n diffused junctions is about one micron, no attemps were made to optimize the junction depth for maximum conversion efficiencies. The processing sequence for the fabrication of the InP/InGaAsP tandem solar cell is illustrated in Fig. 2.

Several InP/InGaAsP tandem solar cells were evaluated at SERI under 1 sun, global AM1.5 illuminations. Shown in Figure 3(a) and 3(b) are the light I-V characteristics for the two most efficient InP/InGaAsP tandem solar cells we have tested so far. The open-circuit voltage ($V_{oc}$), short-circuit current ($J_{sc}$) and Fill factor exhibited by the best device were 1.363 V, 13.85 $mA/cm^2$ and 0.786, respectively. The total-area power conversion efficiency was 14.8%. The second best tandem solar cell which was processed from the same wafer exhibited a conversion efficiency of 14.6%. The $V_{oc}$, $J_{sc}$, and Fill factor exhibited by this second best device were 1.383 V, 12.94 $mA/cm^2$ and 0.816, respectively. The relative quantum efficiency of the InP upper cell and the 0.95 eV InGaAsP lower cell is shown in Fig. 4.

## DISCUSSION

Because of the current matching requirements imposed on a series-connected two-terminal tandem solar cell, its output current is limited by the subcell which generates the least current. For the two-terminal InP/InGaAsP tandem solar cell reported here, the output current is limited by the InGaAsP lower subcell. The short-circuit current density of 13.85 $mA/cm^2$ exhibted by the 14.8% efficient InP/InGaAsP tandem solar cell is comparable in value to what has been reported on the most efficient monolithic $Ga_{0.5}In_{0.5}P$/GaAs tandem solar cell and the most efficient $Al_{0.37}Ga_{0.63}As$/GaAs tandem solar cell [1] [2]. Our results thus confirm that the 0.95 eV InGaAsP solar cell performs quite well underneath an InP solar cell when they are connected in series. With the incorporation of another 1.93 eV wide bandgap solar cell such as AlGaInP solar cell as the top subcell, with the InP subcell in the middle and the InGaAsP subcell at the bottom, the total conversion efficiency can be expected to increase to 30% or more, assuming the output voltage can be enhanced without sacrificing the output current.

REFERENCES:

1. J. M. Olson, S. R. Kurtz, A. E. Kibbler and P. Faine,"A 27.3% efficient $Ga_{0.5}In_{0.5}P$/GaAs tandem solar cell," Appl. Phys. Lett. **56**, 623, (1990).

2. B.- C. Chung, G. F. Virshup, S. Hikido, and N. R. Kaminar, "27.6% efficiency (1 sun, air mass 1.5) monolithic $Al_{0.37}Ga_{0.63}As$/GaAs two-junction cascade solar cell with prismatic cover glass," Appl. Phys. Lett. **55**, 1741, (1989).

3. C. Amano, H. Sugiura, M. YamGuchi, and K. Hane, "Fabrication and numerical analysis of AlGaAs/GaAs tandem solar cells with tunnel interconnections," IEEE Trans. on Electron Device, **ED-36**, 1026, (1989).

4. M.W. Wanless, J.S. Ward, T.A. Gessert. K.A. Emery, G.S. Horner and T.J. Coutts, "Development of High-Performance GaInAsP Solar Cells for Tandem Solar Cell Applications," Proceeding of 21st IEEE Photovoltaic Specialist Conference, (IEEE, New York 1990). p. 172.

5. C.C. Shen, P.T. Chang, and K.Y. Choi, "An $In_{0.53}Ga_{0.47}As$ tunnel diode for monolithic multijunction solar cell applications," Proceeding of 20th IEEE Photovoltaic Specialist Conference, (IEEE, New York 1988) p 771.

6. K.Y. Choi and C.C. Shen "p/n InP homojunction solar cells with modified contacting scheme by liquid phase epitaxy," J. Appl. Phys. **63**, 1198, (1988).

7. C.C. Shen, P.T. Chang and K.Y. Choi,"Photovoltaic properties of 0.95 eV p/n InGaAsP homojunction solar cells prepared by liquid-phase epitaxy," IEEE Trans. on Electron Device, **ED-37**, 464, (1990).

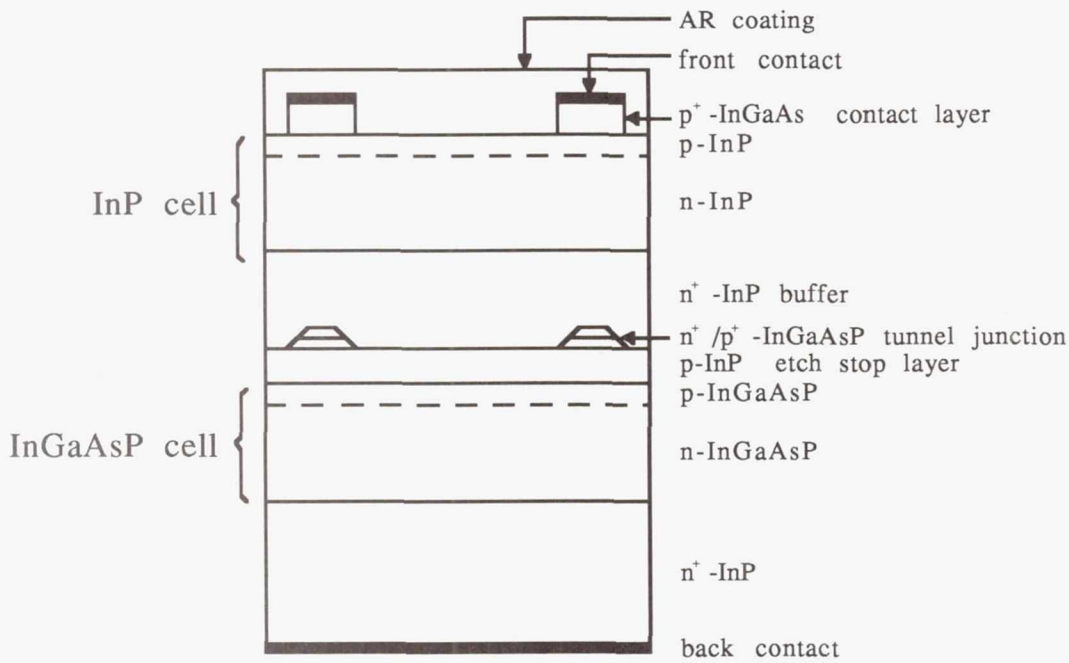


Fig. 1. Schematic cross section of a two-terminal, monolithic InP/InGaAsP tandem cell.

Table 1. Electrical properties of various types of tunnel Junctions

| Material System | Peak current density $J_P$ (A/cm$^2$) | Resistivity R ($10^{-3}$, $\Omega$-cm$^2$) | Ref. |
|---|---|---|---|
| $p^+$-GaAs/$n^+$-GaAs | 34 | 3.0 | a |
| $p^+$-GaAs/$n^+$-GaAs | 15 | 4.7 | b |
| $p^+$-GaAs/$n^+$-GaAs | 23 | 1.7 | c |
| $p^+$-GaAs/$n^+$-GaAs | 45 | 2.0 | d |
| $p^+$-Ge/$n^+$-Ge | 3 | 10 | e |
| $p^+/n^+$-$In_{0.53}Ga_{0.47}As$ | 793 | 0.4 | This Work |
| $p^+/n^+$-InGaAsP | 28 | 2.0 | This Work |

a. D. L. Miller, S. W. Zehr, and J. S. Harris, Jr., *J. Appl. Phys.*, Vol. 53, pp. 744-748, 1982.
b S. K. Ghandhi, R. T. Huang, and J. M. Borrego, *Appl. Phys. Lett.*, Vol. 48, 415-416, 1986.
c. R. E. Hayes *et al.*, *Solar Cells*, Vol. 15, pp. 231-238, 1985.
d. P. Basmaji *et al.*, *J. Appl. Phys.*, Vol. 62, pp. 2103-2106, 1987.
e. P. K. Chiang, M. L. Timmons, G. G. Fountain, and J. A. Hutchby, *Proc. 18th IEEE Photovoltaic Specialist Conf.*, pp. 562-567, 1985.

Table 2. Thicknesses and doping concentrations of epitaxial layers in the InP/InGaAsP tandem cell.

| Layer | Thickness (μm) | Doping Concentration ( $cm^{-3}$) |
|---|---|---|
| **First Crystal Growth** | | |
| undoped InGaAsP | 3.0 | $3.0 \times 10^{17}$ |
| p-InP | 1.0 | $2.5 \times 10^{18}$ |
| $p^+$-InGaAsP | 0.5 | $2.0 \times 10^{19}$ |
| $n^+$-InGaAsP | 0.5 | $2.0 \times 10^{19}$ |
| **Second Crystal Growth** | | |
| $n^+$-InP | 2.5 | $7.0 \times 10^{18}$ |
| undoped InP | 2.5 | $1.0 \times 10^{17}$ |
| $p^+$-InGaAs | 1.3 | $6.0 \times 10^{18}$ |

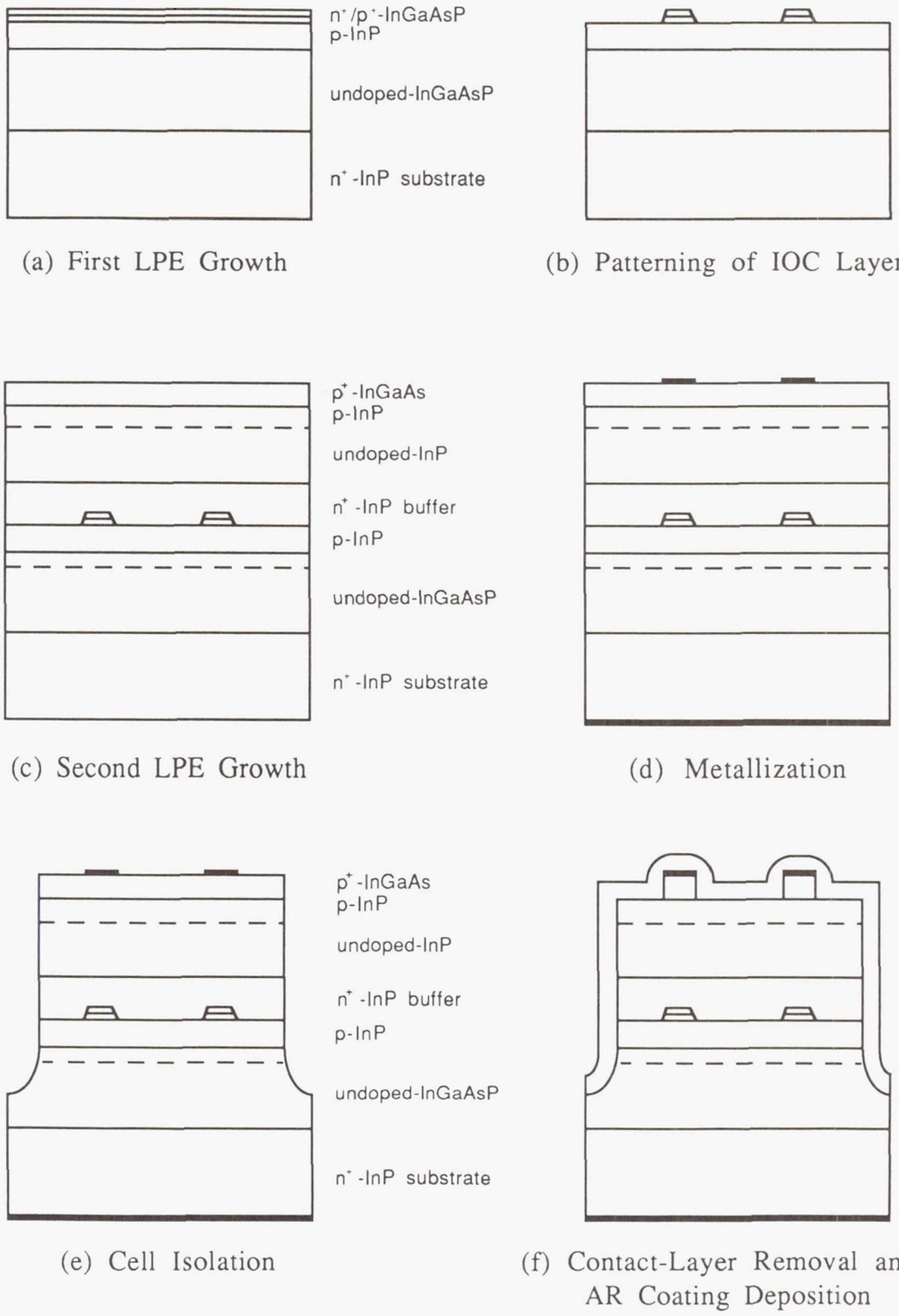


Fig. 2. The Processing sequence for the fabrication of the InP/InGaAsP tandem solar cell.

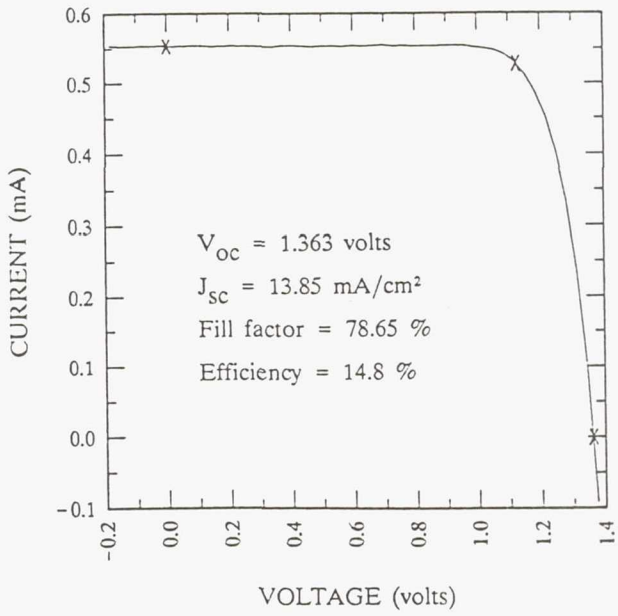


(a)

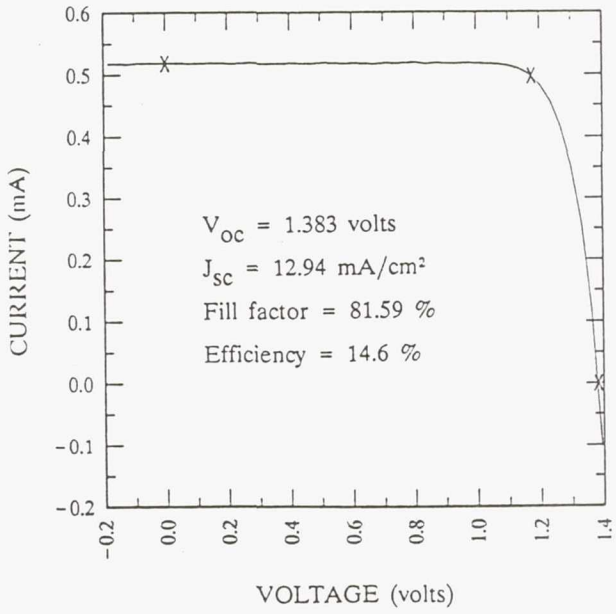


(b)

Fig. 3. Light I-V characteristics under 1 sun, AM1.5 global illuminations for two InP/InGaAsP tandem solar cells. The total surface area is 0.04 $cm^2$.

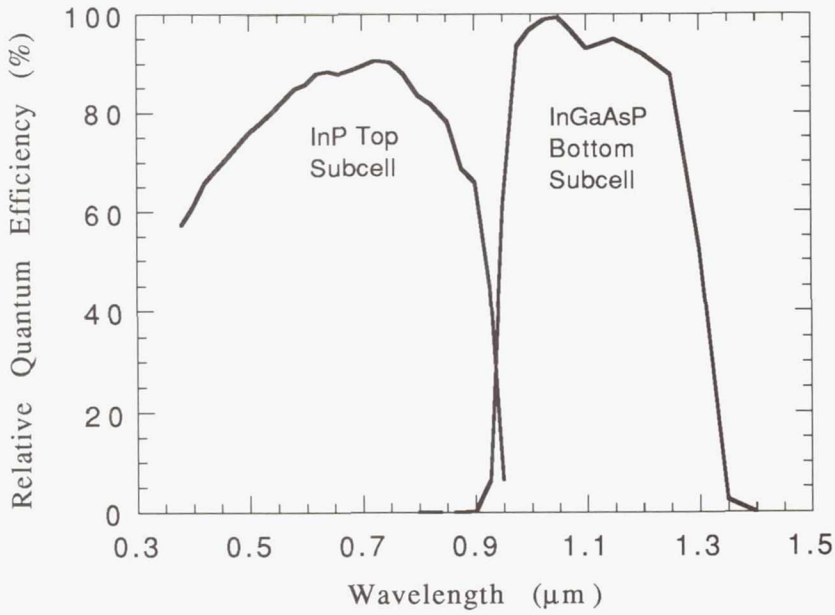


Fig. 4 Spectral response of the InP upper subcell and the 0.95 eV InGaAsP lower subcell.

# GaAs(AlGaAs)/$CuInSe_2$ TANDEM SOLAR CELLS-- TECHNOLOGY STATUS AND FUTURE DIRECTIONS

N.P. Kim, and R.M. Burgess
Boeing Aerospace and Electronics
Seattle, WA. 98124

R.P. Gale, and R.W. McClelland
Kopin Corporation
Taunton, MASS. 02780

Mechanically stacked, high efficiency, light-weight, and radiation resistant photovoltaic cells based on a GaAs thin film top and $CuInSe_2$ thin film bottom cells have been developed under the joint research effort of the Boeing Co. and the Kopin Corp., and are considered one of the most promising devices for planar solar array applications. The highest efficiency demonstrated so far using the 4 $cm^2$ design is 23.1% AM0, one sun efficiency when measured in four-terminal configuration. In this paper, we present the current status of our GaAs(AlGaAs)/$CuInSe_2$ tandem cell program and describe future directions that will lead to cell efficiencies higher than 26% AM0. A new 8 $cm^2$ cell design developed for a two-terminal and voltage-matched configuration to minimize wiring complexity is discussed. Optimization of the GaAs structure for a higher end-of-life performance and further improvement of tandem cells by utilizing AlGaAs as an top absorber are described. Results of environmental tests conducted with these thin film GaAs/$CuInSe_2$ tandem cells are also summarized.

## 1. Introduction

The optimum power system for all spacecraft are the ones that incorporate high efficiency, light-weight, and radiation resistant photovoltaic cells. To meet these goals tandem solar cells have been developed under the joint research effort of the Boeing Co. and the Kopin Corp. The cells are mechanically stacked tandem cells based on a GaAs (AlGaAs) thin film single crystalline top cell and $CuInSe_2$ poly crystalline thin film bottom cell, and are considered one of the most promising devices for planar solar array applications (ref.1).

The top and bottom cells of GaAs (AlGaAs) and $CuInSe_2$ were chosen due to its high efficiency potential associated with its band gap combination (ref.2), relatively good radiation resistance of GaAs (AlGaAs) cells (ref. 3), and superb radiation resistance of $CuInSe_2$ cells compared to Si solar cells (ref. 3 and 4). The mechanical stacked tandem configuration was used to provide wiring flexibility and to minimize cell fabrication processing constraints associated with the monolithically integrated tandem approaches. Furthermore, this approach provides a potential for very high specific power since both cells are incorporated as thin films thus minimizing weight incurred from heavy semiconductor materials.

## 2. Technology Status

The schematic of the GaAs(AlGaAs)/$CuInSe_2$ tandem cell is shown in Figure 1, and consists of a double-heterostructure GaAs (AlGaAs) thin film top cell and a polycrystalline CdZnS/$CuInSe_2$ heterojunction thin film lower cell. The cross-section of the top and the bottom cells are shown in Figure 2 and Figure 3, respectively. The top GaAs(AlGaAs) thin film cell was fabricated by the CLEFT(Cleavage of Lateral Epitaxial Film for Transfer) technique (ref. 5) using MOCVD for cell structure growth. The CdZnS/$CuInSe_2$ (CIS) lower cell was fabricated using coevaporation method for semiconductor film deposition. Interconnection from the top cell bonding pads to glass substrate pads was conducted using gold ribbons to isolate the GaAs thin film from any stress caused by the next level interconnection. Details of cell fabrication process can be found in prior publications. (ref. 1,5, and 6) Electrical measurements were conducted in the four terminal configuration at one sun and

$28^oC$ with an AM0 power normalization of 137.2 $mW/cm^2$ using an XT-10 simulator and a JPL ballon flight calibrated GaAs/CIS reference cell unless noted otherwise.

## 2.1 Cell Efficiency and Cell Design

Cell efficiencies have continuosly improved from 17.4% to 23.1% since the Boeing and Kopin started their joint research work. Cell size also has progressed from the initial 1 $cm^2$ to the current 8 $cm^2$ during the same period. Figure 4 illustrates the major improvements of cell efficiency and size in the past five years (ref. 1,7,8, and 9). The highest efficiency demonstrated so far using the 4 $cm^2$ design was 23.1% AM0, one sun efficiency when measured in four-terminal configuration (ref.1). The best individual cells demonstrated in the completed tandem cells are 20.6% and 3.1% for the upper and the lower cells, respectively. A double layer AR coating of silicon oxide and silicon nitride on the GaAs top surface was incorporated into the base line process and significantly improved IR transmission toward the lower cell. A cell efficiency of 5.2% AM0 of the $CuInSe_2$ cell was demonstrated under a 1.7 eV band gap AlGaAs CLEFT filter, confirming the performance potential at the end-of-life (EOL) as well as at the beginning-of-life (BOL)(ref.9).

A new cell design was developed to enable easy application of these cells by optimizing their configuration for a specific space power application at the cell level and thus minimizing wiring complexity at the array level. The design is based on the 2 cm x 4 cm cell area and features an improved two-terminal configuration with voltage-matched monolithic subcell units, different from the previous four-terminal devices.The configuration of two-terminal and voltage matching was achieved by stacking one GaAs CLEFT cell on top of four $CuInSe_2$ subcells monolithically interconnected in series to form a single cell unit. The ratio of one to four has been determined based on array level circuit analysis conducted at Boeing. The unit was optimized for low-earth-orbit application where operating temperatures are higher than those for other applications. However, the design still provides the flexibility of forming four-terminal devices for various characterization purposes through minor modifications in the intra-cell interconnect. All the unnecessary contact buss area included in the previous design has been eliminated, and contact pads of minimum size are utilized at the four corners of the cell, thus improving cell packing factor significantly.

A recently developed monolithic interconnection method in the GaAs (CLEFT) fabrication process (ref. 10) has been utilized to provide thick buss lines in the GaAs cell to minimize any IR drop. This new technique combines with the $CuInSe_2$ monolithic interconnection capability to allow ratios other than the present one to four and therefore optimization for a wide range of orbital conditions. Fine line lithography has been incorporated into the base line CIS fabrication process to achieve monolithic interconnection of the subcells with minimum area loss. Details of other tandem cell fabrication process have been reported and are found in prior publications (ref. 1,5, and 6). The initial fabrication results using the improved process are encouraging, and the photograph of the GaAs CLEFT and $CuInSe_2$ cells for the voltage-matched, two terminal tandem solar cell are shown in Figures 5 and 6.

The effects of operating temperature on performance of this new device have been analyzed using demonstrated cell performance data and temperature coefficients measured in our laboratory. Two-terminal tandem cell efficiencies of 22.8, 22.3, 21.3, and 20.7% are projected at $28^o$, $40^o$, $55^o$, and $70^oC$, respectively as shown in Table 1.

## 2.2. Cell Weight

One distinct advantage of our cell design is found in the reduced total cell weight. Compared to conventional approaches involving cell growth on a heavy bulk semiconductor substrate, this tandem approach utilizes the CLEFT technique to fabricate a very thin (approximately 5 um thick) GaAs or AlGaAs film. Combined with the thin film CIS cell directly deposited onto thin glass, the optimized weight of a 4 $cm^2$ tandem cell including 2 mil thick coverglass is expected to be about 190 mg (ref.11). Light-weight GaAs/CIS tandem cells were demonstrated on 2 mil thick substrate glasses with efficiencies as high as 20.8% (ref.1). The cell weighed 258 mg using a 1-mil thick coverglass without optimal substrate trimming and adhesive thickness, yielding 442 W/kg cell-coverglass spcific power. When adhesive thickness and substrate trimming is optimized, cell-coverglass specific powers up to 630 W/kg are projected for the GaAs/CIS tandem cell, and up to 700 W/kg is achievable when an AlGaAs top cell is incorporated.

2.3. Environmental Effects

Since the main contributor to the performance degradation of space solar arrays is proton and electron radiation, the effects of these particles on individual cell devices and structures have been extensively studied. These studies have reaffirmed the superior radiation resistance of CIS solar cells when compared with GaAs and Si at comparable proton and electron energies and fluences. CIS solar cells show no measurable degradation occurs when irradiated with 1.0 and 2.0 MeV electrons to a total fluence of $5x10^{15}$ $cm^{-2}$. In addition, CIS solar cells are a factor of ten more radiation resistant to proton radiation between 10.0 and 0.2 MeV energies as compared to GaAs solar cells. These same studies (ref. 3) on the GaAs CLEFT solar cells indicated that the double heterostructure structure is as radiation resistant as the GaAs bulk cells with 1.0 MeV protons, and are slightly more radiation resistant at both the 1.0 MeV electron and 200 keV proton energies. A recent experiment was designed and conducted to optimize the GaAs double heterostructure for a particular mission's end-of-life (EOL) criteria. The designed experiment consisted of a systematic variation of the doping levels and/or thicknesses of the base and emitter layers. The cell efficiencies for the entire experimental matrix are plotted as a function of proton fluence in Figure 7. The EOL efficiencies required for the particular mission are indicated by stars in the figure and were met and exceeded by the optimized cell structure. The degradation curve indicated in the figure corresponds to this cell structure and is representative of the parameters currently used for the devices being fabricated. It was observed from this study that the lower doping in the base structure of the GaAs CLEFT cell improved the radiation resistance while the doping level in the emitter had little effect.

Thermal cycling tests were conducted on these tandem solar cells to confirm the survivability of the devices during the eclipse phase of a given mission. The performance of the tandem solar cells showed negligible degradation when cycled from +80°C to -100°C up to 850 cycles. (ref. 1) Humidity tests performed on the tandem solar cells and unencapsulated CIS solar cells show no degradation when exposed to 80°C and 80% relative humidity for a total of 175 days. These tests results along with addition environmental tests performed on these cells which include UV illumination, off-angle tests and vacuum stability, are summarized in Table 2.

2.4 Array level analysis

On-orbit array level circuit performance analysis was conducted to compare the impacts of the different cell technologies for three generic orbit applications (low earth orbit (LEO), med-earth orbit (MEO), geosynchronous earth orbit (GEO)) and showed that this tandem approach provides significant array weight and area savings over other cell technologies such as silicon or GaAs(Ge) (ref.3). Electrical performance test of demonstration panels fabricated was conducted to confirm optimized circuit configuration. A 30 cell string panel demonstrated 21.7% AM0 efficiency at 28 $^{o}$C based on the nominal cell area including grid lines using the parallel-connected circuit unit of three series-connected CIS cells and three parallel-connected GaAs cells. The I-V characteristics and the picture of the panel are shown in Figure 8 (ref.12). The temperature coefficient for this string was calculated to be 2300 ppm/$^{o}$C.

2.5. Manufacturing process development

Most of our recent effort has been focused on high throughput cell fabrication process development. A major cell fabrication cost reduction is expected to be achieved through the reuse of expensive GaAs substrate material. Substrate reuse has been demonstrated by fabricating GaAs CLEFT devices on reused and re-polished wafers. Performance of devices fabricated on reused substrates was comparable to the controls built on the fresh GaAs wafers. Using an optimized GaAs CLEFT structure for the EOL performance with the base lined double layer AR coating on the front, we were able to fabricate more than 50 tandem cells averaging a BOL efficiency of 21.1% with a standard deviation of 0.7%. These results in addition to the ones of tens of watts of tandem cells fabricated in the past confirmed the producibility and consistency of our current process even though our effort to reduce cell fabrication cost still continues.

3. Future Direction

Much higher performance improvement is expected when the current GaAs top absorber is replaced by high quality AlGaAs material since the band gap of the $CuInSe_2$ cell is better matched to the band gap of the AlGaAs than the GaAs. A 26% AM0 efficiency is projected for the beginning-of-life (BOL) for this device without any further structural change (ref.1). Furthermore, this AlGaAs/$CuInSe_2$ tandem cell offers

significantly more EOL power output than other cell technologies (ref.6 ). Figure 9 shows the calculated power output as a function of 1.0 MeV electron fluence based on the reasonable BOL efficiencies assumed for the different cell technologies (14.5% for thin Si, 19% for GaAs, 2.5% for CIS under GaAs, 5.2% for CIS under AlGaAs, and 17% for AlGaAs). Radiation characteritics of different cells used in this analysis are found in the literature (ref. 4,13, and 14).

Tandem cell fabrication cost can be significantly reduced utilizing an even larger two-terminal cell design. After confirming two-terminal device configuration using the current 2 cm x 4 cm cell design, new cell designs of 4 x 4 $cm^2$ and 7 x 7 $cm^2$ are planned for the 3 inch and the 4 inch GaAs wafer substrate, respectively. These future cell designs will be for high voltage applications and further optimized for the end system use because monolithic interconnection on the GaAs CLEFT cell level is possible using the new process describe elsewhere (ref.10). Since both cells can be interconnected on the cell level to form high voltage device, a new two-terminal design with any combination of subcell ratio will be available for any specified mission environment. This new voltage-matched and two-terminal design can replace any single junction solar cell on the existing array to minimize wiring complexity and thus, reduce array fabrication cost.

Structural changes such as the replacement of the window layer of the CIS cell and replacing or eliminating Dow Corning adhesive in the stack will improve the device performance even further or increase the surviving temperature range of this tandem cell. Concepts are being developed to address these intermediate-term tasks.

Demonstration experiments utilizing these tandem cells are currently being prepared to confirm the viability of this approach The PASP Plus (Photovoltaic Array Space Power Plus Diagnostics) flight experiment conducted by Air Force will contain two strings of two-terminal GaAs/CIS tandem cells. We expect to collect significant space flight data on these cells by 1993.

## 4. Summary

High-efficiency thin-film GaAs/CIS tandem cells have been developed for planar solar array applications. Efficiencies up to 23.1% AM0 have been demonstrated based on four-terminal 4 $cm^2$ cell design. The tandem cells fabricated using our base line process exhibited a reasonable yield and a satisfactory scatter in deveice perfarmance. A new 8 $cm^2$ cell design utilizing the configuration of two-terminal and voltage-matching has been developed to minimize wiring complexity at the array level. Further performance improvement is projected when AlGaAs CLEFT top cell is used in the tandem stack. Environmental test results conducted using these tandem cells were favorable, and the tandem cells are ready for space flight experiment.

References

1. N.P.Kim, R.M. Burgess, R.A.Michelsen,B.J. Stanbery, R.W.McClelland, B.D. King, and R.P. Gale, Proceedings of the 10th Space Photovoltaic Research and Technology (SPRAT) Conference, p.88, 1989

2. J.C.C.Fan, and B.J.Palm, Solar Cells, 12, 401, 1984

3. R.M. Burgess, W.S.Chen, W.E. Devaney, D.H. Doyle, N.P. Kim, and B.J. Stanbery, Conference Record 20th IEEE Photovoltaic Specialist Conference, (IEEE, New York 1988), p. 909

4. H. Dursch, W.S. Chen, and D. Russel, Proceedings of the Space Photovoltaic Research and Technology (SPRAT) Conference, NASA Conf, Pub. 2408, p.165

5. R.W. McClelland, C.O.Bozler, J.C.C. Fan, Appl.Phys. Lett., 37, p.560, 1980

6. R.A. Mickelsen, and W.S. Chen, Conference Record 16th IEEE Photovoltaic Specialist Conference, p. 781

7. B.J. Stanbery, J.E. Avery, R.M. Burgess, W.S. Chen, W.E. Devaney, D.H. Doyle, R.A. Mickelsen, R.W. McClelland, B.D. King, R.P. Gale, J.C.C. Fan, Conference Record 19th IEEE Photovoltaic Specialist Conference, p.280, 1987

8. N.P. Kim, R.M. Burgess, B.J. Stanbery, R.A. Mickelsen, J.E. Avery, R.W. McClelland, B.D. King, M.J. Boden, and R.P. Gale, Conference Record 20th IEEE Photovoltaic Specialist Conference, p.457, 1988

9. R.P. Gale, R.W. McClelland, B.D. Dingle, J.V. Gormley, R.M. Burgess, N.P. Kim, R.A. Mickelsen, and B.J. Stanbery, Conference Record, 21th IEEE Photovoltaic Specialist Conference, p.53, 1990

10. R.W. McClelland, B.D. Dingle, R.P. Gale and J.C.C. Fan, Conference Record, 21th IEEE Photovoltaic Specialist Conference, p.168, 1990

11. N.P. Kim, B.J. Stanbery, R.P. Gale, and R.W. McClelland,Proceedings of the 9th Space Photovoltaic Research and Technology (SPRAT) Conference, p.138, 1988

12. R. Burgess, C.Flora, and M. Schneider, Conference Record 21st IEEE Photovoltaic Specialist Conference, (IEEE, New York 1990), p. 1340

13. R.Y. Loo and G.S. Kamath, Conference Record 20th IEEE Photovoltaic Specialist Conference, (IEEE, New York 1988), p. 635

14. B.E. Anspaugh, JPL Publication 82-69, Addendum 1: 1982-1988, Solar Cell Radiation Handbook

Table 1. Projected Two-terminal Performance

| Temp | Voc (V) | Jsc (mA/cm²) | Fill Factor (%) | Efficiency(%) |
|---|---|---|---|---|
| 28°C | 1.012 | .298 | .83 | 22.80 |
| 40°C | 0.990 | .298 | .83 | 22.30 |
| 55°C | 0.965 | .301 | .82 | 21.30 |
| 70°C | .935 | .302 | .81 | 20.70 |

Table 2. Summary of environmental tests performed on GaAs/CIS tandem solar cells

| Environmental Test | Test Range | Results |
|---|---|---|
| Electron Irradiation | 1.0 and 2.0 MeV<br>Fluences to $5.0 \times 10^{15}$ $cm^{-2}$ | CIS; nodegradation<br>GaAs; same as bulk GaAs |
| Proton irradiation | 0.2, 0.4, 0.8, 1.0, and 2.0 MeV;<br>Fluences to $10^{13}$ $cm^{-2}$ | CIS; Factor of ten more radiation resistant<br>GaAs; Some energies show more radiation resistant than bulk GaAs |
| Thermal Cycling | +80°C to -100°C; 850 cylcles | Negligible degradation |
| UV Exposure | 3 month AM0 equivalent | No UV degradation |
| Photo Illumination | 164 hrs continuous illumination | No degradation |
| Off-Angle Performance | Normal to 50°C off-angle | Follows cosine law |
| Vacuum Stability | $10^{-7}$ torr vacuum pressure<br>25°C to 110°C | No measurable difference to ambient pressure measurements |

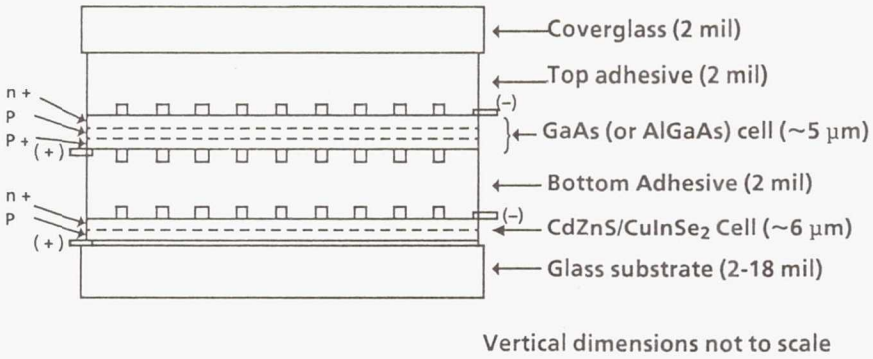


*Figure 1. Schematic of Tandem Cell Structure*

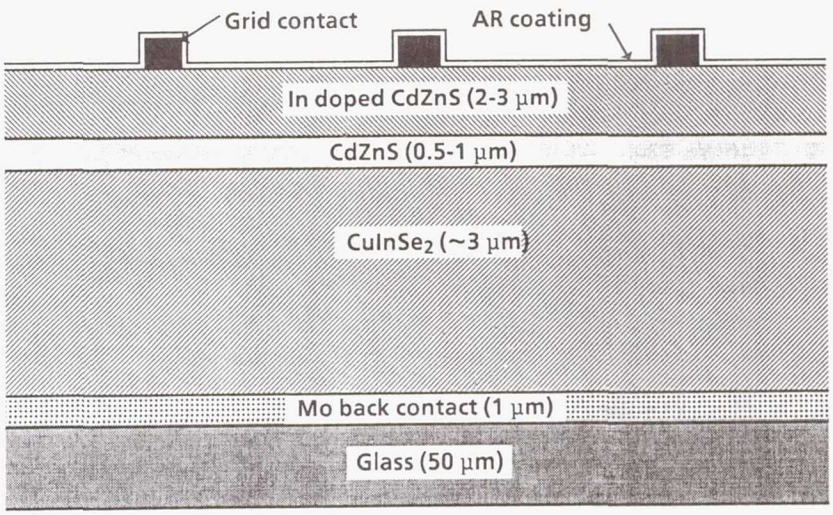


*Figure 2. Cross Sectional View of $CuInSe_2$ Cell*

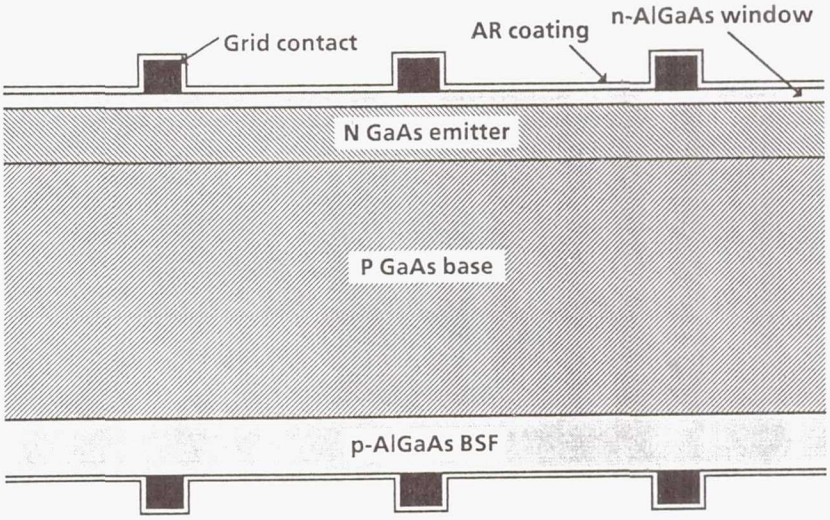


*Figure 3. Cross Sectional View of GaAs Thin-film Cell*

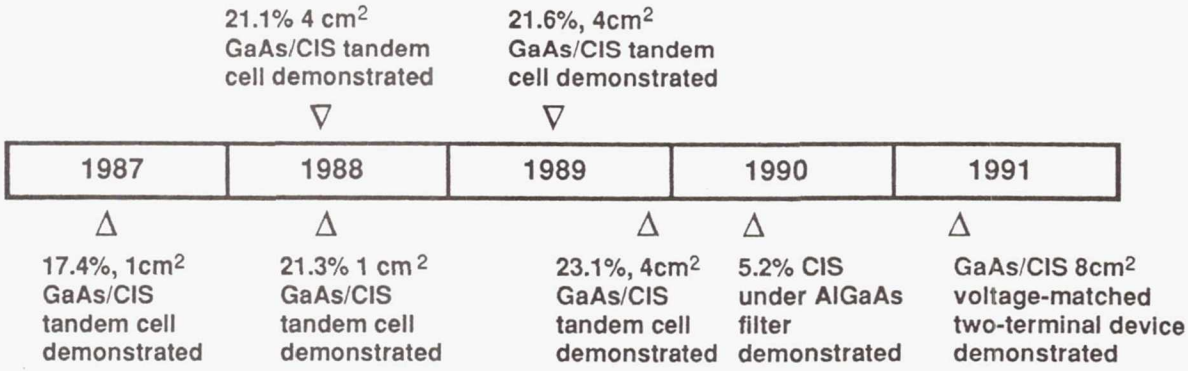


*Figure 4. Key Milesones of GaAs(AlGaAs)/CIS Tandem Cell Project*

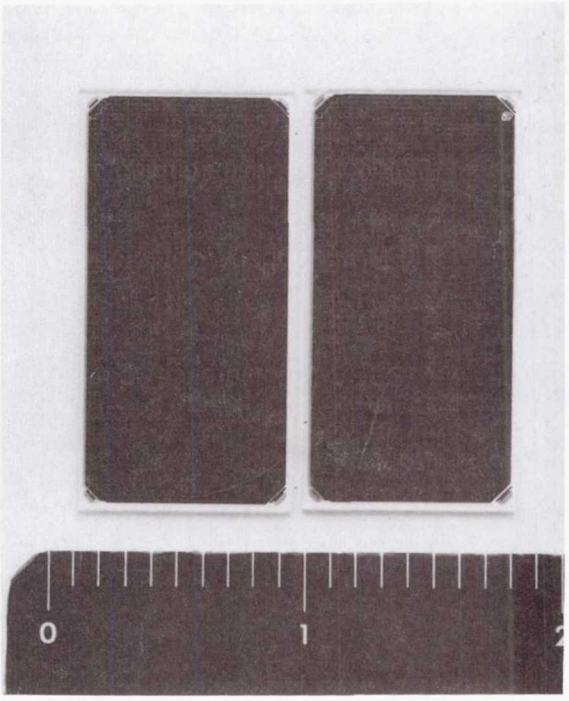


*Figure 5. The GaAs CLEFT Cells (8 cm$^2$ each )*

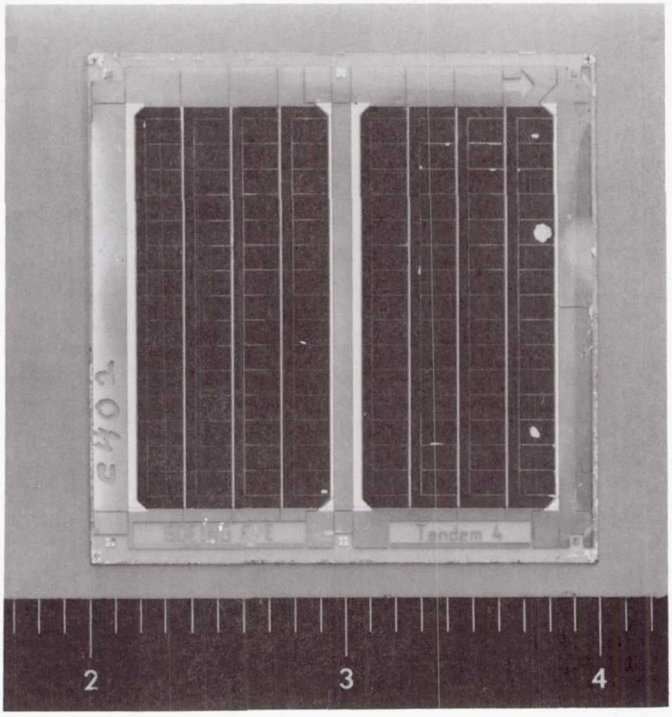


*Figure 6. Two CIS Cells Containing Four Monolithically Interconneted Subcells (8 cm$^2$ each)*

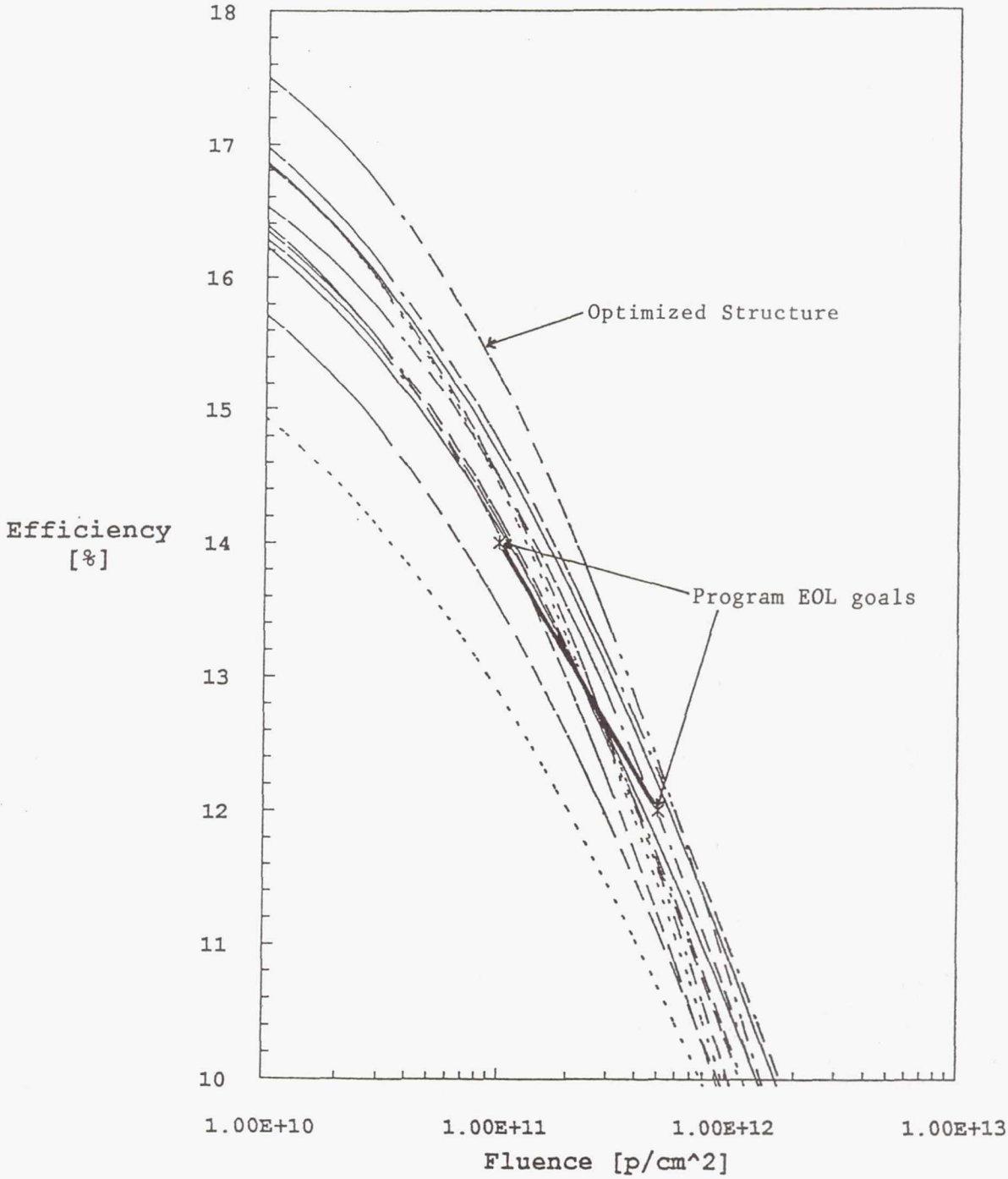


*Figure 7. Efficiency Degradation Curves of GaAs CLEFT Cells with Various Device Parameters vs. 1 MeV Proton Fluence*

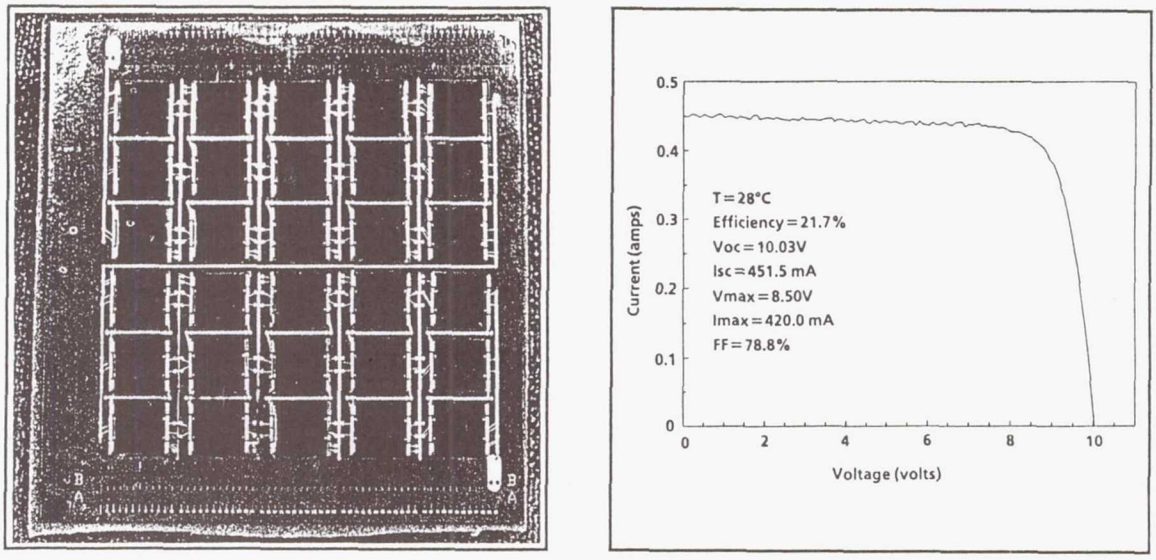


*Figure 8. Voltage-matched 30 GaAs/CIS tandem Cell Demonstration Panel and I-V Curves*

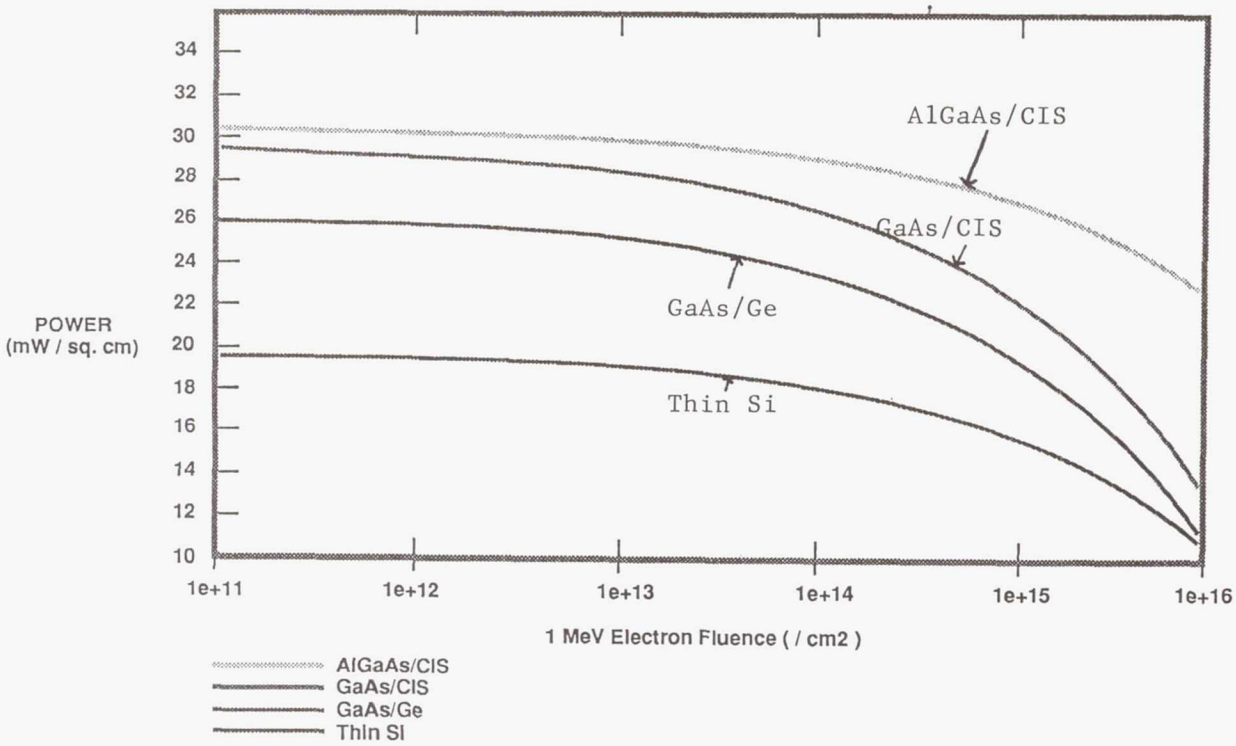


*Figure 9. Calculated Cell Power Output as a Function of 1 MeV Electron Fluence*

# DEVELOPMENT OF N/P AlGaAs FREE-STANDING TOP SOLAR CELLS FOR TANDEM APPLICATIONS*

Gerald H. Negley, Louis C. DiNetta,
John R. Cummings, Margaret H. Hannon
and Paul E. Sims
AstroPower, Inc.
30 Lovett Ave.
Newark, DE 19711

Allen M. Barnett

Department of Electrical
Engineering
University of Delaware
Newark, DE 19716

## ABSTRACT

The combination of a free-standing AlGaAs top solar cell and an existing bottom solar cell is the highest performance, lowest risk approach to implementing the tandem cell concept. The solar cell consists of an AlGaAs substrate layer, an AlGaAs base layer, an AlGaAs emitter, and an ultra-thin AlGaAs window layer. The window layer is compositionally graded which minimizes reflection at the window layer/emitter interface and creates a built-in electric field to improve quantum response in the blue region of the spectrum. Liquid phase epitaxy (LPE) is the only viable method to produce this free-standing top solar cell. We have already demonstrated small (0.125 $cm^2$), transparent p/n AlGaAs top solar cells of the optimum bandgap for combination with a silicon bottom solar cell. The efficiency of an AlGaAs/Si stack using the free-standing AlGaAs device upon an existing silicon bottom solar cell is 24% (1X, AM0). The n/p AlGaAs top solar cell is being developed in order to facilitate the wiring configuration. The two-terminal tandem stack will retain fit, form, and function of existing silicon solar cells. Progress in the development of large area (8 $cm^2$ and 16 $cm^2$), free-standing AlGaAs top solar cells will be discussed.

## INTRODUCTION

During a past development effort, small (0.126 $cm^2$) p/n AlGaAs concentrator solar cells were developed [ref. 1]. Two device structures were investigated: free-standing AlGaAs concentrators and a concentrator based upon a Burrus diode structure [ref. 2]. The results of the early work included the growth and fabrication of a 17.2% AlGaAs solar cell with a bandgap of 1.80 eV. Mechanically stacking this AlGaAs solar cell upon a thin silicon solar cell designed by Spectrolab [ref. 3] (for mechanically stacked applications) should result in a tandem stack efficiency of 24% (1x, AM0) as illustrated in Table I

Table I

Predicted Performance for Two-Terminal Configuration of
AlGaAs/Si Mechanical Stack with Spectrolab Bottom Solar Cell [ref. 3]
(AM0, 135 $mW/cm^2$)

| Material | Eg (eV) | Voc (volts) | Jsc ($mA/cm^2$) | FF | Efficiency (%) |
|---|---|---|---|---|---|
| AlGaAs | 1.80 | 1.295 | 21.4 | 0.84 | 17.2 |
| Silicon | 1.13 | 0.565 | 21.4 | 0.76 | 6.8 |
| | | TWO-TERMINAL STACK ----------> | | | 24.0 |

* This research is being supported in part by the Strategic Defense Initiative/Innovative Science and Technology branch managed by Aero Propulsion and Power Directorate, Wright Laboratory, Wright-Patterson AFB under contract number F33615-91-C-2144.

Presently the effort is targeted to develope large area AlGaAs top solar cells for mechanical attachment to a silicon solar cell flat panel array. Our approach will adapt demonstrated AlGaAs solar cell performance and enhanced growth technology for the fabrication of a self-supporting top solar cell. The top cell will be designed for a two-terminal wiring configuration, hence a n/p configuration is investigated.

## MODELING

The theoretical limits for the proposed tandem stack were determined using a solar cell model by Nell [ref. 4] based upon tabulated standard spectra, the fit of experimentally achieved open circuit voltages, and the assumption of unit quantum efficiency. More recent work [ref. 5] indicates that Nell's model underestimates open-circuit voltages. Incorporating this change, a theoretical AM0 efficiency of 38.5% at 1 sun is predicted for the tandem stack. The theoretical maximum efficiency was analyzed and is shown in Table II. A sub-bandgap transparency of 100% is assumed.

Table II

Predicted Theoretical Maximum Efficiency for a
Two-Terminal AlGaAs/Si Mechanical Stack
(AM0, 135 mW/cm$^2$)

| Material | Eg (eV) | Voc (volts) | Jsc (mA/cm$^2$) | FF | Efficiency (%) |
|---|---|---|---|---|---|
| AlGaAs | 1.76 | 1.414 | 26.6 | 0.91 | 25.3 |
| Silicon | 1.13 | 0.788 | 26.6 | 0.85 | 13.2 |
| | | TWO-TERMINAL STACK ----------> | | | 38.5 |

A goal of 95% transparency to sub-bandgap photons was used in the prediction of the "best case" performance. For direct-bandgap materials, predictions were determined by reducing the open-circuit voltage, short-circuit current, and fill factor to 96%, 91%, and 96%, respectively, of their theoretical limits. Indirect bandgap material reductions are correspondingly 91%, 96%, and 96%, respectively [ref. 6]. This permits stack performance predictions for the various combinations. Performance of the "best case" AlGaAs top solar cell with a 1.76 eV bandgap on a silicon bottom solar cell is listed in Table III.

Table III

"Best Case" Prediction for Two-Terminal
Configuration of AlGaAs/Si Mechanical Stack
(AM0, 135 mW/cm$^2$)

| Material | Eg (eV) | Voc (volts) | Jsc (mA/cm$^2$) | FF | Efficiency (%) |
|---|---|---|---|---|---|
| AlGaAs | 1.76 | 1.35 | 24.3 | 0.87 | 21.1 |
| Silicon | 1.13 | 0.71 | 24.3 | 0.82 | 10.5 |
| | | TWO-TERMINAL STACK ----------> | | | 31.6 |

The "best case" performance of the individual solar cells assumes the following additional reductions in current for the bottom solar cell. The short-ciruit current of the bottom solar cell is decreased by the energy absorbed in the top solar cell. An additional 5% reduction in the short-circuit current is added to account for parasitic absorption or reflection losses in the top solar cell or the inter-cell connection.

## SOLAR CELL DESIGN

Aluminum gallium arsenide is the material of choice for the wide-bandgap top solar cell since it is the most developed of the potential top solar cell materials. This ternary compound exhibits a tunable bandgap while maintaining lattice-matched compositions which permit sophisticated designs leading to high performance devices. Formed on a thick, transparent AlGaAs substrate ($Al_xGa_{1-x}As$, $x \geq 0.45$), device yield is greatly improved due to the relatively robust wafer. Liquid phase epitaxy (LPE) provides the material quality and growth rates necessary for the free-standing AlGaAs top solar cells.

The solar cell consists of an AlGaAs substrate layer (typically 100 microns thick), an AlGaAs base layer (5 microns thick), an AlGaAs emitter, and an ultra-thin AlGaAs window layer (0.05 microns). The AlGaAs emitter is formed by tellurium diffusion from the window layer into the base layer. Using an isothermal growth process permits sufficient time to diffuse the emitter while growing the thin, compositionally graded window layer. The compositionally graded window layer minimizes reflection at the window layer/emitter interface and creates a built-in electric field to improve quantum response in the blue region of the spectrum [ref. 7]. The role of the substrate is two fold: i) support, and ii) formation of a rear cladding layer to enhance carrier confinement. This double heterostructure design results in high open-circuit voltages. The solar cell structure is shown in Figure 1.

Previously, tin (Sn) and beryllium (Be) were used as the n-type and p-type dopants when developing the p/n AlGaAs concentrator solar cells. For the growth of the n/p large area AlGaAs solar cells, these dopants are not compatible with the growth process. Zinc (Zn) and tellurium (Te) are being used as the p-type and n-type dopants. These dopants have been adequately characterized for the production of ultra-bright light emitting diodes (LEDs) which are similar in design [ref. 8].

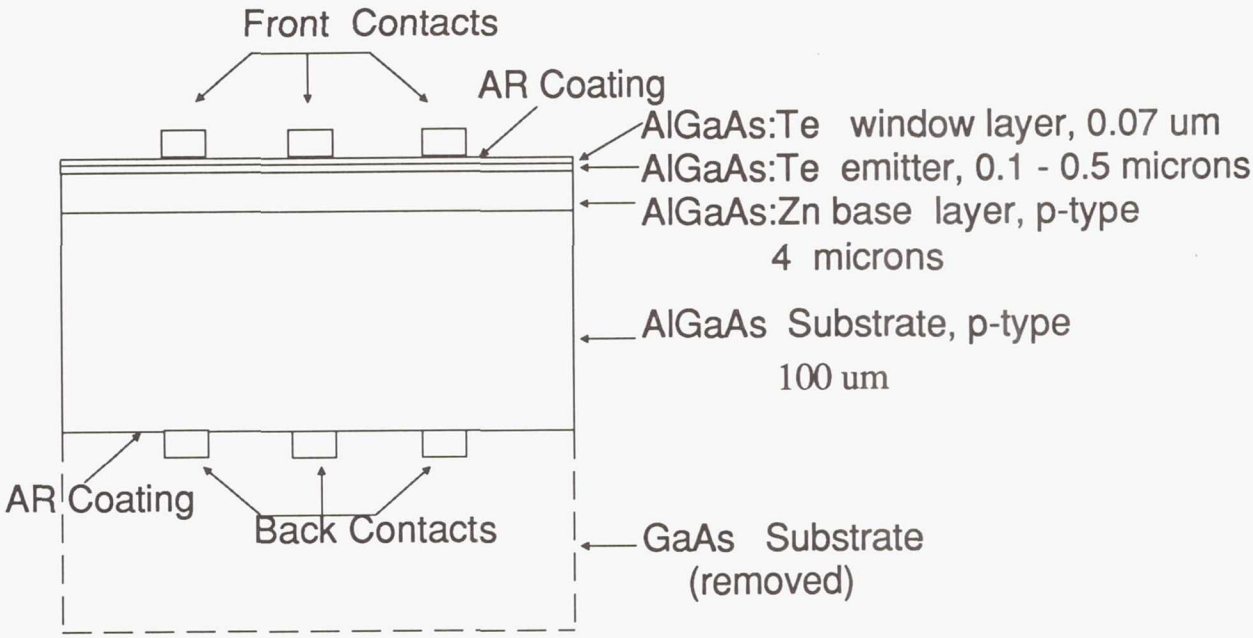


Figure 1. N/p free-standing AlGaAs top solar cell design.

## RESULTS

Building on previous results [ref.1], AstroPower has directed the program to produce large area, free-standing AlGaAs solar cells with a n/p configuration. The n/p AlGaAs top solar cell is being developed to facilitate the wiring configuration. The two-terminal tandem stack will retain fit, form and function of existing silicon solar cells.

Initial work with the n/p configuration has been encouraging. The development effort has been divided into two phases: optimization of the AlGaAs solar cell on a GaAs substrate, and optimization of the AlGaAs substrate. The preliminary emphasis has focused on obtaining high open-circuit voltages. To date, the highest value obtained is 1.320 volts (Device F8719 #2). Figure 2 is the corresponding external quantum efficiency of this device. The I-V characteristics are shown in Figure 3.

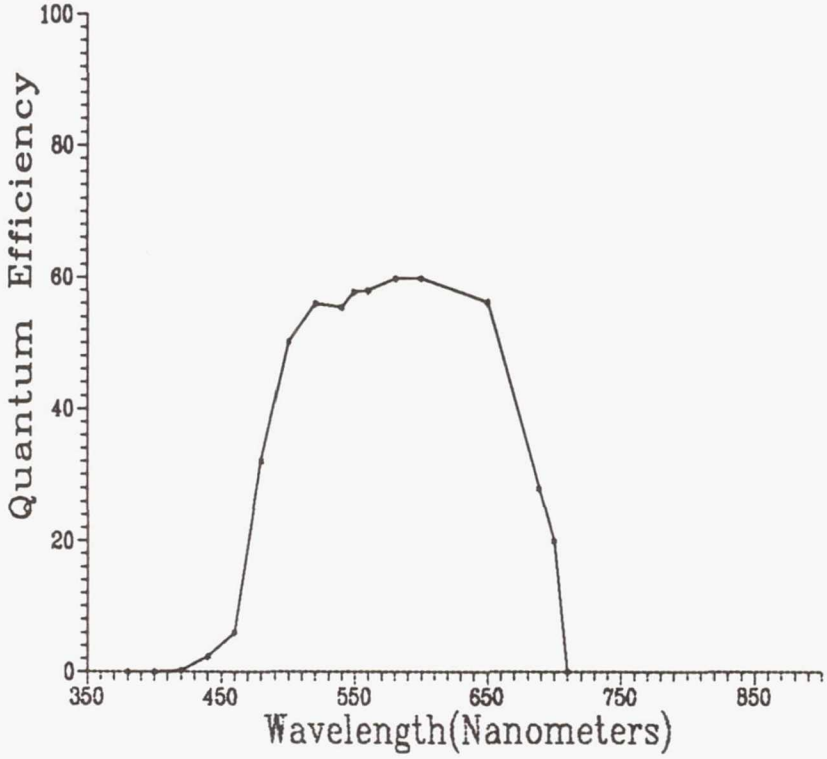


Figure 2. External quantum efficiency of F8719 #2. No AR coating has been applied to this sample. The energy bandgap is estimated to be approximately 1.80 eV.

As can be seen, the current density is limited by the lack of blue response. This problem has been traced to melt-mixing which results in high initial growth rates during the isothermal growth process. Modifications to the epitaxial growth equipment have been made to eliminate this problem.

Presently, our growth process for the AlGaAs structures is limited to a 6 $cm^2$ area. New epitaxial boats have been designed for the growth of 2 cm x 4 cm devices. In addition, a new LPE growth system based upon solute transport has been designed for the fabrication of 5 cm x 5 cm devices or 3 inch diameter wafers. This system is under construction and is expected to be on line shortly. The system has been designed to obtain high growth rates (30 microns/hour) while maintaining the high material quality associated with LPE material.

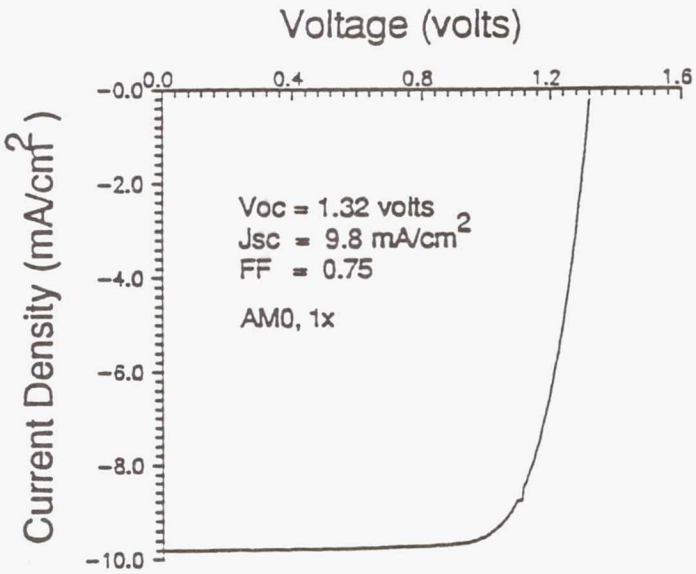


Figure 3. I-V characteristics of F8719 #2 using solar simulator (no AR coating)

During our AlGaAs concentrator development effort, sub-bandgap transparency greater than 91% was obtained [ref.1]. Of the losses, 2% was attributed to free-carrier absorption while the remaining loss was purely reflective. Presently, the AlGaAs substrate is being optimized in terms of doping in order to obtain low specific contact resistance and high sub-bandgap transparency.

## SUMMARY

Large area, free-standing AlGaAs solar cells are being developed for mechanical attachment to existing silicon solar cells. The n/p configuration is being optimized for a two-terminal wiring. Scale up of the areas to 2 cm x 4 cm are presently underway. The growth and fabrication of 4 cm x 4 cm devices will begin in the near future with a large scale LPE system using solute transport to achieve high growth rates.

## REFERENCES

[1] L.C. DiNetta, G.H. Negley, M.H. Hannon, J.R. Cummings, J.B. McNeely, and A.M. Barnett, "AlGaAs Top Solar Cell for Mechanical Attachment in a Multi-Junction Tandem Concentrator Solar Cell Stack," 21st IEEE Photovoltaic Specialists Conference, Kissimimee, p. 58, 1990.

[2] C.A. Burrus and B.I. Miller, "Small Area, Double Heterostructure AlGaAs Electroluminescent Diode Sources for Optical Fiber Transmission," Optics Commun., 4, p.307, 1971.

[3] Private communication, Terry Cavicchi, Spectrolab, Inc.

[4] M.E. Nell and A.M. Barnett, "The Spectral p-n Junction Model for Tandem Solar Cell Design," IEEE Trans. Electron Devices, ED-34, 257-266.

[5] G.H. Negley, unpublished.

[6] A.M. Barnett and J.S. Culik, "New Solar Cell Design Options," 19th IEEE Photovoltaic Specialists Conference, New Orleans, p. 931, 1987.

[7] L. Mayet, M. Gavand, B. Montegu, and A. Laugier, "High Efficiency AlGaAs-GaAs Tandem Solar cells with Three Terminals," 20th IEEE Photovoltaic Specialists Conference, Las Vegas, p. 597, 1988.

[8] See for example, H. Ishiguro, K. Sawa, S. Nagao, H. Yamanaka, and S. Kioke, "High Efficient GaAlAs Light-Emitting Diodes of 660nm with a Double Heterostructure on a GaAlAs Substrate", Appl. Phys. Lett., 43, 11, p.1034, 1983.

# MONOLITHIC $InP/Ga_{0.47}In_{0.53}As$ TANDEM SOLAR CELLS FOR SPACE

M.W.Wanlass, J.S.Ward, T.J.Coutts, K.A.Emery, T.A.Gessert and C.R.Osterwald
*Solar Energy Research Institute (SERI), Golden, CO, 80401, U.S.A.*

## ABSTRACT

This paper provides a review of progress made in the development of $InP/Ga_{0.47}In_{0.53}As$ monolithic tandem solar cells since the last SPRAT conference. Improved one-sun, three-terminal tandem designs have resulted in AM0 efficiencies as high as 23.9% at 25°C. Additionally, high-efficiency concentrator versions of the three-terminal device have been developed. The best concentrator tandem has a peak AM0 efficiency of 28.8% under 40.3 suns at 25°C. For the concentrator tandems, the subcell performance parameter temperature coefficients are reported as a function of the concentration ratio. Results from a computer modeling study are presented which provide a clear direction for improving the efficiency of the concentrator tandem. The prospects for fabricating high-efficiency, series-connected (i.e., two-terminal) $InP/Ga_{0.47}In_{0.53}As$ monolithic tandem cells are also discussed.

## INTRODUCTION

During the last year, the monolithic $InP/Ga_{0.47}In_{0.53}As$ tandem solar cell has emerged as an attractive photovoltaic device for future space power applications. The device has several advantages for space applications over conventional GaAs-based tandems, (e.g., AlGaAs/GaAs and GaInP/GaAs), including a proven radiation-resistant InP top cell, an infrared-scavenging $Ga_{0.47}In_{0.53}As$ bottom cell and a high theoretical AM0 efficiency, particularly under concentration (ref. 1). Additionally, the tandem is based on a lattice-matched structure which is relatively easy to grow in high-quality form using a process such as metalorganic-vapor-phase epitaxy (MOVPE). A wide technology base for the $InP/Ga_{0.47}In_{0.53}As$ materials system has been established due to applications for these materials in other devices, (e.g., photodetectors and heterostructure bipolar transistors), thus allowing for rapid development of the $InP/Ga_{0.47}In_{0.53}As$ tandem cell.

Our first report on the $InP/Ga_{0.47}In_{0.53}As$ tandem cell was presented at the last SPRAT conference (ref. 1). At that time, we had fabricated the first working three-terminal prototype devices which had one-sun AM0 efficiencies of ~14% at 25°C. Since then, we have made considerable progress in several areas, including improved device designs, development of concentrator tandems with high AM0 efficiencies, evaluation of subcell parameter temperature coefficients and new computer modeling capabilities designed to identify key areas for improving the tandem cell performance. The purpose of this paper is to review the present status in each of the above-mentioned areas. Support for this work has been provided by the Naval Research Laboratory under interagency No. RU-11-W70-AD.

## IMPROVED TANDEM CELL STRUCTURE

A schematic representation of the current InP/$Ga_{0.47}In_{0.53}As$ tandem solar cell structure is shown in figure 1. Note that the tandem utilizes three terminals; the middle contact is common to both the top and bottom subcells. In this preliminary work, we have constructed three-terminal devices in order to extract data from the component subcells more easily. Furthermore, in this configuration the subcells can be considered to be independently connected (i.e., much like mechanically stacked tandems). Details of the design and the functional aspects of the component layers in the structure have been described in an earlier publication, however there are two key differences between the current design and the prototype design reported previously (ref. 1). Firstly, a fully interdigitated top/middle contact grid metallization system is used on the latest generation of cells, which results in a square cell mesa geometry. Secondly, Entech prismatic covers are used on the cells to eliminate optical losses due to, 1) obscuration from the top/middle contact grids, and, 2) loss of top cell area due to the trenches required for placement of the middle contact grid. The light ray paths shown in figure 1 illustrate the effect of the Entech cover. Because of the effect of the cover, up to 20% of the cell surface can be covered with grid metallization. Additional details pertaining to the epitaxial growth and processing procedures for the tandem structure have been disclosed previously (ref. 1).

Both one-sun and concentrator tandem cells have been fabricated using this structure, however different cell areas, grid line specifications and Entech covers are used for each type of tandem. The one-sun cells have an area of 0.31 $cm^2$, grid lines which are 80-90 μm wide and 4-5 μm high and utilize Entech covers which are compatible with a grid line-to-grid line spacing of 508 μm. Since the concentrator tandems are designed to operate with much higher current densities, their cell area is reduced to ~0.065 $cm^2$ and Entech covers with lens elements spaced only 127 μm apart are used. Hence, the grid line width on the concentrator version is reduced to 20-25 μm in order to accomodate the tighter grid line spacing.

## ONE-SUN TANDEM CELLS

A limited effort has been devoted to developing one-sun tandems, however, significant increases in efficiency have been realized using the improved structure described above. Illuminated current-voltage data for the most efficient one-sun tandem are shown in figure 2. The combined tandem efficiency is 23.9%. Higher quality structures have since been grown, however one-sun cells were not fabricated in these (see the results for the concentrator cells in the next section). With improved processing, one-sun, three-terminal cells with AM0 efficiencies of ~25% could be achieved. For the present cells, it is important to note the significant efficiency contribution from the $Ga_{0.47}In_{0.53}As$ bottom cell (5.6%). Note also that the subcell current densities are only mismatched by ~10%. Hence, it appears that high-efficiency, series-connected InP/$Ga_{0.47}In_{0.53}As$ tandem cells could be fabricated using a similar structure. For example, subcell current matching could be achieved by thinning the base layer of the InP top cell. Furthermore, suitable tunnel junctions in $Ga_{0.47}In_{0.53}As$ and lattice-matched GaInAsP (0.95 eV) have already been demonstrated (ref. 2), which could be easily incorporated into the present structure as an interconnect between the subcells. Assuming that the subcells could be current matched and a tunnel interconnect with minimal losses could be incorporated into the structure, a one-sun, two -terminal tandem

efficiency of >24% is predicted.

## CONCENTRATOR TANDEM CELLS

The majority of effort in this project has been devoted to the development and characterization of concentrator versions of the tandem. The cell performance has been investigated as a function of the temperature and concentration ratio. The tandem efficiency data at 25°C under concentration are presented here and the subcell temperature coefficients are discussed in the next section.

Figure 3 shows AM0 efficiency data as a function of the concentration ratio for one of the better concentrator tandems. The $Ga_{0.47}In_{0.53}As$ bottom cell shows the expected increase in efficiency with concentration for a cell which is not series-resistance ($R_s$) limited. This behavior can be attributed to the thick lateral conduction layer above the bottom cell in the tandem structure which results in an extremely low effective emitter sheet resistance for the $Ga_{0.47}In_{0.53}As$ cell. In contrast, the InP top cell shows evidence of becoming series-resistance limited as the concentration ratio approaches 20. As the concentration ratio is further increased toward 100, the top cell efficiency behavior shows clear evidence of excessive $R_s$. This behavior is reflected in the tandem efficiency, which is the sum of the subcell efficiencies. The tandem shows a broad efficiency plateau with concentration and AM0 efficiencies ≥28% are observed from 10 to 60 suns. The high-$R_s$ problem for the InP top cell is related to the high sheet resistance of the thin emitter layer coupled with aspects of the top cell grid design. Techniques for solving this problem are discussed in a section to follow on computer modeling.

Figure 4 gives current-voltage data for a three-terminal tandem at peak efficiency under concentration. The efficiencies of both subcells increase substantially under concentration, (compare with the one-sun data given in figure 2), particularly for the $Ga_{0.47}In_{0.53}As$ bottom cell, which adds a substantial contribution (8.1%) to the overall tandem efficiency (28.8%). Presently, the peak efficiency of the tandem occurs at relatively low concentration ratios and is limited by the high $R_s$ of the InP top cell. As shown later, computer modeling studies and empirical studies predict that a small decrease, (as little as a factor of 4), in $R_s$ for the top cell will allow the tandem to operate at a peak efficiency approaching 30% at ≥100 suns. Note, once again, from the data in figure 4 that the subcells are nearly current matched. Under the same assumptions used in the previous section, and using the open-circuit voltage data from figure 4 for each subcell, a series-connected concentrator tandem should have an efficiency ≥28% under 40 suns at 25°C.

## CONCENTRATOR TANDEM SUBCELL TEMPERATURE COEFFICIENTS

Temperature coefficients (TC's) for each of the subcell performance parameters have been calculated as a function of the concentration ratio from measured current-voltage data. In the absence of excessive $R_s$, the TC's for the open-circuit voltage ($V_{oc}$) and fill factor (FF) should improve as the concentration ratio increases due to the logarithmic dependence of $V_{oc}$ on the short-circuit current density. This effect is considered to be one of the advantages of operating under concentration. However, when excessive $R_s$ is present, the TC for FF can actually worsen with increasing concentration.

These effects are illustrated in figures 5 and 6, which give the subcell TC's for $V_{oc}$, FF and efficiency, (each normalized to their values at 25°C), as a function of the concentration ratio. For the top cell data given in figure 5, the TC of $V_{oc}$ is seen to improve with increasing concentration as expected, whereas the TC of FF degrades monotonically due to excessive $R_s$. The net effect is that the TC of efficiency remains relatively constant as a function of concentration. However, the data shown in figure 6 for the bottom cell is characteristic of what one would expect for a nearly ideal concentrator cell. There is no evidence of excessive $R_s$ and the TC's for both $V_{oc}$ and FF improve monotonically with the concentration ratio, resulting in a monotonic improvement in the TC of efficiency.

## COMPUTER-MODELED TANDEM CELL PERFORMANCE

A computer modeling code has been developed which is designed to calculate the tandem cell performance as a function of *measured* subcell parameters and operational parameters such as the temperature and the concentration ratio. This capability has allowed us to study the previously mentioned $R_s$ problem associated with the InP top cell in the concentrator tandem. Using the model, it is possible to track the effect on performance of reducing $R_s$ and thereby set target values for $R_s$ consistent with achieving a desired performance level under a given set of operating conditions. This approach has proven to be very useful as a means of identifying power loss mechanisms as well as avenues for maximizing the performance of existing device structures.

As mentioned above, the computer calculations are based on subcell parameters measured in the laboratory. Thus, the first step in this work involved obtaining the subcell device parameters as a function of temperature. Absolute external quantum efficiency (AEQE) data at 25°C and 80°C were obtained in order to calculate the illuminated short-circuit current density. These measurements showed that only the subcell band gaps changed with temperature, with the shape and level of the AEQE remaining constant. The magnitude of the subcell band gap temperature coefficients were determined from photoluminescence spectra obtained from actual tandem cell structures and taken at a series of temperatures from 20°C to 80°C.

Dark current-voltage (I-V) measurements of the subcells were performed over a similar range of temperatures and were then numerically fitted to obtain the temperature dependence of the diode quality factors, reverse-saturation current densities and series resistances. A computer model was then constructed to calculate the subcell efficiencies as a function of the temperature and concentration ratio. The model output was verified by comparing with measured one-sun subcell performance parameters. Precise agreement with measured open-circuit voltages was obtained by adjusting the reverse-saturation current densities by about a factor of two.

An analysis of the temperature-dependent dark I-V data revealed that $R_s$ for the $Ga_{0.47}In_{0.53}As$ bottom cell was smaller than could be measured using the technique. A low, temperature-independent value of $6.4 \times 10^{-5}$ ohm-cm$^2$ was therefore assumed. The InP top cell, however, had a value of $R_s$ of $5.7 \times 10^{-2}$ ohm-cm$^2$ at 25°C, which decreased linearly to $3.3 \times 10^{-2}$ ohm-cm$^2$ as the temperature was raised to 80°C. Hence, as anticipated, $R_s$ for the top cell was found to be large compared to the bottom cell. These values were then used in the computer model to predict the tandem cell performance over a range of temperatures and concentration ratios.

Figure 7 illustrates the utility of the computer model. In this figure, the modeled AM0 efficiencies for the bottom cell and the complete tandem, (i.e., top cell efficiency plus bottom cell efficiency), are plotted against the concentration ratio for temperatures ranging from 20°C to 80°C. In performing the efficiency calculations, the top and bottom subcells are assumed to be independently connected. The set of curves with solid lines in the figure give the modeled efficiencies using the measured subcell parameters. Note the close correspondence between the modeled data at 25°C in this figure and the measured data given in figure 3 for the same temperature. These results verify the accuracy of the model. In particular, the model correctly predicts the sharp drop in efficiency at high concentration ratios due to the high top cell series resistance. We have used the model to quantify the effect of reducing the series resistance of the InP top cell. The set of curves with dashed lines in figure 7 give the tandem efficiency when $R_s$ of the top cell is reduced by a factor of 10 (i.e., from $5.7 \times 10^{-2}$ ohm cm$^2$ to $5.7 \times 10^{-3}$ ohm cm$^2$ at 25°C). The tandem efficiency shows a remarkable improvement at high concentration ratios for the lower value of $R_s$. In fact, AM0 efficiencies well in excess of 30% are predicted for concentration ratios greater than 100 at 25°C.

In a companion paper presented at this conference (ref. 3), we have shown that the top cell series resistance problem is caused by a high sheet resistance in the the thin emitter layer. The problem is easily solved by reducing the grid line spacing for the top cell metallization. At present, our concentrator cells are based on available Entech cover designs, which limits the smallest grid line spacing to 127 μm. This presents a barrier to further improvements in the performance of the present three-terminal tandem structure without resorting to more complicated metallization schemes (e.g., stacked, electrically isolated contacts). However, results from our work on single-junction InP concentrator cells (ref. 3) suggest that a series-connected version of the tandem, utilizing the grid design used on the single-junction concentrator cells, would experience its peak efficiency (~30% at 25°C) at ≥100 suns. Therefore, the prospect of fabricating high-efficiency, two-terminal InP/$Ga_{0.47}In_{0.53}As$ concentrator tandem cells, which utilize the current subcell device structures and off-the-shelf Entech covers, is very promising.

## SUMMARY

The current status of InP/$Ga_{0.47}In_{0.53}As$ monolithic tandem solar cells has been reviewed. This new tandem cell combines several features which make it very attractive for high-efficiency space power applications. An improved three-terminal device structure has resulted in vastly improved one-sun and concentrator tandem cell efficiencies. One-sun AM0 efficiencies as high as 23.9% at 25°C have been achieved. Concentrator tandems have peak efficiencies of 28.8% under 40.3 suns at 25°C. The data gleaned from the work on three-terminal tandems has been used to demonstrate that high-efficiency, series-connected InP/$Ga_{0.47}In_{0.53}As$ monolithic tandems are possible with AM0 efficiencies ≥24% at one sun, and ≥28% under concentration. However, in order to attain higher tandem cell efficiencies at higher concentration ratios, $R_s$ for the InP top cell must be reduced. This problem has also been shown to degrade the temperature performance of the top cell under concentration. Computer modeling and empirical studies suggest that concentrator tandem efficiencies approaching 30% should be possible through a reduction in $R_s$ for the top cell.

## REFERENCES


1) Wanlass, M.W.; Gessert, T.A.; Horner, G.S.; Emery, K.A. and Coutts, T.J.: $InP/Ga_{0.47}In_{0.53}As$ Monolithic, Two-Junction, Three-Terminal Tandem Solar Cells. Proc. of SPRAT X Conf., NASA Lewis Res. Cen., Nov. 7-9, 1989, pp. 102-116.

2) Shen, C.C.; Chang, P.T. and Emery, K.A.: Two-Terminal, Monolithic, InP-Based Tandem Solar Cells with Tunneling Intercell Ohmic Connections. Technical Session 3, these proceedings.

3) Ward, J.S.; Wanlass, M.W.; Coutts, T.J. and Emery, K.A.: InP Concentrator Solar Cells for Space Applications. Technical Session 6, these proceedings.

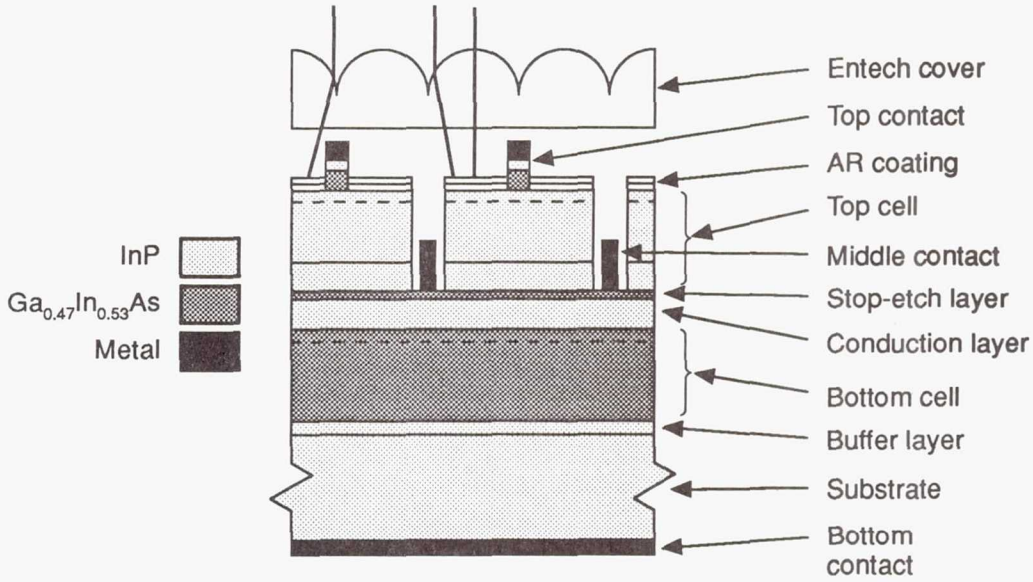


**Figure 1.** Schematic diagram of the three-terminal, monolithic InP/$Ga_{0.47}In_{0.53}As$ tandem solar cell structure.

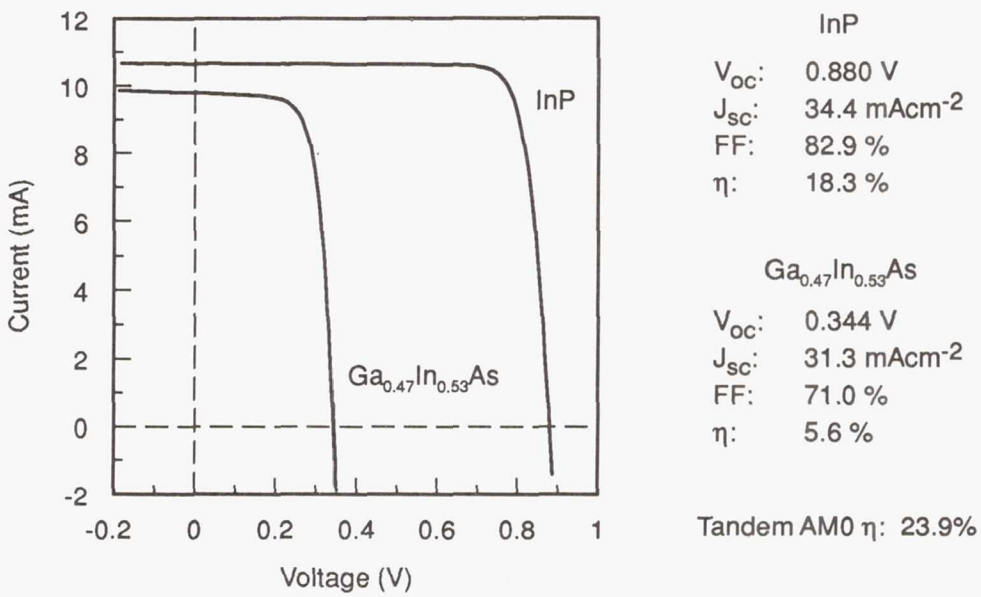


**Figure 2.** Composite one-sun current-voltage AM0-efficiency data for a high-efficiency, three-terminal, monolithic InP/$Ga_{0.47}In_{0.53}As$ tandem solar cell at 25°C.

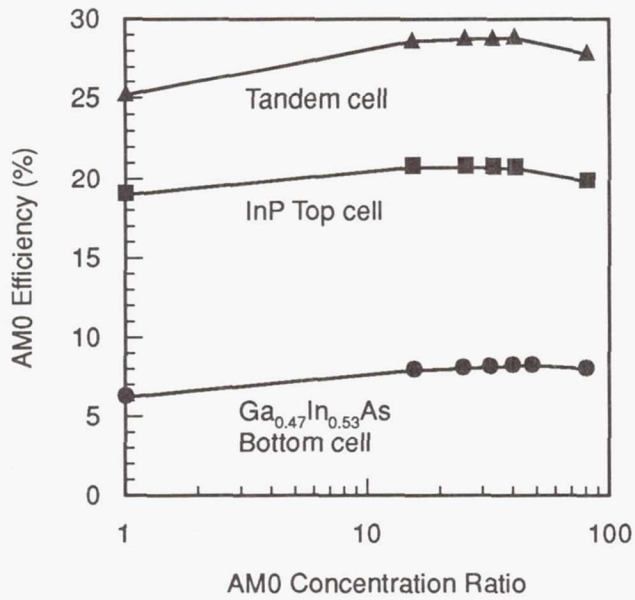


**Figure 3.** AM0 efficiency *versus* concentration ratio data for a high-efficiency, three-terminal, concentrator InP/ $Ga_{0.47}In_{0.53}As$ tandem solar cell at 25°C.

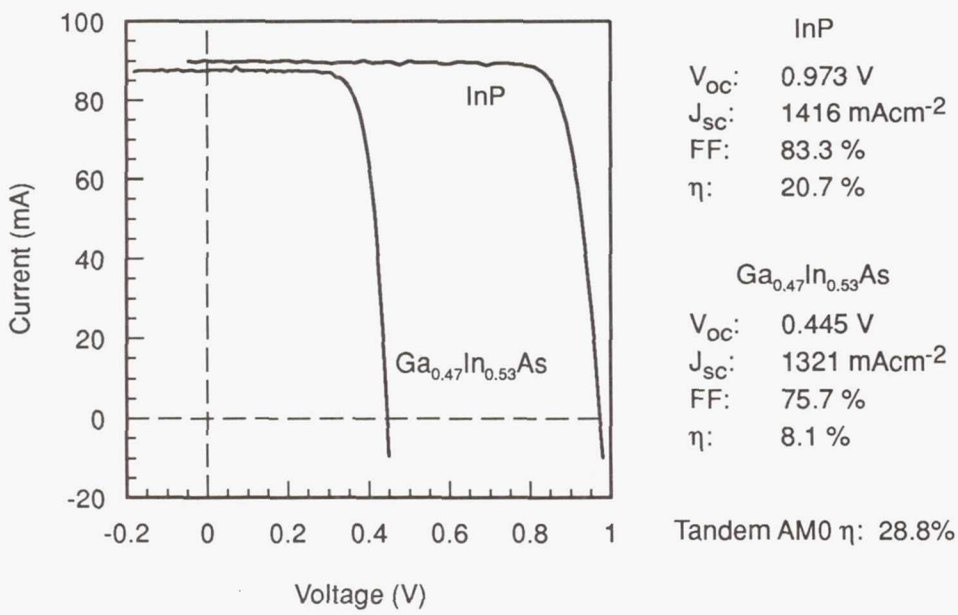


**Figure 4.** Composite current-voltage data for a three-terminal InP/$Ga_{0.47}In_{0.53}As$ tandem solar cell at peak AM0 efficiency under 40.3 suns concentration at 25°C.

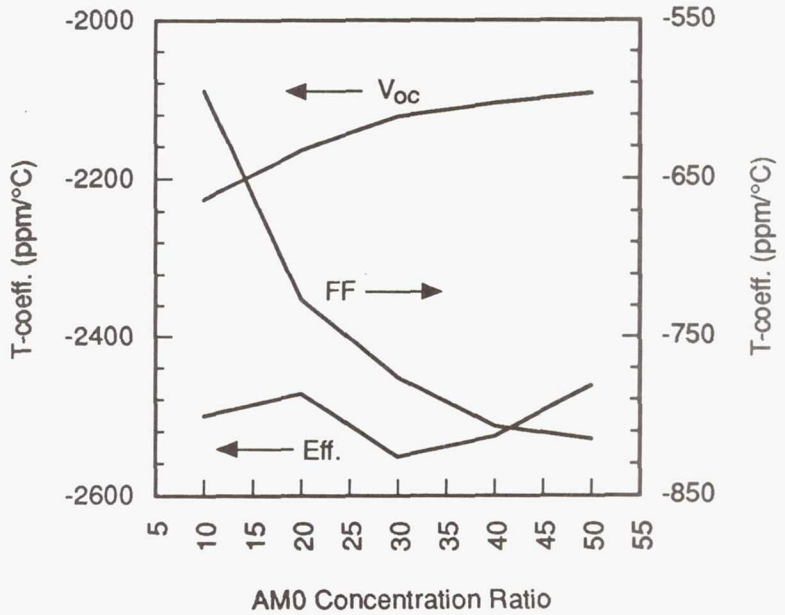


**Figure 5.** InP top cell performance parameter temperature coefficients as a function of the AM0 concentration ratio.

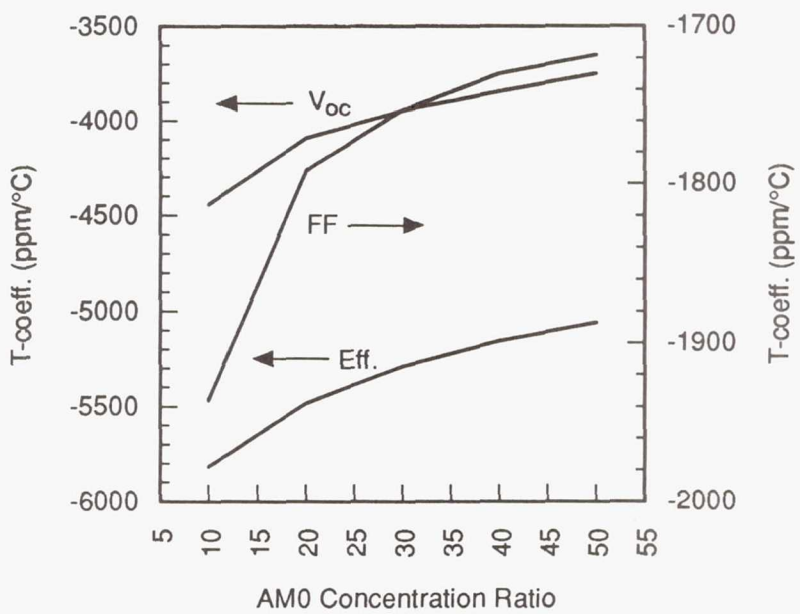


**Figure 6.** $Ga_{0.47}In_{0.53}As$ bottom cell performance parameter temperature coefficients *versus* AM0 concentration ratio.

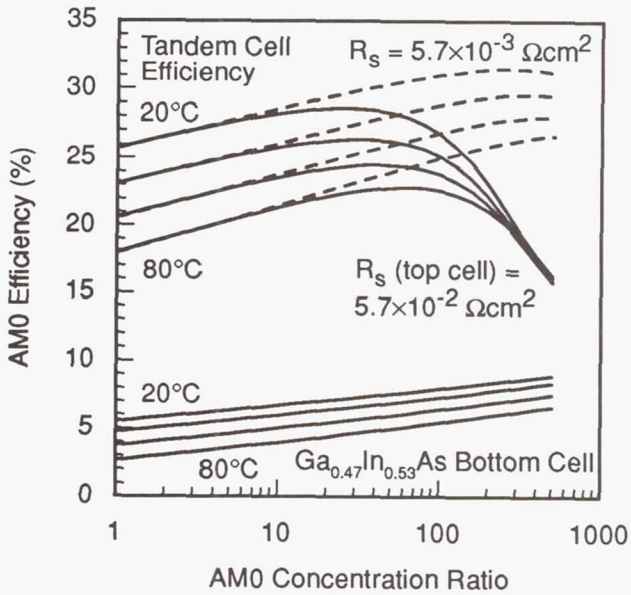


**Figure 7.** Modeled AM0 efficiency as a function of the concentration ratio and temperature for a three-terminal InP/$Ga_{0.47}In_{0.53}As$ concentrator tandem cell based on measured subcell parameters. The dashed set of curves illustrate the effect of reducing the InP top cell series resistance by a factor of 10.

# RECENT ADVANCEMENTS IN MONOLITHIC AlGaAs/GaAs SOLAR CELLS FOR SPACE APPLICATIONS

K. R. Wickham, B-C. Chung, M. Klausmeier-Brown, M. S. Kuryla, M. Ladle Ristow, G. F. Virshup, J. G. Werthen
VS Corporation and Varian Associates
3075 Hansen Way, Palo Alto, CA 94303

## ABSTRACT

High efficiency, two-terminal, multijunction AlGaAs/GaAs solar cells have been reproducibly made with areas of 0.5 $cm^2$. The multiple layers in the cells were grown by OMVPE on GaAs substrates in the n-p configuration. The upper AlGaAs cell has a bandgap of 1.93 eV and is connected in series to the lower GaAs cell (1.4 eV) via a metal interconnect deposited during post-growth processing. A prismatic coverglass is installed on top of the cell to reduce obscuration caused by the gridlines. The best 0.5 $cm^2$ cell has a two-terminal efficiency of 23.0 % at 1 sun, air mass zero (AM0) and 25 °C. To date, over 300 of these cells have been grown and processed for a manufacturing demonstration. Yield and efficiency data for this demonstration will be presented. As a first step toward the goal of a 30 % efficient cell, a mechanical stack of the 0.5 $cm^2$ cells described above, and InGaAsP (0.95 eV) solar cells was made. The best two-terminal measurement to date yields an efficiency of 25.2 % AM0. This is the highest reported efficiency of any two-terminal, 1 sun space solar cell.

## INTRODUCTION

In terms of space qualified photovoltaic cells, the most important variables to control are: weight, cost, efficiency, operating lifetime, and radiation resistance. This paper will address the efficiency of space photovoltaic cells. To get to very high efficiencies (i.e. 25 - 30+ %) without the additional complexity of concentrating optics, one must utilize two or three junctions in tandem. The additional junctions increase the energy range that is usefully absorbed by the cell, and therefore, increase the efficiency. In order to reduce the weight and complexity of a panel of multijunction cells, a monolithic structure is ideal. Up until now, two junction monolithic solar cells have been in the research phase, but in this paper we report the first manufacturing demonstration of these devices. A monolithic three junction cell has never been made. However, attempts at mechanically stacking three junctions have been successful, and will be discussed below.

A computer model, described in detail in reference 1, has been used to determine the optimal design parameters for III-V materials based single and multijunction photovoltaic cells. The program can optimize such structural parameters as doping levels, concentration gradients, layer thicknesses, indices of refraction for anti-reflective (AR) coatings, and gridline aspect ratio and spacing to achieve the highest efficiency for the given solar concentration, air mass and operating temperature. Predictions of efficiency for one, two, and three junction cells as a function of temperature are shown in Fig. 1. At 25 °C, the predicted efficiency for a single junction GaAs cell is approximately 22 %. This value has been achieved with our single junction GaAs cell, and a pilot line for manufacturing has been installed. The expected efficiency for a 1.93 eV AlGaAs on 1.42 eV GaAs two junction cell is approximately 25 % . Currently we have achieved 23.0 % efficiency using a metal interconnect cascade cell (MICC) ( ref. 2). There are other two junction cells which have higher predicted efficiencies than the line shown, but they involve lattice mismatched material structures (i.e. AlGaAs/InGaAs), or quaternary materials which are quite difficult to grow repeatably and uniformly. The three junction line shows the optimized efficiency for the same AlGaAs/GaAs cell as the two junction line, but includes a low bandgap (1.0 eV) InGaAs lower cell. This structure has the potential to achieve efficiencies of up to 31% at 25 °C (1 sun, AM0).

## DEVICE GROWTH AND PROCESSING

The metal interconnect cascade cell (MICC) consists of an upper 1.93 eV AlGaAs cell and a lower 1.42 eV GaAs cell (both in the n on p configuration) which are connected in series by a metal interconnect deposited during post-growth processing. These cells are grown by atmospheric pressure OMVPE on p-type GaAs substrates, as described in reference 3. The schematic cross section of an MICC is shown in Fig. 2. The base

and emitter of the GaAs lower cell are grown first. A highly doped AlGaAs window is grown on top of the emitter to reduce the surface recombination velocity at this interface. Next, p+ and n+ contact layers are grown which will be shorted together during later processing to eliminate the intrinsic p-n junction formed by the two solar cells, and to connect the two cells in series. The AlGaAs base and emitter of the upper cell are grown next, followed by another highly doped AlGaAs window layer. Finally, a GaAs cap layer is added to ensure good ohmic contact to the top metal grid, and to protect the device during processing.

Fig. 3 shows the processing sequence used to fabricate the MICC devices. During processing, the front and back metalizations are deposited by evaporation. The metalization contact to n-type material includes Au/Ge/Ni/Au layers with additional Pt/Au layers on the top metal grid for easy soldering or welding. The p-type metalization contacts are Au/Zn/Au. A wide and a subsequent narrow trench are etched in the upper cell to expose the p+ and n+ contact layers of the device. The metal interconnect consists of two evaporated metal layers deposited in the trench areas which form good ohmic contacts to the p+ and n+ contact layers. Contact resistance after a 400 °C anneal is typically very good, with values below $1 \times 10^{-5}$ $\Omega$-cm$^2$. An isolation etch is performed to allow electrical testing of the devices before they are scribed and separated into individual cells. The n+ GaAs cap layer is selectively etched away between the gridlines prior to the deposition of the AR coating. The two-layer AR coating which includes $TiO_2$ and MgO is sputtered onto the exposed AlGaAs window layer. The indices of refraction of the two layers are designed to minimize reflection when a prismatic coverglass is applied to the surface. This coverglass, supplied by Entech, is a series of lenses which bends light in toward the active area of the cell and away from the gridlines. This effectively eliminates the obscuration caused by the gridlines.

## DEVICE TESTING

The testing of the devices always involves a spectral response measurement of both the upper and lower cell. A separate integrated current density is obtained for the upper and lower cell based on the AM0 spectrum. Current-voltage (I-V) measurements are obtained using a two-color simulator which includes two light sources as shown in Fig. 4. The use of two light sources allows the current in each junction to be controlled independently. The light source for the AlGaAs junction has a short-pass filter, and that for the GaAs junction has a long-pass filter. The intensity of each light source is set so that the current density out of each junction matches the integrated current density obtained from the spectral response measurement of the corresponding junction. After the lamps are set to the appropriate intensity, computer controlled I-V measurements are made. The reason for using this test method is that any AM0 simulator introduces errors because of "spikes" at various wavelengths. By using empirical data for the AM0 spectrum and obtaining the integrated current density from the spectral response, the I-V measurements will be more accurate and the current densities of the two junctions can be realistically compared.

## RESULTS AND DISCUSSION

Our best MICC cell has an efficiency of 23.0 %. An I-V curve for this device is shown in Fig. 5. In addition to this best result, a manufacturing demonstration has been completed for 0.5 cm$^2$ AlGaAs/GaAs MICCs. Twenty-two wafers were grown with the device structure of an MICC. Each wafer contains either fourteen or sixteen 0.5 cm$^2$ cells (depending on whether a D-shaped or a square wafer is used. These 22 wafers resulted in 342 cells grown. During processing and scribing, 45 of the cells were broken. We hope to reduce this breakage rate of 13 % by using a more pointed scribing tip. All of the cells were put through a screening test in wafer form to get an estimate of their performance. The test method was simply to choose one cell on the wafer, set the lamp current so that 15.5 mA/cm$^2$ was obtained out of each junction at short circuit, and then test all the devices on the wafer at that lamp intensity. By doing this we get a wafer map of the expected efficiencies for each cell. After the wafers were scribed, 297 cells were available for individual efficiency measurements.

115 cells which had screening "efficiencies" of at least 20 % were tested with an "electronic" coverglass. When a prismatic coverglass is applied to an MICC the measured increase in device current is 21 % for the upper AlGaAs cell and 9 % for the GaAs cell. We therefore simulated the coverglass effect during testing by multiplying the corresponding integrated current densities by 21 % (AlGaAs) and 9 % (GaAs). This simulation of the coverglass saves installation time, and allows the MICCs to undergo subsequent radiation testing. Seventy-four of the MICCs had actual efficiencies of at least 20 %. Therefore, the yield for good cells is 25 % as compared to the 297 testable cells, and 21.6 % as compared to the 342 cells grown. A histogram showing the efficiencies of these 115 cells is shown in Fig. 6. These results do not show a large number of cells approaching our best MICC efficiency of 23 %. However, this is the first manufacturing demonstration of monolithic two junction cells, and

improvement in both efficiency and yield is to be expected with further process refinements and manufacturing experience.

In addition to the 0.5 $cm^2$ devices we have made, a scale-up to 2x2 $cm^2$ MICC devices is in progress. Our very first attempt at fabricating the devices indicated that our material growth quality was very good, but a problem with one of the metalization steps prevented them from operating properly. Several additional wafers have been grown and the devices are currently being processed using a method which will prevent the metalization problem encountered earlier. If successful, these will be the first monolithic two junction solar cells to be made on an area as large as 4 $cm^2$. They will then me made into a panel of six cells to be flown in a space based experiment.

As a proof of concept project for the near term, a method was developed for stacking a MICC above a low bandgap third junction. Several low bandgap solar cells were used, but the best result was obtained from a InGaAsP cell (ref. 4) which was processed at Varian. The mechanical fixture allowed electrical access to the third junction so that it could be measured independently, and the MICC has the capability to be measured in either a two or three terminal configuration. Table I shows the device parameters of each cell in the stack and the results of a two terminal measurement of the entire stack. The efficiency obtained at 1 sun, AM0 is 25.2 %. This represents the highest 1 sun, AM0 efficiency ever reported. The sum of the efficiencies of each component cell is 25.48 %. This is higher than the two-terminal measurement of the entire stack because the GaAs cell is current limiting the other two cells, thus bringing their efficiencies down slightly. In general, the GaAs component cell has a lower current density than the AlGaAs cell. To remedy this we suggest increasing the bandgap of the AlGaAs cell slightly to allow more light into the GaAs cell. With better current matching, the efficiency of the two terminal configuration will rise. In addition, the MICC cell used had a two terminal efficiency of only about 21 %; this is 2% lower than our best MICC cell so further efficiency gains can be expected. Fig. 7 shows the external quantum efficiency of the three junctions in the stack.

## CONCLUSIONS

Because both component cells can be measured independently, the MICCs have an advantage over tunnel junction based devices in terms of testing and diagnostics. With tunnel junction devices, only two terminal measurements can be made. However, with the MICC one can measure the efficiency of each component cell, determine which cell degrades the most during radiation experiments, and find the current limiting cell. Ultimately, the tunnel junction concept is preferred because it reduces post-growth processing complexity and does not involve reducing the active area of the upper junction. For this reason, tunnel junction development is currently proceeding in parallel with the MICC work.

It is clear that a monolithic integration of three junctions is superior to mechanical stacking if the devices are to actually be used in space. Efficiencies higher than 30 % have been predicted for monolithic three junction devices. Future work in this area should concentrate on monolithic integration of three junctions using grading layers or a superlattice to compensate for the lattice mismatch between GaAs and InGaAs or other low bandgap materials.

---

## REFERENCES


1). H. C. Hamaker; "Computer modeling study of the effects of inhomogeneous doping and/or composition in GaAs solar-cell devices"; J. Appl. Phys., **58**, p. 2344; (1985).

2). B-C. Chung, G. F. Virshup, S. Hikido, and N. R. Kaminar; "27.6% efficiency (1 sun, air mass 1.5) monolithic $Al_{0.37}Ga_{0.63}As$/GaAs two-junction cascade solar cell with prismatic cover glass"; Appl. Phys. Lett. **55**, p. 1741; (1989).

3). B-C. Chung, G. F. Virshup, and J. G. Werthen, High-efficiency, one-sun (22.3% at air mass 0; 23.9% at air mass 1.5) monolithic two-junction cascade solar cell grown by metalorganic vapor phase epitaxy"; Appl. Phys. Lett. **52**, p. 1889; (1988).

4). InGaAsP material grown by M. Wanlass at the Solar Energy Research Institute.

Table I. - Device parameters for the three junction mechanical stack of an MICC on an InGaAsP cell.

| | Efficiency (%) | $V_{OC}$ (V) | Fill Factor | $J_{SC}$ (mA/cm$^2$) |
|---|---|---|---|---|
| AlGaAs | 12.00 | 1.398 | 0.75 | 15.77 |
| GaAs | 9.09 | 0.994 | 0.78 | 15.63 |
| InGaAsP | 4.39 | 0.521 | 0.72 | 15.98 |
| Efficiency Sum | 25.48 | | | |
| Stack | 25.20 | 2.882 | 0.77 | 15.63 |

All measurements are two terminal, and made at 25 °C under 1 sun, AM0 illumination.
Device area 0.5 cm$^2$

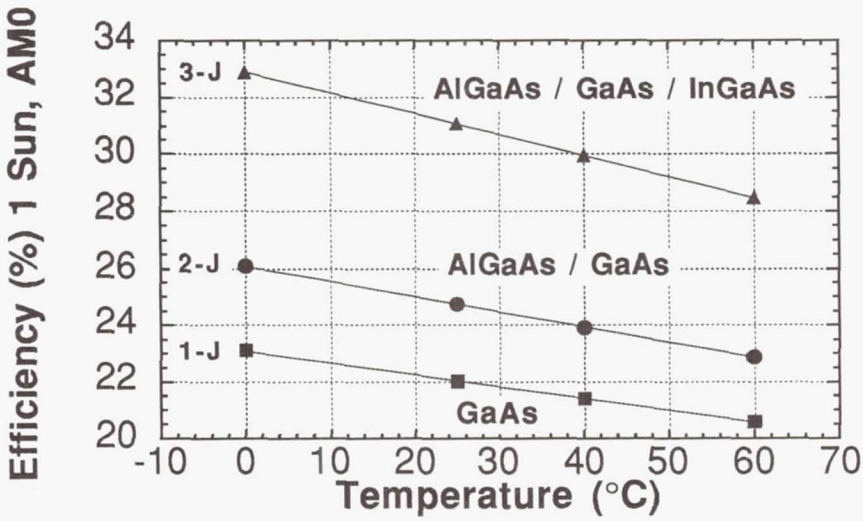


Figure 1. - Predicted efficiency vs. temperature for selected one-, two-, and three-junction solar cells.

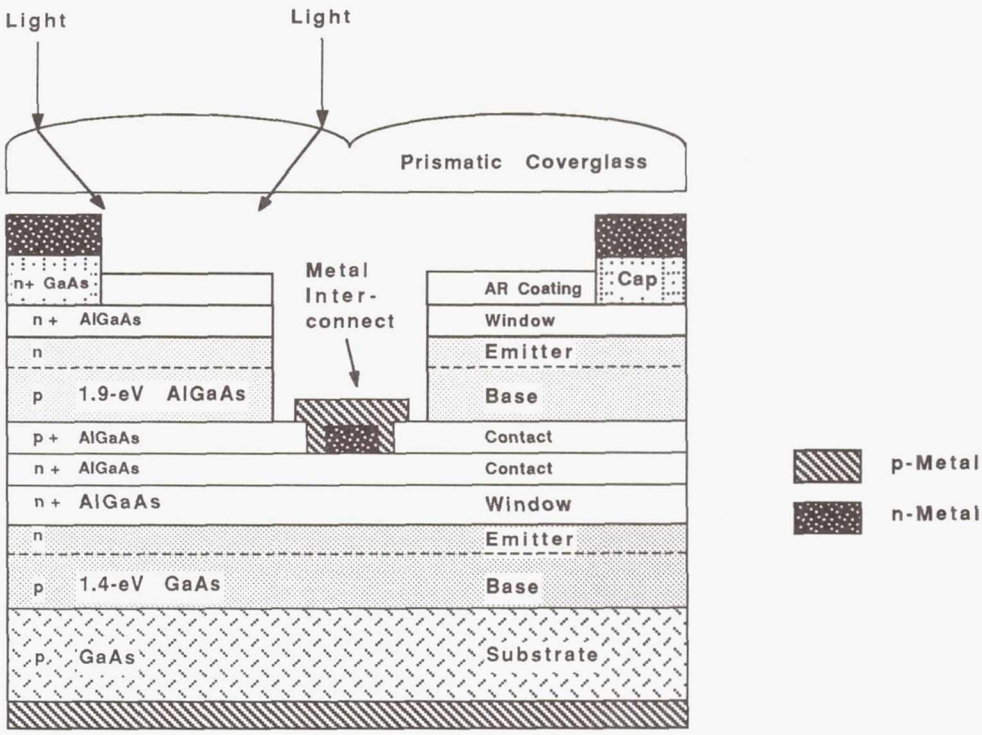


Figure 2. - Schematic cross section of the MICC ( not to scale).

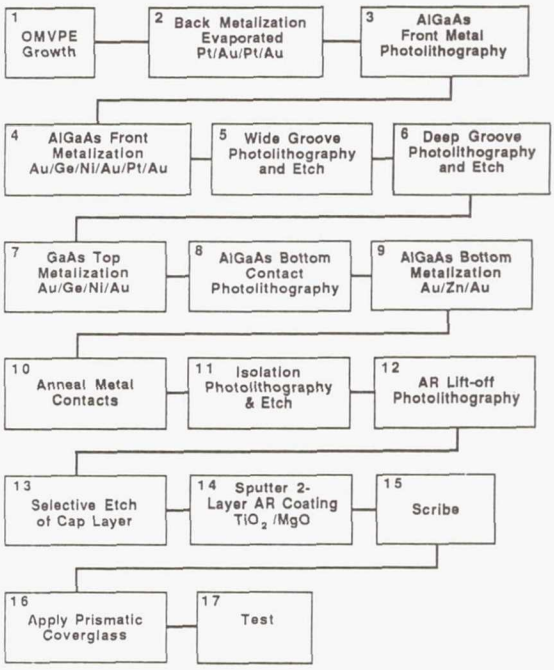


Figure 3. - MICC device processing flow chart

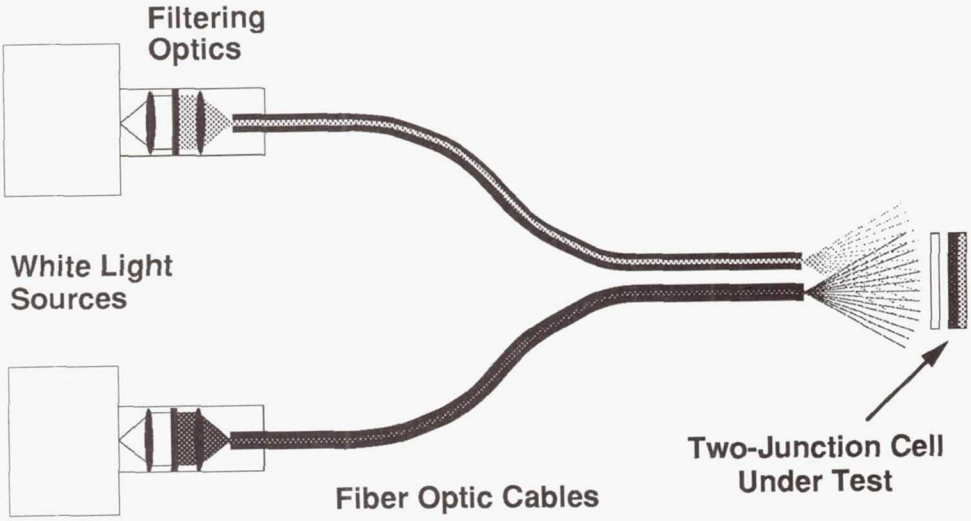


Figure 4. - Testing configuration for I-V measurements of two junction MICCs.

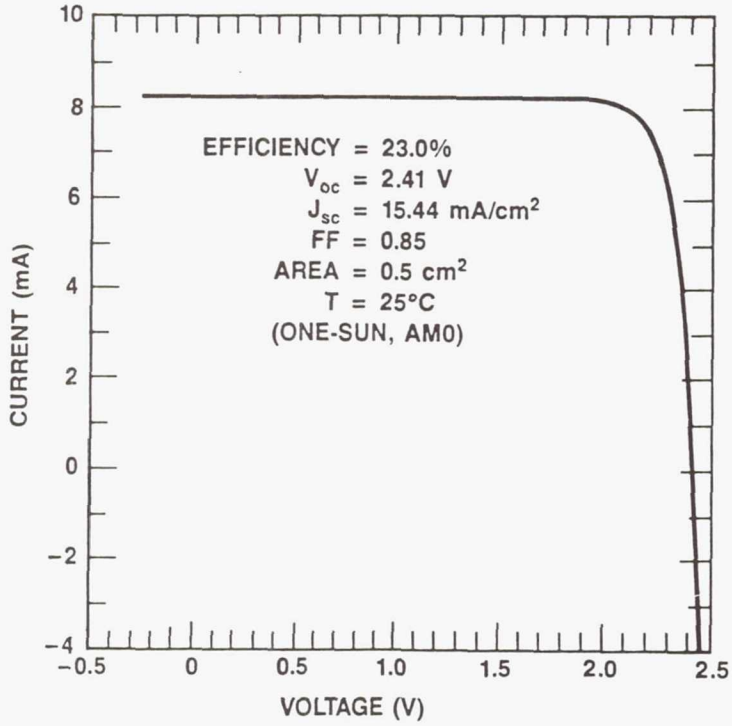


Figure 5. - An I-V curve of the best 0.5 cm$^2$ MICC, showing the measured device parameters.

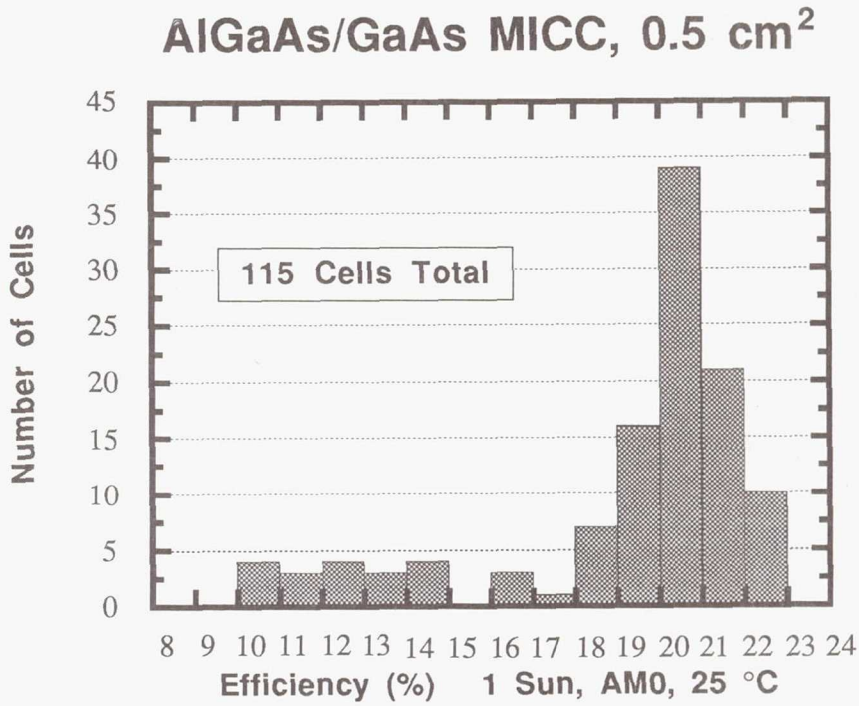


Figure 6. - Efficiency Histogram for 115 of the best 0.5 $cm^2$ MICC cells produced in the manufacturing demonstration.

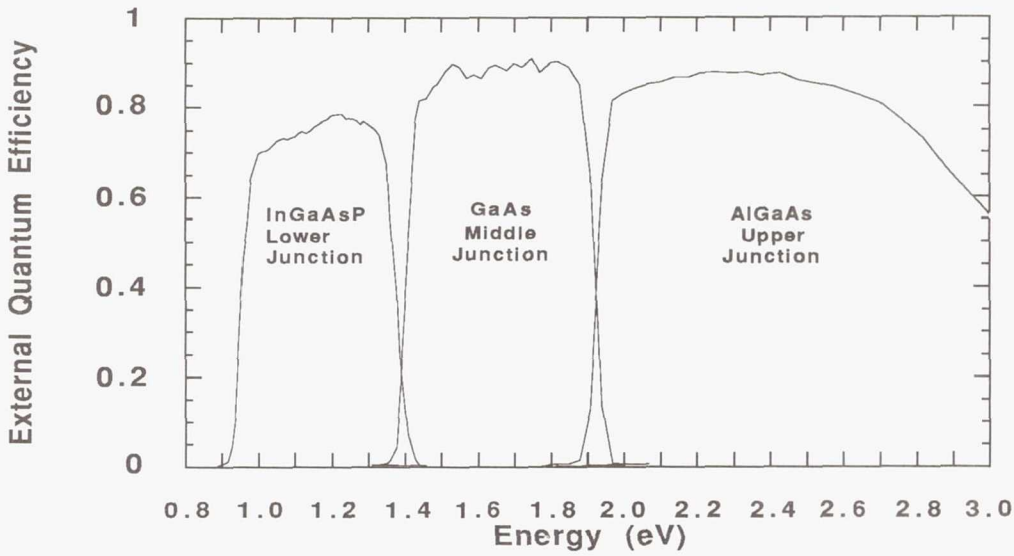


Figure 7. - Spectral Response of the three junction mechanical stack. The stack includes a 0.5 $cm^2$ MICC above a 0.5 $cm^2$ InGaAsP solar cell.

# DIRECT GLASS BONDED HIGH SPECIFIC POWER SILICON SOLAR CELLS FOR SPACE APPLICATIONS

L.C. DiNetta, J.A. Rand, J.R. Cummings,
S.M. Lampo, and K.P Shreve
AstroPower, Inc.
30 Lovett Ave.
Newark, DE 19711

Allen M. Barnett

Department of Electrical Engineering
University of Delaware
Newark, DE 19716

## ABSTRACT

This paper describes a lightweight, radiation-hard, high-performance, ultra-thin silicon solar cell that incorporates light trapping and a cover glass as an integral part of the device. The manufacturing feasibility of high specific power, radiation insensitive, thin silicon solar cells has been demonstrated experimentally and with a model. Ultra-thin, light-trapping structures have been fabricated and the light trapping demonstrated experimentally. Our design utilizes a micro-machined, grooved back surface to increase the optical path length by a factor of 20. This silicon solar cell will be highly tolerant to radiation because the base width is less than 25 microns making it insensitive to reduction in minority-carrier lifetime. Since the silicon is bonded without silicone adhesives, this solar cell will also be insensitive to UV degradation. These solar cells are designed as a form, fit, and function replacement for existing state of the art silicon solar cells with the effect of simultaneously increasing specific power, power/area, and power supply life. Using a 3-mil thick cover glass and a 0.3 g/cm$^2$ supporting Al honeycomb, a specific power for the solar cell plus cover glass and honeycomb of 80.2 W/Kg is projected. The development of this technology can result in a revolutionary improvement in high survivability silicon solar cell products for space with the potential to displace all existing solar cell technologies for single junction space applications.

## INTRODUCTION

The goal of this work was to design and assess the feasibility of lightweight, radiation resistant, high efficiency thin silicon solar cells. This advanced design consists of a 1 mil thick layer of single crystal silicon supported by a 3 mil thick glass superstrate; the glass and silicon are joined using electrostatic bonding (ESB). This novel solar cell design includes several significant advances. These are improved radiation tolerance, increased performance, and high temperature survivability. In the following sections, the advantages of the AstroPower solar cell design are treated in detail.

### Radiation Resistance

Radiation damage is the primary degradation mechanism of silicon solar cells deployed in space. This gradual degradation in solar cell performance is due to a reduction in the minority-carrier lifetime that results from cumulative damage to the crystal lattice. One approach to increasing the silicon solar cell radiation tolerance has been to reduce the silicon base thickness as much as possible. Thin silicon solar cells are available in small quantities with current production thicknesses of 2.7 mils and active areas of 59.8 cm$^2$, however, the best beginning of life efficiencies of these devices are reported to be 14% (ref. 1).

---

This research was suppported in part by the Strategic Defense Initiative/Innovative Science and Technology branch and managed by the Aero Propulsion and Power Directorate, Wright Laboratory, under contract number F33615-90-C-2060.

An opportunity now exists to significantly improve the radiation resistance of silicon solar cells without incurring the yield losses or size limitations of existing thin silicon solar cell technology. The thin silicon solar cell is fabricated by bonding silicon directly to glass, thinning the silicon with a chemical etchant, forming a light trapping structure on the back, and then completing the device fabrication. Before bonding the silicon to the glass coverplate, the emitter and front contacts are formed and the anti-reflection coating is deposited. With this approach, the glass functions as both mechanical support and cover. Device areas will be determined by the cover glass rather than the silicon due to the strength of the glass-silicon laminate. Thin silicon solar cells with an area of over 100 $cm^2$ are certainly feasible since high quality 6" diameter silicon wafers are readily available.

This novel solar cell design is expected to demonstrate the radiation tolerance observed with InP solar cells. Because the absorber layer is very thin, the solar cell will be extremely insensitive to changes in minority-carrier lifetime that may result from radiation damage. The conversion efficiency of the device will not degrade until the minority-carrier diffusion length is less than the thickness of the absorber layer. For silicon layers on the order of 25 microns or less, this is equivalent to a minority-carrier lifetime of less than 250 nanoseconds (as-grown, non-irradiated silicon typically has a lifetime greater than 10 microseconds). In contrast, to obtain high current, present high-performance silicon solar cells require minority-carrier lifetimes on the order of 1 millisecond. Because this new design effectively reduces the minority-carrier lifetime requirement by more than a factor of one-thousand, this solar cell design leads to an important opportunity for substantially increasing the radiation tolerance, and therefore significantly extending the useful life of silicon solar cells deployed in space.

Modelling and experimental data showing the efficiency degradation of candidate space solar cells as a function of 1 MeV electron fluence is shown in Figure 1. Thin, light trapping, silicon solar cells have theoretical radiation resistance similar to InP space solar cells and better radiation resistance than GaAs/Ge space solar cells. To show the validity of AstroPower's model the experimental and modelled values for a 4 mil thick silicon solar cell are also shown.

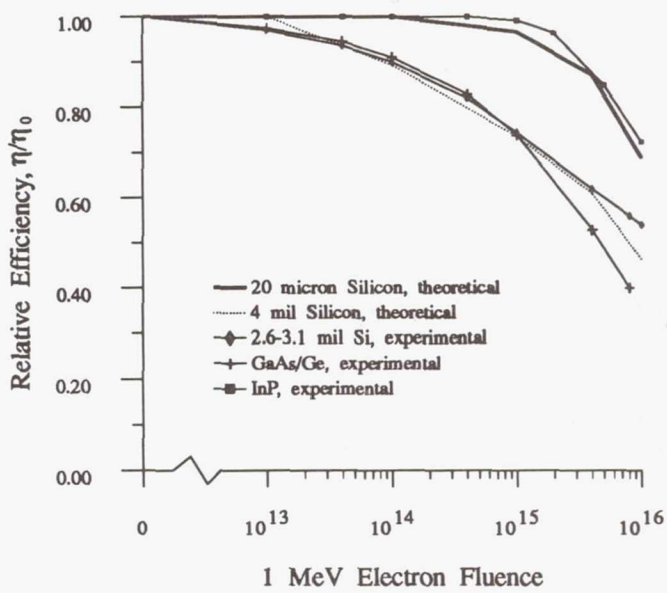


*Figure 1. Radiation resistance of space solar cells (ref. 2, 3, 4).*

Performance Increase

In addition to radiation resistance, this light-trapping thin base device is also a very high performance silicon solar cell design. After the silicon is thinned, it is micro-machined using an orientation dependent etch to produce a grooved surface. A back surface reflector is then deposited. Using this approach, light that enters the silicon is reflected by the back surface in such a way that it is totally reflected at the planar front surface. It is possible to obtain optical path lengths in thin silicon that approach twenty times the base thickness. Higher open circuit voltages will be achieved because higher than conventional doping levels can be used as a result of the thin silicon solar cell having a reduced dependence on diffusion length. Another increase in the open circuit voltage is due to the smaller recombination volume afforded by the thin solar cell and novel back surface passivation methods. Fill factor improvements can be achieved because low resistivity silicon base layers can be employed in this solar cell design compared to the high resistivity base layers currently in use for silicon space solar cells. The result of these enhancements is that the efficiency of the thin, light trapping solar cell can be as high as 19% and still demonstrate good survivability in the space environment.

The high efficiency and light weight of the cover glass supported silicon solar cell can have a significant impact on space solar array technology. Figure 2 shows the power to weight ratio and power density of several candidate solar

cells. As can be seen, this silicon solar cell design offers an increase in the power to weight ratio over that of a 4 mil, 14.5% efficient silicon solar cell. The power to weight ratio is calculated assuming a 0.3 g/cm$^2$ aluminum honeycomb support structure.

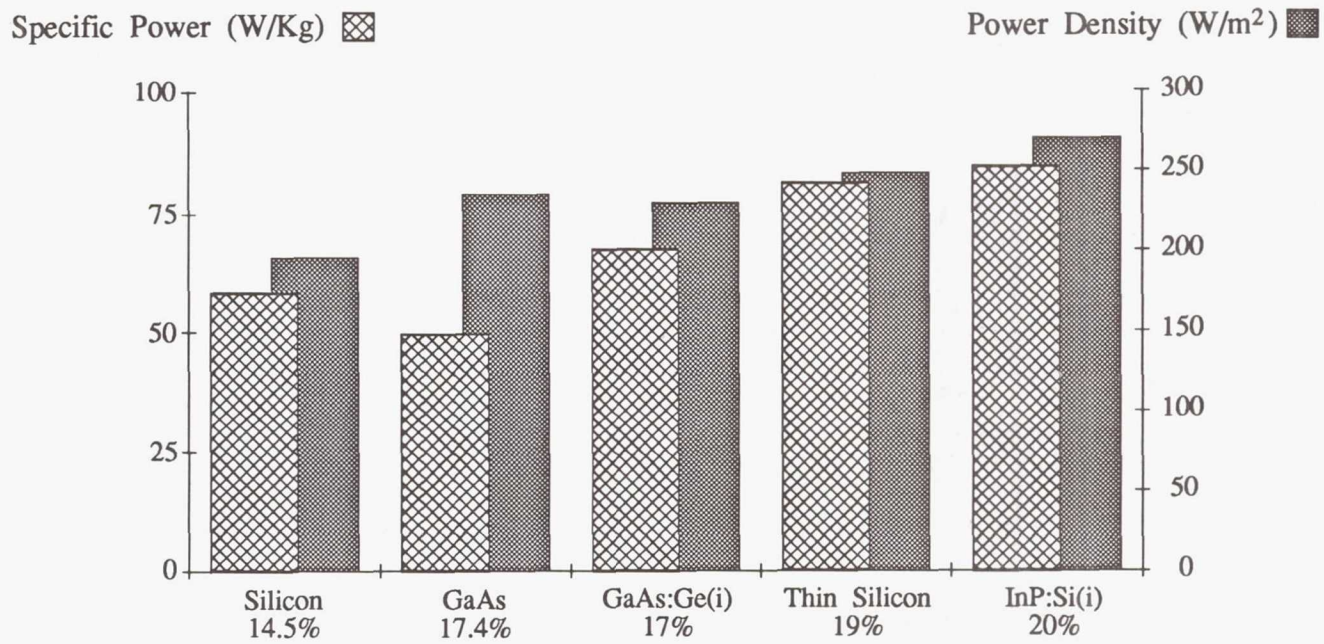


*Figure 2. Comparison of specific power and power density of candidate space solar cells.*

High Temperature Survivability

Finally, this solar cell is designed with contact metallizations that meet the current Air Force goals for high temperature survivability. After bonding, these devices will retain their insensitivity to high temperatures, permitting the solar cell to be deployed for strategic missions where high temperature survivability and radiation hardness are important considerations.

## EXPERIMENTAL RESULTS

A summary of experimental results follows:

- 1 inch x 1 inch, 3 mil thick silicon has been electrostatically bonded to a cover glass;
- 3 mil thick silicon has been thinned to 1 mil while attached to the cover glass;
- light trapping has been accomplished on the 1 mil silicon under glass substrate;
- high temperature survivable contacts have been integrated with the solar cell design;
- a buried contact structure has been developed to present a planar surface to the cover glass for enhanced silicon:glass integrity;
- buried contact solar cells without light trapping have been fabricated and have demonstrated 80.5% fill factors and $V_{OC}$ = 0.606 volts.

A schematic cross-sectional representation of the AstroPower prototype thin silicon solar cell design is shown in Figure 3.

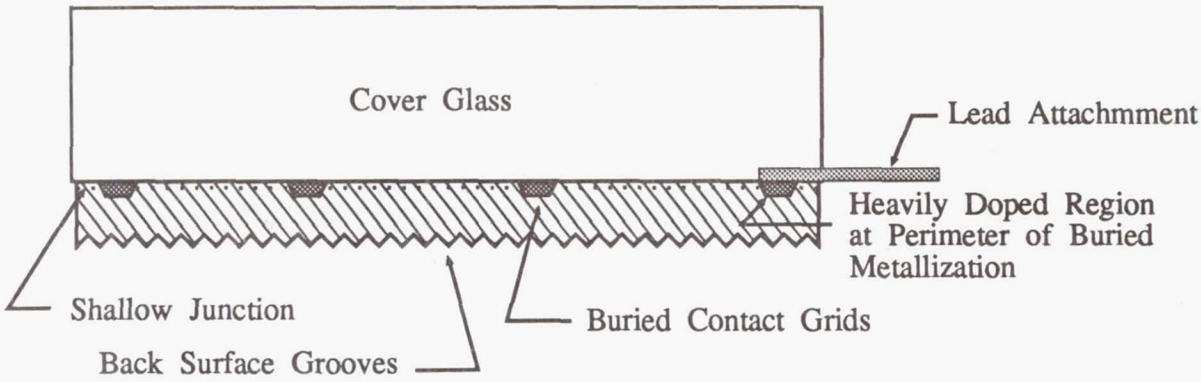


*Figure 3. Glass bonded silicon solar cell cross section.*

Electrostatic Bonding

A key requirement for successful electrostatic glass-silicon bonding is that the glass cover have the same thermal expansion coefficient as silicon over subsequent process and operating temperature ranges. If a thermal mismatch exists, large residual stresses develop in the structure resulting in fracture of the bond or silicon. A coverglass material specifically designed for electrostatic bonding to silicon has recently been made available (Pilkington CMZ). This glass is thermally matched to silicon over the electrostatic bonding temperature range, has a low deformation temperature enabling intimate contact and complete bonds, and also has a low reaction rate with silver ions migrating from the contact metallization.

The general principles of electrostatic bonding are well known. Heat, pressure, and voltage are applied to the silicon-glass laminate for a short period of time. Typical bonding pressures are on the order of 50 psi, the bonding voltages required are 300V with currents of only a few milliamps, and temperatures of 400°C to 500°C. A lab-scale apparatus for electrostatic bonding silicon to glass and for establishing the time, temperature, pressure, and voltage parameters for successful ESB bonding was fabricated.

A schematic diagram of the lab scale bonding apparatus is shown in Figure 4. This bonder is capable of 1 inch x 1 inch silicon to glass bonding. Using 3 mil silicon and 3 mil Pilkington CMZ cover glass material, a zero void bond was obtained at 400°C with a pressure of approximately 50 psi. The successfully bonded 1 inch x 1 inch silicon under glass structure is featureless confirming the uniformity of the electrostatic bond.

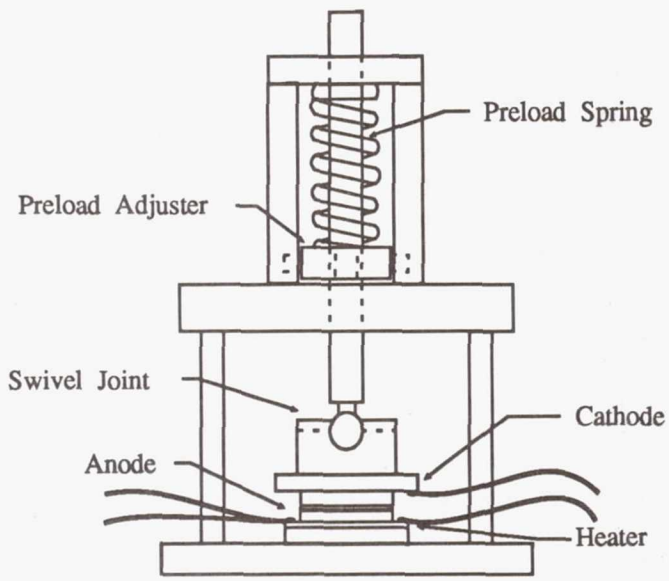


*Figure 4. Lab scale electrostatic bonder.*

High Temperature Survivable Buried Contacts

Electrostatic bonding of the silicon solar cell to a glass superstrate requires a robust and innovative front contact design. Typically, the metallization utilized by silicon solar cell manufacturers relies on a titanium ohmic contact with a palladium barrier layer and silver plating to achieve low series resistance losses. At the required temperatures inherent to the bonding process, the titanium metal will continue to alloy with the silicon and eventually reach the p/n junction where it will cause a loss in solar cell performance. This loss can be attributed to shunting of the solar cell by the titanium-silicon metal interaction and is not reversible. AstroPower is developing a metallization scheme compatible with the ESB process that avoids this problem and, additionally, permits the silicon solar cell to meet the standards for high temperature survivability.

The high temperature survivable metallization scheme is a plated structure. Choosing a plating method for metallization of the solar cell permits the use of a favorable design option, that is, a buried contact structure. Using a buried contact structure the front surface of the solar cell appears planar to the cover glass during the bonding process and there is no need to use excessive pressure or temperature to deform the glass around surface features,,as there are none. As a second benefit it is cheaper and easier to plate the contact than to use vacuum deposition methods, as is customarily the case with space solar cells, leading to a reduction in the cost of manufacturing.

Light Trapping

In order to obtain high efficiencies from a thin, 25μm, solar cell it is necessary to incorporate a high degree of light trapping in the solar cells. Since the ESB solar cell must have a planar front surface, the light trapping must be achieved by back surface texturing. AstroPower has developed a method to micro-machine the back surface of the silicon solar cell to reflect the photons back towards the front surface at an angle sufficient to permit an equivalent optical thickness up to twenty times the physical thickness. In contrast to a planar back surface reflector, the photons are trapped until they are absorbed by the silicon. With a planar back surface reflector, the photons would make only two passes through the silicon and then escape through the front surface of the solar cell.

Curves of absorption normalized for front surface reflection, Figure 5, of various thicknesses of bonded silicon under glass demonstrate the effectiveness of the micro-machined back surface reflector (BSR). An 8 mil glass bonded silicon sample is included for reference. Note that the light trapping structure with the Al reflector matches the 8 mil reference curve up to 850 nm. Beyond 850 nm it differs by only 5% at the most. The cross-over of the absorbtion curve at 1025 nm is caused by a combination of factors involving non-optimized light trapping in the thin silicon and the low absorbtion co-efficient of narrow bandgap photons in the 8 mil sample. This data clearly shows light trapping in a 33 μm thick silicon sample using back surface grooving and a back surface reflector.

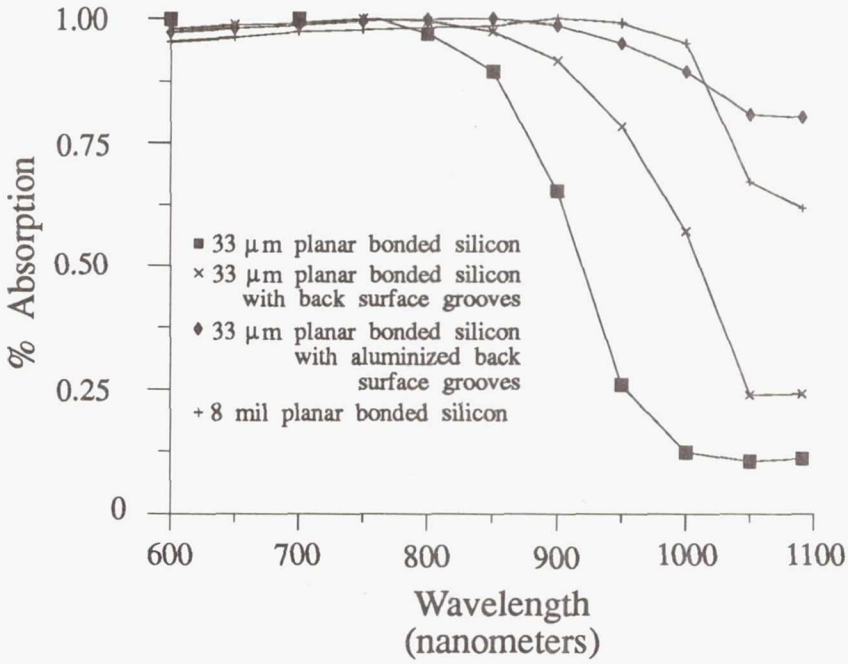


*Figure 5. Optical characteristics of thin silicon compared to thick silicon.*

## CONCLUSION

This work demonstrates the feasibility of the key steps that will be required to produce high specific power, radiation tolerant, thin silicon solar cells. These solar cells will be a form, fit, and function replacement for existing state of the art silicon solar cells with the effect of simultaneously increasing specific power, power density, and power supply life. Followiing is a summary of the necessary processes which when integrated will lead to production of the thin silicon solar cell.

Cover glasses are usually attached to solar cells using an adhesive, which adds weight and eventually degrades and darkens under UV radiation. Electrostatic bonding permits attachment of the silicon to the glass without any intermediate adhesives, provides a permanent chemical bond that adds no weight other than that of the cover glass, and is insensitive to UV degradation. Successful electrostatic bonding of glass to silicon has been achieved on 1 inch x 1 inch, 3 mil thick silicon solar cell substrates.

Although thin silicon solar cells are highly desirable for many reasons already discussed in detail, thicknesses are process limited. The availability of the demonstrated glass:silicon solar cell laminate side steps this issue because the glass:silicon laminate is robust. Silicon attached to the glass by electrostatic bonding can be thinned to any desired thickness. The ability to uniformly thin the silicon has been demonstrated.

Thin silicon is a poor absorber of photons and therefore it is necessary to develop techniques to trap the light in the silicon until it can be absorbed. Micro-machining of the back surface reflector has been achieved and light trapping has been demonstrated.

The electrostatic bonding process requires intimate contact between the cover glass and the silicon to which it is to be bonded. Typical front contact grid metallization designs inhibit this contact. Previous work with electrostatic bonding has shown that the glass can be made to deform over the front contact metallization. The problem with this is that the bond must be made at higher temperatures, near the softening point of the glass, or as has been demonstrated by other researchers, the cover glass can have grooves machined to fit over the metallization. Neither of these solutions is desirable for reasons detailed in the next two paragraphs.

Bonding at temperatures near the softening point of the glass can create stress in the laminate which will lead to lower yields due to breakage. Also the thermal expansion of the cover glass begins to change abrubtly away from that of silicon at 600°C which may inhibit bonding.

Machining of grooves in the cover glass introduces an undesirable cost in the manufacturing of thin silicon solar cells. Not only does the base cost of the cover glass increase but a step must be added to the fabrication process to insure proper alignment of the solar cell grids and the cover glass grooves. Secondly, there are areas of unbonded silicon near the grid structure because the glass machining can not be perfectly matched to the grid. These unbonded areas may lead to stressing in the silicon and certainly will decrease the overall strength of the glass:silicon laminate.

The AstroPower solution to this problem is to bury the contacts in the silicon therefore presenting a planar surface to the cover glass for the electrostatic bonding process. Silicon solar cells have been fabricated with buried contact metallization. Efficiency of these solar cells is greater than 12% with the design capability to reach greater than 18% with process improvement.

During the electrostatic bonding process the solar cell front contact metallization will be exposed to temperatures greater than 400°C. Typically, the metallization used by silicon solar cell manufacturers relies on an alloyed titanium ohmic contact. At the bonding temperatures the titanium metal will continue to alloy and reach the solar cell p/n junction where it will degrade performance. In order to avoid this problem a plated contact system is being developed which is expected to be 700°C survivable for at least 15 minutes. This meets the long term SDI and Air Force goals for high temperature survivability.

The integration of these accomplishments with process improvement, scale up of the solar cell active area, and back surface passivation will result in a demonstration of the manufacturability of this innovative solar cell. A specific power of 80.2 W/Kg and efficiencies of 19%, AM0, are predicted for this thin silicon solar cell design.

## REFERENCES


[1] A.V. Mason, J.R. Kukulka, S.M. Bunyan, and L.M. Woods, "Development of 2.7 mil BSF and BSFR Silicon Wrapthrough Solar Cells", 21st IEEE Photovoltaic Specialists Conference, Kissimee, FL, p. 1378-1382, 1990.

[2] H.Y. Tada and J.R. Carter, "Solar Cell Radiation Handbook", JPL Publication, p. 3-20.

[3] I. Weinberg, D.J. Brinker, C.K. Schwartz, and R.E. Hart, "Progress in Indium Phosphide Solar Cell Research", SPIE Indium Phosphide and Related Materials for Advanced Electronic and Optical Devices, p. 434-444, 1989.

[4] B.E. Anspaugh, "Solar Cell Radiation Handbook", JPL Publication 82-69, Addendum 1, p37, 1989.

# FLEXIBLE COPPER-INDIUM-DISELENIDE FILMS AND DEVICES FOR SPACE APPLICATIONS*

J.H. Armstrong, C.O. Pistole†, and M.S. Misra
Martin Marietta Defense Space and Communications
Denver, CO

V.K. Kapur and B.M Basol
International Solar Electric Technology, Inc.
Inglewood, CA

With the ever-increasing demands on space power systems, it is imperative that low-cost, lightweight, reliable photovoltaics be developed. One avenue of pursuit for future space power applications is the use of low-cost, lightweight flexible PV cells and arrays [1]. Most work in this area assumes the use of flexible amorphous silicon (a-Si), despite its inherent instability and low efficiencies. However, polycrystalline thin-film PV such as copper-indium-diselenide (CIS) are inherently more stable and exhibit better performance than a-Si. Furthermore, preliminary data indicate that CIS also offers exciting properties with respect to space applications. However, CIS has only heretofore only produced on rigid substrates. The purpose of this investigation was first to explore the implications of flexible CIS upon present and future space power platforms. Results from this investigation indicate that space-qualified CIS can dramatically reduce the cost of PV, and in most cases, can be substituted for silicon (Si) based on end-of-life (EOL) estimations. Furthermore, where cost is a prime consideration, CIS can become cost effective than gallium-arsenide (GaAs) in some applications. Second, investigations into thin-film deposition on flexible substrates were made, and data from these tests indicate that fabrication of flexible CIS devices is feasible. Finally, data will also be presented on preliminary TCO/CdS/$CuInSe_2$/Mo devices.

## INTRODUCTION

Emphasis from DoD on large space-power platforms and from NASA regarding the Space Exploration Initiative (SEI) identify the need for advanced photovoltaics for future space-power programs. In particular, prospects for future exploration on the lunar and Martian surface clearly illustrate the need for inexpensive, lightweight power systems. Prospects for a nuclear power solution have fallen into disfavor politically based on safety issues during launch, and increasing weight requirements for shielding. Other power alternatives exist, but photovoltaics (PV) have a definite advantage in that it requires no additional safety considerations and PV have proven reliable in many years of space flight. Concerns regarding this technology are (1) stability in space environment often results in significant reduction of initial power ratings and (2) cost of these facilities is often accelerated by the amount of hand-layup, manual interconnection, and the associated quality control.

While design improvement can attempt to minimize the effects of space environment, inherent material issues remain. A baseline for end-of-life (EOL) for PV after 7 years in geosynchronous orbit (GEO) is a 25-40% reduction in maximum power from a silicon-based array, and 15% for a gallium-arsenide. Based on these numbers, array

* Work Performed under Martin Marietta IR&D Project D-17R, Photovoltaic Technologies
† Martin Marietta Civilian Space and Information Systems

size must be designed not on the basis of beginning-of-life (BOL) efficiencies, but on projected EOL for a particular mission. At this rate, the glamour of multi-junction, high (BOL) efficiency devices is often subdued by the reality of EOL projections of a particular array.

Further concern regarding PV is the weight associated with the PV blanket and the subsequent support structure needed to hold the array. Often, GaAs is used for applications with requirements for high efficiency due to a need for minimum array area and weight. Conventional GaAs, however is both expensive and heavy, although array weight is typically more crucial than blanket weight in these instances. Advanced GaAs on germanium and thin GaAs improve on its weight, but the fragile nature and small size of all GaAs, particularly thin GaAs, could lead to increased cost during fabrication.

One recognized solution to this dilemma is the use of thin-film PV, primarily amorphous silicon (a-Si). Thin-film devices such as these fabricated over large areas (minimizing installation labor) possess high power-to-weight ratios despite moderate beginning-of-life BOL efficiencies. However, a-Si possesses inherent instabilities in ultra-violet light which results in rather dramatic power reduction by EOL [2]. New cell designs utilizing a-Si can improve their performance in space, but the inherent instability in a-Si devices remains [3].

Polycrystalline thin-film PV such as CIS offer the promise of an alternative to Si for most applications, and possible substitution for GaAs where space environment and cost, not array size, is a primary concern. CIS has the highest tolerance of any PV material for radiation (Fig. 1), and has proven itself far more stable than single-junction a-Si (Fig. 2) [2,4]. These devices, which nominally do not exceed 5-8 μm thickness (excluding substrate), have been reported with efficiencies as high as 14% with promise soon to exceed the 15% efficiency goal set by SERI/DOE [5]. Although most of the work on these materials have been towards terrestrial applications, excellent work at Boeing [6] indicate that these materials can indeed excel in a space environment.

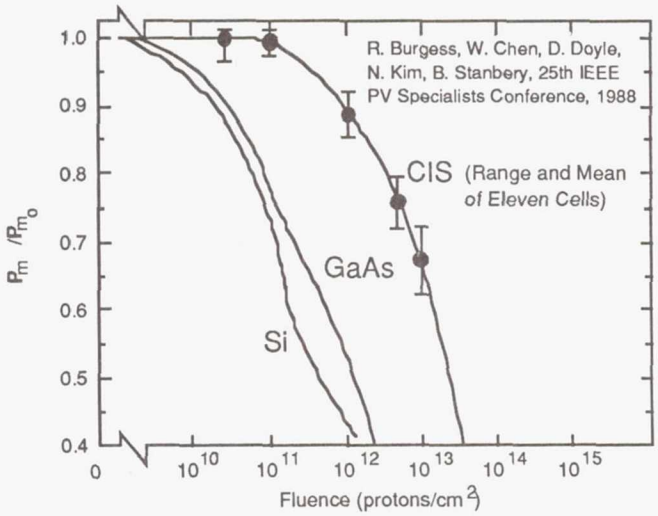


*Figure 1 - Effects of 1 MeV Proton Exposure as a Function of Fluence in Terms of Percent of Original Power Output.*

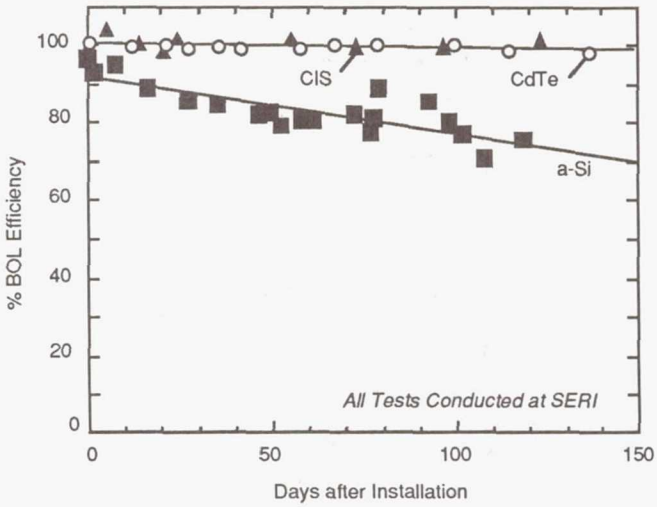


*Figure 2 - Stability of Thin-Film PV Technologies as a Function of Time of AM 1.5 Insolation in Terms of % BOL Efficiency.*

As a result, Martin Marietta has initiated an effort to investigate CIS for space applications. Reported here are the results of investigations into potential cost and weight savings from CIS on future large space-power platforms. Secondly, initial investigations into deposition of CIS and CdS/CIS stacks on flexible substrates will be reported. Finally, the first flexible CIS cells will be shown and preliminary performance values will be given.

## COST ANALYSIS FOR SPACE POWER APPLICATIONS

Most certainly one of the most difficult aspects of PV system design with a new technology is the true cost of array fabrication for space applications. When discussing CIS for terrestrial applications, the cost to produce devices is often clouded by extremely large volume projections that do not coincide with demands in the space power community and lack of stringent reporting and quality control. In this light, special care was taken to evaluate the cost of these materials based on realistic material cost. Emphasis also focused on incorporating the most enticing features of CIS, namely large-area deposition and monolithic integration, into the cost estimate. Chosen for a baseline is a future 10 kW space-based array (with both DoD and NASA significance) presently identified as using silicon.

Table 1 illustrates the calculations used to calculate space-qualified CIS for this investigation. Because of the high labor cost required for space-qualified PV, the size of the individual cells is important to cost reduction. Thus, technologies such as polycrystalline thin-film PV has two major advantages: first, the size of the device can be easily scaled to sizes larger than that found in Si and GaAs technology, and second, low-cost monolithic integration techniques compatible with thin-film deposition technology can produce low-cost modules. These advantages are clearly shown in Table 1 as monolithic integration of modules on only a 30.5 x 30.5 cm scale (1 $ft^2$) will have tremendous cost savings on space-qualified PV arrays. Furthermore, if a large volume market exists for space in the near future, material costs as low as $10-12 per square foot could be realized [7].

*Table 1 — Breakdown Estimates for PV Blanket Fabrication Cost*

| | Single Crystal Silicon | Polycrystalline Thin-Film CIS | Polycrystalline Thin-Film CIS Module§ |
|---|---|---|---|
| Cell Stack Total ($)* | 70.0 | 61.0 | 19.5 |
| Cell Cost ($/$ft^2$) (@99 Cells/$ft^2$, 85% PF) | 6930 | 6039 | 1930.5 |
| Laydown Cost ($/$ft^2$) | 2779 | 2779 | 28.0† |
| Total Cost ($/$ft^2$) | 9709 | 8818 | 1958.5 |
| Total Labor ($/$ft^2$) | 6739 | 6739 | 562.0 |
| Total Material ($/$ft^2$) | 2970 | 2079 | 1396.5 |

* Includes Cell Cost, Interconnects, Testing, Assembly, Cover Glass, and Reporting
§ Monolithically Integrated
† Labor Reduced by Large Device Size

## END-OF-LIFE PERFORMANCE ANALYSIS

The most important criteria when designing a PV power system is the performance of such a device in a space environment. In many cases, cost savings are sacrificed in the process of meeting mission requirements. As was discussed earlier, EOL comparisons of these materials for a chosen mission are the only true basis of comparison. Factors used in this analysis include temperature performance, radiation degradation, packing factors, assembly losses and solar variance (Table 2). For this estimate, 50 μm (2 mil) silicon and 300 μm (≈12 mil) cells were selected as conventional technology. Because CdTe and CIS technologies require thin-film deposition onto a substrate, the specific power of these devices is critically dependent upon the choice of substrate. For CIS, a 6.25 μm (1/4 mil) flexible metal foil was chosen as a substrate (flexible cell design) and 50 μm (2 mil) glass was chosen as a superstrate. While cost projections were made on cells with cover glass, weight estimates for all technologies assume no cover glass. Values for thermal performance were established for Si and GaAs, CIS performance was predicted by typical 2 mV/°C variance from 28°C with a nominal 490 mV output. Efficiency factors for CIS and CdTe were estimated at 11% (AM0) for reasonable near-term efficiencies. Packing factors for Si and GaAs are based on hand layup while CIS and CdTe assumes monolithic integration. Packing factor for CIS and CdTe is assumed to be higher than conventional technology due to monolithic integration.

*Table 2 - Basis of Performance Estimates for Conventional and CIS Space Power*

| Material | Solar Radiance W/m² | Areal Density kg/m² | Blanket Cost k$/m² | Thermal Deg (%/°C) | Radiation Damage (%) | Assembly Loss (%) | Packing Factor (%) | Solar Variance (%) |
|---|---|---|---|---|---|---|---|---|
| Si | 1352.53 | 0.37 | 104.48 | 0.5000% | 25.00% | 98.00% | 85.00% | 98.60% |
| GaAs | 1352.53 | 1.51 | 192.60 | 0.1300% | 15.00% | 98.00% | 85.00% | 98.60% |
| CIS | 1352.53 | 0.08 | 20.98 | 0.3900% | 2.00% | 98.00% | 95.00% | 98.60% |
| CdTe | 1352.53 | 0.12 | 20.98 | 0.2400% | 2.00% | 98.00% | 95.00% | 98.60% |

*Table 3 — BOL Estimates for Arrays*

| Material | BOL Cell Efficiency (%) | BOL Array Efficiency (%) | BOL Cell Power W/m² | BOL Array Power W/m² | BOL Cell Density (W/kg) | BOL Array Density (W/kg) |
|---|---|---|---|---|---|---|
| Si | 14.50% | 11.91% | 196.12 | 161.08 | 535.60 | 439.91 |
| GaAs | 18.00% | 14.78% | 243.46 | 199.96 | 161.02 | 132.25 |
| CIS | 11.00% | 10.10% | 148.78 | 136.57 | 1770.42 | 1625.19 |
| CdTe | 11.20% | 10.28% | 151.48 | 139.06 | 1263.77 | 1160.10 |

### Array Performance at 28°C

EOL array performance projections are shown in Table 3. Strictly on BOL power and efficiency estimates for arrays, CIS cannot compete with GaAs and direct competition with Si is only significant in terms of power-to-weight ratio. Based on these data, one critique of future use of polycrystalline thin-film devices is that their lower efficiency would increase array size, thereby contributing to difficult station-keeping and drag in low earth orb its (LEO). Furthermore, larger array size would contribute to weight gain on the spacecraft. Once again, the required array area must be based on EOL projections alone. On the basis of data presented in Tables 2 and 3, the following results were determined for BOL performance of arrays manufactured with these technologies (Table 4).

*Table 4 — EOL Estimates for Arrays Indicating Stability of CIS and CdTe*

| Material | EOL Cell Efficiency (%) | EOL Array Efficiency (%) | EOL Cell Power W/m² | EOL Array Power W/m² | EOL Cell Density (W/kg) | EOL Array Density (W/kg) |
|---|---|---|---|---|---|---|
| Si | 10.88% | 8.93% | 147.09 | 120.81 | 401.70 | 329.93 |
| GaAs | 15.30% | 12.57% | 206.94 | 169.97 | 136.86 | 112.41 |
| CIS | 10.78% | 9.90% | 145.80 | 133.84 | 1735.01 | 1592.68 |
| CdTe | 10.98% | 10.08% | 148.45 | 136.28 | 1238.49 | 1136.90 |

Data in Table 4 reflect the degradation in performance due to radiation damage after a 7 year mission at GEO. CIS and CdTe exhibit similar to superior performance compared to silicon-based cells in terms of EOL array efficiency and power output. Arrays with CIS have nearly a factor of five higher power-to-weight ratio than silicon, and over 14 times lighter than a comparable GaAs system. Clearly, CIS and CdTe could be substituted for silicon in these cases with a corresponding reduction of weight due to smaller arrays and a lighter PV blanket.

Array Performance from -70 to +100°C

While data presented in Tables 3 and 4 were based on 28°C, it is imperative that estimates as a function of temperature be determined. Typically, high temperature applications (T>70°C) are usually dedicated to GaAs due to its temperature stability. Although performance from CIS and CdTe diminishes more with temperature than GaAs, EOL efficiency and areal power output of CIS and CdTe arrays can come close to the performance of GaAs due to their stability in a GEO environment (Fig. 3). Furthermore, at lower temperatures (martian bases, space probes) these thin-film technologies can outperform GaAs.

Power-to-weight ratio of these PV technologies as a function of operating temperature is shown in Figure 4. As was evident from Tables 2 and 3 earlier, flexible CIS clearly has a tremendous advantage in specific power, while CdTe on thin glass also has significant advantage over conventional technologies. At higher temperatures CIS and CdTe exhibit nearly the same specific power, which is a factor of five higher than Si and even greater than GaAs.

PV Blanket Cost with Respect to Operating Temperature — As was shown earlier in Table 1, cost is also a major advantage to polycrystalline thin-film PV. Based on EOL array performance, CIS and CdTe often exhibit an order of magnitude cost reduction over conventional space-power PV technologies, particularly at higher temperatures when compared to silicon (Fig. 5).

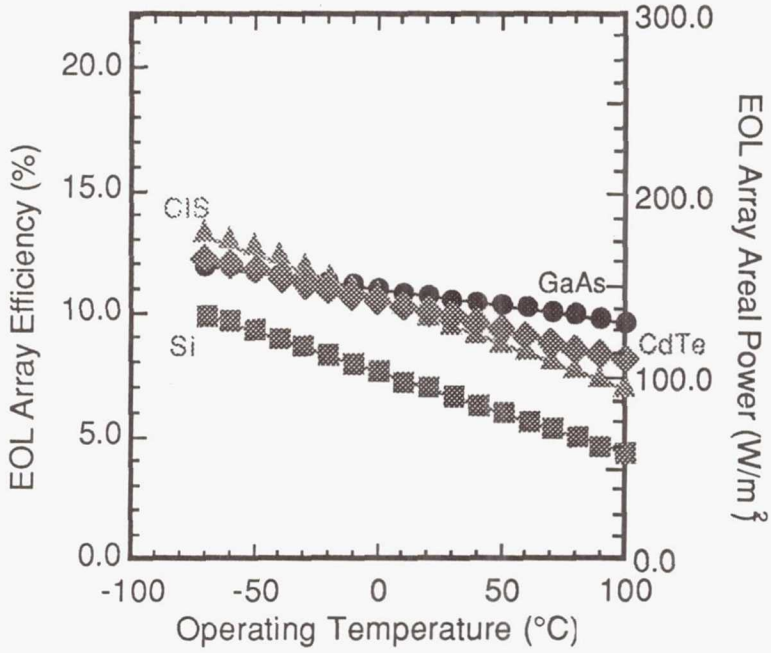


*Figure 3 - EOL Array Efficiency and Areal Power for Conventional and Polycrystalline Thin-Film Technologies.*

## LIGHTWEIGHT, FLEXIBLE CIS DEVICES

By virtue of the thin-film nature of CIS, it should be possible to deposit the necessary layers onto a flexible substrate. This concept has two major advantages: first, the thin-film nature of these cells dictates the majority of the weight will reside in the chosen substrate, and second, techniques commonly used to deposit metallic films on kapton for space applications (e.g. reel-to-reel continuous deposition) lends itself to extremely large-area deposition. Selection of the substrate material must be made not only on the basis of weight, but also with regard to surviving the processing associated with CIS device fabrication. Monolithic integration will be required to minimize the potential for failure of manually-interconnected cells. Finally, a suitable flexible top coating must be investigated which will provide protection from atomic oxygen (AO) for low earth orbits and will serve as an anti-reflective (AR) coating.

Little work has been accomplished in the area of flexible polycrystalline thin-film devices. The majority of the work conducted in this area is in amorphous silicon [8] despite concerns over stability with these devices. However, progress has been made with flexible a-Si over large areas by continuous deposition, thereby validating this concept for CIS as well.

Significant progress has been made by Martin Marietta and ISET in the area of flexible CIS films and devices with suitable adhesion. Experiments with absorber, window, and top contact layers and devices deposited onto thin flexible metallic foils (6.25 -25 µm thick) have proven successful. The $CuInSe_2$ was formed by evaporation using the ISET two-stage process [9, 10], while a CdS window layer was deposited by chemical immersion deposition. Figure 6 shows a glancing incidence diffractometry (GID) scan of a CIS film deposited onto a 25 µm Mo substrate, indicating that both $CuInSe_2$ and $CuIn_2Se_{3.5}$ are observed. Further investigations are in progress to determine if the existence of $CuIn_2Se_{3.5}$ is an

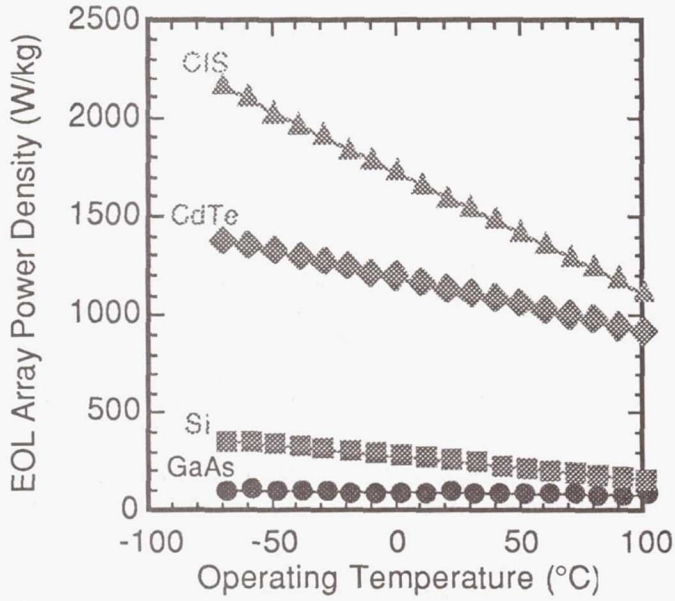


*Figure 4 - EOL Array Power Density for Conventional and Polycrystalline Thin-Film Technologies.*

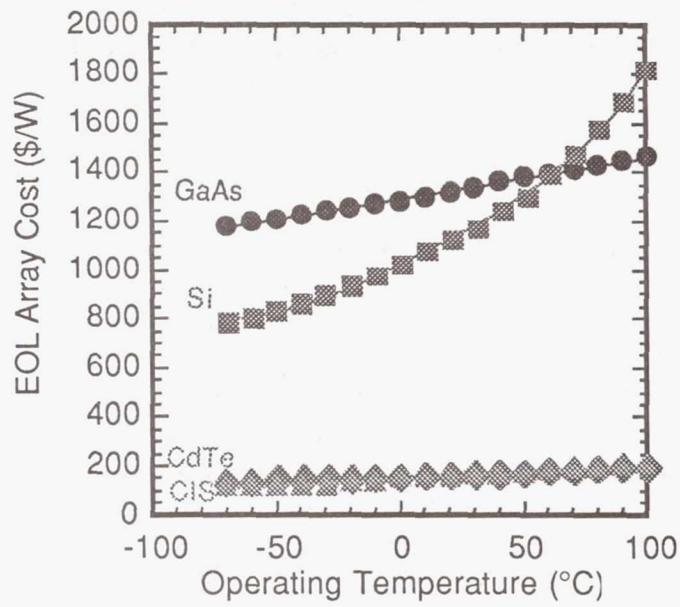


*Figure 5 - EOL Array Cost for Conventional and Polycrystalline Thin-Film Technologies.*

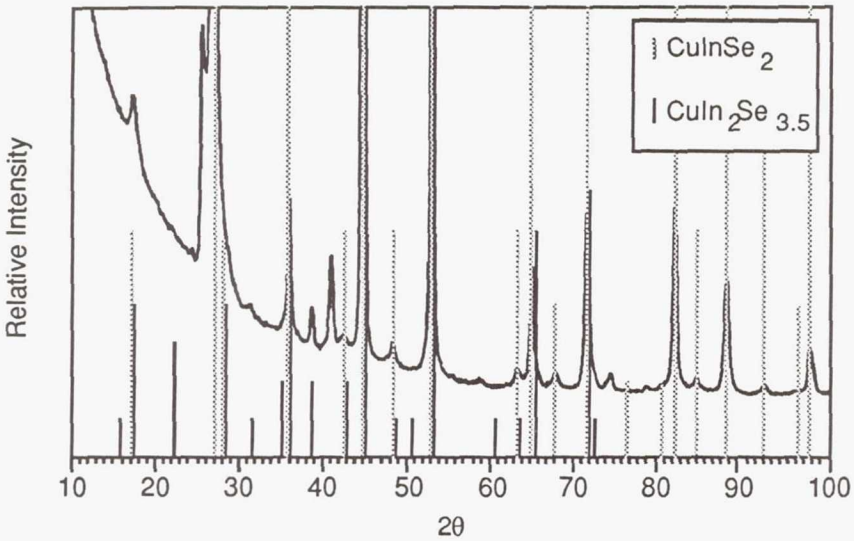


*Figure 6 - Glancing Incidence Diffractometry (GID) of CIS Film on Molybdenum Substrate Indicating Presence of Two Phases.*

artifact of the thin foil substrate or a component previously unseen with other X-ray diffraction technologies. Early coatings failed conventional tape pull tests, although sufficient adhesion existed with later films and devices to allow bending easily to a minimum radius of 0.75 cm. Furthermore, early films on thin substrates exhibited residual stresses which tended to curl specimens slightly upward. Subsequent improvement of deposition techniques has improved adhesion and reduce residual stresses.

Flexible cells were fabricated using this technology. Figure 7 is a schematic of the flexible CIS cell, indicating that a majority of the cross section is the substrate material. This indicates that significant work is still required to develop a lightweight substrate capable of handling temperatures and environments during fabrication while remaining pliable. A photograph of a flexible CIS cell is shown in Figure 8 which exhibited 6% efficiency (AM1.5).

## SUMMARY

Future space-power applications will require PV technologies to be lighter, cheaper, and more stable. These requirements are paramount to the funding of aggressive projects involved with space exploration and large-scale space-power platforms. Three key advantages to polycrystalline thin-film PV for space applications are (1) potential for high power-to-weight ratios, (2) charged-particle environment stability, and (3) low-cost fabrication techniques. From a system design point-of-view, these technologies have great potential for low-cost, lightweight, stable PV for future space power applications. Given the climate within NASA and DoD, the timely development of these polycrystalline thin-film technologies is essential to the future of PV in space exploration.

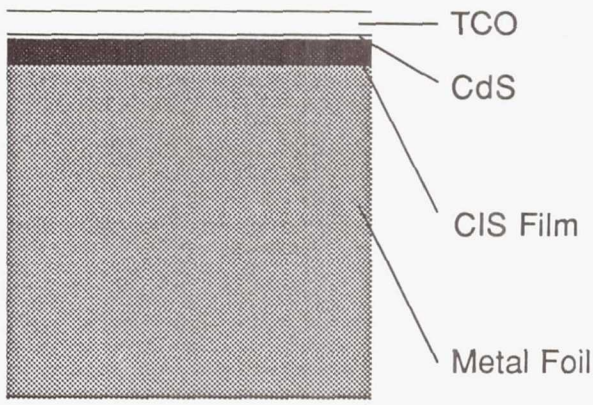


*Figure 7 - Schematic of Flexible CIS Cell.*

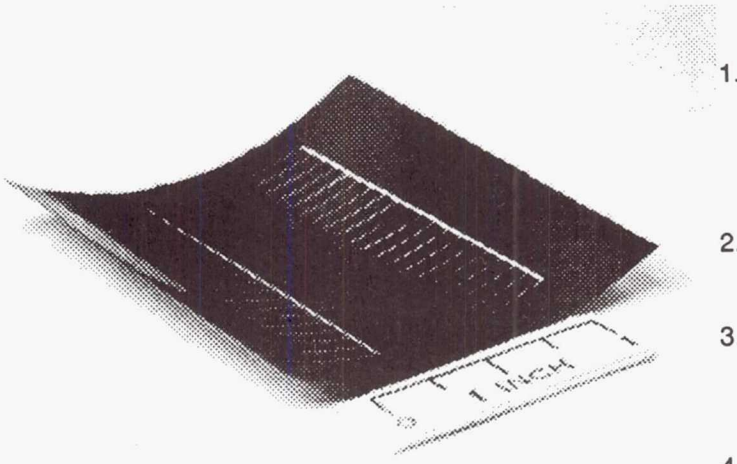


*Figure 8 - Photograph of CIS Cell on Flexible Molybdenum Substrate.*

REFERENCES


1. G. Landis: "Review of Thin Film Solar Cell Technology and Applications for Ultra-Light Spacecraft Solar Arrays," Proc. SPRAT X, NASA CP-3107, 1989, p. 180.
2. L. Mrig: "PV Reliability Issues,: Photovoltaics Workshop, Denver, CO 1990.
3. A. Catalano: Proc. 21th IEEE Photovoltaic Specialists Conf., IEEE, New York, 1990, p. 36.
4. R. Burgess, W. Chen, D. Doyle, N. Kim and B. Stanbery: Proc. 23rd IEEE Photovoltaic Specialists Conf., IEEE, New York, 1988
5. K.Zweibel, H.S. Ullal, and R.L. Mitchell: Proc. 21th IEEE Photovoltaic Specialists Conf., IEEE, New York, 1990, p. 458
6. C.S. Flora and P.A. Dillard: "An Approach for Configuring Space Photovoltaic Tandem Arrays Based on Cell Layer Performance," Proc. SPRAT X, NASA CP-3107, 1989, p. 167
7. V.K. Kapur and B.M. Basol: "Key Issues and Cost Estimates for the Fabrication of $CuInSe_2$ (CIS) PV Modules by the Two-Stage Process," Proc. 21th IEEE Photovoltaic Specialists Conf., IEEE, New York, 1990, p. 467
8. J.J. Hanak and H. Flaisher: "Integral Bypass Diodes in an Amorphous Silicon Alloy Photovoltaic Module," Proc. SPRAT X, NASA CP-3107, 1989, p. 433.
9. V.K. Kapur, B.M. Basol and E.S. Tseng: Proc. 18th IEEE Photovoltaic Specialists Conf., IEEE, New York, 1985, p. 1429.
10. V.K. Kapur, B.M. Basol and E.S. Tseng: Solar Cells, 21, 1987, p. 65.

# KEY RESULTS OF THE MINI-DOME FRESNEL LENS CONCENTRATOR ARRAY DEVELOPMENT PROGRAM UNDER RECENTLY COMPLETED NASA & SDIO SBIR PROJECTS

Mark J. O'Neill
ENTECH, Inc.
DFW Airport, TX

Michael F. Piszczor
NASA Lewis Research Center
Cleveland, OH

Lewis M. Fraas
Boeing High Technology Center
Seattle, WA

## INTRODUCTION

Since 1986, ENTECH and the NASA Lewis Research Center have been developing a new photovoltaic concentrator system for space power applications. The unique refractive system uses small, dome-shaped Fresnel lenses to focus sunlight onto high-efficiency photovoltaic concentrator cells which use prismatic cell covers to further increase their performance. Under Small Business Innovation Research (SBIR) funding provided by both NASA and SDIO, the mini-dome Fresnel lens concentrator array has progressed from a paper concept in 1986 to functional array hardware in 1990-91. Since 1989, Boeing has been a key participant in the development of this concept, providing both record-breaking GaAs/GaSb tandem cell technology and significant expertise in the development of the panel structure and related manufacturing techniques. Other project participants include 3M Company (lens tooling); Fresnel Optics (prism cover tooling); and Varian Associates (GaAs cells).

Highlights of the five-year development include near-AMO Lear Jet flight testing of mini-dome lenses (90% net optical efficiency achieved); tests verifying sun-pointing error tolerance with negligible power loss; simulator testing of prism-covered GaAs concentrator cells (24% AMO efficiency); testing of prism-covered Boeing GaAs/GaSb tandem cells (31% AMO efficiency); and fabrication and outdoor testing of a 36-lens/cell element panel. These test results have confirmed previous analytical predictions which indicate substantial performance improvements for this technology over current array systems. Based on program results to date, it appears that an array power density of 300 watts/square meter and a specific power of 100 watts/kilogram can be achieved in the near term. All components of the array appear to be readily manufacturable from space-durable materials at reasonable cost. This paper presents a concise review of the key results leading to the current array, and briefly discusses further development plans for the future.

## SYSTEM DESCRIPTION

Figures 1 through 4 show the basic mini-dome Fresnel lens space concentrator

array concept. Small, square-aperture, thin, dome-shaped Fresnel lenses focus incident sunlight by a factor of about 100 onto circular photovoltaic cells. The cells are mounted to a backplane radiator for waste heat rejection. Individual lenses are placed within slots in a honeycomb panel, which is structurally integrated with the backplane radiator. Cells are interconnected in series/parallel circuits to build up the desired voltage, current, and power values for the panel. Panels are mounted onto automatically deploying support structures to form large, multi-kilowatt arrays.

Material selection has been one of the key issues in the development of the mini-dome lens array. The current materials have been chosen based on previous successful space use, ease-of-fabrication, and cost. The lens is a laminated assembly of ceria-doped microglass over clear silicone rubber, as shown in Figure 5. The honeycomb and radiator are both made from aluminum. The cell is a tandem structure of gallium arsenide over gallium antimonide, to maximize array performance. The cells use silicone rubber prismatic covers to eliminate grid shading losses, thereby enhancing performance. As discussed in the following section, prototype lenses, cells, prismatic covers, and panels have all been successfully fabricated and tested.

## KEY RESULTS

The unique dome lens design is shown in Figure 6. While every prism in the lens is different from all others, each prism is configured for symmetrical refraction. Specifically, the angle of incidence of the solar rays on the outer smooth surface of the lens is equal to the angle of emergence of these solar rays on the faceted inner surface of the lens. This symmetry minimizes reflection losses, thereby maximizing efficiency. Furthermore, this symmetry greatly improves image quality compared to conventional flat Fresnel lenses. Even more importantly, this refraction symmetry vastly expands allowable inaccuracies encountered in both initial manufacture and long-term operation. Remarkably, the slope error tolerance of the mini-dome lens is more than 100 times larger than for a flat Fresnel lens, and more than 200 times larger than for a reflective concentrator, for equal image defocussing.

By "tweaking" the angles of the individual prisms making up the Fresnel pattern, the dome lens has been designed to focus the sunlight into a circular spot about 2.6 mm in diameter, which is smaller than the cell diameter of 4.0 mm by an amount which was selected to allow a sun-pointing error of 1 degree without loss of power output. Performance goals for the lens were >90% net optical efficiency and $\pm 1$ degree tracking error tolerance with negligible loss of power. Measurements on a pure silicone lens (no glass superstrate) with a square aperture mask coupled with a gallium arsenide cell are shown in Figure 7. Note that the lens indeed achieved 90% efficiency. Note also that the power loss at 1 degree tracking error is only 1%. Later lenses with prototype glass superstrates have achieved about 85% optical efficiency with less than 5% power loss at 1 degree tracking error. Further improvement in the glass superstrates is expected to raise the laminated lens performance back to the pure silicone lens levels. Still higher performance should be achievable through the use of antireflection coatings on the glass superstrate.

Figure 8 shows the Boeing-developed tandem cell approach. The prism-covered gallium arsenide top cell converts about 24% of the available sunlight to electricity. The top cell energy conversion occurs for that portion of the solar

spectrum below about 0.9 micron in wavelength. Longer, infrared wavelengths pass through the top cell onto the prism-covered gallium antimonide bottom cell. The bottom cell converts another 7% of the available sunlight to electricity, for a total tandem cell efficiency of 31%. This value has been confirmed by NASA-Lewis via Lear Jet flight tests coupled with flash solar simulator tests. Higher efficiency values are anticipated in the future, as the newly developed gallium antimonide cell technology matures.

Thermal analyses have been conducted to predict on-orbit cell operating temperature. Figure 9 shows a typical thermal analysis result for the hottest portion of a low earth orbit (LEO) mission. The radiator temperature just beneath the cell is about 96C. Thus, with a well designed cell-to-radiator mount (with a 4C gradient), the cell temperature should be about 100C. Figure 10 shows a similar result for a geosynchronous earth orbit (GEO) mission. The cell temperature will be about 76C for GEO operation.

Mass analyses have been conducted to estimate mass per unit area for the baseline panel, as shown in Figure 11. A value of about 2.4 kg/sq.m. appears achievable in the very near term. Furthermore, automatically deploying support structures designed by others have been identified for use with the mini-dome lens panels. These structures have a mass of about 0.7 kg/sq.m., for a total array mass density of 3.1 kg/sq.m. This array mass density is approximately equivalent to the planned one-sun Kapton blanket array for the Space Station Freedom. Thus, the mini-dome lens array is extremely light-weight.

Figure 12 summarizes the near-term significance of the previously discussed performance and mass parameters. With single junction cells, power density values of 250-260 W/sq.m. will be achieved. With tandem cells, power density values of 300-330 W/sq.m. will be achieved. With single-junction cells, specific power values above 80 W/kg will be achieved. With tandem cells, specific power values above 100 W/kg will be achieved.

## PROTOTYPE PANELS

Over the past year, several prototype panels have been successfully made and tested. The most recent panel is shown in Figure 13. Boeing has developed a computer-controlled milling process for rapidly producing extremely rigid, light-weight, thermally efficient radiator/honeycomb assemblies from a plate of aluminum. Cell assemblies are mounted directly to the panel backplane, while individual lenses are attached to the front of the panel structure. Outdoor testing of these panels has shown performance levels close to expectations for the lenses and cells utilized. These prototype panels have convinced the project participants of the practicality of the mini-dome lens panel concept.

## CONCLUSION

The mini-dome lens array development has progressed successfully to the prototype hardware stage. Performance measurements have closely matched expectations. A small array space flight test is planned for 1992 in conjunction with the PASP+ program (as discussed by Guidice et al in another paper at this conference). Independent comparative array analyses are confirming the relative merits of the new array technology (e.g., as discussed by Kraus in another paper at this conference). Figure 14 summarizes the key features and advantages of the mini-dome Fresnel lens space concentrator approach.

Fig. 1

## DOME LENS PV MODULE CONCEPTUAL DESIGN

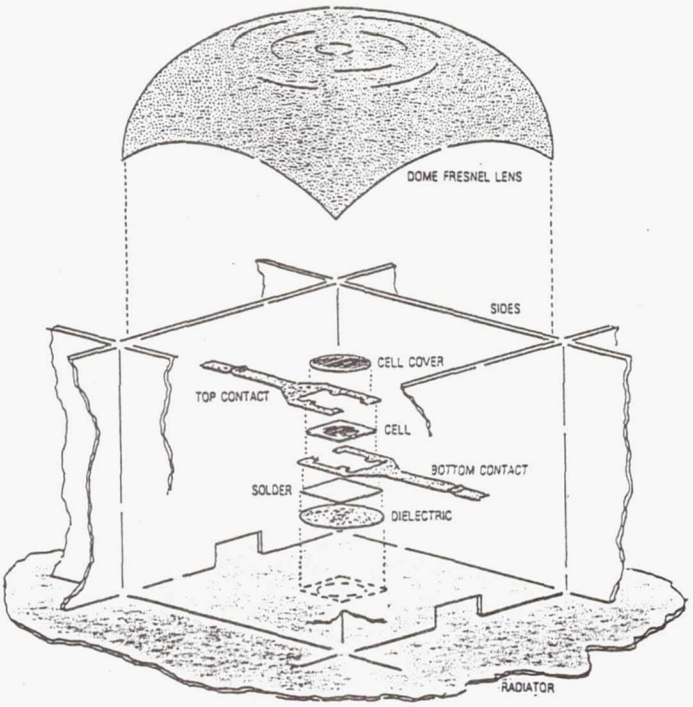


Fig. 2

## ENTECH DOME LENS PV CONCENTRATOR PANEL CONCEPTUAL DESIGN

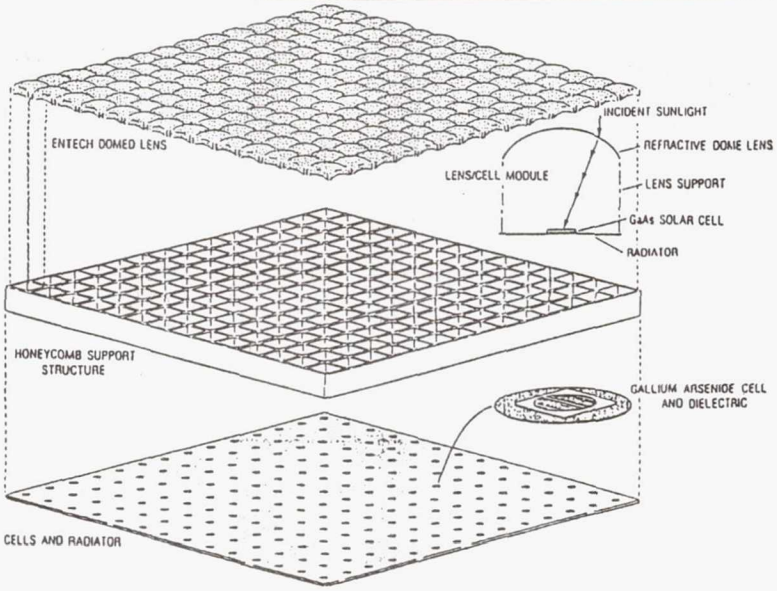

Fig. 3

## CROSS - SECTIONAL VIEWS OF DOME LENS PV PANEL

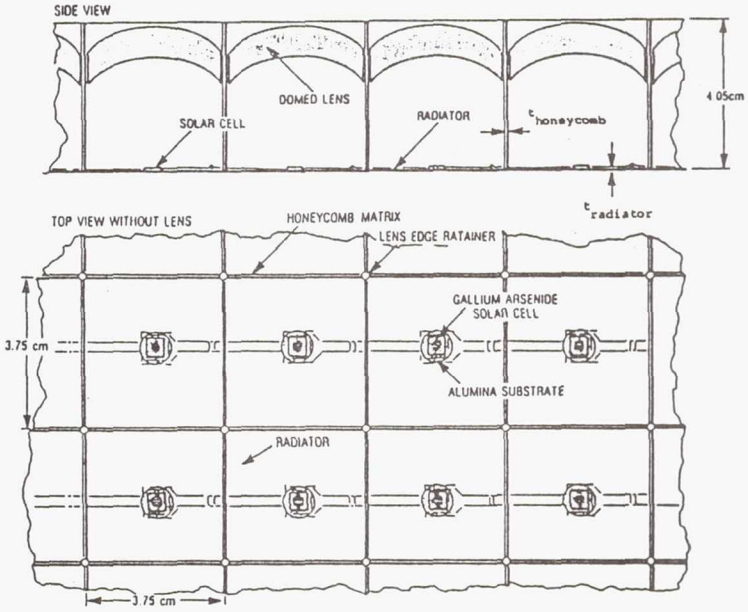


Fig. 4

## DOME LENS PV ARRAYS ON ESS SYSTEM ATTACHED TO SPACE STATION

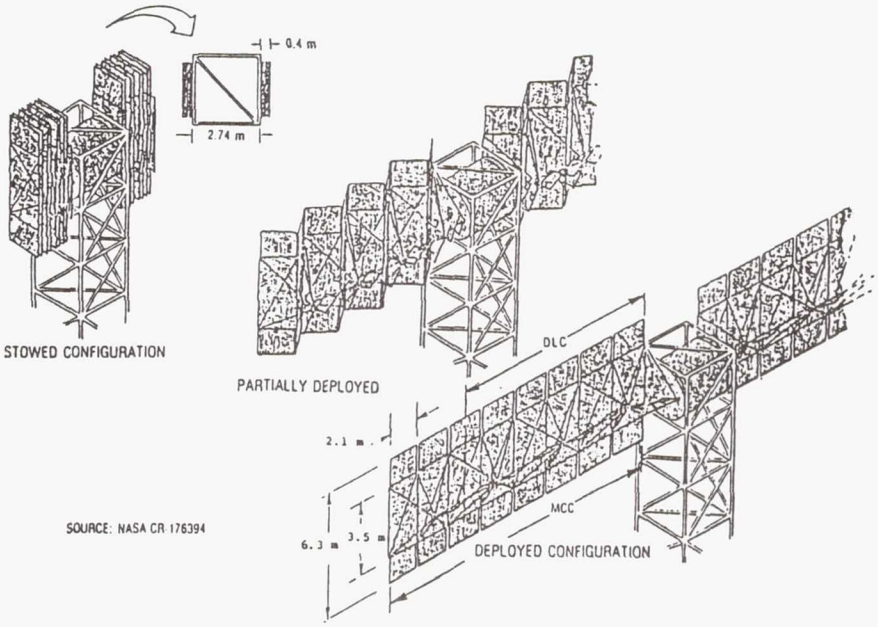


SOURCE: NASA CR-176394

Fig. 5

BASELINE LENS DESIGN FOR LOW-EARTH-ORBIT (LEO) APPLICATIONS
(MICROGLASS SHIELDS POLYMERIC LENS FROM ATOMIC OXYGEN)

## LAMINATED CERIA MICROGLASS/SILICONE RTV MINI-DOME FRESNEL LENS

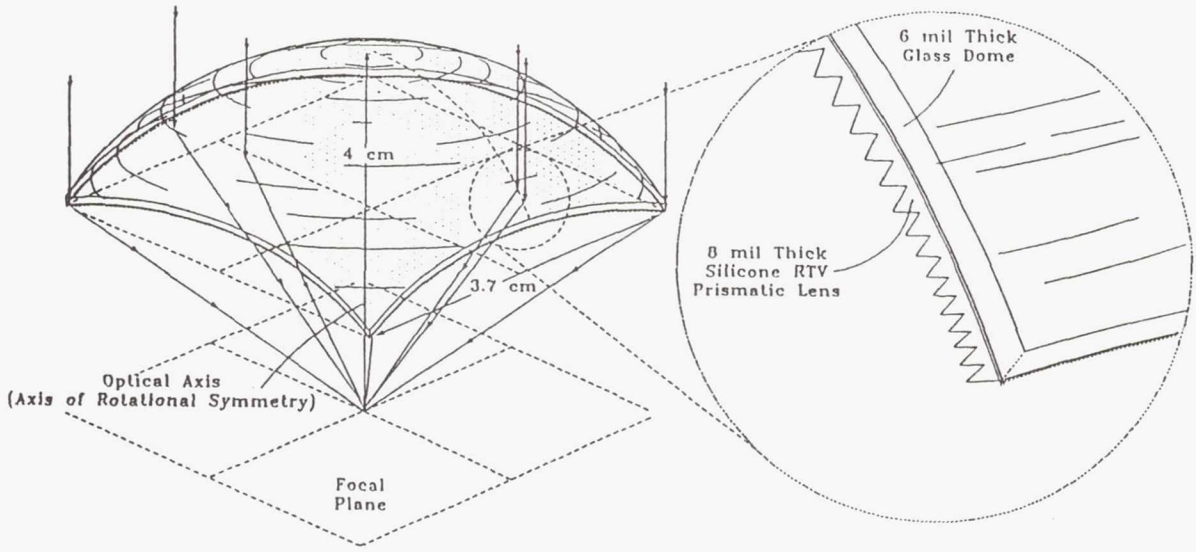


Fig. 6

MAGNIFIED VIEW OF SEVERAL PRISMS WITHIN THE ENTECH DOME LENS, SHOWING REFRACTION SYMMETRY AND BLUNT TIP TOLERANCE

THIS SYMMETRICAL REFRACTION CONDITION MINIMIZES REFLECTION LOSSES FOR A GIVEN RAY TURNING ANGLE, THEREBY MAXIMIZING TRANSMITTANCE.

THE SYMMETRICAL REFRACTION CONDITION ALSO MINIMIZES IMAGE SIZE AND MAXIMIZES TOLERANCE FOR MANUFACTURING ERRORS AND ABERRATIONS.

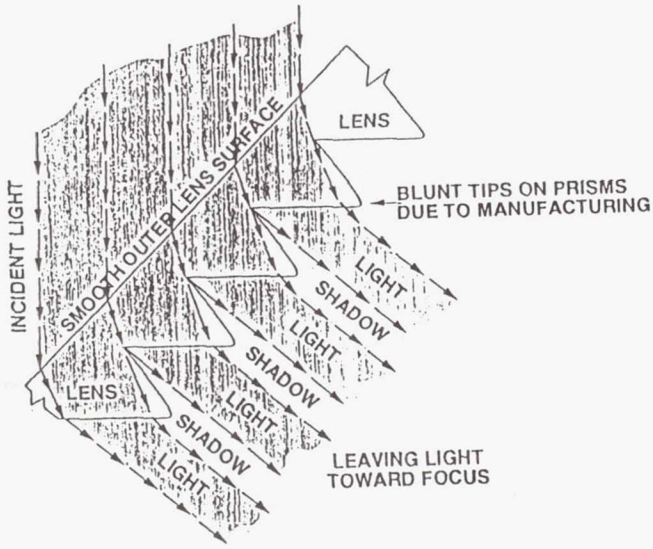

## NASA LEWIS LEAR JET HIGH ALTITUDE TEST FACILITY
## MEASURED LENS PERFORMANCE FOR MODULE #1

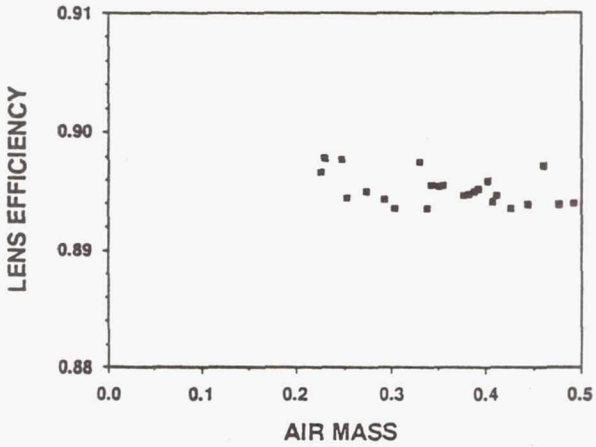


(Prototype Silicone Rubber Lens,
Masked to Simulate Square Aperture
Flown March 1990)

## TRACKING ERROR PERFORMANCE TEST
## FOR PROTOTYPE MODULE #1

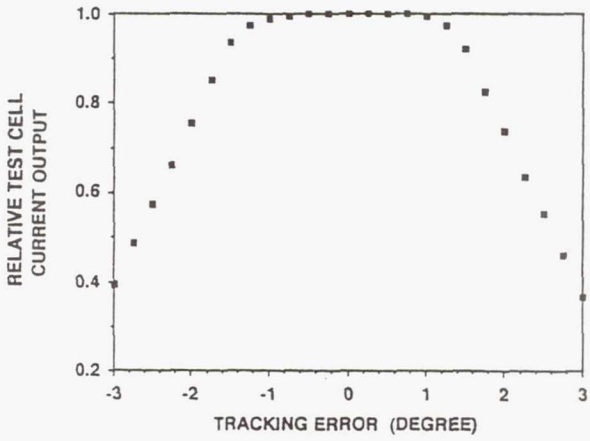


LENS/CELL ELEMENT DESIGNED
FOR 1 DEGREE TRACKING ERROR TOLERANCE

(Prototype Silicone Rubber Lens,
Masked to Simulate Square Aperture)

Fig. 7

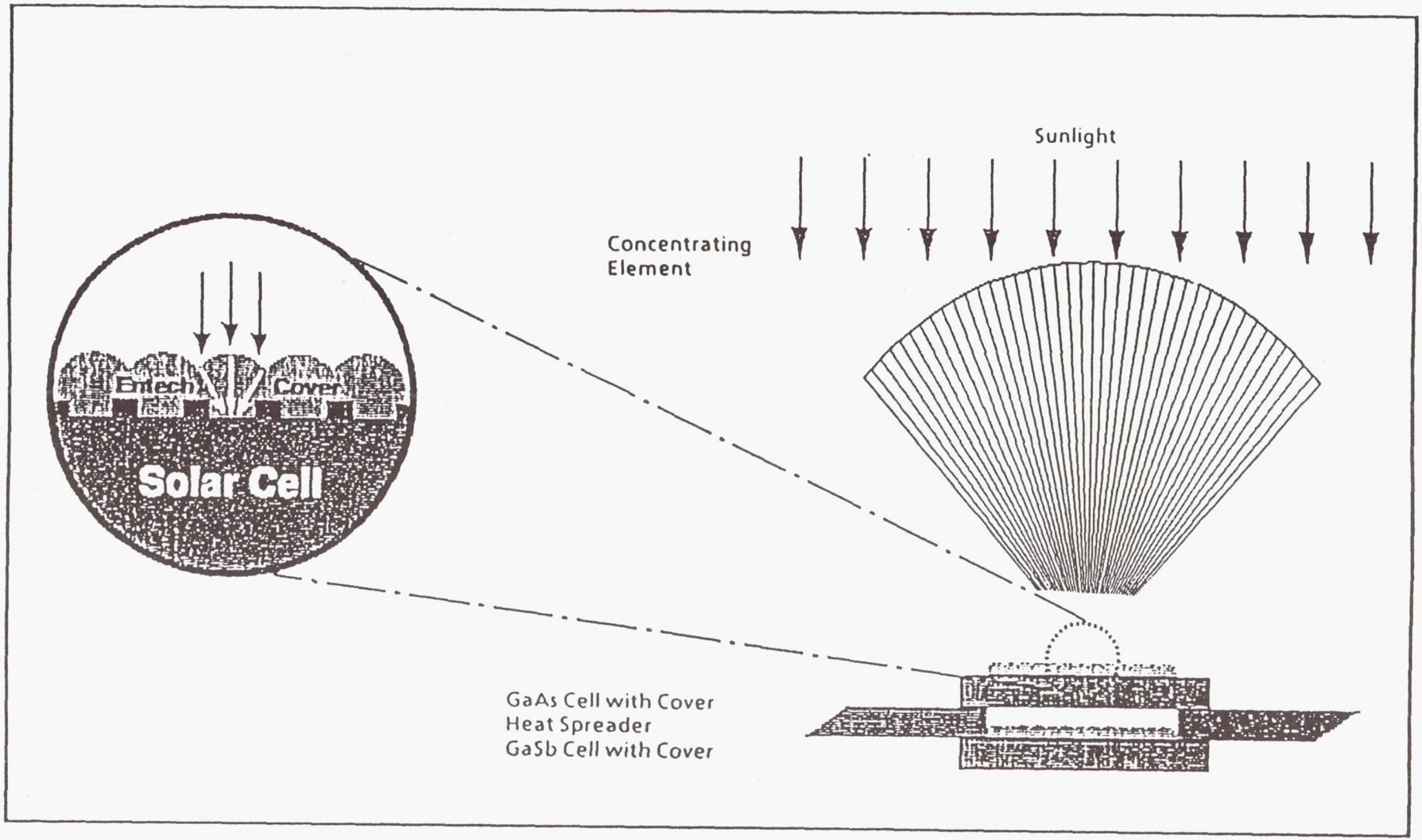


*GaAs/GaSb Concentrator Cell Concept*

Fig. 8

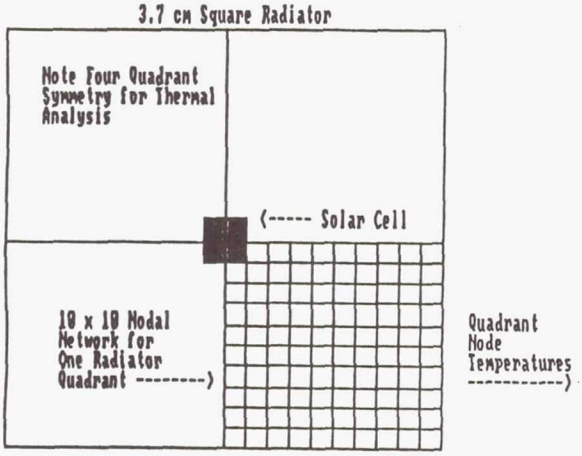


| | | | | | | | | | |
|---|---|---|---|---|---|---|---|---|---|
| 95.910 | 91.381 | 88.713 | 86.947 | 85.697 | 84.787 | 84.125 | 83.660 | 83.364 | 83.219 |
| 91.381 | 89.621 | 87.910 | 86.526 | 85.452 | 84.631 | 84.019 | 83.583 | 83.302 | 83.165 |
| 88.713 | 87.910 | 86.876 | 85.890 | 85.045 | 84.360 | 83.828 | 83.441 | 83.188 | 83.063 |
| 86.947 | 86.526 | 85.890 | 85.208 | 84.572 | 84.025 | 83.585 | 83.255 | 83.036 | 82.927 |
| 85.697 | 85.452 | 85.045 | 84.572 | 84.101 | 83.676 | 83.321 | 83.049 | 82.865 | 82.772 |
| 84.787 | 84.631 | 84.360 | 84.025 | 83.676 | 83.349 | 83.066 | 82.844 | 82.692 | 82.615 |
| 84.125 | 84.019 | 83.828 | 83.585 | 83.321 | 83.066 | 82.840 | 82.659 | 82.533 | 82.469 |
| 83.660 | 83.583 | 83.441 | 83.255 | 83.049 | 82.844 | 82.659 | 82.509 | 82.403 | 82.349 |
| 83.364 | 83.302 | 83.188 | 83.036 | 82.865 | 82.692 | 82.533 | 82.403 | 82.311 | 82.263 |
| 83.219 | 83.165 | 83.063 | 82.927 | 82.772 | 82.615 | 82.469 | 82.349 | 82.263 | 82.218 |

**ASSUMPTIONS**

Thermal Control Coating on Both Sides of Radiator:
Solar Absorptance = 0.20, Infrared Emittance = 0.90

Aluminum Radiator:
Thermal Conductivity = 173 W/m-K

Glass/Silicone Lens on Front Side of Radiator:
Solar Transmittance = 0.92, Infrared Emittance = 0.90

Hottest Portion of Low Earth Orbit (LEO):
Radiator Facing Earth, Lens Facing Sun
Earth Albedo Reflectance = 0.36
Earth Effective Radiation Temperature = 255K
Radiator-to-Earth View Factor = 0.922

Solar Constant = 1371 W/sq.m.

Prism-Covered GaAs Cell:
Solar Absorptance = 0.95
Electrical Conversion Efficiency = 0.20
Cell Area = 0.01 Times Lens Area

Net Waste Heat Rate from Cell To Radiator = 1.30 W
(3.7 cm x 3.7 cm x 0.1371 W/sq.cm. x 0.92 x (0.95 - 0.20))

Fig. 9 Thermal Analysis Results for Low Earth Orbit (LEO) for 200 Micron (8 mil) Radiator Thickness

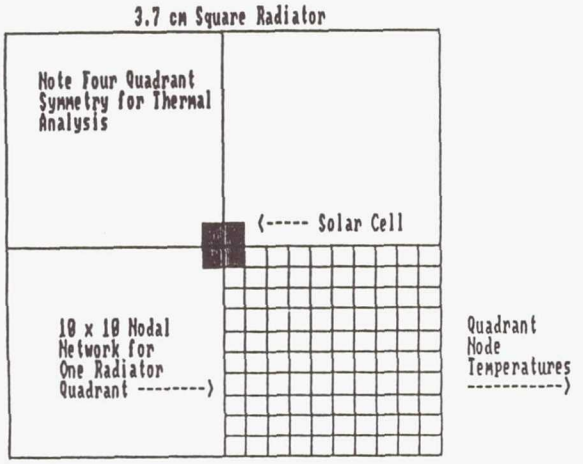


| | | | | | | | | | |
|---|---|---|---|---|---|---|---|---|---|
| 72.207 | 67.677 | 65.008 | 63.240 | 61.988 | 61.076 | 60.412 | 59.946 | 59.649 | 59.504 |
| 67.677 | 65.916 | 64.204 | 62.819 | 61.742 | 60.920 | 60.306 | 59.869 | 59.588 | 59.450 |
| 65.008 | 64.204 | 63.170 | 62.182 | 61.335 | 60.648 | 60.116 | 59.727 | 59.474 | 59.349 |
| 63.240 | 62.819 | 62.182 | 61.499 | 60.861 | 60.313 | 59.872 | 59.541 | 59.322 | 59.212 |
| 61.988 | 61.742 | 61.335 | 60.861 | 60.390 | 59.964 | 59.608 | 59.334 | 59.150 | 59.057 |
| 61.076 | 60.920 | 60.648 | 60.313 | 59.964 | 59.635 | 59.351 | 59.129 | 58.976 | 58.899 |
| 60.412 | 60.306 | 60.116 | 59.872 | 59.608 | 59.351 | 59.125 | 58.943 | 58.817 | 58.753 |
| 59.946 | 59.869 | 59.727 | 59.541 | 59.334 | 59.129 | 58.943 | 58.792 | 58.686 | 58.632 |
| 59.649 | 59.588 | 59.474 | 59.322 | 59.150 | 58.976 | 58.817 | 58.686 | 58.593 | 58.545 |
| 59.504 | 59.450 | 59.349 | 59.212 | 59.057 | 58.899 | 58.753 | 58.632 | 58.545 | 58.501 |

**ASSUMPTIONS**

Thermal Control Coating on Both Sides of Radiator:
Solar Absorptance = 0.20, Infrared Emittance = 0.90

Aluminum Radiator:
Thermal Conductivity = 173 W/m-K

Glass/Silicone Lens on Front Side of Radiator:
Solar Transmittance = 0.92, Infrared Emittance = 0.90

Hottest Portion of Geosynchronous Earth Orbit (GEO):
Radiator Facing Earth, Lens Facing Sun
Earth Albedo Reflectance = 0.36
Earth Effective Radiation Temperature = 255K
Radiator-to-Earth View Factor = 0.023

Solar Constant = 1371 W/sq.m.

Prism-Covered GaAs Cell:
Solar Absorptance = 0.95
Electrical Conversion Efficiency = 0.20
Cell Area = 0.01 Times Lens Area

Net Waste Heat Rate from Cell To Radiator = 1.30 W
(3.7 cm x 3.7 cm x 0.1371 W/sq.cm. x 0.92 x (0.95 - 0.20))

Fig. 10 Thermal Analysis Results for Geosynchronous Earth Orbit (GEO) for 200 Micron (8 mil) Radiator Thickness

Fig. 11

MINI-DOME LENS SPACE PHOTOVOLTAIC CONCENTRATOR
NEAR-TERM BASELINE PANEL MASS BREAKDOWN

| ELEMENT | MATERIAL | DENSITY (G/CU.CM.) | THICKNESS (CM) | SURFACE AREA / PANEL AREA | MASS/PANEL AREA (KG/SQ.M.) |
|---|---|---|---|---|---|
| LENS SUPERSTRATE | MICROGLASS | 2.50 | 0.015 | 1.30 | 0.49 |
| LENS PRISMS | SILICONE | 1.00 | 0.015* | 1.30 | 0.19 |
| RADIATOR | ALUMINUM | 2.77 | 0.020 | 1.00 | 0.55 |
| CELL/COVER/MOUNT | GAAS ET AL | 5.70 | 0.046 | 0.02 | 0.05 |
| HONEYCOMB | ALUMINUM | 2.77 | 0.015 | 2.20 | 0.91 |
| RADIATOR COATING | ALUMINA | 3.88 | 0.001 | 2.00 | 0.08 |
| MISCELLANEOUS | ---------- 7.5% OF ABOVE TOTAL ---------- | | | | 0.17 |
| TOTAL | | | | | 2.44 |

* SILICONE BASE THICKNESS = 0.010 CM
SILICONE PRISM THICKNESS = 0.010 CM (BUT HALF VOID)
EFFECTIVE SILICONE THICKNESS = 0.015 CM

Fig. 12

MINI-DOME FRESNEL LENS ARRAY - NEAR-TERM PERFORMANCE ESTIMATES
BASED ON RECENT TEST RESULTS FOR PROTOTYPE CELLS AND LENSES

| ITEM | NEAR-TERM GaAs | NEAR-TERM TANDEM |
|---|---|---|
| Lens Type | Glass/Silicone | Glass/Silicone |
| Panel Type | 0.02 cm Alum. | 0.02 cm Alum. |
| Cell Type | GaAs | GaAs + GaSb |
| Cell Eff. at 25C | 24% | 24% + 7% = 31% |
| Max. LEO Cell Oper. Temp. | 100C | 100C & 100C |
| Cell Eff. at Max. LEO Temp. | 22% | 22% + 5% = 27% |
| Max. GEO Cell Oper. Temp. | 76C | 76C & 76C |
| Cell Eff. at Max. GEO Temp. | 23% | 23% + 6% = 29% |
| Lens Efficiency | 90% | 90% |
| Packing Factor | 97% | 97% |
| Mismatch/Wiring Factor | 93% | 93% |
| LEO Array Efficiency | 18% | 22% |
| LEO Power Density (w/sq.m.) | 247 | 302 |
| GEO Array Efficiency | 19% | 24% |
| GEO Power Density (w/sq.m.) | 260 | 329 |
| Panel Mass (kg/sq.m.) | 2.4 | 2.4 |
| Structure Mass (kg/sq.m.) | 0.7 | 0.7 |
| Array Mass (kg/sq.m.) | 3.1 | 3.1 |
| LEO Specific Power (w/kg) | 80 | 97 |
| GEO Specific Power (w/kg) | 84 | 106 |

Note: Measured Performance Parameters for Prototype Cells and Lenses Are Underlined.

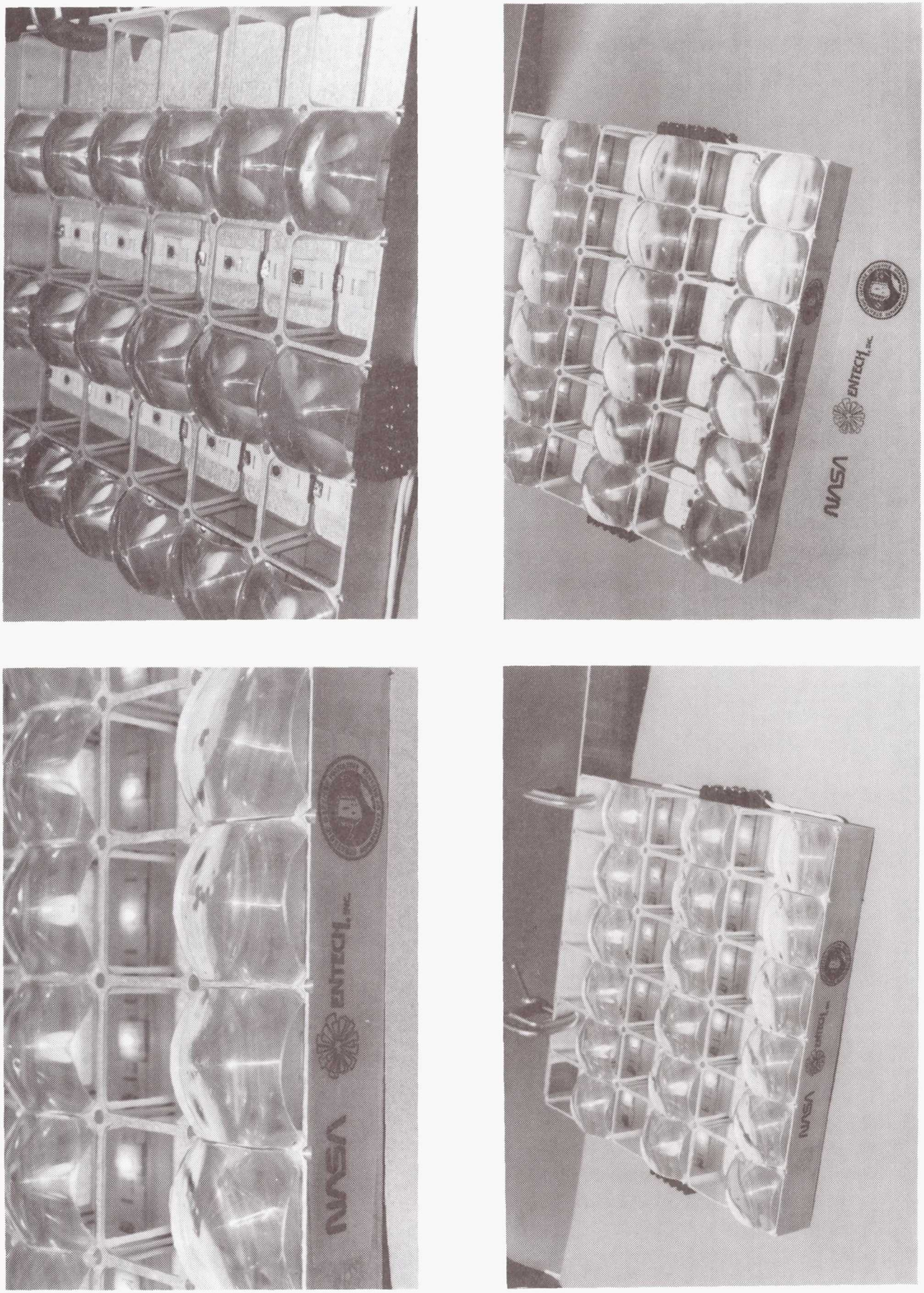


Fig. 13

Fig. 14

## MINI-DOME LENS SPACE PHOTOVOLTAIC CONCENTRATOR KEY FEATURES AND ADVANTAGES

**UNIQUE LENS:** THE TRANSMITTANCE-OPTIMIZED DOME LENS PROVIDES 90% NET OPTICAL EFFICIENCY (WITHOUT THE NEED FOR SECONDARY OR TERTIARY CONCENTRATORS), EXCEPTIONAL TOLERANCES FOR MANUFACTURING AND OPERATIONAL INACCURACIES (E.G., 200 TIMES THE SLOPE ERROR TOLERANCE OF REFLECTIVE CONCENTRATORS, AND 100 TIMES THE SLOPE ERROR TOLERANCE OF FLAT FRESNEL LENSES), AND EXCELLENT AND SELECTABLE TRACKING ERROR TOLERANCE (1 DEGREE FOR 4 MM CELL, 2 DEGREES FOR 5.4 MM CELL, ETC.)

**CELL USAGE:** VARIOUS CELLS CAN BE USED IN THE DOME LENS CONCENTRATOR, INCLUDING BOEING'S GAAS/GASB, VARIAN'S GAAS, NASA'S INP, ET AL. (DUE TO HIGH CONCENTRATION, ONLY 1% OF NORMAL CELL AREA IS NEEDED).

**PRISMATIC COVERS:** ALLOW HEAVY GRID COVERAGE FOR EFFICIENT CURRENT COLLECTION.

**HEAT REJECTION:** CELLS ARE MOUNTED DIRECTLY TO A BACKSIDE RADIATOR.

**PACKING FACTOR:** LENSES CAN BE CUT SQUARE (OR HEX) IN APERTURE TO MAXIMIZE LENS APERTURE/PANEL AREA RATIO (97% IS EASILY ACHIEVED).

**MODULARITY:** THE NUMBER OF LENS/CELL ELEMENTS CAN BE SELECTED FOR OPTIMAL PANEL OUTPUT.

**MATERIALS:** READILY AVAILABLE LIGHTWEIGHT MATERIALS ARE USED THROUGHOUT THE PANEL.

**MANUFACTURABILITY:** ALL PANEL ELEMENTS APPEAR TO BE READILY MANUFACTURABLE.

**DEPLOYABLILITY:** AUTOMATICALLY DEPLOYING STRUCTURES BEING DEVELOPED FOR OTHER CONCENTRATORS CAN BE EASILY ADAPTED TO THE MINI-DOME PANELS. (E.G., THE ASTRO-AEROSPACE ESS OR STACBEAM STRUCTURES).

**COST:** DUE TO THE SMALL CELL AREA REQUIREMENT, THE MASS-PRODUCIBILITY OF ALL ARRAY COMPONENTS, AND THE LARGE ALLOWABLE TOLERANCES, THE MINI-DOME LENS ARRAY OFFERS SIGNIFICANT COST REDUCTION POTENTIAL.

**RADIATION HARDNESS:** THE PANEL CONFIGURATION CAN BE TAILORED TO PROVIDE AN APPROPRIATE LEVEL OF PARTICULATE RADIATION SHIELDING (I.E., ELECTRONS AND PROTONS), MINIMIZING CELL DEGRADATION.

# THE STATUS OF LIGHTWEIGHT PHOTOVOLTAIC SPACE ARRAY TECHNOLOGY BASED ON AMORPHOUS SILICON SOLAR CELLS*

Joseph J. Hanak
Birmingham, MI 48009

and

Jim Kaschmitter
Lawrence Livermore National Laboratory
Livermore, CA 94550

Ultralight, flexible photovoltaic (PV) array of amorphous silicon (a-Si) has been identified as a potential low-cost power source for small satellites. We have conducted a survey of the status of the a-Si PV array technology with respect to present and future performance, availability, cost, and risks. For existing, experimental array "blankets" made of commercial cell material, utilizing metal foil substrates, the BOL performance at AM0 and 35°C includes total power up to 200 W, power per area of 64 W/m$^2$ and power per weight of 258 W/kg. Doubling of power per weight occurs when polyimide substrates are used. Estimated EOL power output after 10 years in a nominal low-earth orbit would be 80% of BOL, the degradation being due to largely light-induced effects (-10 to -15%) and in part (-5%) to space radiation. Predictions for the year 1995 for flexible PV arrays, made on the basis of published results for rigid a-Si modules, indicate EOL power output per area and per weight of 105 W/m$^2$ and 400 W/kg, respectively, while predictions for the late 1990s based on existing U. S. national PV program goals indicate EOL values of 157 W/m$^2$ and 600 W/kg. Cost estimates by vendors for 200 W ultralight arrays in volume of over 1000 units range from $100/watt to $125/watt. Identified risks include the lack of flexible, space compatible encapsulant, the lack of space qualification effort, recent partial or full acquisitions of U. S. manufacturers of a-Si cells by foreign firms, and the absence of a national commitment for a long-range development program toward developing of this important power source for space. One new U. S. developer has emerged as a future potential supplier of a-Si PV devices on thin, polyimide substrates.

## INTRODUCTION

Photovoltaic (PV) arrays serve as very reliable power sources for space application. Recent developments in small satellite technology give rise to several important issues with regard to the use of existing PV arrays. Among them are: the mass of the array, stowed volume, deployability, total power limitation, vulnerability to natural and man-made threats and array cost. Existing arrays for the most part fail to satisfy present small satellite requirements. Stella and Scott-Monck ( ref. 1 ) identified four PV technologies as candidates for advanced photovoltaic space arrays which included (a) thin crystalline silicon (50 µm), (b) thin-layer GaAs CLEFT cells, (c) copper indium diselenide and (d) amorphous silicon (a-Si). Subsequently NASA selected case (a) for a 5 kW prototype demonstration which will result in a deployable and restowable PV array having a beginning-of-life (BOL) specific power of 130 W/kg.

We have conducted a survey with the objective of identifying the best candidate from the preceding four technologies for a PV array for small satellites, having a power output of about 200 W at air mass zero

*This report is based on work sponsored by the University of California, Lawrence Livermore National Laboratory under Contract No. B103159.

(AM0) in normal sun vector at the end of life (EOL) of 10 years in a low earth orbit. Mass limitations of 1 kg for the array and 1 kg for the deployment have been set. It became apparent at the outset that the technical and cost objectives could be possibly best realized with a-Si arrays for a target date in the mid 1990s, hence they became the subject for our survey.

## AMORPHOUS SILICON PHOTOVOLTAIC TECHNOLOGY

The key issues toward a successful product and widespread terrestrial and space application are conversion efficiency and stability, hence their current status will be summarized following a brief review of some aspects of the a-Si solar cell technology.

### Amorphous Silicon Materials and Processes

The semiconductor materials used in a-Si cells are often referred to as a-Si alloys as they consist of a combination of several elements which serve various functions. Thus, hydrogen up to 15% atomic, and fluorine, less than 1%, act as defect passivating agents in the intrinsic, or I-type layer where conversion of photons to photogenerated carriers takes place. Partial substitution of silicon by carbon or germanium widens or narrows the energy gap, respectively, to make the I-layer responsive to a broader spectrum of light. Finally, doping with boron and phosphorus leads to the synthesis of P-type and N-type conductivity layers, respectively, which are needed in the fabrication of solar cell diode structures. The P- and N-type layers can also be made in a microcrystalline form which has certain advantages from the standpoint of higher conductivity and optical transmission. Various thin-film deposition techniques are available, all of which are from the gas phase. The most versatile is plasma-enhanced chemical vapor deposition (PECVD) which is used in large-scale manufacturing. Being amorphous, a-Si alloys do not require epitaxy during the deposition. Hence, they can be deposited on a variety of surfaces, including glass, metals, and high temperature polymers. Deposition on different amorphous or crystalline semiconductors is also possible, which allows fabrication of hybrid diode structures and multijunction solar cells.

### Solar Cell Structures

In its simplest configuration a-Si solar cell consists of an intrinsic (I) layer sandwiched between thin P- and N-type layers. The P-layer is preferably at the front side of the cell, for a more efficient collection of holes, the minority carriers. Transparent conducting metal oxide (TCO), such as indium tin oxide (ITO) is used as the front electrode layer, while a textured metallic layer also known as "back reflector" is used as the rear electrode of the cell.

Multijunction solar cells of a-Si alloys consist of two or more P-I-N cells deposited on top of each other. Each component cell is thinner than a single cell structure, which leads to greater stability. Incorporation of progressively wider bandgap I-type layers from the rear to the front of a multijunction cell structure leads to the absorption of a broader range of the solar spectrum and thereby to enhanced conversion efficiency.

### Conversion Efficiency of a-Si Solar Cells and Modules

Progress in conversion efficiency of a-Si cells and modules worldwide has been summarized most recently by Stone ( ref. 2 ). Selected data appear in Table 1, which shows that the highest efficiency for a-Si cells to date of 13.7% has been obtained with a triple-junction, dual-gap cell structure. A historical progress of the efficiency of cells and modules appears in Fig. 1 which shows that the difference between the efficiency of small cells (1 $cm^2$) and modules (1200 $cm^2$) is shrinking. In the case of Fuji Electric the difference is only 11%, because of good material uniformity, the use of the monolithic structure and laser patterning. Data in Table 1 have been used to calculate the AM0 power at the beginning of life (BOL) output of potential space PV modules. For this purpose the AM1.5 values were multiplied by a factor of 1.25 determined independently by two sources, Gay et al. ( ref. 3 ) and Abdulaziz et al. ( ref. 4 ).

TABLE 1. PERFORMANCE OF AMORPHOUS SILICON SOLAR CELLS AND MODULES AT BOL

| Efficiency* at AM1.5 (%) | Device Area ($cm^2$) | Pmax (W) | **Calculated Pmax at AM0 ($W/m^2$)** | Cell Structure | Source |
|---|---|---|---|---|---|
| Single Junction | | | | | |
| 12.0 | ≤ 1.0 (act) | | **150** | glass/p-i-n (all used a-SiC p-type and a-Si i-type layers) | Hitachi, TDK-SEL, MitsuiToatsu, Osaka University Solarex |
| 11.28 | 1.2 (act) | | **141** | a-Si/polymer | Teijin |
| 9.8 | 933 (ap) | 9.2 | **115** | glass/a-Si | Solarex |
| 6.4 | 1200 (t) | 7.3 | **80** | a-Si/polymer | Teijin |
| 8.4 | 4800 (t) | 40.3 | **105** | glass/a-Si | Fuji Electric |
| 6.4 | 11613 (t) | 74.3 | **80** | glass/a-Si | Chronar |
| Multijunction | | | | | |
| 13.7 | 0.25 (act) | | **171** | a-Si/a-Si/a-SiGe/SS | ECD |
| 12.4 | 1.0 (act) | | **155** | glass/a-Si/a-Si/a-SiGe | Sumitomo |
| 11.3 | 1.0 (act) | | **141** | glass/a-Si/a-Si/a | Fuji Electric |
| 8.4 | 838 (ap) | 6.84 | **105** | a-Si/a-Si/a-SiGe/SS | ECD |
| 9.27 | 940 (ap) | 8.7 | **111** | glass/a-Si/a-Si/a-SiGe | Solarex |
| 10.05 | 1200 (t) | 12.06 | **125** | glass/a-Si/a-Si | Fuji Electric |
| 5.8 | 4104 (t) | 23.9 | **72** | a-Si/a-Si/SS | Sovonics |
| 9.06 | 4800 (t) | 43.5 | **113** | glass/a-Si/a-Si | Fuji Electric |

*Efficiency for (act) active cell area, (ap) aperture area and (t) for total area

Conversion Efficiency of Large, Terrestrial a-Si Arrays

Since mid 1980s amorphous silicon PV arrays have been subjected to field tests with the goal of large-scale utility applications. Numerous arrays with an initial DC power output in the range of 1 to 100 kW have been constructed and are now providing valuable data base on longevity and reliability. A summary of initial and current performance data are given in Table 2 for three selected arrays which are representative of the state of the art. Calculated EOL power output at AM0 is also included to assess the power output of larger potential space arrays, having a power output up to about 22 kW, based on the technology of the late 1980s.

TABLE 2. PERFORMANCE OF LARGE TERRESTRIAL AMORPHOUS SILICON PV ARRAYS*

| BOL Power Rating (kW) | BOL Efficiency (%) | Period of Operation (months) | Power Degradation (%) | **Calculated EOL Pmax at AM0 ($W/m^2$)** | Location of Array | Source & (Substrate or Superstrate) |
|---|---|---|---|---|---|---|
| 17.4 | 5.3 | 21 | 17 | **55** | Florida | ARCO Solar (glass) |
| 4.0 | 4.16 | 38 | 12.5 | **46** | Michigan | Sovonics (stainless steel) |
| 22.0 | 4.0 | 10 | 3.3 | **48** | Maui, HI | Sovonics (stainless steel) |

*Data based on Townsend et al. ( ref. 5 ), Atmaran et al. ( ref. 6 ) and Pratt ( ref. 7 ).

Factors Affecting the Long-Term Performance of a-Si PV Arrays

A-Si solar cells are subject to degradation in power output by exposure to light via the Staebler-Wronski effect. Furthermore, in the space environment, they will be affected by strong ultraviolet light, electron and proton radiation, atomic oxygen and severe temperature cycling. The effects of these ambients on EOL performance are discussed next.

The Staebler-Wronski effect, is marked by a sharp decrease of dark and photoconductivity in a-Si materials upon prolonged exposure to light. In solar cells it is manifested by an asymptotic decrease in conversion efficiency. While early a-Si cells have shown a degradation of as much as 50% in a few days of exposure to light, recent results indicate the first year degradation to be in the range of 10 to 14%. In addition, degradation has been shown to saturate to a constant value within about a year for ground-based modules. Wagner and coworkers ( ref. 8 ) have shown that the limit of degradation is governed by saturated defect density $N_{sat}$ which is independent of light intensity and further illumination. There is a consensus that the most probable causes for the degradation are hydrogen, impurities, nanometer-scale inhomogeneities and strained bonds. Recent improvements in the stability of a-Si cells include a partial replacement of hydrogen by deuterium reported by Suzuki et al. ( ref. 9 ), exposure to intense light followed by annealing reported by Nevin et al ( ref. 10 ), and chemical annealing in hydrogen plasma described by Shirai et al. ( ref. 11 ). The latter leads to a-Si material having reduced hydrogen content and energy gap and a tenfold increase in photoluminescence. In addition to showing a slow photodegradation rate, these materials may be suitable for multi-gap, multijunction cells. The most practical partial cure to date for a-Si cell degradation follows from the work of Hanak and Korsun (ref. 12 ) who observed an inverse relationship of cell stability with cell thickness and a higher stability for multijunction than for single junction cells. Cell degradation is a reversible process which can be annealed by heating the cell above 160$^{o}$C for one or more hours, less at higher temperatures. Furthermore degradation is lower at elevated temperatures. This is quite evident from data on large arrays, such as that reported by Pratt ( ref. 7 ), which show a seasonal variation in efficiency. In space, where array temperatures are expected to be about 80$^{o}$C, compared with a maximum of about 50$^{o}$C for terrestrial arrays, the saturated value of degradation is expected to be about 7 %.

Effect of Electron Irradiation. Effects of 1.0 MeV electron irradiation at fluences of 1E14 to 1E16 have been reported by Gay et al ( ref. 3 ) for a a-Si cell structure consisting of Al/N-I-P/$In_2O_3$/glass. The cells were irradiated at fluences of 1E14 to 1E16 cm$^{-2}$ through 1.1 mm thick glass layer (D. Tanner, private communications). Initial AM1.5 efficiency was given as 8.5%. The degradation in efficiency at a fluence of 1E16 cm$^{-2}$ was 30%, with most of the change occurring in the fill factor, 7% in $V_{oc}$ and 4% in $I_{sc}$. Byvik et al. ( ref. 13 ) with an older, inverted cell structure (the light entering through the N-layer) observed cell efficiency degradations of 7.4, 25 and 99.8%, respectively, at 1.0 MeV fluences of 1E14, 1E15 and 1E16 cm$^{-2}$. The significant differences in radiation damage are due partly to the difference in the cell structure and to partial shielding by glass in the prior case. In both cases a nearly complete recovery of PV efficiency occurred after annealing at 175 to 200$^{o}$C.

Effect of Proton Irradiation. Radiation damage studies of both single junction and tandem a-Si cells with 1 MeV protons at fluences ranging from 1E11 to 1E15 cm$^{-2}$ have been reported by Hanak et al. ( ref. 14 ). The single cells included a-Si and a-SiGe alloy I layers, with $E_g$ of 1.7 and 1.5 eV, respectively. The tandem cells contained same gap, a-Si I-layers. Additional studies by Hanak et al ( ref. 15 and 16 ) included radiation damage with 200 keV protons and with dual-gap, tandem junction cells, containing a-Si and a-SiGe I-type layers. It has been shown that the a-Si dual-gap, tandem cells have 50 to 100 times higher radiation resistance than c-Si or GaAs cells and also higher than InP and $CuInSe_2$ (CIS) cells. It was also shown that the 200 keV protons produced about 5 to 10 times more degradation than 1.0 MeV protons in a-Si alloy cells and that the radiation damage was fully annealable at a modest temperature of 160$^{o}$C. The superior tolerance to proton radiation is believed to be due to primarily the small thickness of a-Si cells and consequently a low number of knockon collisions. A further improvement in radiation resistance of a-Si cells to 1.0 MeV protons has been reported by Payson et al. ( ref. 17 ) who made a side-by side comparison of solar cells fabricated in 1989 with cells of the preceding studies, made in 1985.

Effect of Operating Temperature on a-Si PV Array Performance. Osterwald et al. ( ref. 18 ) have conducted a study of the effect of temperature on PV performance parameters for a variety of crystalline and a-Si solar cells. They have found that the variation of the maximum power output Pmax with increasing temperature is most favorable for a-Si cells, falling off at a rate of only -1320 +/- 105 ppm/$^{o}$C, followed by GaAs at -2300, Si at -4210, and CIS at -5870 ppm/$^{o}$C. This means that at higher operating temperatures in space a-Si array will make substantial gains in power output on other types of arrays.

Effect of Ultraviolet Light on a-Si Solar Cell Performance. U. v. light is converted to electricity by a-Si cells. Besides the Staebler-Wronski effect, no other effects of u. v. light are known. The main concern is the effect of u. v. light on the encapsulation, which still awaits development, in lowering its optical transmission.

Effect of Thermal Cycling on the Longevity of a-Si PV Arrays. Commercial a-Si arrays for ground use have been temperature cycled satisfactorily between -40$^{o}$C and 90$^{o}$C in acceptance testing over several hundred cycles. For space use, several ten thousand cycles are required over a much wider temperature range. With existing a-Si array the concern is about low-temperature printed silver grids, copper busbars utilizing organic adhesives and soldered contacts. Adhesion of encapsulation, still not defined, constitutes another unknown.

Ablation by Atomic Oxygen. For applications in low earth orbit a-Si solar cells and flexible polymeric substrate would be subject to rapid ablation by atomic oxygen. Hence, at least the external layers must consist of a transparent, inorganic material such as silica.

Tolerance to Physical Damage. PV modules on a-Si have been found extremely tolerant to physical damage as reported by Hanak (ref. 19 ). These tests included repetitive rollup (or flex) tests to diameters of 3 cm and penetration by projectiles. Nakatani et al. ( ref. 20 ) have measured the effect of linear elongation on a-Si solar cells on polyimide and found that they can tolerate a strain of up to 0.7%, without damage. Calculations based on this result indicated that a-Si cells encapsulated in a thin flexible material can be bent to a radius of about 0.004 cm without damage.

Bypass Diodes. Bypass diodes are used to protect PV arrays against reverse bias voltage, which occurs when a cell is selectively shaded. The diode is connected across one or more cells. In the case of a-Si tandem cells it has been shown by Hanak and Flaisher ( ref. 21 ) that a bypass diode should be placed across at least every 3 tandem cells (each 5 V). For the monolithic ultralight cells incorporation of diodes externally is cumbersome and counterproductive with respect to array mass. For this case they have developed "integral diodes" which are made of the same material and on the same substrate as the cells. Every cell in the module can be protected individually at the expense of 2% of the cell area and with no additional processing steps.

Estimate of EOL Performance of a-Si Arrays in LEO

Estimates of normallized EOL efficiencies have been calculated for several LEO orbits for a-Si arrays. Only the effects of electron and proton radiation and of Staebler-Wronski effect were considered. Worst-case radiation damage estimates were made for a single-junction PIN a-Si cell consisting of $SiO_2$(5μm)/ITO/P-I-N/Al/St.Steel (20μm). The procedure and the fluence data were based on the JPL Radiation Handbook which gives fluence data relating to crystalline silicon. Equivalent 1.0 MeV electron fluences for trapped electrons and trapped protons were added. The value for the protons was divided by 50, which is the observed factor for the difference in proton-induced damage between c-Si and a-Si. Radiation resistance data for 1.0 MeV electrons of Gay et al. ( ref. 3 ), corrected for glass shielding, were used to predict 1, 5 and 10 year EOL values of normallized efficiency for 3 assumed LEO orbits. The resulting data, presented in Table 3, indicate that for orbits up to 450 nmi and EOL of 10 years space radiation would decrease a-Si array power output only by of 1 to 4.6%. Estimates have been also made for a-Si PV arrays of the EOL power output as percent of the BOL values after combined degradation by light and electron and proton radiation in various LEO orbits. For this purpose an estimated 15% saturated degradation for multijunction a-Si cells due to light was combined with the EOL radiation results for single-junction cells given in Table 3. The resulting EOL power output normallized to the BOL values are shown in Table 4.

TABLE 3. ESTIMATED NORMALLIZED EFFICIENCY OF A PIN AMORPHOUS SILICON CELL vs. TIME FOR SELECTED CIRCULAR ORBITS AFTER COMBINED TRAPPED ELECTRON AND PROTON IRRADIATION

| Time in Orbit (years) | EOL Cell Efficiency (% of BOL) for Various 60° Orbit Heights | | |
|---|---|---|---|
| | 150 nmi | 300 nmi | 450 nmi |
| 1 | 99.0 | 98.7 | 97.8 |
| 5 | 98.2 | 97.3 | 96.2 |
| 10 | 97.9 | 96.8 | 95.4 |
| Equivalent Total1 MeV Electron Fluence ($cm^{-2}year^{-1}$) | 5.96E11 | 1.91E12 | 7.00E12 |

TABLE 4. ESTIMATED EOL NORMALLIZED POWER OUTPUT OF AN AMORPHOUS SILICON PV ARRAY AFTER DEGRADATION BY LIGHT AND ELECTRON AND PROTON RADIATION AT AMO AND 25°C

| Time in Orbit (years) | EOL Array Power Output (% of BOL) for Various 60° Orbit Heights | | |
|---|---|---|---|
| | 150 nmi | 300 nmi | 450 nmi |
| 1 | 84.0 | 83.7 | 82.8 |
| 5 | 83.2 | 82.3 | 81.2 |
| 10 | 82.9 | 81.8 | 80.4 |

Flexible Lightweight a-Si PV Modules and Arrays

Solar arrays of a-Si cells are less than one micrometer thick and utilize about 11 pounds (5 kg) of a-Si per acre. When constructed with thin, flexible substrates and encapsulants, the arrays are very thin, ultralight weight and flexible. One of two types of ultralight arrays made consists of monolithic modules, reported by Hanak ( ref. 19 ) and Hanak et al. ( ref. 15 ). It employs series and parallel cell interconnections in a rectangular matrix of relatively small solar cells. This type of module utilizes an insulating substrate such as polyimide. The modules are fabricated from large sheets of tandem a-Si cells coated in the roll-to-roll processor. The fabrication consists of patterning the layers into cells by masking and etching, screen printing of grids and cell interconnections, application of terminal busbars and encapsulation. For a 2 sq. ft. unencapsulated module, on a 7-μm thick polyimide substrate, specific power of 2.4 $kw/m^2$ has been reported at AM1.5 illumination.

The monolithic lightweight flexible array has been the subject of subsequent development effort at Energy Conversion Devices, Inc., sponsored by the SDIO under a Phase II SBIR contract NAS3-25458. Data for the monolithic array developed in this program are given in Table 5. Currently, NASA-funded development of monolithic a-Si space array is taking place at Iowa Thin Film Technologies, Inc., under SBIR Phase II contract No. NAS3-26244.

The second type of lightweight, flexible a-Si PV array consisting of "giant cells" has been reported by Hanak et al ( ref. 22 ). These cells utilize a stainless steel substrate, thinned by etching to 20 μm. The PV array consisted of 20 cells 1566 $cm^2$ each in area and had a power output of 207 W at AM0. Data on this type of an array, the UL-200, are given in Table 6.

TABLE 5. CHARACTERISTICS OF ECD ULTRALIGHT AMORPHOUS SILICON PHOTOVOLTAIC ARRAY DEVELOPED UNDER CONTRACT NAS3-25458

Design characteristics

| | |
|---|---|
| Aperture area | 0.49 $m^2$ |
| Mass | 137 g |
| Substrate | Kapton |
| Front encapsulation | Tefzel (Dupont) |
| Rear encapsulation | Thin Cr film over Kapton substrate |
| Array design | Consisting of 36 monolithic submodules |

Calculated BOL and estimated 10 year EOL power output at AMO and 25°C

| | BOL | EOL |
|---|---|---|
| Power output (W) | 30.4 | 24.8 |
| Power per weight (W/kg) | 222 | 181 |
| Power per area ($W/m^2$) | 62 | 51 |

TABLE 6. CHARACTERISTICS OF UL-200 LIGHTWEIGHT FLEXIBLE AMORPHOUS SILICON PHOTOVOLTAIC ARRAY ( REF. 22 )

Design characteristics

| | |
|---|---|
| Size (deployed) | 2.92 m x 1.11 m x 0.01 cm |
| Size (stowed) | 1.11 m (length) x 6.3 cm (diameter), roll |
| Mass | 800 g |
| Substrate | stainless steel, 0.002 cm thick |
| Encapsulation* | polyester, 0.0038 cm, both sides |
| Array design | 20 "giant cells" in series, each 1566 $cm^2$ in area, each protected with bypass diodes |

BOL and estimated 10 year EOL power output at AMO and 35°C for a 300 nmi, 60° orbit

| | BOL | EOL** |
|---|---|---|
| Power output (W) | 207 | 169 |
| Power per weight (W/kg) | 258 | 211 |
| Power per area ($W/m^2$) | 64 | 52 |

*This encapsulation is not space compatible.

**Projected values for an array having a top encapsulation of 5μm of $SiO_2$.

Projections for Ligtweight a-Si PV Arrays Based on Existing Results

Data in Table 1 for modules 0.08 to 1.2 $m^2$ (1 to 12.5 $ft^2$) in area are used as a basis for projecting 1995 performance for small space arrays, having a power output of about 200 W. The projected BOL power output ranges from 72 to 125 W/ $m^2$. Higher values of up to 171 $W/m^2$ for small cells indicate that arrays up to 152 $W/m^2$ are possible (using a derating factor of 11%). The data for cells on polymer substrates indicate a BOL value of 141 $W/m^2$, close to the best value of 150 $W/m^2$ for a similar cell on a glass substrate, which indicates that power per area for ultralight flexible devices should approach those on rigid substrates. Based on these results a conservative BOL value of 130 $W/m^2$ is projected for ultralight, flexible arrays for 1995. A summary of other performance parameters and 10 year EOL data for LEO is given in Table 7.

TABLE 7. FORECAST FOR 1995 BOL AND EOL PV PERFORMANCE FOR 200 W ULTRALIGHT FLEXIBLE A-Si ARRAYS BASED ON 1990 DATA FOR SOLAR CELLS AND MODULES

| | BOL | EOL |
|---|---|---|
| Power output (W) | 244 | 200 |
| Power per area ($W/m^2$) | 130 | 105 |
| Power per weight (W/kg) | 500 | 409 |
| Deployed area ($m^2$) | 1.88 | 1.88 |
| Mass (kg) | 0.5 | 0.5 |

TABLE 8. DEVELOPERS AND MANUFACTURERS OF AMORPHOUS SILICON PV DEVICES

| Organization | Kind | Type of PV Product | | | | Comments |
|---|---|---|---|---|---|---|
| | | Rigid | Flexible | Single | Tandem | |
| ARCO Solar | M | x | | x | | Sold in 2/90 to Siemens Solar Industries |
| Chronar | M | x | | x | | Chapter 11 |
| Solarex | M | x | | x | x | See Table 1 |
| UPG | M | x | | | x | |
| Energy Conversion Devices/Sovonics Solar Systems | M | | x | | x | Ceased mfg. in '90; formed partnerships with Soviet# and Japanese* firms. |
| (*) United Solar Systems Systems | M | | x | | x | To start mfg. in mid '91 in former, upgraded Sovonics plant in Troy, Michigan. |
| (#) Sovlux (USSR) | M | | x | | x | A plant for a-Si dual-gap, triple-junction cells is being built by ECD for manufacture in the USSR. |
| Center for Amorphous Semiconductors Inc. (CASI) (Iowa State University) | D | | x | x | x | A roll-to-roll pilot plant operational in 1991. |
| Iowa Thin Film Technologies, Inc. | D | | x | x | x | Contractor for CASI; also for space PV development. |
| Teijin | D | | x | x | | See Table 1. |
| Fuji Electric | D | x | | x | x | See Table 1. |
| Kanegafuchi Chemical | M | x | | x | | |
| Sanyo Electric Co. | M | x | | x | | Has made flexible cells for an experimental manned airplane |
| Hitachi, Ltd. | D | x | | x | x | |

Projections Based on Nationally Funded PV Programs.

Both USA and Japan have maintained a substantial support for more than a decade toward the development of low-cost, thin-film photovoltaics as a potential power fource for the future. The FY 1993 SERI goals call for 10% and 13% stabilized AM1.5 efficiency for same-gap and multiband-gap multijunction, large-area (>900 $cm^2$), a-Si modules, respectively. Somewhat less ambitions goals for 1992 exist for Japan's NEDO program. The SERI goals translate to an EOL power output at AM0 of 121 and 157 $W/m^2$, for same-gap and different-gap cells, respectively, after 10 years in a circular, 300 nmi, $60^o$ orbit, which includes degradation by light and radiation. At this point it is too early to forecast successful fabrication of lightweight flexible arrays based on these goals.

## AVAILABILITY OF FLEXIBLE LIGHTWEIGHT a-Si PHOTOVOLTAIC ARRAYS

To date, most of the a-Si PV products have been made for terrestrial applications. For space use, suitable materials are preferably tandem-junction cells deposited on high temperature polymer substrates such as polyimide, or metal foil, or on polyimide-coated metal foil. Cells deposited on glass substrates are not suitable because of excessive mass. Manufacturing processes consist of two general types, one being deposition on discrete areas such as glass plates, the other being a roll-to-roll process suitable for long, continuous flexible substrates supplied on a roll. Table 8 lists the manufacturers (M) and developers (D) in the USA and abroad who have a near-term capability of a limited production and who have been contacted for this survey. Table 8 identifies five manufacturers or developers having past or future capability of producing lightweight, flexible a-Si cells by the roll-to roll process.

## PROJECTED COST OF FLEXIBLE LIGHTWEIGHT a-Si PHOTOVOLTAIC ARRAYS

Estimated cost and delivery data in Table 9 on 200 W, lightweight, flexible a-Si arrays have been provided by one manufacturer in early 1990. Although this data is no longer relevant, it is to be noted that in large quantities, the manufacturer projected cost of a-Si arrays was about one order of magnitude less than existing crystalline arrays.

TABLE 9. PROJECTED COST AND DELIVERY FOR 200 W LIGHTWEIGHT a-Si PV ARRAYS

| Number of arrays | 1 Prototype | 10-99 | 100-999 | 1000+ |
|---|---|---|---|---|
| Delivery of 1st unit (months) | 4 | 6 | 12 | 24 |
| Delivery per month | 1 | 10-50 | 100 | 100 |
| Estimated unit cost ($/W) | 500 | 200 | 150 | 100 |

## REFERENCES


1. Paul Stella and J. Scott-Monck, Proc. Ninth Space Photovoltaic Research and Technology (SPRAT) Conf., NASA CP-2475, 1986, p.145.

2. Jack Stone, "Recent Advances in Thin-Film Solar Cells", Tech. Digest Int'l. Photovoltaic Solar Energy Conf.-5 (PVSEC-5), Kyoto, Japan, Nov. 26-30, 1990.

3. C. F. Gay, R. R. Potter, D. P. Tanner and B. E. Anspaugh, Proc. 17th IEEE Photovoltaic Specialists Conf., 1984, p. 151.

4. Salman Abdulaziz, J. Scott Payson, Yang Li, and James R. Woodyard, Proc. 21st IEEE Photovoltaic Specialists Conf., 1990, p. 1510.

5. T. Townsend and P. Hutchinson, Photovoltaic Module Reliability Workshop, Lakewood, CO, Oct. 25-26, 1990, vol. SERI/CP-4079, p.1.

6. G. Atmaran and Bill Marion, Ibid., p.25.

7. R. G. Pratt, Ibid., p. 53.

8. M. Isomura, X. Xu and S. Wagner, Tech. Digest Int'l. PVSEC-5, Kyoto, Japan Nov. 26-30, 1990.

9. A. Suzuki, G Ganguly, K. Nomoto, Y. Takeuchi, Y. Urano, J. Guizot, S. Yamasaki, H. Matsuura, H. Oheda, and A. Matsuda, Abstracts of the Jpn. Soc. Appl. Phys. Spring Meeting No. 37, Tokyo 1990, pp. 705, 706.

10. W. A. Nevin, H. Yamagishi, K. Asaoka, H. Nishino, and Y. Tawada, Abstracts of the 22nd Conf. Solid Devices and Materials, Sendai 1990, p.693.

11. H. Shirai, D. Das, J. Hanna and I. Shimizu, Tech. Digest Int'l. PVSEC-5, Kyoto, Japan, Nov. 26-30, 1990.

12. J. J. Hanak and V. Korsun, Proc. 18th IEEE Photovoltaic Specialists Conf., 1982, p. 1381.

13. C. E. Byvik, W. S. Slemp, B. T. Smith and A. M. Bonchristiani, Proc. 17th IEEE Photovoltaic Specialists Conf., 1984, p.155.

14. J. J. Hanak, A Myatt, P. Nath, and J. R. Woodyard, Proc. 18th IEEE Photovoltaic Specialists Conf., 1985, p. 1718. (The paper erroneously listed the tandem-junction cells as dual-gap cells with an a-Si,Ge:H,F bottom cell. The cells were a-Si:H,F single bandgap cells.)

15. J. J. Hanak, Englade Chen, C. Fulton, A. Myatt and J. R. Woodyard, Proc. 8th Space Photovoltaic Research and Technology Conf., 1986, vol. NASA Conf. Publication 2475, p. 99, 1986.

16. J. J. Hanak, E. Chen, A. Myatt, and J. R. Woodyard, Proc. 19th IEEE Photovoltaic Specialists Conf., 1987, p. 630.

17. J. S. Payson, S Abdulaziz, Y. Li and J. R. Woodyard, Proc. Tenth Space Photovoltaic Research and Technology (SPRAT) Conf., 1989, vol. NASA Conference Publication 3107, p. 389.

18. C. R. Osterwald (SERI), T. Glatfelter and J. Burdick (ECD), Proc. 19th IEEE Photovoltaic Specialists Conf., 1987, p.188.

19. J. J. Hanak, Proc. 18th IEEE Photovoltaic Specialists Conf., 1985, p.89.

20. K. Nakatani, M. Ogasawara, K. Suzuki, and H. Okaniwa, Applied Physics Letters vol. 54, 1989, p.1678.

21. J. J. Hanak and H. Flaisher, Proc. Tenth Space Photovoltaic Research and Technology (SPRAT) Conf., 1989, vol. NASA CP-3107.

22. J. J. Hanak, Lee Walter, David Dobias and Harvey Flaisher, DGLR/AIAA.JSASS 20th nternational Electric Propulsion Conf. Proceedings, Garmisch-Partenkirchen, W. Germany, 1988, p.121.

23. M. Yano, K. Suzuki, K Nakatani, and H. Okaniwa, Thin Solid Films vol.146, p. 75.

24. K. Nakatani, K. Suzuki and H. Okaniwa, Solar Energy Materials vol. 17, 1988, p. 265.

25. K. Nakatani, K. Suzuki, H. Okaniwa, and S. Sobajima, Technical Digest of International PVSEC-4, Australia, 1989, p.639.

# REVERSE BIAS VOLTAGE TESTING OF 8 CM X 8 CM SILICON SOLAR CELLS

T. Woike, S. Stotlar, C. Lungu
Applied Solar Energy Corporation
City of Industry, CA

## ABSTRACT

This paper describes a study of the reverse I-V characteristics of the largest space-qualified silicon solar cells currently available (8 cm x 8 cm) and of reverse bias voltage (RBV) testing performed on these cells. This study includes production grade cells, both with and without cover glass. These cells span the typical output range seen in production. Initial characteristics of these cells are measured at both 28°C and 60°C. These measurements show weak correlation between cell output and reverse characteristics. Analysis is presented to determine the proper conditions for reverse bias voltage stress to simulate shadowing effects on a particular array design. After performing the reverse bias voltage stress the characteristics of the stressed cells are remeasured. The degradation in cell performance is highly variable which exacerbates cell mismatching over time. The effect of this degradation on array lifetime is also discussed. Generalization of these results to other array configurations is also presented.

## I. INTRODUCTION

The use of large area solar cells in solar arrays for space applications has become more pervasive as the fabrication technology and the cost-effectiveness of these cells improve. These large cells are more defect prone than smaller cells of equivalent defect density. This results in an adverse effect on the reverse current - voltage (I-V) characteristics of the cells. These characteristics become important during periods of partial shadowing in solar arrays that do not incorporate shunting or bypass diodes. The impact of the quality of cell reverse I-V characteristics on the cell lifetime is manifested as the well-known "hot spot" effect (Blake,1969). Reverse bias voltage stress testing is a standard technique that is used to simulate the effects of shadowing when investigating cell lifetime under shadowed conditions (Rauschenbach, 1972).

The objectives of this study were to determine the relationship between cell output and reverse I-V characteristics, if any, and to examine the effects of shadowing on cell forward and reverse I-V characteristics when installed into a particular array configuration without the benefit of bypass diodes.

A number of silicon 8 cm x 8 cm solar cells were obtained from the production line. These were Class I Electrical cells. One-fourth of these cells had cover glass applied, and the remainder were unglassed. The AM0 output data of these cells were measured in production. The reverse characteristics of these cells were later measured at both 28°C and 60°C. These data sets are discussed in Section II.

An analysis was performed to establish the bias conditions that would be produced on a shadowed cell in the array. This analysis required the use of the physical and electrical layout of the array design, the forward and reverse I-V data of the cells, and some assumptions about the size, location, and duration of shadows. The shadowing analysis is presented in Section III.

Reverse bias voltage (RBV) stress testing was then performed on a number of cells. The cells that were used in this phase of the study were chosen to provide a distribution of initial output levels and reverse characteristics. Prior to RBV the cells chosen for the sample were measured for output at $10 mW/cm^2$ (2800°K source). Each cell was then stressed at a reverse bias voltage that was based on the cell's individual reverse characteristics. This relationship was determined from the shadowing analysis. Various stress durations from a minimum of 2 minutes to a maximum

of 48 hours were used. After RBV stress testing, the output was remeasured at 10 $mW/cm^2$ and the resulting degradation analyzed. The results of the RBV stress testing are discussed in Section IV.

## II. INITIAL CELL CHARACTERISTICS

### Cell Distribution among Output Groups

132 silicon 8 cm x 8 cm solar cells were obtained from production. These were Class I Electrical cells. One-fourth of these cells had cover glass applied, and the remainder were unglassed. The AM0 output data of these cells were measured in production. The distribution of cells among the output groups is shown in Figure 1. The definition of these groups is provided in Table 1.

### Initial Reverse I-V Characteristics

The reverse characteristics of these cells were measured at both 28°C and 60°C. The results are given in Figures 2 and 3, respectively. Each figure shows the I-V data for the best and worst cells, along with the median cell. This information is presented for both glassed and unglassed cells. Near ambient temperature (Figure 2), the glassed cells exhibit significantly more leakage than their unglassed counterparts. The worst glassed cell is about a factor of four leakier than the worst unglassed cell, the median glassed cell is roughly a factor of three leakier than the median unglassed cell, and the best glassed cell is nearly two orders of magnitude leakier than the best unglassed cell. At slightly elevated temperature (Figure 3), the glassed and unglassed leakage characteristics become nearly indistinguishable, with a typical glassed cell only 25% leakier than an unglassed one. In fact, the leakage of all three benchmark cells (best, worst, median) actually decreases as the cell temperature is increased from 28°C to 60°C. This behavior may be due to residual contamination from the clean performed on the cells prior to glassing. The 60°C leakage current data is more germane to operation in a solar array, provided that power dissipation of a reverse-biased cell is small, as defined in the next paragraph.

Neglecting the effects of power dissipated in the array interconnect and the cell metallization, the temperature of a cell will remain the same when it is shadowed if the additional power dissipation from the reverse-biased condition exactly balances the loss of power absorbed from illumination. If the front-facing absorptance is 0.4, then 3.46 W may be dissipated by a shadowed cell without affecting cell temperature, assuming only radiative heat loss.

### Relationship of Initial Cell Reverse Characteristics to Initial Output

The relationship of cell reverse electrical characteristics at 60°C to the output is shown in Figures 4 and 5 with both glassed and unglassed cells identified separately. Figure 4 shows the dark reverse leakage current $I_{dr}$ for all the cells included in this study as a function of cell group number. $I_{dr}$ was measured at 1 V. Figure 5 depicts the reverse breakdown $V_{br}$ as a function of cell group number at a dark reverse current of 1 A. All measurements were taken instantaneously so that the cell would not have time to heat.

There seems to be a rather weak correlation between reverse characteristics and output. The higher group cells generally have better reverse characteristics: lower leakage current and higher breakdown voltage. This is expected since the defects that contribute to the leakage current (bulk and surface defects) will also cause a lower minority carrier lifetime, resulting in lower cell output. Although this general trend is observed in the data, there is a great deal of variability in the data ($r^2 < 0.2$), so there are also other significant factors involved (for example, perimeter defects).

## III. SHADOWING ANALYSIS

A worst-case analysis was performed to establish the bias conditions that would be produced on a shadowed cell in the array. This analysis was performed for an array that uses series strings of 120 cells. The following assumptions were made about the solar array and various conditions which affect it. All cells in the array are assumed to have identical electrical characteristics. All series strings of solar cells are assumed to be connected directly to the bus, so that all strings have the same voltage. Resistive losses in the cell and array interconnect are assumed negligible.

A shadow is assumed to not affect the array voltage. The cells in fully illuminated strings are assumed to be biased at the maximum power level. The shadow is assumed to cover the area of a single cell only, since this results in the worst-case reverse bias across the shadowed cell (Blake, 1969). The shadow is assumed to persist long enough to allow the shadowed cell to reach steady-state temperature.

Figure 6 shows the 28°C and 60°C output characteristics that were used for the cells. The cell output parameters are also tabulated in Figure 6. Based on the above assumptions, if the array is operating at 60°C, each illuminated cell will supply 0.438 V, leading to a voltage $V_a$ = 52.6 V across a fully-illuminated string of 120 cells in series. This voltage will also appear across a partially-shadowed string according to the assumptions. This information along with the reverse characteristics of a shadowed cell can be used to determine the voltage and current levels in the shadowed string (Rauschenbach, 1972) as demonstrated in Figure 7. The bias point is determined by the intersection of the characteristics of the 119 illuminated cells with the reverse characteristics of the shadowed cell offset by $V_a$. The cell reverse characteristics at 60°C (Figure 3) are represented by the relation $I = CV^{1.02}$ where C is the leakage current measured at -1 V.

The bias point for the single shadowed cell was determined for various array configurations as a function of cell leakage current at -1 V using the above technique. The results of this analysis are presented in Figure 8.

## IV. REVERSE BIAS VOLTAGE (RBV) STRESS TESTING DISCUSSION AND RESULTS

Reverse bias voltage (RBV) stress testing was performed on a number of cells. The cells that were used in this phase of the study were chosen to provide a good representation of initial output levels and reverse characteristics. Prior to RBV the cells chosen for the RBV sample were measured for output at 10mW/cm$^2$ (2800°K source). This source was chosen because of better availability than the AM0 simulator. The relation of Figure 8 was used to determine the appropriate stress voltage for each cell.

### Short-term RBV Stress

Six cells, four glassed and two unglassed, were subjected to RBV for a series of short duration stresses. Two of these cells underwent a series of three stresses, another two underwent two stresses, and the final two underwent only one stress. The durations of these stresses were such that the total stress times on the cells at the readpoints were 2 minutes, 10 minutes and 40 minutes. After each RBV stress, the output was remeasured at 10 mW/cm$^2$. The results of the changes in $I_{sc}$, $V_{oc}$, and power output are given in Figures 9 through 11, respectively. The changes in $I_{sc}$ dominate the changes in power output of the cells. $V_{oc}$ changes relatively little. At the end of 40 minutes of total stress, all six cells had degraded in power output, with the changes ranging from 2% to 16%. Some cells apparently exhibited stages of healing, perhaps through some sort of self-annealing, but the level of improvement never exceeded the measurement reproducibility.

### Long-term RBV Stress

Thirteen different cells were subjected to long-term RBV stress, seven for two hours and the other six for 48 hours. This study was performed to extend the stress duration significantly beyond the usual level (Williams, 1984) and develop a lifetime model for shadowed cells. The post-stress characteristics appear in Figures 12 through 16. The short-term RBV results discussed above have been included in these figures for completeness. As before the output changes are determined mostly by $I_{sc}$ changes, with $V_{oc}$ changes being relatively minor. The unglassed cells show a definite trend toward long-term degradation, as do the glassed cells with the notable exception of three cells that underwent the 48 hour RBV stress and improved slightly from their pre-stress output levels.

Six of the 19 cells studied had their output power degrade by more than 25%, half after 2 hours total stress and the other half after 48 hours stress. Half of these cells were glassed and half were unglassed.

These same six cells also had their reverse breakdown voltage degrade by more than 50%. Three cells (all unglassed) had their reverse leakage current degrade by greater than a factor of ten. The leakage current of the

glassed cells probably did not degrade as rapidly because they have a significant strain-induced leakage component which is not affected by RBV stress aging.

Relationship of Output Degradation to Initial Output

The relationship between cell output degradation and the initial output is demonstrated in Figure 17. It does appear more likely for a higher output cell to undergo more rapid output degradation. This effect has been previously observed (Rauschenbach, 1972) and may be attributed to the higher voltage at which these cells are stressed per Figure 8.

Relationship of Output Degradation to Initial Leakage

The relationship between cell output degradation and the initial leakage was examined since a potential relation between the initial cell output and the leakage had been noted. The power degradation is plotted against the initial cell leakage in Figure 18. The power degradation exhibits a moderate relationship to the initial leakage current level, with the lower leakage cells having more rapid output degradation. This result provides additional validation for the behavior presented in the previous section.

Relationship of Change of Reverse Characteristics to Initial Output

The relationship between the change of cell reverse characteristics and the initial cell output level was also examined because it could help corroborate the results of the previous sections. The results as shown in Figure 19 indicate that the cells having lower output do not degrade as quickly as the better cells.

Relationship of Output Degradation to Change of Reverse Characteristics

Having noted that the poorer cells both in the forward and reverse directions fare better during RBV stress testing, the change in reverse cell characteristics due to RBV was examined to see if this could be used as a predictor of output degradation. The results are presented in Figure 20. A moderate correlation does exist between the change in power output and the change in reverse leakage current, with an increase in leakage indicating a decrease in power output. However these data have a sufficient amount of scatter to preclude any hope of using change in $I_{dr}$ as the only measure of cell degradation without having to perform the output test.

Predicted Lifetime of Shadowed Cell

A simple model for the lifetime of a shadowed cell was developed from a regression performed on the output power degradation data. The results are shown in Figure 21. Selected values from this data set are given in Table 2. Unglassed cells will reach half power with a mean time to occurrence of 116 hours (0.7 weeks) of shadow while the equivalent value for glassed ones is 497 hours (3.0 weeks) of shadow. When the variability of the data is considered, the earliest time ($-3\sigma$) to degrade to the half power level is 15.7 minutes of shadow for glassed cells and 44.6 minutes of shadow for unglassed cells. This model can aid in the prediction of array lifetime when combined with shadowing patterns, end-of-life power requirements and other system-level information.

## V. CONCLUSIONS

A study of the behavior of 8 cm x 8 cm silicon solar cells under worst-case shadowing conditions was performed for a particular solar array without the benefit of bypass diodes. This study involved analyzing the bias conditions expected to be generated by shadowing and the subsequent RBV stressing of production grade solar cells consistent with the shadowing analysis.

Approximately 32% of the cells that underwent RBV stress testing degraded significantly. This strongly indicates the reliability benefits of incorporating bypass diodes into the design of space-based solar arrays.

With some exceptions, RBV stress testing degraded solar cell output between 2% and 59%. The level of degradation is highly variable and indicates that an initially perfectly matched string of solar cells will become unmatched over time. Furthermore, this variability may be understated since the harsh space environment could not be fully reproduced in this study. A few cases of increases in output after RBV stress testing were observed, but even these may be considered undesirable because this further disturbs the cell matching characteristics of the array.

Glassed cells were predicted to degrade to half power with a mean time to occurrence of 497 hours of shadow while unglassed cells will do so after 116 hours. Initial ($-3\sigma$) occurrences are predicted after 15.7 and 44.6 minutes of shadow for glassed and unglassed cells, respectively.

There is a rather weak relationship between the initial reverse characteristics of a cell and that cell's initial output, with the higher output level cells having better reverse characteristics. This correlation is too weak to permit a prediction of cell output performance from its reverse characteristics.

Cell output is inversely related to degradation level from RBV stress testing. Cells having higher output degraded more rapidly than lower output cells. Also cell output and reverse characteristics appear to be correlated both in initial values and change levels. Cells having poorer reverse characteristics did not degrade as rapidly as better cells. These results may be due to the lower voltage levels at which the poorer cells are stressed.

Reverse voltage on a shadowed cell is greatly dependent on the cell's reverse characteristics in high voltage arrays, but in low voltage arrays the reverse voltage is nearly independent of cell reverse characteristics. The highest stress voltage is generated on low leakage cells in high voltage arrays.

The correlation between reverse change and output change was not observed to be strong enough to obviate the need for a cell output test when evaluating cell degradation.

Shadowing on a solar array which does not utilize bypass diodes is predicted to create a permanent output mismatch in a string of cells and exacerbate this mismatch over time. This effect is accelerated in high-voltage arrays since the bias levels on shadowed cells are higher. This undesirable and somewhat unpredictable effect can be avoided by incorporating bypass diodes into the design of solar arrays.

## REFERENCES

Blake, F.A., and K.L. Hanson. 1969. The "Hot-spot" Failure Mode for Solar Array. Proceedings of the IECEC. pp. 575-581.

Rauschenbach, H.S., and E.E. Maiden. 1972. Breakdown Phenomena in Reverse Biased Silicon Solar Cells. Proceedings of the Ninth IEEE Photovoltaic Specialists Conference. pp. 217-225.

Williams, R.D., G.S. Goodelle, and N. Mardesich. 1984. Solar Cell Reverse Bias Testing to meet New Cell Technology and Satellite Applications Demands. Proceedings of the Seventeenth IEEE Photovoltaic Specialists Conference. pp. 306-309.

TABLE 1

*Solar Cell Output Groups*

Output Current
$I_L$ Measured @ 0.495 V; 28°C

| Group | Minimum $I_L$ (mA) | Maximum $I_L$ (mA) |
|---|---|---|
| 1 | 2217 | 2253.9 |
| 2 | 2254 | 2290.9 |
| 3 | 2291 | 2327.9 |
| 4 | 2328 | 2364.9 |
| 5 | 2365 | 2401.9 |
| 6 | 2402 | 2438.9 |
| 7 | 2439 | 2475.9 |
| 8 | 2476 | 2512.9 |
| 9 | 2513 | 2549.9 |
| 10 | 2550 | None |

TABLE 2

Predicted Total Shadow Time to Degrade
Shadowed Cells to Specified Power Level

(120 cells in a string)

| | Glassed | | Unglassed | |
|---|---|---|---|---|
| Normalized Power | Earliest Predicted Occurrence | Mean Time to Occurrence | Earliest Predicted Occurrence | Mean Time to Occurrence |
| 1.00 | 0.0 hr | 0.0 hr | 0.0 hr | 0.0 hr |
| 0.75 | 0.1 min | 4.3 hr | 1.5 min | 3.9 hr |
| 0.50 | 15.7 min | 497.4 hr | 44.6 min | 116.1 hr |
| 0.25 | 30.6 hr | 6.6 yr | 22.0 hr | 0.4 yr |

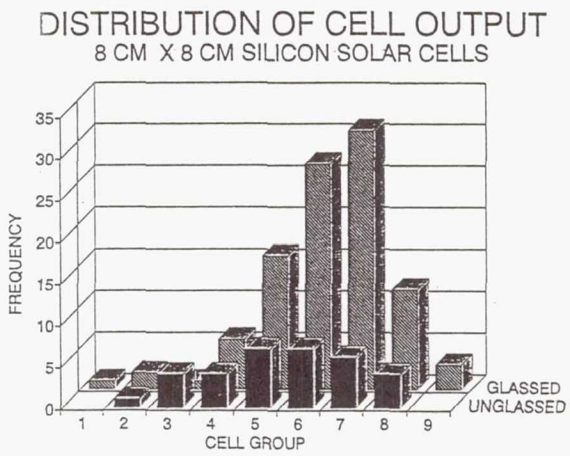


FIGURE 1

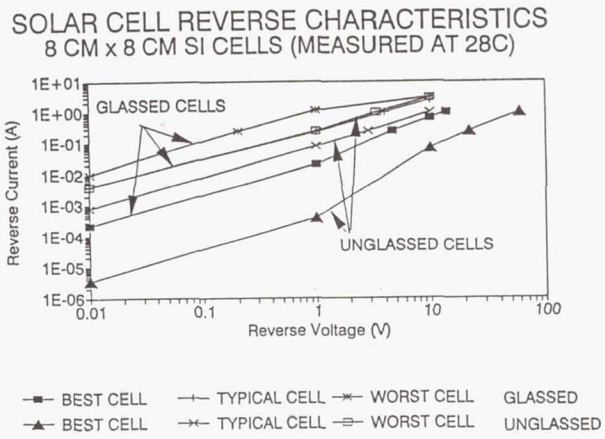


FIGURE 2

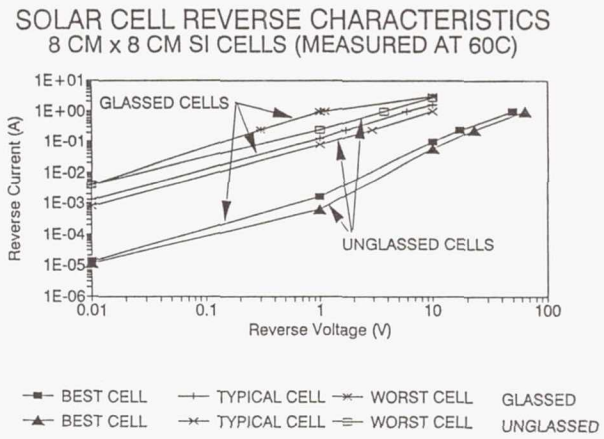


FIGURE 3

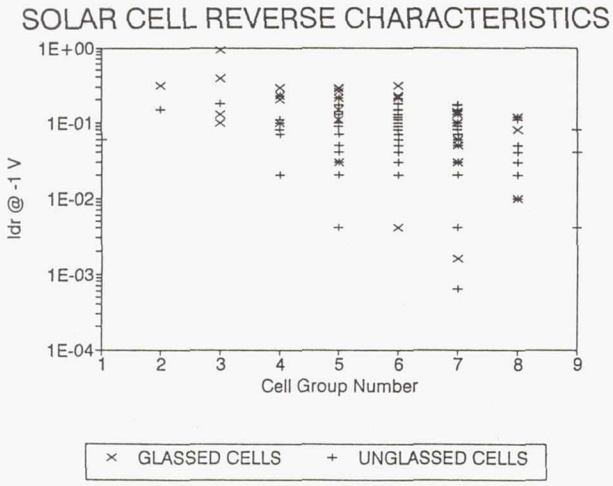


FIGURE 4

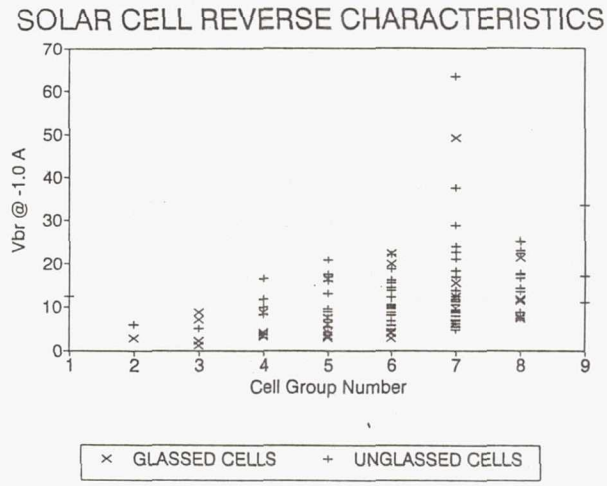


FIGURE 5

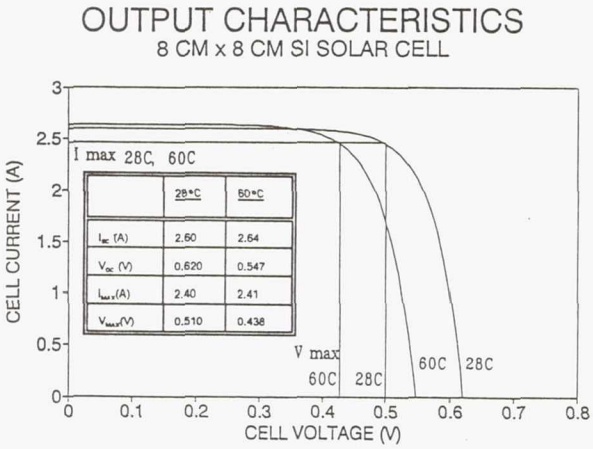


FIGURE 6

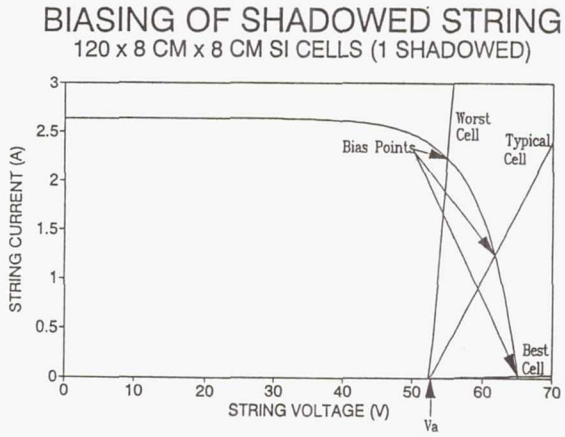


FIGURE 7

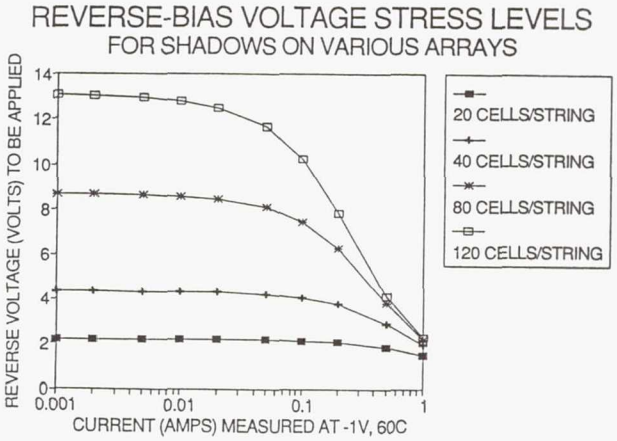


FIGURE 8

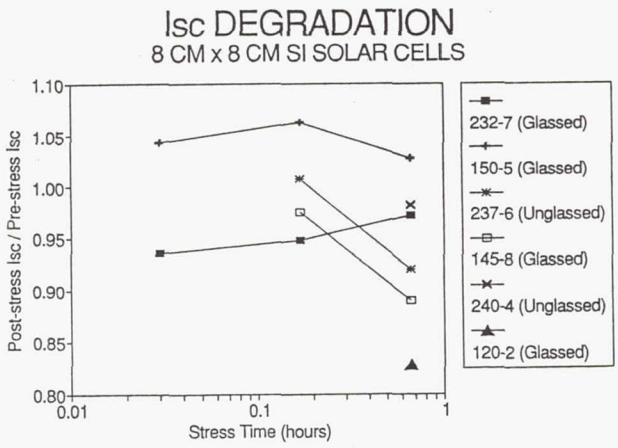


FIGURE 9

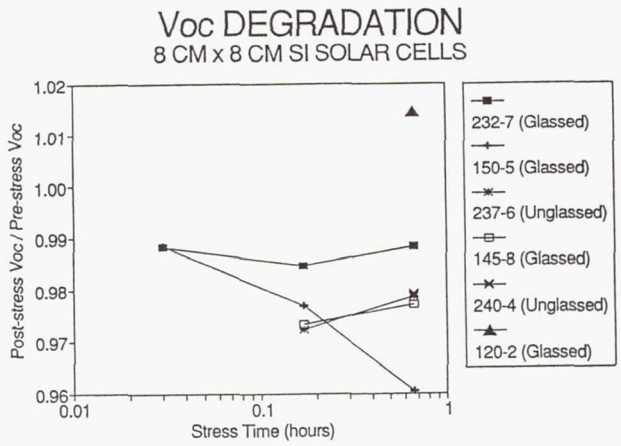


FIGURE 10

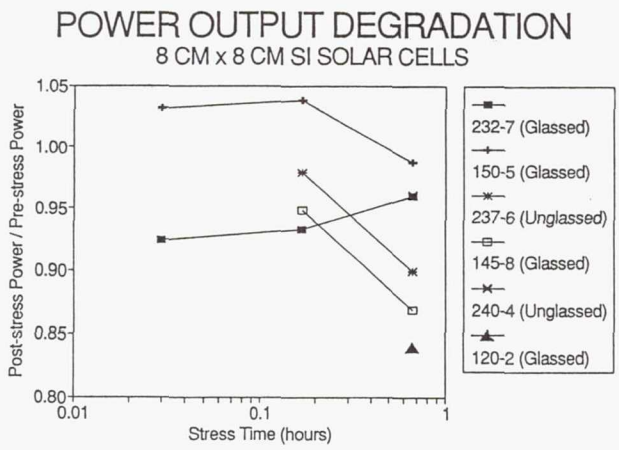


FIGURE 11

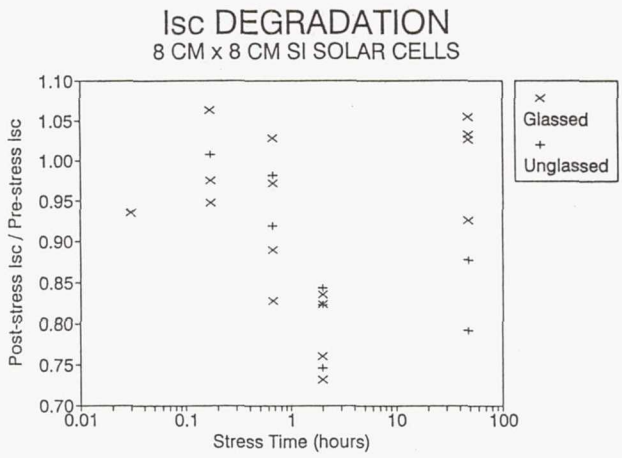


FIGURE 12

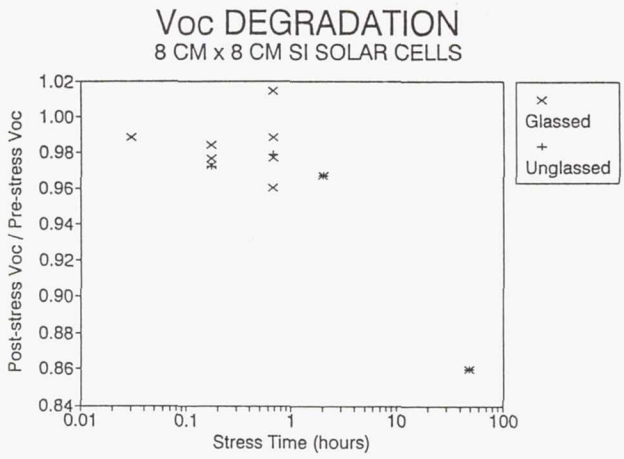


FIGURE 13

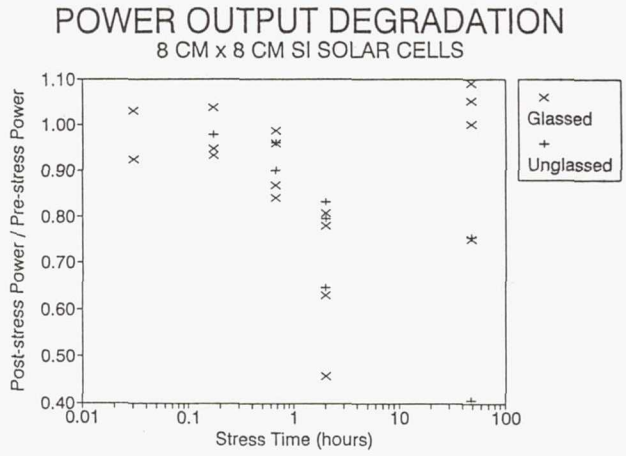


FIGURE 14

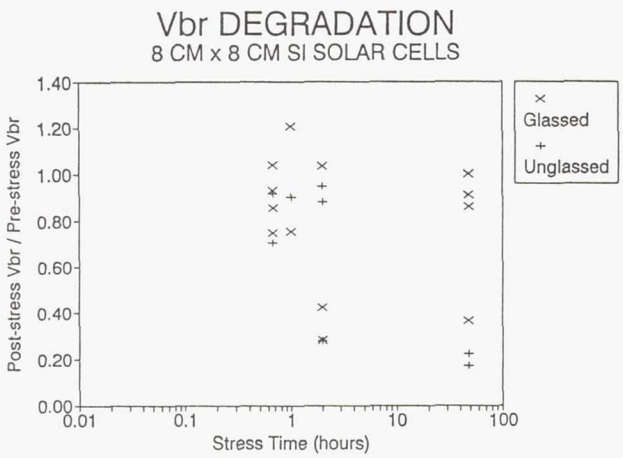


FIGURE 15

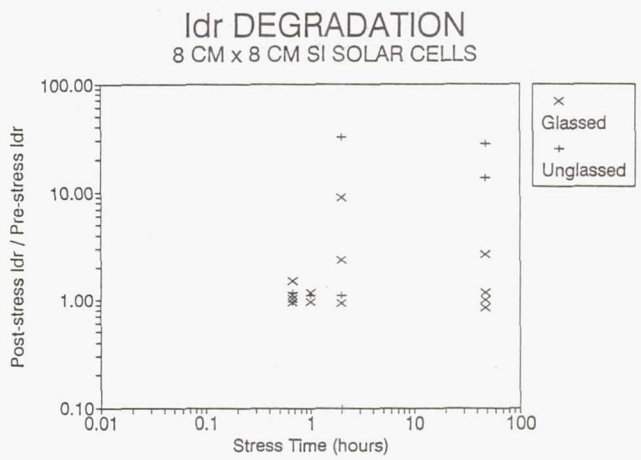


FIGURE 16

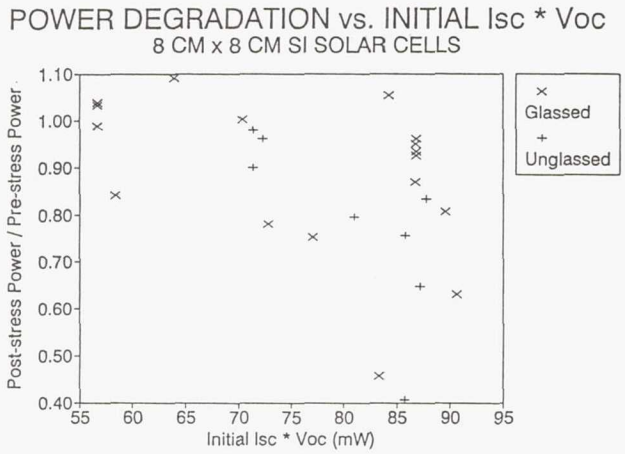


FIGURE 17

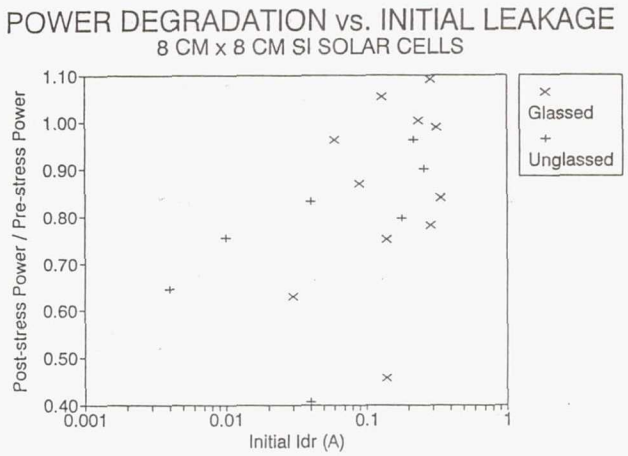


FIGURE 18

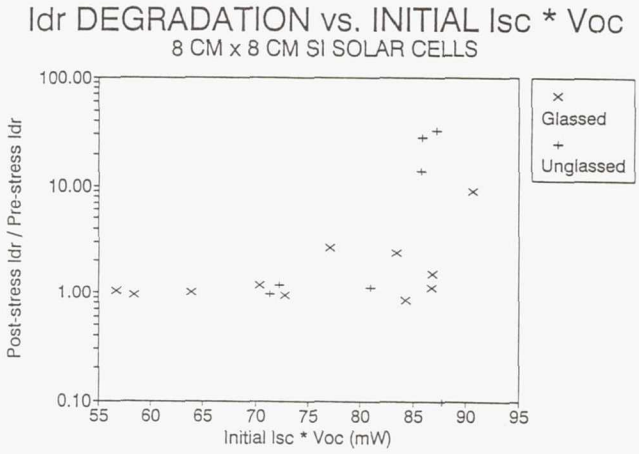


FIGURE 19

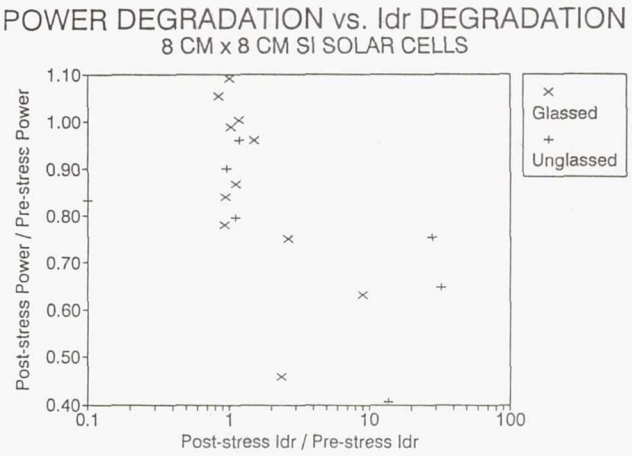


FIGURE 20

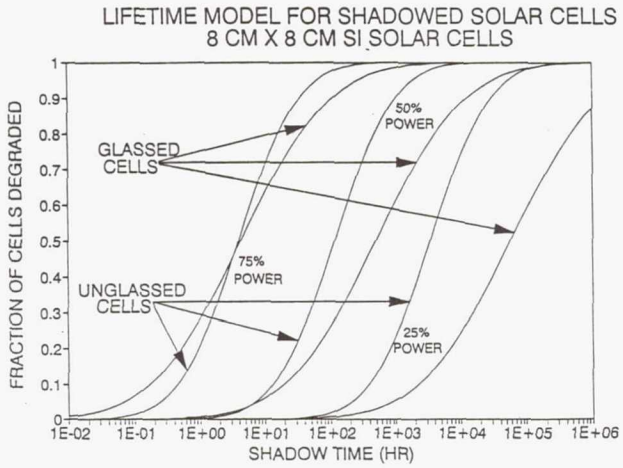
LIFETIME MODEL FOR SHADOWED SOLAR CELLS
8 CM X 8 CM SI SOLAR CELLS
FRACTION OF CELLS DEGRADED
1
0.9
0.8
0.7
0.6
0.5
0.4
0.3
0.2
0.1
0
GLASSED CELLS
UNGLASSED CELLS
50% POWER
75% POWER
25% POWER
1E-02
1E-01
1E+00
1E+01
1E+02
1E+03
1E+04
1E+05
1E+06
SHADOW TIME (HR)

FIGURE 21

# MASS PROPERTIES SURVEY OF SOLAR ARRAY TECHNOLOGIES

Robert Kraus
W.J. Schafer Associates
Arlington, VA 22209

## INTRODUCTION

An overview of the technologies, electrical performance, and mass characteristics of many of the presently available and the more advanced developmental space solar array technologies is presented. Qualitative trends and quantitative mass estimates as total array output power is increased from 1 kW to 5 kW at EOL from a single wing are shown.

The array technologies are part of a database supporting an ongoing solar power subsystem model development for top level subsystem and technology analyses. The model is used to estimate the overall electrical and thermal performance of the complete subsystem, and then calculate the mass and volume of the array, batteries, power management, and thermal control elements as an initial sizing. Technology tradeoffs and advantages can then be quantified within a consistent, system-level framework.

The array types considered here include planar rigid panel designs, flexible and rigid fold-out planar arrays, and two concentrator designs, one with one critical axis and the other with two critical axes. Solar cell technologies of silicon, gallium arsenide, and indium phosphide were included in the analyses.

Comparisons were made at the array level; hinges, booms, harnesses, support structures, power transfer, and launch retention mountings were included. It is important to note that the results presented here are approximations, and in some cases revised or modified performance and mass estimates of specific designs; this was necessary to fit the objective of this paper - an apples to apples comparison of array technologies.

## SOLAR ARRAY TECHNOLOGIES

Planar rigid panel arrays have been the most commonly used design to date. The substrate used here comprises 10 mil graphite epoxy facesheets over an 0.75 inch aluminum honeycomb. Graphite epoxy facesheets provide more strength than aluminum facesheets at approximately two-thirds the mass density. Additional components are an insulation layer, adhesives, harness, and thermal control paint. The areal mass density of the substrate components was 1.6 kg/m2, including a 10% contingency. This represents an equivalent fused silica shield thickness of approximately 29 mils; 30 mils was used for degradation calculations. The packing factor of the cells was 0.90.

Solar cells of silicon (Si) and gallium arsenide on germanium (GaAs/Ge) were considered for GEO applications. Indium Phosphide (InP) was considered for an orbit closer to the radiation belts. Cell parameters are given in Table 1.

Three conceptually similar lightweight fold-out blanket designs of varying technical maturity were considered. The solar cells are mounted to thin blankets of kapton or lightweight metal that are a few mils thick. Electrical harnesses run along the outside longitudinal edges of the blanket. For launch, the blankets are folded and sandwiched in a foam housing. The arrays are then deployed using a continuously coiled lattice mast. Once deployed, the blanket is tensioned by a hanger/spring assembly.

The fold-out arrays considered were the Advanced Photovoltaic Solar Array (APSA) under development by NASA and JPL [1], another lightweight array of silicon on kapton under development at Lockheed [2], and the recently completed design of the SDIO planar Survivable Power Subsystem (SUPER) array [3]. The APSA array uses small (2 x 4 cm) thin (2.2 mil) silicon cells (13.8 % efficient BOL) on a kapton blanket. The blanket housing, mast, and deployment structures for the APSA array are very light. The Lockheed array under development has larger, thicker silicon cells (7.1 x 7.1 cm, 4 mils) on a kapton blanket with a lower packing factor than the APSA array. The SDIO planar SUPER design has large gallium arsenide on germanium cells (5.9 x 5.9 cm, 3.5 mils, 18% efficient) on a beryllium substrate. Because of the similarity in the designs, the fold out SUPER structures (boom, mast, etc) were used for the Lockheed Si on kapton array.

## ORBIT ENVIRONMENT AND DESIGN DRIVERS

A geosynchronous (GEO) orbit of 35760 km, 0 deg inclination was selected for the flexible and rigid fold-out blanket designs, as it is the designed application. EOL performance was determined after 10 years. For the analyses here of both flexible blanket designs, the kapton blanket provided 3 mils of equivalent fused silica shielding on the back side of the solar cell. The planar SUPER substrate provided 12 mils of shielding, including the germanium cell substrate. The APSA array has 2 mil coverglasses, the lightweight silicon on kapton and the planar SUPER arrays have 3 mil coverglasses. Mass characteristics of rigid panels with 3 mils of coverglass in this environment were also determined and were compared to the lightweight blankets.

An orbit of 1111 km (600 nmi) at 80 degrees inclination was used for concentrator and InP technologies that are more resistant to the moderate natural radiation levels of this environment. In GEO, most of the damage to solar cells is due to electrons, whereas at 1111 km the damage is due primarily to protons. The equivalent 1 MeV fluence at 1111 km is approximately twice that at GEO.

The SUPER concentrator array is under development by SDIO to survive nuclear and laser threats.[4] The design provides a great deal of shielding to the 21.5% efficiency GaAs solar cells (at least 60 mils with infinite backshielding). It is also designed for a heavy lift launch vehicle, so extra structural mass for strength is included. Another novel concentrator using fresnel domes and very high efficiency (30%) GaAs on gallium antimidide is under development by Boeing after earlier development by NASA and Entech through an SDIO SBIR. The reference design used here is based on a Space Station design and has an aluminum concentrator structure.[5] For this study 9 mils front, and 12 mils equivalent back shielding were used.

The optical efficiency of the SUPER concentrator given in Table 3 includes the product of geometric off-pointing factors and mirror contamination. The fresnel concentrator optical efficiency is the product of lens absorption and darkening.

Degradation for the solar cells was determined using the technique outlined in reference [6]. The 1 Mev equivalent flux was determined from reference [6], and degradation factors specified in reference [7] were used for Si and GaAs/Ge cells. InP degradation was determined from unpublished Naval Research Laboratory documents.

Power from the array is calculated assuming full perpendicular solar insolation of 1350 W/m2. Cell power output is adjusted for operating temperature and environment degradation. An additional 4% loss due to micrometeorites, uv darkening, and harness line loss is also factored into the calculations. The electrical characteristics of the fold-out and concentrator arrays is summarized in Tables 2 and 3.

## ARRAY SCALING AND ALGORITHM DEVELOPMENT

In order to make a more complete and consistent comparison between technologies, a total single wing array concept design consisting of solar cells, panel substrate, deployment, power transfer and harness, and support and launch retention structures was developed for each of the array designs.

An earlier rigid planar array study assumed boom and mechanisms to be 30% of cell-covered panel mass for 5 kW designs.[8] More detailed weight statements recently obtained for arrays indicated multipliers that were much larger for multi-kilowatt arrays; scaling parameters became even more difficult to determine because of the uniqueness of each reference design. Some estimates were made, however, such as limiting the area of individual panels, and using spring hinges between panels. A solar array drive motor, hinge, boom, and launch support mass were constant for all power levels. The power harness and power transfer slip ring mass were calculated as a ratio of the power output. When incorporated into the scaling algorithms and recalculated, the mass of the additional hardware represented 80% of the panel-only mass at 5 kW, and 170% of the panel mass at 1 kW.

For each of the fold-out array designs, mass properties information was available for a specific point design of 3000 to 4000 W array power at EOL. Blanket housing, mast canister, mast motor, array/spacecraft hinge, support tube, and support structure mass remained constant as power output was increased for each design. A diode box was not included. The APSA program does not include some of the components listed above, so an averaged value based on the other designs was used. As output power was increased, blanket panels and mast mass were added. Power transfer and harness masses were added as a ratio of array power.

These ratios were based on a range of design points. After setting the scaling parameters, the recalculated mass for each array was within a few per cent of its reference design point.

At 1111 km, only power producing panels are considered due to the variations of the technologies. The SUPER concentrator design is based on modularity; panels are available in full (~6 m2) or half (~3 m2) sizes. The fresnel concentrator design was converted to a W/kg ratio to determine mass at each power level. A major mass driver for this design is the fresnel dome. Two domes were considered, a high mass dome that has been demonstrated, and a low mass version under development. Due to the developmental nature of the design, a 15% contingency was added to the estimates. The InP panels were calculated using the same procedure as the GEO Si and GaAs/Ge panels.

Although the scaling approach described above may not represent the "best" array configuration, and may provide insufficient or extra mechanical support especially at the extremes (1000 and 5000 W), it does provide a consistant approach and seemed reasonable within the scope and limits of the study.

## RESULTS AND SUMMARY

A graph of the Si and GaAs/Ge rigid panel mass as a function of increasing array output power is shown in Figure 1. The solid lines represent the mass of only the cell covered panels. The Si panels provide approximately 43 W/kg, the GaAs/Ge 54 W/kg. The lines would pass through the origin if the power was extended to 0 W. The dashed lines of Fig. 1 represent the estimates of the total array mass. The mass of the additional hardware is 80% of the panel-only mass at 5 kW, and 170% of the panel mass at 1 kW. The uncertainty is higher at 1 and 5 kW; the mass may be overestimated at 1 kW and underestimated at 5 kW.

The mass of the lightweight blanket mass as a function of increasing array output power is shown in Figure 2. The slope of the mass growth is much less than that for the rigid panel designs, because the blanket provides 110-190 W/kg, depending on the array technologies. This design concept clearly accommodates power growth with a lower weight penalty than rigid planar designs. Substantial structural mass is still required, however.

If the two design types are compared for a 3000 W array, the lightweight silicon on kapton is 16% lighter than the rigid silicon array. The lightweight silicon on kapton array has a 40% larger array, however, because of its much lower packing factor and greater degradation. The planar SUPER provides the same power for the same mass as the lightweight silicon on kapton, but is 12% smaller than the rigid silicon. The APSA array is yet another 30% lighter, even with the additional hardware added for this study.

A comparison of the concentrator and InP panels is shown in Fig. 3. The 'staircase' nature of the SUPER half panels is evident. The envelope of the fresnel concentrators ("Lo" mass and "Hi" mass domes) indicates a very light weight concentrator array is possible. The baseline design used here was intended for a LEO orbit. The InP panel mass is very close to the high mass fresnel panel due to its inherent resistance to natural space radiation. With a very small amount of extra shielding near the cells, EOL performance of concentrators could be improved for high radiation environments with a very small mass penalty. The InP panels would also require much more structural support than the concentrator here, however, because the InP array has a 50% larger area.

It is important to note that the SUPER concentrator has only one critical axis for sun tracking; a cosine loss (and a slight shadowing loss) occurs in the other axis similar to planar designs. The fresnel concentrator requires the mass of an additional gimbal for close tolerance tracking in the other axis as well.

Solar cell efficiency improvements and novel array designs continue to dramatically reduce solar array mass. Mass of the structures to support the array and mechanisms to transfer power also are a large fraction of total array mass. Technology or design improvements in these areas will also contribute to reducing weight of satellites.

## REFERENCES


[1] P. Stella and R. Kurland, "Latest Developments In The Advanced Photovoltaic Solar Array Program", Proceedings of the 25th Intersociety Energy Conversion Engineering Conference, Reno, NV, 1990.

[2] Lockheed Missiles and Space Co., "Summary of Lockheed Solar Arrays"

[3] "Planar SUPER Program Overview, Dec.9, 1990", Maj. S. Vining, Wright Laboratories program manager; L. Chidester, Lockheed program manager

[4] "SUPER Program Overview, Dec.4-6,1990", Maj. Steve Vining, Wright Laboratories program manager; N. Freeman, Martin Marietta program manager

[5] M. Piszczor, NASA Lewis Research Center, and J.W. Yerkes, Boeing Defense & Space, private communication

[6] B. Anspaugh, R. Downing, H. Tada, and J. Carter, "Solar Cell Radiation Handbook, Third Edition", JPL Publication 82-69, November 1982

[7] B. Anspaugh "Solar Cell Radiation Handbook, Addendum 1: 1982-1988" JPL Publication 82-69, Addendum 1, February 1989

[8] M. Mills and R. Kurland, "The Impact of Solar Cell Technology on Planar Array Performance", Proceedings of the 1988 Space Photovoltaic Research and Technology Conference, NASA Lewis Research Center


Table 1. Rigid Panel Solar Cell Technologies

| Cell Technology | Size (cm) | Thickness (mils) | BOL Eff'y | Degradation |
|---|---|---|---|---|
| Si | 4.4 x 4.4 | 4 | 13.7 | 0.76 |
| GaAs/Ge | 4 x 4 | 3.5 | 18.0 | 0.83 |
| InP | 4 x 4 | 10 | 18.0 | 0.95 |

Table 2. Fold-Out Array Parameters

| Design | Cell | BOL Eff'y | Packing | Degradation |
|---|---|---|---|---|
| APSA | Si | 13.8 | 0.76 | 0.63 |
| Si on Kap | Si | 13.7 | 0.67 | 0.72 |
| Planar SUPER | GaAs/Ge | 18.0 | 0.77 | 0.81 |

Table 3. Concentrator Parameters

| Design | Cell | BOL Eff'y | Temp (deg C) | Optics Eff'y | Degradation |
|---|---|---|---|---|---|
| SUPER | GaAs | 21.5 | 130 | 0.87 | 0.93 |
| Fresnel | GaAs+GaSb | 30.0 | 80 | 0.87 | 0.80 |

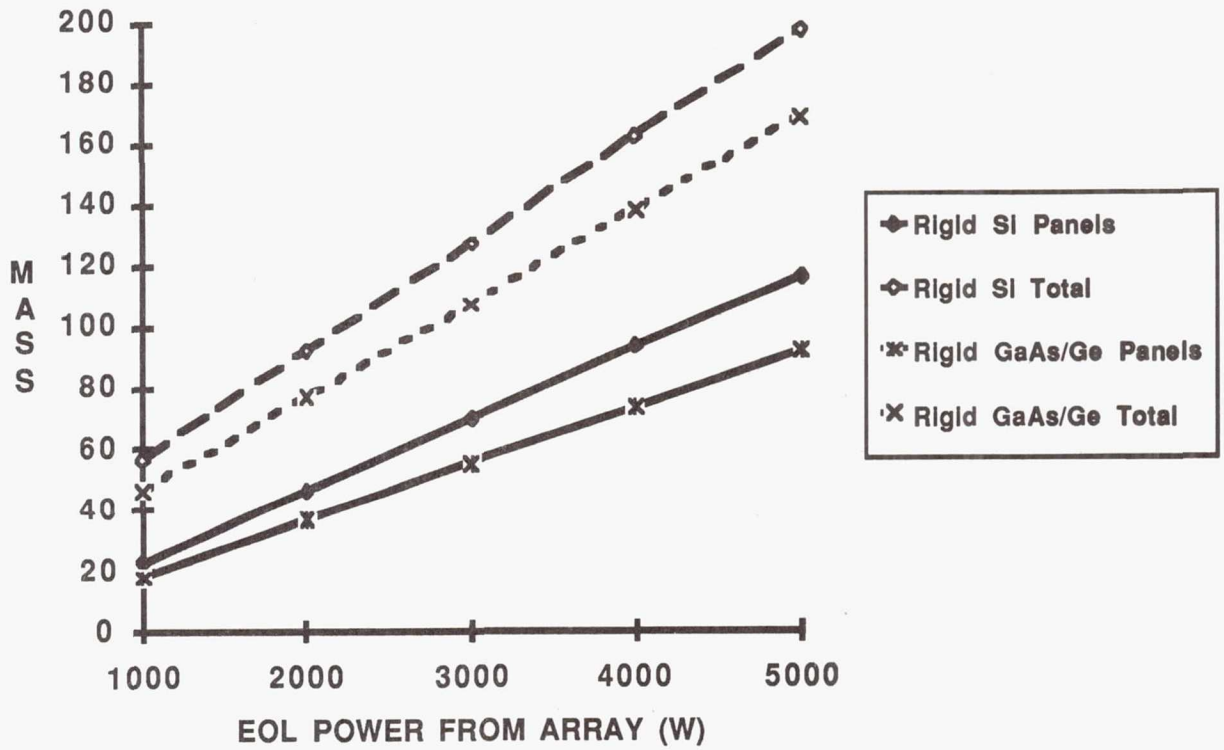


Figure 1. Rigid planar array mass

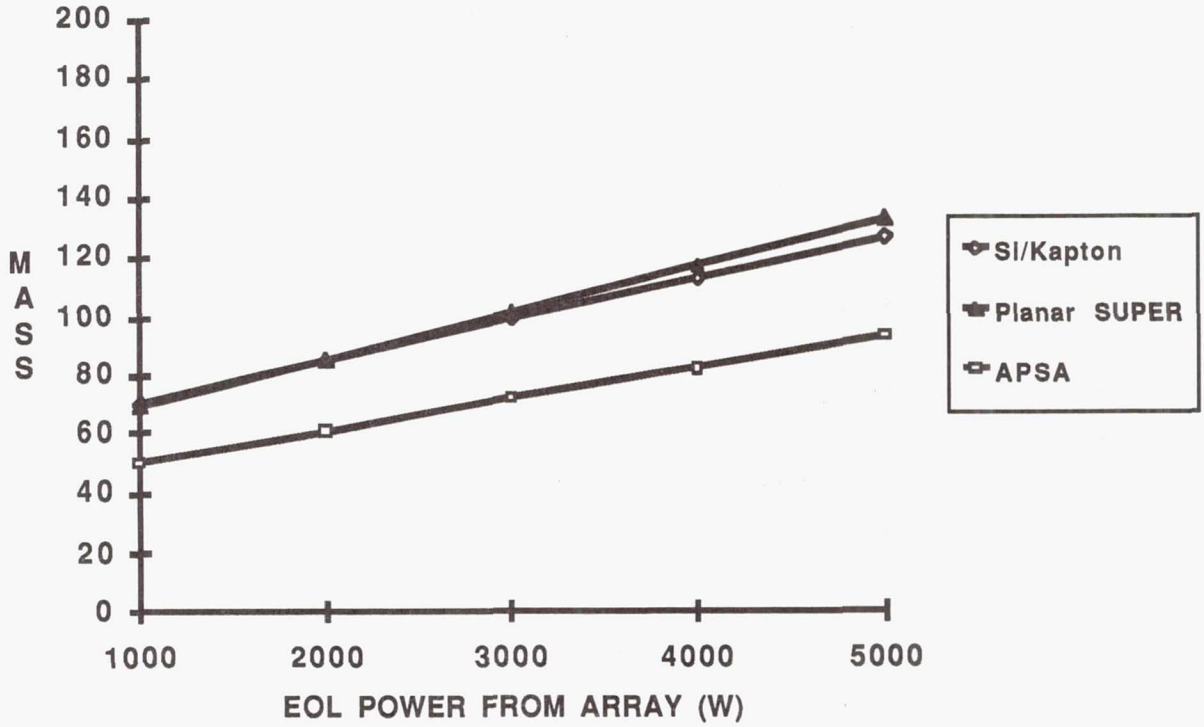


Figure 2. Foldout array mass

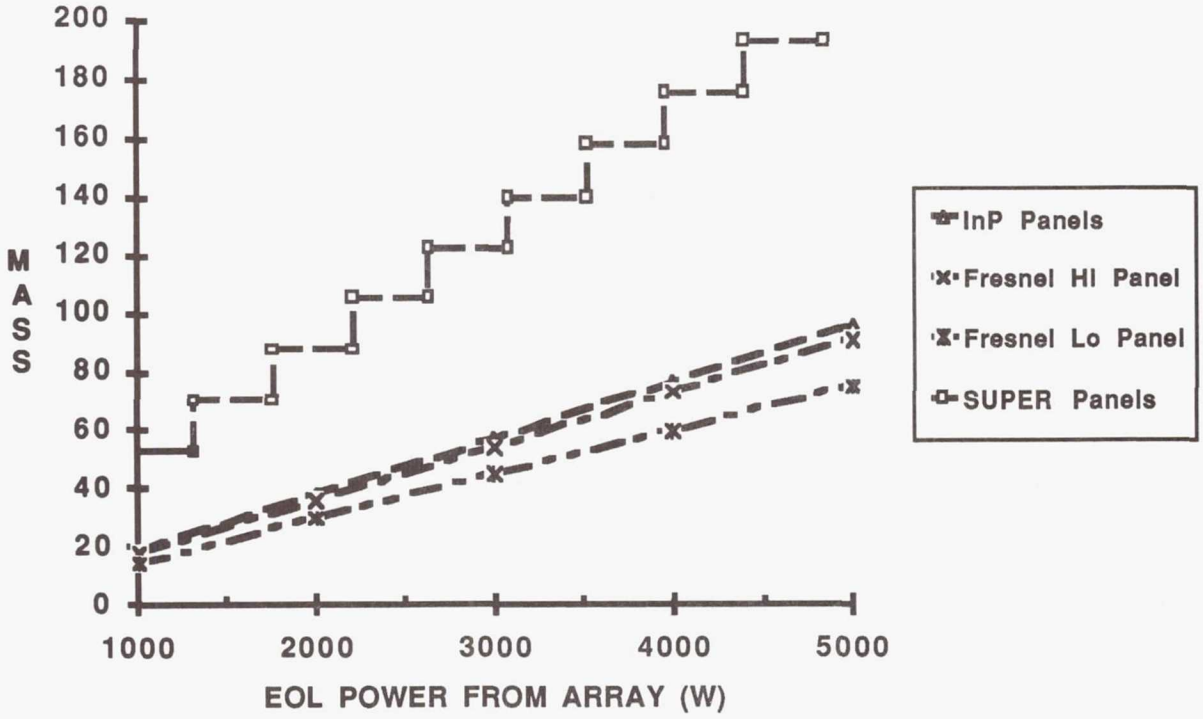


Figure 3. Concentrator and InP array mass

# Space Power by Laser Illumination of PV Arrays

**Geoffrey A. Landis**
Sverdrup Technology Inc.
NASA Lewis Research Center 302-1
21000 Brookpark Rd.,
Cleveland, OH 44135
(216) 433-2238

## *Introduction*

There has recently been a resurgance of interest in the use of beamed power to support space exploration activities. This paper will examine the utility of photovoltaics and identify problem and research areas for photovoltaics in two beamed-power applications: to convert incident laser radiation to power at a remote receiving station, and as a primary power source on space-based power station transmitting power to a remote user.

A particular application of recent interest is to use a ground-based free-electron laser as a power source for space applications. Specific applications include: night power for a moonbase by laser illumination of the moonbase solar arrays; use of a laser to provide power for satellites in medium and geosynchronous Earth orbit, and a laser powered system for an electrical-propulsion orbital transfer vehicle. These and other applications are currently being investigated at NASA Lewis as part of a new program to demonstrate the feasibility of laser transmission of power for space.

## *Example Case: Laser Night Power for the Moon*

Providing power over the 354 hour lunar night provides a considerable challenge to solar power concepts for a moonbase. While some systems can be run at reduced power, others, such as air recycling, may even have increased power consumption during the night. The storage required for night operation is the major mass component of a photovoltaic system. An alternative possibility is to beam power to the lunar base to eliminate the need for storage. Solar arrays on the lunar base can be illuminated by laser power beamed directly from the Earth. The advantage is that electric power is cheap on Earth, and there is no need to transport a large solar array or power beaming equipment to space.

No added elements are needed for the base night power system over the system used for daytime operation. The solar array needed to receive the beamed power is already in place. At each laser station, laser power is required for 12 hours a day for two-week periods. This allows ample time for laser refurbishment and preventative maintenance. The fact that the laser is on the Earth allows considerable design simplification; unlike in-space systems, where any failure is fatal, terrestrial systems can be easily repaired, so highly redundant systems are not required.

The best photovoltaic cells have been shown to convert 60% of monochromatic incident light at the optimum wavelength into electricity. The efficiency drops to zero for wavelengths much longer than the optimum. For wavelengths shorter than the optimum, the conversion efficiency for monochromatic light is approximately proportional to the wavelength.

The minimum spot radius of a transmitted laser beam is set by diffraction,

$$r_{spot} = 0.61\, d\, \lambda / r_{lens} \qquad (1)$$

The opacity of the atmosphere to short-wavelength ultraviolet places a lower limit to the wavelength at about 350 nm. A key element in achieving small spot sizes is the use of a large

optical aperture on the ground system. For optimal systems, the lens size should be in the scale of meters. Pointing accuracy and atmospheric turbulence degrade the effective spot size. Achievable pointing accuracy is high enough that this is not a limiting factor. Atmospheric turbulence can be corrected by use of optical systems which correct for atmospheric distortion. Such techniques have been demonstrated to give nearly diffraction-limited performance.

Candidate laser technologies are the semiconductor diode laser and the free-electron laser.

The highest power GaAs diode lasers operate at about 795-820 nm, which is nearly optimal for existing silicon solar cells. Arrays of diode lasers have recently demonstrated power densities as high as 100 W/cm$^2$. 25-watt CW integrated arrays have been demonstrated. An array consisting of a very large number of individual diode lasers could yield the required power.

Free-electron lasers (FELs) have potentially very high high power and are, in principle, tunable over a range of wavelengths down to as low as <200 nm.

Consider a baseline system with a wavelength $\lambda$ of 400 nm ($4 \cdot 10^{-7}$ m). The distance d at maximum is $4 \cdot 10^8$ m, and the lens diameter is 2 meters. For diffraction limited beam spread, the diffraction-limited spot radius at the moon is is 100 m. The illuminated area is 31,000 m$^2$.

For 100 kw of baseline daytime power, the required solar array area is about 400 m$^2$. This is augmented by supplementing the array area by a factor of four using fixed, reflective sheets of thin plastic. Libration, the apparent motion of Earth in the lunar sky, limits the maximum possible concentration achievable by a non-tracking concentrator. The total solid angle subtended by libration is 1.1 steradians; thus, the maximum concentration without tracking is 11x. The array area is then increased over that required for daytime power by an additional factor of two. The array intercepts 10% of the incident power, and the laser power needed is ~2 MW.

The required 2 MW could be provided, for example, by twenty 100-kw laser units, to allow any single unit to be taken off line without system failure. Twice as many stations will be required as are actually in use, since half will be on the wrong side of the Earth.

## *PV Issues*

Eight issues are identified as subject areas for development in the photovoltaic receiver area:

*1. Choice of cell type and material and verification of cell performance under laser (monochromatic) light.*

Cell theoretical models must be made and measurements of cell parameters (efficiency; spectral response; intensity variation of efficiency; temperature coefficients) to verify the models.

*2. Investigation of cell operation in pulsed mode*

The duty cycle of the baseline free electron laser system is $10^{-6}$, with a typical pulse width of 1 to 10 ns. Thus, the cell operates at extremely high power levels for very brief periods, separated by longer unilluminated periods. Cell operation depends on pulse width and rate compared to minority carrier lifetime ($\tau$) of solar cell. If pulse spacing (1/rep rate) is less than $\tau$, then the pulsed input is effectively continuous to the solar cell. If pulse spacing > $\tau$, there are two cases:

pulse width > $\tau$ : solar cell reaches equilibrium during pulse.

pulse width < $\tau$ : solar cell does not reach equilibrium during pulse.

Since typical $\tau$ is 1-10 ns for GaAs and 10-100 µsec for Si, silicon cells and GaAs cells operate in different regimes under pulsed power conditions.

The pulse rate is high compared to the thermal time constant of the system. Overall, the system will behave thermally as a continuous wave system.

High peak power will produce series resistance losses by $I^2R$. The cell, system and PMAD resistance all may be important; the cell grid will have to be designed to handle peak current, not average.

*3. Power management and distribution (PMAD)*

The PMAD must be capable of utilizing power from pulsed input. Capacitance or inductance can be deliberately added to the system, either distributed or lump, to smooth the pulse. The RC

time constant of the array, junction capacitance in the cell, and capacitance and inductance in the wiring will all increase the pulse width.

*4. Ambient temperature*

Lunar: Daytime maximum ~85°C, night minimum temperature ~100°K; satellites may see slightly lower temperature variations between eclipse and in-sun operation. The temperature coefficient for power conversion for monochromatic light is different than for solar spectrum, since the temperature coefficient of Eg leads to large changes in absorption with temperature near the band edge.

*5. Array issues*

PV Array design issues will have to be addressed; in particular, design for deployment; maintanance; dust avoidance, and optimum thermal design.

*6. Design of cells for dual use.*

For many applications (such as the lunar base described), the cells will be required to operate under laser illumination during "night" operation, and solar illumination during "day" operation.

*7. Optimum design of cells for laser conversion*

Trade-off of high-performance vs. llightweight, low efficiency arrays. The cell will be designed to maximize performance at wavelengths close to band edge, cells may include light trapping to maximize long-wave response. Cells design for high peak power levels may includes large coverage of grid metallization and use of a prismatic cover. Optimum thermal design is required to maximize $\alpha/\varepsilon$.

*8. Radiation Damage*

Radiation preferentially damages the long wavelength response of a solar cell, which is the most efficient part for laser conversion. On the moon, there is some radiation damage effect due to solar flare protons. This is expected, on the average, to degrade the cells by a few percent per year on the average, although actual degradation will be in discrete events. Transfer vehicles will experience severe radiation damage effects due to crossing the Van Allen belts. This radiation damage will likely drive the mission mass due to the requirement of shielding. It will be important to evaluate the use of radiation-tolerant cells such as InP, radiation-tolerant cell design strategies, and the possibility of in-situ annealing (possibly using the ground based laser as the heat source) to periodically remove the radiation damage.

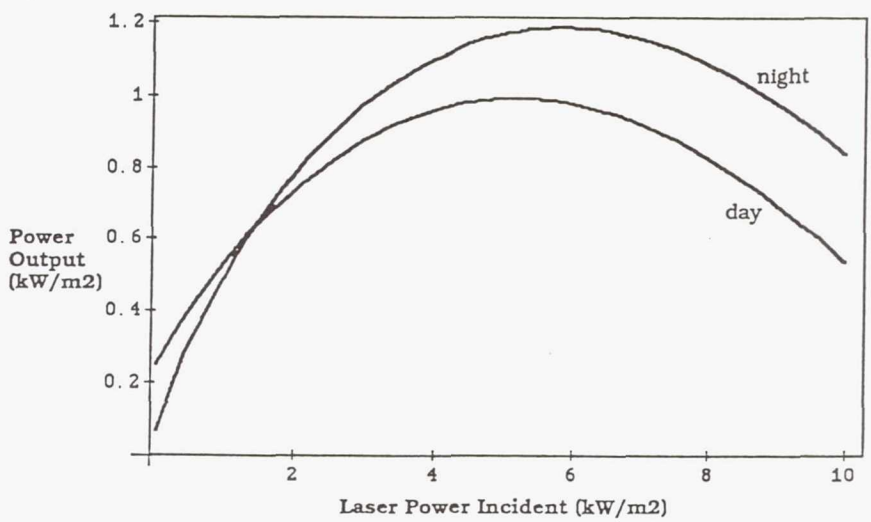


**Figure 1.**
**Power output from a laser-illuminated GaAs array on the Moon.**
The power produced by a PV array increases as the intensity of the laser illumination increases. The temperature rise at high power levels means that there is a maximum power density that can be achieved before the actual power decreases as the intensity of illumination increases. The maximum is higher at night, when the lunar ambient temperature is low and the array is not heated by the sun.

## Table 1: PV Converters for Laser Beamed Power
*Approaches*

| | |
|---|---|
| Flat-Plate Array | GaAs (Efficiency ~ 50%) or Si (Efficiency ~40%)<br>Cell cost may be important for large areas and for GaAs cells<br>Thermal management not required for power <~2 kW/m2<br>low pointing accuracy required (cosine loss) |
| Thin-Film Array | amorphous Si, $CuInSe_2$ or CdTe. Efficiencies will low (≤20%)<br>Cost and Mass are low<br>Roll-out "carpet" approach possible but needs development |
| Concentrator Array | GaAs developed; other III-V possible; High efficiencies (>70%?)<br>Cell cost not a major driver since area is low<br>Thermal management required<br>High pointing accuracy required<br>Dust is more of a problem |

## Table 2: PV Converters for Laser Beamed Power
*Choice of Converters for VariousWavelength Choice*

| Wavelength Range | | Cell |
|---|---|---|
| **Visible** | 0.4 to 0.8 μ | η of Si or GaAs cells decreases linearly with λ.<br>Specially designed cell will have high η<br>and good temperature coefficient; development needed |
| **GaAs Optimum** | 0.8 to 0.86 μ (GaAs)<br>0.8 to 0.90 μ (InP) | Optimum for GaAs; InP and a-Si;<br>η of GaAs cells ~50%;temperature coefficient moderate |
| **Si Optimum** | 0.8 to ~1.0 μ | Optimum for Si and $CuInSe_2$; η of Si cells ~40%<br>Temperature coefficient worse |
| **Nd:YAG** | 1.06 μ | Standard Si bad; a new cell design may give ok response<br>should be okay for $CuInSe_2$<br>Optimum for InGaAs quaternary (development needed)<br>η of $CuInSe_2$ cells ~20%<br>Temperature coefficient worse |
| **Near IR** | 1-2 μ | Specially designed cell needed;<br>III-V quaternary or HgCdTe<br>will have low η and poor temperature coefficient;<br>development needed |
| **Mid IR** | >2 μ | Not practical for PV conversion<br>Specially designed cell needed<br>may need cooling to operate |

**Table 3: Radiation Environment**

**LEO**
Negligible radiation; any cell type okay
(atomic oxygen and debris are the problem in LEO)

**Transfer orbits**
Pass through the radiation belts; high doses (mostly protons)--Si or GaAs cells with 3 mil cover will lose ~30% in ~100 days . Want radiation-resistant cell, concentrator, or shielding.

**GEO**
Moderate radiation; subject to solar flare protons and electrons from the outer fringe of belts. Standard Si cells can be used with coverglass; some degradation.

**Moon**
No trapped radiation; subject to solar flare protons
Expect slight degradation after large solar flares.

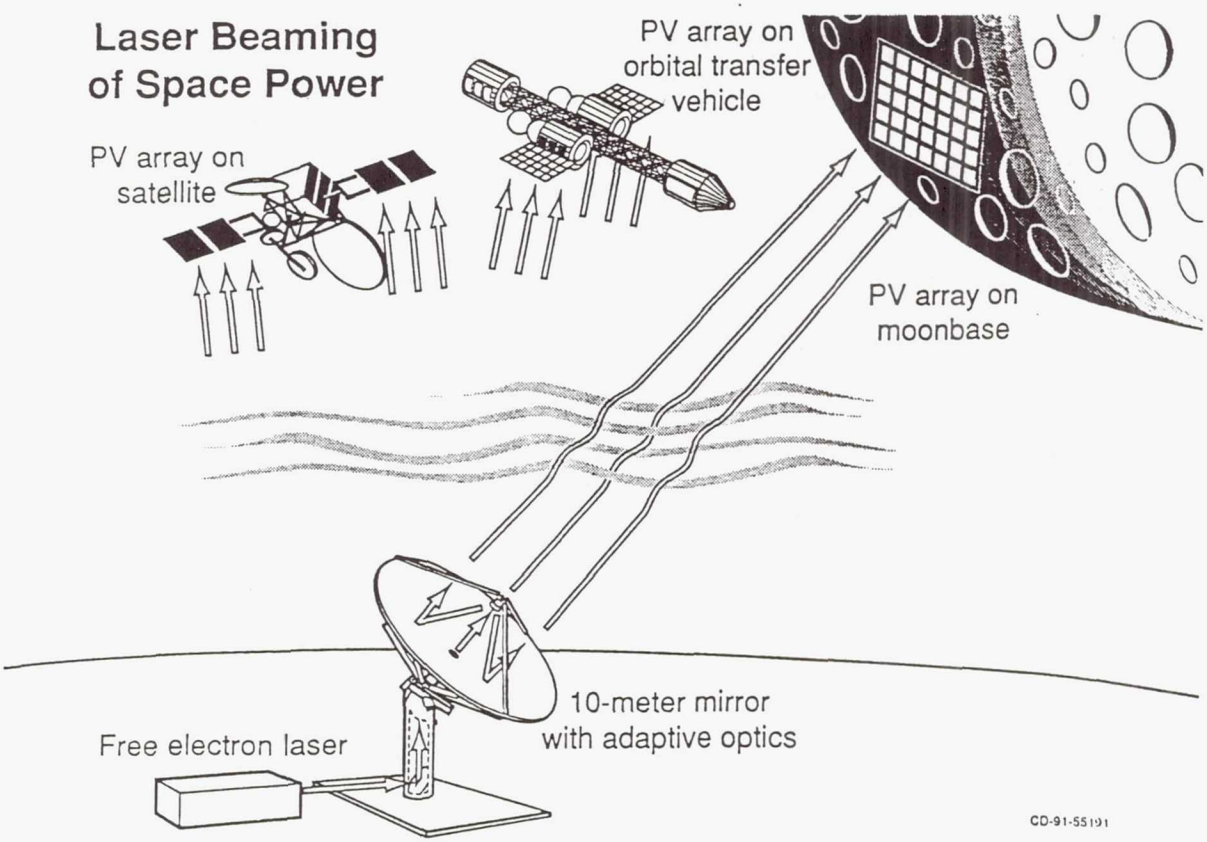

# POTENTIAL CONVERTER FOR LASER-POWER BEAMING

# USING DIODE LASERS

Gilbert H. Walker, Michael D. Williams, and Gregory L. Schuster
Mail Stop 493
High Energy Science Branch
Space Systems Division
NASA Langley Research Center
Hampton, VA 23665-5225
804-864-1411

Peter A. Iles
Applied Solar Energy Corporation
City of Industry, CA 91746-1212

Future space missions, such as those associated with the Space Exploration Initiative (SEI), will require large amounts of power for operation of bases, rovers, and orbit-transfer vehicles. One method for supplying this power is to beam power from a space-based or Earth-based laser- power station to a receiver where laser photons can be converted to electricity. Previous research has described such laser-power stations orbiting the Moon and beaming power to a receiver on the surface of the Moon by using arrays of diode lasers. This paper describes photovoltaic converters that can be efficiently used with these diode lasers.

## INTRODUCTION

A number of space-related missions and objectives which require large amounts of power have been identified by NASA (reference 1 and 2). Two such missions are the establishment of a lunar habitat and exploration of the lunar surface by a roving vehicle. The power for these (and many other) missions could be supplied by laser beam transmission. Reference 3 describes a typical system for beaming power to a habitat or rover on the Moon.

This system consists of three laser satellites which orbit the Moon in a plane oriented to receive continuous solar irradiation (figure 1). The orbit precesses and the satellites are separated by 120 degrees of arc to provide continuous coverage directly below the satellites and intermittent coverage to each side of the orbital plane.

As shown in figure 2, each satellite is composed of a solar collector/concentrator, solar photovoltaic cells, power conditioning equipment, heat radiators, a powerful laser subsystem and

transmission optics. Power from the Sun is collected and concentrated 300 times to irradiate the solar cells which power the laser. Power in the laser beam is transmitted to receivers at the habitat or on the rover. Figure 3 is a flow diagram for such a rover system. The receivers use GaAs photovoltaic converters to convert laser radiation to electrical power.

There are other scenarios for transmitting power by laser beam. Examples are: (1) transmitting from L1 LaGrange point, making most of the visible half of the Moon accessible by one satellite and (2) transmitting from Earth's surface through the atmosphere (with adaptive optics) to the lunar surface or to satellites. However, all scenarios have a common element - the power converter at the destination of the laser beam. This paper describes preliminary efficiency measurements for a GaAs concentrator photovoltaic converter irradiated by a diode laser.

## LASER

The light source used for these measurements was a 10-watt CW laser diode (SDL-3490-S). It emitted light at a wavelength of 813 nanometers through a slit-like aperture with dimensions of 1 centimeter (horizontal) and 1 micrometer (vertical). The aperture was composed of 30 ten-stripe, phase-coupled arrays. Beam divergence angles were 50 × 10 degrees full width, half maximum (FWHM) (vertical plane, horizontal plane). The output beam was focused by two plexiglass cylinders 2 inches in diameter by 6 inches long into a square area that covered the solar cell or an equal aperture (through which power measurements were made with a heat-sensitive detector).

The laser diode was driven by a DC power supply which limited the diode's output to about 7.5 watts. At that output power, about 22.5 watts of heat were conducted away from the diode through a thermoelectric cooler into a circulating water coolant. The thermoelectric cooler provided fine temperature control, and the diode operated at 29.9° C within 0.1° C.

## PHOTOVOLTAIC CONVERTER

The concentrator converter was a GaAlAs/GaAs photovoltaic device on a Ge substrate. Table I shows the characteristics of this converter. Figure 4 is a photograph of the converter-laser experimental setup. The outer portion of the converter's surface is completely covered with a metal contact, while the center of the converter consists of a circular region 0.412 $cm^2$ in area. For the measurements described in this paper, the laser-beam diameter was adjusted to just fill this circular region. Although 22.6 percent of this circular region was covered with a metal contact grid, power density, current density, and efficiency are based on the total area of this circular region, uncorrected for contact area. Figure 5 shows the current density-voltage characteristics of this converter with the laser beam incident at a power density of 2.45 $W/cm^2$. At this power density, the power-conversion efficiency was 45.0 percent.

Figure 6 shows the efficiency and fill factor as functions of laser-power density. The efficiency initially increases with increasing power density because of an increase in converter voltage; however, the decrease in fill factor causes a decrease of efficiency above a laser-power density of 2.45 W/cm$^2$. The corresponding current density obtained at 2.45 W/cm$^2$ is approximately 45 times the current density that would be expected from this converter at air mass zero (AM0).

In conclusion, a peak power conversion efficiency of 45 percent has been demonstrated for a GaAs concentrator device irradiated with a diode laser. Further optimization of the converter structure will be required for efficient operation at power densities above 2.45 W/cm$^2$.

## REFERENCES


1. Ride, Sally K.: LEADERSHIP and America's Future in Space. A Report to the Administrator, August 1987.

2. The Report of the National Commission on Space. PIONEERING THE SPACE FRONTIER, May 1986.

3. Williams, M. D.; Kwon, J. H.; Walker, G. H.; and Humes, D. H.: Diode Laser Satellite Systems for Beamed Power Transmission. NASA TP 2992, July 1990.

*Table 1: GaAs photovoltaic converter.*

| | | |
|---|---|---|
| p - $Ga_{.15}Al_{.85}As$ | | |
| Thickness | = | 600 Å |
| p - GaAs | | |
| Thickness | = | 0.5 μm |
| Doping Density | = | $2 \times 10^{18}/cm^3$ |
| Diffusion Length | = | 4 μm |
| Surface Recombination Velocity | = | $1 \times 10^4$ cm/sec |
| n - GaAs | | |
| Thickness | = | 6 μm |
| Doping Density | = | $2 \times 10^{17}/cm^3$ |
| Diffusion Length | = | 2 μm |
| Surface Recombination Velocity | = | $1 \times 10^4$ cm/sec |

Substrate is inactive n - Ge

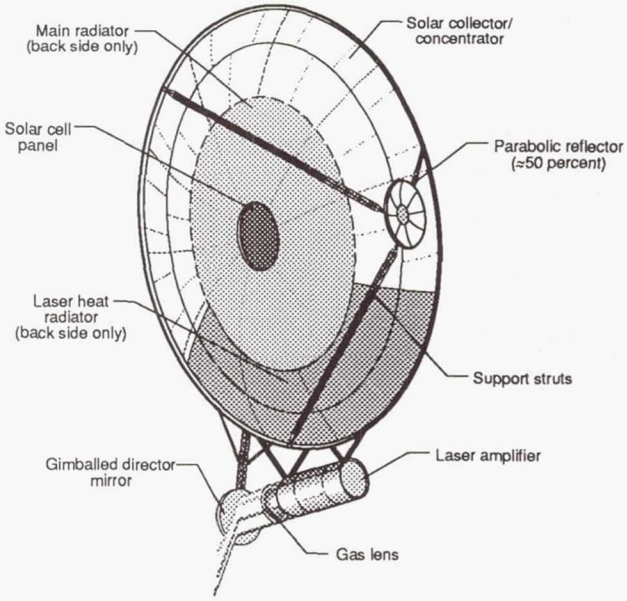


*Figure 2: Diode laser satellite.*

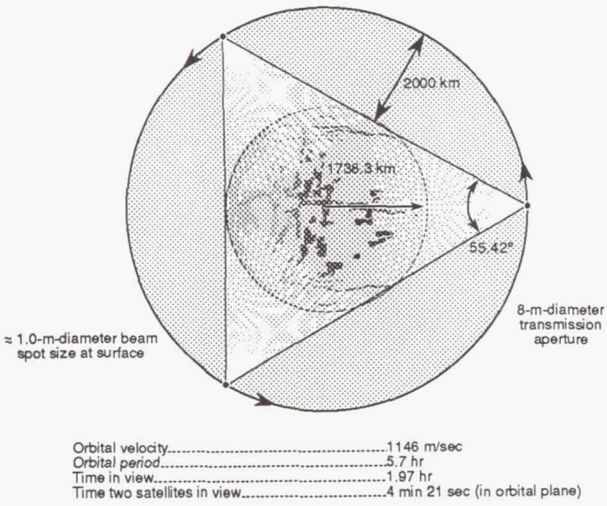


*Figure 1: Lunar orbit data.*

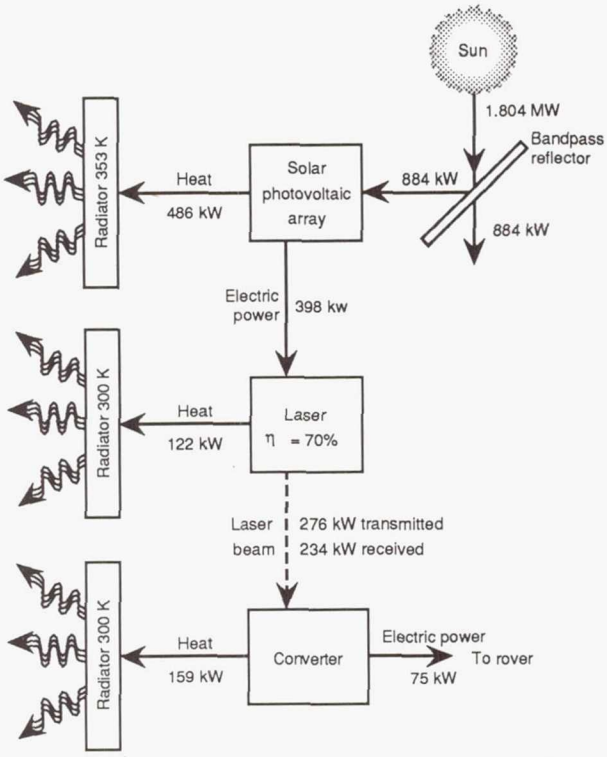


*Figure 3: Power flow of laser satellite for rover.*

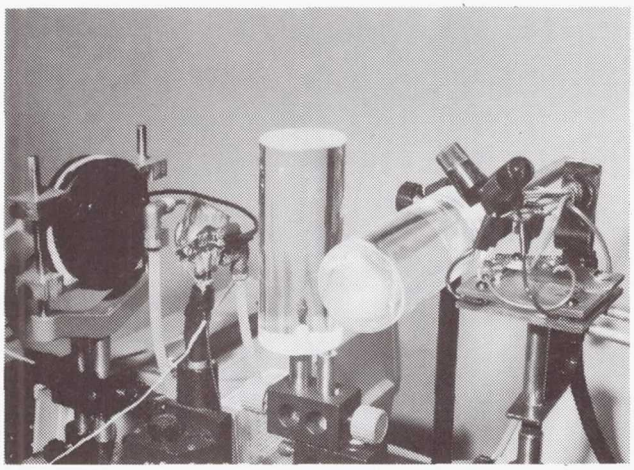

*Figure 4: Experimental arrangement of laser diode and converter.*

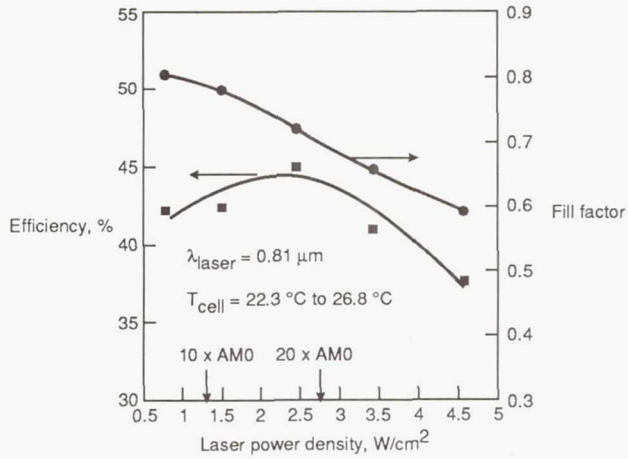


*Figure 6: Response of diode converter to laser radiation.*

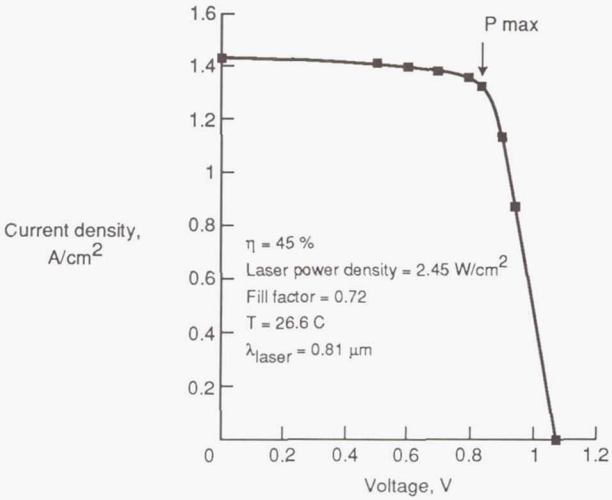


*Figure 5: GaAs converter diode irradiated with laser.*

# GaAs SOLAR CELLS FOR LASER POWER BEAMING

Larry C. Olsen, Glen Dunham, Daniel A. Huber, and F. William Addis
Washington State University at Tri-Cities, Richland, Washington
And
Norman Anheier And E.P Coomes
Battelle Pacific Northwest Laboratory, Richland, Washington

## ABSTRACT

This paper describes efforts to develop GaAs solar cells for coupling to laser beams in the wavelength range of 800 to 840 nm. The work has been motivated primarily by interests in space-to-space power beaming applications. In particular, the Battelle Pacific Northwest Laboratories is conducting studies of the utilization of power beaming for several future space missions. Modeling calculations of GaAs cell performance have been carried out using PC-1D to determine an appropriate design for a p/n cell structure. Epitaxial wafers were grown by MOCVD and cells fabricated at WSU Tri-Cities. Under simulated conditions, an efficiency of 53% was achieved for a cell coupled to 806 nm light at 400 mW/cm$^2$.

## 1. INTRODUCTION

This paper describes efforts to develop GaAs solar cells for coupling to laser beams in the wavelength range of 800 to 840 nm. The work has been motivated primarily by interests in space-to-space power beaming applications. In particular, the Battelle Pacific Northwest Laboratory is conducting studies of the utilization of power beaming for future space missions. However, high efficiency monochromatic GaAs cells will also be useful for numerous applications requiring isolated power and voltage, or transmission of power without electromagnetic interference. This paper considers cell design calculations, cell fabrication, testing procedures with a laser beam, and experimental results for GaAs cells.

When coupled to laser light comprised of photons with an energy equal to the cell material bandgap, a cell can convert the laser beam beam power to electrical power quite efficiently. Before considering the potential efficiency of GaAs cells specifically, it is intersting to consider the efficiency of monochromatic cells over a range of bandgaps. The approach used here is similar to that used to discuss the limiting efficiency of cells coupled to the solar cell spectrum. Figure 1 indicates some of the important considerations. The limiting efficiency is determined by choosing a $Q_{ext}$ of 1.0 ; thus, $J_{sc}$ is set equal to $J_{max}$.which can be expressed as a fuction of photon energy. If we assume that the monochromatic cell is tuned to the photon energy, then $J_{max}$ is expressed as a function of bandgap. The complete I-V curve is defined if we assume that the current losses are limited by minority carrier injection, and express $J_o$ as a function of bandgap. The constant indicated in Figure 1 has been selected to agree with the best results we are aware of for GaAs cells, namely, the highest efficiency cells reported by Spire Corporation. Once a value of bandgap is selected, the I-V curve is determined and the maximum power can be calculated . Results for the maximum efficiency of monochromatic cells vs bandgap assuming an input laser beam intensity of 500 mW/cm$^2$ are plotted in Figure 2. If we consider GaAs specifically, the limiting efficiency for a 'tuned' cell at 500 mW/cm$^2$ is on the order of 70 %. Results for more realistic limiting conditions are given in Table 1. Performance calculations were conducted assuming an incident laser beam intensity of 100 mW/cm$^2$ and a wavelength of 806 nm. As indicated, the limiting efficiency for $Q_{ext}$ = 1.0 is 62 % and for $Q_{ext}$ = 0.95 it is 58.8 %. If

one assumes an incident intensity of 400 mW/cm$^2$ and a wavelength of 840 nm, the corresponding efficiencies are 65 % and 62 %.

## 2. ARRAY CONCEPTS

Preliminary considerations have been given to array concepts because of the impact on cell design. It is assumed that passive cooling will be utilized. Thus the input beam intensity is assumed to be in the 100 to 500 mW/cm$^2$ range. Such an incident intensity condition will result in short circuit current values typical of a concentrated AMO spectrum of 2X to 8X. Thus, it is desirable to have fairly large busbars so that the current can be extracted without significant losses. Figure 3 provides an isometric view of an array concept that is being considered for this application, namely, a hidden busbar arrangement. Triangular reflectors would be bonded to relatively large busbars so that photons normally obscured by the busbars are reflected to active cell area. Based on this approach to array design, the cell collector grid design depicted in Figure 4 was selected Since an array design is assumed for which photons are not obscured by busbars, cell efficiency is calculated by neglecting busbar area. This method of calculating cell efficiency is equivalent to that used for concentrator cells. Thus, we will refer to a concentrator cell efficiency measurement.

## 3. DETAILED MODELING OF GaAs CELL PERFORMANCE

Modeling calculations were conducted for GaAs p-on-n (p/n) solar cells coupled to a monochromatic light for wavelengths ranging from 600 nm to 900 nm, and with incident power covering the range of 100 mW/cm$^2$ to 500 mW/cm$^2$. The basic cell structure is described by Figure 5. The values for the various layer thicknesses are those determined to be optimum for a cell coupled to an 806 nm laser beam. Modeling calculations of cell performance involving variation of layer thicknesses and dopant densities were conducted using the one dimensional code PC-1D, supplemented by the use of computer codes to account for power losses due to sheet resistance and grid finger resistance. Most of the performance calculations have been carried out for a laser wavelength of 806 nm, since initial experimental studies have been based on this wavelength. Figure 6gives cell efficiency versus emitter depth for a range of emitter-concentration values. The calculated results plotted in Figure 6assume a collector grid density of 30 cm$^{-1}$ , collector grid fingers that are 10 μm wide and 4 μm high, and a cell array configuration that provides for photon deflection away from the bus bar (Hidden Busbar Concept). As indicated by Figure 6, the optimum p/n cell design involves a relatively thick emitter , 1.5 μm to 2.0 μm, and doped at a relatively low concentration, 5E17 cm$^{-3}$. These calculations assume a base dopant concentration of 1E17 cm$^{-3}$, and front and back surface recombination velocities of 1E4 cm/sec.

Figure 7 describes calculations of monochromatic GaAs cell performance for a range of laser wavelengths (assuming such lasers are available). The limiting performance is based on an assumed external photoresponse of 100 % while the results based on the present collector grid assume 1.5 % obscuration due to the collector grid, an internal photoresponse of 96 % , and a reflectance from the semiconductor surface of 0 %.

## 4. CELL FABRICATION

Cells were fabricated from epi-wafers grown on the WSU MOCVD reactor (SPIRE 500XT). The front surface collector metalliaztion is established using photolithography and liftoff of vapor deposited Au. Maximum transmission is required only at 806 nm. Vapor deposited SiO (1000 Å) with an index of 1.75 is combined with the 500 Å AlGaAs window to provide a double AR coating yielding 0 % reflection at 806 nm. Cells have been fabricated with dimensions of 0.4 cm x 2.0 cm. as well as with the area indicated in Figure 4.

## 5. EXPERIMENTAL RESULTS

Best results are shown in Figure 8. The figure gives simulated I-V characteristics for a GaAs cell coupled to a 806 nm laser beam at 400 mW/cm$^2$ . The I-V characteristics were obtained by first determining the expected short circuit current based on the measured external photoresponse at 806 nm, and then adjusting illumination by an ELH light source to an intensity level such that the appropriate value of short circuit current was achieved. As indicated in Figure 8, this GaAs cell ((91-24-3) converts the laser beam to electrical power with an efficiency of 53.0 %. Internal photoresponse data for a cell made from the same epi wafer as Cell 91-24-3 are given in Figure 9. These data have been fit with theory yielding estimated values for minority carrier parameters are indicated in Figure 9. The minority carrier diffusion lengths are quite satisfactory, but improvements can be made in the values of surface recombination velocity.Results for the external photoresponse of Cell 91-24-3 are given in Figure 10 along with the internal photoresponse data of Figure 9. Note the cell has been tuned to a wavelength near 806 nm. The external photoresponse at 806 nm is 92 %. This value can be improved to 95 % by decreasing the grid line widths and improving the internal photoresponse to 98 %. Experimental results for cell efficiency vs beam intensity at 806 nm are shown in Figure 11. The upper curve describes the limiting efficiency and the middle curve describes the realistic estimate of cell performance based on the present cell design. In order to close the gap between the experimental results and estimated potential cell performance (53.0 % to 59.5 % at 400 mW/cm$^2$), the external photoresponse must be improved to 95 % and improvement must be made in $J_0$.

## 6. LASER POWER BEAM TEST BED

Battelle Pacific Northwest Laboratories has established a power beam testing station that utilizes a 10 W, 806 nm AlGaAs laser diode array as a laser source. The testbed is controlled with a Macintosh II ci computer with a National Instruments interface. Analog I/O lines control the voltage to the laser array and monitor the drive current. A detector monitors the laser power and power reflected from the cell under test. Cells under test are placed on a temperature controlled, nickel-coated vacuum chuck. Four point probe contacts are utilized to measure I -V characteristics. The laser beam intensity can be varied from zero to 500 mW/cm$^2$ , and is uniform over a 3 cm x 4 cm area. Work is underway to insure that the calibration procedure is satisfactory. A schematic diagram of the test setup is shown in Figure 13. A significant effort has been devoted to obtaining a uniform distribution ofthe laser beam intensity at the cell plane. Figure 14 shows an intensity profile over a 3x4 cm area.

TABLE 1 :

**CALCULATED MONOCHROMATIC GaAs CELL EFFICIENCY FOR LASER AT 806 nm & 100 mW/cm$^2$**

| $Q_{EXT}$ ( % ) | $J_{SC}$ ( mA/cm$^2$ ) | $V_{OC}$ (VOLTS) | FILL FACTOR | EFFICIENCY ( % ) |
|---|---|---|---|---|
| 100 | 64.9 | 1.07 | .891 | 62.0 |
| 95.0 (1) | 61.7 | 1.07 | .891 | 58.8 |

(1) Assumed Internal Photoresponse Is 98 % And Obscuration Due To Collector Grid Is 3 %.

(2) $J_0$ = 6.0 x $10^{-20}$ A/cm$^2$ . This Value Is An Experimentally Determined Value Based On Spire's Results For GaAs Cells.

MAXIMUM CURRENT

$$J_{max} = q \times [\text{PHOTON FLUX}]$$

$$= \frac{P_{in}\,(mW/cm^2)}{h\nu\ (eV)} \quad \frac{mA}{cm^2}$$

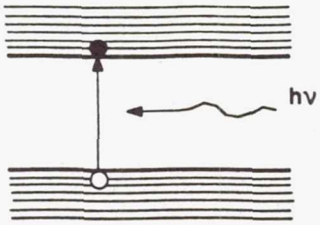


CURRENT-VOLTAGE CHARACTERISTICS

$$J_{sc} = Q_{EXT} \times J_{max}$$

$$J = J_{sc} - J_o [\exp(V/kT) - 1]$$

$$P_{max} = \text{MAX}(J \cdot V)$$

$$\text{EFFICIENCY} = \frac{100 \times \text{MAX POWER}}{\text{INCIDENT POWER}}$$

FOR LIMITING EFFICIENCY

$$Q_{EXT} = 1.0$$

$$J_o = 4 \times 10^4 \exp(-E_g/kT)\ A/cm^2$$

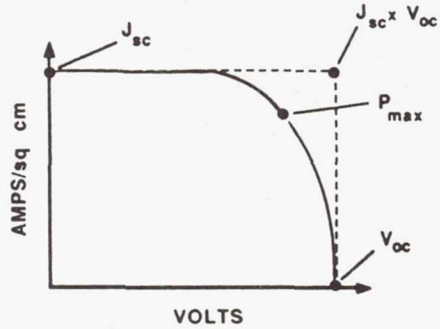


**Figure 1. Approach To Calculating The Limiting Efficiency Of Monochromatic Cells.**

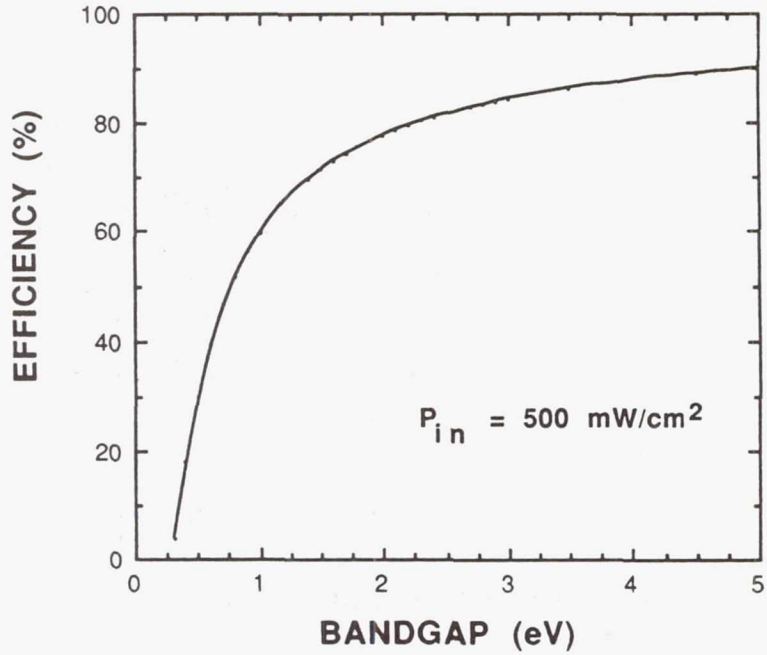


**Figure 2. Calculated Efficiency For Monochromatic Cells Coupled To Laser Light Tuned To The Cell Material Bandgap, And Assuming An Input Power Of 500 mW/cm².**

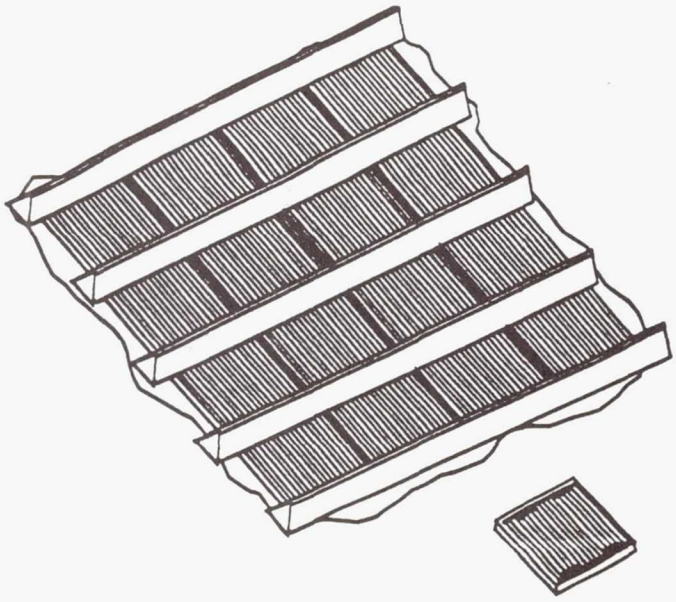

Figure 3. Isometric View Of A Cell Array Utilizing A Hidden Busbar Approach.

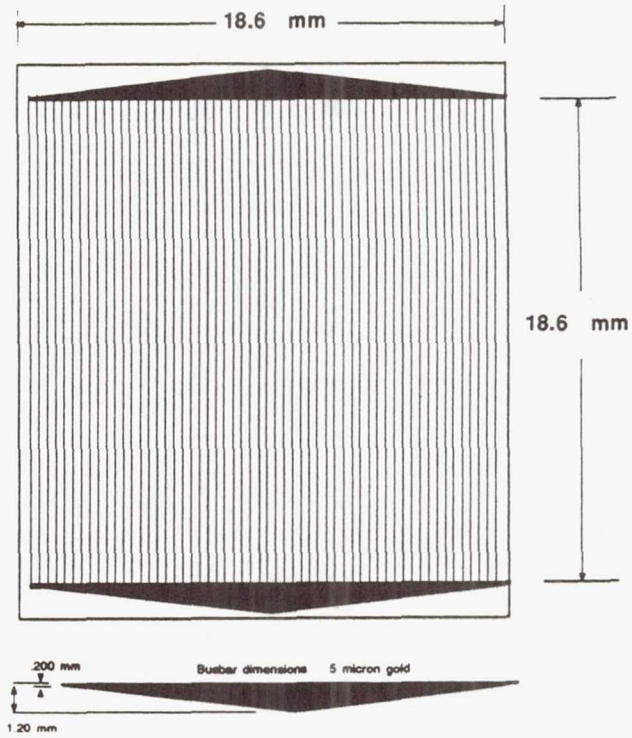


Figure 4. Collector Grid Design Used For GaAs Cells Grown And Fabricated By WSU.

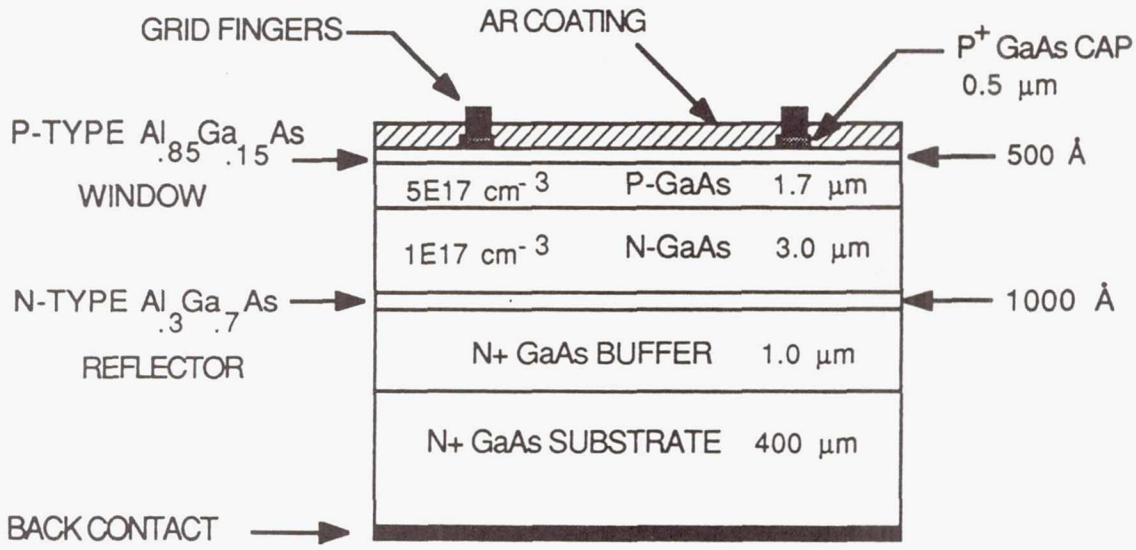


Figure 5. Optimum Cell Structure For p/n GaAs Cells Coupled To Laser Light At 806 nm.

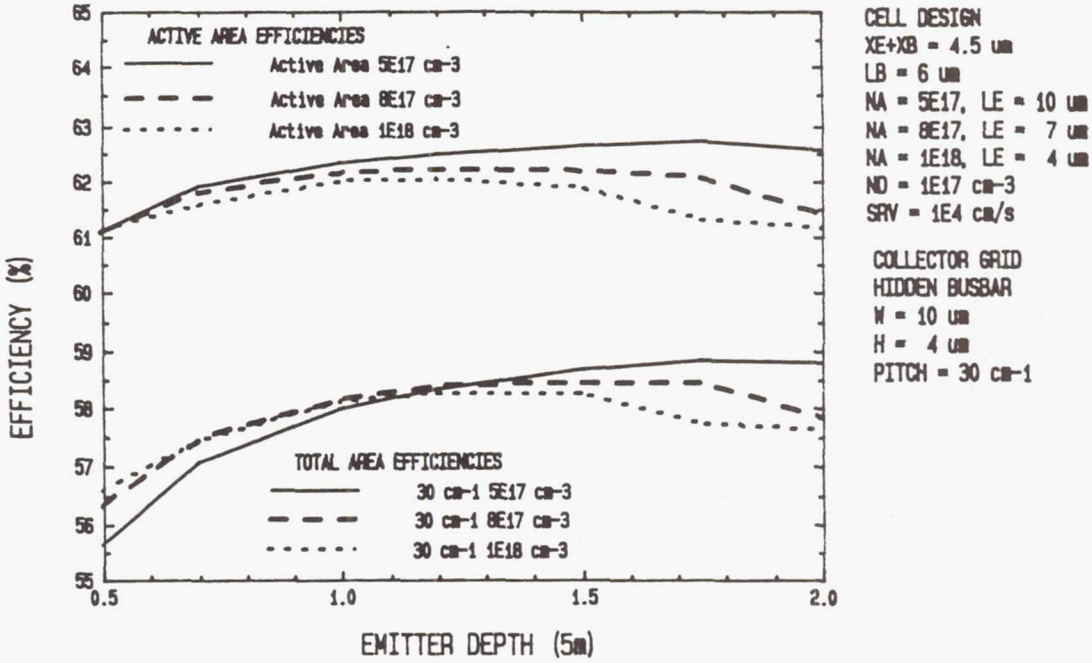


Figure 6. Calculated Efficiency vs Emitter Depth, And Emitter Doping, For a p/n GaAs Cell Coupled To 806 nm Light At 400 mW/cm$^2$.

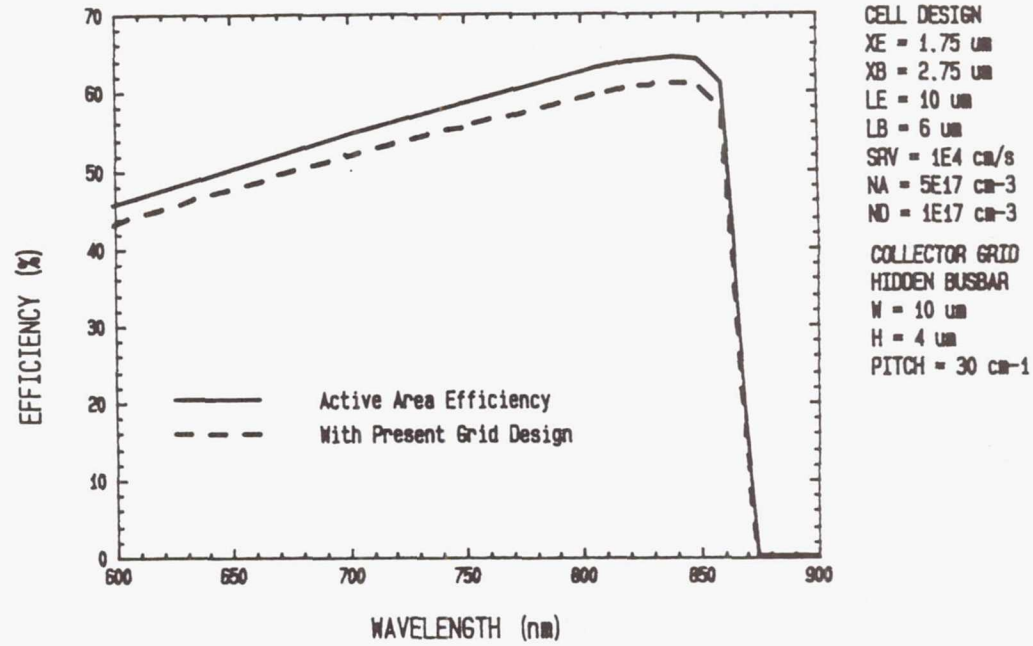


Figure 7. Calculated Efficiency vs Laser Wavelength For A p/n GaAs Cell. The Incident Beam Intensity Is Assumed To Be 400 mW/cm$^2$.

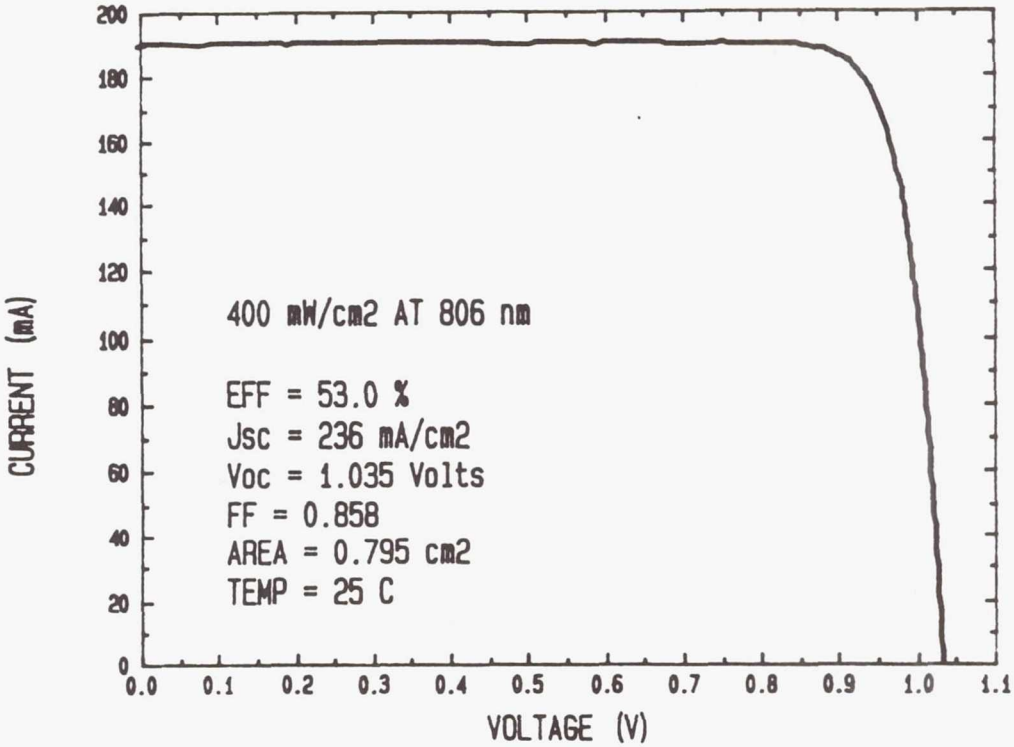


Figure 8. Simulated I-V Characteristics For p/n GaAs Cell 91-24-3 Coupled To 806 nm Light At 400 mW/cm$^2$. The GaAs Cell Was Grown And Fabricated At WSU Tri-Cities.

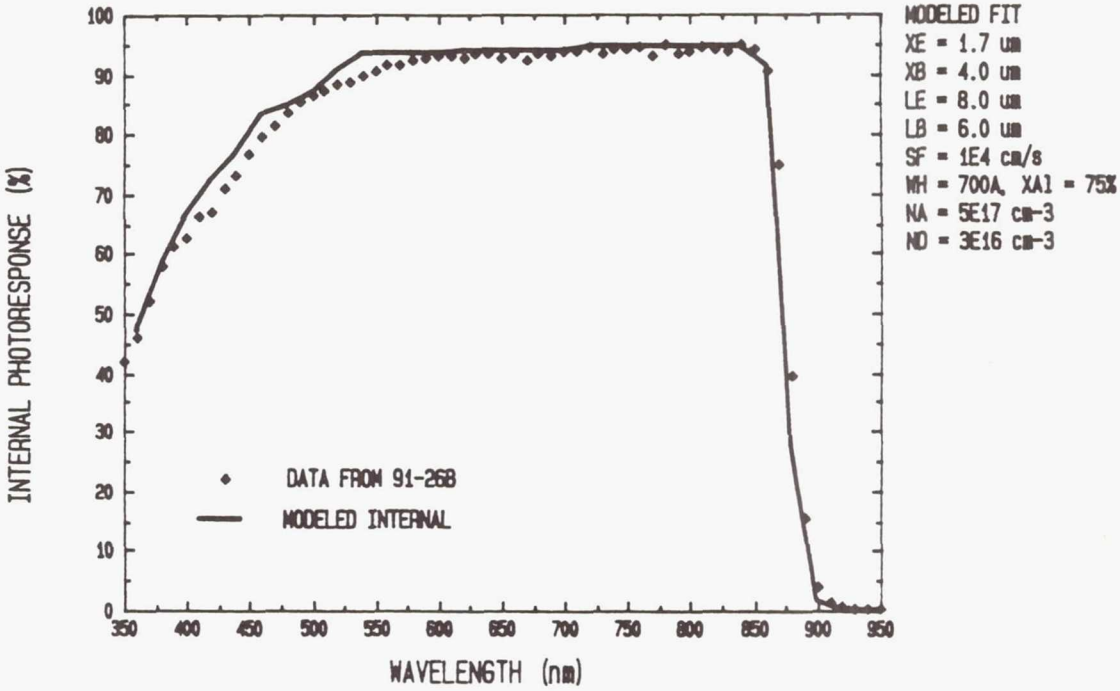


Figure 9. Internal Photoresponse Measured For A GaAs Cell Fabricated From The Same Epi-Wafer As Cell 91-24-3. Minority Carrier Parameters Determined From Fitting The Photoresponse Data Are Indicated.

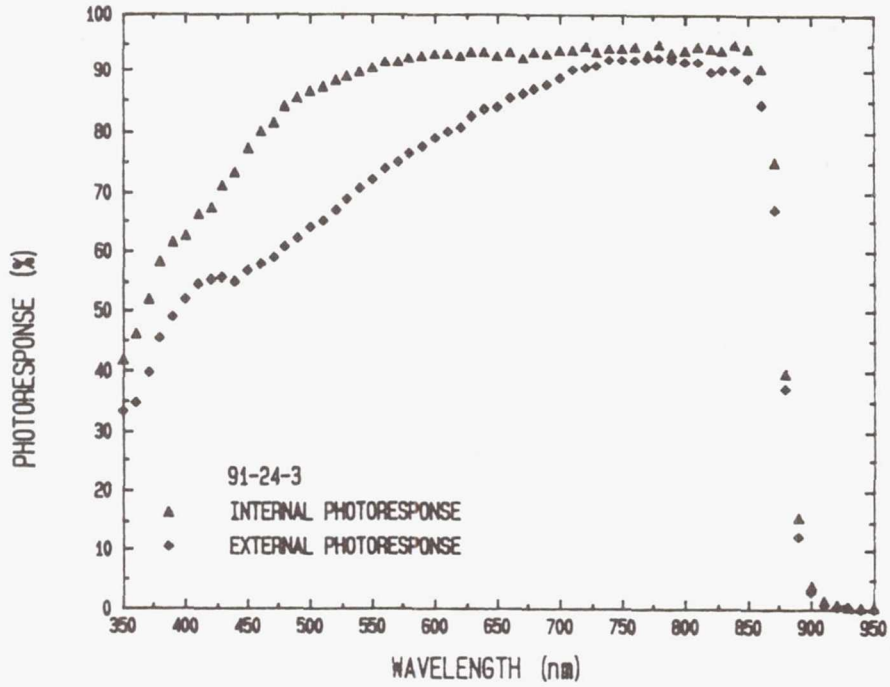


Figure 10. External Photoresponse And Internal Photoresponse Data For 53 % Cell (91-24-3). An AR Coating Of 1000 Å Of SiO Was Used To Tune The Cell To The 800 To 850 nm Wavelength Range.

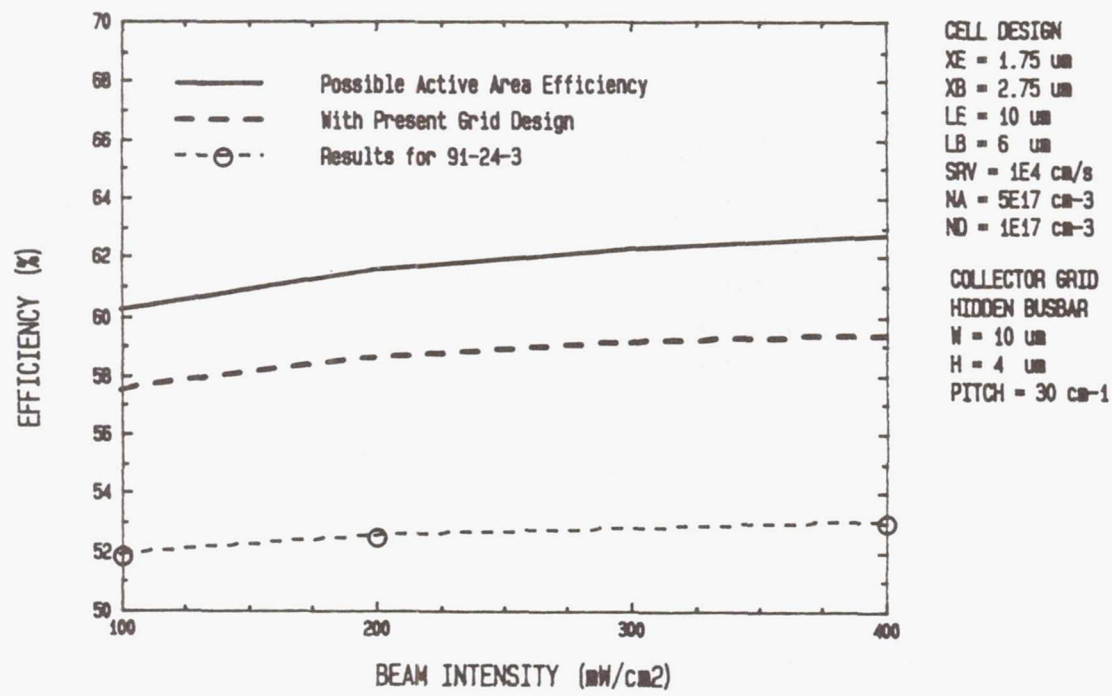


Figure 11. Experimental And Theoretical Results For Efficiency vs Laser Beam Intensity. Experimental Results Are Simulated Measurenments As Discussed In Text,.

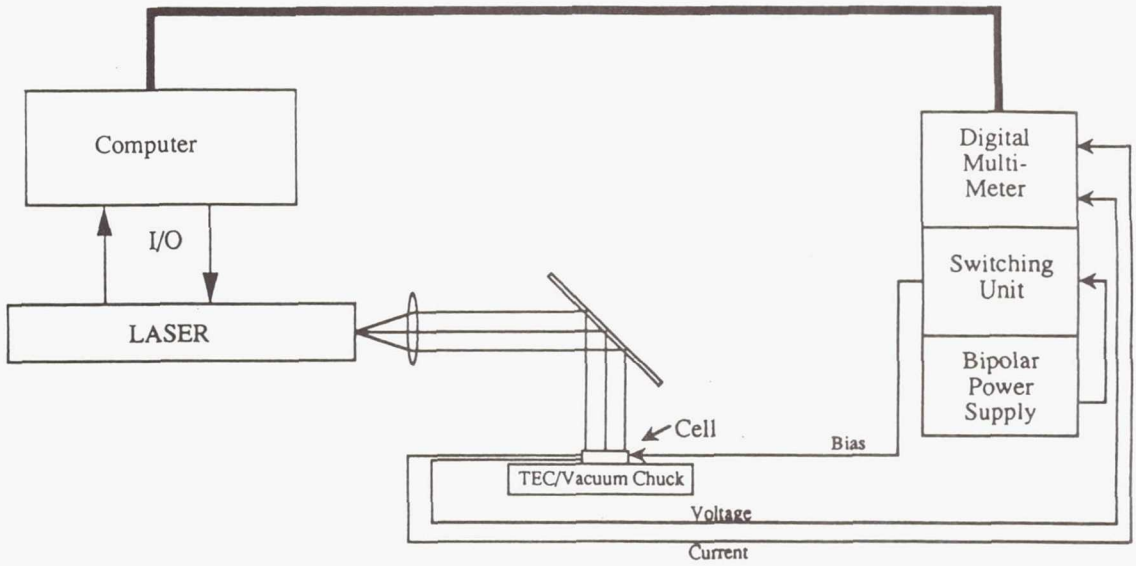


**Figure 12. Schematic Of Battelle Northwest Laboratory's Arrangement For A Laser Beaming Test Bed.**

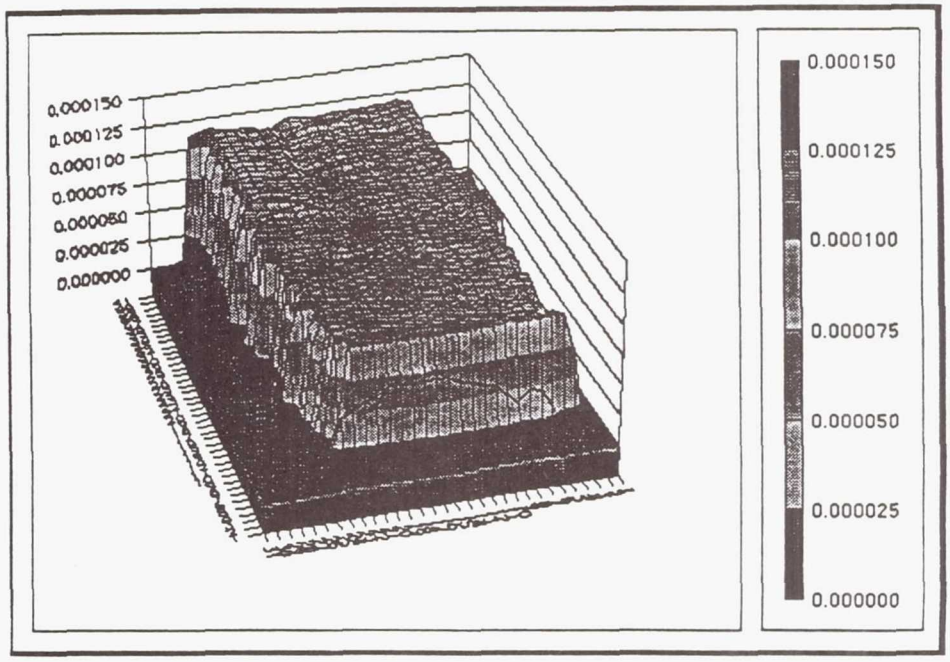


**Figure 13. Laser Intensity Profile Over A 3x4 cm Area At Cell Test Plane.**

# HIGH-EFFICIENCY HETEROEPITAXIAL InP SOLAR CELLS

M.W.Wanlass, T.J.Coutts, J.S.Ward and K.A.Emery
*Solar Energy Research Institute (SERI), Golden, CO, 80401, U.S.A.*

## ABSTRACT

High-efficiency, thin-film InP solar cells grown heteroepitaxially on GaAs and Si single-crystal bulk substrates are being developed as a means of eliminating the problems associated with using single-crystal InP substrates (e.g., high cost, fragility, high mass density and low thermal conductivity). A novel device structure employing a compositionally graded $Ga_xIn_{1-x}As$ layer (~8 μm thick) between the bulk substrate and the InP cell layers is used to reduce the dislocation density and improve the minority carrier properties in the InP. The structures are grown in a continuous sequence of steps using computer-controlled atmospheric-pressure metalorganic vapor phase epitaxy (APMOVPE). Dislocation densities as low as $3x10^7$ $cm^{-2}$ and minority carrier lifetimes as high as 3.3 ns are achieved in the InP layers with this method using both GaAs or Si substrates. Structures prepared in this fashion are also completely free of microcracks. These results represent a substantial improvement in InP layer quality when compared to heteroepitaxial InP prepared using conventional techniques such as thermally cycled growth and post-growth annealing.

The present work is concerned with the fabrication and characterization of high-efficiency, thin-film InP solar cells. Both one-sun and concentrator cells have been prepared from device structures grown on GaAs substrates. One-sun cells have efficiencies as high as 13.7% at 25°C. However, results for the concentrator cells are emphasized. The concentrator cell performance is characterized as a function of the air mass zero (AM0) solar concentration ratio (1-100 suns) and operating temperature (25-80°C). From these data, the temperature coefficients of the cell performance parameters are derived as a function of the concentration ratio. Under concentration, the cells exhibit a dramatic increase in efficiency and an improved temperature coefficient of efficiency. At 25°C, a peak conversion efficiency of 18.9% (71.8 suns, AM0 spectrum) is reported. At 80°C, the peak AM0 efficiency is 15.7% at 75.6 suns. These are the highest efficiencies yet reported for InP heteroepitaxial cells. Approaches for further improving the cell performance are discussed.

## INTRODUCTION

InP solar cells are particularly attractive for space applications due to their resistance to radiation damage and demonstrated high energy conversion efficiency under the AM0 spectrum [ref. 1, 2]. Single-crystal InP wafers, however, have characteristics which make them generally undesirable for solar cell fabrication and operation. These

include high cost, high fragility, high mass density and low thermal conductivity. Thus, in order to promote the widespread use of InP cells in space it is critical that techniques are developed for fabricating high-efficiency, thin-film InP cells. Three approaches are currently under investigation for solving this problem and they include CLEFT [ref. 3] using a bulk InP wafer, chemical separation [ref. 4] from an InP wafer and heteroepitaxy onto single-crystal materials with more desirable characteristics. Of the three options, heteroepitaxy may prove to be the preferred choice since, ultimately, large-area thin films of InP may be too difficult to handle and process on a large scale. Furthermore, it is uncertain whether the InP bulk substrates used in the CLEFT and chemical separation processes will actually be reusable. Heteroepitaxial cells have the advantage of being fully compatible with existing cell processing technologies as well as being based on mature single-crystal wafer technologies in materials such as GaAs, Ge and Si.

Due to the large differences in lattice constant and thermal expansion coefficient between InP and the above-mentioned materials, problems generally arise which inhibit the growth of high-quality InP heteroepilayers. For example, the lattice constant mismatch is 3.7% between InP and GaAs and 7.5% between InP and Si. Such large mismatches result in high mechanical stresses in the resulting epilayers which, in turn, lead to the generation of a high density of defects. The defects include dislocations, stacking faults and even microcracks. Several techniques have been investigated for reducing the density of defects in the InP layers, thereby reducing their deleterious effects. These have included thermally cycled growth, post-growth annealing and inclusion of an intermediate GaAs layer for the case of InP grown on a Si substrate. Limited success has been realized with these procedures and InP epilayers with dislocation densities of ~$3x10^8$ $cm^{-2}$ and minority carrier lifetimes of ~1 ns or less in undoped material are reported for the best cases when grown on GaAs substrates [ref. 5]. Unfortunately, InP layers with these properties are of insufficient quality for the fabrication of high-efficiency solar cells. Using post-growth annealing, the highest efficiency for InP cells grown directly on GaAs substrates is 10.8% (one-sun, AM0, 25°C) [ref. 6]. Even lower efficiencies have been reported for InP cells grown on Si substrates [ref. 7].

In previous work [ref. 8], we reported on the use of a novel structure for the growth of high-quality InP epilayers on substrates such as GaAs, Ge and Si. A full description of the device structure concept is given in [ref. 9]. The structure utilizes a compositionally graded $Ga_xIn_{1-x}As$ layer disposed between the bulk substrate and the InP device layers. This serves to reduce the dislocation density in the InP device layers substantially when compared to the conventional techniques discussed above. In this work, substrates of GaAs and GaAs/Si were placed side by side in the growth reactor and identical structures were deposited on each. The resulting InP epilayers were then characterized using transmission electron microscopy (TEM), electron-beam-induced current (EBIC) and photoluminescence-decay (PL-decay) lifetime techniques to assess the defect density and minority carrier lifetime. $n^+/p$ shallow homojunctions were grown into the InP layers and solar cells with grids designed for one-sun operation were processed from the structures grown on the GaAs substrates only. Additionally, structures with three different $Ga_xIn_{1-x}As$ graded layer thicknesses (8, 12 and 20 μm) were grown and characterized; however the InP material and solar cell quality was essentially independent of the thickness chosen in this range. With this structure, dislocation densities of $3x10^7$ $cm^{-2}$ and minority carrier lifetimes of over 3 ns were achieved in the InP layers using either GaAs or GaAs/Si substrates. Furthermore, the InP epilayers were completely free of microcracks

in both cases, which is an extremely important result for high-quality solar cell fabrication. InP solar cells with one-sun efficiencies of 13.7% (AM0, 25°C) and 15.7% (global, 25°C) were fabricated on GaAs substrates using an 8μm-thick $Ga_xIn_{1-x}As$ graded layer. Unfortunately, pinholes in the InP layers grown on the GaAs/Si substrates resulting from surface contamination prior to growth precluded the fabrication of cells in this case. However, it seems reasonable to assume that InP cell efficiencies similar to those achieved using GaAs substrates should be possible on Si substrates due to the similar dislocation densities and minority carrier lifetimes observed in the InP layers grown on either substrate type.

In the remainder of this paper, we describe the epitaxial growth, fabrication and characterization of concentrator heteroepitaxial InP solar cells grown on GaAs substrates using a compositionally graded intermediate structure similar to that described above. The cell performance has been determined as a function of the concentration ratio and the operating temperature. We have also investigated the behavior of the cell performance parameter temperature coefficients as a function of the concentration ratio. The details of this work are described in the sections which follow. Support for this work was provided by the U.S. Department of Energy under contract No. DE-AC02-83CH10093 through an award from the SERI Director's Development Fund.

## DEVICE STRUCTURE

A schematic diagram of the heteroeopitaxial (HE) InP solar cell structure grown on a GaAs substrate is given in figure 1. The structure is initiated with a thin buffer layer of p-GaAs which is then followed by the p-$Ga_xIn_{1-x}As$ linearly graded layer (LGL) which has a thickness of 8 μm for the results reported here. The LGL is followed by a buffer layer of $Ga_{0.47}In_{0.53}As$ which is lattice matched to InP. The InP solar cell layers are finally deposited at the top of the structure and these comprise a high-efficiency n+/p shallow homojunction (SHJ) cell structure (in figure 1, "BSFL" is an acronym for "back-surface field layer"). A back contact of pure Au is applied to the exposed bottom surface of the GaAs substrate. The top grid contact on the surface of the InP cell emitter is also composed of pure Au. A 2-layer antireflection coating is deposited on the front surface of the cell structure and an Entech prismatic cover is also incorporated into the structure to allow for a high top-contact-metallization coverage (~20%). Further details of the device structure are discussed below.

## EXPERIMENTAL

The heteroepitaxial solar cell structures were grown by atmospheric-pressure metalorganic vapor-phase epitaxy (APMOVPE) using a specially designed, RF-heated vertical reactor vessel [ref. 10] which yields highly uniform epilayers. The growth system is a home-built, run-vent type and uses palladium-purified hydrogen as the carrier gas through the main mixing manifold and through each of the metalorganic source cylinders. The primary reactants used in the growth process included trimethylindium, trimethylgallium, pure phosphine and pure arsine. The sources for p- and n-type doping were diethylzinc and 500 ppm hydrogen sulfide in hydrogen, respectively. Zn-doped p+-GaAs wafers oriented 2° off the (100) were supplied by Sumitomo Electric, Inc. and used as substrates. These were loaded directly into the growth reactor as received from the vendor (i.e., without any pre-growth cleaning or etching steps). Prior to growth, the GaAs substrates were heated to 700°C for 10 minutes with

arsine flowing into the reactor vessel. Growth was then carried out at a constant temperature of 650°C. The structures were grown at a rate of 75 - 175 nm $min.^{-1}$ in a continuous sequence of steps (i.e., without stop-growth periods at the heterointerfaces). A typical growth run takes about 2.5 hours, including the time required for warm-up and cool-down of the reactor vessel. The entire process is controlled and monitored using a home-built, PC-based control system.

The epitaxial structures were then processed into completed concentrator solar cells using conventional techniques. Ohmic, low-resistance contacts were made to both the back surface of the $p^+$-GaAs substrate and the $n^+$-InP emitter surface using electroplated Au as deposited. The back surface of the GaAs substrate was etched in 1% by volume bromine in methanol for 5 minutes at room temperature prior to applying the metallization. The top contact and device mesa geometries were defined by photolithographic techniques using positive photoresist. The top contact grids were specially designed to accomodate an overlying Entech prismatic cover which was originally designed for concentrator GaAs solar cells [ref. 11]. A center-to-center grid line spacing of 127 μm was used and the individual gridlines have a cross-sectional area of ~125 $\mu m^2$ (~25 μm wide by ~5 μm high). A busbar is included at both ends of the grid lines in this design to allow for the simultaneous placement of test probes at both ends. This aspect of the grid design results in better performance under concentration. Through the use of the Entech cover, it is possible to cover ~20% of the cell surface with the grid metallization without incurring any photocurrent losses due to grid obscuration. This allows for ample grid metallization on the cell which results in low electrical power losses within the top contact. As such, the Entech cover has proven to be a very important component in the fabrication of high-efficiency concentrator cells. Electrical isolation of the individual cells was accomplished by etching moats through the $n^+/p$ InP junction with concentrated HCl. A two-layer antireflection coating of ZnS (~55 nm) followed by $MgF_2$ (~95 nm) was then deposited on the front surface of the device wafer. The concentrator cells were completed by installing the Entech cover. A typical array of completed heteroepitaxial InP concentrator cells is shown in figure 2. The effect of the Entech cover is also illustrated in this figure. Each individual cell has an area of 0.0746 $cm^2$ which is computed by subtracting the areas of the two busbars from the total device mesa area (this is a standard area definition for concentrator solar cells [ref. 12]).

The performance of the concentrator cells was characterized by measuring the absolute external quantum efficiency (AEQE) as a function of temperature as well as the illuminated current-voltage characteristics as a function of the temperature and the concentration ratio. The latter data sets were used to calculate the dependence of the cell performance parameter temperature coefficients on the concentration ratio. The measurement techniques have been described previously [ref. 13]. All of the results reported here are referenced to the AM0 spectrum [ref. 14]. A discussion of the cell performance is given in the following section.

## RESULTS AND DISCUSSION

Initially, the current-voltage characteristics for the cells were measured as a function of temperature under one-sun AM0 conditions in order to obtain the necessary information for evaluating the efficiency under concentration (i.e., the one-sun short-circuit current ($I_{sc}$) is needed to calculate the concentration ratio for

concentrator measurements). To within experimental error, we found $I_{sc}$ to be independent of temperature. The AEQE data shown in figure 3 illustrates why $I_{sc}$ is temperature independent. As expected, the InP band edge shifts to longer wavelengths as the temperature increases and one would normally expect an increase in $I_{sc}$ due to this effect. However, a concomitant decrease in the short- and mid-wavelength response is also observed for these devices as the temperature increases which offsets any increase in $I_{sc}$ due to the band gap shift. Thus, $I_{sc}$ remains essentially constant as the temperature is increased. Note that the blue response for these cells is relatively low. This characteristic is typical of shallow-homojunction solar cells which have a high surface recombination velocity. We have shown in previous work that graded emitter doping profiles can be used to improve the blue response in these cells [ref. 15]. However, a technique for effectively passivating the emitter surface needs to be developed in order to realize InP cells with near-theoretical performance characteristics.

The HE InP cell performance was then tested as a function of the temperature and the AM0 concentration ratio and the results from these measurements are shown in figures 4 and 5. The AM0 efficiency (figure 4) increases rapidly at low concentration ratios and then reaches a broad plateau for concentration ratios of ~40 or more. At 25°C, the cells have efficiencies of close to 19% over a broad range of concentration ratios. This value decreases to ~16% as the temperature is increased to 80°C. The broad plateau in efficiency can be understood by examining the open-circuit voltage ($V_{oc}$) and fill factor (FF) *versus* concentration ratio data given in figure 5. The behavior of $V_{oc}$ is as expected. In fact, when the $V_{oc}$ data are plotted against *ln*(concentration ratio) a straight line is obtained. However, the FF data indicate that the cells quickly become series-resistance limited as the concentration ratio is increased beyond ~20 suns. Additionally, this effect appears to be enhanced as the operating temperature is increased. An analysis of the resistance components contributing to the overall series resistance for these cells shows that the emitter sheet resistance is primarily responsible for limiting the concentrator cell performance. A lower emitter sheet resistance or a smaller grid line spacing will be necessary in order to improve this aspect of the cell performance. The broad plateau in efficiency *versus* concentration ratio is seen to be due to offsetting effects of the $V_{oc}$ and FF as the concentration ratio increases.

Current-voltage data for an HE InP concentrator cell at peak efficiency are shown in figure 6. At 25°C, the efficiency reaches 18.9% under the AM0 spectrum at 71.8 suns. As shown in figure 4, the peak efficiency at 80°C is 15.7% at 75.6 suns. These values are very encouraging and demonstrate that HE InP cells have the potential to reach high efficiencies at high concentration ratios and high temperatures. Additionally, these results show that the HE cell efficiencies improve dramatically when operated under concentration.

Using the data shown in figures 4 and 5, we have calculated the temperature coefficients for the HE InP cell performance parameters as a function of the concentration ratio. As a basis for comparison, we have also fabricated homoepitaxial (HO) InP concentrator solar cells on single-crystal InP substrates with junction structures which are similar to those used in the HE InP cells. Similar concentrator measurements and temperature coefficient calculations have been performed for the HO InP cells. In figure 7, we compare the $V_{oc}$ temperature coefficients for the two types of cells as a function of the concentration ratio. At low concentration ratios, the HO cells clearly out-perform the HE cells. However, at high concentrations, the HE cell temperature performance improves substantially and approaches that of the HO cells. This result highlights an additional advantage of operating the HE cells under

concentration.

Efficiency and FF temperature coefficient data for the HE InP cells as a function of the concentration ratio are plotted in figure 8. The data indicate that the temperature performance of the FF actually degrades with increasing concentration. This behavior is linked to the series resistance problems discussed previously. Nevertheless, the temperature performance of the conversion efficiency actually improves as the concentration ratio is increased due to the behavior of the $V_{oc}$ temperature coefficient (shown in figure 7). The temperature coefficient of efficiency would improve much more rapidly with concentration if the cell series resistance were reduced. This problem remains as an important one to solve for these devices in order to realize higher efficiencies at high concentration ratios.

## SUMMARY

High-efficiency heteroepitaxial InP solar cells have been fabricated on GaAs substrates using a novel compositionally graded intermediate layered structure. One-sun cells have AM0 efficiencies as high as 13.7% at 25°C. The concentrator cell performance has been characterized as a function of the temperature and the AM0 concentration ratio. Peak concentrator AM0 efficiencies of 18.9% at 71.8 suns, 25°C and 15.7% at 75.6 suns, 80°C have been obtained with these cells, which are the highest efficiencies yet reported for InP heteroepitaxial solar cells. It has also been shown that the conversion-efficiency temperature coefficient for these cells improves substantially as the concentration ratio is increased. The advantages of operating the HE InP cells under concentration include reduced cell area, higher conversion efficiencies and improved temperature performance.

The cell performance is presently limited by three main loss factors including 1) recombination at the surface of the emitter layer, 2) a high emitter-layer sheet resistance leading to reduced FF values at high concentration and 3) a high density of threading dislocations in the active cell layers. Improvements in any of these areas will lead to increased cell efficiencies.

Technologically, it would be important and immediately useful if the results obtained in this work for InP cells grown on GaAs substrates could be duplicated using Si substrates. Such a result would make HE InP cells a viable contender for space power applications and efforts toward this goal are currently underway.

## REFERENCES


1) Yamaguchi, M. et al.; Jap. J. Appl. Phys., **23**, 302, 1984.

2) Keavney, C.J. et al.; Conf. Record 21st IEEE Photovoltaic Specialists Conference, 141, 1990.

3) McClelland, R.W. et al.; Appl. Phys. Lett., **37**, 560, 1980.

4) Spitzer, M.B. et al.; Conf. Record 21st IEEE Photovoltaic Specialists Conference, 196, 1990.

5) Vernon, S.M. et al.; Proc. Mat. Res. Soc. Symp., **198**, 163, 1990.

6) Keavney, C.J., Spire Corp.; private communication, Mar. 1991.

7) Keavney, C.J. et al.; Conf. Record 20th IEEE Photovoltaic Specialists Conference, 654, 1988.

8) Al-Jassim, M.M. et al.; Proc. Mat. Res. Soc., 1990 Spring Meeting, San Francisco, CA, April 16-21, 1990.

9) Wanlass, M.W. et al.; U.S Patent No. 4,963,949, Oct. 16, 1990.

10) Wanlass, M.W.; U.S. Patent No. 4,649,859, Mar. 17,1987.

11) O'Neill, M.J.; U.S. Patent No. 4,711,972, Dec., 1987.

12) Terrestrial Photovoltaic Measurement Procedures, Report ERDA/NASA/102277/16, June, 1977.

13) Wanlass, M.W. et al.; Proc. 10th Photovoltaic Advanced Research and Development Meeting, Lakewood, CO, U.S.A., Oct.23-25, 1990. To be published in *Solar Cells*, 1991.

14) Wehrli, C.; Extraterrestrial Solar Spectrum, Physical Meteorological Observatory and World Radiation Center, tech. rep. no. 615, Davos-Dorf, Switzerland, July 1985.

15) Wanlass, M.W. et al.; Proc.1st Int. Conf. on InP and Rel. Mat., Norman, OK, U.S.A., March, 1989, **1144**, 445-458, SPIE (1989).

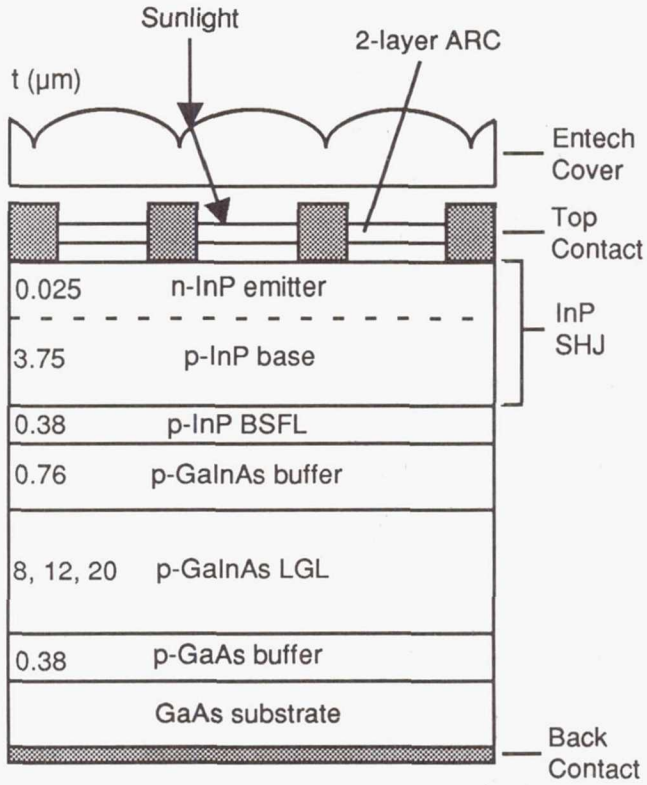


**Figure 1.** Schematic diagram of the HE InP concentrator solar cell structure on a GaAs substrate.

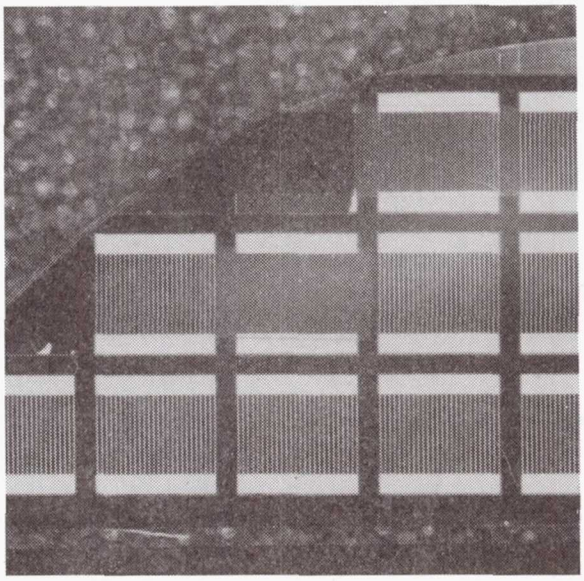

**Figure 2.** Plan-view photomicrograph of a typical array of HE InP concentrator cells. The cell in the center of the micrograph has an Entech cover properly installed.

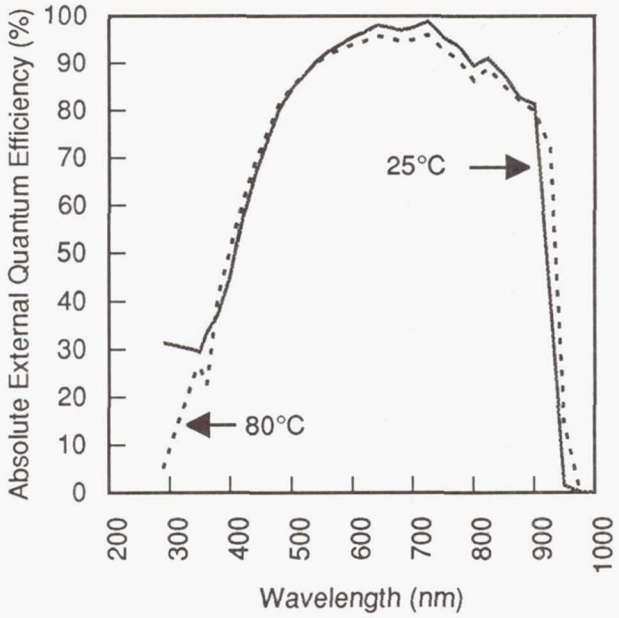


**Figure 3.** AEQE data for an HE InP concentrator cell at 25°C and 80°C.

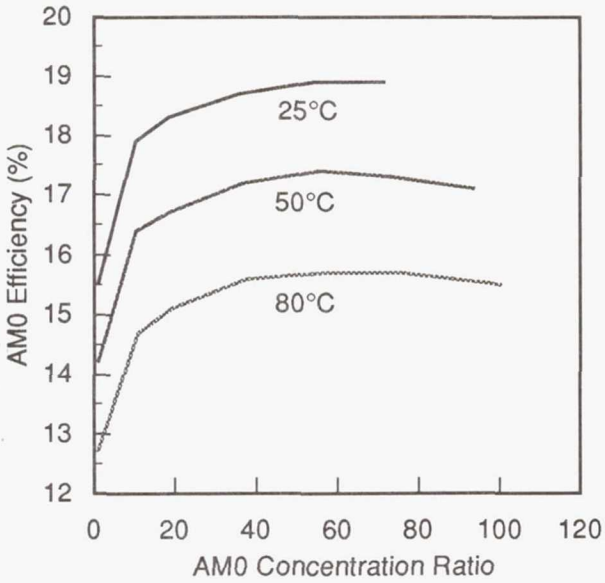


**Figure 4.** AM0 conversion efficiency data for an HE InP concentrator cell as a function of the operating temperature and AM0 concentration ratio.

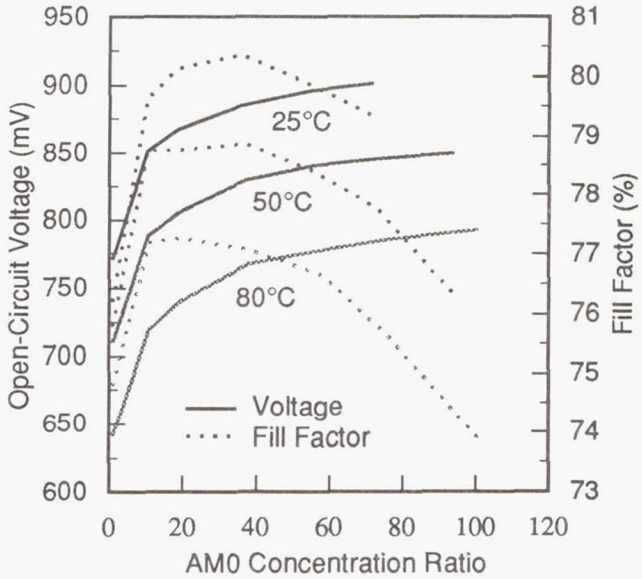


**Figure 5.** Open-circuit voltage and fill factor data for an HE InP concentrator cell as a function of the operating temperature and AM0 concentration ratio.

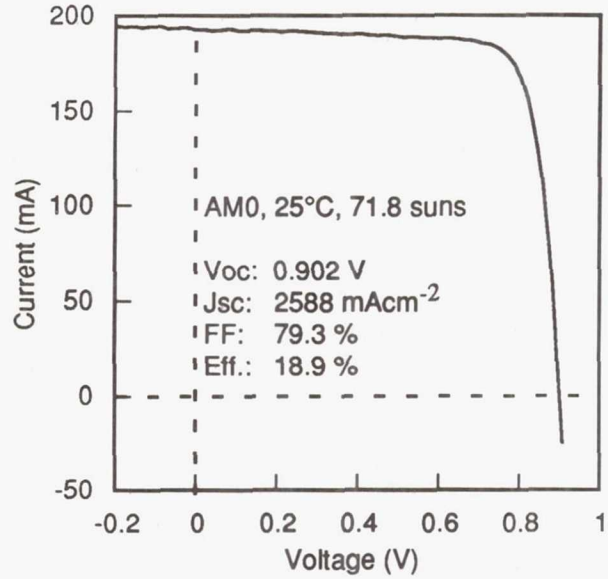


**Figure 6.** Current-voltage data for an HE InP concentrator cell at peak efficiency under concentrated AM0 illumination.

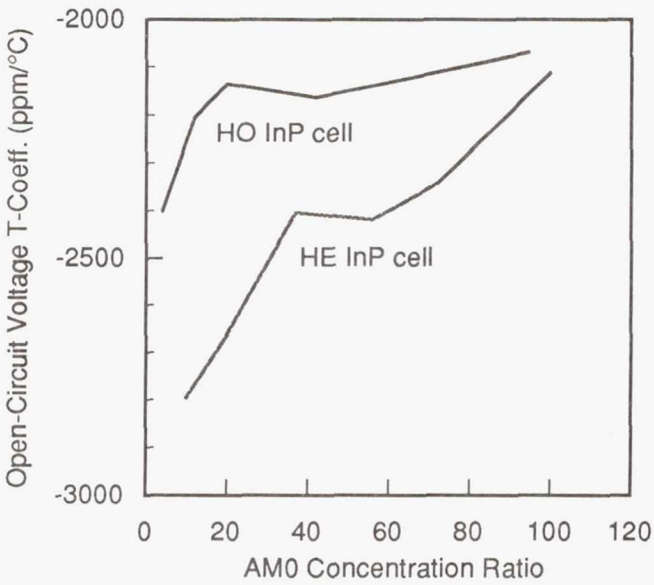


**Figure 7.** Open-circuit voltage temperature coefficient data as a function of the AM0 concentration ratio for HO and HE InP concentrator cells.

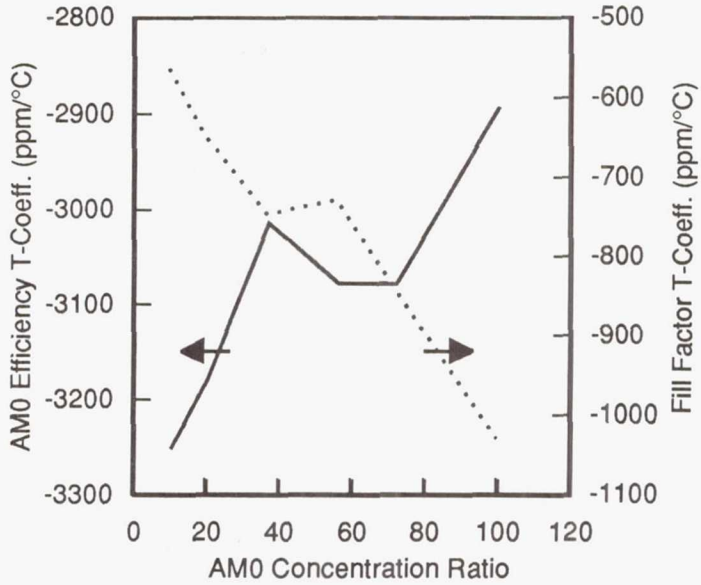


**Figure 8.** AM0 conversion efficiency, and fill factor, temperature coefficient data as a function of the concentration ratio for an HE InP concentrator cell.

# InP Concentrator Solar Cells for Space Applications

J. S. Ward, M. W. Wanlass, T.J. Coutts and K.A. Emery
*Solar Energy Research Institute*
*Golden, CO 80401*

## ABSTRACT

The design, fabrication and characterization of high-performance, $n^+/p$ InP shallow-homojunction (SHJ) concentrator solar cells is described. The InP device structures were grown by atmospheric-pressure metalorganic vapor phase epitaxy (APMOVPE). A preliminary assessment of the effects of grid collection distance and emitter sheet resistance on cell performance is presented. At concentration ratios of over 100, cells with AM0 efficiencies in excess of 21% at 25°C and 19% at 80°C are reported. These results indicate that high-efficiency InP concentrator cells can be fabricated using existing technologies. The performance of these cells as a function of temperature is discussed, and areas for future improvement are outlined.

## INTRODUCTION

In the past several years, InP solar cell performance has begun to approach the high conversion efficiencies predicted by the early modeling efforts [ref.1]. With reported end-of-life/begining-of-life ratios (EOL/BOL) for efficiency of about 90%, the radiation resistance of InP is generally acknowledged to be superior to both GaAs and Si [ref. 2 ]. At this point, one of the major obstacles to a more widespread use of InP in space is the price of high-quality, single-crystal substrates. Various strategies have been suggested to limit the impact of this cost. These strategies include the development of multijunction cells to boost efficiency, heteroepitaxial growth techniques, which would eliminate the need for InP substrates, and concentrator cells, which would greatly reduce the impact of their cost. Overlapping efforts in all three of these approaches are currently being pursued at the Solar Energy Research Institute.

Recent work on space photovoltaic concentrator arrays indicate that attractive power densities and power-to-mass ratios are achievable with these systems [ref.3]. While excellent work is being done concerning the effects of the space environment on concentrator modules, the possibility that radiation effects may prove to be problematic for these systems cannot be overlooked. InP may prove to be a radiation-resistant alternative to GaAs. InP concentrator cells have the potential for high conversion efficiencies [ref. 2] and their high EOL/BOL could make space photovoltaic concentrator arrays competitive with more conventional flat-plate systems.

The work done on InP concentrator cells should yield information that will be directly applicable to the emerging heteroepitaxial cell technology. We have already seen dramatic improvements in the performance parameters of heteroepitaxial InP cells when measured under solar concentration.

Improving the performance of the SERI-designed InP/$Ga_{0.47}In_{0.53}As$ monolithic tandem cell requires advances in the design of the InP top cell [ref. 4]. The $Ga_{0.47}In_{0.53}As$ bottom cell is exhibiting near theoretical performance levels but the InP top cell is showing evidence of series resistance problems at concentration ratios above 40 suns. Minimization of these series resistance losses may allow the tandem efficiency to exceed 30% AM0, (At 28.8%, AM0, 40 suns, 25°C, this is already the most efficient monolithic photovoltaic device yet demonstrated).

In previous work [ref.5], we performed an empirical investigation of the InP SHJ solar cell designed to operate at one sun. Optimum design parameters were identified and devices were fabricated that yielded one-sun AMO efficiencies of 17.6% at 25° C. A thin (25 nm) emitter was found to be essential to minimize the roll off in the blue response attributable to the unpassivated InP surface. For concentrator cells, the benefits of this

enhanced blue response must be weighed against the high sheet resistance associated with thin emitter designs. At one-sun current densities (~35 mA $cm^{-2}$) the negative effects of the high sheet resistance can be minimized by adjusting the grid finger spacing. However, our concentrator cells utilize Entech prismatic covers [ref.6] originally designed for GaAs concentrator cells operating at 100 suns. This aspect of our concentrator cell design results in the grid line spacing being fixed at 127 μm. Therefore, it is reasonable to expect that the optimum concentrator cell structure may differ from the optimum one-sun structure. In this paper we describe our initial efforts to fabricate high-performance InP concentrator cells designed to operate under 100 AM0 suns.

## DEVICE DESIGN

A schematic diagram of the InP concentrator solar cell structure is given in figure 1. The devices are grown by APMOVPE on Zn-doped, $p^+$ substrates oriented in the (100) direction. Growth is carried out in a vertical reactor vessel at a temperature of 620°C and in a purified hydrogen ambient. The primary reactants are trimethylindium and phosphine. The dopants consist of hydrogen sulfide and diethylzinc. A $p^+$- back-surface-field layer that is grown to a thickness of 0.38 μm, is followed by a p-base layer that is doped to ~ $10^{17}$ $cm^{-3}$ and grown to a thickness of 3.8 μm. The thin $n^+$ emitter layer, that is doped to 3.7 x$10^{18}$ $cm^{-3}$ completes the growth.

After etching the back surface in a 1% by volume Br in MeOH solution for 5 minutes, an ohmic contact is formed by electroplating 0.1 μm of Au, 0.1 μm of Zn, and 3 μm of Au onto the back surface and then annealing it on a graphite strip heater at 375° C for 90 seconds. The grid pattern on the emitter surface is defined by standard photolithography and pure Au is electroplated to a thickness of 5 μm. Cell isolation is accomplished by an HCL etch after a photolithographic mesa definition. The devices are completed with the deposition of a $ZnS/MgF_2$ anti-reflection coating and application of prismatic covers. (See fig.1)

The Entech prismatic cover is an essential component of the cell design. With the resistivity of electroplated gold often in excess of five times the bulk value [ref. 7], metalization schemes designed to handle current densities of 3.6 A per $cm^2$ necessarily entail a high grid coverage (~20%). We have found that with a properly designed anti-reflection coating, the optical losses associated with the use of the prismatic cover are under 5%. The major limitation associated with the use of the cover for this device is that the grid line spacing is fixed.

## EXPERIMENTAL

Our primary objective in this work was to demonstrate the potential of InP concentrator cells. However, development of the single-junction InP concentrator cells is important as a basis of comparison with the heteroepitaxial cells and the $InP/Ga_{0.47}In_{0.53}As$ tandem. As a starting point in our attempt to optimize the InP SHJ cell structure for operation under concentration, we decided to examine the effects of grid finger spacing and emitter layer sheet resistance on cell performance.

The three-terminal design of the monolithic $InP/Ga_{0.47}In_{0.53}As$ tandem cell uses a prismatic cover slip with a fixed center-to-center grid line spacing of 127 μm. In the three terminal configuration, every other grid line must be used for the middle contact. Both the top contact fingers and the middle contact moats are 25 μm wide, resulting in a grid finger collection distance (S/2) of 102 μm. Hall and electron probe measurements on our $n^+$-InP layers provide values of 1200 $cm^2$ $V^{-1}$ $s^{-1}$ for the electron mobility and 3.7 x $10^{18}$ $cm^{-3}$ for the free electron density. This results in a resistivity value of 1.4 x $10^{-3}$ ohms-cm. Using the emitter thickness of 24 nm, the computed power loss at 100 suns due to lateral current spreading in the emitter is about 8%. This is an unacceptably high level for this component of the series resistance. When measured under solar concentration, the top cell of the tandem exhibits evidence of becoming series resistance limited beyond a concentration ratio of 40 suns. From the power loss calculation, we conclude that the drop in efficiency for the top cell of the tandem at concentration ratios above 40 is caused primarily by a non-optimum grid line spacing.

As a test of this hypothesis, we fabricated single-junction InP concentrator cells that use a grid line spacing of 127 μm. The effective collection distance in this case is one-half of the tandem's collection distance, or

51 μm. Due to the $S^2$ dependence of the power losses in the emitter, this gives a reduction by a factor of four from 8% to 2%, which is a more reasonable level for this loss mechanism. We also fabricated cells with emitter thicknesses of 33 and 240 nm in order to test whether a lower emitter sheet resistance would result in a further power loss reduction under concentration. The computed lateral sheet resistance power losses associated with these designs are 1.6% and 0.02%, respectively.

The performance of these cells was characterized by absolute external quantum efficiency (AEQE) measurements as well as illuminated current-voltage characteristics as a function of the concentration ratio. All measurements were made at both 25 and 80°C. All efficiencies reported here are referenced to the AM0 spectrum [ref.8]. The cell performance is discussed in the following section.

## RESULTS AND DISCUSSION

When one compares the efficiency as a function of concentration for the single-junction cells with that of the top cell of the InP/$Ga_{0.47}In_{0.53}As$ tandem (fig. 2), it is apparent that the series resistance problem occuring between 40 and 100 suns is greatly reduced in the single-junction design. Furthermore, when the fill factor as a function of current density for the single-junction device with the 33 nm emitter is compared to that of the device with the 240 nm emitter (fig. 3), the similarity in behavior suggests that the resistance due to lateral current spreading in the emitter is not a major power loss mechanism for this concentrator grid design. The above mentioned power losses for this component of the series resistance are consistent with the observed performance of the cells. This implies that a grid pattern with a finger spacing compatible with available Entech prismatic cover material is adequate for the fabrication of high-performance InP SHJ concentrator cells operating at 100 suns.

The single-junction InP concentrator cell design utilizing a 33 nm-thick emitter has achieved high efficiency levels at concentration ratios of over 100 suns. Peak efficiency under the AM0 spectrum at 25°C was 21.4% at a concentration ratio of 106.5 suns. This represents a gain of 2.3 efficiency percentage points compared to the best reported one-sun result of 19.1% at 25°C [ref. 9]. The efficiency dropped to 19.1% at 80°C and 125 AM0 suns (fig. 4). This high-temperature result is particularly relevant to operation under concentration where 80°C is considered to be a realistic temperature for passive cooling at 100 suns.

Analysis of the AEQE data (not shown here), indicates that improvements in the performance of these cells will likely be achieved by fabricating devices with even thinner emitters, which will enhance the blue response and increase $J_{sc}$. Development of a passivating window layer should have a similar effect as well as providing a possible increase in $V_{oc}$.

## SUMMARY

As part of an ongoing effort to make InP-based solar cells a realistic option for the space community, InP concentrator cells have been fabricated and characterized as a function of concentration ratio and temperature. AM0 conversion efficiencies of 21.4% at 25°C and 19.1% at 80°C have been achieved. The power loss due to lateral current spreading in the emitter layer was found to be within acceptable limits using a grid design that incorporates an available Entech prismatic cover. These results indicate that the necessary technologies presently exist for the fabrication of high-performance InP concentrator solar cells.

The InP concentrator cells described in this paper have attained a high level of performance utilizing well developed growth and processing techniques. Areas for further research include a more detailed look at the optimum emitter thickness for the present shallow-homojunction design. Higher efficiencies are expected for devices with slightly thinner emitters. We intend to apply low-resistance, highly adhesive metalization schemes currently being developed at SERI to these cells in the near future. Surface passivation is perhaps the best approach to further reducing the losses due to the sheet resistance of the emitter since thicker emitter layers could ultimately be employed. Experimental evidence suggests that at 80°C and at the current densities observed at 100 suns, these devices may become self-annealing. The power-to-mass ratios of certain space concentrator systems can be improved if radiation tolerance can be eliminated as a design constraint.

The InP concentrator cell comprises the top cell of the most efficient monolitic device yet demonstrated (the InP/$Ga_{0.47}In_{0.53}As$ tandem). This work has shown that minor design changes in the top cell of the tandem will result in an improved level of performance. When these designs are incorporated into the InP/$Ga_{0.47}In_{0.53}As$ tandem, AM0 conversion efficiencies in excess of 30% are anticipated.

## REFERENCES


1) J.J. Loferski: Theoretical Considerations Governing the Choice of Optimum Semiconductors for Photovoltaic Solar Energy Conversion. J. Appl. Phys.,**27**, 777, 1956.

2) C. Gordia, I.V. Geier and I. Weinberg: Predicted Performance of Near-optimally Designed Indium Phosphide Space Solar Cells at High Intensities and Temperatures. Conf. Record 20th IEEE PhotovoltaicSpecialists Conference, 695, 1988.

3) M.J. O'Neil and M.F. Piszczor: Mini-Dome Fresnel Lens Concentrator Development. Conf. Record SPRAT 1989, 443,1991.

4) M.W. Wanlass et al.: Monolitic InP/$Ga_{0.47}In_{0.53}As$ Tandem Solar Cells for Space. Technical Session 3, these proceedings.

5) M.W. Wanlass et al.: An Empirical Investigation of the InP Shallow-Homojunction Solar Cell. Conf. Record 20th IEEE Photovoltaic Specialists Conference, 491, 1988.

6) M.J. O'Neil, U.S. Patent No. 4,711,972, Dec., 1987.

7) T.A. Gessert and T.J.Coutts: Requirements of Electrical Contacts to Photovoltaic Solar Cells. MRS Symp. Proceed.,Vol 181, pp. 301-312,1990.

8) C. Wehrli, "Extraterrestrial Solar Spectrum," Physical Meteorological Observatory and World Radiation Center, tech. rep. no. 615, Davos-Dorf, Switzerland, July 1985.

9) C.J. Keavney, V.E.Haven and S.M. Vernon: Emitter Structures in MOCVD InP Solar Cells. Conf. Record 21st IEEE Photovoltaic Specialists Conference, 141, 1990.

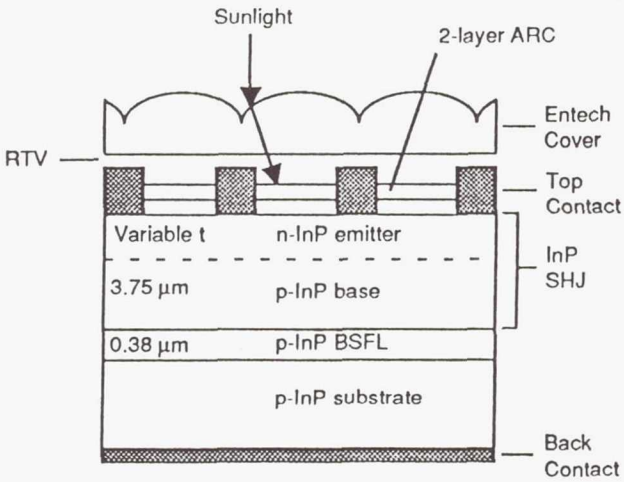


**Figure 1.** Cross-sectional schematic diagram of the InP shallow-homojunction concentrator solar cell structure.

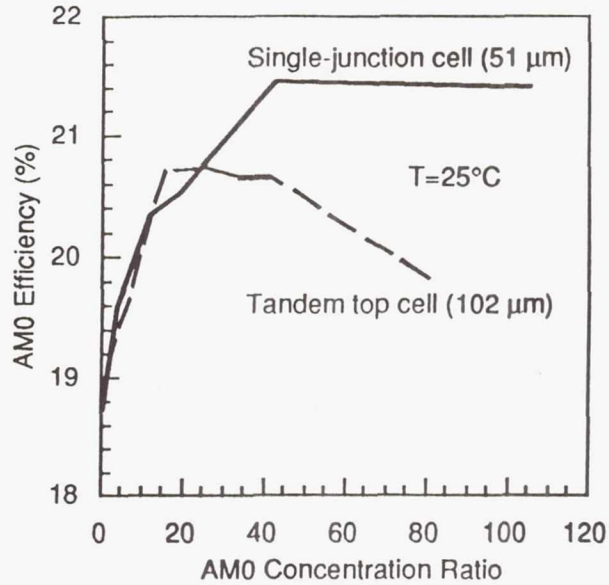


**Figure 2.** AM0 efficiency *versus* concentration ratio data for InP concentrator cells with similar structures, but different grid collection distances.

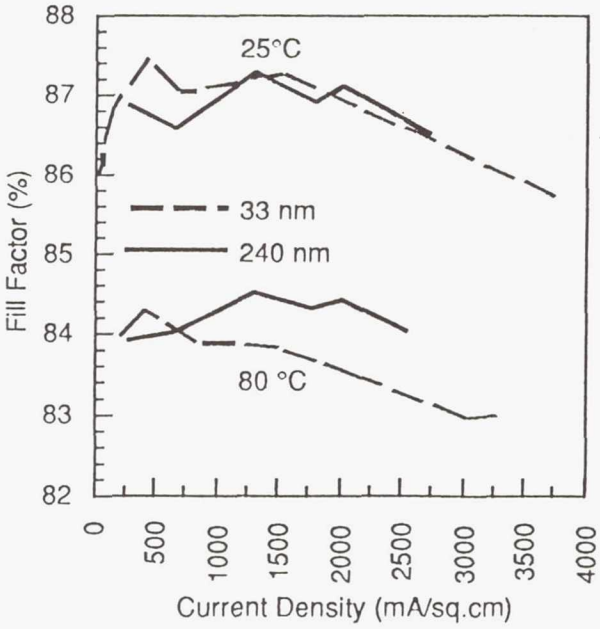


**Figure 3.** Fill factor *versus* current density data for InP concentrator cells with the same grid collection distance (51 µm), but different emitter thicknesses.

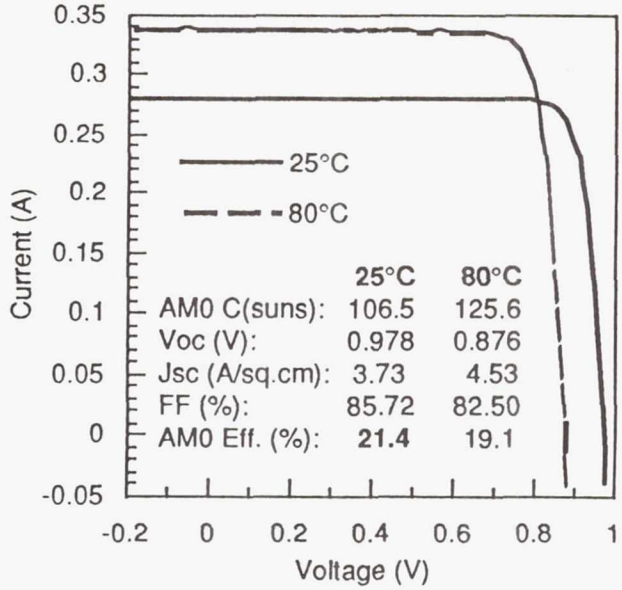


**Figure 4.** Current-voltage data for an InP shallow-homojunction cell at peak AM0 efficiency under concentration at 25°C and 80°C.

# COMPARATIVE MODELING OF InP SOLAR CELL STRUCTURES

R. K. Jain*, I. Weinberg and D. J. Flood
NASA Lewis Research Center
Cleveland, OH 44135

This work describes the comparative modeling of $p^+n$ and $n^+p$ indium phosphide solar cell structures using a numerical program PC-1D. The optimal design study has predicted that the $p^+n$ structure offers improved cell efficiencies as compared to $n^+p$ structure, due to higher open-circuit voltage. The various cell material and process parameters to achieve the maximum cell efficiencies are reported. The effect of some of the cell parameters on InP cell I-V characteristics has been studied. The available radiation resistance data on $n^+p$ and $p^+n$ InP solar cells are also critically discussed.

## INTRODUCTION

Recently indium phosphide has emerged as an attractive material for space power applications. Keavney et al. (ref. 1) have been successful in fabricating the highest efficieny (19.1% AM0 at 25°C) homoepitaxial $n^+p$ InP solar cells using the MOCVD growth technique. To date a majority of the work has been devoted to the development of n/p type cells and very limited work has been reported on p/n type InP cells. In spite of the various reasons which might have hampered the work on the development of p/n type cells, the results of initial R&D work reported in references 2 and 3 have been quite encouraging. LPE and MOCVD growth techniques have been used to fabricate p/n cells and laboratory efficiencies as high as 15.9% AM0 have been achieved by Choi et al. (ref. 3). During the last few years no work on p/n cells has been reported. The aim of this study is to compare the optimally designed performance of $n^+p$ and $p^+n$ InP solar cells. PC-1D, a one-dimensional numerical program (ref. 4) has been used to model the two structures considered in this work. The effect of minority carrier diffusion lengths on $p^+n$ InP cell performance have been considered. The scope of this paper does not allow for discussion of the complete parametric study and a critical comparison with the various modeling studies available in the literature. This work will be reported in a future paper. The radiation resistance of p/n and n/p InP cells has been compared and the results indicate the need for a systematic reevaluation of the comparative radiation resistance of the two InP cell configurations.

---

* This work was done while the author held a National Research council-NASA LeRC Research Associateship.

## MODELING APPROACH

The PC-1D computer program developed by Basore et al. (ref. 4) was used to model and optimally design $n^+p$ and $p^+n$ InP solar cells. This one-dimensional program solves the standard semiconductor device equations a finite-element method. Relevant InP solar cell material and process parameters have been varied to arrive at the maximum cell performance. The effect of a single parameter on the cell I-V characteristics has been studied by varying the parameter of interest and keeping all other parameters constant.

## RESULTS AND DISCUSSION

Figure 1 and 2 show the calculated current-voltage characteristics (AM0, 1 sun, 137.2 mW/cm$^2$, 25°C) for the $p^+n$ and $n^+p$ InP solar cell

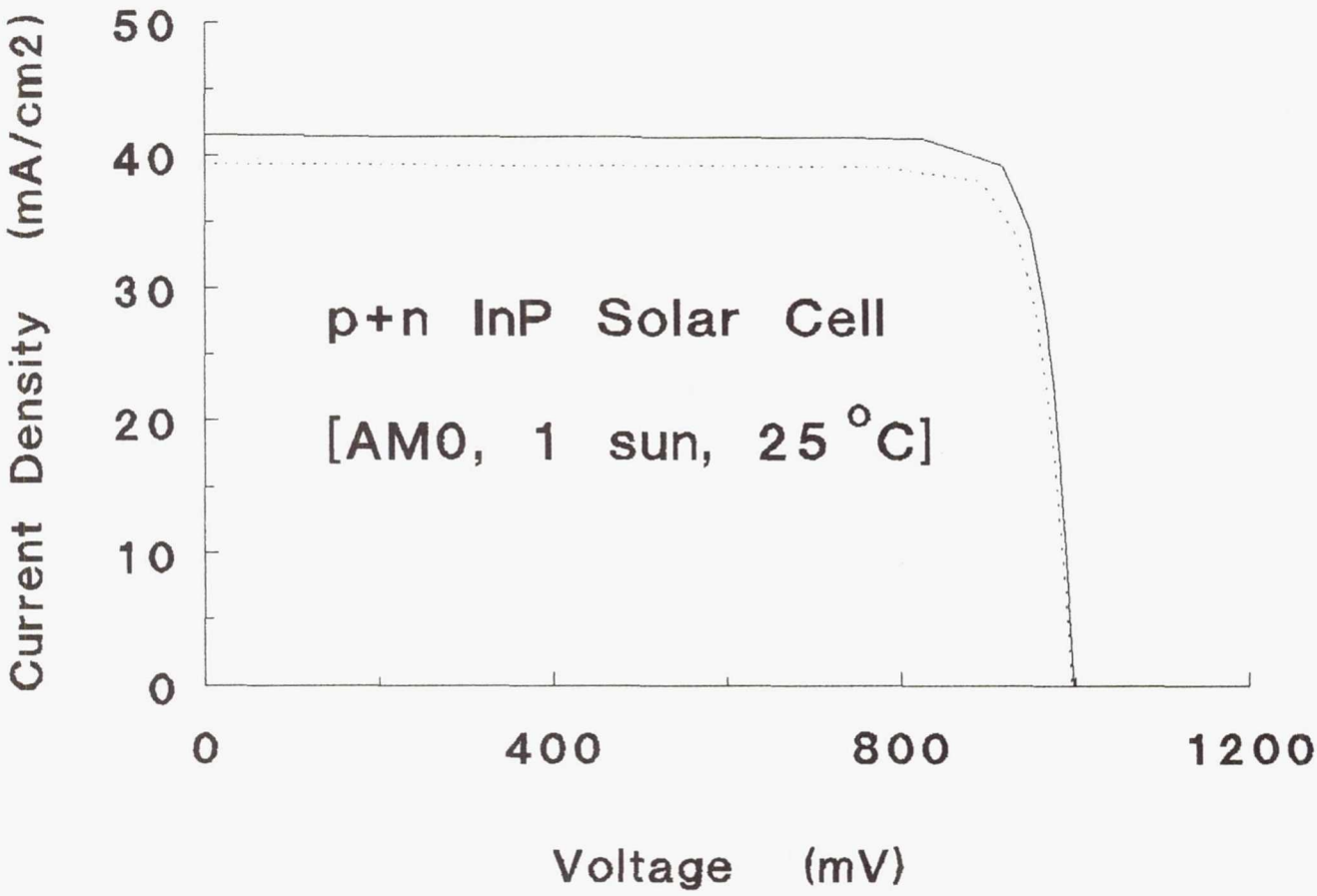


Fig. 1 Calculated I-V Characteristics of Optimally Designed $p^+n$ InP Solar Cells. The Solid Line Curve ($J_{sc}$=41.49 mA/cm$^2$, $V_{oc}$=998 mV, FF=0.869, Eff=26.2%) is for Grid Shadowing Losss of 0% and Series Resistance of 0.1 ohm cm$^2$. The Dotted Line Curve ($J_{sc}$=39.35 mA/cm$^2$, $V_{oc}$=996 mV, FF=0.867, Eff=24.8%) is for Grid Shadowing Loss of 5% and Series Resistance of 0.3 ohm cm$^2$. The other parameters are as per Table I.

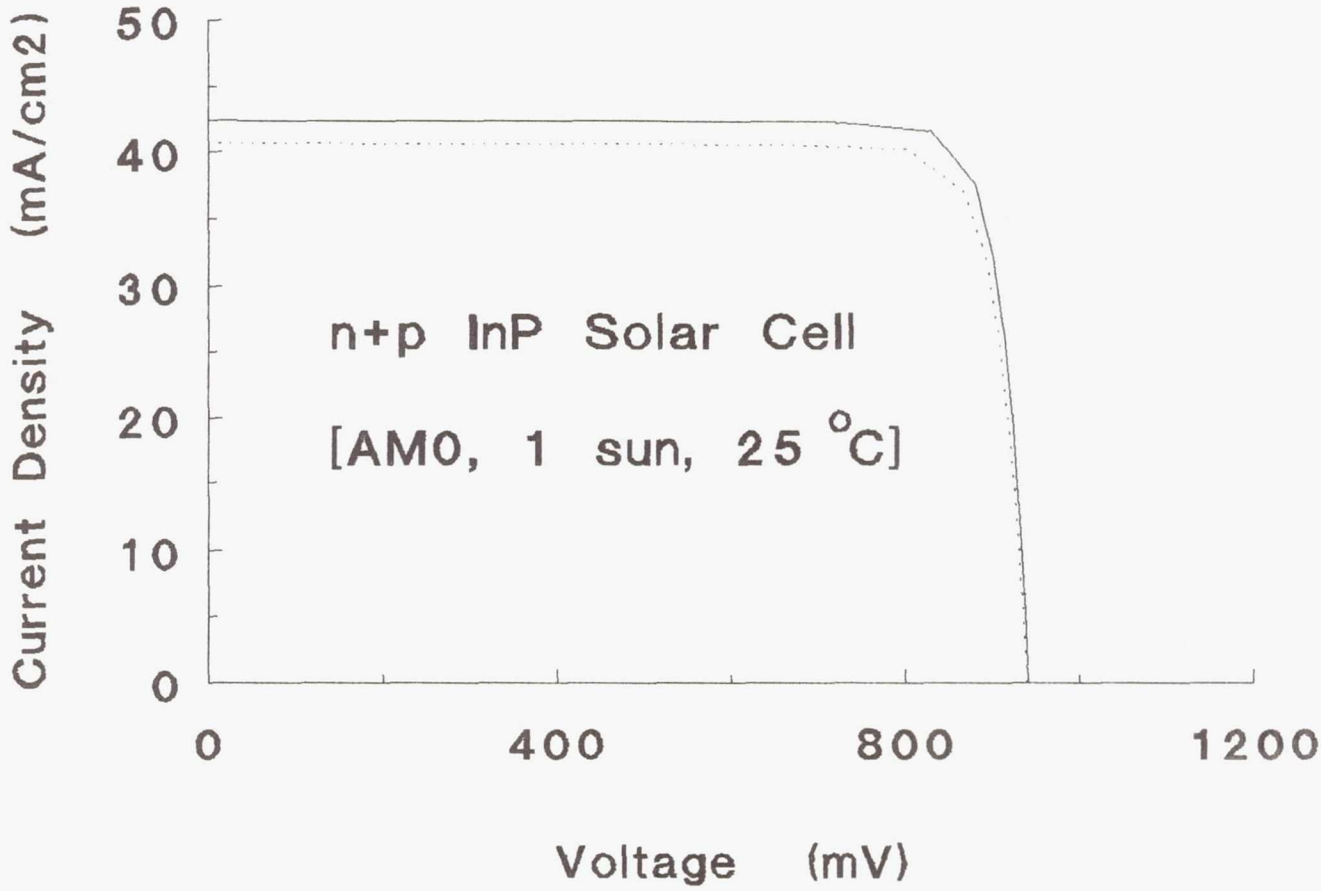


Fig. 2 Calculated I-V Characteristics of Optimally Designed $n^+p$ InP Solar Cells. The Solid Line Curve ($J_{sc}$=42.4 mA/cm$^2$, $V_{oc}$=941 mV, FF=0.863, Eff=25.1%) is for Grid Shadowing Loss of 0% and Series Resistance of 0.1 ohm cm$^2$. The Dotted Line Curve ($J_{sc}$=40.6 mA/cm$^2$, $V_{oc}$=940 mV, FF=0.845, Eff=23.5%) is for Grid Shadowing Loss of 4% and Series Resistance of 0.2 ohm cm$^2$. The other parameters are as per Table I.

configurations by solid lines respectively. The material and cell process parameters for the optimal design of $p^+n$ and $n^+p$ structures are described in Table I. From Table I following observations are made. The emitter of the $n^+p$ InP solar cell structure (20 nm) is relatively shallower than the $p^+n$ structure (0.15 $\mu$m). Emitter dopings of moderate concentrations are considered to avoid any dead layer and bandgap narrowing effects. Base dopings in the range of 1 to 2x10$^{17}$ cm$^{-3}$ are needed for the optimally designed cell. Front surface recombination velocities (10$^4$ cm/sec) are required to achieve the high efficiencies. This requires the development of suitable passivation layers. Present day InP cells do not have any passivation layers and SRV's are in the range of 10$^7$ cm/sec, which has been responsible for relatively low efficiencies. Minority carrier diffusion lengths in the emitter and

Table I Emitter and Base Material/Process Parameters for the Optimal Design of InP Solar Cell.

| | $p^+n$ Structure | $n^+p$ Structure |
|---|---|---|
| Emitter | | |
| Thickness, nm | 150 | 20 |
| Doping, $cm^{-3}$ | $10^{18}$ | $10^{18}$ |
| Front SRV, cm/sec | $10^4$ | $10^4$ |
| Diffusion Length, $\mu m$ | 2 | 0.1 |
| Lifetime, nsec | 0.73 | 0.1 |
| Mobility, $cm^2/V$ sec | 2123 | 39 |
| Base | | |
| Thickness, $\mu m$ | 5 | 5 |
| Doping, $cm^{-3}$ | $10^{17}$ | $10^{17}$ |
| Back SRV, cm/sec | $10^7$ | $10^5$ |
| Diffusion Length, $\mu m$ | 5 | 20 |
| Lifetime, nsec | 151.5 | 56 |
| Mobility, $cm^2/V$ sec | 63 | 2772 |
| Grid Coverage Loss, % | 0 | 0 |
| Series Resistance, ohm $cm^2$ | 0.1 | 0.1 |
| Double Layer AR Coating, nm | 50 (ZnS)/ 100 ($MgF_2$) | 50 (ZnS)/ 100 ($MgF_2$) |

base are also very critical in controlling the cell efficiency and can be improved by better quality material growth. For $p^+n$ cell optimal design, electron and hole diffusion lengths of 2 and 5 $\mu m$ are required. Minority carrier lifetimes which would yield diffusion lengths of similar order have recently been measured on n and p type InP substrates by photoluminescence technique (ref. 5). In the case of $n^+p$ cell design, minority carrier diffusion length in the base on the order of 20 $\mu m$ is required to achieve optimal efficiency. Electron diffusion lengths as high as 30 $\mu m$ in $n^+p$ InP cells have been estimated from the red quantum efficiency (ref. 6). The solar cell design calculations are performed assuming zero front contact shadowing loss, 0.1 ohm $cm^2$ series resistance and two layer $ZnS/MgF_2$ antireflection coating. Zero contact shadowing loss assumes the availability of a prismatic cell cover, which helps in diverting the incoming light from grid lines on to the cell active area. This assumption also helps in considering a lower value of series resistance, because larger portion of cell could be covered by metal grid lines. In Fig. 1 and 2 we have also plotted the calculated I-V characteristics (dotted line curves) assuming grid coverage (i.e. no

prismatic covers) and higher series resistance. The $p^+n$ results (dotted line) shown in Fig. 1 are for grid coverage of 5% and series resistance of 0.3 ohm $cm^2$. The $n^+p$ results (dotted line) shown in Fig. 2 are for grid coverage of 4% and series resistance of 0.2 ohm $cm^2$. It is observed that one could achieve better series resistance in $n^+p$ structures than $p^+n$. From these results it is observed that the open circuit voltage values remain almost the same, but the cell efficiency reduces due to grid coverage losses and the corresponding increased series resistance. However, even in this case $p^+n$ and $n^+p$ cell efficiencies as high as 24.8 and 23.5% respectively are predicted. In all the calculations reported in this work the InP bandgap energy of 1.35 eV and an average value of intrinsic concentration ($n_i$) of $8 \times 10^6$ $cm^{-3}$ (ref. 6) have been used. It is important to point here that there exist an uncertainty in the value of $n_i$ and various researchers have used different values.

In Fig. 3 we have shown the comparison of the calculated I-V characteristics for the optimally designed $n^+p$ and $p^+n$ configurations assuming the parameters of Table I. From Fig. 3 it is clear that one

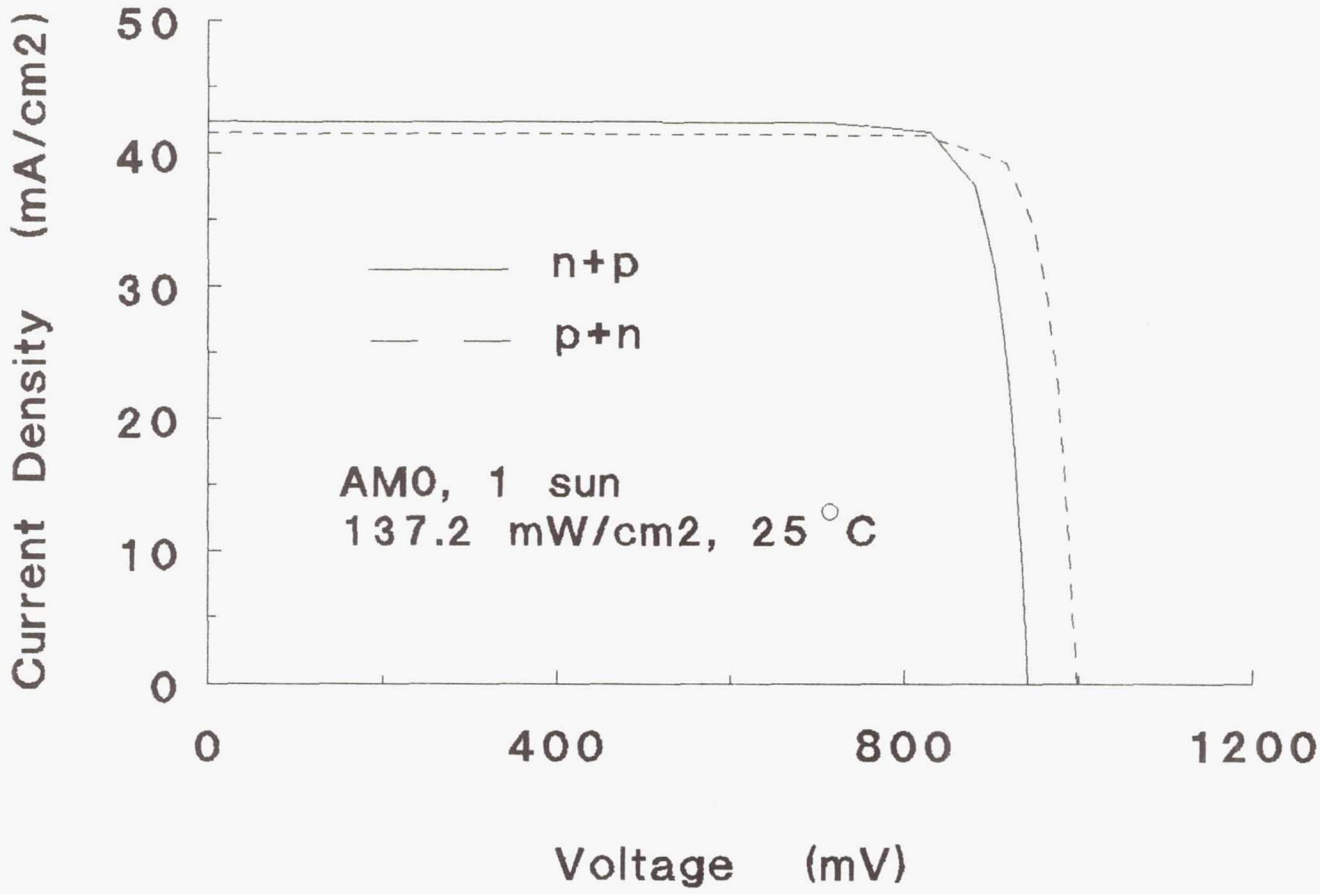


Fig. 3 Comparison of the I-V Characteristics of the Optimally Designed $p^+n$ and $n^+p$ InP Solar Cell Structures (Grid Shadowing Loss 0%, Series Resistance 0.1 ohm $cm^2$).

could achieve higher efficiencies in $p^+n$ configuration compared to $n^+p$, due to higher open circuit voltage even though the short circuit current density is somewhat lower as compared to $n^+p$ structure. Similar observation is true, even when the effect of grid shadowing loss is considered (dotted curves of Fig. 1 and 2).

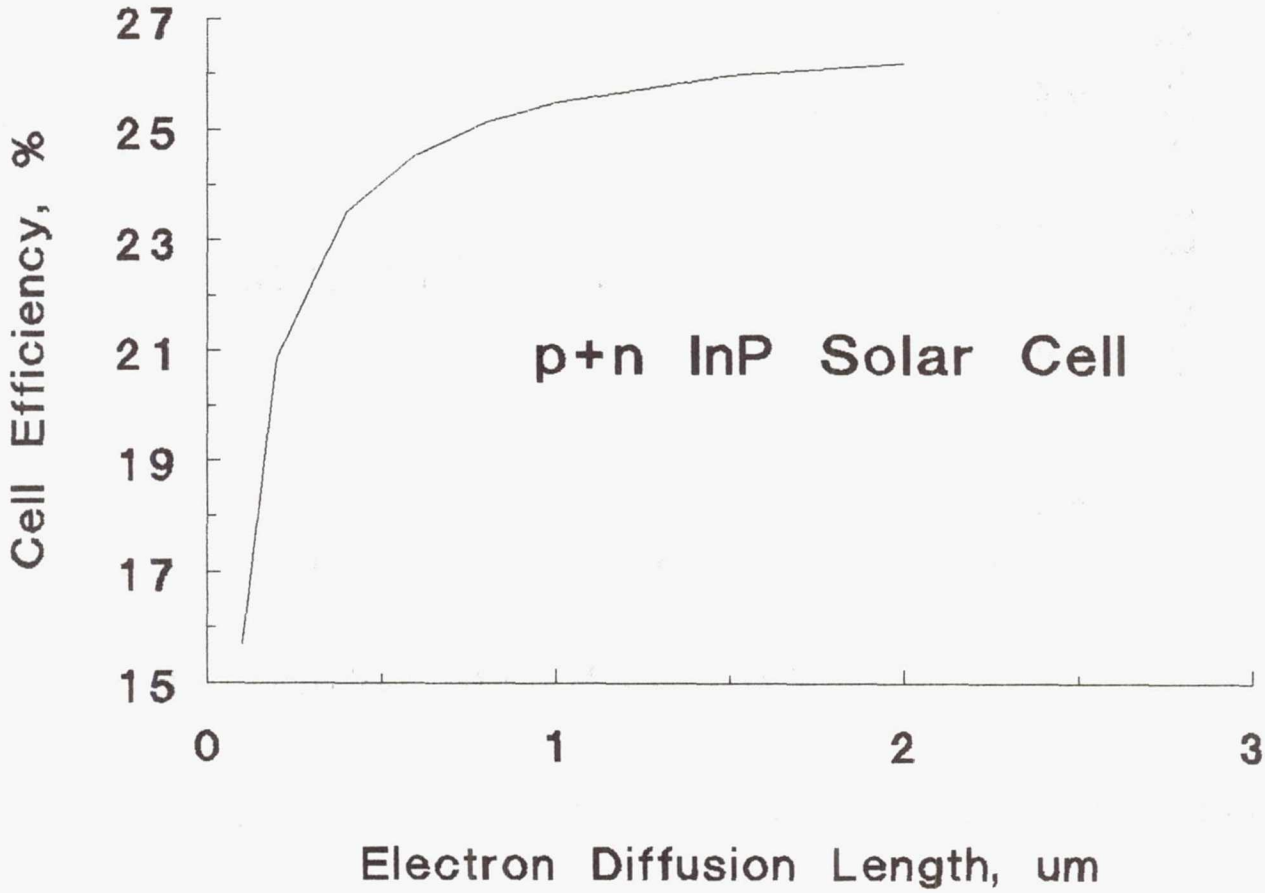


Fig. 4 Effect of Electron Diffusion Length on the $p^+n$ InP Solar Cell AM0 Efficiency.

Minority carrier diffusion lengths in the emitter and base regions greatly influence the cell efficiency. Figures 4 and 5 describe the effect of electron and hole diffusion length respectively on the $p^+n$ InP solar cell efficiency. These results have been obtained by varying the minority carrier diffusion length of interest and keeping all other parameters constant as per Table I. From Figs. 4 and 5 we observe that the cell efficiency vs minority carrier diffusion length curve starts saturating for electron diffusion length of 2 $\mu m$ and hole diffusion length of 5 $\mu m$ respectively. This observation allowed us to choose these values in the optimal design of $p^+n$ InP solar cell. Longer minority carrier diffusion lengths could be obtained by improving the material growth and cell process techniques.

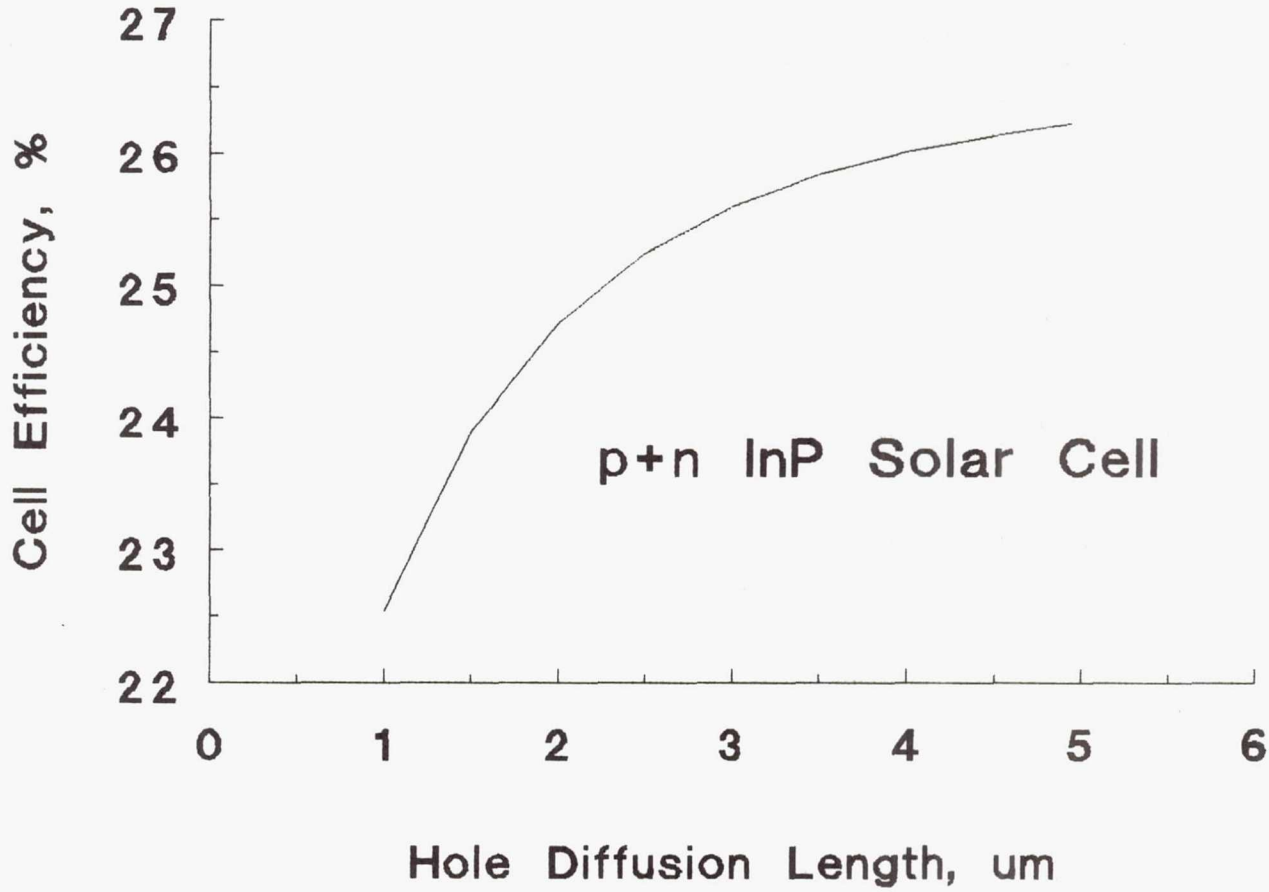


Fig. 5 Effect of Hole Diffusion Length on the $p^+n$ InP Solar Cell AM0 Efficiency.

InP solar cells have shown superior radiation resistance (ref. 7,8) as compared to GaAs and Si cells. This would lead to higher end-of-life (EOL) efficiencies. This is an important criterion as space solar arrays are designed on the basis of EOL efficiencies. In Fig. 6 we have plotted the normalized efficiency results as a function of 1 MeV electron fluence for $n^+p$ and $p^+n$ structures reported independently by Yamaguchi et al. (ref. 9), and Weinberg et al. (ref. 10). From Fig. 6 it is observed that the results reported by these two groups are conflicting as to which structure is better under electron irradiation. To date limited work on the development of $p^+n$ cells has been initiated. This has also restricted electron irradiation studies on such cells. No proton irradiation results have been reported for $p^+n$ cells. However, it is important to note that the cells used to obtain the results plotted in Fig. 6 were made from different material growth and cell process techniques. A meaningful comparison would require both types of cells to be processed under identical conditions. It is also observed that the cells used in reference 9 are more radiation resistant at the lower fluence than the cells used in reference 10, but degrade rapidly in the $10^{15}$ - $10^{16}$ $cm^{-2}$ electron fluence range. The efficiency measure-

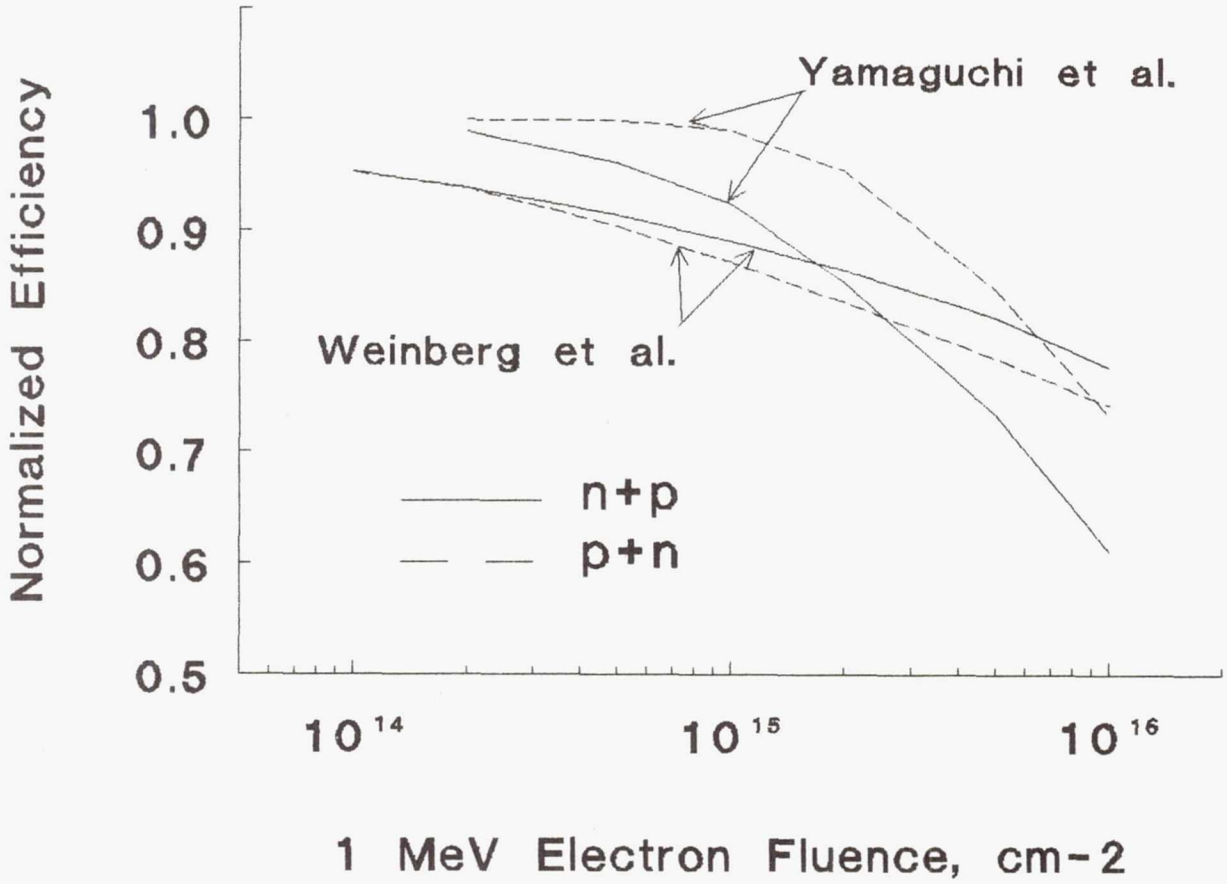


Fig. 6 Effects of 1 MeV Electron Irradiation on the Normalized Efficiency of $p^+n$ and $n^+p$ InP Solar Cells.

ment results of reference 9 are made under AM1.5 spectrum (100 mW/cm$^2$), while reference 10 uses AM0 spectrum (137.2 mW/cm$^2$). The discrepancy between the comparative results in Fig. 6, suggests a need for a systematic work on the electron and proton irradiation damage on these two types of cell configurations.

## CONCLUSIONS

Optimal design calculations for the $p^+n$ and $n^+p$ indium phosphide solar cells have been performed using a computer code PC-1D. It is shown that AM0 cell efficiencies in excess of 23% at 25°C are possible. The optimal cell material and process parameters have been given. Surface passivation and improved material growth techniques require serious attention in order to obtain the minimum possible surface recombination velocities and maximum possible minority carrier diffusion lengths. Comparison of $p^+n$ and $n^+p$ cell configurations has shown that $p^+n$ offers better efficiency due to higher open circuit voltage as compared to $n^+p$ configuration. The effect of minority carrier diffusion length on InP cell efficiency has been studied. Extensive and systematic electron and proton irradiation damage studies are required. Enhanced and renewed efforts are needed to develop $p^+n$ type InP cells.

## REFERENCES


1. Keavney, C. J.; Haven, V. E.; and Vernon, S. M.: Emitter Structures in MOCVD InP Solar Cells. 21st IEEE Photovoltaic Specialists Conference, vol. 1, IEEE, 1990, pp. 141-144.

2. Itoh, Y.; Ando, K.; Yamaguchi, M.; and Uemura, C.: Mg Doped $p^+$-n InP Solar Cell by LPE. First International Photovoltaic Science and Engineering Conference, Kobe, Japan, 1984, pp. 245-248.

3. Choi, K. Y.; Shen, C. C.; and Miller, B. I.: P/N InP Homojunction Solar Cells by LPE and MOCVD Techniques. 19th IEEE Photovoltaic Specialists Conference, IEEE, 1987, pp. 255-260.

4. Basore, P. A.; Rover, D. T.; and Smith, A. W.: PC-1D Version 2: Enhanced Numerical Modeling. 20th IEEE Photovoltaic Specialists Conference, vol. 1, IEEE, 1988, pp. 389-396.

5. Landis, G. A.; Jenkins, P.; and Weinberg, I. : Photoluminescence Lifetime Measurements in InP Wafers. 3rd International Conference on InP and Related Materials, IEEE/LEOS, 1991 (To be published).

6. Yahia, A. H.; Wanlass, M. W.; and Coutts, T. J. : Modeling and Simulation of InP Homojunction Solar Cells. 20th IEEE Photovoltaic Specialists Conference, vol. 1, IEEE, 1988, pp. 702-707.

7. Yamaguchi, M.; Uemura, C.; Yamamoto, A.; and Shibukawa, A.: Electron Irradiation Damage in Radiation-Resistant InP Solar Cells. Jpn. J. Appl. Phys., vol. 23, 1984, pp. 302-307.

8. Weinberg, I.; Swartz, C. K.; and Hart, R. E.: Potential for use of InP Solar Cells in the Space Radiation Environment. 18th IEEE Photovoltaic Specialists Conference, IEEE, 1985, pp. 1722-1724.

9. Yamaguchi, M.; Yamamoto, A.; Itoh, Y.; and Uemura, C.: 22% Efficient and High Radiation-Resistant InP Solar Cells. Second International Photovoltaic Science and Engineering Conference, Beijing, China, 1986, pp. 573-576.

10. Weinberg, I.; Swartz, C. K.; Hart, R. E.; and Statler, R. L. : Radiation and Temperature Effects in Gallium Arsenide, Indium Phosphide, and Silicon Solar Cells. 19th IEEE Photovoltaic Specialists Conference, IEEE, 1987, pp. 548-557.

# A Theoretical Comparison of the Near-Optimum Design and Predicted Performance of n/p and p/n Indium Phosphide Homojunction Solar Cells

Chandra Goradia, William Thesling
Space Photovoltaic Research Center*, Electrical Engineering Department
Cleveland State University,
Cleveland, Ohio 44115
and
Irving Weinberg
NASA Lewis Research Center, Cleveland, Ohio 44135

## ABSTRACT

Using our detailed simulation model of $p^+nn^+$ and $n^+pp^+$ Indium Phosphide (InP) homojunction solar cells, we have done extensive parametric variation computer simulation runs to help us arrive at near-optimum designs of these two solar cell configurations. In this paper, we present the values of all the geometrical and material parameters corresponding to the near-optimal designs of both these configurations. Next, for each configuration, we present the results of parametric variation runs showing how the performance parameters $J_{sc}$, $V_{oc}$ and $\eta$ vary with each of the cell design parameters for the near-optimally designed cell. Finally, we discuss the theoretical results obtained and compare the relative merits and drawbacks of the two configurations.

## INTRODUCTION

In recent years, in laboratory irradiation tests, indium phosphide (InP) homojunction solar cells have shown a markedly higher tolerance to 1 MeV electron and 10 MeV proton irradiation than silicon (Si) and gallium arsenide (GaAs) solar cells [1]; this fact makes indium phosphide solar cells very attractive for space applications [2]. The main task in the design of InP solar cells is, then, to design them as to yield the maximum possible beginning-of-life (BOL) energy conversion efficiency, comparable to, or greater than that obtained from gallium arsenide solar cells (≈22% at AM0, 25°C).

Using a fairly complete computer simulation model of the homojunction InP solar cell [3], we have done an extensive parameter variation study which has allowed us to come up with near-optimum designs of the InP homojunction solar cell in both its $n^+pp^+$ (n-on-p) and $p^+nn^+$

*Funded by NASA Lewis Research Center

(p-on-n) configurations. Having obtained the near-optimum designs of the two configurations, we then re-did the parameter variation study such that while each parameter was being varied individually, all other parameters were kept fixed at their near-optimum values. It is the results of such a parameter variation study of the near-optimum cell design that we present in this paper. While so doing we also compare the theoretically predicted performance of near-optimally designed $n^+pp^+$ (n-on-p) and $p^+nn^+$ (p-on-n) InP homojunction space solar cell configurations. Such a comparison is necessary and useful since, there is no a priori reason why a particular one of these two configurations should have the higher beginning-of-life (BOL) efficiency. In addition, we had shown in an earlier paper [4], that the primary factor limiting the open circuit voltage and efficiency of the $n^+pp^+$ InP homojunction solar cell is the relatively large heavy doping factor in the heavily doped $p^+$ back-surface field (BSF) region and had mentioned there that since the heavy doping factor in heavily doped n-type InP is quite likely much smaller than that in p-type InP, it was worth investigating the BOL performance of the near-optimally designed $p^+nn^+$ InP solar cell.

## RESULTS AND DISCUSSION

### A. Near-Optimum Designs

Table 1 gives the geometrical, material and performance parameters of the near-optimum designs of the $n^+pp^+$ and $p^+nn^+$ (p-on-n) homojunction InP solar cell configurations. In this table, the values of the minority carrier indirect or Hall-Shockley-Reed lifetime coefficients in n- and p-type InP are assumed to be ten times the values obtained by matching (curve-fitting) the measured curves of illuminated I-V, $\log_{10} I_{sc}$ versus $V_{oc}$ and spectral response, to the corresponding calculated curves, for an $n^+pp^+$ homojunction InP solar cell made by the Spire Corporation (Cell Spire 6 [5]). This is along the same lines as we have done earlier [4] As indicated in the table, the heavy doping factors in the various regions were also obtained by matching the calculated and measured curves for the above measurements for the Spire 6 solar cell. The minority carrier mobilities and diffusivities in the various regions were obtained in the same manner as we have explained before [3]. The design parameters, namely, the thickness of and doping in each cell region were obtained from an extensive parametric variation study and are those values which yield the maximum efficiency.

In comparing the $n^+pp^+$ and $p^+nn^+$ near-optimum cell designs, note the considerable difference in the emitter thickness of the two configurations. Because of the significantly higher electron mobility compared to hole mobility in InP, the minority carrier diffusion length is much longer in p-type InP than in n-type InP. Hence, it is advantageous to have most of the incoming photons be absorbed in the p-type InP, regardless of configuration. This means that the p-region should be as close to the surface as possible and should be wide enough to absorb most of the incoming photons. This is achieved by choosing either the $p^+nn^+$ configuration with a wide emitter or the $n^+pp^+$ configuration with a thin emitter. An immediate implication of this fact is that a larger fraction of the short circuit current $I_{sc}$ comes from the emitter in the $p^+nn^+$ configuration compared to that in the $n^+pp^+$

Table 1 **Geometrical, Material and Performance Parameters of Near-Optimum $n^+pp^+$ and $p^+nn^+$ Homojunction Indium Phosphide Solar Cells.**

a) $n^+pp^+$ Structure

| | |
|---|---|
| Grid Shadow | 4.0% |
| Front SRV | $1 \times 10^4$ cm/sec |
| $W_E$ | 200 Å |
| $N_{D,\text{emitter}}$ | $3 \times 10^{18}$ cm$^{-3}$ |
| * $HD_E = n_{iE} / n_{i0}$ | 0.837 |
| * $\tau_{HSR}$ | 6.667 ns |
| $\tau_{Rad}$ | 0.469 ns |
| $\tau_{p,E}$ | 0.437 ns |
| $L_{p,E}$ | 0.229 µm |
| $W_{base}$ | 4.0 µm |
| $N_{A,base}$ | $8 \times 10^{15}$ cm$^{-3}$ |
| $HD_{base}$ | 1.0 |
| * $\tau_{HSR}$ | 3.750 µs |
| $\tau_{Rad}$ | 0.176 µs |
| $\tau_{n,B}$ | 0.168 µs |
| $L_{n,base}$ | 43.29 µm |
| $W_{BSF}$ | 250 µm |
| $N_{A,BSF}$ | $7.5 \times 10^{16}$ cm$^{-3}$ |
| $HD_{BSF}$ | 1.0 |
| * $\tau_{HSR}$ | 400 ns |
| $\tau_{Rad}$ | 18.74 ns |
| $\tau_{n,BSF}$ | 17.89 ns |
| $L_{n,BSF}$ | 12.45 µm |

* Quantities obtained from Spire 6 match.

$J_{SC}$ = 39.94 mA / cm$^2$
$V_{OC}$ = 901.3 mV
$J_{max}$ = 38.57 mA / cm$^2$
$V_{max}$ = 804.4 mV
$FF$ = 86.21 %
$\eta$ = 22.60 %

b) $p^+nn^+$ Structure

| | |
|---|---|
| Grid Shadow | 4.0% |
| Front SRV | $1 \times 10^3$ cm/sec |
| $W_E$ | 3500 Å |
| $N_{A,\text{emitter}}$ | $1 \times 10^{18}$ cm$^{-3}$ |
| * $HD_E = n_{iE} / n_{i0}$ | 3.0 |
| * $\tau_{HSR}$ | 30 ns |
| $\tau_{Rad}$ | 1.406 ns |
| $\tau_{n,E}$ | 1.327 ns |
| $L_{n,E}$ | 2.971 µm |
| $W_{base}$ | 3.0 µm |
| $N_{D,base}$ | $1 \times 10^{16}$ cm$^{-3}$ |
| $HD_{base}$ | 1.0 |
| * $\tau_{HSR}$ | 2.0 µs |
| $\tau_{Rad}$ | 140.6 ns |
| $\tau_{p,B}$ | 131.3 ns |
| $L_{p,base}$ | 7.349 µm |
| $W_{BSF}$ | 300 µm |
| $N_{D,BSF}$ | $5.0 \times 10^{18}$ cm$^{-3}$ |
| $HD_{BSF}$ | 1.0 |
| * $\tau_{HSR}$ | 4.0 ns |
| $\tau_{Rad}$ | 0.281 ns |
| $\tau_{p,BSF}$ | 0.249 ns |
| $L_{p,BSF}$ | 0.152 µm |

* Quantities obtained from Spire 6 match.

$J_{SC}$ = 39.65 mA / cm$^2$
$V_{OC}$ = 915.3 mV
$J_{max}$ = 38.32 mA / cm$^2$
$V_{max}$ = 808.5 mV
$FF$ = 85.35 %
$\eta$ = 22.56 %

configuration, as shown in Table II. This table gives, for the $n^+pp^+$ and $p^+nn^+$ configurations, the components of the short circuit current density $J_{SC}$ from each of the emitter, space charge and base regions, both in terms of mA/cm$^2$ and as fractions of the total current density. Note that in the $p^+nn^+$ configuration, over 92% of the short circuit current $I_{SC}$ comes from the emitter and space charge regions while in the $n^+pp^+$ configuration, only 30.5% of $I_{SC}$ comes from these regions. This fact has strong implications on the radiation damage in these two configurations. For a radiation environment in which the radiation-induced defect creation in the InP material occurs primarily at a depth ≥ 1 µm, the $p^+nn^+$ structure will suffer very little degradation of its $I_{SC}$ compared to the $n^+pp^+$ structure for which about 70% of its $I_{SC}$ comes from deeper in the base region. For a radiation environment in which defect creation in the InP

material occurs close to the surface (≤ 1 μm), the $p^+nn^+$ structure will suffer more degradation of its $I_{SC}$ than the $n^+pp^+$ structure.

Table 2 Fractions of $I_{SC}$ coming from various regions of near-optimally designed n/p and p/n solar cells.

| | Emitter | SCR | Base | Total |
|---|---|---|---|---|
| n/p | 6.36<br>15.9 % | 5.83<br>14.6 % | 27.74<br>69.6 % | 39.94 mA/cm²<br>100 % |
| p/n | 31.6<br>79.7 % | 4.97<br>12.5 % | 3.06<br>7.72 % | 39.65 mA/cm²<br>100 % |

In comparing the beginning-of-life (BOL) performance of the near-optimum designs of the $n^+pp^+$ and $p^+nn^+$ solar cell configurations, we see from Table I that the near-optimum designs of both the $n^+pp^+$ and $p^+nn^+$ configurations are capable of yielding essentially the same 1 AM0 25°C efficiency of slightly over 22.5%. The $p^+nn^+$ configuration has a somewhat higher $V_{OC}$ but somewhat lower $J_{SC}$ and FF than the $n^+pp^+$ configuration.

## B. Parametric Variation Study

1) Front Surface Recombination Velocity $S_F$.

Figures 1a,b,c show, respectively, the $J_{SC}$, $V_{OC}$ and $\eta$ of $n^+pp^+$ and $p^+nn^+$ near-optimum InP solar cells as functions of the front surface recombination velocity $S_F$. Note that all performance parameters, $J_{SC}$, $V_{OC}$ and $\eta$ degrade heavily with increasing $S_F$ in the upper ranges of $S_F$ for only the $p^+nn^+$ configuration. The performance

Fig. 1a Current Density $J_{SC}$ of Near-Optimum Cell vs. front SRV $S_F$

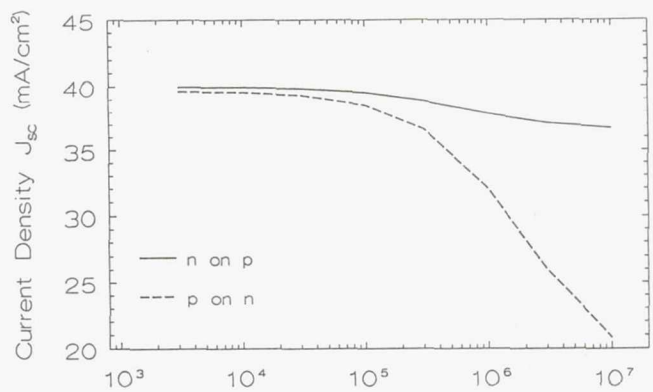


Fig. 1b Open Circuit Voltage of Near-Optimum Cell vs. front SRV $S_F$

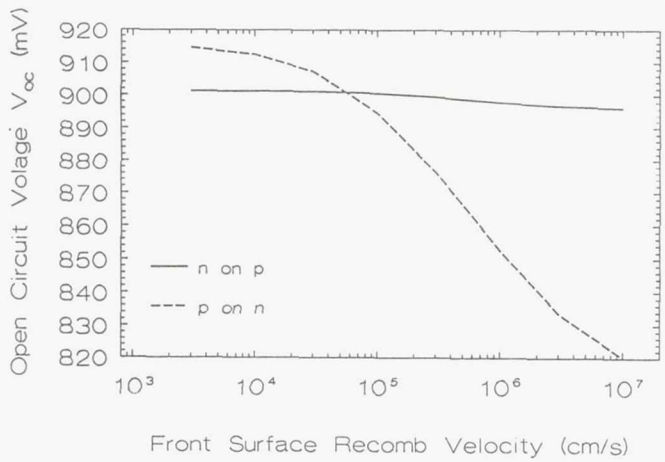


Fig. 1c Efficiency $\eta$ of Near-Optimum Cell vs. front SRV $S_F$

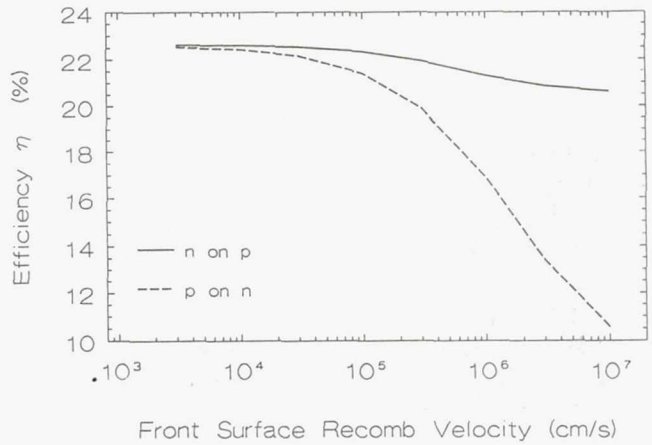

degradation is relatively minor for the $n^+pp^+$ configuration even at $S_F$ values approaching its limiting value of $v_{th}/2 \sim 10^7$ cm/s. This grossly different dependence on $S_F$ for the $n^+pp^+$ and $p^+nn^+$ configurations is easy to explain if we consider that because of its substantially thicker emitter, the $p^+nn^+$ configuration has most of its photocurrent coming from the emitter and this makes the $p^+nn^+$ configuration much more sensitive to all the emitter parameters (front SRV, emitter doping, emitter thickness etc.) than the $n^+pp^+$ configuration.

2) Emitter Thickness $W_E$.

Fig. 2a Current Density $J_{SC}$ of Near-Optimal cell vs. Emitter Width

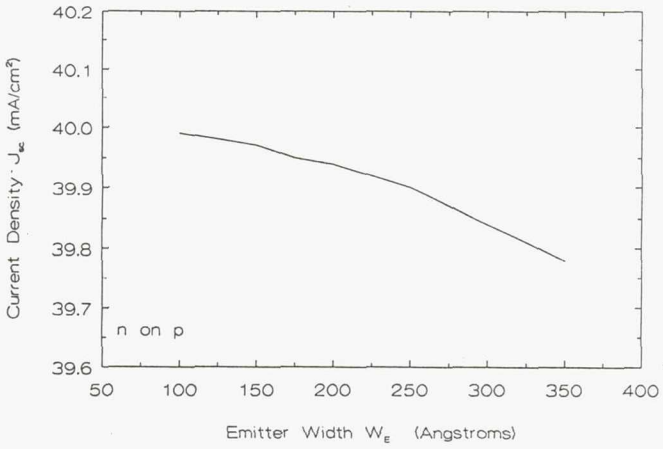


Fig. 2b Current Density $J_{SC}$ of Near-Optimal Cell vs. Emitter Width

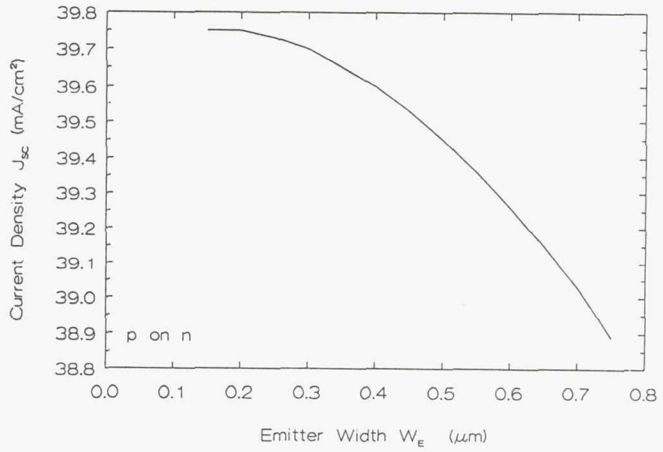


parameters, $J_{SC}$, $V_{OC}$ and $\eta$ vary little, less than 2%, as the emitter thickness varies from 100Å to 350Å for the $n^+pp^+$ and from 0.1 μm to 0.75 μm for the $p^+nn^+$ configuration. Note also that all the three performance parameters $J_{SC}$, $V_{OC}$ and $\eta$ initially increase monotonically as the emitter

Figures 2a,b show, respectively, the $J_{SC}$ for the $n^+pp^+$ and $p^+nn^+$ configurations while Figures 2c,d show the $V_{OC}$ and $\eta$ for the same two configurations, all as functions of the emitter thickness $W_E$. Here, note that for both the $n^+pp^+$ and $p^+nn^+$ configurations, all performance

Fig. 2c Open Circuit Voltage & Efficiency of Near Optimal cell vs. Emitter Width

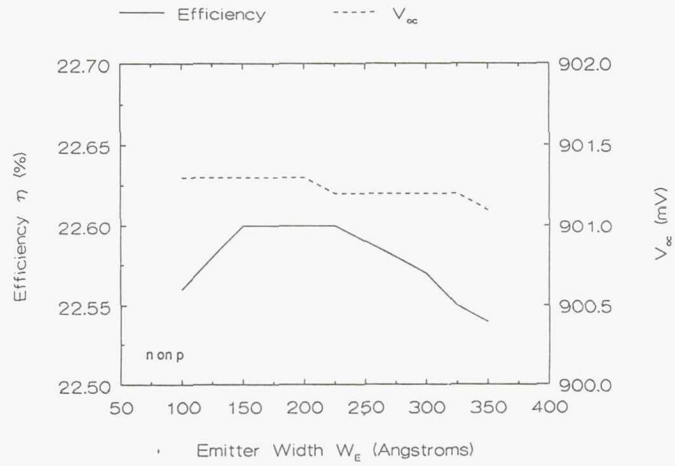


Fig. 2d Open Circuit Voltage & Efficiency of Near Optimal cell vs. Emitter Width

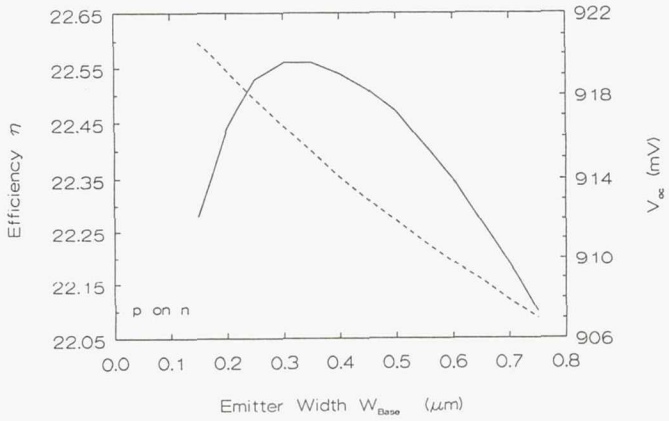

thickness $W_E$ decreases. While this trend holds for $J_{SC}$ and $V_{OC}$ all the way down to $W_E$ = 100Å for the $n^+pp^+$ configuration and $W_E$ = 0.1μm for the $p^+nn^+$ structure, the curve for η peaks in the range of $W_E$ between 150Å and 225Å for the $n^+pp^+$ and $W_E$ between 0.3 and 0.4 μm for the $p^+nn^+$ structure. For $W_E$ shorter than the lower limits of these ranges, the efficiency η decreases with further decreases in $W_E$. This is because in these ranges of $W_E$ values, the overall series resistance of the solar cell is dominated by the emitter sheet resistance which increases with decreasing $W_E$, causing the fill factor FF and thereby also the efficiency η to decrease with decreasing $W_E$. Thus for both the $n^+pp^+$ and $p^+nn^+$ configurations, there is an optimum range of values of $W_E$, which yield the highest efficiency. For the $n^+pp^+$ structure this optimum range of $W_E$ is from ~150Å to ~225Å, while for the $p^+nn^+$ structure, the optimum range of $W_E$ is 0.25-0.425 μm.

Fig. 3a Current Density $J_{SC}$ of Near-Optimum Cell vs. Emitter Doping $N_E$

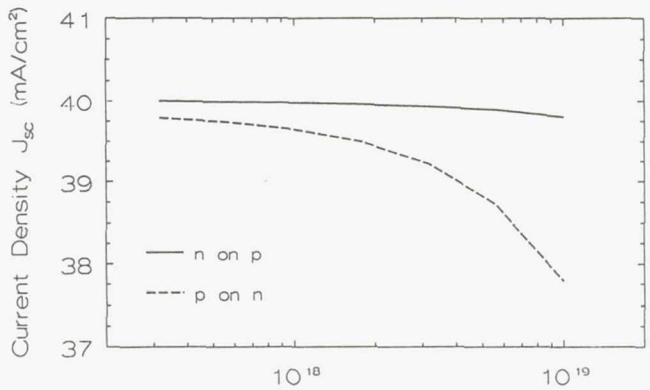


3) Emitter Doping $N_{dE}$ or $N_{aE}$.

Figures 3a,b,c show, respectively, the $J_{SC}$, $V_{OC}$ and η of $n^+pp^+$ and $p^+nn^+$ near-optimum InP solar cells as functions of the emitter doping concentration $N_{dE}$ or $N_{aE}$. The calculations for these figures take into account heavy doping effects in the emitter, in the same manner as we have done earlier [4], when the doping there exceeds $10^{17}$ donor or acceptor atoms per $cm^3$. As the emitter

Fig. 3b Open Circuit Voltage of Near Optimum Cell vs. Emitter Doping $N_E$

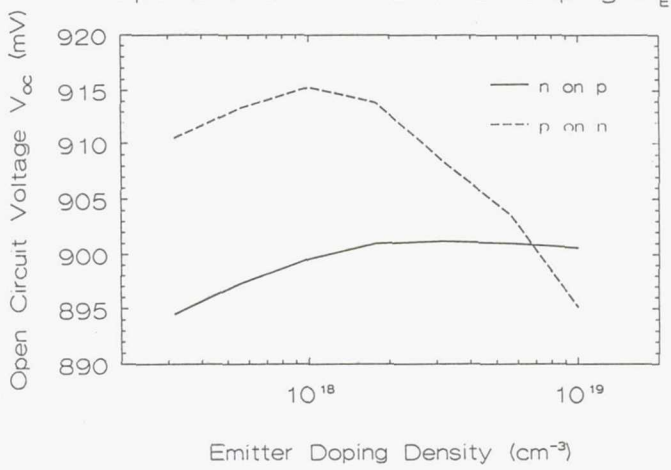


Fig. 3c Efficiency η of Near-Optimum Cell vs. Emitter Doping $N_E$

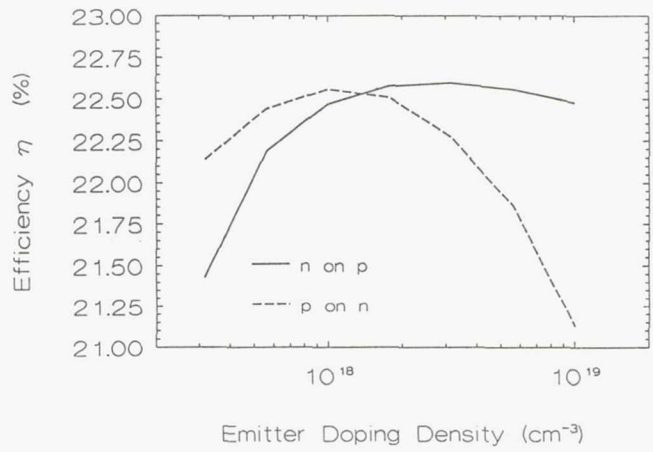


doping increases from $10^{17}$ to $10^{19}$ $cm^{-3}$, two detrimental effects come into play. First, the radiative lifetime in the emitter decreases in inverse proportionality to the doping increase and secondly, the effective bandgap narrowing significantly increases the effective intrinsic carrier

concentration, thereby increasing the dark saturation or loss current. Of these, it is primarily the first effect, namely, the reduction of lifetime, which is responsible for the degradation of $J_{sc}$ with increased emitter doping. However, both detrimental effects affect $V_{oc}$ and cause it to degrade with increasing doping.

Here, in comparing the $n^+pp^+$ and $p^+nn^+$ configurations, we see that the $n^+pp^+$ cell suffers only a ~0.6% drop in its $J_{sc}$ as the emitter doping increases from $10^{17}$ to $10^{19}$ $cm^{-3}$ while the $p^+nn^+$ cell suffers a 5.12% reduction in its $J_{sc}$ over the same range of emitter doping increase. This difference in behavior is easily explained, knowing that in the $p^+nn^+$ structure about 80% of the $J_{sc}$ comes from the emitter as compared to only about 16% from the emitter for the $n^+pp^+$ structure. Thus, as the minority carrier lifetime and diffusion length in the emitter reduce with increased doping in that region, a larger current is affected in the $p^+nn^+$ structure than in the $n^+pp^+$ structure, giving a larger amount of degradation in the $p^+nn^+$ compared to the $n^+pp^+$ structure.

As to the variation of $V_{oc}$ and $\eta$ with emitter doping, we see a somewhat different behavior between the $n^+pp^+$ and $p^+nn^+$ structures. For the $n^+pp^+$, both $V_{oc}$ and $\eta$ first rapidly increase with increasing emitter doping, and then very very gradually decrease with further increases in emitter doping. For the $p^+nn^+$ cell, $V_{oc}$ first decreases, reaches a minimum at an emitter doping of $3*10^{17}$ $cm^{-3}$, then increases, reaches a maximum, and then decreases continually up to an emitter doping of $10^{19}$ $cm^{-3}$. The observed behavior of $V_{oc}$ versus emitter doping is explainable by considering the fact that in p-type InP, heavy doping causes a substantial increase in $n_{ie}$, the effective intrinsic carrier concentration, thereby increasing the loss current (dark saturation current) and reducing $V_{oc}$ [4]. In n-type InP, heavy doping causes the bandgap to widen rather than become narrow [4]. Therefore, $n_i$ either reduces or, at worst, stays the same. Thus, for the $n^+pp^+$ cell, there is no degradation of $V_{oc}$ due to heavy doping effects and the rather slight reduction of $V_{oc}$ with increasing emitter doping seen in Figure 3b is due to the reduction of the minority carrier lifetime in the emitter with increasing doping there. For the $p^+nn^+$ cell, at emitter dopings higher than ~$10^{18}$ $cm^{-3}$, $V_{oc}$ decreases with increasing emitter doping due to both, the heavy doping factor and the reduction in lifetime. Hence, a much steeper decline in $V_{oc}$ with increasing emitter doping is seen for the $p^+nn^+$ structure as compared to the $n^+pp^+$ structure.

4) Base Width $W_B$

Figures 4 a,b,c show, respectively, the $J_{sc}$, $V_{oc}$ and $\eta$ of $n^+pp^+$ and $p^+nn^+$ InP homojunction solar cells as functions of the base thickness $W_B$. First considering figure 4a, we see that $J_{sc}$ increases monotonically with base thickness for both the $n^+pp^+$ and $p^+nn^+$ configurations and substrates at a value of slightly below 40 $mA/cm^2$ at a base thickness of about 4μm. In this regard, both the $n^+pp^+$ and $p^+nn^+$ configurations behave similarly and there is no unexpected behavior anywhere. Figure 4b,c show the $V_{oc}$ and $\eta$ of the two configurations as functions of the base thickness. In comparing the two configurations with respect to their $V_{oc}$ as a function of base thickness, we note that the $n^+pp^+$ cell shows $V_{oc}$ initially rising with increasing base thickness, reaching a maximum of about 905 mV at a

Fig. 4a Current Density $J_{sc}$ of Near-Optimum Cell vs. Base Width

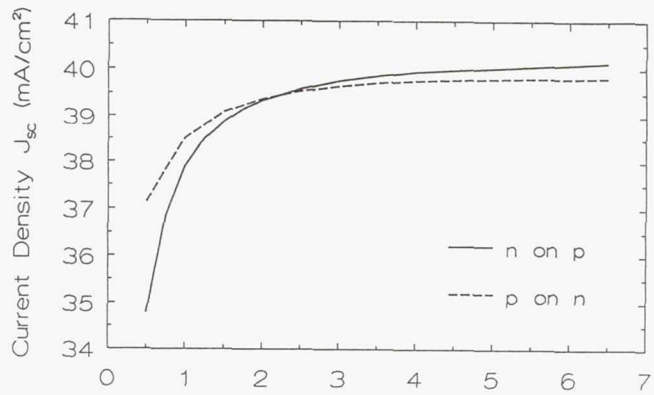


Fig. 4b Open Circuit Voltage of Near-Optimum Cell vs. Base Width

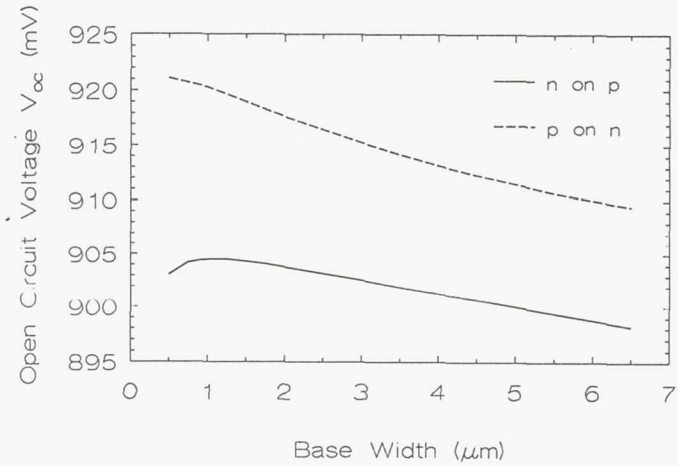


Fig. 4c Efficiency $\eta$ of Near-Optimum Cell vs. Base Width

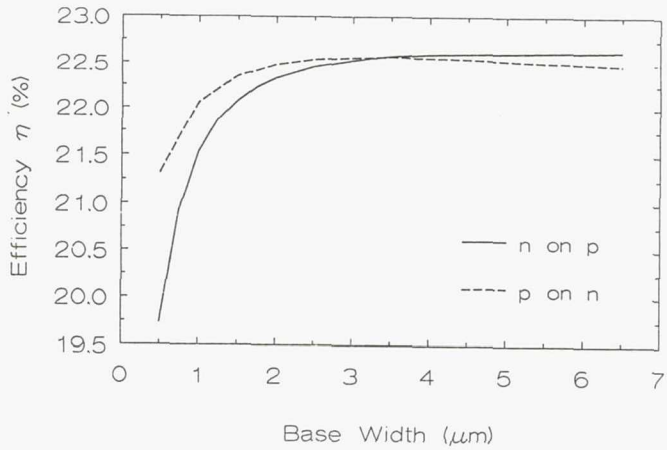


thickness of about 1μm and then falling with increasing base thickness. For the $p^+nn^+$ configuration, the maximum $V_{oc}$ is about 921 mV and occurs at a base thickness of approximately 0.5μm. As to the variation of efficiency with base width, figure 4c shows $\eta$ rising rapidly with increasing base thickness, reaching $\eta$ = 19.7% at $W_B$ = 0.5μm, for the $n^+pp^+$ cell and $\eta$ = 21.3% at $W_B$ = 0.5μm for the $p^+nn^+$ cell. Both configurations saturate to 1AM0, 25°C $\eta$ of very close to 22.5% for base thickness greater than ~3.5μm.

5) Base Doping $N_{aB}$ or $N_{dB}$.

Figures 5a,b,c show, respectively, the $J_{sc}$, $V_{oc}$ and $\eta$ of $n^+pp^+$ and $p^+nn^+$ InP homojunction solar cells as functions of the base doping $N_{aB}$ or $N_{dB}$. First, considering figure 5a, we see that the $J_{sc}$ of the $n^+pp^+$ device is slightly but consistently higher than $J_{sc}$ of the $p^+nn^+$ device. This difference is due to the fact that most of the photogenerated carriers in the $p^+nn^+$ cell come from the emitter where, because of the heavier doping needed to reduce the sheet resistance to a reasonable value, the minority carrier lifetime is shorter and the collection efficiency of these photogenerated carriers is poorer than in the less heavily doped base region, where most of the photocurrent comes from for the $n^+pp^+$ cell.

Next, looking at figure 5b, which shows $V_{oc}$ versus base doping, we see that the $V_{oc}$ of the $p^+nn^+$ near-optimum cell is consistently higher than that of the near-optimum $n^+pp^+$ cell. This is explainable on the basis that heavy doping effects play a detrimental role only in p-type InP. Then, for the $n^+pp^+$ structure, the increased recombination in the $p^+$ BSF

Fig. 5a Current Density $J_{sc}$ of Near-Optimum Cell vs. Base Doping

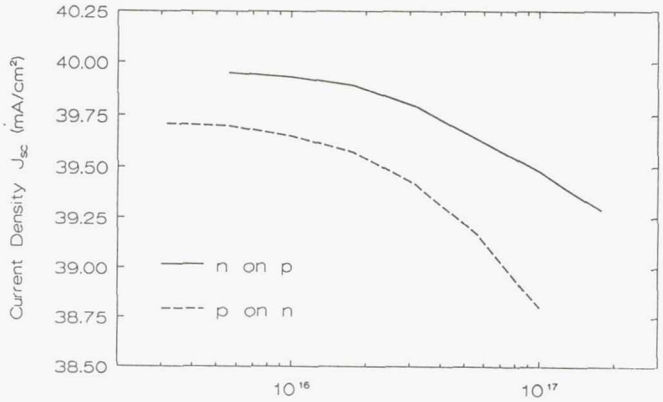


Fig. 5b Open Circuit Voltage of Near-Optimum Cell vs. Base Doping

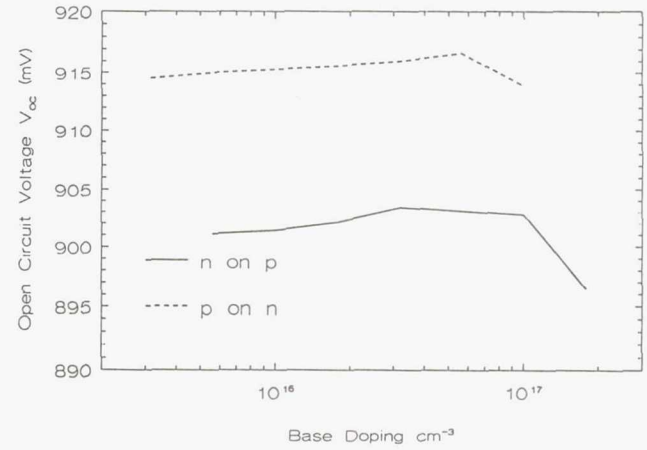


Fig. 5c Efficiency $\eta$ of Near-Optimum Cell vs. Base Doping

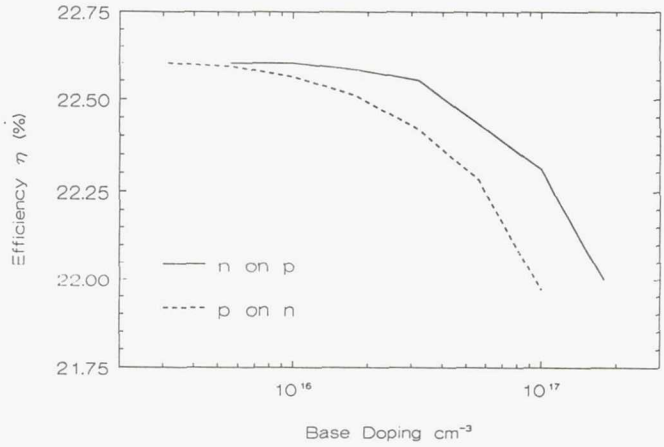


increases the effective SRV at the base/BSF $pp^+$ interface and increases the dark forward current or loss current component from the base and reduces the $V_{oc}$. For the $p^+nn^+$ structure, on the other hand, the increased recombination in the $p^+$ emitter due to heavy doping effects is not as detrimental in terms of the amount of $V_{oc}$ reduction as is the increased recombination in the $p^+$ BSF region in the $n^+pp^+$ structure. This is because of the much smaller volume of the emitter, with its thickness of only 400Å, compared to the volume of the BSF region, with its thickness of $\gtrsim$ 10μm.

Finally, looking at figure 5c, showing $\eta$ as a function of base doping for both structures, we see that for a base doping less than ~ $5*10^{15}$ $cm^{-3}$, both near-optimum structures have the same efficiency of 22.6% at 1AM0, 25°C. However, as the base doping increases, the $n^+pp^+$ structure starts showing a higher $\eta$ than the $p^+nn^+$ structure and the difference in $\eta$ between the two structures keeps widening with increasing base doping.

## CONCLUDING REMARKS

1. From Table 1 as well as the figures showing the efficiency $\eta$ versus any of the parameters, we see that the near-optimal designs of both the $n^+pp^+$ and $p^+nn^+$ InP homojunction solar cell configurations appear capable of yielding beginning-of-life (BOL) 1AM0, 25°C efficiency of slightly over 22.5%. It should be noted that our near-optimum designs use realistically achievable values of 4% grid shadowing, a two-layer AR coating of $ZnS/MgF_2$, front SRV values of $10^4$ cm/s on top of th $n^+$ emitter

and $10^3$ cm/s on top of the $p^+$ emitter. The thickness of and doping in each region also have realistic values. The primary requirement to achieve the efficiency of 22.5% is that the indirect or Hall-Shockley-Reed minority carrier lifetime coefficients for n-type and p-type InP be ten times their values found from the solar cell Spire6.

With the materials technology of InP constantly improving, we expect this to be achievable in the very near future, if it is already not so.

2. For both the $n^+pp^+$ and $p^+nn^+$ configurations, the largest fraction of the photocurrent comes from the p-type region - $p^+$ emitter in the $p^+nn^+$ cell and p-type bases in the $n^+pp^+$ cell. Hence the performance of the cell is most sensitive to the geometrical and material parameters of the p-type region in each configuration.

3. The maximum efficiencies of the two configurations being nearly equal, the choice of configuration ($n^+pp^+$ or $p^+nn^+$) is dictated by other considerations such as ease and cost of fabrication and radiation tolerance under a specific radiation environment.

## REFERENCES


[1] M. Yamaguchi, C. Uemuer and A. Yamamoto, "Radiation Damage in InP Single Crystals and Solar Cells", J. Appl. Phys., 55 (1984) p. 1429

[2] I. Weinberg, C. K. Swartz, R. E. Hart, Jr., "Potential for use of InP Solar Cells in the Space Radiation Environment", Conf. Rec. 18th IEEE Photovoltaic Specialists Conf., Las Vegas, Oct. 1985, pp. 1722-1724. (See also I. Weinberg, "Indium Phosphide Solar Cells for use in Space", Solar Cells, vol. 29, pp 225-244, 1990.)

[3] C. Goradia, J.V.Geier, I. Weinberg, "Theory of the InP Shallow Homojunction Solar Cell", Solar Cells, vol 25, (1988), pp.235-253

[4] C. Goradia, W. Thesling and I. Weinberg, "Key Factors Limiting the Open Circuit Voltage of n+pp+ InP Solar Cells", Conf. Rec. 21st IEEE Photovoltaic Specialists Conf., Orlando, Fla., May 1990, pp. 386-393

[5] C.J. Keavney, M.B. Spitzer, Appl. Phys. Lett. 52(17) 25 April 1988, pp. 1439-40

# FIESTA ROC: a New Finite Element Analysis Program for Solar Cell Simulation

Ralph O. Clark
Space Photovoltaic Research Center*, Electrical Engineering Department
Cleveland State University
Cleveland, Ohio

## INTRODUCTION

FIESTA ROC (FInite Element Semiconductor Three-dimensional Analyzer by Ralph O. Clark) is a computational tool for investigating in detail the performance of arbitrary solar cell structures. As its name indicates, it uses the finite element technique to solve the fundamental semiconductor equations in the cell. It may be used for predicting the performance (thereby dictating the design parameters) of a proposed cell or for investigating the limiting factors in an established design.

## THE FINITE ELEMENT METHOD

The fundamental semiconductor equations solved by FIESTA ROC are [1]

$$\nabla \cdot (\epsilon \mathcal{E}) = \rho \qquad \text{(Poisson's Equation)} \tag{1a}$$

$$\nabla \cdot \mathcal{F}_n = G - R \qquad \text{(Electron Continuity Equation)} \tag{1b}$$

$$\nabla \cdot \mathcal{F}_p = G - R \qquad \text{(Hole Continuity Equation)} \tag{1c}$$

Here $\mathcal{E}$ is the electric field, $\epsilon$ the permittivity, $\rho$ the volume charge density, $G - R$ the net carrier generation rate (generation minus recombination), and $\mathcal{F}_n$ and $\mathcal{F}_p$ the electron and hole flux densities. In turn, $\mathcal{E}$, $\mathcal{F}_n$, and $\mathcal{F}_p$ are related to the electrostatic potential $\psi$ and the quasi-Fermi potentials $\phi_n$, $\phi_p$ by

$$\mathcal{E} = -\nabla \psi \tag{2a}$$

$$\mathcal{F}_n = n_i \mu_n e^{(\psi - \phi_n)/V_T} \nabla \phi_n \tag{2b}$$

$$\mathcal{F}_p = -n_i \mu_p e^{(\phi_p - \psi)/V_T} \nabla \phi_p \tag{2c}$$

As boundary conditions, we assume that the domain of simulation, $\Omega$, has a boundary $\partial\Omega$ that can be partitioned into two segments: the Dirichlet boundary $\partial\Omega_D$, on which $\psi$, $\phi_n$, and $\phi_p$ are prescribed, and the Neumann boundary $\partial\Omega_N$, on which the components of $\nabla\psi$, $\nabla\phi_n$, and $\nabla\phi_p$ normal to the surface all vanish. In particular, on the Dirichlet boundary, which corresponds to the contacts of a device, an infinite surface recombination velocity is assumed, pinning $n$ and $p$ to their levels at thermal equilibrium and $\phi_n$ and $\phi_p$ both to $\psi - \psi_0$. On the Neumann boundary, arbitrary surface recombination velocities are possible. Note that, for a one-dimensional model of a two-terminal device under these assumptions, we cannot model finite surface recombination velocities at the ends of the device because both ends represent contacts, i.e. Dirichlet boundaries.

Equations (1) can all be written in the generic form

$$\nabla \mathbf{f} - s = 0 \tag{3}$$

To solve (3) by the finite element method, we first write it in its weak form, as follows. Let $w$ be an arbitrary piecewise-continuous function on $\Omega$, vanishing identically on $\partial\Omega_D$. Multiplying (3) by $w$, integrating over the entire volume, and integrating the first term by parts, we obtain

$$0 = \int_\Omega w(\nabla \cdot \mathbf{f} - s) = \int_{\partial\Omega} w\mathbf{f} \cdot \mathbf{n} - \int_\Omega (\nabla w \cdot \mathbf{f} + ws),$$

*funded by NASA Lewis Research Center, Cleveland, Ohio

where $\mathbf{n}$ is the unit outward normal to the surface. Note that since $w$ vanishes on the Dirichlet boundary and $\mathbf{f} \cdot \mathbf{n}$ on the Neumann boundary, the surface integral vanishes, leaving us with the weak form of equation (3):

$$\int_{\Omega} (\nabla w \cdot \mathbf{f} + ws) = 0 \qquad (4).$$

We now discretize the problem by fixing $N$ points, called nodes, between which $w$, $\psi$, $\phi_n$, and $\phi_p$ all vary in a continuous way. In particular, we express $w\{\psi, \phi_n, \phi_p\}$ as a linear combination of continuous, piecewise smooth functions $W_i\{\Psi_i, \Phi_i^n, \Phi_i^p\}$, $i = 1, \ldots, N$, each of which assumes the value of 1 at node $i$ and zero at all other nodes. Thus, $w = \sum_{i=1}^{N} w_i W_i$, $\psi = \sum_{i=1}^{N} \psi_i \Psi_i$, $\phi_n = \sum_{i=1}^{N} \phi_i^n \Phi_i^n$, $\phi_p = \sum_{i=1}^{N} \phi_i^p \Phi_i^p$, where the $w_i$ are arbitrary coefficients (to keep $w$ arbitrary) and $\psi_i$, $\phi_i^n$, $\phi_i^p$ are just the values assumed by $\psi$, $\phi_n$, and $\phi_p$ at node $i$. Now equation (4) becomes

$$\sum_{i=1}^{N} w_i \int_{\Omega} (\nabla W_i \cdot \mathbf{f} + W_i s) = 0 \qquad (5).$$

Since the $N$ coefficients $w_i$ are arbitrary, equation (5) really represents the system of $N$ equations

$$\int_{\Omega} (\nabla W_i \cdot \mathbf{f} + W_i s) = 0, \qquad i = 1, \ldots, N \qquad (6).$$

In fact, with our three coupled equations (1) and three dependent variables $\psi$, $\phi_n$, $\phi_p$, we now have $3N$ coupled non-linear equations in the $3N$ unknowns $\psi_i$, $\phi_i^n$, $\phi_i^p$, $i = 1, \ldots, N$. These are solved by the finite element code by means of a generalized Newton's method.

## ADVANTAGES OF FINITE ELEMENT

Because the finite element method is an integral method, with only first derivatives appearing, many complications associated with boundary value problems disappear. First of all, surface effects, whether at a boundary between regions of the device (e.g. the junction) or at the physical surface of the device (e.g. surface recombination) are effectively a special case of bulk effects where the integrand includes a Dirac delta function to localize the effect to the boundary. The delta function converts volume integrals into surface integrals. Thus, surface recombination and interface charge density may be handled easily by including surface integrals in equation (6). In addition, the perennial problem of matching the electric field at a jump discontinuity of $\epsilon$ does not even come up, having been integrated out of existence. Thirdly, multiple non-interacting recombination levels are dealt with simply by including additional terms in R (which appears in the $s$ in equation (6)). Finally, non-rectilinear elements are readily handled by performing the integrations in (6) numerically.

## IMPLEMENTATION

We have implemented a one-dimensional prototype of FIESTA ROC in C, running on an IBM-PC compatible and on a Cray XMP. The prototype features automatic mesh generation and automatic dark and light $I$–$V$ simulations, as well as spectral response. Arbitrary numbers of recombination levels, degenerate statistics, and heavy doping effects are supported. Finite surface recombination velocities, as noted earlier, are imcompatible with our choice of boundary conditions in the one-dimensional case, so they have been left out of the prototype. Once the solution to equation (6) has been found for a given bias and illumination, many quantities of interest can be examined at any point in the cell. These include the electron and hole current densities, electric field, electric potential and quasi-Fermi potentials, net recombination, $n$, and $p$.

## EXAMPLE

As an example of the use of FIESTA ROC, we have modeled an InP shallow homojunction $n^+pp^+$ cell from Spire Corporation which has been extensively studied with analytical models [2]. The growth parameters and modeling parameters found in [2] are reproduced in Tables I and II. Without any change in the parameters of either table, the results of light $I$–$V$ and spectral response simulations by the prototype are shown in Figures 1 and 2. In addition, the measured and calculated solar cell parameters are shown in Table III.

Table I: Growth Parameters for Spire 6 Cell

| | |
|---|---|
| emitter width | 400 Å |
| $n^+$ emitter doping (Si) | $1 \times 10^{18}$ cm$^{-3}$ |
| base width | 3 $\mu$m |
| $p$ base doping (Zn) | $2 \times 10^{16}$ cm$^{-3}$ |
| BSF width | 250 $\mu$m |
| $p^+$ BSF doping (Zn) | $5 \times 10^{18}$ cm$^{-3}$ |
| cell area | 0.25 cm$^2$ |
| grid shadowing | 4.8% |

Table II: Modeling Parameters for Spire 6 Cell [2]

| | |
|---|---|
| indirect lifetime of holes in emitter | 2.0 ns |
| hole mobility in emitter | 75 cm$^2$/V-s |
| indirect lifetime of electrons in base | 150 ns |
| electron mobility in base | 3988 cm$^2$/V-s |
| indirect lifetime of electrons in BSF | 0.60 ns |
| electron mobility in BSF | 2456 cm$^2$/V-s |

The real utility of a numerical solver, however, lies in its ability to show what is happening in various regions of the cell. In this respect, it functions as a sort of computational microscope, allowing the investigator to probe all regions of the cell to determine, for example, which contribute most to the total recombination, light-generated current, and so on. In Figure 3, we show the calculated net recombination for three different bias points—short circuit, maximum power, and open circuit—plotted against the spatial coordinate $x$. Here $x = 0$ represents the metallurgical $p$-$n$ junction and $x = 3\mu$m the base-BSF low-high junction. The emitter, being only .04$\mu$m wide, is invisible on this scale. The junction space charge region is visible as a low-recombination valley at short circuit and a high-recombination peak under forward bias. Note, however, the additional peak in recombination in the BSF region. In Figure 4, we show the same curve, at maximum power only, calculated for the same cell and for another differing only in the doping in the BSF, namely $5 \times 10^{17}$ rather than $5 \times 10^{18}$ cm$^{-3}$. The indirect recombination lifetime in the BSF is also correspondingly higher (6.0 ns instead of .60). The peak in the BSF almost disappears when the BSF doping is decreased. Such an analysis can aid cell fabricators in designing and producing more efficient cells.

## CONCLUSIONS

We have demonstrated a one-dimensional prototype of a flexible finite element package that will enable cell designers to simulate a variety of effects and to pinpoint problems in proposed or existing cells. The two- and three-dimensional versions are currently under development.

## REFERENCES


[1] Markowich, Peter. *The Stationary Semiconductor Device Equations*, Springer-Verlag, Vienna, 1986.

[2] Thesling, William. "Theoretical Modeling, Optimal Design and Performance Predictions of the Shallow Homojunction Indium Phosphide Solar Cell in Space Applications", Master's Thesis, Cleveland State University, Cleveland, Ohio, August 1990.

Table III: Solar Cell Parameters for Spire 6 Cell

| | Measured | Calculated |
|---|---|---|
| $I_{sc}$, mA | 8.47 | 8.37 |
| $V_{oc}$, mV | 868 | 869 |
| $I_{max}$, mA | 8.19 | 8.03 |
| $V_{max}$, mV | 751 | 754 |
| $FF$, % | 83.8 | 83.3 |
| $\eta$, % | 17.94 | 17.64 |

at 1AM0, 25°C

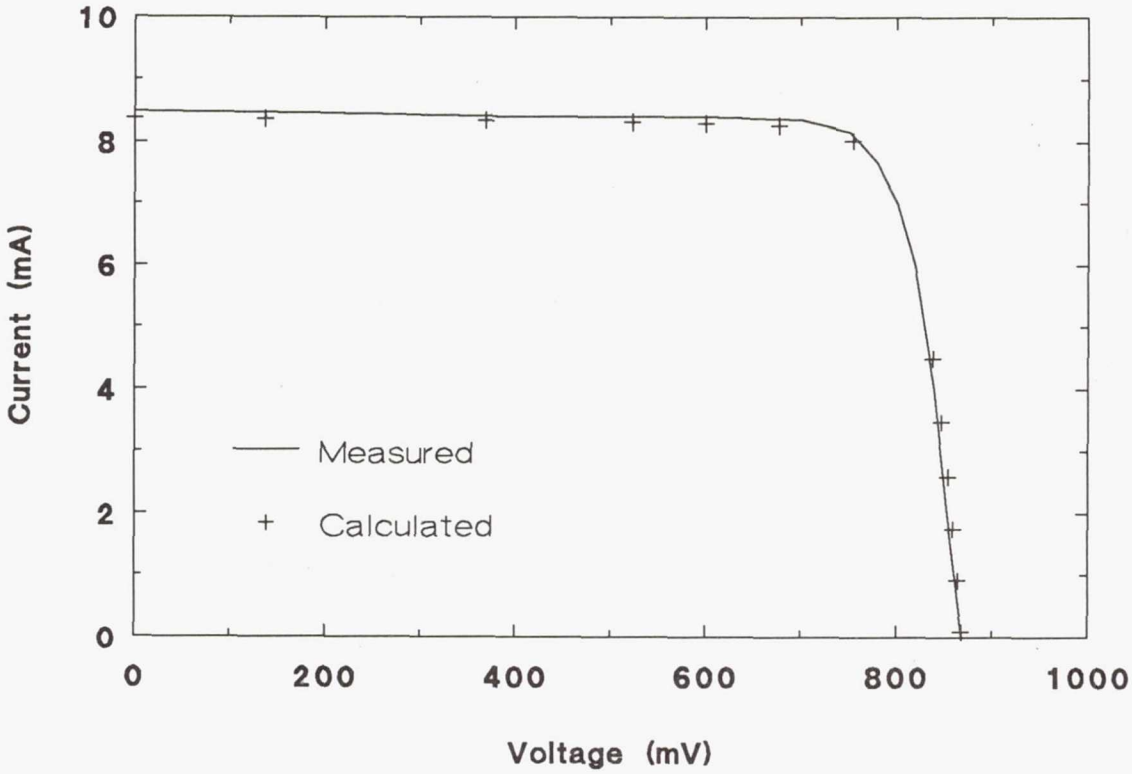


Figure 1: Illuminated $I$–$V$ characteristic for cell Spire 6, with calculated results by FIESTA ROC prototype.

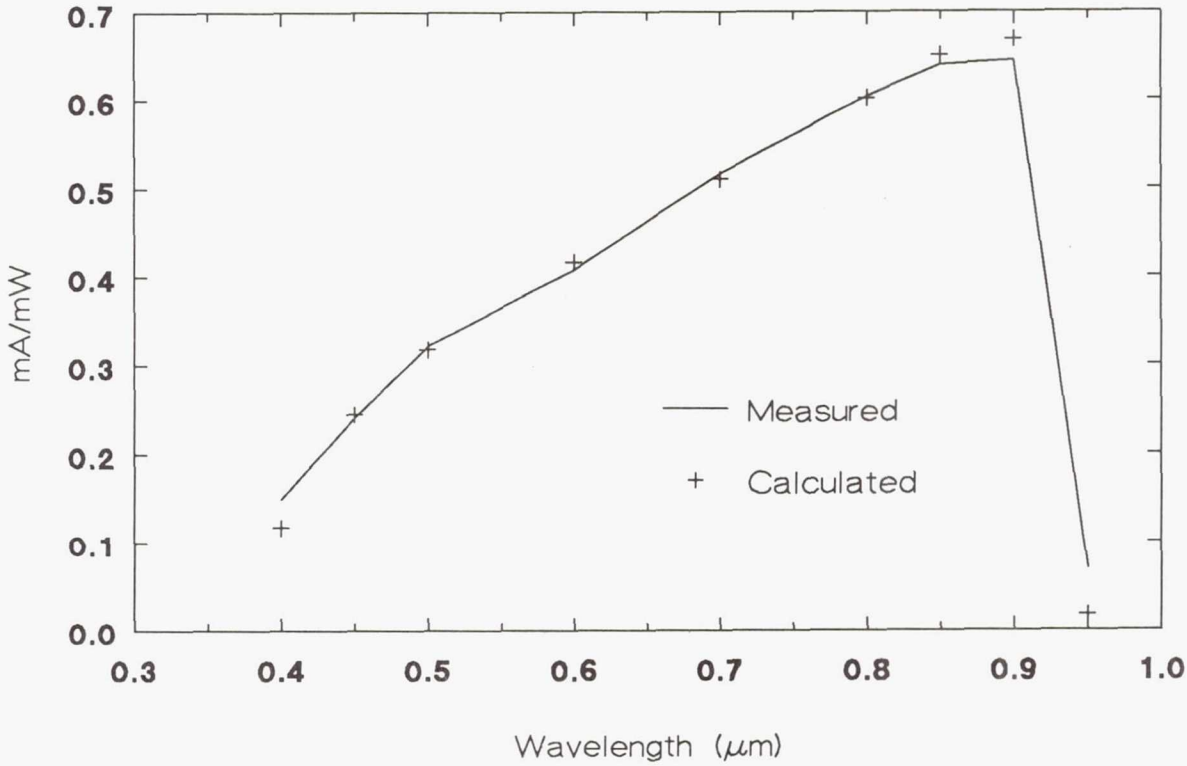


Figure 2: Spectral response for cell Spire 6, with calculated results by FIESTA ROC prototype.

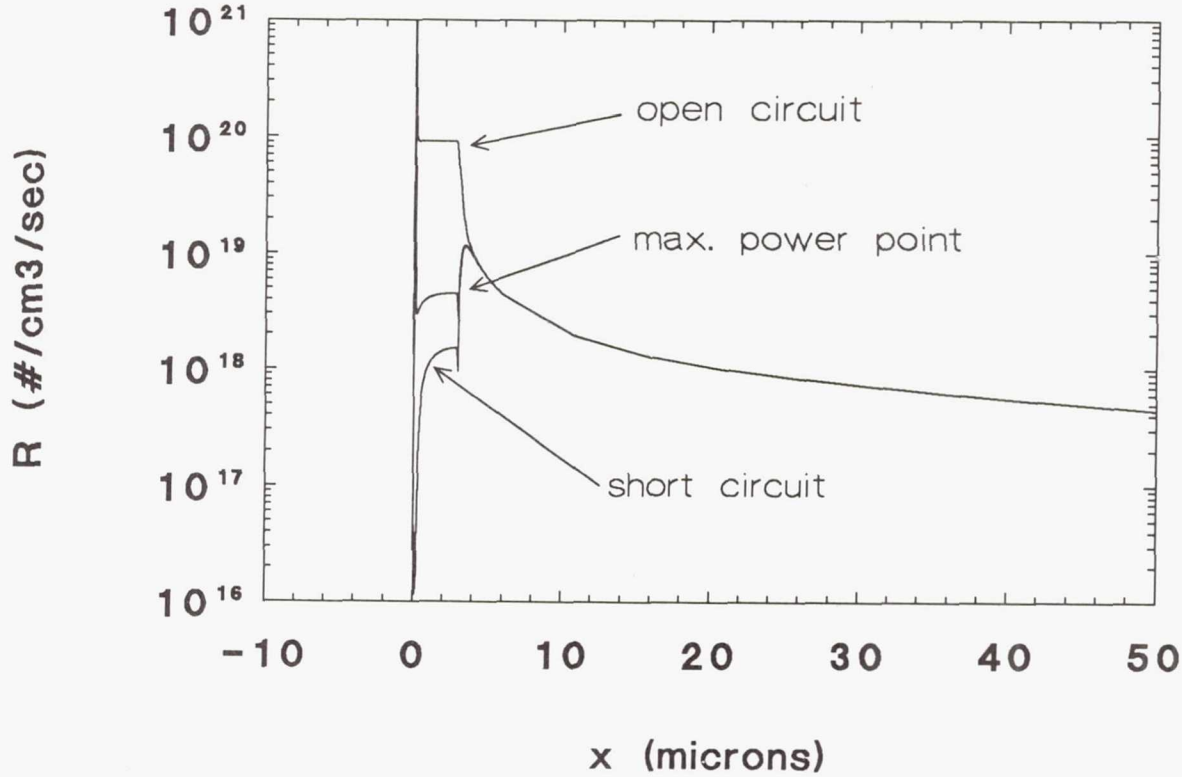


Figure 3: Net recombination calculated by FIESTA ROC prototype at three bias conditions. The $n^+p$ junction is at $x = 0$ and the $pp^+$ junction at $x = 3\mu$m.

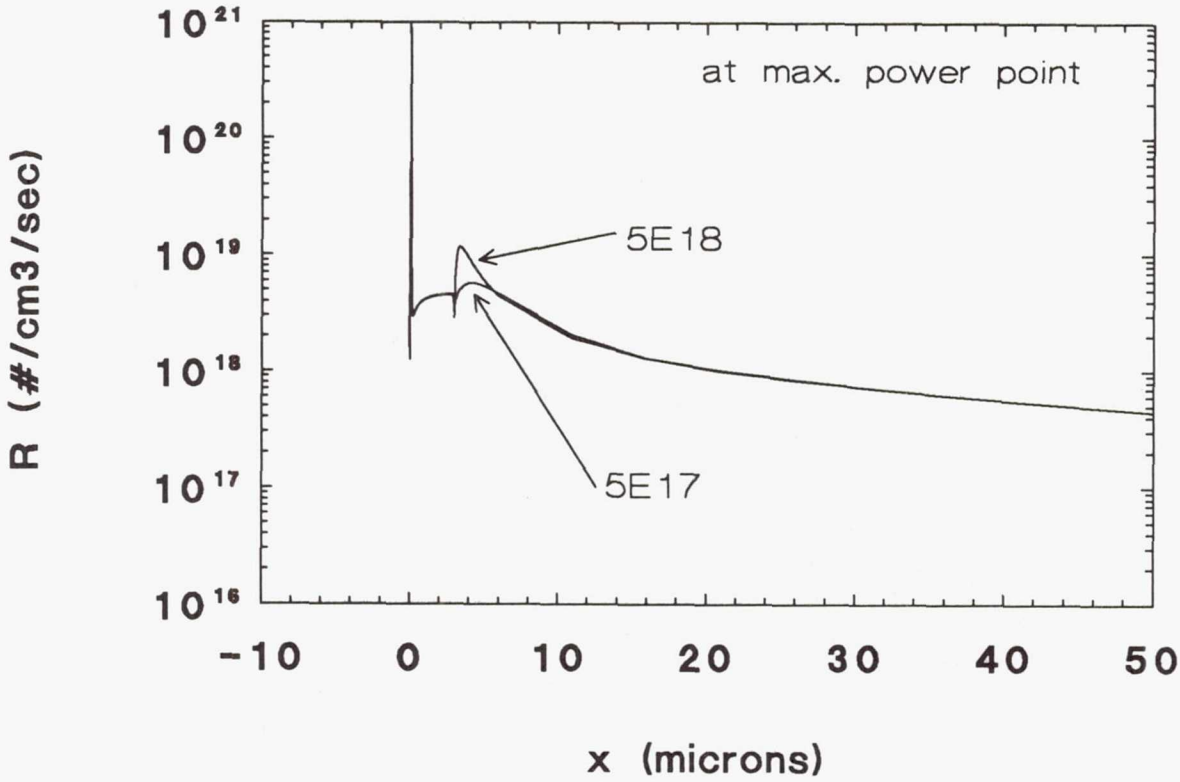


Figure 4: Net recombination calculated at max power voltage for cells with different BSF dopings.

# Significant Reduction in Arc Frequency of Negatively Biased Solar Cells: Observations, Diagnostics, and Mitigation Technique(s)

B.L. Upschulte, G.M. Weyl, and W.J. Marinelli
Physical Sciences Inc.
Andover, Massachusetts

E. Aifer
Boston University
Boston, Massachusetts

D. Hastings
Massachusetts Institute of Technology
Cambridge, Massachusetts

D. Snyder
NASA LeRC

A variety of experiments have been performed which identify key factors contributing to the arcing of negatively biased high voltage solar cells. These efforts have led to reduction of greater than a factor of 100 in the arc frequency of a single cell following proper remeditation procedures. Experiments naturally lead to and focussed on the adhesive/encapsulant that is used to bond the protective cover slip to the solar cell. An image-intensified CCD camera system recorded UV emission from arc events which occurred exclusively along the interfacial edge between the cover slip and the solar cell. Microscopic inspection of this interfacial region showed a bead of encapsulant along this entire edge. Elimination of this encapsulant bead reduced the arc frequency by two orders of magnitude.

Water contamination has also been identified as a key contributor which enhances arcing of the encapsulant bead along the solar cell edge. Spectrally resolved measurements of the observable UV light shows a feature assignable to OH(A-X) electronic emission, which is common for water contaminated discharges. Experiments in which the solar cell temperature was raised to 85°C showed a reduced arcing frequency, suggesting desorption of $H_2O$. Exposing the solar cell to water vapor has been shown to increase the arcing frequency. Clean dry gases such as $O_2$, $N_2$, and Ar show no enhancement of the arcing rate. Elimination of the exposed encapsulant eliminates any measurable sensitivity to $H_2O$ vapor.

## INTRODUCTION

The demands on future space power systems encourage all of us to investigate every possible avenue to increase output power, reduce weight, and improve efficiency. High voltage arrays, i.e., several hundred volts, have the distinct advantage of higher output power with minimal design changes and little weight penalty. Unfortunately, high voltage arrays exhibit undesirable arcing phenomena. In particular, for negatively biased solar cell arrays this arcing leads to disruptive RF noise, and may potentially damage sensitive electronic components or the solar array itself. It has been experimentally observed (Refs. 1 through 6) that arcing begins at bias voltages more negative than -300V. Although several mechanisms have been suggested to explain the

arcing phenomena/behavior, very little hard evidence is available which unambiguously identifies the physical processes which control arc initiation or maintenance.

In this paper we will describe a set of experiments which identify key factors contributing to arcing of negatively biased solar cells. We begin by describing the unique ultra-high vacuum plasma test facility and its performance characteristics. Following this we will describe several arc diagnostics which were instrumental in our findings; then we will describe in detail the most relevant measurements, observations, and analysis. In our conclusion, we will suggest future mitigation techniques to make high voltage solar cell arrays of practical use, and suggest complimentary testing techniques to identify the microscopic mechanism associated with arcing.

## APPARATUS

All experiments were conducted in an ultra-high vacuum (UHV) chamber. The chamber is a 21 in. long by 10 in. o.d. cylinder in which all ports are sealed with Cu gaskets and knife edge flanges to allow operation at pressures as low as $2 \times 10^{-11}$ torr. The chamber is shown schematically in Figure 1 and described below. In the forward section of the chamber are four 6-in. clear aperture ports employed for operation of sample diagnostics. An Auger electron spectrometer is located on the top flange and may be positioned to within 0.25 in. of the sample for surface analysis. A differentially pumped quadrupole mass spectrometer (0 to 300 amu range) is located on the lower port and is configured to detect species desorbed from the sample as well as the background environment. Ports on either side of the chamber and on the end wall are available for optical access. In these experiments the end wall port is used for optical access and may be equipped with a fast, low resolution optical spectrometer for discharge characterization. A camera system may be employed to photograph arcing events from this port as well. One of the side ports is fitted with the plasma source. The end-wall of the chamber may also be equipped with a retarding potential electron energy analyzer which may be employed to sample emission from the surface. The side ports were used to support retractable planar and cylindrical Langmuir probes.

In the mid-section of the chamber four small access ports are provided for pressure measurement (ionization gauge), gas dosing, and a 0 to 5 keV ion sputtering gun for sample cleaning. In the rear section of the chamber, ports are provided for a 1000 1/s turbomolecular pump and sample viewing.

The samples to be tested are mounted in the cradle of a 5 degree-of-freedom sample manipulator which provides access to all of the forward ports in the chamber. High voltage and low-voltage isolated feedthrough are used for precise electrical measurements.

The plasma source is a 3 cm Kaufmann type charge-neutralized ion source purchased from Ion Tech Inc. It has been mounted on a vacuum flange and slides into a full nipple extension attached to an 8 in. conflat flange port on the UHV chamber. The plasma source mounting bracket slides on threaded rods to allow the source to solar cell distance to be varied from 13 to 35 cm. The three rods are arranged in an optical mount pattern so that small angular adjustments may be specifically and reproducibly set. Argon plasmas are typically used in our measurements. The flow of argon used during plasma source operation is roughly 1 sccm and produces a chamber pressure of $1 \times 10^{-5}$ torr. Although this argon pressure is relatively high, the largest partial pressure of a contaminant is $\leq 1 \times 10^{-7}$ torr. This background pressure is due to $H_2O$ desorbed from the chamber walls when the hot Kaufmann ion source is in operation. Typical plasma densities are presented in Table 1. The electron temperature was found to be 1.25 eV ± 0.15 eV. Samples were positioned 25 cm downstream from the plasma source. The radial profile of the ion beam at this position was measured using the cylindrical Langmuir probe in ion saturation mode. Figure 2 shows the size of the ion beam, full width at half maximum, to be at least 5 cm, i.e., larger than the sample solar cells used in our measurements.

Several diagnostics played a crucial role in these experiments. A capacitively coupled current sensor based on an experimental design by Snyder[3] was utilized for all measurements, and provided a master trigger signal for many of the other diagnostics. A high voltage probe (Tektronix Model P6015) was attached to the solar cell interconnect to monitor time dependent voltage variations during arc events. Time bandwidths in excess of 8 MHz were realizable with the voltage probe, and bandwidths in the range of 100 MHz were

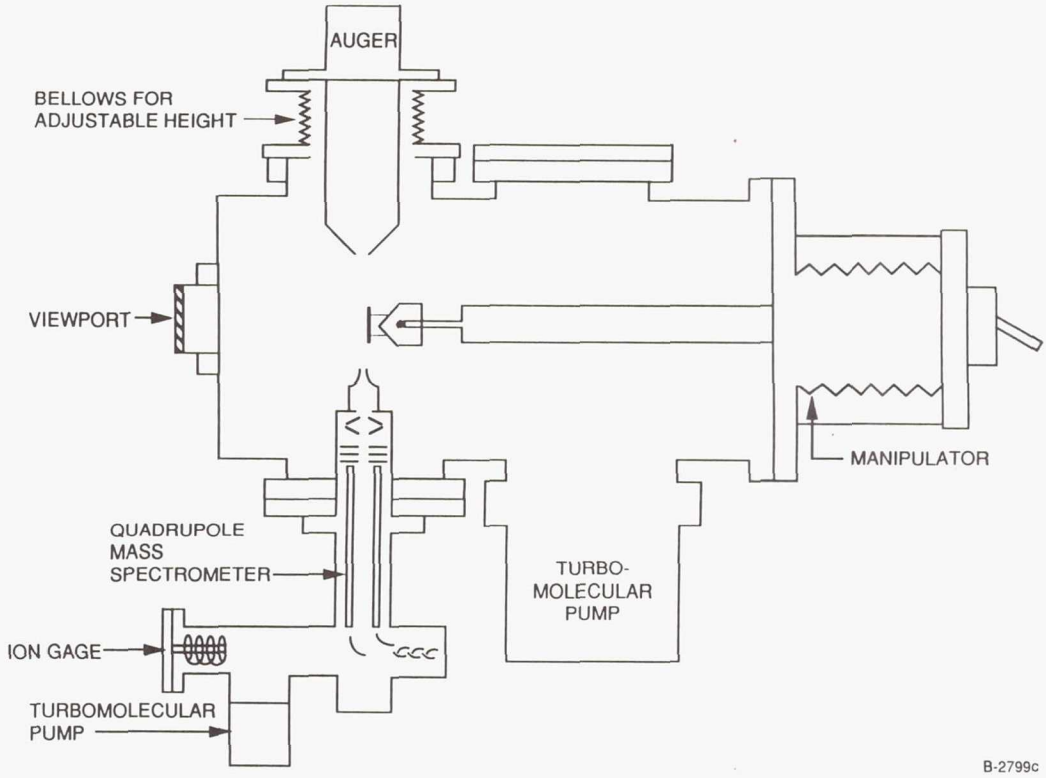


(a) Side View

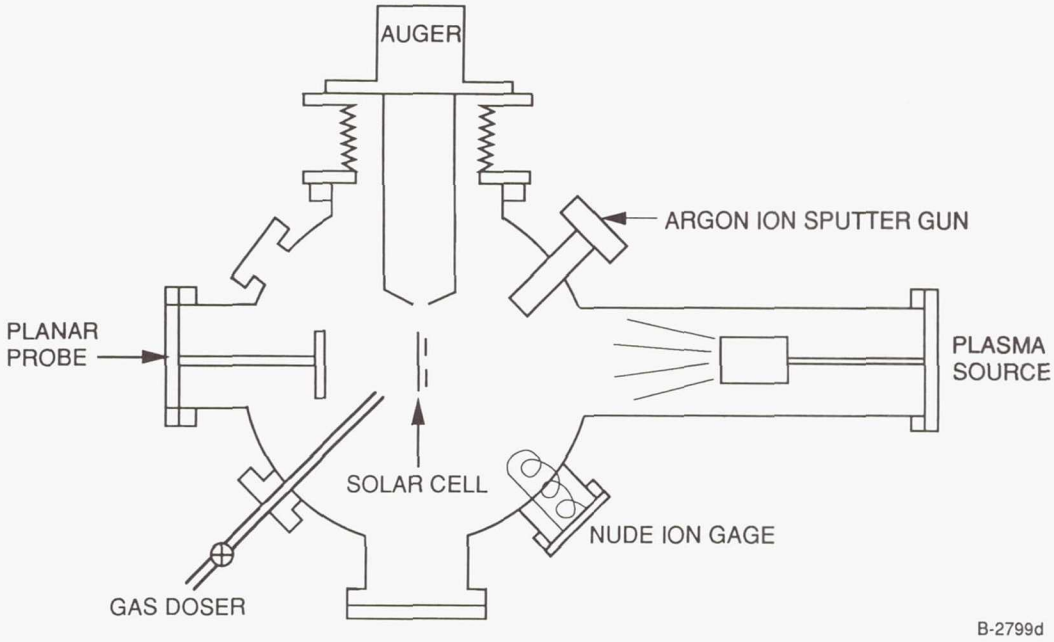


(b) View Along Manipulator Axis

Figure 1. - Schematic drawing of the UHV chamber showing location of diagnostics.

TABLE 1. - PLASMA CHARACTERISTICS

| Beam Energy (eV) | Electron Density ($10^6$ $cm^{-3}$) | Ion Density ($10^6$ $cm^{-3}$) |
|---|---|---|
| 20 | 7.4 ± 1.5 | 5.6 ± 1.0 |
| 30 | 7.4 | 5.5 |
| 40 | 8.8 | 6.0 |
| 50 | 10.0 | 7.5 |
| 60 | 12.1 | 10.0 |

obtainable with the current sensor. A UV radiometer was implemented and viewed arc events through the end viewport. This device consisted of a Hamamatsu Model R1220 solar blind photomultiplier tube in an EMI-Gencom Model SRI/F housing. This tube provides an active photocathode of about 3/4 in. in diameter and response from the air transmission cutoff at, around 190 nm, to 305 mm with a quantum efficiency of approximately 0.2. The same UV light was spectrally resolved using a Princeton Instruments Optical Multichannel Analyzer (OMA) coupled to a Jarrell-Ash 1/4 meter monochromator. The dispersed light from the monochrometer's 300 line/mm grating is detected on a 712 element diode array. The multiplex advantage of the OMA allows simultaneous detection of all light throughout the 200 to 400 nm region for each arc event. The diagnostic most useful in our measurements is a unique PSI designed and built intensified CCD camera system. The CCD array is a Model NXA 1060 by Amperex and is coupled to a Nikon F/4.5 compound quartz lens system. Custom gating circuitry and software allowed us to trigger the gated image intensifier with the current sensor. Using a UG-5 ultraviolet filter, we were able to capture arc emission in a 5 $\mu$s gate width. Actual images of individual arc events were displayed in false color video format. Finally, we made excellent use of an Olympus Model BH2 phase sensitive microscope to inspect and photograph changes in the solar cell edges.

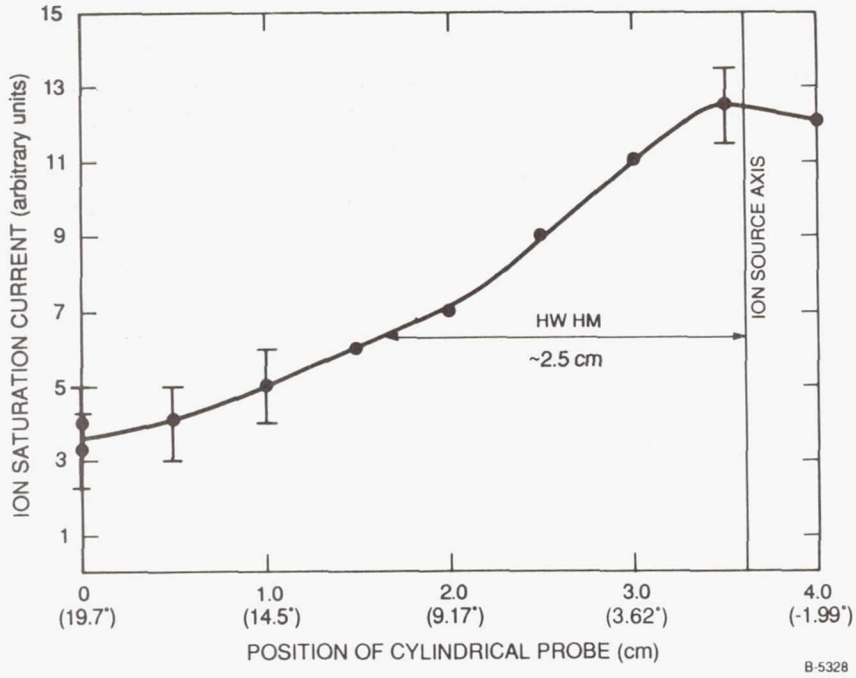


Figure 2. - Radial profile of ion saturation current, cylindrical probe.

## Experimental Observations

The relevant experiments to be described below were performed on "thin" solar cells, (i.e., ~250 $\mu$m thick) provided to us by Spectralab, Inc. These cells measured 2 x 1 $cm^2$ and had silica cover plates that extended beyond the edge of the cell on all sides by approximately 100 $\mu$m. The cells were mounted individually on the manipulator, where they were exposed to the plasma from the ion source. High voltage leads, which were determined to be free of arcing sites, were used to bias the solar cell to the test voltages. Plasma ion energies for all these tests reported here were 40 eV, and most tests were performed at a cell bias of -1000V.

A lengthy set of initial electrical/optical correlations were first measured to confirm that the UV light emission arises from the arc event. Figure 3 presents digitized oscilloscope traces of the UV Radiometer, the high voltage probe, and the current sensor. It is immediately obvious that the UV emission and the instantaneous current are extremely well correlated. A running integral of the current has been shown to produce a curve matching the interconnect voltage change as prescribed by dQ = CdV. In fact, a very accurate measurement of the sensor capacitance can be obtain from this linear relationship. In addition, we found the integral of the UV light emission was well correlated with the interconnect voltage change as well.

Polaroid pictures of the CCD camera images, as displayed on the computer screen, are used for the presentation of the observed arc event. The images are false color encoded and the brighter total emission level corresponds to the white regions of the picture while the blue-black color corresponds to the lower light emission regions. Figure 4 shows a full screen picture of an arc event. The entire profile of the solar cell is observable. The solar cell interconnect is located at the right edge. The brighter line observed along this edge of the cell is the result of light from the arc event scattering off of the embedded interconnect. All arc events occurred at the lower edge of the solar cell, not in the interconnect region. This entire lower edge is a triple junction point due to the silver conducting film on the bottom of the solar cell and due to the dielectric adhesive extruded along this edge as a result of attaching the cover slip to the cell. The luminosity dispersed around the cell arises due to light scattered off the Kovar interconnect/support. The white center of the arc is sufficiently bright to bleach/bleed across to other pixels on the CCD array and should not be interpreted as a measurement of the size of the arc spot. Arc spots have been measured as small as 200 $\mu$m, but most measurements suggest the characteristic size of the spot to be order of 500 $\mu$m. Although many images of arc events were acquired, we never observed detectable light emission at any location other that at this lower edge of the solar cell.

Our observation led us to examine the lower edge region of the cell where arc events had been recorded. Upon inspection, we observed a bead of adhesive along this edge; apparently squeezed out from between the silicon and cover slip during assembly. We did not observe any indication of damage due to the arc events or any unique site that might have been responsible for the large frequency of arc events at this edge. Indeed, the inspection of all the edges appeared very similar. Our next inclination was to inspect a new solar cell which had never been exposed to the plasma. This cell showed an identical accumulation of adhesive as observed for the plasma irradiated cell. An example picture (X50) is shown in Figure 5. This photo concentrates

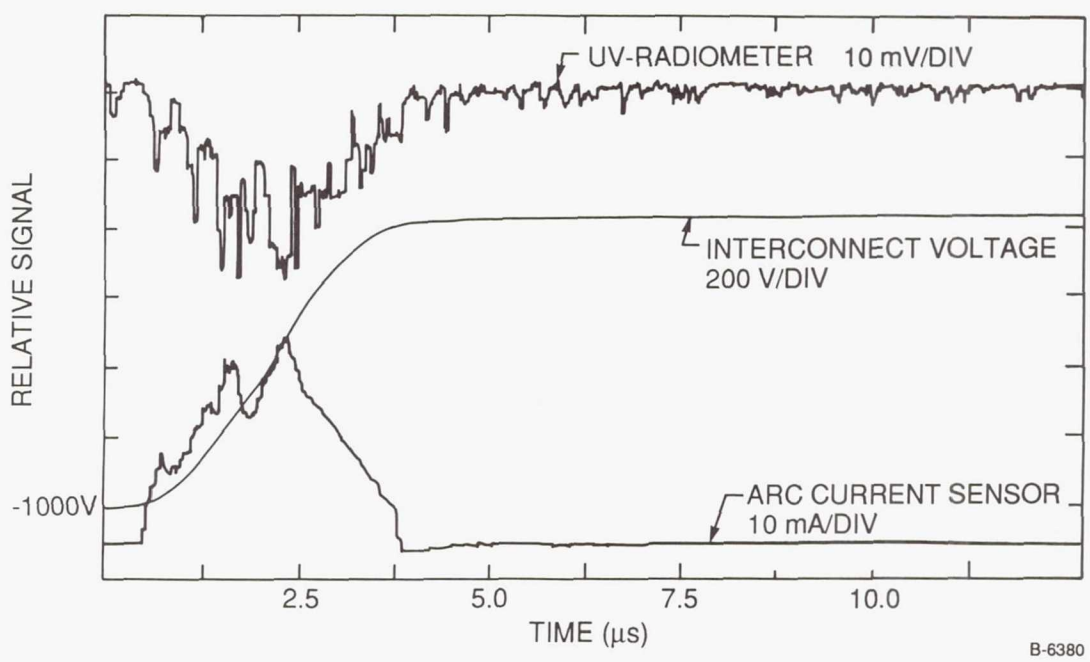


Figure 3. - Time-resolved record of current flow, voltage change, and UV emission during an arc event.

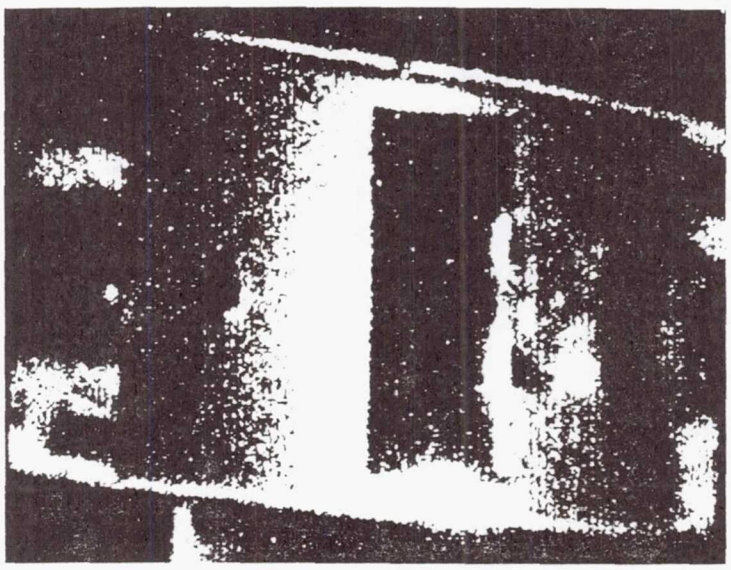

Figure 4. - CCD camera image of a solar cell arc event.

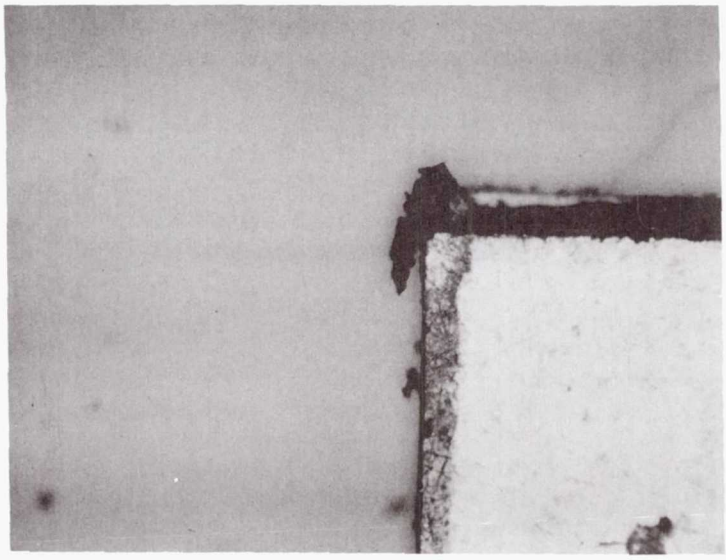

Figure 5. - Exposed adhesive/encapsulant along the edge and corner of the solar cell.

on a corner of this particular solar cell, where a substantial amount of adhesive is observed. The adhesive edge displays both flake-like and globular structures. The adhesive is clear to opaque and difficult to discern on normal contrast film. The phase sensitive polarizer of the microscope was utilized to invert the contrast, making the adhesive look dark. Some flakes are quite large, on the order of 10 to 100 $\mu$m. In a variety of places filaments or hairlike fibers of adhesive were observed to be protruding from the edges. These features are much smaller and particularly difficult to photograph because of magnification, depth of field, and contrast problems.

During the course of many of our experiments, we had observed the arcing rate decrease with continual exposure to the plasma. At first we believed this to be an irreversible morphology change in the triple junction region due to the plasma coupling current. Later we observed that the arc frequency would recover to a higher arc rate after cycling the vacuum system to atmosphere and back to $10^{-9}$ torr. We also performed some experiments to monitor the temperature of the support plate and the Kovar interconnect during the plasma exposure period. The results of these experiments are shown in Figure 6. This chart plots the arc frequency on a log scale versus the cumulative plasma exposure time on the horizontal axis (bottom) and cross correlates that exposure time with the interconnect temperature shown on the top horizontal axis. The interconnect temperature rises due to the radiative heating from the plasma neutralizing filament. The arc rate is observed to decrease with time/temperature. Several experiments were then conducted to investigate this phenomenon. First, following an atmosphere to vacuum cycling, the solar cell was subjected to only the radiative heating due to the filament but no plasma exposure. The cell was then exposed to the plasma and arcing rate measurements were performed. The results of 40 min and 3 hr of heating are shown in Figure 7. These experiments clearly demonstrate that the arcing rate is dependent upon the time spent by the cell at elevated temperatures, where the outgassing rates are greatest. In these experiments the cell is not exposed to the plasma during the heating period. Hence, the reduction in arcing rate can clearly be correlated with a temperature increase rather than

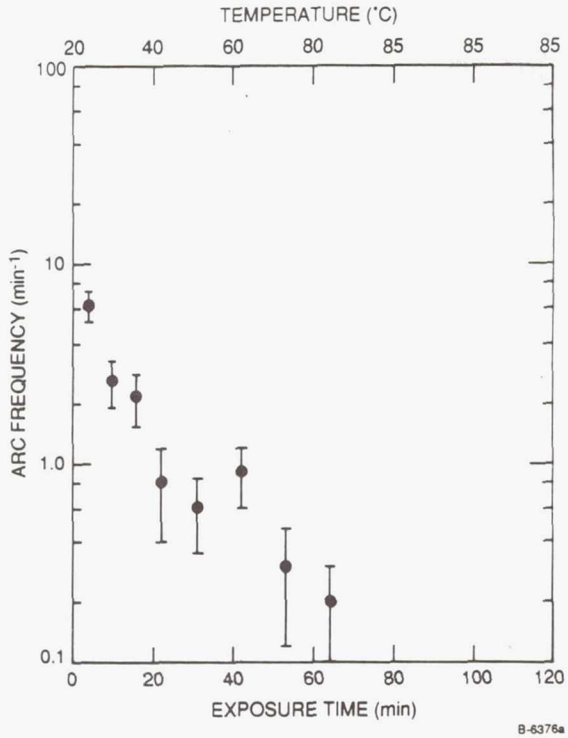


Figure 6. - Arc frequency versus plasma exposure time.

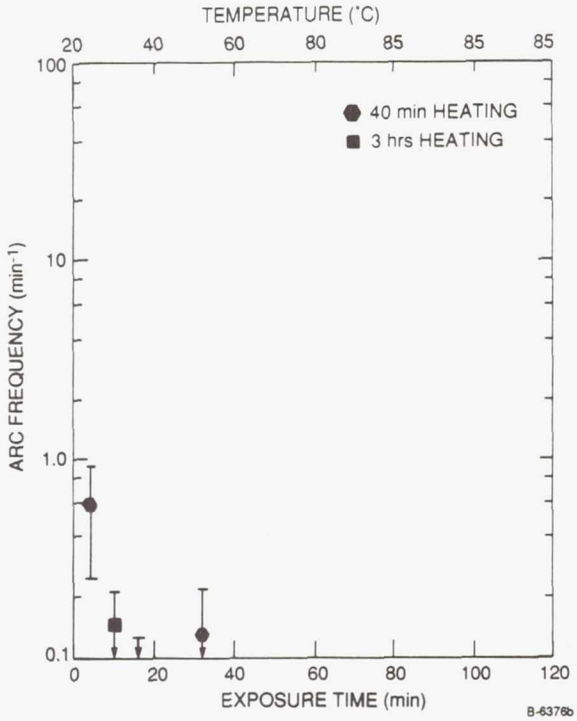


Figure 7. - Arc frequency after solar cell heating.

plasma exposure. Furthermore, upon cooling the cell to room temperature, this reduced arcing rate persists for a period of several hours to as long as 2 days. During this time the cell slowly readsorbs ambient water vapor in the UHV chamber (base pressure $10^{-9}$ torr) and the arcing rate will slowly rise to the rate observed upon initially placing the cell into the chamber. Hence, the role of temperature in controlling the arcing rate is through its effect on adsorbate vapor pressures. This hypothesis was further confirmed in our next set of experiments.

In this experiment we used the OMA to spectrally resolve the arc emission. The spectra shown in Figure 8 suffers from poor signal-to-noise levels, but clearly shows the presence of the $OH(A^2\Sigma\ v'=0 - X^2\Pi\ v''=0)$ feature at 306 nm. This feature is commonly observed in all types of electrical discharges contaminated with water.

The larger features at 350 and 380 nm cannot be uniquely identified at this low signal level and poor resolution. Possible contributors are AgO, Fe, and CN. Some of the features below 290 nm are suspected to be $NO(A^2\Sigma - X^2\Pi)\ \gamma$ or $(B^2\Pi - X^2\Pi)\ \beta$ bands, but once again the poor signal and resolution prohibit a unique identification.

Our next set of experiments investigated arc frequency with controlled exposure to likely adsorbates. Mass spectrometer measurements in our UHV chambers suggested the most ubiquitous contaminant is water. We controlled the temperature of the solar cell with the radiative heat load of the neutralizing filament, then exposed the solar cell to varying amounts of water vapor using a variable leak valve and reservoir of distilled degassed water. The arc frequency was observed to increase with additional exposure to the $H_2O$ vapor. The data is shown in Figure 9. The $H_2O$ exposure is cumulative, with the step size of the exposures being $2.5 \times 10^{-4}$ torr-min. The arc frequency is determined with three consecutive 2-min counts of the observed arcs using the capacitively coupled sensor. Radiative heating was continued through the $H_2O$ exposure period to maintain the temperature near 80°C. Analysis of this data suggests the arc rate increases with the 0.6 power of the dosing of $H_2O$ on the solar cell. One might expect the arc frequency to

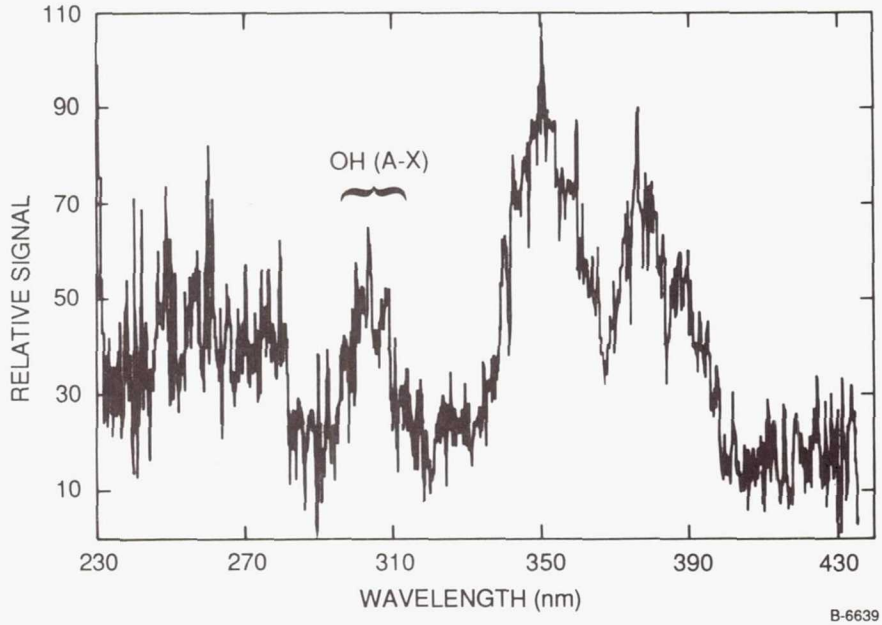


Figure 8. - Spectra of solar cell arc emission at 8 nm resolution.

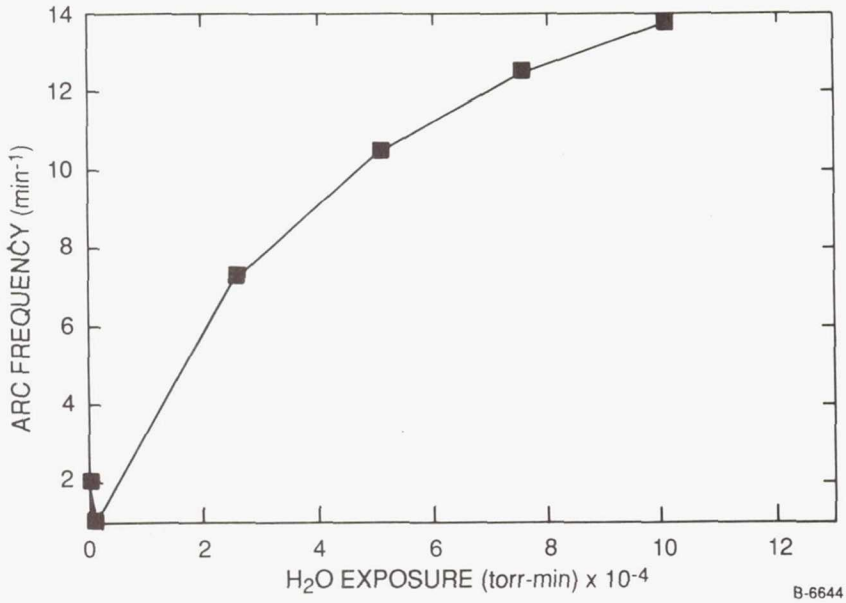


Figure 9. - Arc frequency of heated solar cell as a function of cumulative $H_2O$ exposure.

increase with $H_2O$ dosing to the first power. This would resemble the adsorption of a contaminant with negligible desorption during the measurement. Our measured 0.6 power dependence is most likely the result of some desorption occurring during the period of the experimental measurement. The desorption of $H_2O$ contamination from the cell surface should be quite rapid at elevated temperatures. The apparent arcing rate observed in these measurements does not reflect this type of desorption phenomenon. Rather, the experiments suggest that $H_2O$

is absorbed in depth into the adhesive. Under these conditions the arcing rate is a function of the temperature-dependent diffusion rate of absorbed $H_2O$ into the material. This observation is consistent with the properties of the adhesive used to attach the protective cover slip to the cell surface. As applied, these epoxies are hydrophilic and often contain metallic impurities. As a cross check, the same solar cell was exposed to clean dry gases, i.e., argon, oxygen, and nitrogen. In no case did these gases produce an arc frequency increase.

Our last experiment involved removal of the excess encapsulant along the solar cell edge. This was performed by soaking the solar cell in Dynasolve 220, a silicon solvent recommended by Dow Corning for their encapsulant(s). The solar cell was removed from the solvent and rinsed with methanol. The edges of the solar cell were inspected with the microscope. The adhesive appeared removed, but liquid (either methanol or Dynasolve 220) remained trapped under the cover slip. Figure 10 presents a low magnification view of a cleaned edge. The cleaned solar cell was placed in the vacuum system for testing and pumped down to $10^{-7}$ torr. Initially, this clean solar cell did arc, however, it exhibited a marked faster decline in arc frequency than for an uncleaned solar cell. After a 40-min bakeout, the solar cell could not be induced to arc. We now suspect this initial arcing was associated with trapped solvent. The inducements included: exposure to room air overnight and exposure to greater than $2 \times 10^{-3}$ torr-min of $H_2O$ vapor. Both of these treatments caused significant arc frequency increases on an uncleaned solar cell.

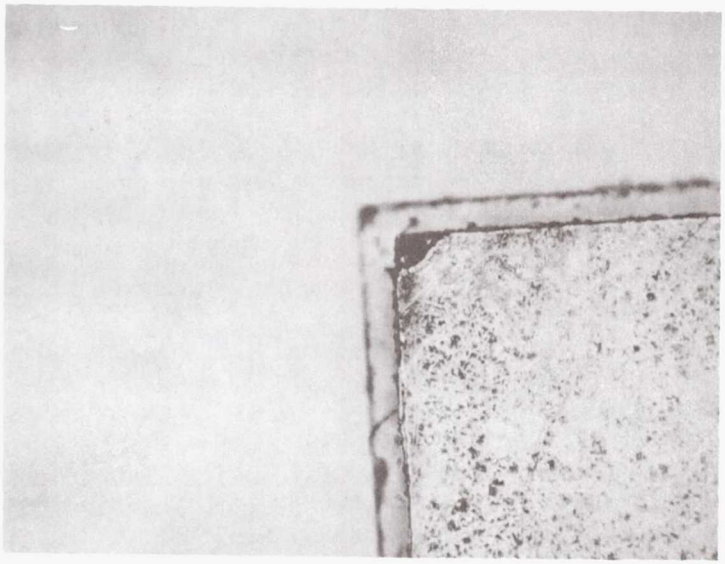

Figure 10. - Microscope picture of the cleaned edge of a solar cell.

Experimental Conclusion

Moisture ladden adhesive that may simultaneous come in contact with the space plasma and the high voltage base of a solar array will exhibit arcing phenomena at voltages more negative than -300V.

Migitation Strategies

Our findings confirmed at least one means of reducing arcing phenomena, but several others might be considered. Clearly elimination of the edge adhesive significantly reduces arcing frequency. This may be accomplished via several techniques, such as the solvent removal of the excess adhesive that we utilized above. We have investigated at least three other removal techniques including: pulsed water/methanol jet, high-speed rotary brush, and laser ablation. A continuous water jet at 300 psig through a 650 $\mu$m orifice showed no substantial effects. Pulsed water/methanol/Dynasolve 210 jets showed only slight removal of the edge adhesive. In all cases the use of a solvent leads to lengthy drying times, i.e., days, and produces some undercutting of the adhesive layer between the cover glass and the silicon cell.

Laser ablation using a focused excimer laser beam at 193 nm, 0.5 J/cm$^2$ pulse and 25 Hz successfully removes the adhesive. However, great care must be utilized to mask the edge. This laser power is capable of ablating the silver base layers of the solar cell. Any higher power levels are capable of damaging even the UV transmitting cover glass material. Some charring may occur but typically wipes off with either $H_2O$ or methanol. Times to ablate a 2 mm illuminated length of a solar cell edge required 30 to 60 seconds at the 25 Hz repetition rate.

High-speed rotary microbrushes are relatively successful. Custom fabricated brushes using one to three rows of roughly 100 $\mu$m diameter wire bristles are recommended. Larger brushes can damage the corners of the solar cell, actually removing/rounding away the edge. Nylon brushes appear to have very little effect, and grinding stones or burrs are much too abrasive. Typical removal times are 30 to 60 seconds for a 2 cm length solar cell edge using a rotary speed of 10,000 rpm. A significant drawback for brushes occurs along the embedded interconnect edge. Great care must be used to avoid tearing or damaging the interconnect. Of course, for solar cells with unexposed interconnects located away from the cover slip edge, this issue is not a concern.

Arcing along the solar cell edge suggests the local electrostatic field contributes to the arc phenomena. This leads us to believe that a redesign of the cover glass edge geometry may help mitigate arc events. This redesign could be as simple as a larger overhang to protect the adhesive washout, however this leads to a size and weight penalty. Sloping or angled cover glass edges may be alternative approaches without associated weight penalties, however additional research must be conducted to verify these strategies.

The potentially best solution to the adhesive problem is new bonding technology. Currently efforts are underway to perfect and commercialize electrostatic or molecular bonding techniques to attach cover glass to the solar cell. It is our opinion that such a technique will significantly reduce arcing while possibly providing a weight savings.

## Future Experiments

Our immediate efforts are to further document the arc frequency reduction and establish a threshold measurement technique/criteria. In addition, we are anxious to investigate the influence of plasma density, ion impact energy, and temperature on both the adhesive ladden and clean solar cells. Very soon we will have an electrostatic probe available to monitor the disposition of cover glass charge before and after an arc event. The most significant need is to investigate the arc initiation process. We also need to identify the microscopic role of water as an adsorbate and the adhesive as the arc propagator/carrier. We clearly need to identify any chemical/physical changes arising when adhesive, water, plasma are combined.

The authors would like to acknowledge technical assistance from Drs. David Sonnenfroh and Mark Allen, and helpful discussions with Drs. B.D. Green, A. Gelb, and Herb Cohen. We would also like to thank NASA Lewis Research Center for financial support through the SBIR program and Mr. Jim Albec of Spectralab Inc. for providing us with sample solar cells.

## References

1. Kennerud, K.L.. 1974. High Voltage Solar Array Experiment, NASA Report CR-121280.

2. Synder, D.B.. 1984. Discharges on a Negatively Biased Solar Array, NASA TM-83644.

3. Synder, D.A.. 1984. Characteristic of Arc Currents on a Negatively Biased Solar Cell Array in a Plasma, NASA TM-83723, July.

4. Grier, N.T. 1983. Plasma Interaction Experiment II: Laboratory and Flight Results. 1983. Spacecraft Environment Interactions Technology Conference, Colorado, October 4-6, 1983, NASA CP-2359, p. 333-349.

5. Fujii, H., Y. Shibuya, T. Abe, K. Ljichi, R. Kasaia, and K. Kuriki. 1986. "Laboratory Simulation of Plasma Interactions with High Voltage Solar Arrays," Proceedings of the 15th International Symposium on Space Technology and Science, Tokyo.

6. Thiemann, H., and K. Bogus. 1986. ESA Journal, 10, 43-57.

# MEASUREMENT OF HIGH-VOLTAGE AND RADIATION-DAMAGE LIMITATIONS TO ADVANCED SOLAR ARRAY PERFORMANCE

D.A. Guidice and P.S. Severance
Phillips Laboratory, Geophysics Directorate
Hanscom AFB, Massachusetts 01731

and

K.C. Reinhardt
Wright Laboratory
Wright-Patterson AFB, Ohio 45433

## SUMMARY

A description is given of the reconfigured PASP Plus experiment: its objectives, solar-array complement, and diagnostic sensors. Results from a successful spaceflight will lead to a better understanding of high–voltage and radiation–damage limitations in the operation of new-technology solar arrays.

## INTRODUCTION

Before new-technology photovoltaic space-power subsystems are developed for use on operational spacecraft, increased knowledge is required in the area of space environmental effects on solar arrays. To carry out an appropriate investigation, the Geophysics Laboratory (now part of Phillips Laboratory, PL) and the Aero-Propulsion and Power Laboratory (now part of Wright Laboratory, WL), starting in 1985, decided to put together an experiment to measure the effects of the space environment on solar-array performance. The experiment was called Photovoltaic Array Space Power Plus Diagnostics, or PASP Plus for short.

The original objectives of the PASP Plus experiment were limited to the investigation of the effects of space-plasma interactions on high-voltage solar array operation at low altitudes. The Jet Propulsion Laboratory (JPL) developed a brassboard instrument capable of biasing as many as six arrays in various voltage steps up to limits of +500 V and –500 V. The JPL brassboard consisted of a digital controller, a high-voltage generation/distribution unit, four solar arrays (two planar and two concentrator designs), and various diagnostic sensors (Ref 1, 2).

In early 1990, the Space Test Program (STP) of the Air Force's Space Systems Division (SSD) offered the PASP Plus experiment a flight on a Pegastar satellite put into orbit by a Pegasus launch vehicle (both built by Orbital Sciences Corp., OSC). PASP Plus was to be part of the APEX (Advanced Photovoltaic and Electronics Experiments) mission, set up to fly PASP Plus and two small "radiation effects on electronics" experiments, CRUX and FERRO. The Spaceflight Plan for APEX was approved by Hq USAF on 3 October 1990. Because of the enhanced opportunity provided by APEX—an elliptical [350 km by 1850 km] near-polar [i = 70°] orbit with a one to three year lifetime, Phillips Laboratory (PL) and Wright Laboratory (WL) decided to broaden the scope of the PASP Plus experiment to include the investigation of the effects of space radiation dosage on long-term solar array performance. PL also decided to put on additional diagnostic instruments appropriate to PASP Plus's new scope and mission profile. When the availability of a ride for PASP Plus became known to the photovoltaic array development community, additional new-technology arrays were

offered to WL for flight on PASP Plus. PL and WL then decided to increase the number of different arrays to be flown on PASP Plus from four to eleven.

In October 1990, a meeting was held at Wright-Patterson AFB to discuss the measurements, instrumentation, and flight requirements for PASP Plus. Scientists from Phillips Laboratory, Wright Laboratory, Aerospace Corp., Naval Research Laboratory, and NASA Lewis Research Center participated. From the various discussions at this meeting, the objectives of the new PASP Plus experiment were defined.

## PASP PLUS OPERATION AND INSTRUMENTATION

The objectives of the reconfigured PASP Plus experiment are:

(1) To measure the limitations in solar-array high voltage operation caused by space-plasma interactions.

(2) To quantify the long-term deterioration in the electrical performance of many different types of solar cells when exposed to the space radiation environment.

(3) To collect sufficient environmental sensor data to be able to establish cause-and-effect relationships between environmental conditions and array performance.

(4) To provide a means for "flight qualifying" various new photovoltaic technologies (new materials and/or designs).

Extensive investigations of high-voltage interactions have been carried out by groups at the NASA Lewis Research Center (LeRC), including laboratory and flight-test work (Ref. 3,4,5). Several explanations of the causes of arcing from high negative voltage operation have been given. Jongeward et al. (Ref. 6) suggest that arcing is initiated as a result of ion neutralization and associated charge buildup on a thin insulating layer over the metallic interconnects. Hastings et al. (Ref. 7) propose that arcing is due to the breakdown of gas that is emitted under electron bombardment from the coverglass on the solar cells. The arcing rate (beyond threshold voltage) appears to be roughly proportional to plasma density, but has a large power-law dependence on voltage level (Ref. 8). For high positive voltage operation, there is the problem of the draining of array power by electron currents flowing between the array and the surrounding space plasma (Ref. 9). The magnitude of the "leakage" current will depend on the operating voltage, plasma density, exposure of the interconnects, nature of the coverglass material (secondary electron emission), and the geometry of the sheath surrounding the array. Various computer simulations have been used to study the plasma leakage current problem (Ref. 10). Data from the PASP Plus experiment, with its many different kinds of array technology, should be very helpful in determining the relationships between various parameters.

To simulate large arrays operating at high voltage levels, we apply high bias voltages to our small arrays. Some of PASP Plus's eleven arrays will be partitioned into two or three sections, resulting in 16 electrically isolated, individual modules. Ten of our 16 modules will be biased. The high-voltage biasing sequences for each module (one at a time) will consist of <u>four</u> all-positive or all-negative steps (each 20 sec long) of successively greater voltage levels. The minimum difference between step values is 10 volts. Early in the APEX mission, lower bias voltages will be used, gradually increasing to higher levels after determining that the higher voltages do not disable the particular module. After satisfactorily reaching the highest voltage levels (+500 V and –500 V), a standard positive and negative data-gathering sequence [e.g., 350 V, 400 V, 450 V, 500 V] will be used to obtain detailed statistical data on array leakage (positive biases) and arcing (negative biases) as functions of bias-voltage level, array temperature, satellite altitude (ambient plasma density), and velocity-vector orientation (ram, wake, in-between).

The partitioning of some arrays will allow us to apply high-voltage biasing to only <u>part</u> of an array and not the remaining part. In some cases, we want to investigate long-term radiation damage to array performance for that part of the array <u>not</u> subjected to biasing. The high-voltage biasing, besides causing possible performance deterioration itself (detectable at the time of the bias measurements), could also increase the <u>susceptibility</u> of the biased part to later (or longer-term) contamination or radiation damage. Instrumentation included in PASP Plus will allow us to distinguish between different damage effects.

The electrical performance of each of the 16 array modules, whether biased or not, is monitored by taking numerous current-voltage measurements (I–V curves) of the module over the course of mission lifetime. The I–V curves for each module are obtained from the rapid application of dynamically varying resistance values between $R = \infty$ to $R = 0$ (corresponding to open-circuit voltage $V_{OC}$ and short-circuit current $I_{SC}$) to the sun-illuminated array module. Thirty-two digitized measurements of current and voltage are recorded (all within about 2 sec) for each array module. The optimum I–V curve voltage range for an array would be from zero to just beyond $V_{OC}$. However, $V_{OC}$ (and, consequently, the I–V curve) is highly dependent on array temperature, with the highest voltage levels occurring at the lowest array temperatures. Hence, we must allow for a $V_{OC}$ corresponding to when the sun-viewing array will be coldest—coming out of eclipse into solar illumination. Temperature sensors are affixed to each array so that array performance can be correlated with temperature.

Diagnostic sensors for the PASP Plus experiment will include:

a. a sun incidence-angle sensor to measure the alignment of the arrays to the incident solar energy, especially important for concentrator arrays. To meet PASP Plus requirements, the Pegastar satellite will point its upper-deck honeycomb panel (on which any concentrator arrays will be mounted) to within 0.5° of the sun.

b. a Langmuir probe (LP) to measure low-energy plasma parameters (density and temperature). To sweep the appropriate voltage range [with respect to the space plasma], our LP will be equipped with a potential sensor (SENPOT) capable of sensing how far negative the satellite frame-ground is below space-plasma reference and compensating for this deviation. The vehicle-frame negative potential is due to the fact that Pegastar's spacecraft-power solar arrays are configured (like all space vehicles) with the positive terminal ($\approx +32$ V) high and the negative terminal connected to vehicle frame-ground. Because of the greater mobility of incoming electrons over incoming ions, the positive (high) end of Pegastar's arrays goes to only several volts (5 to 10) positive with respect to the space plasma while the negative end (and vehicle frame-ground) goes to 22 to 27 volts negative.

c. electrical transient sensors (E-field sensors for detection of radiated pulses and a current-loop sensor for detection of power-line pulses) connected to a transient pulse monitor (TPM) to obtain the characteristics (amplitude, rise time, integral, and pulses per time period) of arc-discharge pulses that will occur during high-voltage biasing of the arrays.

d. an electrostatic analyzer (ESA) to measure 10 eV to 30 keV electron/ion spectra and detect the passage of Pegastar through an auroral region.

e. an electron/proton radiation dosimeter to measure the short-term and long-term particle radiation that damages solar cells, leading to deterioration in array performance (as measured by the I–V curves). The design of one of the four detection domes has been altered (see Figure 1) to facilitate the measurement of 5-10 MeV protons shown to be particularly damaging to solar-cell material, especially silicon (Ref. 11); see Figure 2.

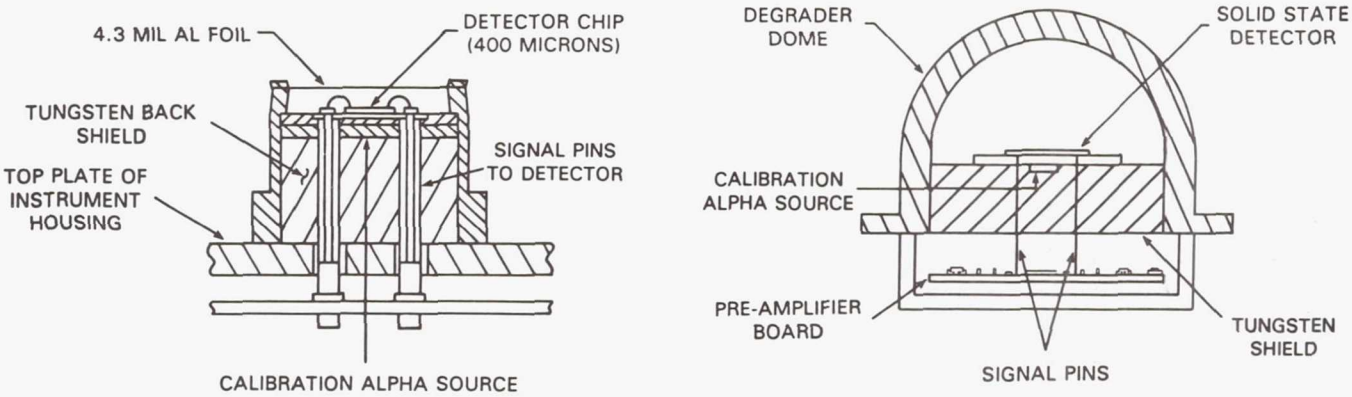


Figure 1. Domes of PASP Plus dosimeter: modified design to measure 5 - 10 MeV protons [left] and customary design for higher energy particles [right].

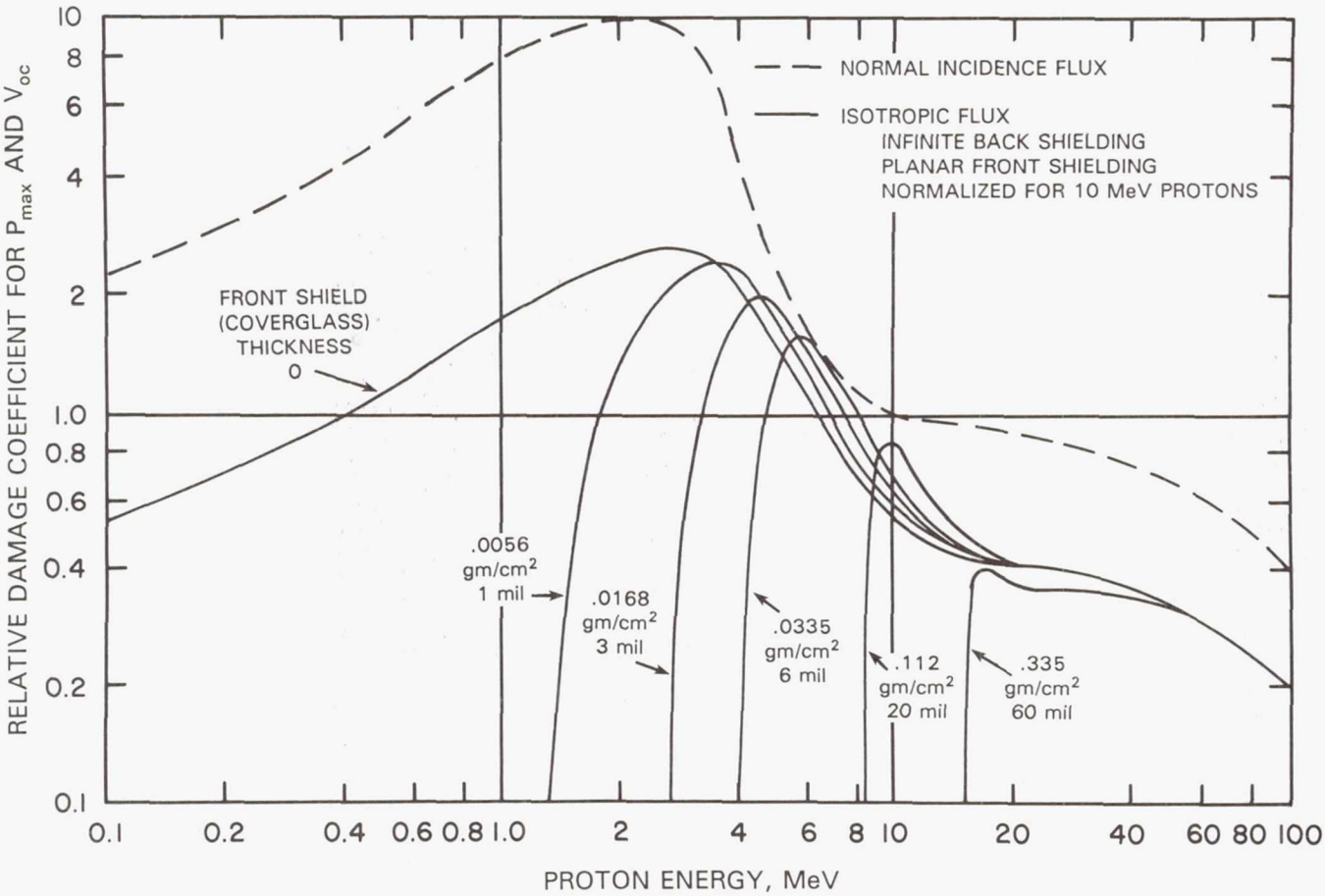


Figure 2. Relative damage coefficients for space proton irradiation of coverglass-shielded N/P silicon cells (based on $P_{max}$ or $V_{oc}$).

f. *a set of contamination monitors to give an indication of the amount of effluents deposited on array surfaces* (this leads to decreased sunlight collection and array output power—as measured by the I–V curves). Contamination sensors will include QCMs (quartz crystal microbalances) and calorimeters. The information from these monitors will allow us to differentiate the solar-array performance degradation caused by radiation-dosage damage from that caused by contamination.

## PASP PLUS SOLAR ARRAY COMPLEMENT

To maximize the utility of the PASP Plus experiment, a wide variety of conventional and advanced-concept solar cell designs will be investigated. Eleven unique solar array designs, comprising a total of 16 individual solar-cell strings (modules), will be studied on PASP Plus. The criteria used for selecting each of the solar array designs was based on electrical performance and potential for use on current and future DoD and NASA spacecraft missions. The solar array designs to be investigated on PASP Plus are shown in Table 1.

Two silicon (Si) solar cell designs will be studied. The first Si array is comprised of 2 cm × 4 cm 8-mil conventional Si solar cells laid down with conventional interconnects and coverglass. These are representative of practically all DoD and NASA solar array designs flying today (see Figure 3). The first Si array contains three electrically isolated solar-cell strings. The first of the three Si modules (strings) will <u>not</u> be high-voltage biased to provide a benchmark for the second and third modules that will be. The area of the third Si module

will be three times that of the second to help establish a relationship between high-voltage induced solar-cell leakage current and cell area.

The second Si solar array is comprised of 8 cm × 8 cm, 8-mil, wrap-through contact solar cells (see Figure 4). These are baselined to fly on NASA's Space Station Freedom. The wrap-through contact design is important because it reduces cell laydown manufacturing costs and increases cell survivability. This array will also be biased to determine how the cell's isolated wrap-through contact design affects its high-voltage performance.

TABLE 1. PASP PLUS SOLAR ARRAYS

| ARRAY | CELL TYPE | DESCRIPTION | SIZE (in × in) | BIASED SEGMENTS |
|---|---|---|---|---|
| 1 | Si | 2cmx2cm, BSF | 10 × 20 | 2 of 3 |
| 2 | Si | 8cmx8cm, WTC Space Stati n | 8 × 9.5 | 1 of 1 |
| 3 | GaAs/Ge | 4cmx4cm, 3.5-mil | 10 × 20 | 2 of 3 |
| 4 | GaAs/Ge | 4cmx4cm, 7-mil | 5 × 10 | 1 of 1 |
| 5 | GaAs/Ge | 4cmx4cm, 7-mil, WTC | 5 × 10 | 1 of 1 |
| 6 | GaAs/Ge | 4cmx4cm, 3.5-mil, w/ICG | 4 × 4.5 | 1 of 1 |
| 7 | InP | 2cmx2cm | 4 × 5.5 | 0 of 1 |
| 8 | AlGaAs/GaAs | 2cmx2cm, monolithic MBG | 3 × 6 | 0 of 1 |
| 9 | GaAs/$CuInSe_2$ | 2cmx2cm, mech-aligned MBG | 6 × 6 | 0 of 2 |
| 10 | GaAs | SLATS Concentrator | 11 × 13.5 | 1 of 1 |
| 11 | GaAs/GaSb | Mini-Dome Fresnel Lens Concentrator, MBG | 4.5 × 7.5 | 1 of 1 |

BSF = Back Surface Field
WTC = Wrap-Through Contact
MBG = Multiband Gap

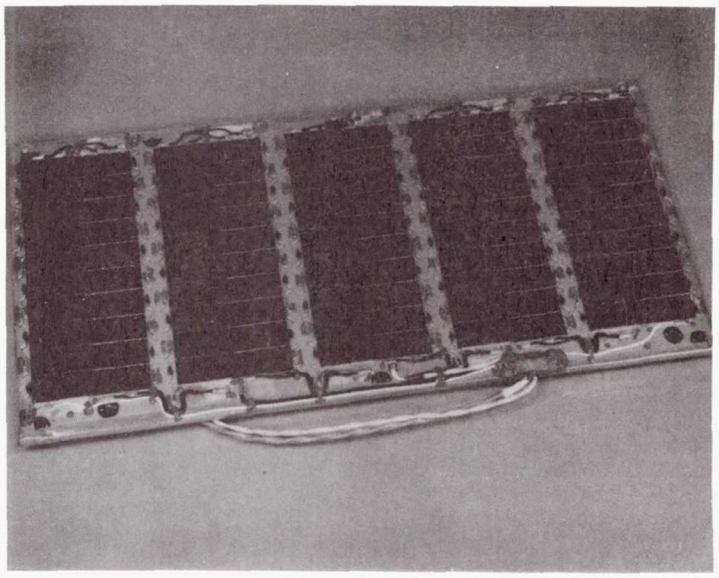

Figure 3. Silicon array (#1 above) to be partitioned into three separate modules.

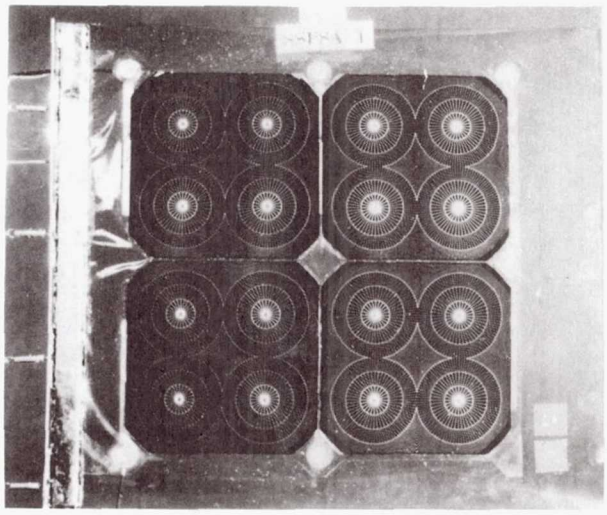

Figure 4. Si array with wrap-through contact solar cells baselined for flight on NASA's Space Station Freedom.

All of the next four solar array designs shown in Table 1 utilize GaAs on Ge solar cells, but all differ in electrical and/or mechanical configuration. The GaAs/Ge solar cell represents a very important technology because GaAs offers better energy conversion, radiation resistance, and high temperature performance over Si solar cells.

The first of the four GaAs/Ge arrays is comprised of 4 cm × 4 cm, 3.5-mil GaAs/Ge solar cells. This array is similar to the first Si array in that it has three separate electrical strings laid down with conventional interconnects and coverglass. The first module (string) will not be biased to provide a control for the second and third high-voltage biased modules. Also, the area of the third module will be twice that of the second module to help establish a relationship between cell leakage current and cell area.

The second GaAs/Ge array consists of one string of 4 cm × 4 cm, 7-mil GaAs/Ge solar cells laid down with conventional interconnects and coverglass. This array will be biased and compared in high-voltage performance with the third GaAs/Ge array, which will consist of 4 cm × 4 cm, 7-mil GaAs/Ge solar cells with wrap-through contacts. The second and third GaAs/Ge arrays will be identical in all respects (solar cell material, cell area, array substrate, and mounting and wiring design) except for the conventional top-bottom versus wrap-through contact design differences. The fourth GaAs/Ge array will consist of one string of 4 cm × 4 cm, 3.5-mil GaAs/Ge solar cells coated with an alumina/silicate based CVD-deposited coverglass. The glass coating will conformally cover the entire area of the array, including interconnects and cell edges, with the intent of providing conductor to space plasma isolation resulting in improved high-voltage performance.

The seventh, eighth, and ninth arrays shown in Table 1 (InP, GaAs/ $CuInSe_2$, and AlGaAs/GaAs cell designs, respectively) will not be high-voltage biased, but their performance will be measured as a function of exposure to the natural space environment and orbital temperature excursions. The cell size for each of these three designs will be 2 cm × 2 cm, and all strings will be laid down with conventional interconnects and coverglass. The InP solar cell is important because of its high conversion efficiency and extremely high radiation resistance. The GaAs/$CuInSe_2$ solar cell is a dual-junction mechanically stacked design which offers high conversion efficiency and extremely high radiation resistance to electrons. The AlGaAs/GaAs cell design is important because it is dual-junction and monolithic and promises to yield very high conversion efficiencies.

The last two PASP Plus solar arrays shown in Table 1 are concentrator designs. The first is the survivable low-aperture trough system (SLATS) concentrator array which collects and focuses (concentrates) light onto GaAs solar cells using trough-shaped (venetian blind like) metal mirrors. The solar cells are mounted to the backside of the mirrors and are illuminated by the mirrors to which they are adjacent. This design is important for enhancing the survivability of the solar array against man-made threats (e.g., high-powered lasers) and the natural space environment, as well as having the capability to operate at higher voltages. This capability arises from the fact that the solar cells are effectively shielded from the space plasma environment. The second concentrator is the mini-dome fresnel-lens GaAs/GaSb design which promises extremely high conversion efficiencies through the use of its dual-junction mechanically stacked GaAs and GaSb solar cells and prismatic coverglass. This design is important not only for its high conversion efficiency, but for its potential use in operating at higher voltages. In this design, the GaAs/GaSb solar cells are isolated from the space plasma environment by the concentrator elements and the array support structure.

## CHARACTERISTICS OF PEGASTAR SATELLITE

PASP Plus will be integrated onto a Pegastar satellite bus and placed into orbit by a Pegasus launch vehicle. With the enhanced capability afforded by the Pegasus/Pegastar system, an elliptical (350 km × 1850 km) near-polar (70° inclination) orbit was made available to satisfy PASP Plus's objectives. The launch will take place from a B-52 aircraft in the Western Test Range off the coast of California (see Figure 5). Both the Pegastar satellite and Pegasus are being designed and built by Orbital Sciences Corporation (OSC) as a low-cost DoD alternative for small payload missions. The first Pegasus launch from a B-52 was successfully completed in April 1990. PASP Plus is scheduled for the fourth Pegasus launch in November 1992.

Figure 5. The Pegasus launch vehicle accelerating into orbit after being released by the B-52.

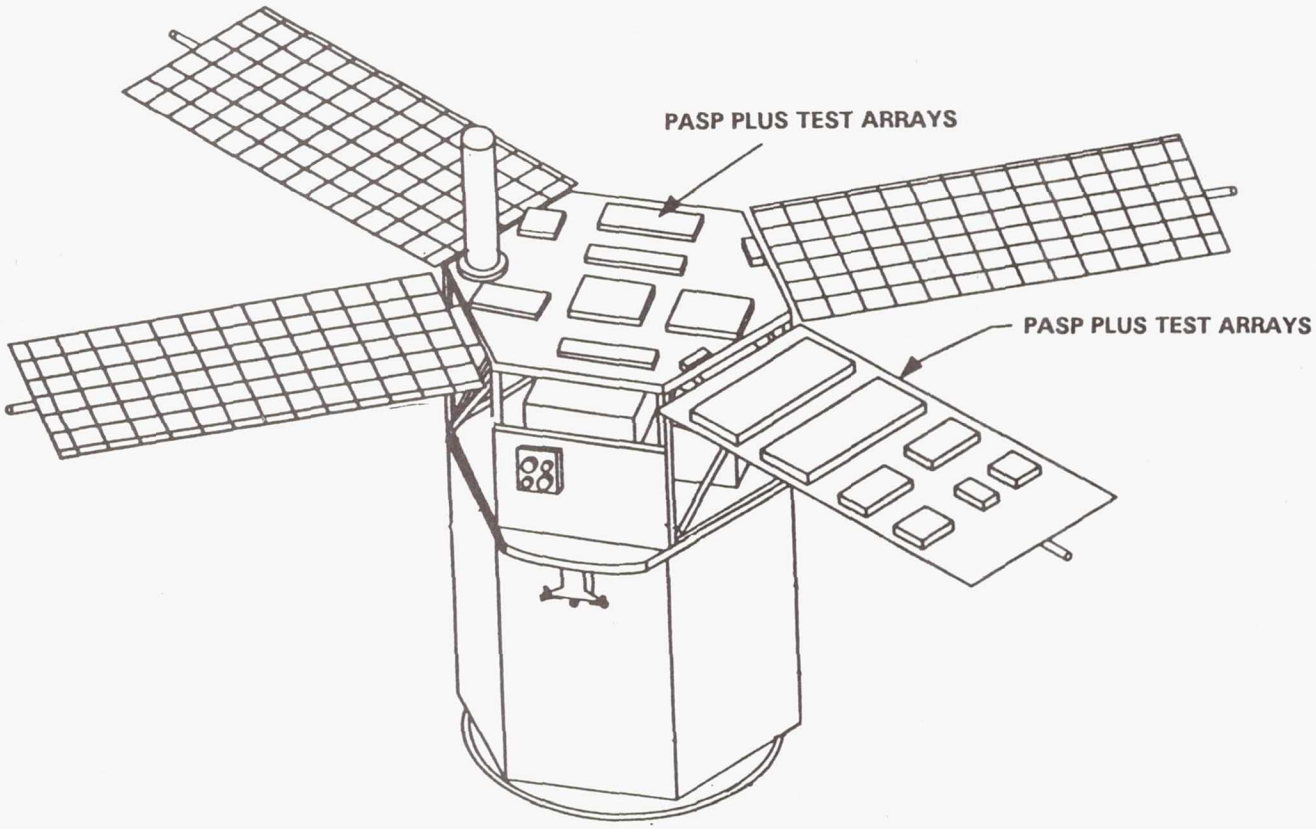


Figure 6. The Pegastar satellite bus showing the general location of the PASP Plus test arrays.

The Pegastar satellite with integrated PASP Plus experiment is shown in Figure 6. The satellite bus will measure approximately 60 inches in height and 44 inches in diameter. Power for PASP Plus and other satellite subsystems is provided by three 60 in x 22 in solar array panels producing between 320 and 380 watts of power for up to three years on orbit. Total weight to orbit of the Pegastar vehicle including PASP Plus is approximately 820 pounds. The Pegastar satellite will be three-axis stabilized and oriented so the PASP Plus test arrays will be continuously sun-pointing to within ±0.5 degrees. The PASP Plus test arrays are mounted on a combination of the hexagonally shaped upper shelf and one deployable panel (see Figure 6). PASP Plus electronic subsystems are mounted on the lower avionics payload shelf.

The dosimeter and ESA each have special pointing requirements. The dosimeter domes will view a direction parallel to the ecliptic plane and normal to the sun-satellite line. This will provide the optimum look direction for the dosimeter throughout the orbit while minimizing the time facing the earth. The ESA apertures will view a direction normal to the ecliptic plane and 90° from the dosimeter's pointing direction. This will orient the ESA so as to look along the earth's magnetic field lines when the vehicle is in the auroral regions.

Most of the high-voltage plasma interactions objectives of PASP Plus will be achieved while the vehicle is near perigee passing through the ionospheric F–region and/or through auroral regions. Most of the radiation degradation objectives of PASP Plus will be achieved while the vehicle is near apogee in the *equatorial* regions (Pegastar's line of apsides will rotate ~1.5° a day in its orbital plane). During the 1–3 year lifetime of the APEX mission, measurable radiation-induced degradation will be seen in the performance of the PASP Plus test arrays. An orbit maintenance capability might be provided on Pegastar to enable it to remain at high apogee for the duration of the mission or possibly the initial apogee would be increased. This will assure the continued high-altitude radiation exposure necessary to satisfy PASP Plus objectives.

The PASP Plus solar arrays will be tested and assembled as a completed subsystem at WL. Diagnostic instruments and electronics equipment will be tested and calibrated at PL's Geophysics Directorate (GP). The completed PASP Plus system (arrays and electronics) will be environmentally tested at PL/GP and delivered to OSC for integration onto the Pegastar satellite bus. PASP Plus delivery to OSC is planned for April 1992. The completed Pegastar system will be shipped to Edwards AFB, CA in October 1992 for integration onto the Pegasus launch vehicle at NASA's Dryden Research Center. PASP Plus data will be collected in both a real-time mode and recorded play-back mode. Continuous 24-hour operation of the experiment is planned for the mission lifetime.

## EXPECTED RESULTS FROM A SUCCESSFUL FLIGHT

Achievement of PASP Plus's experimental goals is highly dependent on maintaining the proper orientation (sun pointing) and achieving the proper orbit for the Pegastar satellite.

Pegastar's sun-pointing accuracy of ±0.5° is obviously essential for the concentrator arrays (e.g., the SLATS power generation decreases significantly beyond 0.5° and drastically beyond 1.5°). However, even for the planar arrays, in an experiment where the interaction effects may be small and/or slowly developing and where we wish to distinguish one effect from another (e.g., radiation vs. contamination degradation), it is important to minimize any undesired variation in sun illumination that would cause even small changes in array I–V curves.

APEX's nominal 350 km (190 naut mi) perigee will provide the maximum electron density (in the order of $10^5$ to $10^6$ $cm^{-3}$) in the region around perigee and allow investigation of space-plasma induced effects over the largest useful range of electron density variations. After six months of flight, a very large data base on arc-pulse parameters (negative biasing) and plasma-leakage current parameters (positive biasing) as functions of bias levels and types of array will be collected over the flight achievable ranges of the controlling parameters: array temperatures, plasma density (perigee through apogee), auroral passage, and velocity-vector orientation. This large data base will permit examination of the correlations between all the linkable variables and lead to the establishment of cause-and-effect relationships for high-voltage space-environment interaction effects.

These relationships will then be available for analytic study, modeling, and code development. The information on array operating voltage limitations developed through analysis of PASP Plus results can be used to decide on the choice of operating voltage levels for particular kinds of arrays in various orbital regimes.

APEX's nominal 1850 km (1000 naut mi) apogee will allow passage of Pegastar through the lower portion of the inner radiation belt only when apogee occurs near equatorial geomagnetic latitudes. The line of apsides (the perigee–apogee line in the orbital plane) continuously rotates about 1.5° per day throughout the mission. On a long-term basis, Pegastar's apogee will pass through the radiation belt at equatorial latitudes only a small fraction (about one-quarter) of the rotation period. A higher apogee (up to 2000 or 2200 km) would significantly increase the dosage (or lessen the time to reach a specific dose accumulation), but there are limitations in the Pegastar-Pegasus boosting capability.

With some modest improvement in apogee, we expect to obtain sufficient radiation dosage in one year to see array performance degradation (as measured by the I–V curves) in Si cells in the order of 8 to 12 percent. For the more rad-hard materials (GaAs and especially InP) and the concentrators, the degradation may be only a few percent. If Pegastar's apogee is limited to 1850 km, we may need two or three years to see radiation-induced degradation to these levels. Information from the contamination sensors (QCMs and calorimeters) will be used to separate contamination effects from radiation effects. The radiation-induced performance degradation data for all the PASP Plus test arrays will be correlated with the radiation dosage data gathered from our electron/ proton dosimeter to try to establish cause-and-effect relationships. A section of the PASP Plus dosimeter has been designed to measure 5–10 MeV proton radiation, an important source of solar cell degradation. The information on radiation-damage limitations developed through analysis of PASP Plus results can be used to decide on the choice of solar-cell material or array configuration for operation in particular orbital regimes.

Within the first year after a successful PASP Plus flight, correlated PASP Plus data would be made available to the space-power communities in DoD and NASA. PL and WL, working closely with NASA LeRC, will conduct a series of workshops which will be targeted to major topics of interest such as high-voltage operation and EMI-generation effects. As data on array performance degradation from radiation effects becomes available (1½–3 years, depending on flight apogee), additional workshops will be held on radiation effects on new cell technologies and concentrator arrays. Results from these workshops will be directed towards upgrading relevant space-power design guidelines and test standards.

## CONCLUSIONS

PASP Plus's complement of solar arrays and diagnostic sensors and APEX's mission profile provide us with a unique opportunity to investigate both the high-voltage and the radiation-damage limitations to advanced solar array performance. Full utilization of the results of the PASP Plus experiment should be made by space systems developers before fielding future space-power subsystems that might be subjected to unwanted environmental interactions. Failure to determine the extent of interactions problems by experiments such as PASP Plus could lead to serious flaws in future space-power subsystems.

## REFERENCES


1. Guidice, D.A., "Photovoltaic Array Space Power Plus Diagnostics Experiment", Third Annual Workshop on Space Operations, Automation and Robotics (SOAR '89), NASA Conf. Publ. 3059, 1990, pp. 515–519.

2. Burger, D.R., Photovoltaic Array Space Power Plus Diagnostics Experiment, PL-TR-91-2002, 1990, pp. 12–42.

3. Snyder, D.B., "Discharges on a Negatively Biased Solar Cell Array in a Charged-Particle Environment", Spacecraft Environmental Interactions Technology - 1983, NASA CP-2359, AFGL-TR-85-0018, 1985, pp. 379-388.

4. Grier, N.T., "Plasma Interaction Experiment II (PIX II): Laboratory and Flight Results", Spacecraft Environmental Interactions Technology - 1983, NASA CP-2359, AFGL-TR-85-0018, 1985, pp. 333-348.

5. Ferguson, D.C., "The Voltage Threshold for Arcing Solar Cells in LEO—Flight and Ground Test Results", AIAA 86-0362, AIAA 24th Aerospace Sciences Meeting, Reno, Nevada, Jan. 6-8, 1986.

6. Jongeward, G.A., Katz, I., Mandell, M.J., and Parkes, D.E., "The Role of Unneutralized Surface Ions in Negative Potential Arcing", IEEE Trans. Nucl. Sci., Vol. NS-32, No. 2, 1985, pp. 4087–4091.

7. Hastings, D.E., Weyl, G., and Kaufman, D.,"Threshold Voltage for Arcing on Negatively Biased Solar Arrays", J. of Spacecraft and Rockets, Vol. 27, No. 5, 1990, pp. 539–544.

8. Ferguson, D.C., "Solar Array Arcing in Plasmas", Third Annual Workshop on Space Operations, Automation and Robotics (SOAR '89), NASA Conf. Publ. 3059, 1990, pp. 509-513.

9. Mandell, M.J., Katz, I., Steen, P.G., Schnuelle, G.W., "The Effect of Solar Array Voltage Patterns on Plasma Power Losses", IEEE Trans. Nucl. Sci., Vol. NS-27, No. 6, 1980, pp. 1797-1800.

10. Thiemann, H., and Schunk, R.W., "Particle-in-Cell Simulations of Sheath Formation Around Biased Interconnectors in a Low-Earth-Orbit Plasma", J. of Spacecraft and Rockets, Vol. 27, No. 5, 1990, pp. 554–562.

11. Tada, H.Y., and Carter, J.R., Solar Cell Radiation Handbook, JPL Publ. 77-56, 1977, Chap. 4.

# LEO MICROMETEORITE/DEBRIS IMPACT DAMAGE*

Paul M. Stella
Jet Propulsion Laboratory
California Institute of Technology
Pasadena, CA 91109

The school bus sized LDEF (Long Duration Exposure Facility) was retrieved in 1990, after nearly six years of 250 nautical mile altitude LEO (Low Earth Orbit) environmental exposure (Figure 1). The recovery of LDEF experiments has provided extensive information on space interactions, including micrometeorite, debris, atomic oxygen, U.V. and particulate radiation.

JPL provided a test plate as part of SAMPLE (Solar-Array-Materials Passive LDEF Experiment). The test plate contained thirty thin silicon solar cell/cover assemblies. The cover samples included a variety of materials such as Teflon and RTV silicones, in addition to conventional microsheet. This paper discusses the nature of the approximately 150 micrometeorite/debris impacts on the cell/cover samples, cell interconnects and aluminum test plate.

## Introduction

The JPL subplate consists of an 11" x 16.3" (28 cm x 41.4 cm) aluminum plate with thirty (30) cell/cover samples. The cells are 50 micron thick 2x2 $cm^2$ silicon devices fabricated by Solarex Corporation. Silver-plated Invar tabs are welded to the N and P contacts of each cell to facilitate pre and post flight electrical performance measurements. Each cell is bonded to a slightly oversize sheet of Kapton insulation bonded to the aluminum plate. The bonding materials are standard silicone RTVs. A protective cover is attached to the front surface of each cell. These covers consist of a variety of materials, including cerium doped microsheet, teflon film and various silicone-based encapsulants.

The preparation of samples and experiment assembly was performed by the G.E. Company. The LDEF flight provided a means to directly evaluate the behavior of the cover materials in the space environment, including their ability to protect cells from that same environment.

---

*The research described in this paper presents the results of one phase of research carried out by the Jet Propulsion Laboratory, California Institute of Technology, under contract with the National Aeronautics and Space Administration

The planned post flight review at JPL consisted of visual examination, cell electrical performance measurements and data analysis. The detailed visual examination (up to 200X power) has been completed and is discussed in this paper. The electrical performance measurements will be completed before the end of May, 1991.

Observation of the recovered test plate revealed a number of obvious changes (Figure 2). All exposed (uncovered by adhesive or encapsulant) tab surfaces darkened (black and dark blue) from the original shiny silver appearance. In many cases, the darkened silver tab surfaces showed signs of stress by the formation of platelets, much like dried mud in texture. The dark surface material is readily removed by gentle mechanical abrasion revealing a shiny, albeit rough, surface underneath. In some areas, it appeared that the original surface had flaked off. The resultant surface region was slightly lower than the surrounding regions and the color was less dark -- more gray than blue/black -- suggesting less exposure time to the pertinent environment.

As might be expected, the least disturbed cover system was that of the conventional microsheet platelet. Encapsulant behavior varied widely, with some materials appearing to have been essentially removed. In those cases, the cell grid lines darkened, probably through interaction with the space environment. In other cases, although encapsulant materials degraded, becoming embrittled for example, the cell grid lines were still protected sufficiently that they remained shiny. Areas of the aluminum plate appeared stained, most likely due to environmental interactions (atomic oxygen and/or UV) with the residue of materials used in assembly.

Survey of the plate reveals a large number of impact craters, predominantly in the aluminum plate, ranging in size from 0.05 mm (Figure 3) to 1 mm (Figure 4) in diameter. Most impacts appear to be normal to the plate (circular crater), although a small number of elongated craters indicate off normal incidence. The physical appearance of these impacts is discussed in the following section.

## Micrometeorite/Debris Impacts

SAMPLE was located in a near ram position (direction of motion) on LDEF. The LDEF investigators have determined that the position was not only subject to a very high number of impacts, but also that the majority were due to manmade debris, such as solid fuel particles, and paint chips, rather than micrometeorites (reference 1). This is due to the fact that debris in the vicinity of LDEF tends to have the same magnitude of orbital velocity. Consequently, impacts from the forward direction will have large velocity differentials and impacts from the wake direction will have small velocity differentials. Ram impacts will then be highly energetic, leaving visible impacts or penetrations. By the same argument, wake impacts are unlikely to leave significant impressions.

Micrometeorites, being of extraterrestrial origin, will approach LDEF with high velocity differentials from many directions due to their high velocities. As a result, they will likely produce a comparable number of visible impacts in the ram and wake direction. Review of the entire LDEF structure has shown a roughly 10 to 1 ratio for ram to wake impacts. For the SAMPLE experiment, these considerations imply that the majority of impacts were of debris origin. Conversely, the majority of impacts on experiments in the wake are most likely due to micrometeorites.

## Cratering in the Aluminum Plate

Since the majority of the test plate area consists of the uncovered aluminum mounting plate, the majority of impacts are located in the plate. These are generally similar visually, and typified by the example in Figure 4. The impact has formed a circular crater with a surrounding ridge ejected out from and over the plate surface. The crater bottom is crystalline in appearance, unlike the scratched and machined plate surface, showing evidence of melting and resolidifying. This crater pattern was observed for all sizes from 1mm diameter on down. Of the 157 impacts observed (over the entire test plate/sample surface), seven were 0.5mm or larger. Depth measurements of the seven indicated a crater depth (measured from crater bottom to top of surrounding ridge) ranging from one-half to one-third the crater diameter. Only a few craters were noted with an elliptical shape that might be attributable to an impact with a particle with a large non-normal velocity component.

## Invar Interconnector Impacts

Although the total area occupied by the silver-plated Invar tabs was relatively small, the debris/micrometeorite fluence was sufficient that tab impacts did occur. The results of the impacts were visually surprising, but offer clear indication of the high particle impact velocities and corresponding impact energies. Figure 5 is a typical example of one such impact. It is observed that the tab has been completed penetrated. The region of Invar immediately surrounding the 0.5mm diameter through hole shows clear indication of melting and resolidifying. In addition, the impact generated gases have peeled the top silver plating away from the Invar and blown those layers out from the impact area. The silver/Invar separation is well-identified by the lack of any atomic oxygen darkened residual silver. Indeed, the inner surface of the peeled back silver plating has now darkened from atomic oxygen interaction. The remainder of the silver plated Invar tab still appears shiny due to a thin layer of silicone adhesive which has provided protection during the mission. This kind of impact well illustrates the nature of the typical LEO particulate impacts -- small and violent.

## Impacts with Polymer Cell Covers

The appearance of impacts with a relatively thick polymer cell cover, such as Teflon FEP, shown in Figure 6, is remarkably similar to

the above-described silver-plated Invar tab. For Teflon, the incident particle readily penetrates and impacts the silicon cell below. The impact with the silicon has generated gases which, in turn, lift the Teflon away from the cell and blow out the central area. The flexible Teflon, unlike the rigid silver metallization, settled back somewhat onto the cell surface. A light colored ring can be observed around the blowout region, corresponding to an area of Teflon/silicon delamination, where physical contact has been recovered, if not adherence. It is clear that the Teflon provides essentially negligible protection against the high energy impacts. Again, due to the small damage area, cell power degradation may not be significant. It is intended to examine for any impact/cell power loss correlation in subsequent electrical performance tests.

## Impacts to Silicon and Microsheet

The silicon and microsheet impacts are discussed together because of the many similarities. Both materials are rigid and tend to shatter under severe loading. Figure 7 is a photograph of an impact in silicon (through a few micron thick polymer cover) and Figure 8 is a view of an impact into a microsheet coverslide. Both impact areas are comparable in size (~0.1mm central "hole"), the difference in the photographs being due to different magnification levels. In view of the limited number of such impacts, it is not clear if these are truly typical. However, both materials have a well-defined crater with any ejected material blown completely away. Both crater perimeters appear rectangular. For the silicon, this would reflect the crystalline nature of the material, however, this would not be expected for the microsheet. Of interest, the silicon cell has been completely penetrated, with the formation of a near hexagonal through hole. The microsheet impact appears well limited in size, and radiating cracks were not visible. In the case of the microsheet impact, it was not possible to determine with certainty that damage was limited to just the microsheet and immediately underlying silicone adhesive. However, it is believed that the impact was spent in the microsheet and that the adhesive was able to absorb any residual gas/debris, without a significant silicon interaction.

## Conclusions

The LDEF experiment was subject to a wide variety of environmental interactions, in particular, space debris impacts and atomic oxygen. The extent of these interactions is strongly dependent on orbital altitude -- the LDEF orbit favored intensive interactions -- and care must be used in extrapolating to other, more commonly used higher altitude orbits. The advantage of LDEF is that the combination of long duration (~ 6 years) and environmentally active orbit altitude essentially accelerates interactions to better reveal the results.

For the particular case of debris/micrometeorite impacts, a relatively high fluence was observed for the SAMPLE experiment (~1300 impacts/$m^2$) over the mission duration. These typically were of small area

(0.05mm-1.0mm in diameter) and of high energy, allowing for penetration of Invar interconnector tabs and a thin silicon solar cell. At present, there is no evidence that these impacts incurred any significant electrical degradation in the solar cells. In particular, the Invar penetration only removed a small fraction of available interconnector material.

Although polymer-type covers may look attractive for low cost cell protection and may someday be suitable for protection against U.V. and low energy protons, there is negligible ability to shield against debris/micrometeorite impacts. If these impacts are cell degrading, then more robust covers, such as the standard fused silica or microsheet materials may be required at these low altitudes.

## References


1. Ellis, David, "Micrometeoroid and Debris SIG is Focus for Many Issues", LDEF Spaceflight Environmental Effects Newsletter, Vol. 1, No. 8, January 23, 1991.

Figure 1. Retrieval of LDEF (Jan. 1990) - SAMPLE at upper left

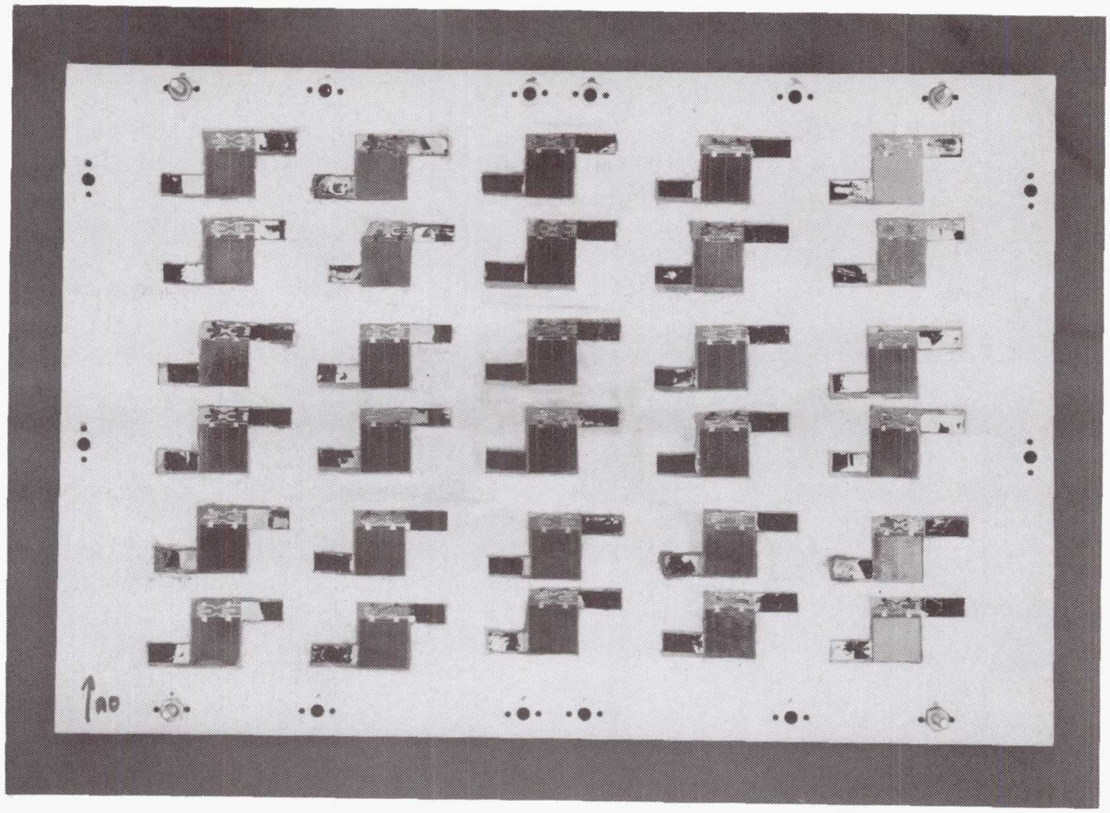

Figure 2. JPL SAMPLE Plate After Retrieval

Figure 3. Typical small Al craters ~0.05mm diameter

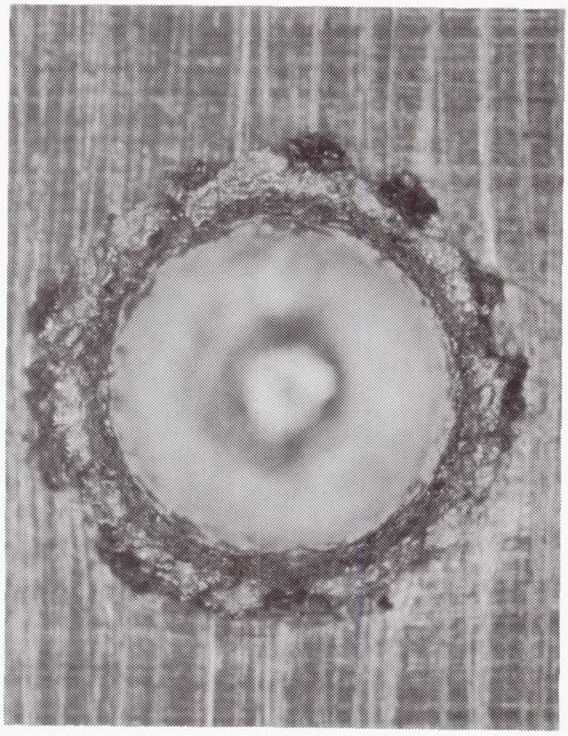

Figure 4. Largest crater ~1mm diameter

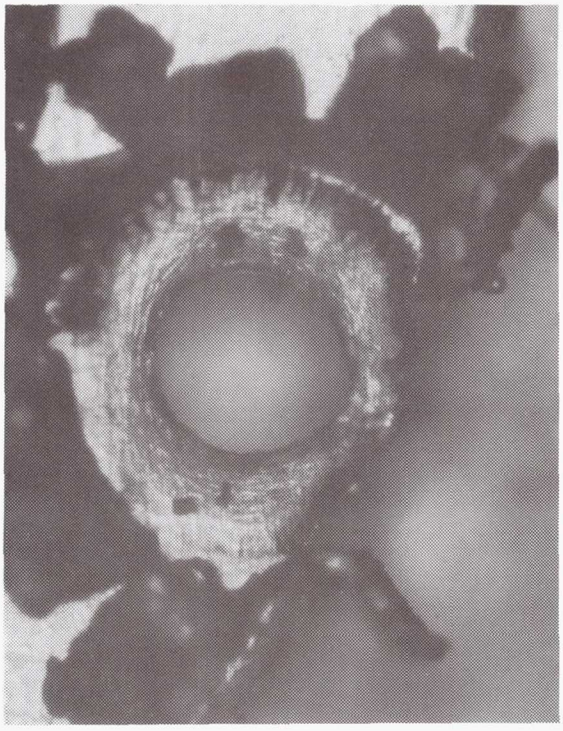

Figure 5. Invar Interconnector (~0.2mm diameter hole)

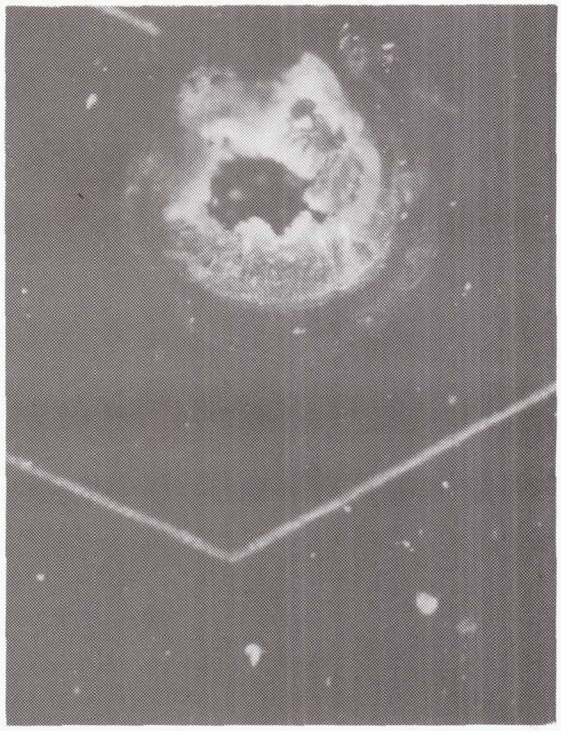

Figure 6. Teflon cover (~0.3 mm diameter hole)

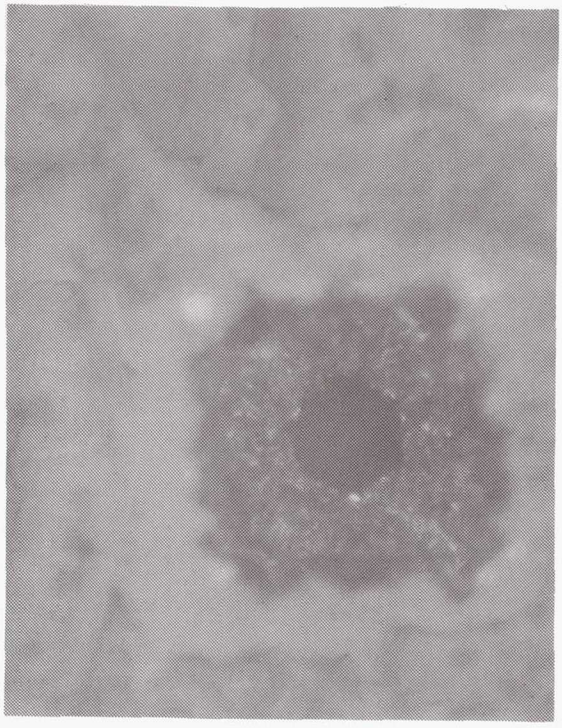

Figure 7. Impact in silicon (~0.1mm diameter hole)

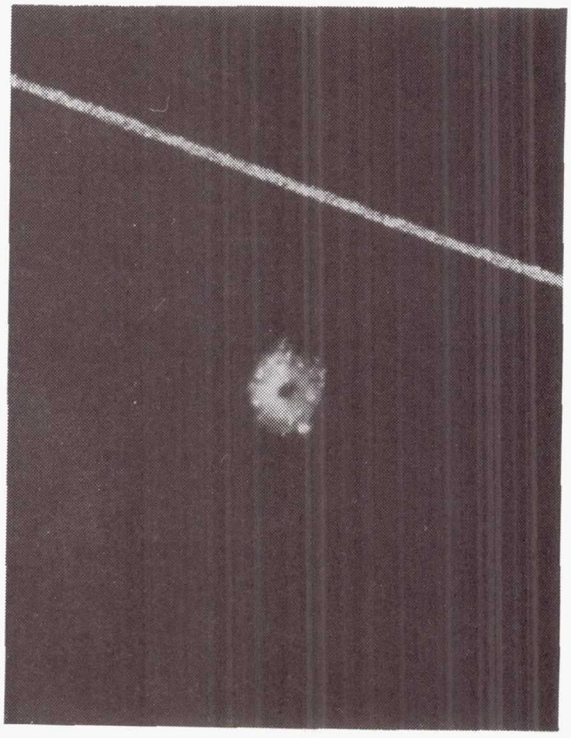

Figure 8. Impact in microsheet cover

# THE EFFECTS OF LUNAR DUST ACCUMULATION ON THE PERFORMANCE OF PHOTOVOLTAIC ARRAYS*

Cynthia M. Katzan
Sverdrup Technology, Inc.
Brook Park, Ohio

David J. Brinker
NASA Lewis Research Center
Cleveland, Ohio

and

Robert Kress
University of Akron
Akron, Ohio

## ABSTRACT

Lunar base activity, particularly rocket launch and landing, will suspend and transport lunar dust. From preliminary models, the resulting dust accumulation can be significant, even as far as 2 km from the source. For example, at 2 km approximately 0.28 mg/cm$^2$ of dust is anticipated to accumulate after only 10 surface missions with a 26,800 N excursion vehicle. The possible associated penalties in photovoltaic array performance were therefore the subject of experimental as well as theoretical investigation.

To evaluate effects of dust accumulation on relative power output, current-voltage characteristics of dust-covered silicon cells were determined under the illumination of a Spectrolab X-25L solar simulator. The dust material used in these experiments was a terrestrial basalt which approximated lunar soil in particle size and composition. Cell short circuit current, an indicator of the penetrating light intensity, was found to decrease exponentially with dust accumulation. This was predicted independently by modeling the light occlusion caused by a growing layer of dust particles. Moreover, the maximum power output of dust-covered cells, derived from the I-V curves, was also found to degrade exponentially. Experimental results are presented and potential implications discussed.

## INTRODUCTION

The suspension and transport of lunar dust can occur by many processes. These include natural mechanisms, such as ejection during meteoroid impact (ref. 1-3) and electrostatic levitation (ref. 4-7), as well as mechanisms associated with human activity on the lunar surface (ref. 8). Disturbance can result from any activity, including walking, rover transport, mining/construction, and rocket launch and landing. Once lunar dust is suspended, it follows pure Newtonian motion in the absence of any atmospheric effects, and thus has the ability to travel great distances and accumulate indiscriminately. Vulnerable power system components such as photovoltaic arrays and radiator surfaces may be at risk of performance reductions due to lunar dust accumulation. Therefore the potential effects of dust accumulation on these surfaces may impact future lunar base design and perhaps even advanced component concepts.

---

* This work was supported by NASA Lewis Research Center under Contract NAS3-25266.

Of all the mechanisms for lunar dust suspension, the launch and landing of lunar excursion vehicles is anticipated to disturb the greatest amount of lunar dust, and transport it the furthest. Therefore an effort was made to assess the amount of dust that may be expected to accumulate as a result of launch and landing, both as a function of distance from the launch pad, and as a function of the number of supply missions from Earth. To generate an understanding of lunar dust transport behavior, available information from the Apollo experiences was collected and analyzed. Particularly important were the clues provided by the Surveyor III, an unmanned lunar exploratory craft which experienced the nearby landing of the Apollo 12 lunar module (LM). The Apollo 12 astronauts returned some of the Surveyor's components for analysis, and it was discovered that significant dust accumulations, directly related to the LM's engine blast, occurred even at a distance of 155 m (ref. 9). In general the craft acquired roughly 1 $mg/cm^2$ of lunar dust (ref. 10), and some parts collected a layer as thick as 8.7 $\mu m$ (ref. 11). The investigators who examined the components were able to estimate that the dust was ejected almost horizontally at an average velocity on the order of 40 - 100 m/s, but with some particles travelling as fast as 2000 m/s in order to cause the observed pitting in glass (ref. 9, 12, 13).

Based on this information, a particle velocity distribution was generated for the landing LM. The relationship between velocity and distance was introduced to convert the relative number of particles of a given velocity to the relative number of particles travelling a given distance. The resulting function was integrated over angles from 0° to 1° to produce a lunar particle accumulation distribution for the 13,400 N LM engine. The accumulation distribution was subsequently scaled to a future possible lunar excursion vehicle employing $O_2/H_2$ propulsion at a thrust of 26,800 N. As the thrust is doubled, particles attain twice the distance and the number of particles disturbed (flux) is squared. Finally, assuming that the dust trajectories resulting from launch are equivalent to those from landing, and assuming that two service or supply missions are required each year during normal lunar base operations, the anticipated dust accumulations with time were determined for various distances from the landing site (see Figure 1). By this optimistic model, surfaces within 1000 m can be expected to acquire accumulations in excess of 2 $mg/cm^2$ after 10 missions (5 years). At 2 km, cells would collect 0.28 $mg/cm^2$ over the same time period. The development of this model is described in more detail in Reference 8.

To address the potential implications of this level of lunar dust accumulation on a photovoltaic array, a light occlusion model was developed. This model was generated by incorporating particle overlap probabilities and particle optical absorption to calculate the attenuation of light by a growing layer of dust. The reduced light intensity into a cell is associated with a reduction in relative short circuit current, which is in turn an indicator of relative cell power reductions. The preliminary occlusion model was based on a fixed particle size and shape, and was confirmed by laboratory measurement of the transmittance of dust-covered glass coverslips under the illumination of a tungsten filament light source. The lunar dust simulant used in these experiments, "Minnesota Lunar Simulant-1," or MLS-1, is a basaltic material mined from a quarry in Duluth, MN, for its close compositional match to the material from the lunar lowlands, or "maria." Both the occlusion model and the experiments showed an exponential decay in relative transmittance, and therefore relative cell power, with lunar dust accumulation (see Figure 2). The model was then generalized to describe the occlusion caused by a continuous distribution of particle sizes, more representative of lunar soil. Two particle morphologies were considered: spherical and cubic. The predicted decay in relative transmittance with increasing dust accumulation is shown in Figure 3. As expected, particles with a greater surface area-to-volume ratio are more mass-efficient at light attenuation. Lunar particle morphologies have been observed to vary from spherical to very highly pocketed and irregular due to the unusual erosion processes on the moon. Therefore, the curve representing actual lunar soil is likely to fall below that for cubic particles. The evolution of the occlusion model is described in Reference 8.

The predicted relative transmittance for cubic particles was combined with the anticipated launch/landing-related dust accumulation described above to estimate the amount of solar power incident upon a photovoltaic array as a function of time for arrays located at various distances from the landing site. The predicted reduction in available solar power relative to that for a dust-free cell is shown in Figure 4. It can be seen that over 5 years the dust coverage attenuates more than 10 % of the solar intensity at 2000 m, and more than 60 % at 1000 m. Arrays within 500 m will experience a 50 % reduction in available solar power in one year. It is important to note that these estimates do not include to dust suspended from the host of other sources. As the lunar base is expected to survive 30 years of operation, it is clear that the issue of lunar dust management must receive attention during the design stages.

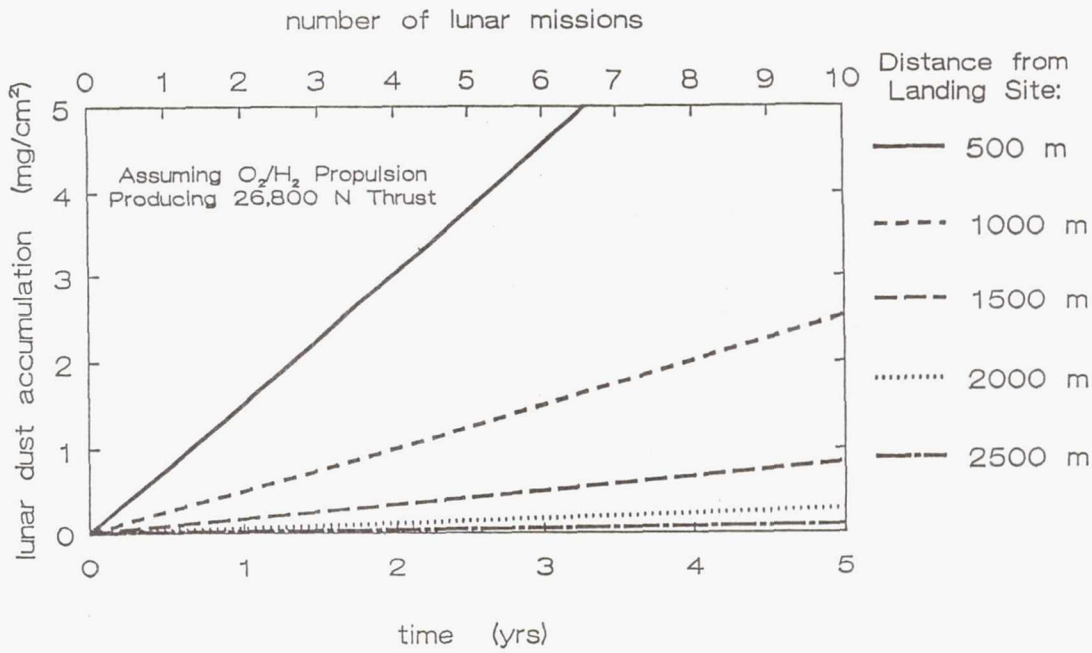


Figure 1. Predicted lunar dust accumulation distribution resulting from launch and landing of a 26,800 N lunar excursion vehicle as a function of time for different distances from the landing site.

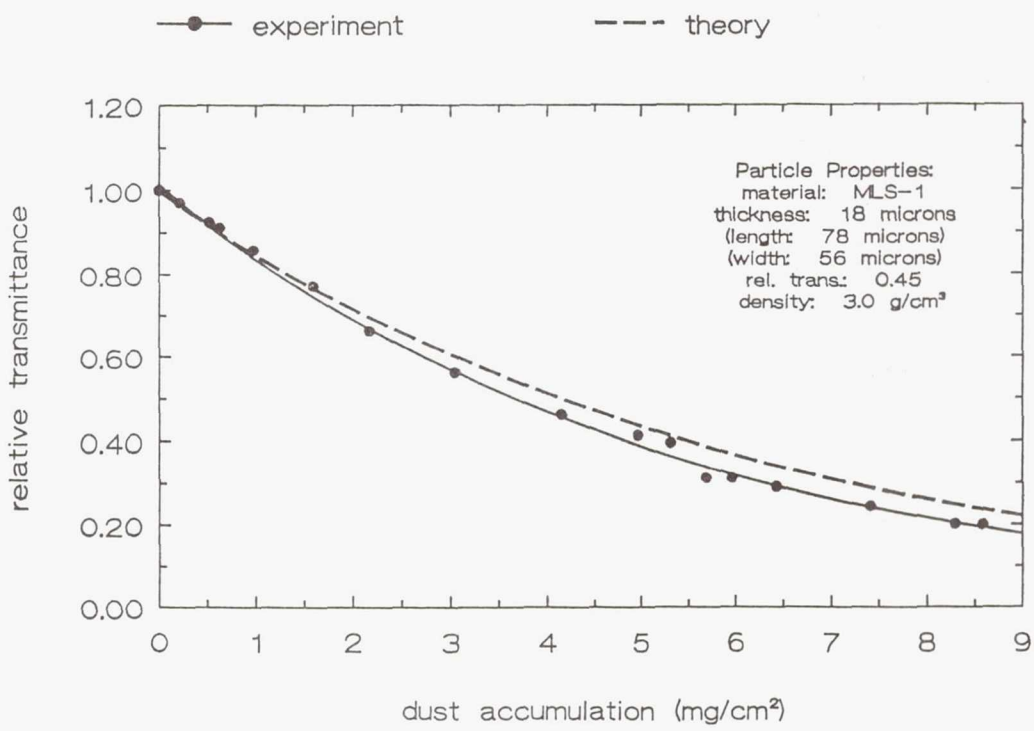


Figure 2. Transmittance of a glass coverslip with varying amounts of dust. Theory and experiment are compared for a specific particle size and shape.

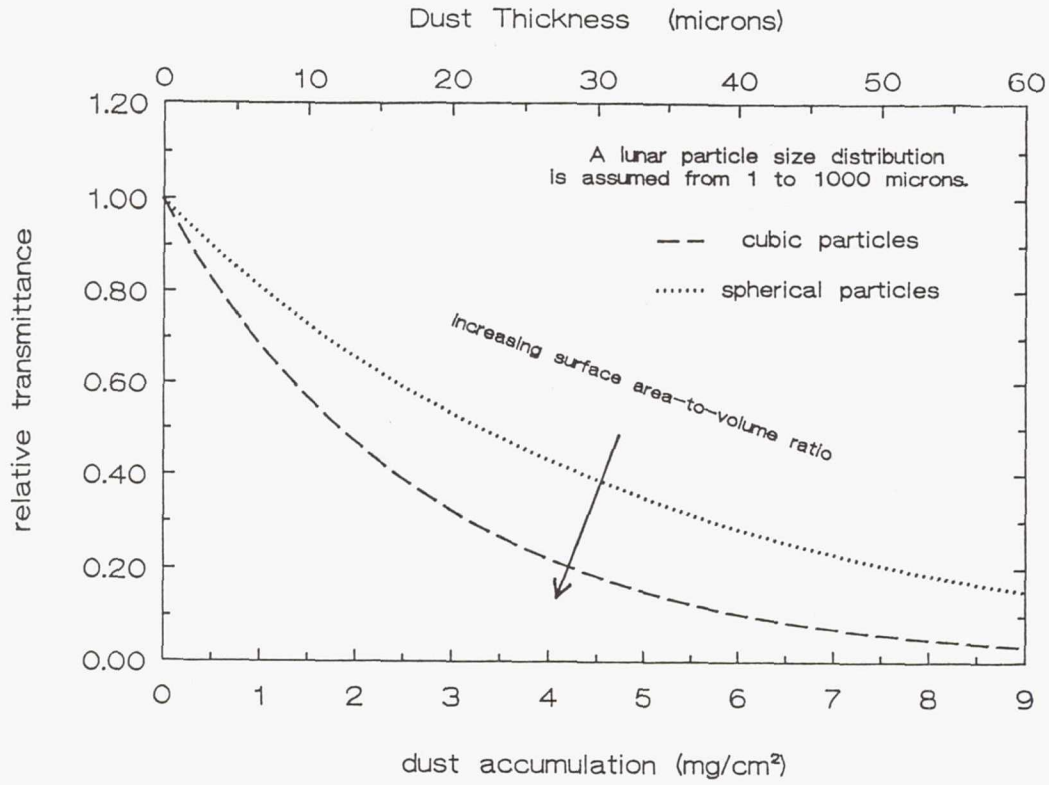


Figure 3. Predicted transmittance of a glass coverslip with varying amounts of dust which includes the range of particle sizes found in lunar dust. Spherical and cubic particles are compared.

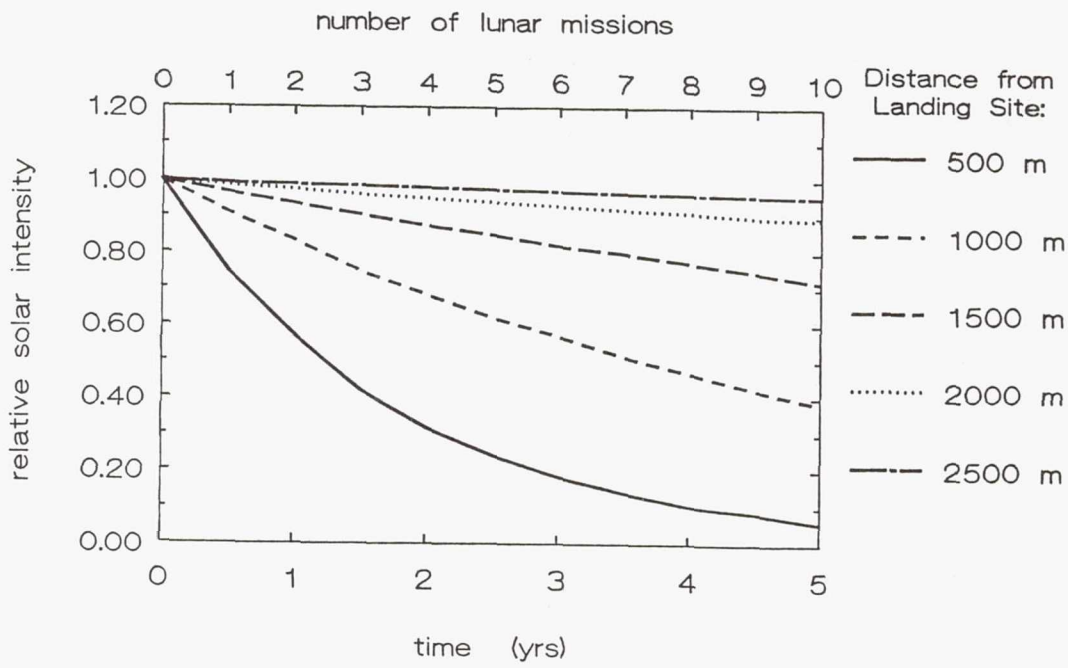


Figure 4. Predicted temporal dependence of relative solar intensity entering solar cells due to accumulated dust resulting from the launch and landing of 26,800 N lunar supply vehicles.

## I-V CURVES OF DUST-COVERED CELLS

In order to more directly determine the effects of dust accumulation on the power output of photovoltaic arrays, current-voltage characteristics were measured for solar cells covered with differing amounts of dust. Small silicon space solar cells (2x4 $cm^2$) were used so that the mass of applied dust would be detectable by means of a Sartorius microbalance. The cells, provided by Applied Solar Energy Corporation, had antireflective coatings, fused silica coverslips bonded with Dow-Corning 93-500 adhesive, and ultraviolet filters.

The illuminated cell characteristics were measured prior to and after dusting in a Spectrolab X-25L xenon arc solar simulator. Air mass zero calibration was assured by the use of an aircraft calibrated silicon reference standard.

The dust material, MLS-1, was ground and dry-sieved with stainless steel mesh. The sieve fraction used in these experiments was collected between 20 $\mu$m and 38 $\mu$m meshes, but it was observed that the diagonal dimension of the mesh openings allowed passage of somewhat larger particles. In addition, very fine particles were present due to electrostatic effects created during sieving. The charge was allowed several weeks to drain, and the dust material was held at 200 °C when not in use in order to eliminate the clumping effects of moisture.

Dust layers were applied to the cells by a simple sedimentation procedure which produced homogeneous sub-monolayers of simulant particles with a minimum of clumping. Before and after dusting, each cell was weighed and the complete I-V curve was measured, proceeding from open-circuit voltage to short circuit current, with computer-controlled increments in voltage. Short circuit current and maximum power for each cell were determined from the I-V curves.

## RESULTS AND DISCUSSION

While the occlusion model and measured transmittance of coverslips provide a useful estimation of the effects of dust, the I-V curves directly demonstrate the impact of dust accumulation on photovoltaic array performance. Cell short circuit current more accurately represents the exponential decrease in light intensity penetrating the cell. As can be seen in Figure 5, a difference exists between the measured relative transmittance of glass coverslips with MLS-1 of 20-38 $\mu$m and the relative short circuit current of cells with the same type and amount of dust. The difference would indicate that in fact more light enters the cell than suggested by tungsten source transmittance measurements. This is thought to be attributable to spectral differences in the light sources; the xenon arc source provides wavelengths in the blue-ultraviolet end of the spectrum which are not represented in tungsten illumination. The results suggest that these short wavelengths are not as significantly absorbed or reflected by the lunar simulant particles, as are the redder wavelengths. An evaluation of the spectral absorption of both the simulant and actual lunar dust, as well as the spectral response of the cells, may elucidate these subtleties. Other factors which may also be involved include cell optics and illumination intensity.

It is possible to adjust the optical absorption coefficient used in the occlusion model to more closely match the model to the observed change in relative short circuit current (See Figure 5). Ideally, the best correction would incorporate the spectral properties of both cell and dust, which is beyond the scope of this paper. The improvements, however, would not significantly affect the predictions of Figure 4.

The I-V curves also allow direct observation of the exponential decay in relative maximum cell power as a function of dust accumulation for the specific silicon cells used (Figure 6). The data show that an accumulation of 5 $mg/cm^2$ of MLS-1 in the size range 20-38 $\mu$m will reduce power output to less than 40 %. Smaller particles, such as those most readily disturbed and transported in the lunar environment, would be expected to cause greater reductions because dust monolayer coverage can be achieved at a lower mass per unit area with smaller particles.

Unfortunately, once lunar dust has accumulated it may be very difficult to remove. According to Apollo observations, lunar dust adhesive forces are very strong (0.01 to 0.1 $N/cm^2$ (ref. 9)), dominated by electrostatics with van der Waals contributions. Dust removal may be labor-intensive and at best only partially successful. Therefore, a defensive position is recommended to prevent array surfaces from collecting dust. The location and placement of

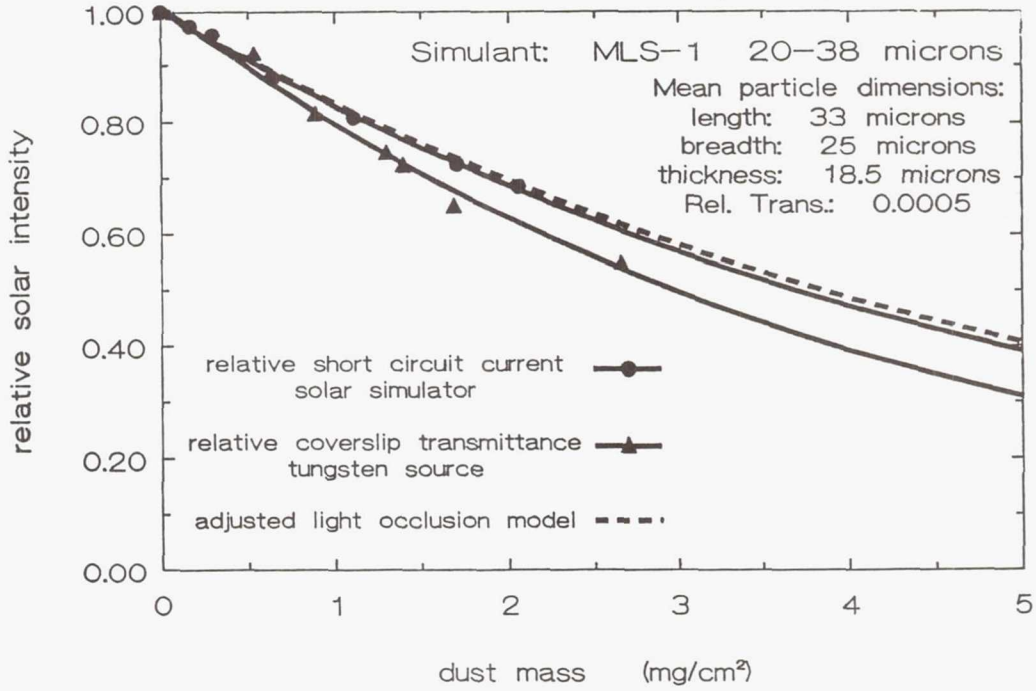


Figure 5. Relative light intensity entering a solar cell through an accumulation of dust, as predicted by three methods: relative short circuit current measurements of dusted cells under simulated solar illumination, relative transmittance measurements of dusted coverslips under tungsten illumination, and predictions of a light occlusion model.

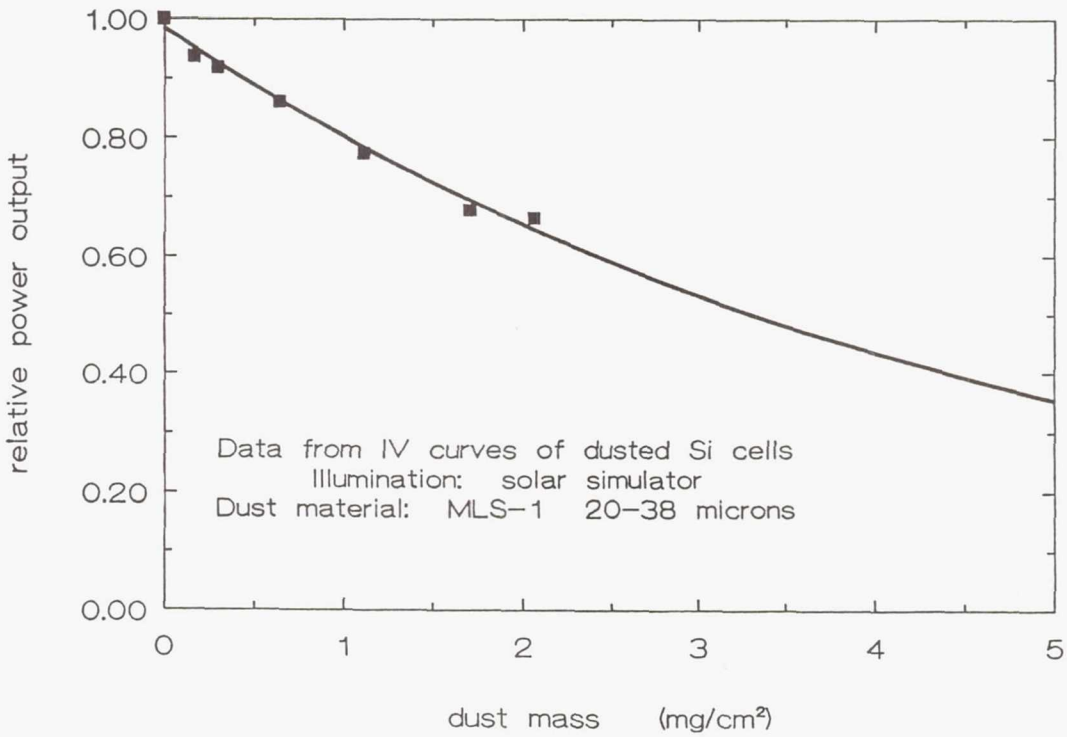


Figure 6. Relative power output as determined from the IV curves of dust-covered silicon cells.

arrays at a lunar base with respect to launch pads and other major sources of suspended dust is an important consideration. Advanced array design concepts may be found which incorporate array materials, operating voltages, or mounting arrangements to reduce the tendencies for particles to collect. However, these may not be enough to eliminate dust accumulation. Unless it becomes feasible for arrays to be compensationally oversized, it is likely that additional strategies must be implemented to reduce the amount of dust generated. These might include glazing launch pad areas, refining rocket approach patterns, improving rover fenders, laying packed-earth roads, restricting traffic in array zones, and even improving space suit mobility. Moreover, supplementary measures, such as mechanical or electrostatic fences, may be necessary to divert the dust that is inevitably suspended from accumulating on important surfaces.

## CONCLUSIONS

Lunar dust accumulations resulting from the launch and landing of a 26,800 N surface vehicle have been anticipated, using available Surveyor III data. Substantial dust accumulations are predicted for surfaces within a 2 km radius of the landing site over a 5 year period. Therefore, the impact of dust accumulation on the performance of photovoltaic arrays has been addressed both theoretically and experimentally; both a light occlusion model and transmittance measurements indicate that the attenuation of light by dust accumulations at 1 km may be in excess of 60 %, and at 2 km more than 10 % after 10 surface missions.

Relative cell short circuit current changes derived from I-V measurements confirmed the predictions of the light occlusion model and transmittance measurements: an exponential decay in solar intensity results from the accumulation of dust particles. However, the relative short circuit current data suggests that solar ultraviolet is not as significantly attenuated by the dust simulant as the visible wavelengths produced by a tungsten source, and therefore indicates a more gradual exponential decay than predicted by the model or transmittance data.

Cell power output was directly determined from the I-V curves of silicon space cells covered with MLS-1 particles in the 20-38 $\mu$m size range. This also degrades exponentially with dust accumulation such that 50 % reductions result when accumulations reach 3 mg/cm$^2$. As actual accumulations of lunar dust will likely be comprised of even smaller particles, power output is expected to degrade more dramatically.

The findings of this investigation indicate that the performance of photovoltaic arrays on a lunar base is so threatened by the potential accumulation of lunar dust that measures must be incorporated into design to minimize degradation. As lunar dust adhesive forces have been observed by Apollo astronauts to be very strong, driven by electrostatic as well as van der Waals forces, dust removal appears to be a difficult solution. Instead, a preventative strategy is recommended to protect vulnerable surfaces such as photovoltaic arrays from ever acquiring enough dust to significantly affect performance. Such measures might include special attention to array orientation and location on a lunar base, as well as improved rover fenders, glazed launch pads, and perhaps even electrostatic fences.

## REFERENCES


1. Zook, H.A., Lange, G., GrÜn, E., and Fechtig, H.: The Interplanetary Meteoroid Flux and Lunar Primary and Secondary Microcraters. Properties and Interactions of Interplanetary Dust. R.H. Giese and P. Lamy (eds.), D. Reidel Publishing Company, Dordrecht-Holland, 1985, pp. 89-96.

2. Zook, H.A., Lange, G., GrÜn, E., and Fechtig, H.: Lunar Primary and Secondary Microcraters and the Meteoroid Flux. Lunar Planet. Sci. Conf. XV, 1984, pp. 965-966.

3. West, Jr., G.S., Wright, J.J., and Euler, H.C. (eds.): Space and Planetary Criteria Guidelines for Use in Space Vehicle Development, 1977 Revision. NASA TM-78119, 1977.

4. Criswell, D.R.: Horizon-Glow and the Motion of Lunar Dust. Photon and Particle Interactions with Surfaces in Space. R.J.L. Grard (ed.), D. Reidel Publishing Company, Dordrecht-Holland, 1973, pp. 545-556.

5. Pelizzari, M.A., and Criswell, D.R.: Lunar Dust Transport by Photoelectric Charging at Sunset. Proc. 9th Lunar Planet. Sci. Conf., 1978, pp. 3225-3227.

6. Rennilson, J.J., and Criswell, D.R.: Surveyor Observations of Lunar Horizon-Glow. The Moon, vol. 10, D. Reidel Publishing Company, Dordrecht-Holland, 1974, pp. 121-142.

7. Rhee, J.W., Berg, O.E., and Wolf, H.: Electrostatic Dust Transport and Apollo 17 LEAM Experiment. COSPAR Space Res., vol. XVII, Pergamon Press, NY, 1977, pp. 627-629.

8. Katzan, C.M., and Edwards, J.L.: Lunar Dust Transport and Potential Interactions with Power System Components. NASA LeRC Contract NAS3-25266, 1991, in press.

9. Nickel, N.L., and Carroll, W.F.: Summary and Conclusions. Analysis of Surveyor 3 Material and Photographs Returned by Apollo 12, NASA SP-248, 1972.

10. Carroll, W.F., and Blair, Jr., P.M.: Spacecraft Changes: Lunar Dust and Radiation Darkening of Surveyor 3 Surfaces. Analysis of Surveyor 3 Material and Photographs Returned by Apollo 12, NASA SP-248, 1972.

11. Satkiewicz, F.G., and Marmo, F.F.: Spacecraft Changes: Sputter-Ion Source Mass Spectrometer Analysis of Samples Cut from the Surveyor 3 Camera. Analysis of Surveyor 3 Material and Photographs Returned by Apollo 12, NASA SP-248, 1972.

12. Jaffe, L.D.: Spacecraft Changes: Blowing of Lunar Soil by Apollo 12: Surveyor 3 Evidence. Analysis of Surveyor 3 Material and Photographs Returned by Apollo 12, NASA SP-248, 1972.

13. Cour-Palais, B.G., Flaherty, R.E., High, R.W., Kessler, D.J., McKay, D.S., and Zook, H.A.: Micrometeorite Impact Analysis: Results of Examination of the Returned Surveyor 3 Samples for Particulate Impacts. Analysis of Surveyor 3 Material and Photographs Returned by Apollo 12, NASA SP-248, 1972.

# RAPID THERMAL CYCLING OF SOLAR ARRAY BLANKET COUPONS FOR SPACE STATION FREEDOM

David A. Scheiman *
*Sverdrup Technology, Inc.*
*Brook Park, Ohio*

Bryan K. Smith
*NASA Lewis Research Center*
*Cleveland, Ohio*

**ABSTRACT**

NASA Lewis Research Center has been conducting rapid thermal cycling on blanket coupons for Space Station Freedom. This testing includes two designs (8 coupons total) of the solar array. Four coupons were fabricated as part of the Photovoltaic Array Environmental Protection Program (PAEP), NAS3-25079, at Lockheed Missiles and Space Company. These coupons began cycling in early 1989 and have completed 172,000 thermal cycles. Four other coupons were fabricated a year later and included several design changes; cycling of these began in early 1990 and has reached 90,000 cycles. The objective of this testing is to demonstrate the durability or operational lifetime (15 yrs.) of the welded interconnects within a Low Earth Orbit (LEO) thermal cycling environment. The paper presented describes the blanket coupons, design changes, test description, status to date including performance and observed anomalies, and any insights related to the testing of these coupons. The paper also includes the description of a third design.

## INTRODUCTION

Power for Space Station Freedom (SSF) will be generated by four photovoltaic power modules which each employ two solar array wings. The solar array wings are comprised of two blankets that each are an assembly of 82 active solar panels. A panel contains 200 solar cells in series, with each cell connected to an underlying circuit interconnect by 10 welded contact points. The peak power output for each cell is slightly over 1 watt. The on-orbit deployed envelope of the solar array wing is 38 ft. by 110 ft.

SSF will have an operating altitude range of 180 to 240 nautical miles at an inclination of 28.5 degrees. At this altitude SSF will orbit the earth approximately once every 90 minutes or 6000 times per year. With each orbit SSF will pass into and out of the sun's view causing temperature excursions of over 160°C. These temperature extremes can induce thermal stresses in the blanket materials of the array and can, over time, result in structural fatigue of the panel components. This is just one of the many detriments of the low earth orbit (LEO) space environment which include atomic oxygen, micrometeoroids, vacuum, plasma, and radiation.

The thermal stresses induced on the array blanket are the focus of rapid thermal cycling. Different materials of the array have different coefficients of thermal

* Work supported under NASA Lewis contract NAS3-25266

expansion (CTE); for example, silicon is 2 x $10^{-6}$ (cm./cm.)/°C and Kapton (ref 1) is 26 x $10^{-6}$ (cm./cm.)/°C. Various CTE's for different materials used in the array blanket can be seen in Figure 1 (ref. 2). The resultant effects of thermal stresses are difficult to predict and therefore warrant physical testing. In addition to verifying mechanical integrity, thermal cycling data will also serve to verify assumptions used in calculating array performance over the design lifetime.

Solar array blanket coupons have been tested to 172,000 cycles for 1989 samples and 90,000 cycles for 1990 samples. Both of these sample groups have had only slight degradation in performance. A third test coupon which represents the latest design has completed 6,000 cycles. These coupons will also run to 90,000 cycles.

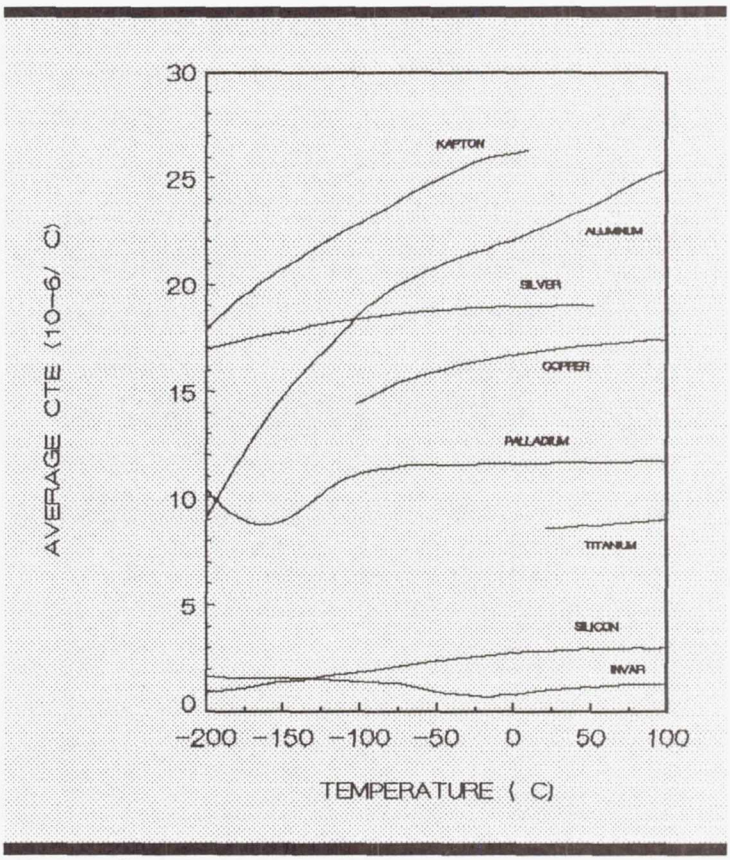


Figure 1: CTE vs. Temperature for Solar Array Materials

## TEST ARTICLE DESCRIPTION AND DESIGN EVOLUTION

All of the coupons used for testing were fabricated by Lockheed Missiles and Space Company (LMSC) under the Photovoltaic Array Environmental Protection Program (PAEP), NAS3-25079. Between 1989 and 1991 three different designs, designated blanket design I (SSF 1989), II (SSF 1990) and III (SSF 1991), were delivered to NASA-LeRC for thermal cycle testing. Four coupons of each design were delivered, the cells used for these coupons are secondary cells and therefore efficiency is below nominal.

Each coupon contains four 8x8 cm silicon solar cells with CMX coverglass connected in series. The coverglass is bonded to the solar cell with Dow Corning DC93-500 silicone adhesive. The SSF solar cells are an N on P type silicon cell with a boron back surface field (BSF) and a 10 ohm-cm nominal base resistivity. The collection grids and contact points are layers of titanium, palladium, aluminum and silver. Four holes in the cell bring the front N contacts through to the back side where they are welded to the copper circuitry along with the six P backside contacts. Solar cells for SSF will be supplied by both Applied Solar Energy Corporation and Spectrolab Inc.

It is difficult to assess the integrity of a solar cell weld without destructive testing. One solar array wing alone will contain over 164,000 cell to circuit welds, therefore, LMSC must maintain tight control over their production welding operation to assure adequate welding. LMSC addressed this in the PAEP program by completing a weld optimization task. The task determined voltage, emissivity, and IR sensing settings that will be used to control the weld pulse energy and duration on the production welders. Pull tests, photomicrographs, thermal cycling and illumination tests were used to evaluate the quality of the solar cell to copper interconnect weld. From this effort a weld schedule was selected that exhibited statistically the highest pull strengths and showed no obvious failure mechanisms such as gross melting, voids,

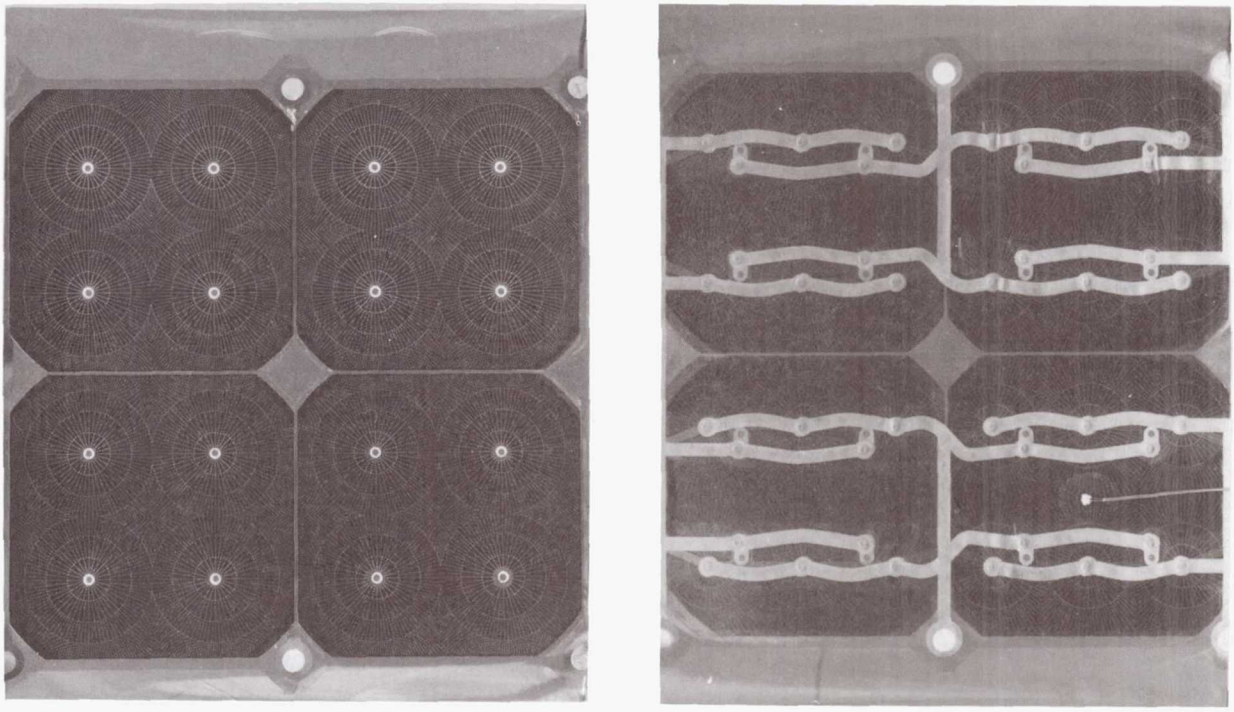

Figure 2: SSF 1989 (design I) Test Coupon -- Front and Back

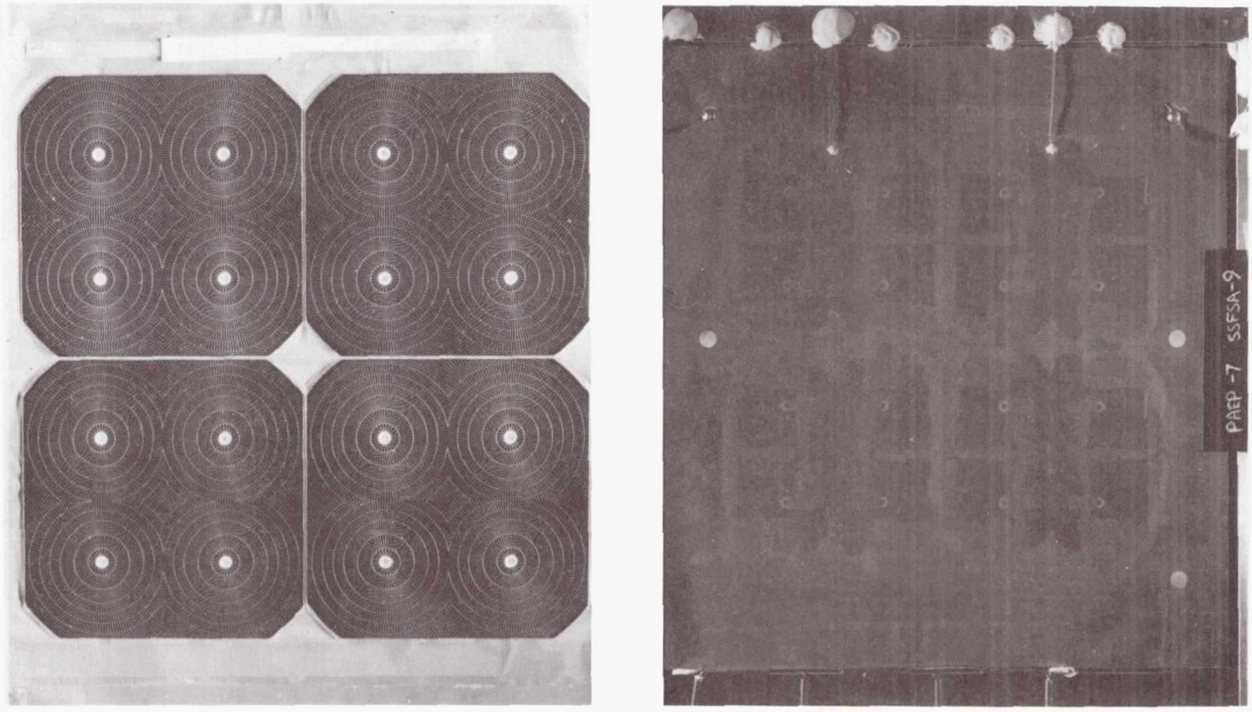


Figure 3: SSF 1990 (design II) Test Coupon -- Front and Back

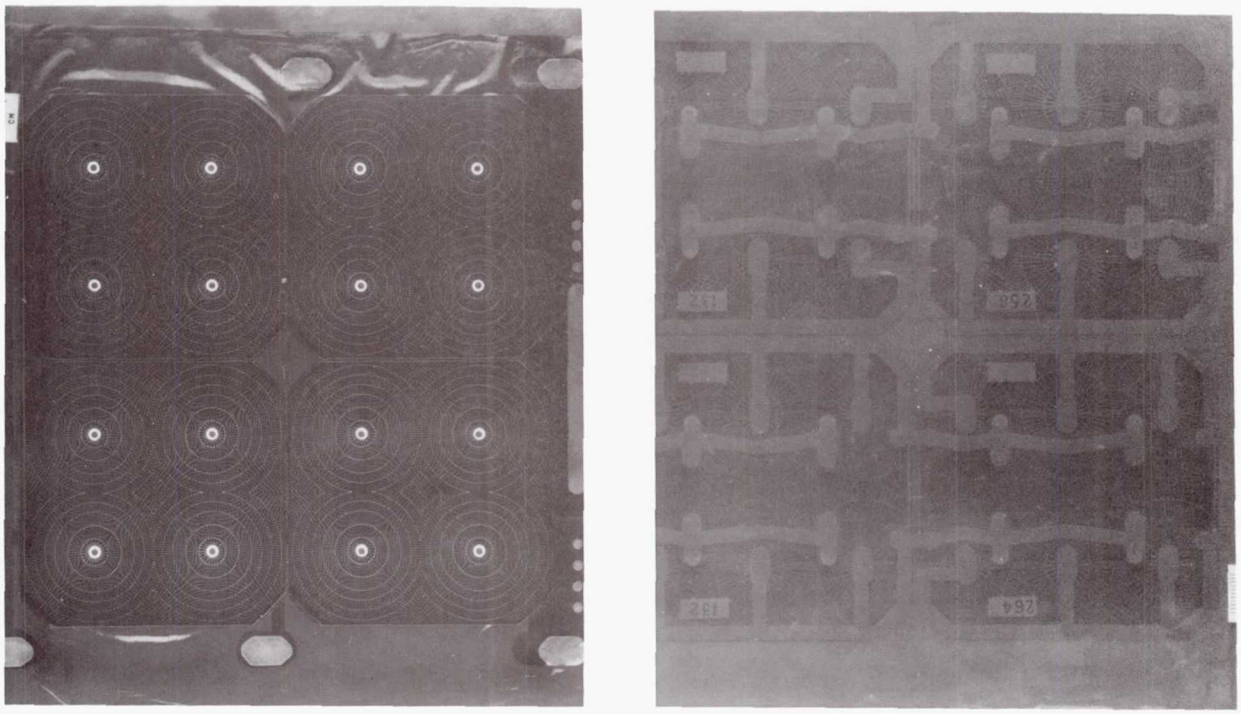

Figure 4: SSF 1991 (design III) Test Coupon -- Front and Back

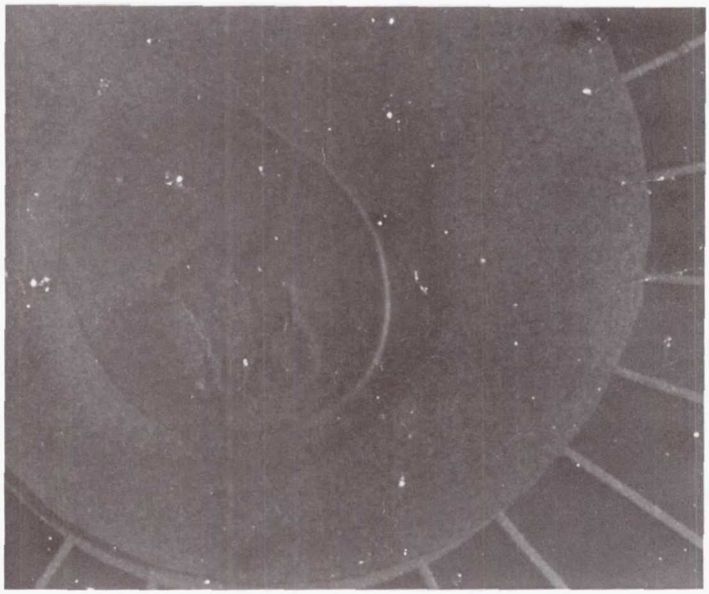

Figure 6: Copper Fatigue of SSF 1989 at 150,000 cycles

or cracking. In addition to deriving a weld schedule and closely monitoring the weld parameters, thermal cycling will also be used throughout the production process to assure quality welds.

Blanket design I employed two layers of Kapton H polyimide film with the copper circuit in between the layers (Fig. 2). The first layer of Kapton was cut to insulate the cell from the copper circuitry and allow the second layer of Kapton an adhesive bond path to the back of the solar cell. The copper circuitry was bonded to the first layer of Kapton with a polyester adhesive. The solar cells were welded to the circuitry through access holes in the first layer of Kapton. The second layer of Kapton or coverlay provides the structural component for the blanket and also contains the Kapton hinge loops that are used to connect the panels together to form the blanket assembly. The second sheet of Kapton is bonded with DC93-500 to the exposed circuitry, the first layer of Kapton and the back of the solar cells.

Atomic oxygen protection on blanket design I was achieved by coating both layers of Kapton on both sides with 1300 angstroms of silicon dioxide. The coupons were also configured with aluminum foil covered Kapton hinges. The aluminum foil was considered the most effective way of protecting the critical hinge area from atomic oxygen.

Blanket design II coupons substituted the Kapton H with an experimental atomic oxygen resistant Kapton (AOR Kapton) (Fig. 3). The solar cells were changed to include redundant weld contact points that allowed for repair or replacement of a solar cell once it had been welded into a panel assembly. The copper circuitry was also changed to control adhesive flow in the manufacturing process and to accommodate the redundant weld contact. Two of the four design II coupons delivered featured bypass diodes that are used within the flexible panel assemblies to protect individual solar cells from reverse biasing resulting from transitory shadowing. The SSF design will use one bypass diode every eighth solar cell which will also provide a shunt path if an open circuit develops within an eight cell unit. The diodes used on design II had Kovar leads and were welded to the circuitry in four places.

Blanket design III coupons returned to the silicon dioxide coated Kapton H for the copper circuit layer but replaced the back surface Kapton with a laminate (Fig. 4). The laminate consists of two layers of silicon dioxide coated Kapton with a glass scrim cloth bonded in between the layers. Development tests have demonstrated that this design will provide adequate atomic oxygen protection to the blanket over the 15 year design lifetime. The coupons also incorporated additional copper circuitry under the bypass diode that will act as a sink and allow the diode to operate at a reduced temperature. Two of the four design III coupons have bypass diodes with copper leads.

## TEST DESCRIPTION

### TEST CHAMBER

The thermal cycling chamber, Figure 5, is designed to cycle a test article between two temperature extremes. The chamber consists of two smaller chambers that each maintain a constant hot and cold temperature. Test frames are installed in the chamber and are the vehicle by which the test articles are moved between the hot and cold chambers. The movement of the frames is controlled by a computer which receives temperature information from a thermocouple mounted on each test article. When a given temperature is achieved, the computer activates the movement of the test frame to the adjacent chamber. Test frames are individually controlled and switching depends only on temperature. One thermal cycle is the completion of exposure to both temperature extremes. Cycle times range from 2 to 5 minutes and can vary depending on coupon mass and chamber temperature. Because the chamber is computer controlled, timed cycling and limited temperature profiling can also be used.

The thermal cycling test rig is an insulated box with an oven over a freezer. The oven is heated using two 500 watt resistive heaters which provide radiative and

convective heat. The freezer is cooled using liquid nitrogen fed directly into the chamber. This also supplies an inert atmosphere for both chambers. The system is capable of temperature extremes between +120°C and -180°C with a 10° gradient in either chamber. Disadvantages of this method include the lack of information regarding the effects of outgassing of the components, stresses due to pressure differentials, and local temperature gradients (ref. 3).

Up to four 8" x 8" x .5" solar array test articles can be tested simultaneously. Temperatures are read at approximately 16 second intervals and cycle counts are printed hourly. The chamber shuts down automatically when cycling is completed. At set intervals, the test articles are removed from the chamber for performance testing and visual inspection.

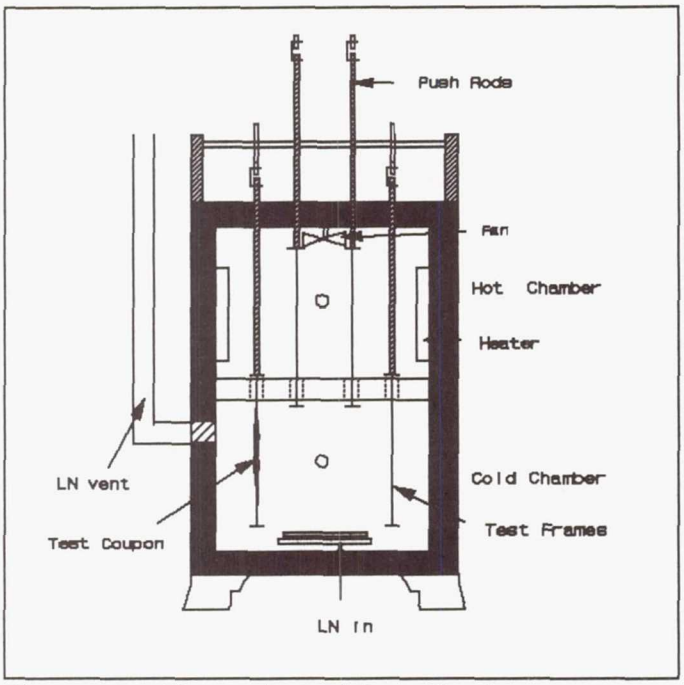

Figure 5: Thermal Cycling Chamber cross-section

ARRAY PERFORMANCE

Performance of the test article is measured by the range of its electrical power output under illumination. This power output is characterized as a curve of current vs. voltage or an I-V curve. The I-V curve is generated by varying a load resistance on the coupon from 0 to infinity (ohms) while it is illuminated. The solar constant of 1.36 $mW/cm^2$ is used in efficiency calculations. The array efficiency is also based on the cell area only. The following information from the I-V curve is used in performance evaluation: short circuit current in amps, denoted $I_{sc}$; open circuit voltage in volts, denoted $V_{oc}$; current at maximum power out in amps, denoted $I_{max}$; voltage at maximum power out in volts, denoted $V_{max}$; maximum power out in watts, denoted $P_{max}$; fill factor, denoted FF; peak efficiency in percent, denoted eff.; measured peak power over initial peak power, denoted $P/P_o$

I-V curves were obtained by flash testing. Flash testing is performed by using a short burst of light (Xenon arc lamp) with a normalized solar intensity at air mass zero (AM0). A complete I-V curve containing 30-80 data points is generated in about 1.5 milliseconds. This flash test provides curve data with virtually no heat generated in the array and therefore data comparisons can be made because repeatability is very good. This measurement is performed at room temperature with the coupons removed from the chamber.

If an interconnect failure were to occur in the array, series resistance would increase. Series resistance would most prominently affect the slope of the I-V curve between $P_{max}$ and $V_{oc}$ and would result in a drop in FF and $P_{max}$. The coupons have electrical test pads after each cell in the series circuit that can be used to isolate failures to a single solar cell if a loss in performance is detected at the coupon level.

An additional check is made on samples which contain bypass diodes. The bypass diode is forward biased (array is reverse biased) and a dark I-V curve is created using a curve tracer with the coupons at room temperature. Any loss of continuity could easily be detected using this method.

SOLAR CELL VISUAL INSPECTION

In addition to performance characteristics, the solar array test coupons are visually inspected. The test coupons are viewed under 10X magnification with incident light at varying angles. Because of the coverglass and the reflective nature of the cell, light angles are varied to detect any flaws in the surface of the cell or coverglass. These flaws are mapped on a paper image of the cell and subscripted with the type of flaw and time observed. Both the front and back side of the test coupon are mapped. The following flaws are noted:

1) B -- break/crack in cell surface
2) C -- break/crack in coverglass
3) V -- void, open area i.e. lack of adhesive
4) W -- wrinkle in interconnect/ blanket
5) A -- adhesive, typical evidence of migration or elongation
6) O -- other, any other nonconformity in the cell; bubbles, contamination, peeling, delamination, etc.

Visual mapping with subscripted notations are performed at regularly scheduled intervals. Ultimately, the visual inspection is used to observe any trends that would lead to or cause performance degradation.

## TEST RESULTS

Rapid thermal cycling of the solar array coupons for SSF has been an ongoing project for more than two years. Test articles have accumulated well over 500,000 cycles. Four 1989 coupons have been cycled to 90,000 cycles with two completing 172,000 cycles, two 1990 coupons have been cycled to 90,000 cycles, and four 1991 coupons are currently being tested. Based on this testing several observations have been made to establish confidence in the welded interconnects and array design.

Performance degradation was observed in both the 1989 and 1990 test coupons. The amount and rate of degradation varied between the two designs. Performance of the 1989 dropped less than 1% after 90,000 cycles (ref. 4) and was down 3% after 172,000 cycles. Performance of the 1990 coupons was down 2% after 66,000 cycles and 6% after 90,000 cycles. The 1991 coupons have just completed 6,000 cycles with no performance degradation. Overall performance parameters are included in Table 1.

Visual inspection of all the coupons revealed only very slight changes in the cells. Fine cracks were observed in the cell and coverglass. Most of the cracks were observed prior to cycling and only tended to elongate fractionally during the first 12,000 cycles. These changes in the cell were viewed as posing no threat to the integrity of the array.

The backside of the coupon, interconnect side, exhibited a change in the copper interconnects, Kapton, and adhesive layers. Within the first 12,000 cycles, motion of the copper and Kapton was evident. The copper went from being flat to having wrinkles or ripples. This out of plane rippling, resulting from initial thermal stresses, has actually provided a stress relief for subsequent thermal cycling. Rippling of the copper interconnects was random and even ran up to the weld joints. The adhesive also appeared to have elongated in some places. This elongation is characterized by round voids in the adhesive that have changed to oval shapes. The Kapton also wrinkled, which usually fit the mold of the underlying Kapton. After 12,000 cycles the motion continued but was stabilized, i.e. no significant changes in size or quantity were apparent. The 1990 coupon design had less adhesive area. This resulted in the Kapton pulling away from the cell in the four corners although the adhesive did retain the bond.

As the cycling and rippling continued, fatigue in the copper near the welds was more apparent. The copper areas around the weld were brittle due to the heating incurred during the weld process. In areas where the rippling was occurring at or close to the weld, copper fatigue resulted around the weld joint (Fig. 6). This was first observed after 150,000 cycles in the 1989 coupons and after 72,000 cycles in the

**Table 1: Selected Solar Array Coupon Electrical Performance**

SSF 1989 Test Coupons, Design I (SSFSA-4)

| CYCLES : | 0 | 30000 | 60000 | 90000 | 172000 |
|---|---|---|---|---|---|
| Isc (A) | 2.7070 | 2.6654 | 2.6759 | 2.6323 | 2.6504 |
| Voc (V) | 2.4470 | 2.5127 | 2.5097 | 2.4885 | 2.4454 |
| Imax (A) | 2.4740 | 2.3993 | 2.4368 | 2.3591 | 2.3329 |
| Vmax (V) | 1.8360 | 1.9289 | 1.9115 | 1.9028 | 1.9016 |
| Pmax (W) | 4.5430 | 4.6279 | 4.6580 | 4.4889 | 4.4363 |
| F.F. | 0.686 | 0.691 | 0.694 | 0.685 | 0.684 |
| effic. | 13.4 % | 13.6 % | 13.7 % | 13.2 % | 13.1 % |
| P/Po | 1.0000 | 1.0187 | 1.0253 | 0.9881 | 0.9765 |

SSF 1990 Test Coupons, Design II (SSFSA-9)

| CYCLES : | 0 | 32000 | 66000 | 90000 |
|---|---|---|---|---|
| Isc (A) | 2.6158 | 2.6722 | 2.6211 | 2.6223 |
| Voc (V) | 2.4916 | 2.5013 | 2.5001 | 2.4615 |
| Imax (A) | 2.3397 | 2.3430 | 2.3058 | 2.3420 |
| Vmax (V) | 1.9078 | 1.9152 | 1.8979 | 1.7863 |
| Pmax (W) | 4.4636 | 4.4874 | 4.3761 | 4.1835 |
| F.F. | 0.685 | 0.671 | 0.668 | 0.648 |
| effic. | 13.2 % | 13.2 % | 12.9 % | 12.3 % |
| P/Po | 1.0000 | 1.0053 | 0.9804 | 0.9372 |

SSF 1991 Test Coupons, Design III (SSFSA-12)

| CYCLES : | 0 | 3000 | 6000 * |
|---|---|---|---|
| Isc (A) | 2.6048 | 2.6722 | 2.4477 |
| Voc (V) | 2.4116 | 2.5013 | 2.1440 |
| Imax (A) | 2.2221 | 2.3430 | 2.0943 |
| Vmax (V) | 1.8173 | 1.9152 | 1.5460 |
| Pmax (W) | 4.0382 | 4.4874 | 3.24 |
| F.F. | 0.643 | 0.671 | 0.617 |
| effic. | 11.9 % | 12.1 % | 9.5 % |
| P/Po | 1.0000 | 1.0162 | ------ |

* data not accurate (non-uniform light source)

1990 coupons. The copper fatigue occurred primarily by the corner welds (P contacts) and was a result of less adhesive around that weld. The 1989 coupons had approximately 3 visible copper fatigue weld areas after 172,000 cycles and the 1990 coupons had approximately 16 copper fatigue weld areas. The 1990 coupons had considerably more copper fatigue failures due to the lack of stability in the AOR Kapton and the smaller adhesive area. The 1991 coupons utilize the Kapton H of the 1989 samples, however they will have the smaller adhesive area of the 1990 samples.

One of the 1990 coupons was assembled with a bypass diode. The diode was welded to the copper interconnect in four places, two on each side. After 72,000 cycles the weld connections completely separated although there was no loss of continuity. The cause for this separation was the thermal expansion mismatch between the copper interconnect and the Kovar lead of the diode. The 1991 coupons now use a bypass diode with a copper lead to match the interconnect.

## CONCLUSIONS

Based upon test data from blanket design I and II coupons the SSF solar array will experience some performance degradation due to thermal cycling over the 15 year LEO mission. Performance degradation in the coupons can be attributed to a combination of fatigue cracks in the dimpled area of the copper interconnect adjacent to the solar cell weld and increased series resistance of the solar cells and interconnects.

Although the results represent a small statistical sample of the total welds on the SSF solar array, the test data strongly suggests that the weld between the solar cell and copper interconnect is adequate for the 15 year design life in LEO. However, repeatability in the welding process and sufficient adhesive distribution around the welds will be important to assure this in the production program. A transient plasticity analysis of the solar array blanket also indicated that the fatigue life of the solar array blanket should be higher than the program requirement (ref. 5). Considering blanket design I and II coupon test data, assembly level circuits and connections and a statistical treatment of the welding and manufacturing process, performance losses for the SSF solar array due to thermal cycling will be between 0.5% to 1% for 5 - 10 years and 1% - 2% for 10 to 15 years in LEO. Data for blanket design III will be available in December of 1991 and the final flight design is scheduled to begin thermal cycling testing at NASA-LeRc in April 1992.

## REFERENCES


1. Kapton is a registered trademark of E. I. DuPont De Nemours and Co., Inc.

2. Jet Propulsion Laboratory: Solar Cell Array Design Handbook Volume II. NASA October 1976 pp. 7.11-4,5.

3. Brinkmann, P. W.; Reimann, J.: Efficient Thermal Cycling of Solar Panels in Solar Simulation Facilities With a Multi-Panel Test Rig. Proc. 2nd European Symposium "Photovoltaic Generators in Space", Heidelberg, 15-17 April 1980 (ESA SP-147, June 1980) pp. 195-197.

4. Scheiman, D. A.; Smith, B. K.; Kurland, R. M.; Mesch, H. G.: Rapid Thermal Cycling of New Technology Solar Array Blanket Coupons. 25th IECEC , Volume 1 pp. 575-580.

5. Armand, S. C.; Liao, M-H; Morris R. W.: A Transient Plasticity Study and Low Cycle Fatigue Analysis of Space Station Freedom Photovoltaic Solar Array Blanket. NASA LeRc Technical Memorandum 102516.

# Radiation Resistance of Ge, $Ge_{0.93}Si_{0.07}$, GaAs, and $Al_{0.08}Ga_{0.92}As$ Solar Cells*

M.L. Timmons and R. Venkatasubramanian
*Research Triangle Institute*
*Research Triangle Park, NC*

P.A. Iles and C.L. Chu
*Applied Solar Energy Corporation*
*City of Industry, CA*

Solar cells made of Ge, $Ge_{0.93}Si_{0.07}$ alloys, GaAs and $Al_{0.08}Ga_{0.92}As$ have been irradiated in two experiments with 1-meV electrons at fluences as great as $1 \times 10^{16}$ cm$^{-2}$. Several general trends have emerged. Low-band-gap Ge and $Ge_{0.93}Si_{0.07}$ cells show substantial resistance to radiation-induced damage. $Al_{0.08}Ga_{0.92}As$ cells have shown in the two experiments that degradation is less than for GaAs cells similarly irradiated. Compared to homojunctions, cells with graded-band-gap emitters did not show the additional resistance to damage in the second experiment that had been seen in the first. The thickness of the emitter is a key parameter to limit the degradation in GaAs devices.

## Introduction

Radiation damage to devices is a key factor for space photovoltaics since the end-of-life (EOL)/beginning-of-life (BOL) ratios largely determine how much extra array area must be launched to meet EOL mission requirements. At the previous SPRAT, we presented preliminary radiation exposure data using 1-meV electrons at fluences as high as $5 \times 10^{15}$ cm$^{-2}$ for $Al_{0.08}Ga_{0.92}As$ and GaAs solar cells[1]. In that study, the AlGaAs emitter configurations were varied and included homojunctions, grade compositions, and heterojunctions. GaAs cells grown on Ge (with inactive GaAs/Ge interfaces) were included. All of these cells were grown in production-type reactors.

The preliminary data showed that AlGaAs cells, regardless of emitter configuration, degraded less than GaAs cells. But beyond this, the graded-emitter cells degraded the least of all in the experiment.

In this paper, we describe a second experiment that extends the results presented previously. The 1-meV electron fluence has been increased to $1 \times 10^{16}$ cm$^{-2}$, and Ge and $Ge_{0.93}Si_{0.07}$ alloy cells have been added. Again, AlGaAs and GaAs cells form the major focus of the study.

---

* This work was funded by the Department of the Air Force under Contract Nos. F33615-87-C-2804 and F33615-88-C-2847. Mr. K. Reinhardt and Mr. J. Scofield are the respective Project Engineers.

## Experimental

All the $Al_{0.08}Ga_{0.92}As$ cells used in this study were grown at RTI in a research-type reactor. This reactor is horizontal and operates at atmospheric pressure. Trimethylgallium (TMG), trimethylaluminum (TMA), and arsine ($AsH_4$) are the sources of Ga, Al, and As, respectively, and Se from a 50 ppm $H_2Se/H_2$ mixture and Zn from dimethylzinc (DMZ), and diethylzinc (DEZ) are the n- and p-type dopants, respectively. The AlGaAs layers were grown at 780 °C using a V/III ratio of about 35 to 40. The RTI GaAs cells were grown at 700 °C.

The Ge and $Ge_{0.93}Si_{0.07}$ cells were grown in a vertical low pressure reactor. The reactor was operated at 250 Torr and at 700 °C for Ge and 900 °C for $Ge_{0.93}Si_{0.07}$. Mixtures of germane ($GeH_4$), disilane ($Si_2H_6$), $AsH_4$, and diborane ($B_2H_6$) in $H_2$ were the source and dopant gases. The junctions evaluated in this study, using p-on-n polarity, were all epitaxially grown.

The RTI-grown devices were also processed at RTI. The current-voltage (I-V) characteristics were measured under a xenon-lamp solar simulator. The devices were sent to ASEC where the I-V measurements were repeated; generally, there was good agreement between the two sets of measurements. Several AlGaAs cells were evaluated by deep-level-transient spectroscopy (DLTS) at SERI, under the direction of Dr. R.K. Ahrenkiel, to establish a baseline deep defect level prior to irradiation. The only observed level was the DX center, present in most AlGaAs DLTS data, and the defect densities were low.

As in the first experiment, ASEC added several GaAs cells grown on Ge with inactive GaAs/Ge interfaces. These cells have an emitter thickness of about 0.5 $\mu$m compared to the 0.25-$\mu$m-thick emitters found in the GaAs and AlGaAs cells grown at RTI.

The irradiation of the devices was effected at JPL under the direction of Dr. B.E. Anspaugh. The cells, those grown and processed at RTI and GaAs/Ge cells from the ASEC process line, were divided into three groups. One group was irradiated at a fluence of $10^{15}$ cm$^{-2}$, the second at $5 \times 10^{15}$ cm$^{-2}$, and the third at $10^{16}$ cm$^{-2}$. Unfortunately, there was no sequential irradiation with measurement after each level of exposure.

After irradiation, workers at ASEC remeasured the I-V characteristics and the quantum efficiencies at wavelengths of 450 and 800 nm. The cells were then returned to RTI, where they were also remeasured. There was again good agreement between the two sets of measurements. Several of the AlGaAs and GaAs samples were returned to SERI for remeasurement of the defect content by DLTS.

The BOL efficiencies for the cells used in the second experiment were typically higher than those of the cells from the first experiment. The Ge-cell efficiencies

ranged from 4 to 6 percent, and $Ge_{0.93}Si_{0.07}$ efficiencies were about 5 percent. These values were measured under a xenon-lamp simulator and may be slightly high because of high currents. $Al_{0.08}Ga_{0.92}As$ homojunction cells varied from 15 to 19 percent, and graded-emitter cells varied from 14 to 17 percent. AlGaAs cells for which the emitter changed composition in discrete steps had BOL efficiencies of 14 to 17 percent. GaAs cell efficiencies were 17 to 20 percent, and cells with AlGaAs graded-composition emitters and GaAs bases had 13 to 19 percent efficiencies. The BOL efficiencies of these cells are high enough to extract useful information and are important because cells with lower efficiencies will generally show less effects of radiation damage.

## Results

While, overall, the experiment went smoothly, some difficulties were encountered. A decision to test separate groups of cells at different fluences, rather than using sequential irradiation, was made to reduce the risk of damaging the cells during repeated measurements between irradiations, but this decision also reduced the sample size for each fluence. These smaller sample sizes prevented resolution of some discrepancies in the observed degradation data. Attempts to extract quantitative damage coefficients were hampered by the spread in the initial quantum efficiency values. The relatively small changes in quantum efficiencies at lower fluences made determination of the diffusion lengths $L_n$ difficult. And since the damage coefficient K and $L_n$ are related usually by the expression

$$\frac{1}{L_{n\phi}^2} = \frac{1}{L_{no}^2} + K\phi$$

where $L_{n\phi}$ and $L_{no}$ and the diffusion lengths after and before irradiation, respectively, at the fluence of $\phi$, uncertainty in $L_n$ produces uncertainty in K.

Despite these difficulties, several conclusion about the trends in the data can be made.

1. Ge and $Ge_{0.93}Si_{0.07}$ cells show substantial resistance to radiation damage even at the highest fluences, confirming predictions made in our original proposal.

2. Although having lower beginning values for the product of $J_{sc}$ and $V_{oc}$, the AlGaAs cells, regardless of emitter configuration, degrade less than the GaAs and GaAs-on-Ge cells.

3. Within the AlGaAs group, the graded-band-gap cells fail to show the performance advantage that was observed in the first experiment, i.e., shallow homojunction cells performed as well or better.

4. The GaAs cells with the 0.25-$\mu$m-thick emitters degrade less than the cells with 0.5-$\mu$m-thick emitters, which is a trend generally observed for cells.

These trends can be seen in Figure 1 that shows the post-irradiation efficiencies normalized to pre-irradiation values as a function of fluence. The data points are the averages of the cells irradiated at that fluence, and because of dividing the samples that is mentioned above, each point represents usually no more than three to four cells, which, unfortunately, is a small sampling size.

From the data shown in Figure 1, the performance of the Ge and $Ge_{0.93}Si_{0.07}$ cells is clearly outstanding. Even at a fluence of $10^{16}$ electrons/cm$^2$, these cells have retained 85 percent of the BOL efficiency. And a single Ge cell, upon which a 3-$\mu$m-thick $Al_{0.08}Ga_{0.92}As$ layer had been grown, performed even better, retaining about 94 percent of the BOL efficiency. This latter cell represents the structure of an AlGaAs/Ge cascade cell and clearly indicates that this cascade cell, or any other using Ge as the bottom junction, will likely by limited by the radiation resistance of the top cell.

Since cell fill factors changed by no more than two to five percent for all of the cells in the test, the differences in the normalized GaAs and AlGaAs data must reflect differences in $V_{oc}$ and/or $J_{sc}$. For the GaAs and AlGaAs cells, the ratios of pre- and post-irradiated $V_{oc}$ and $J_{sc}$ are plotted versus the fluence in Figure 2. The data show that the voltage degrades comparably for both GaAs and AlGaAs, indicating that the changes in the normalized efficiencies must come from changes in the current collection, i.e., changes in diffusion length and minority-carrier lifetime. The AlGaAs cells retain about 70 to 75 percent of the current. The thickness of the GaAs cell emitters significantly impacts current collection. The 0.25-$\mu$m-thick-emitter cells retain about 50 percent more current than the cells with the thicker emitters at $10^{16}$ electrons/cm$^2$.

The change in the current collection in the GaAs and AlGaAs cells was examined further by considering the spectral response of these cells. This is shown in Figures 3 and 4. The data in Figure 3 were gathered with ASEC's two-source (tungsten and xenon) simulator, using the sources separately to illuminate the samples. For the AlGaAs cells, the "red" and "blue" responses from tungsten and xenon, respectively, degrade at about the same rate although the normalized ratio is lower for the "red". For the GaAs cells with thin emitters, the degradation is only slightly greater than for the AlGaAs cells. The thick-emitter GaAs cells show an initial rapid decrease in both the "red" and "blue" regions followed by a slowing of the degradation rate, but still greater than for the AlGaAs cells.

Figure 4 shows measured quantum efficiencies at wavelengths of 450 and 800 nm as a function of fluence for the AlGaAs and GaAs cells and confirms the simulator data shown in Figure 3. The higher starting values for the GaAs-based cells indicate longer diffusion lengths, but the slower rate of decrease for the AlGaAs-based cells supports the conclusion that the diffusion length changes less, producing the observed

higher current ratios for those cells. And since this is the case for both short and long wavelengths, we infer qualitatively that the degradation coefficient is lower in AlGaAs than GaAs for both the base and emitter regions.

Normalized data present only part of the necessary information to evaluate radiation damage characteristics. Efficiency data must also be considered. Since the fill factor changes were small, plotting the $J_{sc}$ $V_{oc}$ product provides the additional information. This is shown in Figure 5. The key result here is that, while initially having lower $J_{sc}$ $V_{oc}$ products than GaAs cells, the AlGaAs-cell performance equals the GaAs-cell performance at an EOL fluence of $10^{16}$ electrons/cm$^2$, and, because the AlGaAs degradation proceeds at a slower rate, will outperform GaAs at higher fluences. This may be pivotal for long-duration flights or high-radiation-intensity orbits. In Figure 6 also note the stability of the output of the Ge and GeSi cells.

The DLTS data for the cells are currently being analyzed and will be reported at a later date.

## Conclusions

In summary, a second radiation-resistance experiment has shown qualitatively that AlGaAs solar cells degrade more slowly the GaAs cells. We were somewhat disappointed that clear evidence favoring graded-band-gap emitters over homojunction emitters could not be concluded from the data. Because of the slower degradation, the performance of the AlGaAs cells equalled that of GaAs at a 1-MeV electron fluence of $10^{16}$ cm$^{-2}$. Because of some discrepancies in the data, we were unable to determine quantitative damage coefficients for AlGaAs to compare with the published data for GaAs.

Ge and GeSi cells, added for this experiment, showed remarkable resistance to damage. Both Ge and $Ge_{0.93}Si_{0.07}$ cells demonstrated BOL/EOL ratios of about 0.85 at $10^{16}$ electrons/cm$^2$. A Ge junction with a 3-$\mu$m-thick AlGaAs cap showed a BOL/EOL ratio of 0.94 at that fluence.

And, finally, thin emitter GaAs cells outperformed thicker-emitter cells. While this is not unexpected, it may suggest that there are processing optimizations yet to be done to examine the trade-offs between emitter thickness influence on yield versus the resistance to radiation-induced damage. It was clear that the thinner emitter cells produced at RTI were more susceptible to probing damage during I-V and spectral measurements.

## References

1 M.L. Timmons, R. Venkatasubramanian, T.S. Colpitts, J.S. Hills, J.A. Hutchby, P.A. Iles, and C.L. Chu, *Graded Bandgap AlGaAs Solar Cells for AlGaAs/Ge Cascade Cells*, Proceedings of the Space Photovoltaic Research and Technology Conference, 1989, (NASA Conference Publication 3107), p. 48.

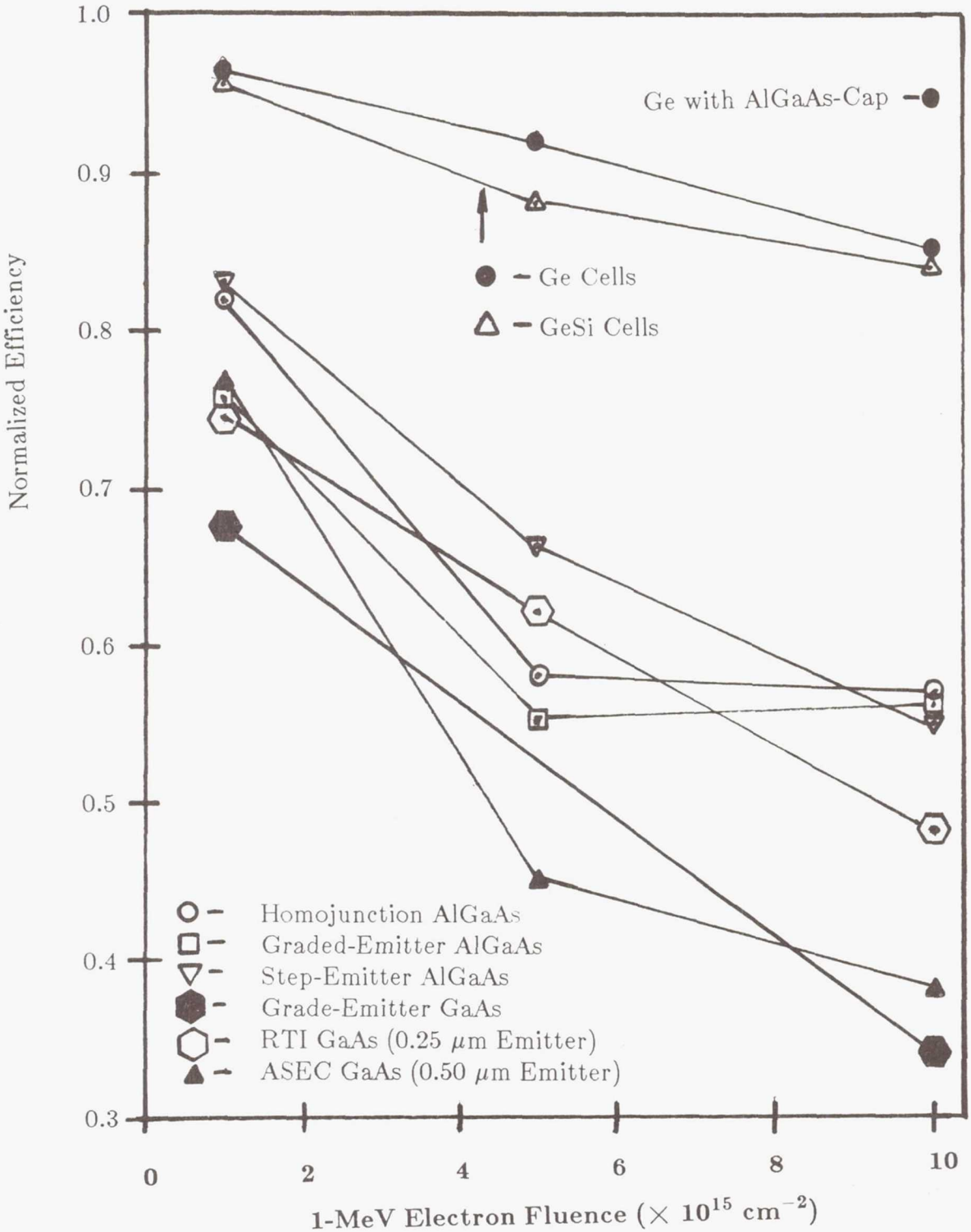


**Figure 1.** Normalized efficiencies versus fluence for the AlGaAs, GaAs, Ge, and GeSi solar cells after irradiation with 1-MeV electrons.

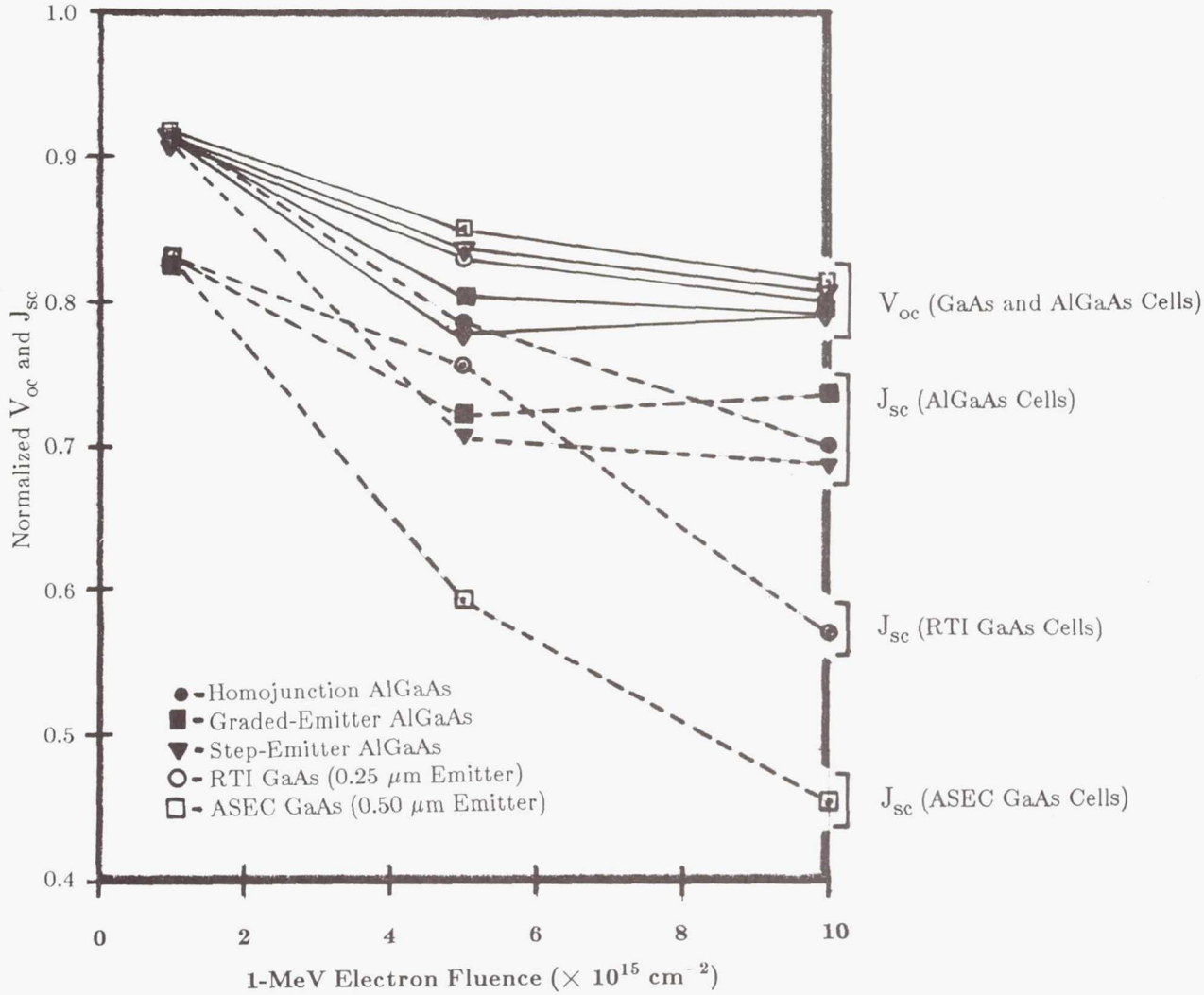


**Figure 2.** Normalized values of $J_{sc}$ and $V_{oc}$ versus fluence for the GaAs and AlGaAs solar cells that were part of this experiment. The dashed lines show current, and solid lines show voltage.

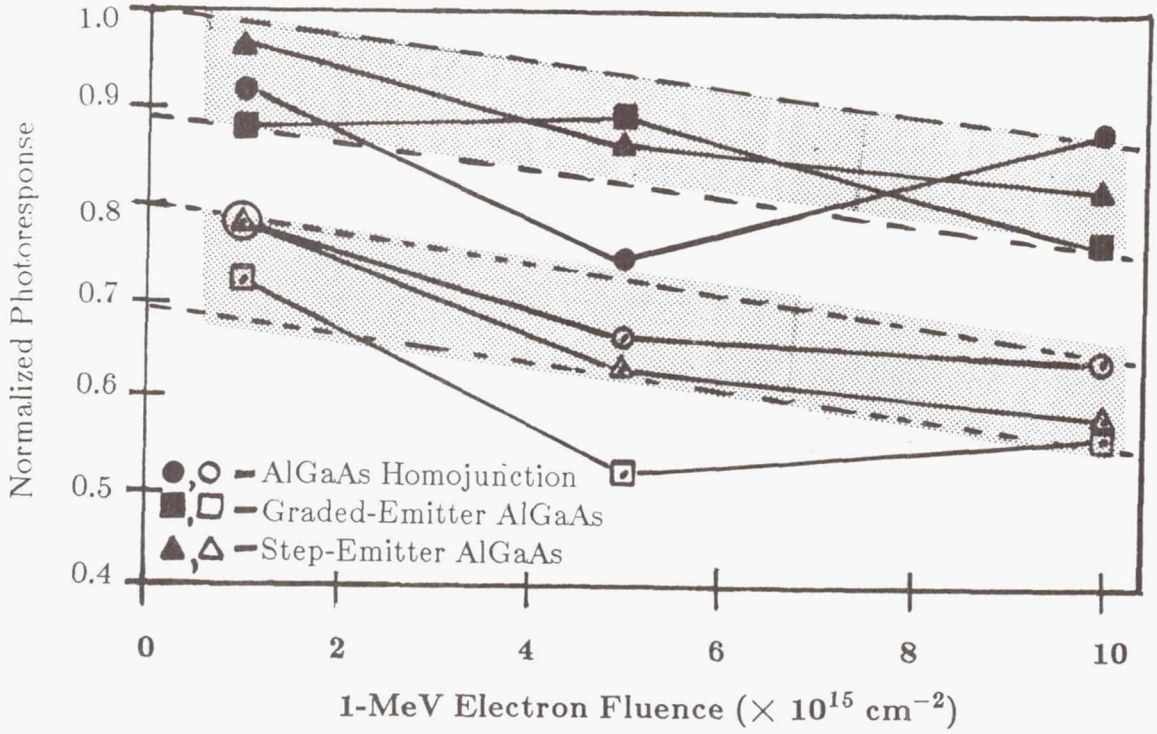


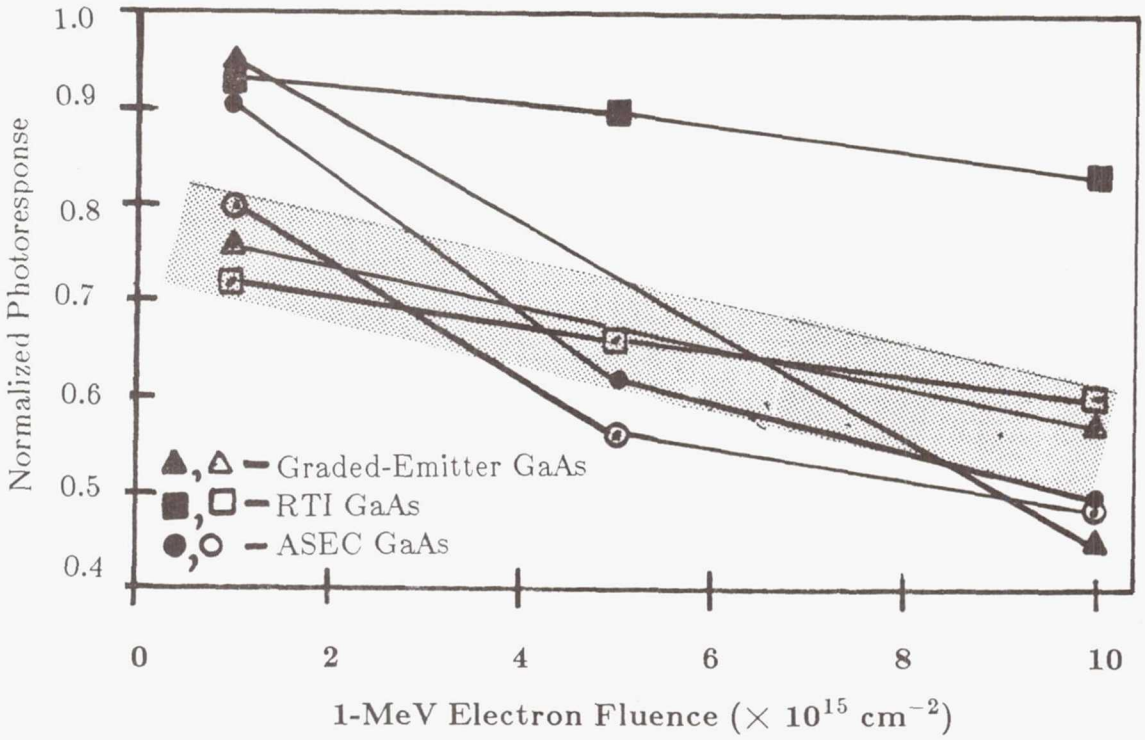


**Figure 3.** Normalized photocurrents versus fluence from a two-source solar simulator using the xenon and tungsten sources separately to illuminate the cells. This technique produces qualitative "blue" (closed symbols) and "red" (open symbols) responses.

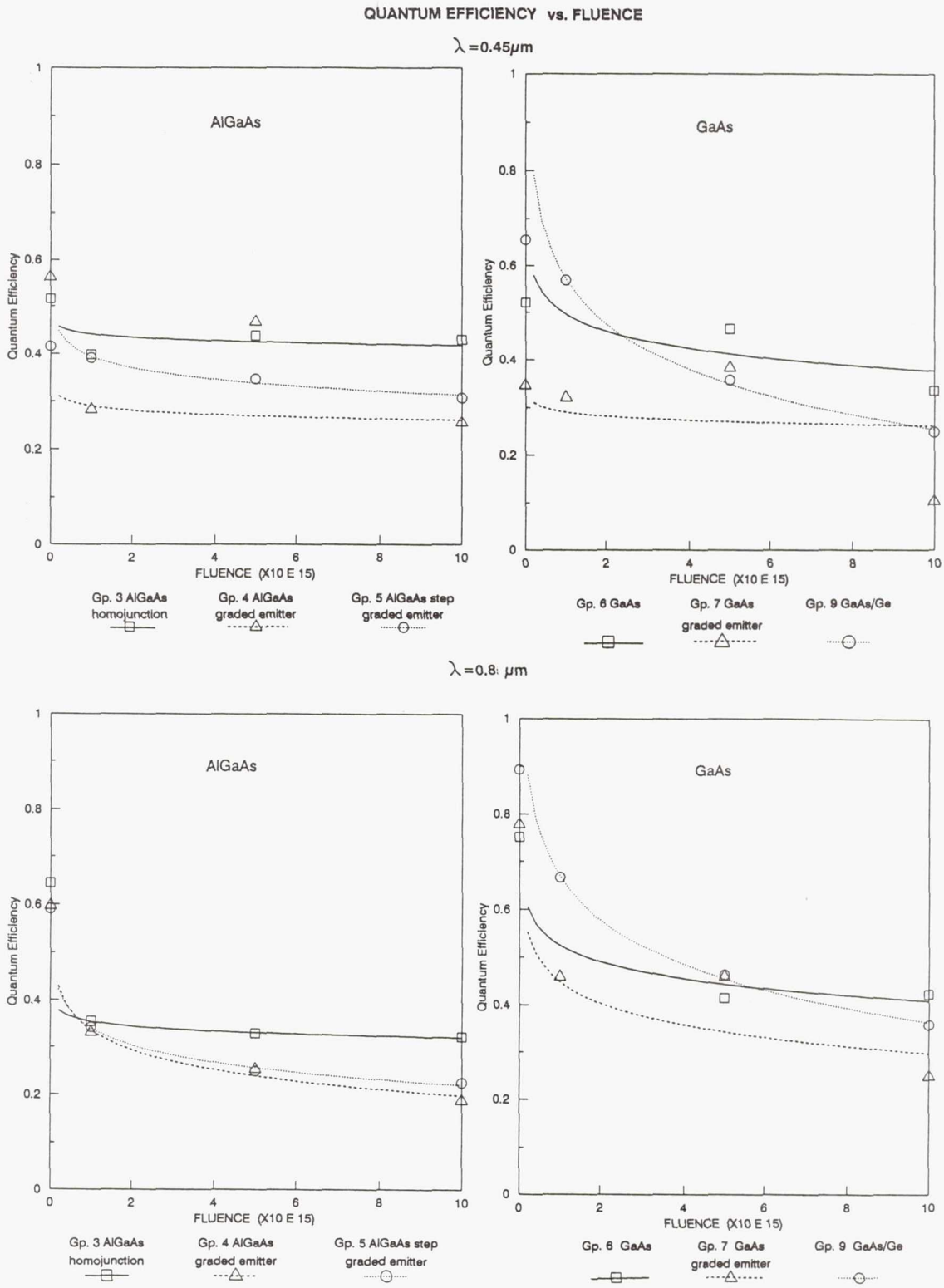


**Figure 4.** Quantum efficiency measurements as a function of fluence made at wavelengths of 450 and 800 nm for GaAs and AlGaAs solar cells.

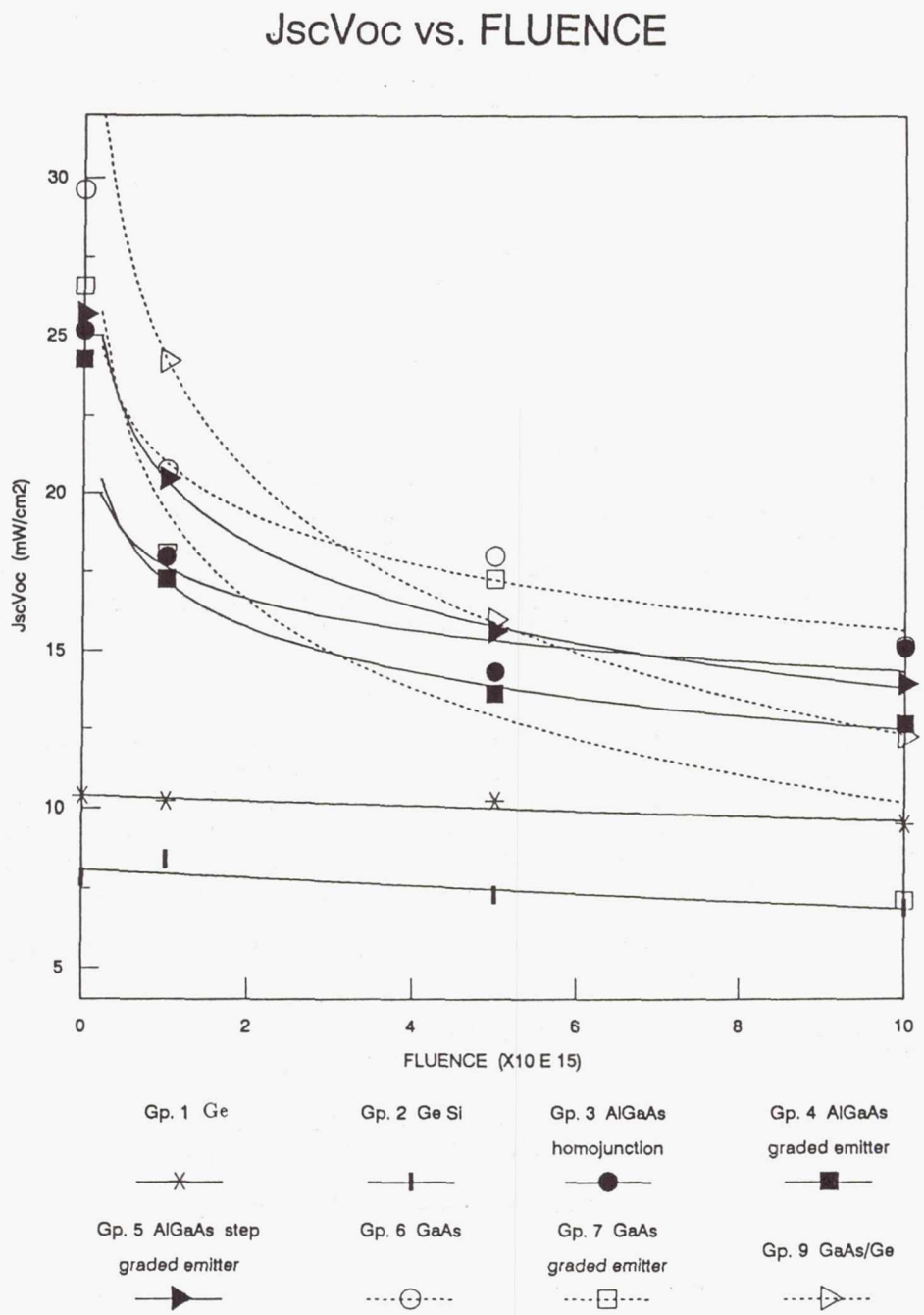


**Figure 5.** The product of $J_{sc}$ and $V_{oc}$ as a function of fluence for GaAs and AlGaAs solar cells. The a fluence of $10^{16}$ $cm^{-2}$, the performance of the GaAs and AlGaAs cells are equal.

# GALLIUM ARSENIDE SOLAR CELL RADIATION DAMAGE EXPERIMENT

R. H. Maurer, J. D. Kinnison, and G.A. Herbert
The Johns Hopkins University Applied Physics Laboratory
Laurel, Maryland

and

A. Meulenberg
COMSAT Laboratories
Clarksburg, Maryland

## ABSTRACT

Gallium arsenide (GaAs) solar cells for space applications from three different manufacturers were irradiated with 10-MeV protons or 1-MeV electrons. The electrical performance of the cells was measured at several fluence levels and compared. Silicon cells were also included for reference and comparison. All of the GaAs cell types performed similarly throughout the testing and showed a 36-56% power areal density advantage over the silicon cells. Thinner (8-mil versus 12-mil) GaAs cells provide a significant weight reduction and the use of germanium (Ge) substrates to improve mechanical integrity can be implemented with little impact on end-of-life performance in a radiation environment.

## INTRODUCTION

Interest in gallium arsenide (GaAs) solar cells for space applications is increasing to the point where a significant percentage of near-future space missions will employ these cells as the primary power source. With these applications in mind, The Johns Hopkins University Applied Physics Laboratory (APL) was funded by the joint NASA-CNES MFE-Magnolia study program to carry out the radiation testing described in this paper. This electron and proton radiation experiment was a follow-on to some previous work performed by APL (ref. 1). The fundamental goals of this experiment were to do the following:

1. Verify the suitability of all of these GaAs cell types, primarily of production line quality (and availability), for use in a low-earth radiation environment.

2. Provide data on the bare and covered Mitsubishi cells for the Magnolia program (CNES-France). CNES is responsible for the solar cell array design and delivery for this program.

3. Compare the performance, both before and after charged particle irradiation, of present-day GaAs cells from different manufacturers, including a check against silicon cells.

4. Increase the precision of the measurements by using larger sample sizes and fewer variables than previous experiments.

A total of 48 cells were tested from three manufacturers: Mitsubishi Corporation, Applied Solar Energy Corporation (ASEC), and Spectrolab, Inc.

APL purchased bare cells from ASEC and Spectrolab, made electrical connections, bonded the cells to a small plate, and mounted the cover slides. The Mitsubishi cells were provided by Mitsubishi (through CNES) with tabs and covers already attached. Electrical data were taken at APL; proton irradiation was accomplished using the Brookhaven National Laboratory (BNL) tandem Van de Graaff, and electron irradiation was supplied by the Van de Graaff at Goddard Space Flight Center (GSFC). Compatibility with existing radiation data was achieved by using 10-MeV protons and 1-MeV electrons in addition to providing a damage equivalence factor measurement. Described below are the solar cells tested, the test and measurement techniques used, and significant results and conclusions.

## TEST ARTICLES

Five different cell types were included in the testing and are defined in Table 1. It was assumed that the cell types were "production line quality," meaning that the manufacturing specifications were reasonably well established and large quantities of the cells could be purchased at the present time.

## TEST AND MEASUREMENT TECHNIQUES

### CELL USAGE AND MOUNTING

Two separate wheels were rotated through the radiation beam: one for electron irradiation and one for proton irradiation. Each wheel could hold a total of 24 cells. Two of the silicon cells, two of the Spectrolab GaAs/Ge cells, and five each of the remaining four types were mounted on the wheel. The cover slides were 6-mil ceria-doped Microsheet; these were used on all cells except for two Mitsubishi cells on the proton wheel and three on the electron wheel, which remained bare. In addition to the 48 irradiated cells, 12 were used as control cells (two of each type).

### PROTON IRRADIATION

The proton doses were obtained using the BNL tandem Van de Graaff. Particle energy was 10 MeV, and beam currents ranged from 5 to 200 nA. The beam was rastered up and down at a frequency of four cycles per second as the wheel was rotated at 33 rpm. The shortest run time was 129 s, which corresponded to 71 rotations of the wheel. Dosimetry was performed by taking several readings with a Faraday cup before exposing the wheel and repeating this procedure once during and following the exposure. By averaging several readings and adjusting the run time to compensate for slight drifts in the beam current, the actual total doses are within a few percent of what was desired.

Data (solar cell I-V curves) were taken at fluence levels of 0 (beginning-of-life—BOL), $10^{10}$, $5 \times 10^{10}$, $10^{11}$, $10^{12}$, and $10^{13}$ (end-of-life—EOL) protons/cm$^2$.

### ELECTRON IRRADIATION

As in reference 1, the GSFC Van de Graaff was used to achieve the electron fluences. By breaking the beam pipe, a flux level of $10^{13}$ 1-MeV electrons/cm$^2$ per second was achieved, resulting in the final run time of approximately 6 hours. The electron energy was 1 MeV. The fluence was calculated by using measurements from a Faraday cup before and after the exposures and monitoring the beam current during the run. The beam current chosen (0.5 $\mu$A) remained quite stable over time.

Data were taken at fluence levels of 0, $5 \times 10^{13}$, $10^{14}$, $5 \times 10^{14}$, $10^{15}$, and $10^{16}$ electrons/cm$^2$.

### CELL ELECTRICAL CHARACTERISTICS MEASUREMENT

Care was taken throughout this testing to maintain consistency and accuracy of the measurement of the cell electrical characteristics.

#### Solar Simulation

A xenon flash lamp, formally termed a medium area pulsed solar simulator (or MAPSS), located at APL was used to measure the current-voltage (I-V) curves of the cells. The light pulse covers an area of 60 ft$^2$ for a duration of 2 ms, during which time the I-V curve is swept. The test articles were always placed in the same spot in the test plane, very close to the standard cells, and were tested at room temperature (23°C).

The spectral quality of this source is not ideal for testing damaged solar cells but provides accurate BOL data (±0.5%) on all cells and EOL ($10^{16}$ 1-MeV electrons/cm$^2$) data that is conservative by 2-5% in current and power. Reference 3 discusses the cross calibration work that was done between this simulator and a modified X-25 solar simulator in use at COMSAT Laboratories. The modifications of the COMSAT X-25 include additional filtering to provide a nearly ideal spectral match to the sun. However, the data presented in the figures below are not corrected for spectral match.

The inaccuracies of the MAPSS are due to the excess red (infrared) and blue energy of the xenon lamp as compared to 1 sun in space (AM0). The intensity in the mid-region of the spectrum is actually less than 1 sun AM0 to compensate for these excesses. For undamaged cells, this is easily overcome by using calibrated standards of the same type as the test article. As the cells are damaged, their spectral response changes such that they are not receiving a full 1 sun AM0 (in the mid-spectrum region), but the undamaged standard cell still does receive the proper illumination, resulting in a low reading on the test article. As the damage gets worse, so does the accuracy. This problem could also be overcome by using cells that are damaged to the same level as the test articles and then calibrated as standards, but this would be difficult and expensive. The voltage measurements are primarily dependent on the cell temperature and are typically within 2 mV (~1°C).

The MAPSS does have the advantage of not heating the cell during the measurement, producing consistent results and performing many measurements in a short time period. A wheel of 24 cells could be tested in about an hour.

### Standard Cells

Two secondary standards were used throughout this testing: a 2 × 4 cm K6 silicon cell from Spectrolab and a 2 × 4 cm GaAs cell made by ASEC. The silicon cell was provided by Spectrolab as a standard to be used with a recent flight program and was of the same type as the K6 cells used in the test. The GaAs cell was calibrated using a primary standard at COMSAT Laboratories with the X-25 solar simulator mentioned above.

Both of these standards, along with a 2 × 2 cm K4 type silicon, were mounted on blocks with 28°C water circulating through them. All data are referenced to 28°C. The small silicon cell was used as a standard when the other standards were put through the test input as a system check. This was done following each set of measurements on each wheel.

### Measurement Temperature Corrections

Typically, a 5°C temperature correction was made by the MAPSS computer to adjust between the 23°C test cell temperatures and the 28°C standard cell temperatures. The correction factors used were 2.2 mV/°C and 0.025 mA/°C/cm$^2$ for the silicon cells and 2.0 mV/°C and 0.020 mA/°C/cm$^2$ for the GaAs cells (ref. 4). Any errors in these correction values would result in quite small errors in the final electrical data, well within the overall uncertainty of the measurements.

## EXPERIMENTAL RESULTS

The mean values of the parametric results on five samples each of the ASEC GaAs, Mitsubishi GaAs, Spectrolab GaAs, and ASEC GaAs/Ge solar cells, as well as two samples of the K6 silicon cells were analyzed. These 22 solar cells were subjected to each type of radiation, 1-MeV electrons or 10-MeV protons. Analysis of these two data sets consisted of graphical displays and a statistical analysis of variance (ANOVA). The ANOVA on the initial maximum power density ($P_{max}$) values gave an experimental error of 3.13 mW for cells with mean values from 185 to 210 mW.

## GALLIUM ARSENIDE SOLAR CELL DISPLACEMENT DAMAGE

Figures 1-6 show the electrical responses of cell open-circuit voltage ($V_{oc}$), short-circuit current density ($I_{sc}$), and $P_{max}$ versus both electron (Figures 1, 3, and 5) and proton (Figures 2, 4, and 6) fluences in particles/cm$^2$. The Spectrolab GaAs/Ge cells are excluded from this part of the discussion because of their classification as prototype cells instead of production line cells.

Initially, the GaAs cells from all three manufacturers have efficiencies in the 18-19% range and power densities in the 24-26 mW/cm$^2$ range (see Table 2). The five ASEC GaAs cells selected for electron exposure were statistically better (at a 95% confidence level), with a mean efficiency exceeding 19% and a mean power density exceeding 26 mW/cm$^2$, by small margins in each case. Otherwise, there were no significant differences among the six cell groups (three for electron exposure and three for proton exposure). The less mature ASEC GaAs/Ge cells have a lower efficiency and power density (16.5-17.5% and 22.5-23.5 mW/cm$^2$). We note that prototype GaAs cells studied around 1978 had power densities of 22 mW/cm$^2$ (ref. 5).

Figures 1-6 show that the GaAs cell electrical parameters from the various manufacturers degrade in a similar manner, with their degradation curves having similar shapes. After $10^{16}$ 1-MeV electrons/cm$^2$, the Mitsubishi cells are the superior performers with efficiencies 9.4% and power densities of 12.7 mW/cm$^2$. After $10^{13}$ 10-MeV protons/cm$^2$, the Mitsubishi GaAs cells are also superior (at a 95% confidence level), with a mean efficiency of 9.7% and a mean maximum power density of 13.2 mW/cm$^2$. However, in less severe radiation environments ($<10^{15}$ e/cm$^2$ or $<10^{12}$ p/cm$^2$), the lower starting efficiences of the Mitsubishi and GaAs/Ge cells may be a handicap. The lower BOL efficiences for the ASEC GaAs/Ge cells are due to their being early cells coming off the production line. Efficiences equal to the pure GaAs cells have been subsequently reported by the manufacturer for these cells.

## GALLIUM ARSENIDE VERSUS SILICON SOLAR CELLS

Figures 1-6 include the degradation curves for the K6 series silicon solar cells, a space industry standard. The most interesting of these are Figures 5 and 6, which compare the maximum power densities of the silicon and GaAs cells.

The degradation curves for $P_{max}$ of the silicon cells versus particle fluence are quasi-linear on these semi-log plots, whereas the like curves for the GaAs cells exhibit a sharp increase in slope above $10^{15}$ electrons/cm$^2$ and $10^{12}$ protons/cm$^2$. This increase in rate of degradation for the GaAs cells is such that their absolute maximum power densities will eventually be less than those of the silicon cells at very high fluence levels ($>10^{16}$ electrons/cm$^2$ and $>10^{13}$ protons/cm$^2$). This phenomenon has been observed before (refs. 4,5). For space missions of moderate duration in nominal natural environments, GaAs cells are obviously superior; however, in extremely severe environments, silicon cells would have better EOL values.

Figures 7 and 8 show the absolute spectral responses of typical individual silicon and GaAs cells before and after 1-MeV electron irradiation to $2 \times 10^{16}$ electrons/cm$^2$. Figure 7 shows that the bulk of the electron displacement damage affects the red part of the spectrum. Figure 8 shows that GaAs cells suffer electron displacement degradation to both red and blue wavelength response.

As a final comment we note that our previous experiment showed that the maximum power of thin silicon cells (2.5-3 mils) was not significantly different from that of K6 series cells (8 mils thick) after very high fluences ($2 \times 10^{16}$ 1-MeV electrons/cm$^2$) (ref. 1). However, in the denser GaAs cells a 4-mil thickness differential (from 12 to 8 mils) removes about twice the amount of material as contrasted to the 5-mil differential in the 8-mil and 3-mil silicon cells.

## DAMAGE EQUIVALENCE FACTORS

By using the data on relative $P_{max}$ versus electron fluence or by examining the fits to the data, we can determine damage equivalence factors between 10-MeV protons and 1-MeV electrons for the GaAs so-

lar cells. These factors are calculated by taking the ratio of 1-MeV electron fluence to 10-MeV proton fluence at the same damage level, e.g., 80% relative or normalized $P_{max}$. For a baseline comparison we compute a damage equivalence factor for the K6 silicon cells. Table 3 shows these data. These data are in good agreement with those of Anspaugh and Downing (ref. 6), except for the silicon cells at relative $P_{max}$ values of 0.5 and 0.6, where 10-MeV protons become more damaging for the K6 cells with back surface reflectors (BSR) (ref. 6). (The Anspaugh and Downing data were for cells with no BSR.)

The damage equivalence factors for the GaAs cells remain fairly constant over two orders of magnitude in proton ($10^{11}$-$10^{13}$ protons/cm$^2$) and electron ($10^{14}$-$10^{16}$ electrons/cm$^2$) fluence. The low end of the ranges for GaAs is for the Mitsubishi 8-mil GaAs and ASEC GaAs/Ge cells, the two sets of cells with lower starting efficiences.

The bare Mitsubishi cells suffered less damage (~2% in power) than those with 6-mil cover slides, as expected for protons but not, a priori, for electrons. (Cover slide reduction of beam intensity and average energy may be less important than its reduction in net backscattering from the GaAs.) This means that cells to be tested should be covered and with the same cover slide thickness.

Of course, any predictions for space missions must take into account the variation of damage equivalence factors with proton energy (lower-energy protons are relatively more damaging, particularly in GaAs) and the omnidirectional incidence of the particles as contrasted to the normally incident particles used to generate these data.

The similarity of the shapes of the degradation curves for both proton and electron irradiated cells and associated damage analysis are discussed in detail elsewhere (ref. 7). The differences between silicon and GaAs cells in Figures 1-6 are attributed to the monatomic and diatomic crystal structures. Under heavy irradiation by electrons (producing only point defects), the monatomic structure provides annealing by recombination of silicon vacancies and interstitials. The diatomic structure provides additional permanent defects by recombination of Ga interstitials with As vacancies (and vise versa). The difference between silicon and GaAs cells in Table 3 results from the competition of the proton-generated cluster defects with the annealing and increased degradation effects above. Cluster defects reduce annealing in silicon, thereby increasing the damage equivalence factors at high fluences. They reduce point-defect formation, by trapping primary mobile defects, thereby decreasing the damage equivalence factors at high fluences for GaAs.

## EFFECTS OF JUNCTION DEPTH AND MATERIAL PROPERTIES IN GALLIUM ARSENIDE CELLS

Figure 9 shows a plot of mean relative $P_{max}$ versus electron fluence for three types of ASEC GaAs solar cells. In the previous experiment we had a 12-mil thick GaAs cell with a 0.7-$\mu$m junction depth (ref. 1). In this experiment we had both 12-mil GaAs cells with a 0.45-$\mu$m junction depth and 8-mil GaAs/Ge cells with a 0.45-$\mu$m junction depth.

It is readily seen from Figure 9 that junction depth is more important with respect to electron displacement damage than substrate material. After exposure to $10^{16}$ electrons/cm$^2$, the GaAs/Ge cell has a relative $P_{max}$ of 0.51 as compared to 0.47 for the GaAs cell of the same junction depth. In contrast, the GaAs cell with the 0.7-$\mu$m junction depth had a relative $P_{max}$ of 0.23. The effects of substrate material (Ge versus GaAs), ~8.5%, is probably negligible (since this difference is close to the difference in BOL maximum power values) whereas shallower junctions give improvement of a factor of 2. The importance of having junctions in GaAs cells less than 0.5 $\mu$m deep has been known for some time (ref. 4). The selection of doping levels to maximize EOL performance, common for silicon cells in a radiation environment, might be seen for GaAs in the differences between the BOL $V_{oc}$ and EOL $I_{sc}$ values for the Spectrolab and Mitsubishi cells (Table 2 and Figure 4). The crossover in $P_{max}$ (Figures 5 and 6) may be accidental or the result from a deliberate attempt to optimize performance at BOL.

## DISCUSSION AND CONCLUSIONS

Gallium arsenide solar cells and the manufacturing processes have matured to a level that makes them quite attractive for use in many space applications. Sample sizes of five give a high level of confidence in the results since standard deviations were relatively small. Coefficients of variation for the initial values of $P_{max}$ are in the range of 1-2.5%. All of the goals stated in the introduction were met satisfactorily by this experiment.

A typical low-earth orbit (LEO) mission may have a total radiation fluence in the range of $1\text{-}5 \times 10^{14}$ equivalent 1-MeV electrons/cm$^2$. Our data show (Figure 3) that the EOL power per unit area will be 36-56% greater for a typical GaAs cell than for a K6-type silicon cell for such a mission. For very severe environments ($>10^{16}$ electrons/cm$^2$), we have corroborated previous results for the greater EOL power density of silicon cells. However, this may be overcome by in-orbit annealing techniques since defects in GaAs are repaired at much lower temperatures than those in silicon. We found the damage equivalence factor for 10-MeV protons (to 1-MeV electrons) to be approximately 1000 and slowly varying over 2 orders of magnitude in proton and electron fluence.

The doping densities of the Mitsubishi GaAs cells give them a slight edge over the U.S. GaAs cells. The data on these thinner cells and the data on the 12-mil ASEC cells with two significantly different junction depths (Figure 9) provided a quantitative comparison of the effects of junction depth and material properties. Assuming BOL efficiencies equal to pure GaAs cells, GaAs/Ge cells should show a significant advantage for any use because of the structural integrity of Ge, the ability to make these cells thinner (as thin as the thinnest silicon cells, ~3 mil), and the equivalent EOL performance.

## REFERENCES


1. Herbert, G. A.; et al.: "Electron and Proton Displacement Damage in Production Line Quality Silicon and Gallium Arsenide Solar Cells," Proceedings of the 4th Int. Photovoltaic Science and Engineering Conf., Sydney, Australia, February 1989.

2. Tobin, S. P.; et al.: "High Efficiency GaAs/Ge Monolithic Tandem Solar Cells," Proceedings of the 20th IEEE Photovoltaics Specialists Conf., Las Vegas, September 1988.

3. COMSAT Laboratories Final Report, 602979-L, October 1988.

4. Weinberg, I.; et al.: "Radiation and Temperature Effects in Gallium Arsenide, Indium Phosphide and Silicon Solar Cells," Proceedings of the 19th IEEE Photovoltaics Specialists Conf., New Orleans, 4-8 May 1987, p. 548.

5. Rahilly, W. P.: "Radiation Effects on Solar Cells," in Space Systems and Their Interactions with Earth's Space Environment, H. P. Garrett and C. P. Pike, Editors, vol. 71, AIAA, New York, 1980.

6. Anspaugh, B. E.; and Downing, R. G.: Radiation Effects in Silicon and Gallium Arsenide Solar Cells Using Isotropic and Normally Incident Radiation, Jet Propulsion Laboratory Publication 84-61, September 1984.

7. Maurer, R. H.; et al.: "Gallium Arsenide Solar Cell Radiation Damage Study," IEEE Trans. Nucl. Sci., vol. 36, pp. 2083-2091, December 1989.

Table 1. - SOLAR CELL SPECTIFICATIONS

| Manufacturer | Cell Type | Area Dimensions (cm) | Thickness (mil) | Junction Depth ($\mu$m) | Manufacturing Process |
|---|---|---|---|---|---|
| 1. Mitsubishi | GaAs P/N | 2 × 4 | 8 | <0.6 | MOCVD |
| 2. ASEC | GaAs P/N | 2 × 4 | 12 | 0.45 | MOCVD |
| 3. Spectrolab | GaAs P/N | 2 × 4 | 12 | 0.5 | LPE |
| 4. ASEC | GaAs/Ge P/N Inactive Ge Substrate | 2 × 4 | 8 | 0.45 | MOCVD |
| 5. Spectrolab BSR, BSF N/P | K6 Si | 2 × 4 | 8 | 0.12 | Diffusion |

Table 2.—INITIAL MEAN ELECTRICAL PARAMETER DATA

| Cell | Maximum Power Density (mW/cm$^2$) | Efficiency (%) | Short Circuit Current (mA/cm$^2$) | Open Circuit Voltage (mV) | No. of Samples |
|---|---|---|---|---|---|
| Mitsubishi GaAs | | | | | |
| (e group) | 24.8 | 18.3 | 31.6 | 971 | 5 |
| (p group) | 24.6 | 18.2 | 31.5 | 970 | 5 |
| ASEC GaAs | | | | | |
| (e group) | 26.0 | 19.2 | 31.9 | 1000 | 5 |
| (p group) | 25.3 | 18.7 | 31.6 | 996 | 5 |
| Spectrolab GaAs | | | | | |
| (e group) | 25.0 | 18.6 | 29.8 | 1011 | 5 |
| (p group) | 25.3 | 18.7 | 30.0 | 1011 | 5 |
| ASEC GaAs/Ge | | | | | |
| (e group) | 23.4 | 17.3 | 31.2 | 956 | 5 |
| (p group) | 22.5 | 16.6 | 31.5 | 940 | 5 |
| Spectrolab K6 silicon | | | | | |
| (e group) | 19.7 | 14.6 | 43.0 | 606 | 2 |
| (p group) | 19.7 | 14.6 | 42.8 | 608 | 2 |

Table 3.—DAMAGE EQUIVALENCE FACTORS, $f = Q_e/Q_p$, FOR 1-Mev ELECTRONS AND 10-MeV PROTONS.

| Relative $P_{max}$ | GaAs | Silicon |
|---|---|---|
| 0.9 | 1130–1460 | 3880 |
| 0.8 | 1020–1470 | 3220 |
| 0.7 | 1000–1160 | 3600 |
| 0.6 | 960–1030 | 5220 |
| 0.5 | 890 | 6820 |

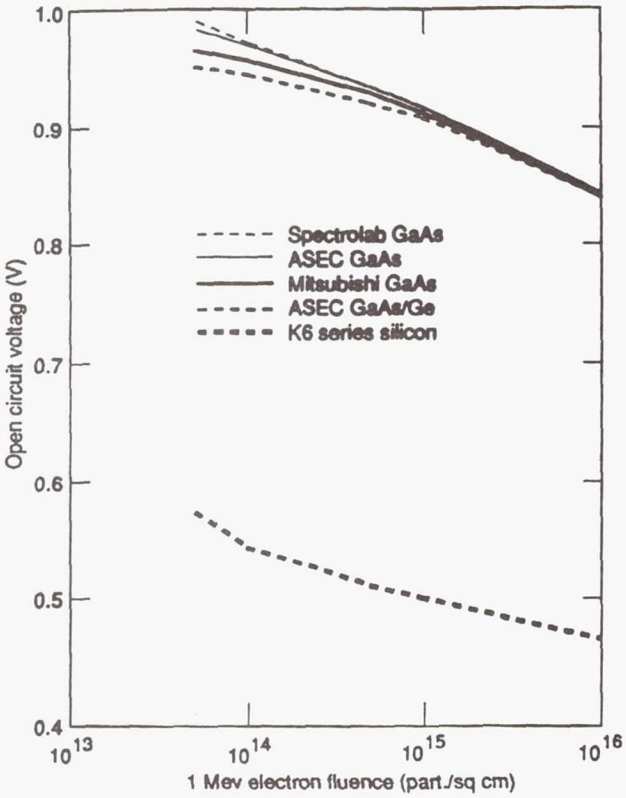


**Fig. 1 Solar cell open circuit voltage versus electron fluence**

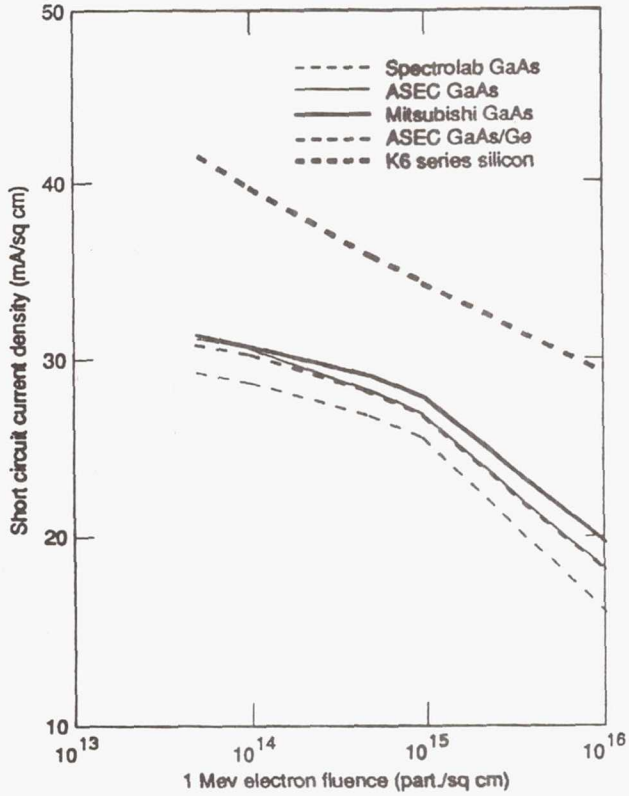


**Fig. 3 Solar cell short circuit current density versus electron fluence**

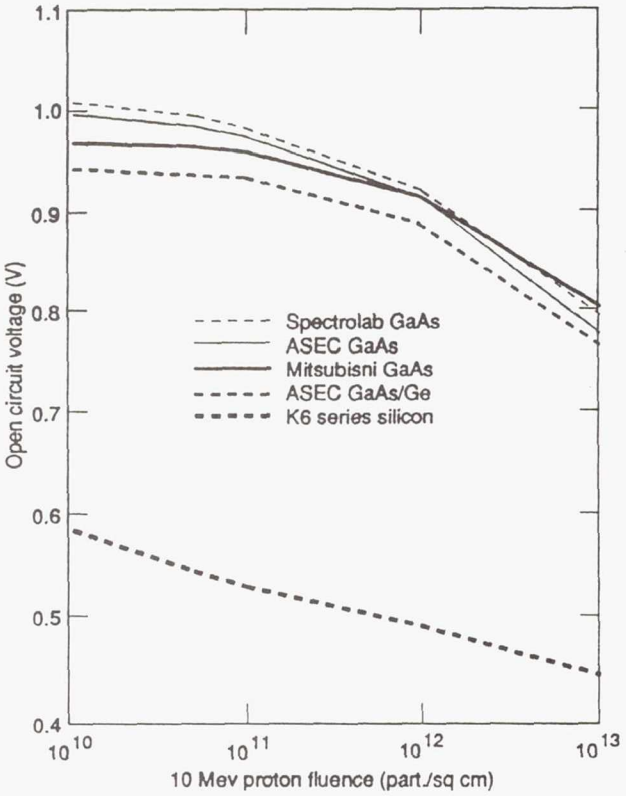


**Fig. 2 Solar cell open circuit voltage versus proton fluence**

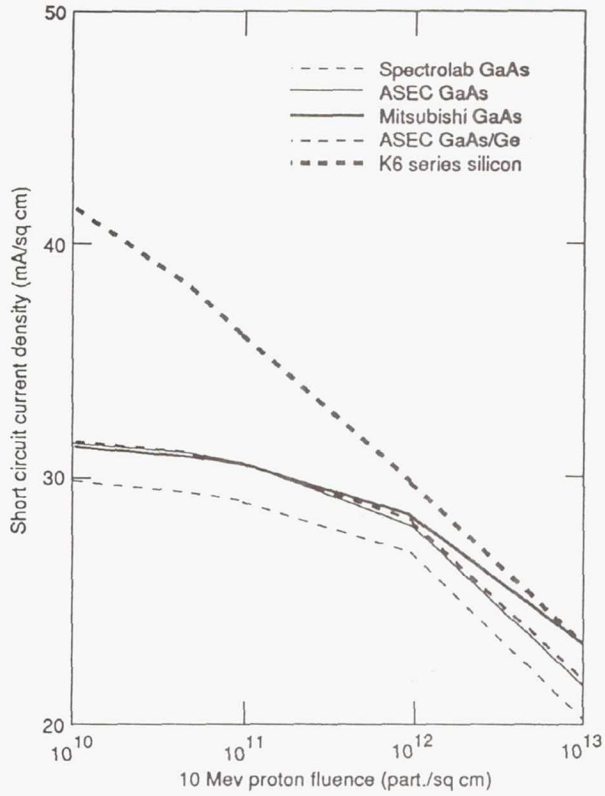


**Fig. 4 Solar cell short circuit current density versus proton fluence**

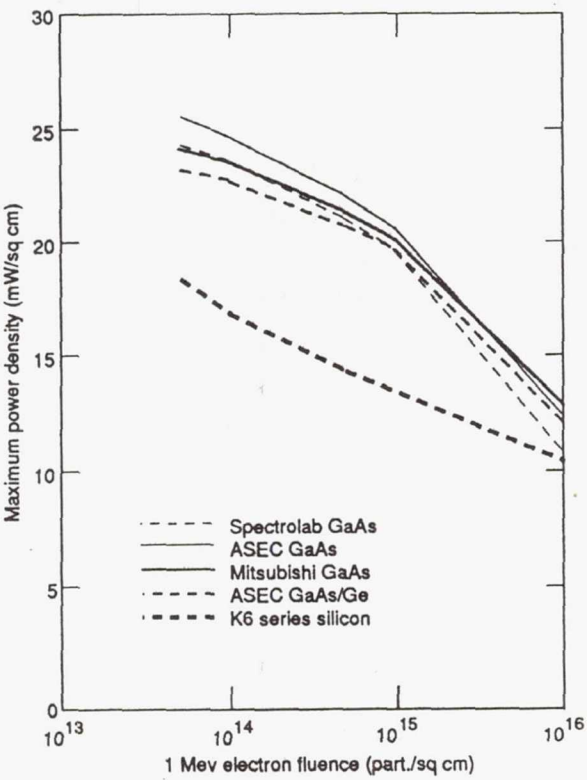


**Fig. 5 Solar cell maximum power density versus electron fluence**

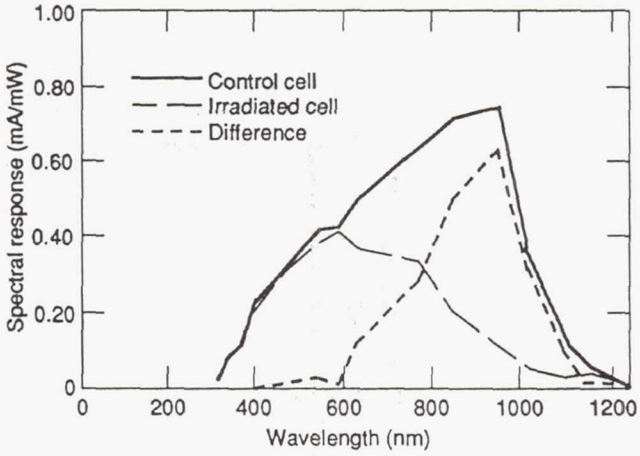


**Fig. 7 Control cell versus electron irradiated cell spectral response-Spectrolab K6.**

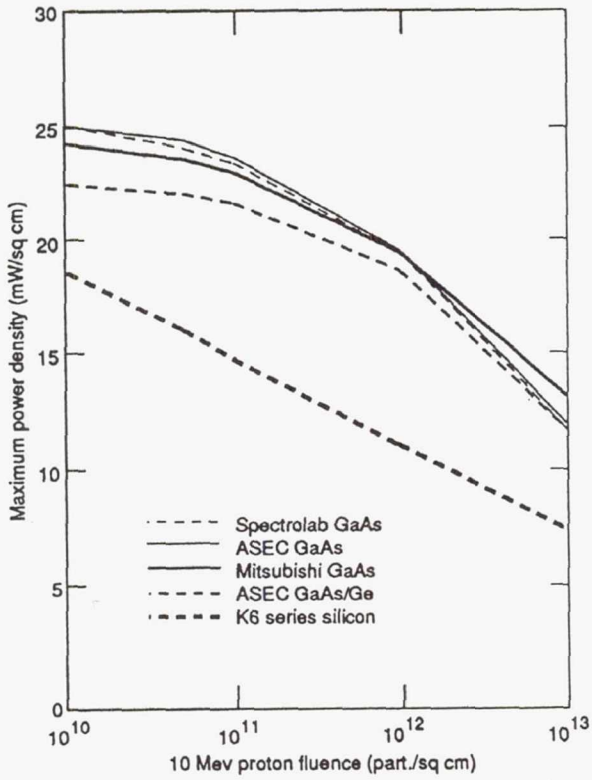


**Fig. 6 Solar cell maximum power density versus proton fluence**

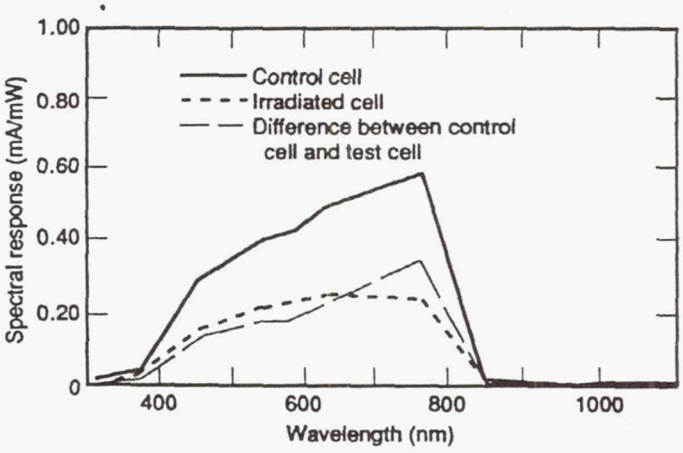


**Fig. 8 Spectrolab GaAs - electron irradiated**

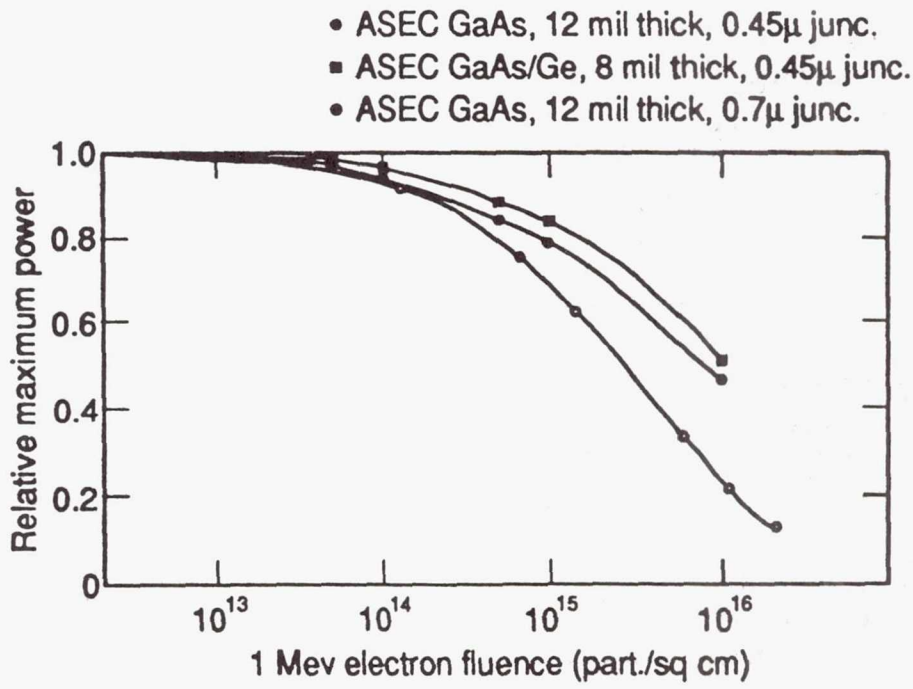


**Fig. 9 Relative maximum power versus electron fluence for GaAs solar cells of different thickness and junction depth.**

# I-V ANALYSIS OF IRRADIATED GALLIUM ARSENIDE SOLAR CELLS*

A. Meulenberg
COMSAT Laboratories
Clarksburg, Maryland

and

R. H. Maurer and J. D. Kinnison
The Johns Hopkins University Applied Physics Laboratory
Laurel, Maryland

While a spacecraft designer may only be interested in end-of-life (EOL) solar cell output power, analysis of the full I-V characteristics of unirradiated and irradiated cells can benefit both the solar cell designer and manufacturer, as well as those responsible for determining solar cell acceptance criteria. COMSAT Laboratories has used a computer program to analyze the illuminated I-V characteristics of four sets of gallium arsenide (GaAs) solar cells irradiated by the Johns Hopkins University Applied Physics Laboratory (APL) with 1-MeV electrons and 10-MeV protons.

The illuminated I-V characteristic provides the values (under operating conditions) for series resistance ($R_s$), minority carrier lifetime, internal electric fields, and other cell parameters which may depend on photo-generated carrier concentrations. A multi-regression fit of these data is made to the following equation:

$$I = I_{ro}\left[e^{q(V-IR_s)/2kT} - 1\right] + I_{do}\left[e^{q(V-IR_s)/kT} - 1\right] - (V - IR_s)/(R_{sh}) - I_L \qquad (1)$$

where

$I$ = output current

$I_{ro}$ and $I_{do}$ = coefficients of the junction recombination and bulk dark currents, respectively

$I_L$ = photo-generated short-circuit current

$V$ = cell voltage ($V - IR_s = V_j$, the junction voltage)

$R_{sh}$ = junction shunt resistance.

The short-circuit current, $I_L$, is subtracted and the data are fitted (with $R_s$ being stepped to obtain the best correlation) to determine values for $R_s$, $R_{sh}$, $I_{do}$, and $I_{ro}$. In the simplest analysis, these are all constants. The two currents separate the equation into contributions from bulk regions, $J_d$, and junction regions, $J_r$. (Current densities are used to remove area effects.) More detailed analysis (ref. 1) employs the full Sah-Noyce-Schockley formulation for $J_{ro}$, which allows determination of non-midgap defect levels, and band gap narrowing due to the Franz-Keldysh effect.

*This work was sponsored in part by the Communications Satellite Corporation and in part by NASA.

I-V analysis has been used for silicon solar cells (ref. 2) to measure the effectiveness of the following:

- $p^+$ back contact treatments.
- Treatments to reduce surface recombination.
- Dot contacts vs grids.
- Altered junction profiles.
- Gettering to increase diffusion lengths.
- Many other processing changes.

This method has also been used for analyzing silicon solar cells to determine the following:

- Band gap narrowing from heavy doping (ref. 1).
- Band gap narrowing from intense electric fields (ref. 1).
- The presence of A-centers in the junction, resulting from oxygen diffusion during $n^+$ layer formation (unpublished data).
- The presence and nature of junction leakage paths caused by heavy-ion bombardment (ref. 3).
- The best approach for improving beginning-of-life (BOL) or EOL performance (ref. 4).

Since I-V analysis had been successfully applied to silicon cells (ref. 2), it was thought that it might be equally beneficial when used for GaAs cells, such as those irradiated by APL (ref. 5, 6). The analysis of representative unirradiated GaAs cells in this experiment indicates that the junction recombination current density ($J_r$) dominates the contributions to the dark current. At 0.82 V, which is the voltage at maximum power, the bulk dark-current density ($J_d$) is not even 10 percent of $J_r$. Below this voltage, $J_d$ is even less important. The dominance of $J_r$ is presumably due to defects initially present in the junction region of the cell. The $J_r$ term increases linearly with junction thickness ($W_j$) and exponentially with the electric field in the junction, $E_j$. Since $E_j \cong V_j/W_j$, $J_r$ is high for both thick and thin junctions, with an optimum thickness that is between the two.

Figure 1 is characteristic of unirradiated high-quality [18- to 19-percent air mass zero (AM0)] GaAs solar cells. The three current contributions in this semi-log plot add up to the calculated cell current (LIDC) for comparison with the experimental data (LIDX). Beyond the illuminated data, the cell area (8 $cm^2$), base doping ($3 \times 10^{23}/m^3$), and principal junction defect level (with respect to mid-gap) are included. For simplicity, a trap gap of 0.12 eV is selected to keep the $J_r$ line straight at this stage. The correlation coefficient of 0.99983 is weighted heavily by the higher density of points at high voltages. The apparently poor fit at low voltages results from a nonlinear shunt current which was fitted with a linear term. The actual difference between the data and the model is less than 1 mA (out of an $I_{sc}$ of 251 mA). The current resolution is seen to be approximately ±0.2 mA.

For solar cells that have been irradiated, the contribution of $J_r$ remains greater than that of $J_d$ except near the maximum voltage, where the two terms are approximately equal. Figure 2 is a typical analysis result for electron-irradiated GaAs solar cells. Note that both $J_d$ and $J_r$ have increased so that the relative contributions of the terms are similar to those from the unirradiated cells. For cells from U.S. vendors, this trend continues to at least $10^{16} e^-/cm^2$. The correlation coefficient and best value for series resistance are nearly unchanged from those of the unirradiated sample; however, the diode current data and calculated shunt current at low voltages have both increased slightly.

Figure 3 shows the effects of proton irradiation on GaAs solar cell current contributions. Two major differences from electron-irradiated cells are seen: the bulk current contribution is now negligible, and the series resistance has increased significantly (from 0.001 to 0.041 Ω). Comparison of electron- and proton-irradiated cells, degraded to the same power, indicates more degradation in $J_r$ (and $R_s$) and less in $J_d$ from protons. The relative effect on cell characteristics from protons is a lower $V_{oc}$ and higher $I_{sc}$. Study of these combined effects provides two possible explanations. One is that protons damage junctions more than do electrons, and that they lower the bulk carrier concentration more with less change in carrier lifetime. The second explanation is that the higher reduction in carrier concentration increases the junction field-region thickness (and thereby $J_r$) and provides a drift field to increase carrier collection (greater effective diffusion length) and $I_{sc}$.

In Figure 4, the same data as in Figure 3 have been reanalyzed; however, the expression for shunt current has been changed in the model. The modification is based on earlier studies which indicated that most of the observed shunt currents result from a few individual leakage paths through the junction. These paths are shortened as the junction depletion layer collapses under forward bias. Thus, the effective resistance decreases with increasing junction voltage. As a second approximation, a fixed value was maintained for $R_{sh}$, but $(V - IR_s)^2/R_{sh}$ was substituted for the shunt term in equation 1. The results in Figure 4 are a closer fit to data in the low-voltage region, but provide a lower correlation coefficient than in Figure 3. The other terms are not significantly changed except for $J_d$, which is at the noise level. This exercise demonstrates that, while the fit can be improved at low voltages, the effect on the critical currents ($J_r$ in this case) is quite small.

Figure 5 is an example of the large differences noted in analyses of Mitsubishi GaAs cells compared to those from U.S. manufacturers. At $10^{16}/cm^2$ 1-MeV electrons, the results appear much closer to the proton results of Figure 3 than to the electron results of Figure 2. The proton irradiation results for the Mitsubishi cells are similar to those from the U.S. cells, but with a higher series resistance (0.27 vs ~0.04 Ω) and higher $I_{sc}$. The conclusion is that the Mitsubishi cells have lower doping in either (or both) the emitter or base layers. Radiation reduces the carrier concentration further, and the junction field reaches further into the low doped layer(s).

Analysis of GaAs-on-germanium cells (ref. 4) indicates that the principal difference between these cells and GaAs/GaAs is at BOL, where a higher level of junction defects is proposed. With exposure to radiation, the difference in $J_r$ diminishes as radiation-induced defects come to dominate the results. Table I gives typical values for cell characteristics before and after irradiation.

Table I. Results of I-V Analysis on GaAs Solar Cells

| Condition | $J_d$ ($A/cm^2$) | $J_r$ ($A/cm^2$) | $R_s$ (Ω) |
|---|---|---|---|
| GaAs | | | |
| Initial | $2 \times 10^{-19}$ | $1 \times 10^{-10}$ | <0.01 |
| $10^{15}$ e/cm² | $4 \times 10^{-18}$ | $6 \times 10^{-10}$ | <0.01 |
| $10^{16}$ e/cm² | $4 \times 10^{-17}$ | $2 \times 10^{-9}$ | <0.01 |
| $10^{13}$ p/cm² | $3 \times 10^{-18}$ | $8 \times 10^{-9}$ | 0.04 |
| GaAs/Ge | | | |
| Initial | $5 \times 10^{-20}$ | $4 \times 10^{-10}$ | <0.01 |
| $10^{15}$ e/cm² | $4 \times 10^{-18}$ | $1 \times 10^{-9}$ | <0.01 |
| $10^{16}$ e/cm² | $5 \times 10^{-17}$ | $2 \times 10^{-9}$ | <0.01 |
| $10^{13}$ e/cm² | $5 \times 10^{-17}$ | $1 \times 10^{-8}$ | 0.04 |

The separation of cell I-V curves into junction and bulk contributions, and the differences observed in degradation rates for $V_{oc}$ and $I_{sc}$ from protons and electrons, provide a basis for understanding why a distinction must be made between cell I-V degradation parameters for proton-irradiated solar cells. The greater effect of protons on $J_r$, relative to that from electrons, increases GaAs solar cell degradation because the $J_r$ term is dominant here, while $J_d$ is dominant in silicon solar cells. The I-V analysis technique provides not only a tool in the design of solar cells for benign and radiation environments, but also a means of studying radiation damage at the defect level.

It can be concluded from this study that $J_r$ dominates nearly all GaAs cells tested, except for unirradiated Mitsubishi cells, which appear to have a different doping profile. Irradiation maintains or increases the dominance by $J_r$, and proton irradiation increases $J_r$ more than does electron irradiation. The U.S. cells have been optimized for BOL and the Japanese for EOL. I-V analysis indicates ways of improving both the BOL and EOL performance of GaAs solar cells.

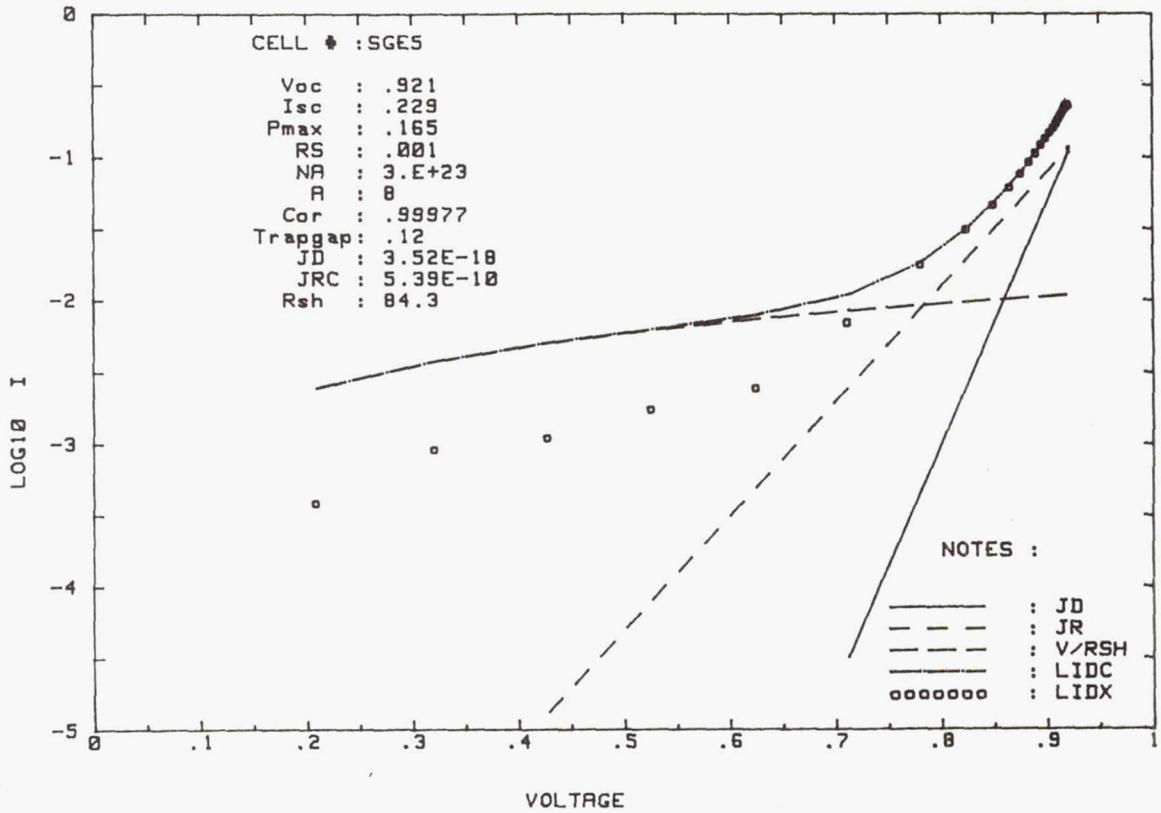


Figure 2. Spectrolab GaAs Solar Cell After $10^{15}/cm^2$ 1-MeV Electrons

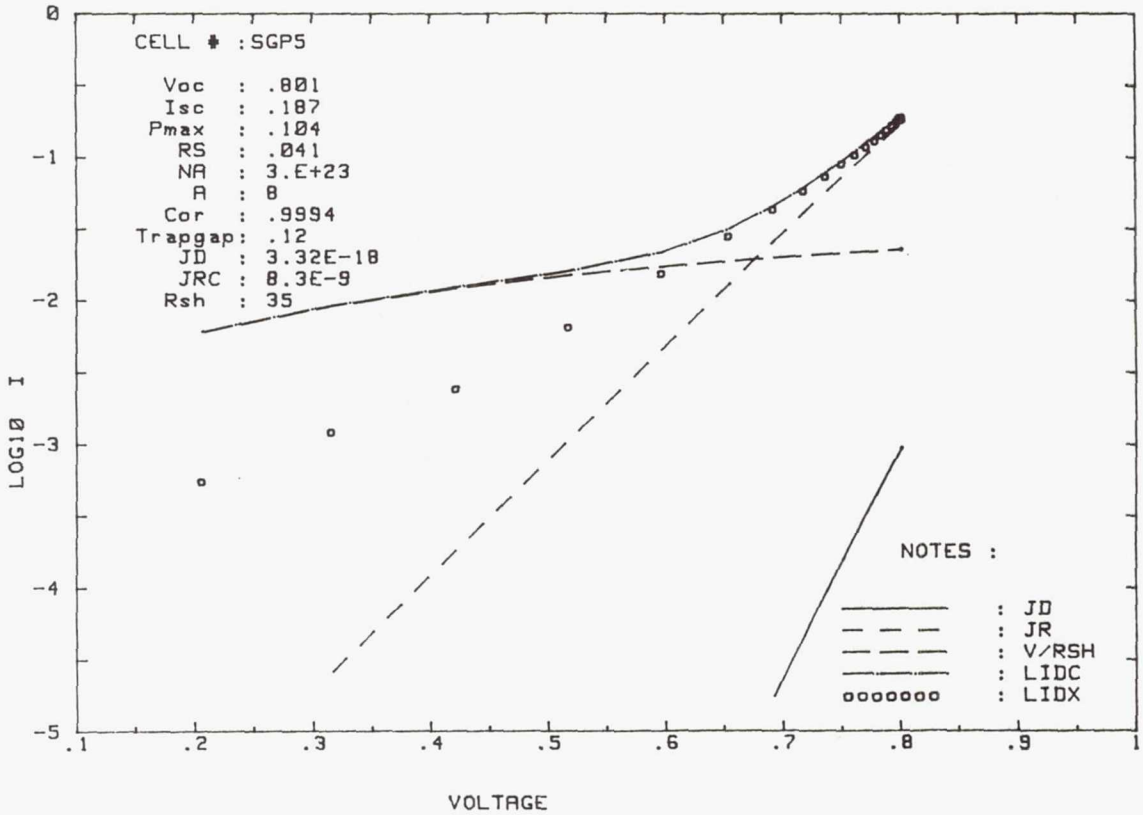


Figure 3. Spectrolab GaAs Solar Cell After $10^{13}/cm^2$ 10-MeV Protons

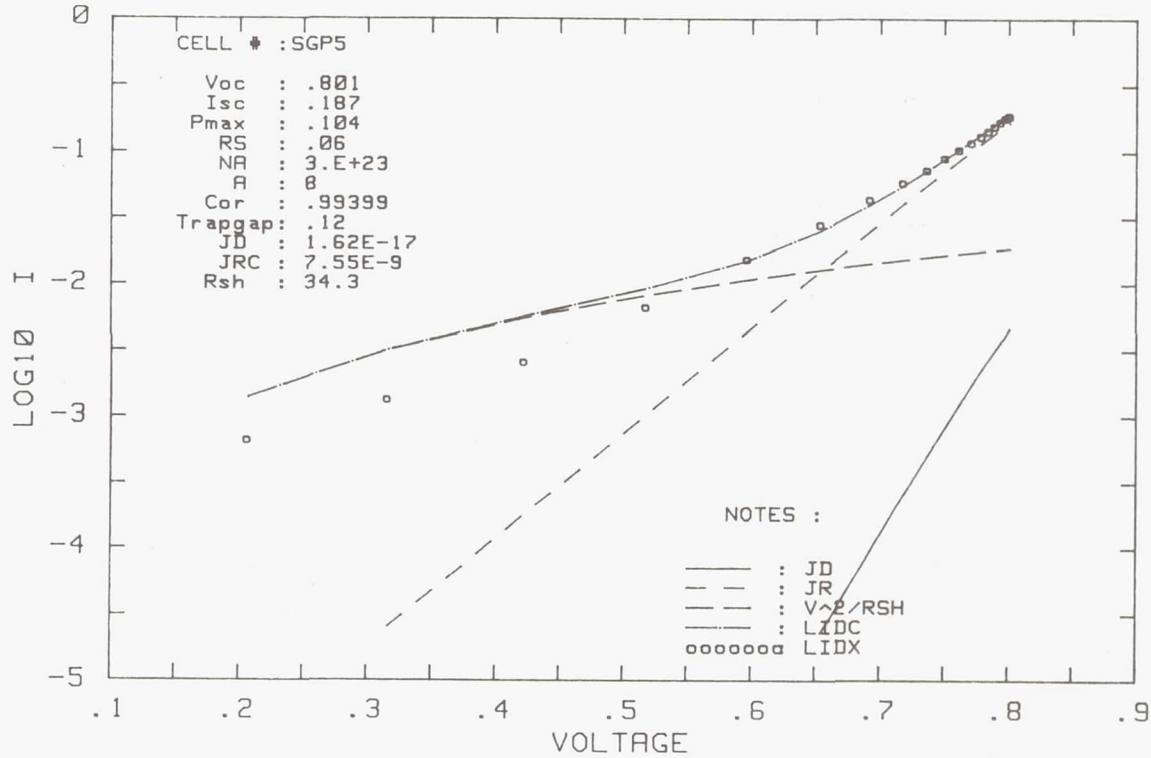


Figure 4. Proton-Irradiated Spectrolab Cell With $V^2$ Dependence In Shunt Term

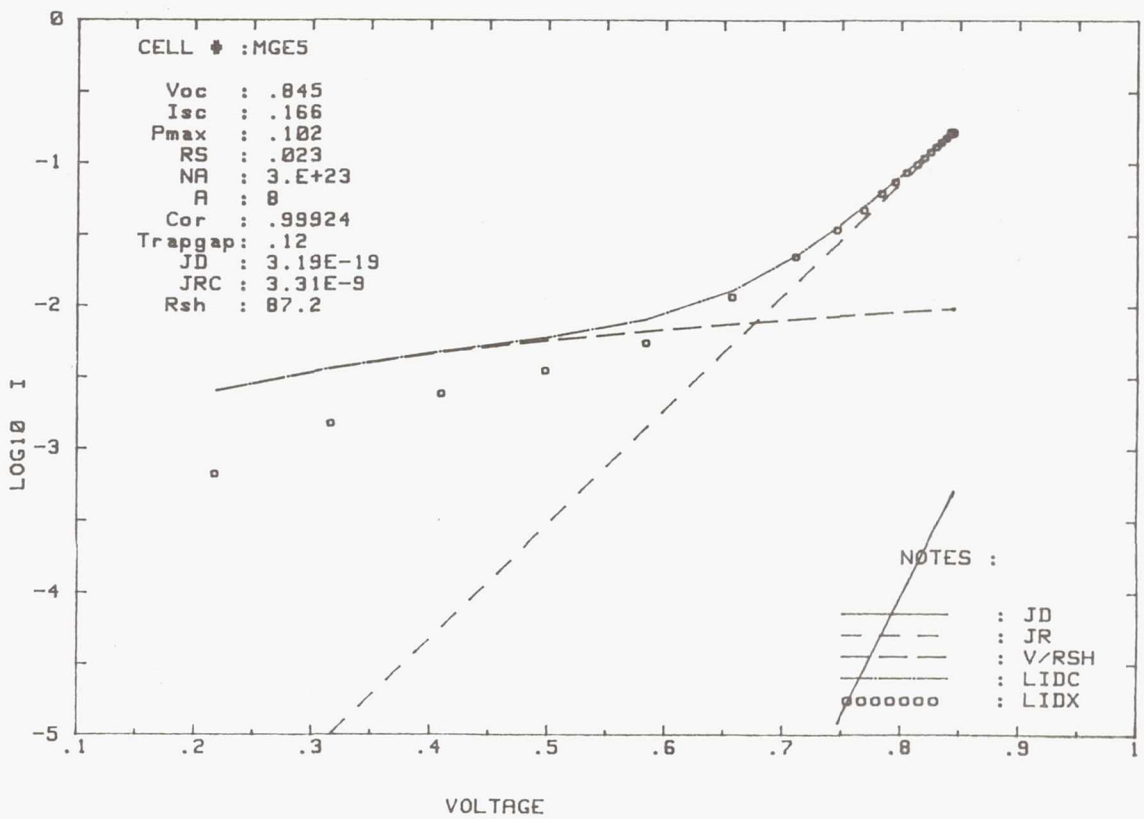


Figure 5. Mitsubishi GaAs Solar Cell After $10^{16}/cm^2$ 1-MeV Electrons

## REFERENCES


1. Rittner, E. S.; Meulenberg, A.; and Allison, J. F.: "Dependence of Efficiency of Shallow Junction Silicon Solar Cells on Substrate Doping," *Journal of Energy*, Vol. 5, No. 1, January–February 1981, pp. 9–14. [See also: Rittner, E. S, "An Improved Theory for the Si p-n Junction Solar Cell," *Journal of Energy*, Vol. 1, No. 1, January–February 1977, pp. 9–17.]

2. Meulenberg, A., Jr.: "Developments Toward an 18% Efficient Silicon Solar Cell," Final Report for Contract NAS-3-22217, NASA CR 168141, April 1983.

3. Meulenberg, A.: "Evidence for a Permanent Single-Event Upset Mechanism," *IEEE Transactions on Nuclear Science,* Vol. NS-31, No. 6, December 1984, pp.1280–1283.

4. Meulenberg, A.; and Rittner, E. S.: "Limiting Processes in Shallow Junction Solar Cells," 3rd Solar Cell High Efficiency and Radiation Damage Meeting, NASA Lewis Research Center, June 1979.

5. Herbert, G. A., *et al.*: "Electron and Proton Displacement Damage in Production Line Quality Silicon and Gallium Arsenide Solar Cells," 4th International Photovoltaic Science and Engineering Conference, Sydney, Australia, February 1989.

6. Maurer, R. H., *et al.*: "Gallium Arsenide Solar Cell Radiation Damage Study," *IEEE Transactions on Nuclear Science,* Vol. NS-36, No. 6, December 1989, pp. 2083–2091. (See also these *Proceedings.*)


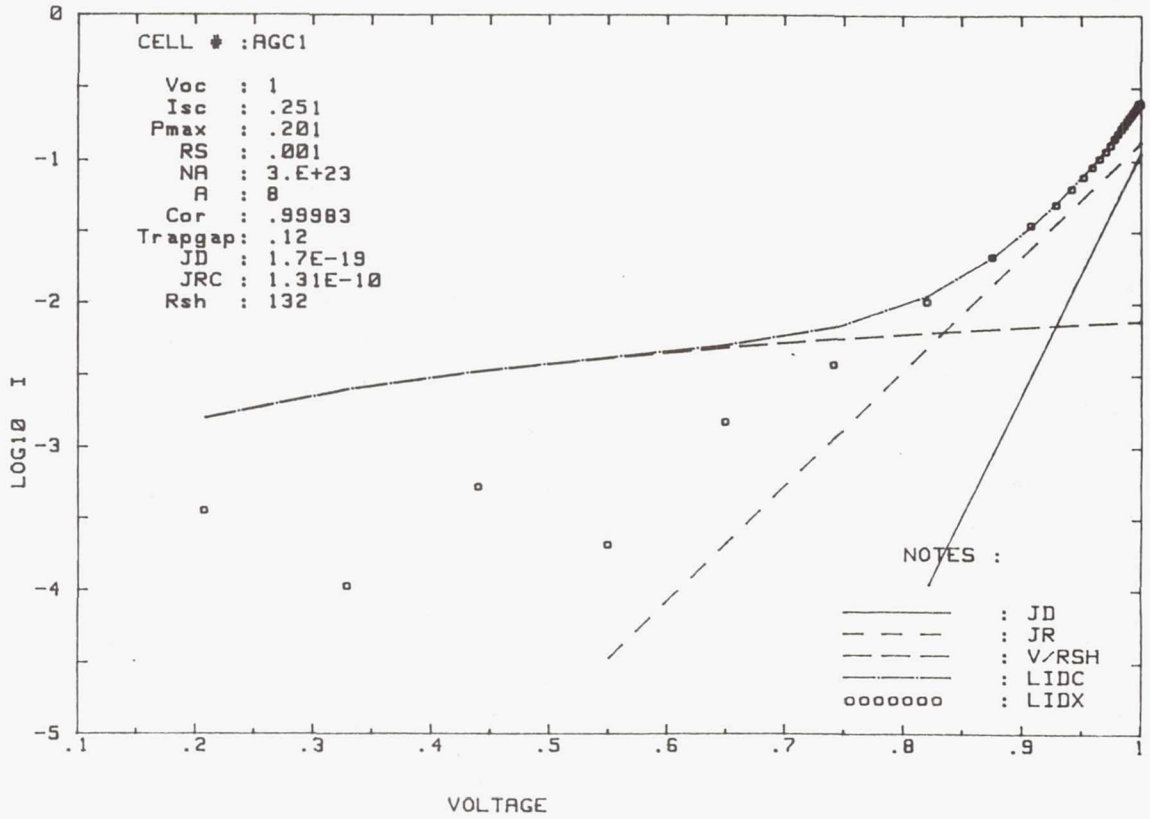


Figure 1. Unirradiated ASEC GaAs Solar Cell

# RADIATION HARDNESS OF $Ga_{0.5}In_{0.5}P$/GaAs TANDEM SOLAR CELLS

Sarah R. Kurtz, J. M. Olson, K. A. Bertness, D. J. Friedman, and A. Kibbler
Solar Energy Research Institute
Golden, Colorado

and

B. T. Cavicchi and D. D. Krut
Spectrolab Inc.
Sylmar, California

The radiation hardness of a two-junction monolithic $Ga_{0.5}In_{0.5}P$/GaAs cell with tunnel junction interconnect is investigated. Related single-junction cells are also studied to identify the origins of the radiation losses. The optimal design of a $Ga_{0.5}In_{0.5}P$/GaAs cell is discussed. The air mass (AM)0 efficiency of an optimized tandem cell after irradiation with $10^{15}$ $cm^{-2}$ 1 MeV electrons is estimated to be 20% using currently available technology.

## INTRODUCTION

Two-junction monolithic device efficiencies have recently surpassed those of single-junction devices (Chung, 1989; Olson, 1990). These devices present the advantages of higher efficiencies with lower currents and low temperature coefficients while avoiding use of a mechanical stack. A monolithic, two-junction device with a tunnel-junction interconnect can easily be incorporated into existing systems without changes in the wiring or processing schemes. The advantages of the choice of $Ga_{0.5}In_{0.5}P$ and GaAs for fabrication of a monolithic, two-junction device including a current state-of-the-art efficiency of 27.3% (Olson, 1990) are presented in detail elsewhere (Olson, 1991).

Although the $Ga_{0.5}In_{0.5}P$/GaAs tandem cell is very attractive for space applications because of its high efficiency, ease of introduction into existing GaAs processing lines, low temperature coefficient, and relatively low current and high voltage, its sensitivity to radiation has not been established. The sensitivity of the GaAs bottom cell to radiation can easily be extrapolated from the literature (for example, Yamaguchi, 1985; Fan, 1980; Markvart, 1990). There is also substantial data on the radiation sensitivity of InP (for example, Yamaguchi, 1988), but it is not known whether $Ga_{0.5}In_{0.5}P$ responds to radiation in a similar manner, and it has not been established how the added complexity of a multijunction device may affect the radiation sensitivity. This paper presents data on the effect of electron radiation on the performance of the $Ga_{0.5}In_{0.5}P$/GaAs cells and discusses the implications of these data in terms of the design of the tandem cell and the anticipated radiation hardness. It will be shown that using a thin $Ga_{0.5}In_{0.5}P$ top cell not only improves the current matching but reduces the radiation damage in the top cell.

## EXPERIMENTAL METHOD

Schematics of the device structures used in this study are shown in Fig. 1. The structures were grown in a vertical, air-cooled reactor at one atmosphere using organometallic chemical vapor deposition, the details of which are described elsewhere (Olson, 1986). The group III source gases were trimethylindium, trimethylgallium and trimethylaluminum; the group V source gases were arsine and phosphine. The dopant sources were diethylzinc, carbon tetrachloride, disilane, and hydrogen selenide. All of the structures were grown at 700°C, with the exception of the back-surface field of the top cell and the preceding GaAs layer, which were grown at 625°C. The phosphides were grown under a V/III (ratio of group V sources to group III sources) of 30 for the $10^{17}$ $cm^{-3}$ p-type layers and 240 for the $10^{18}$ $cm^{-3}$ n-type layers. The base GaAs layer was grown with a V/III of 35. Most of the layers were grown with a growth rate of 100 nm/min. The tunnel junction layers were grown at lower rates, as low as 10 nm/min. The front and back contacts were made by electroplating gold. A heavily doped GaAs layer was used for the top contact. This layer was removed before adding the double layer antireflection (AR) coating (ZnS and $MgF_2$). A more detailed description of the cell fabrication is given elsewhere (Olson, 1990).

The cells were irradiated to a fluence of $10^{15}$ $cm^{-2}$ of 1 MeV electrons by B. Anspaugh at the Jet Propulsion laboratory. The devices were characterized at both the Solar Energy Research Institute (SERI) and Spectrolab before and after irradiation. The device parameters reported here were measured by K. Emery at SERI for one-sun, AM1.5 global conditions. The tandem cells were measured after adjusting the spectrum of the solar simulator to achieve the appropriate currents for two reference cells (with spectral response curves similar to those of the top and bottom cells), as described by Glatfelder, 1987. The spectral response curves were measured using a monochromator-based system. The relative response of this system was calibrated using a thermopile. The absolute calibration was obtained by integrating the product of the spectral response curve and the solar spectrum and comparing this with the short-circuit current ($J_{SC}$). The separate top- and bottom-cell quantum efficiency curves for the tandem cell were measured using light biasing and, in some cases, electrical biasing.

(a) (b) (c)

Figure 1. Device structures for the (a) tandem cell, (b) thin top ($Ga_{0.5}In_{0.5}P$) cell, and (c) bottom (GaAs) cell. The thicknesses and dopant for each layer are indicated. The alloys are all nominally lattice matched to GaAs. The thick ($Ga_{0.5}In_{0.5}P$) top cell had a structure as shown in (b) except that the base layer was 6 μm instead of 0.6 μm.

## RESULTS

Four device structures were chosen for the study (as shown in Fig. 1): a tandem cell, top and bottom cells similar to those in the tandem cell, but grown separately, and, a thick top cell. The bottom cell included a GaAs tunnel junction and a $Ga_{0.5}In_{0.5}P$ layer of thickness comparable to a top cell so that the single-junction bottom cell is optically very similar to the bottom cell in the tandem structure. The tandem cell differed from the single-junction cells as to the passivating layers on the front and back and the dopants used in the tunnel junction. The results of the study imply that these differences are not major factors in determining the radiation sensitivity of the device. Although it is possible to separately evaluate the currents of the two junctions in the tandem cell, it is not possible to separately evaluate the voltages. Thus, the single-junction cells were grown for this purpose. In Fig. 1, the GaAs contacting layer, Au grid, and AR coating are not shown. The heavily doped GaAs layers used for the tunnel junction and contacting layer approached $10^{19}$ $cm^{-3}$ in carrier concentration. The emitter layers were doped n-type with Se to about $10^{18}$ $cm^{-3}$. The $Ga_{0.5}In_{0.5}P$ base layers had a hole concentration of about $10^{17}$ $cm^{-3}$, while that of the GaAs base layers was 2-5 X $10^{17}$ $cm^{-3}$. The thick top cell had the same structure as shown for the thin cell (Fig. 1b), but it had a base thickness of 6 μm. The thick $Ga_{0.5}In_{0.5}P$ top cell would not be used in an actual tandem cell structure, but it gives us more information about the radiation hardness of $Ga_{0.5}In_{0.5}P$ itself. Four devices were fabricated for each device structure. We present here the average results, or specific results for a representative cell. After analysis of the four device structures, it became apparent that the doping level of the GaAs base layer is a very important parameter. An additional conventional GaAs device was grown with a base doping level of 2 X $10^{16}$ $cm^{-3}$. This device had $Ga_{0.5}In_{0.5}P$ as the passivating layers for both the front and back surfaces.

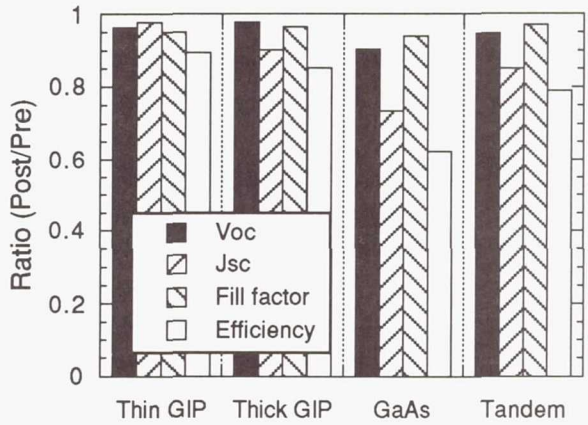


Figure 2. The degradation of device parameters after irradiation with $10^{15}$ $cm^{-2}$ 1 MeV electrons.

Figure 2 shows the relative performance of the four devices after irradiation. The relative values shown here were measured under AM1.5 conditions, but we expect that the relative performance under AM0 would be similar. The degradation of current in the thin top cell was negligible compared to the uncertainty of the measurement. However, the open-circuit voltage ($V_{oc}$) and fill factor (FF) both degraded by about 5%. The thick top cell did show a significant (10%) loss of current, indicating that the $Ga_{0.5}In_{0.5}P$ base diffusion length does decrease after irradiation, highlighting the advantage of using a top-cell thickness less than the post-radiation diffusion length. The degradation of the GaAs bottom cell was dominated by the loss of current (more than 25% of the current was lost) with significant (5% -10%) degradation also observed in the $V_{oc}$ and FF. Clearly, both of the $Ga_{0.5}In_{0.5}P$ cells showed superior radiation hardness to the GaAs cell. The degradation of the tandem cell was less than that of the GaAs cell but greater than that of the $Ga_{0.5}In_{0.5}P$ cell, as would be expected for the $V_{oc}$ and

FF. The better performance of the $J_{SC}$ (which would be expected to reflect the GaAs bottom cell since it degraded more) is likely to be due to a lack of current matching in the device before irradiation, (*i.e.*, before irradiation the bottom cell produced more current than the top cell, indicating that the top cell was thicker than optimal.

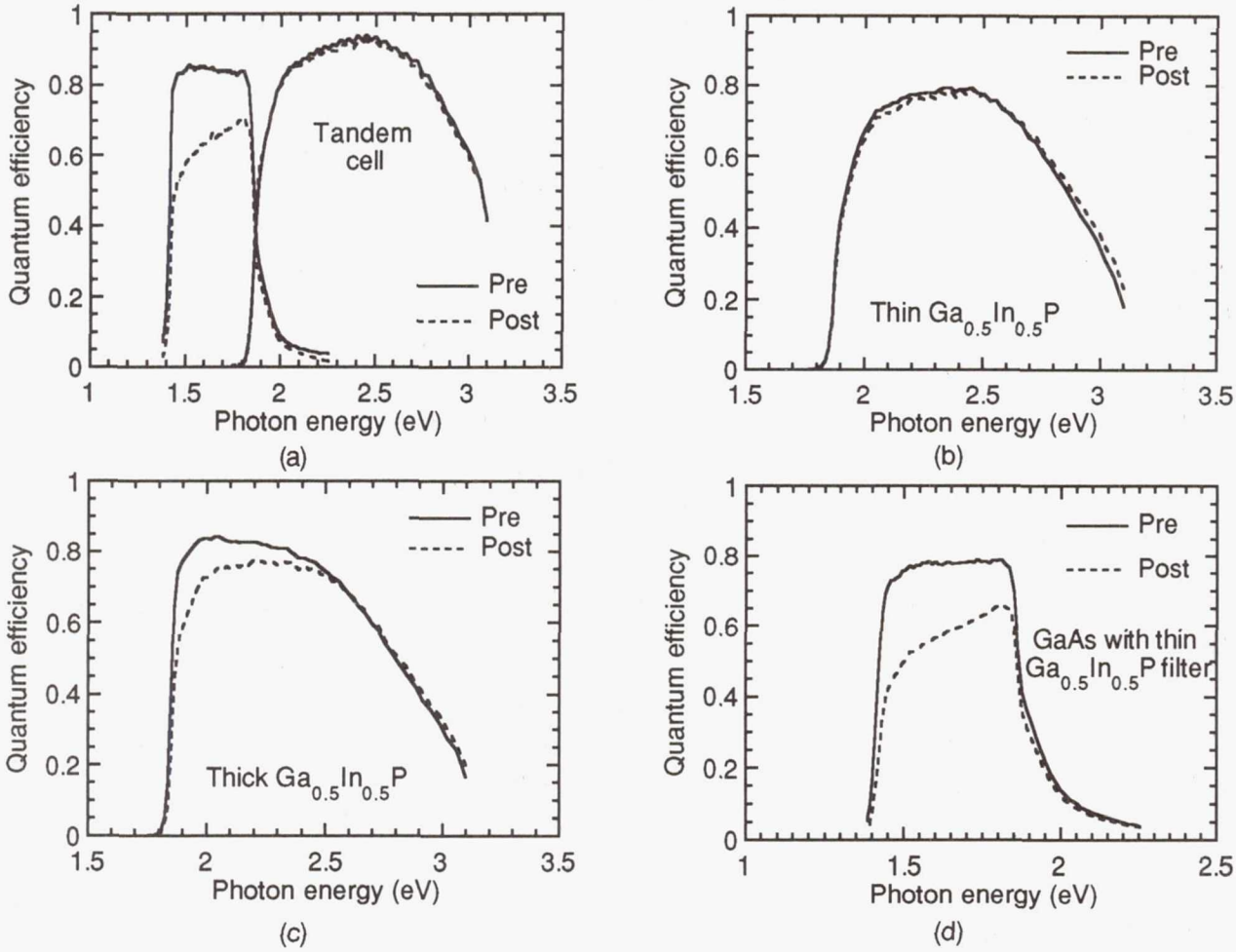


Figure 3. Quantum efficiency curves for (a) a tandem cell, (b) a thin top cell, (c) a thick top cell, and (d) a bottom cell before and after irradiation with $10^{15}$ $cm^{-2}$ 1 MeV electrons. These data and the data in Fig. 2 pertain to the same samples.

Figure 3 shows the quantum efficiency curves for the four cells both before and after irradiation. What appears to be poor red response in the top cell (Figs. 3a and 3b) is a result of the thinness of the top cell. Some of the light passes through and is collected by the bottom cell, resulting in a tail toward the high-energy side of the quantum efficiency curves as shown in Figs. 3a and 3d. The thick $Ga_{0.5}In_{0.5}P$ cell shows about a 10% loss in $J_{SC}$ after irradiation. As can be seen from Fig. 3c, most of this loss is in the red response of the cell. This loss is substantially greater than the loss observed for the thin $Ga_{0.5}In_{0.5}P$ cell. For the thin cell, the loss in quantum efficiency was not consistent between the four devices measured. Two devices lost more toward the blue end of the spectrum, and two lost more toward the red end of the spectrum. However, none of the four devices lost more than 3% of the total current, implying that these differences are less than the uncertainty of the experiment. The GaAs cell degraded significantly in red response. From the literature, this large degradation can be directly related to a high doping concentration in the base of the cell, and it motivated the study presented below for a GaAs cell with a lower base doping level. One of the GaAs bottom cells had a low FF (caused by a shunt) before irradiation. This device degraded more than the others (to 56% compared to 62% of beginning of life efficiency), so the data

for that device were not averaged with those of the other devices. The results from the tandem cell (Fig. 3a) are consistent with those from the single-junction cells (Figs. 3b and d). That is, the top cell showed almost no degradation while the bottom cell showed substantial degradation.

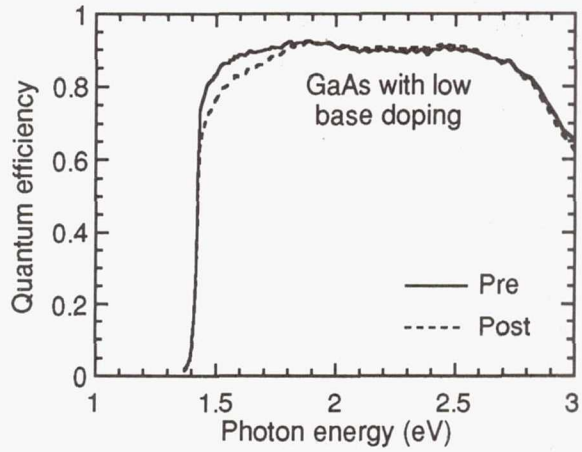


Figure 4. Quantum efficiency before and after electron irradiation for a GaAs cell with a base doping of 2 X $10^{16}$ $cm^{-3}$.

Figure 4 shows quantum efficiency results from a conventional single-junction GaAs cell grown with a lightly doped base layer (2 X $10^{16}$ $cm^{-3}$). This sample was irradiated on a different date than the other samples. However, other cells irradiated on the same date but that had larger base doping levels showed degradation similar to that shown in Figs. 3a and 3d. It should be noted that the degradation in FF for the lightly doped GaAs cell was comparable to those for more heavily doped cells and similar to that of the GaAs bottom cell presented above (Figs. 2 and 3d). However, the $V_{oc}$ showed a somewhat larger degradation (to 85% of beginning-of-life (BOL) compared with 90% of BOL for the more heavily doped cells).

## DISCUSSION

The thin $Ga_{0.5}In_{0.5}P$ top cell clearly showed excellent radiation resistance, retaining 90% of its BOL efficiency. However, the GaAs bottom cell showed large degradation, primarily because of degradation of the $J_{sc}$. This large degradation in the current of the GaAs n-on-p bottom cell can be related to a high doping level in the p-type base region (Yamaguchi, 1985; Fan, 1980). The results presented here are consistent with the predictions of Yamaguchi and Fan. Specifically, the GaAs cells fabricated with a base doping level of 2 X $10^{16}$ $cm^{-3}$ showed substantially less degradation than those with high base doping levels. Yamaguchi estimated that the optimal base doping level is 2 X $10^{16}$ $cm^{-3}$, while Flood (1987), in reporting Fan's work, shows a very broad end-of-life (EOL) efficiency maximum centered on 1 X $10^{16}$ $cm^{-3}$. This difference can be predicted from analyses similar to that presented by Yamaguchi, 1985. The change in minority carrier diffusion length $L$ with irradiation is related to $K\phi$ by

$$\Delta(1/L^2) = K\phi$$

where $K$ is the damage constant and $\phi$ is the electron flux. The better performance is a result of both a smaller $K$ for the more lightly doped p-type GaAs, and a longer diffusion length for the preirradiated material. It is not clear which of these effects is more important since Yamaguchi (1985) shows very little variation of $K$ with p-type doping level in this range, while Fan shows $K$ almost directly proportional to the p-type doping level (this work was

originally reported by Fan (1980) and subsequently included in reviews by Markvart (1990) and Flood (1987)).

In the tandem cell chosen for this study, the largest degradation came from a loss of current in the bottom cell. This is especially problematic for a series-connected device because a similar amount of current is lost from the top cell simply because it can't be carried out of the device. This limitation of series-connected devices has discouraged many from considering series-connected tandem cells for use in space. However, this is not a necessary loss. If the tandem cell is grown with a lower base doping level in the bottom cell, the loss of current for the bottom cell will be substantially less. Using the degradation of the spectral response of the lightly doped GaAs and applying this loss to the pre-radiation spectral response curve of the bottom cell shown in Fig. 3d, the expected EOL current for a bottom cell with a lightly doped base layer would be 91% of the BOL current instead of the 73% measured here. Even this lower value of 91% is still a substantially greater loss than the loss in current measured for the top cell, implying that there will still be some loss after irradiation associated with the series connection. However, this loss does not prevent the device from being useful. In fact, as shown below, this loss from series connection can be helpful in tailoring the performance profile of the solar cell.

In some cases, it is advantageous to have extra power at the beginning of a mission, and other times it would be more useful to have a constant power source throughout the mission. Table I shows the efficiencies we estimate would be obtained for a tandem cell of the quality of the 27.3% efficient AM1.5 global cell if it were redesigned for AM0 one-sun efficiency. The redesigning of the device involves only two changes: (1) a decrease of the base doping level of the bottom cell to improve its radiation resistance and, (2) an adjustment of the top cell thickness to achieve current matching under the desired conditions. Specifically, it was assumed that the current of the bottom cell would degrade to 91.3% of BOL, but that the voltage would degrade to 85% of BOL, and that the total BOL AM0 current of the device (*i.e.,* the sum of the top and bottom cell currents) would be 33.4 mA/cm$^2$. The 24.4% efficiency was calculated from device parameters of 2.296 V, 16.7 mA/cm$^2$, and 87% FF. The efficiencies were estimated for optimizing both BOL and EOL performance. This was done by adjusting the top cell thickness so that the device would be current matched at BOL or EOL, respectively. It is clear that the choice of optimization for BOL or EOL makes little difference in the absolute efficiency. However, the ratio of EOL to BOL changes from 82% to 87%, which may be significant depending on the desired performance profile. Most important to note is that in either case we estimate that with appropriate optimization and existing $Ga_{0.5}In_{0.5}P$/GaAs technology an EOL, AM0 efficiency of 20% can be achieved.

We emphasize that this study only used a small number of cells and that, although we investigated ways to improve the stability of the current, we have not investigated ways to improve the stability of the voltage, leaving some room for improvement. Additional studies are planned for tandem devices with lower base doping and appropriate top cell thicknesses.

Table I. Estimated AM0 efficiencies for tandem cells before and after irradiation with $10^{15}$ cm$^{-2}$ 1 MeV electrons.

| Tandem Cell | Before (%) | After (%) | Ratio E.O.L/BOL (%) |
|---|---|---|---|
| Optimized for BOL | 24.4 | 20.0 | 82 |
| Optimized for EOL | 23.7 | 20.7 | 87 |

## SUMMARY

The radiation hardness was investigated for a monolithic, two-junction tandem $Ga_{0.5}In_{0.5}P/GaAs$ cell with a tunnel-junction interconnect. The device was shown to retain approximately 80% of its beginning of life efficiency. The primary degradation was a result of a large loss of current from the bottom cell. This degradation can be controlled by lowering the base doping level, although this may contribute to an increased degradation of the voltage. The top cell degradation was minimal with end-of-life parameters $J_{sc}$, 98%; $V_{oc}$, 96%; FF, 95%; and efficiency, 90% of BOL. This degradation is minimized as a result of the thin base layer in the top cell. It would appear that the damage coefficients for $Ga_{0.5}In_{0.5}P$ lie between those of GaAs and InP, but this depends on the doping levels of interest. With low base doping and appropriate top-cell thickness, an end-of-life ($10^{15}$ $cm^{-2}$ 1 MeV electrons) AM0 efficiency of 20% can be achieved with existing technology.

## REFERENCES

Chung, B.-C., G. F. Virshup, S. Hikido, and N. R. Kaminar. 1989. 27.6% Efficient (One Sun, Airmass 1.5) Monolithic $Al_{0.37}Ga_{0.63}As/GaAs$ Two-Junction Cascade Solar Cell With Prismatic Cover Glass. Appl. Phys. Lett. 55:1741-1743.

Fan, J.C.C. 1980. GaAs Shallow Homojunction Solar Cells. Final Report, NASA CR-165167.

Flood, D. , and H. Brandhorst. 1987. Space Solar Cells. Current Topics in Photovoltaics, 2:143-202.

Glatfelter, T., and J. Burdick. 1987. A Method for Determining the Conversion Efficiency of Multiple-cell Photovoltaic Devices. Proceedings of the 19th IEEE Photovoltaic Specialists Conference (IEEE, New York, 1987) 1187-1193.

Kurtz, S. R., P. Faine, and J. M. Olson. 1990. Modeling of Two-Junction, Series-Connected Tandem Solar Cells Using Top-Cell Thickness as an Adjustable Parameter. J. Appl. Phys. 68:1890-1895.

Markvart, T. 1990. Review Radiation Damage in Solar Cells. J. Mat. Science: Mat. in Elec. 1:1-12.

Olson, J. M., and A. Kibbler. 1986. In situ Characterization of MOCVD Growth Processes by Light Scattering Techniques. J. Cryst. Growth 77:182-187.

Olson, J. M., S. R. Kurtz, A. E. Kibbler, and P. Faine. 1990. A 27.3% Efficient $Ga_{0.5}In_{0.5}P/GaAs$ Tandem Solar Cell. Appl. Phys. Lett. 56:623-625.

Olson, J. M., S. R. Kurtz, A. E. Kibbler, K. Bertness, and D. Friedman. 1991. $GaInP_2/GaAs$ Tandem Cells for Space Applications. This volume.

Yamaguchi, M. and C. Amano. 1985. Numerical Analysis for Radiation-Resistant GaAs Heteroface Solar Cell Structures. J. Appl. Phys. 57:537-544.

Yamaguchi, M. and K. Ando. 1988. Mechanism for Radiation Resistance of InP Solar Cells. J. Appl. Phys. 63:5555-5562.

# THE EFFECTS OF ELECTRON AND PROTON RADIATION ON GaSb INFRARED SOLAR CELLS

P.E. Gruenbaum, J.E. Avery, and L.M. Fraas
Boeing High Technology Center
Seattle, WA 98124-2499

Gallium Antimonide (GaSb) infrared solar cells were exposed to 1 MeV electrons and protons up to fluences of $1x10^{15}$ $cm^{-2}$ and $1x10^{12}$ $cm^{-2}$ respectively. In between exposures, current-voltage and spectral response curves were taken. The GaSb cells were found to degrade slightly less than typical GaAs cells under electron irradiation, and calculations from spectral response curves showed that the damage coefficient for the minority carrier diffusion length was $3.5x10^{8}$. The cells degraded faster than GaAs cells under proton irradiation, but we expect the top cell and coverglass to protect the GaSb cell from most damaging protons. Also, some annealing of proton damage was observed at low temperatures (80-160°C).

## Introduction

Mechanically stacked Gallium Arsenide (GaAs) and Gallium Antimonide (GaSb) solar cell assemblies have been shown to have efficiencies over 30% under concentrated AM0 conditions (ref. 1) . In this design, the GaAs cell converts the visible light, but passes infrared light through to the GaSb cell underneath, which has a bandgap of 0.7 eV. The GaSb cell will provide an extra 6% to the GaAs cell's 24% efficiency. In combination with light-weight concentrator structures, these assemblies have the potential for providing power in space using significantly less area and weight than standard silicon space cells. However, in order to survive the space environment, the cells must be able to withstand high energy electrons and protons. GaAs cells have been shown to be more radiation resistant than silicon cells, but the effects on GaSb have never been studied previously. In this paper, we report the effects of 1 MeV electrons and protons on GaSb solar cells measured by current-voltage and spectral response curves.

## Experimental Details

The 5.4 mm diameter GaSb cells used in this experiment were processed as described in reference 2. They consist of n-type tellurium-doped substrates with a zinc diffusion on the front. The zinc diffusion was partially etched off between the gridlines to reduce heavy doping effects, and then an antireflection coating was deposited. Cells with various beginning of life efficiencies were used for each type of exposure. The cells were soldered down to ceramic pads, and the front of the cells were contacted by wirebonds. With some of these, GaAs cells were added, creating a finished assembly (except for a coverglass). This assembly is shown in Fig. 1.

Spectral response and current-voltage curves were taken before and after each radiation exposure. The one-sun short-circuit current was calculated by convolving the spectral response with the AM0 spectrum (and for the bare GaSb cells, convolving the transmission of a GaAs filter as well). A small correction factor (1.06) was required to match the calculated currents before radiation exposure with the currents measured under a GaAs filter using an XT-10 simulator calibrated with a balloon-flight standard. Voltage and fill factor values were found from current-voltage curves taken under concentrated light. The short circuit current was approximately 50 times the one-sun current. The assemblies were measured on a temperature-controlled plate at 25°C.

Cells were exposed to 1 MeV electrons and 1 MeV protons in a Dynamitron system. The total exposure was $1x10^{15}$ $cm^{-2}$ for electrons and $1x10^{12}$ $cm^{-2}$ for protons. (The electron and proton irradiations were made

possible by Dennis Russell and Tom Nirider of the Boeing Radiation Effects Laboratory.) All annealing after exposure was done in air.

## Results

Tables I and II show the average values from the measurements between each radiation exposure for 1 MeV electrons and 1 MeV protons. (Note that these are average values, and some low efficiency cells were included. Good GaSb cells have efficiencies over 6% in AM0 sunlight under a GaAs filter.) Figures 2 and 3 show these measurements normalized to their beginning of life values. The error bars indicate the spread in data among the different cells. Note that the electron-irradiated cells degraded uniformly, but the proton-irradiated cells had some variations. No correlation with beginning of life values was found, so the spread may be due to non-uniformities in the proton beam.

For GaSb cells in tandem assemblies, the damage due to 1 MeV electrons was reduced significantly due to absorption by the GaAs cell. Figure 4 compares the degradation in efficiency for cells in assemblies vs. bare cells. For 1 MeV protons, no degradation was observed for GaSb cells in tandem assemblies.

The spectral response curves for GaSb cells during electron exposure is shown in Figure 5. These show a decrease in the infrared region during electron irradiation, which suggests that the bulk minority carrier lifetime is being decreased. By modeling the cells, we have been able to calculate the hole diffusion length $L_p$ (ref. 3) ; according to our calculations, it begins at 3.2 μm and ends at 1.5 μm after $1 \times 10^{15}$ electrons/cm$^2$. (Electron beam induced current measurements done by R. Matson of the Solar Energy Research Institute have confirmed a beginning of life diffusion length of about 3 μm.) Plotting $1/L_p^2$ vs. dose (fig. 6) has allowed us to find a damage coefficient of $3.5 \times 10^8$ (compared to $7 \times 10^8$ for GaAs found in reference 4 ).

The spectral response curves for 1 MeV proton exposure is shown in Fig. 7. It also shows a decrease in the bulk lifetime, although we cannot assume it is uniform as we did with electron exposure (ref. 5) , so we cannot calculate a valid damage coefficient.

We have performed annealing experiments in order to determine if the radiation damage can be reversed. Since these particular assemblies can only withstand temperatures below 180°C, the maximum temperature applied to them was 160°C. In one case, we annealed samples for one hour at increasing temperatures; we observed no effect on the electron-irradiated samples, but the proton-irradiated samples partially recovered (Fig. 8). Partial recovery of proton-damaged cells has been observed at temperatures as low as 80°C, which is what we calculate is the maximum operating temperature of the assembly under concentrated sunlight in space.

## Discussion

For 1 MeV electron exposure, the normalized degradation of the GaSb cells is slightly better than a typical GaAs cell (ref. 6) . However, proton exposures have shown that GaSb cells are more susceptible to 1 MeV protons than GaAs. Protons do most of their damage where they stop, so we are most concerned with low energy protons that are absorbed near the junction (ref. 5) . Fig. 9 shows the minimum proton energy required to get through a coverglass and 450 μm of GaAs at normal incidence. (This is calculated from data in reference 7.) Although the low energy protons do not reach the GaSb cell, some higher energy protons will lose their energy in the coverglass and the top cell, and become low energy protons by the time they reach the GaSb cell. Nonetheless, the proton flux decreases rapidly with higher energies, often down an order of magnitude from 1 MeV to 30 MeV (ref. 8) . In a concentrator system the coverglass can be considerably thicker than in a flat-plate system; since only the area where the light is focused needs to be covered, the weight is significantly reduced. The choice of coverglass thickness would depend on the orbit, but we expect to be able to heavily protect the GaSb cell from protons. In addition to the protection, there may be some annealing of proton damage.

We conclude that GaAs/GaSb tandem assemblies are a very good candidate for space concentrator photovoltaic arrays since GaAs cells are known to be radiation resistant, and we have shown that GaSb cells have good electron resistance and are protected from protons. Further radiation tests and annealing experiments will improve our estimates of how much the GaSb cells will degrade in a space environment.

## References


1. Avery, J.E. ; Fraas, L.M. ; Sundaram, V.S. ; Mansoori, N. ; Yerkes, J.W. ; Brinker, D.J. ; Curtis, H.B.; and O'Neill, M.J. : Lightweight Concentrator Module with 30% AM0 Efficient GaAs/GaSb Tandem Cells. *Proc. 21st IEEE Photovoltaic Specialists Conf.* (Kissimimee, FA), May 1990, p. 1277.

2. Fraas, L.M. ; Girard, G.R. ; Avery, J.E. ; Arau, B.A. ; Sundaram, V.S. ; Thomson, A.G. ; and Gee, J.M.: GaSb Booster Cells for over 30% Efficient Solar-Cell Stacks. *J. Appl. Phys.*, vol. 66, no. 8, Oct. 1989, p. 3866.

3. Sze, S.M.: *Physics of Semiconductor Devices,* 2nd ed., John Wiley and Sons, Inc., 1981.

4. Loo, R.; Goldhammer, L.; Anspaugh, B.; Knechtli, R.C.; and Kamath, G.S.: Electron and Proton Degradation in (AlGa)As-GaAs Solar cells. *Proc. 13th IEEE Photovoltaic Specialists Conf.* (Washington, DC), January 1978, p. 562.

5. Tada, H.Y.; Carter, J.R.; Anspaugh, B.E.; and Downing, R.G.: *Solar Cell Radiation Handbook* , 3rd ed., JPL Publication 82-69, Nov. 1, 1982.

6. Bertness, K.A.; Ristow, J. Ladle; Klausmeier-Brown, M.E.; Grounner, M.; Kuryla, M.S.; and Werthen, J.G.: 16% Efficient GaAs Solar Cell after $10^{15}$ $cm^{-2}$, 1 MeV Radiation. *Proc. 21st IEEE Photovoltaic Specialists Conf.* (Kissimimee, FA), May 1990, p. 1231.

7. Janni, J.F.: *Atomic Data and Nuclear Data Tables*, vol. 27 (Academic Press Inc.), p. 268 (1982).

8. Sawyer, D.M.; Chan, K.W.; Teague, M.J.; and Schofield, J.J. Jr.: *Proc. 13th IEEE Photovoltaic Specialists Conf.* (Washington, DC), January 1978, p. 545.


Table I. – AVERAGE CHARACTERISTICS FOR GaSb CELLS EXPOSED TO 1 MeV ELECTRONS. (Efficiency, open-circuit voltage and fill factor were measured at 50X AM0 concentration.)

| Dose, $e/cm^2$ | Efficiency, % | $J_{sc}$ (1-sun), $mA/cm^2$ | $V_{oc}$, V | Fill factor |
|---|---|---|---|---|
| 0 | 4.7 | 23.8 | 0.408 | 0.654 |
| $1x10^{14}$ | 4.5 | 22.9 | 0.403 | 0.647 |
| $3x10^{14}$ | 4.1 | 21.8 | 0.396 | 0.643 |
| $1x10^{15}$ | 3.7 | 19.9 | 0.386 | 0.642 |

Table II. – AVERAGE CHARACTERISTICS FOR GaSb CELLS EXPOSED TO 1 MeV PROTONS. (Efficiency, open-circuit voltage and fill factor were measured at 50X AM0 concentration.)

| Dose, p/cm$^2$ | Efficiency, % | $J_{sc}$ (1-sun), mA/cm$^2$ | $V_{oc}$, V | Fill factor |
|---|---|---|---|---|
| 0 | 4.8 | 23.8 | 0.410 | 0.665 |
| $3x10^{10}$ | 3.9 | 20.3 | 0.400 | 0.660 |
| $1x10^{11}$ | 3.3 | 18.0 | 0.390 | 0.630 |
| $3x10^{11}$ | 2.3 | 15.1 | 0.360 | 0.590 |
| $1x10^{12}$ | 1.5 | 12.4 | 0.300 | 0.520 |

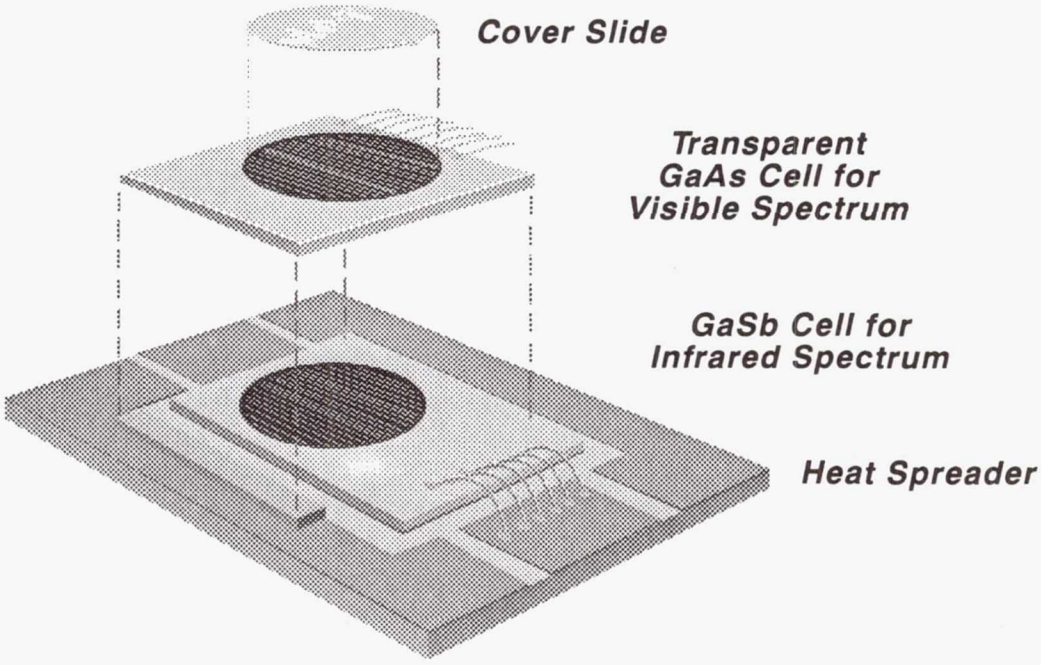


Figure 1. The GaAs/GaSb tandem assembly. The two cells are mechanically stacked, but electrically isolated.

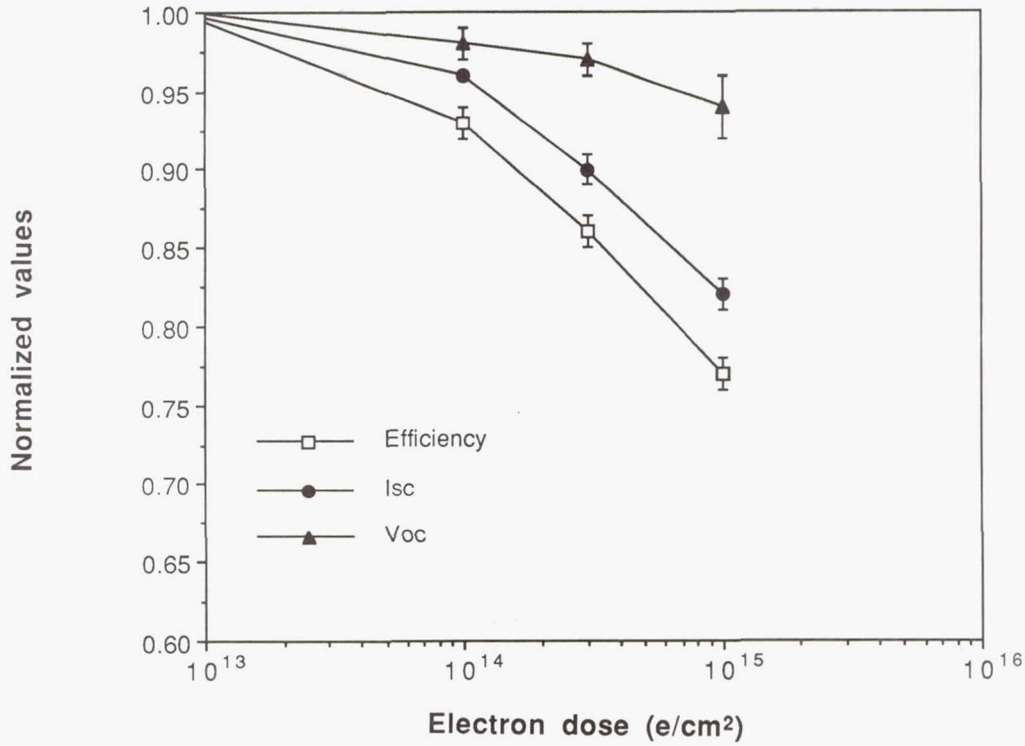


Figure 2. Normalized efficiency, short-circuit current an open-circuit voltage for GaSb cells during 1 MeV electron irradiation.

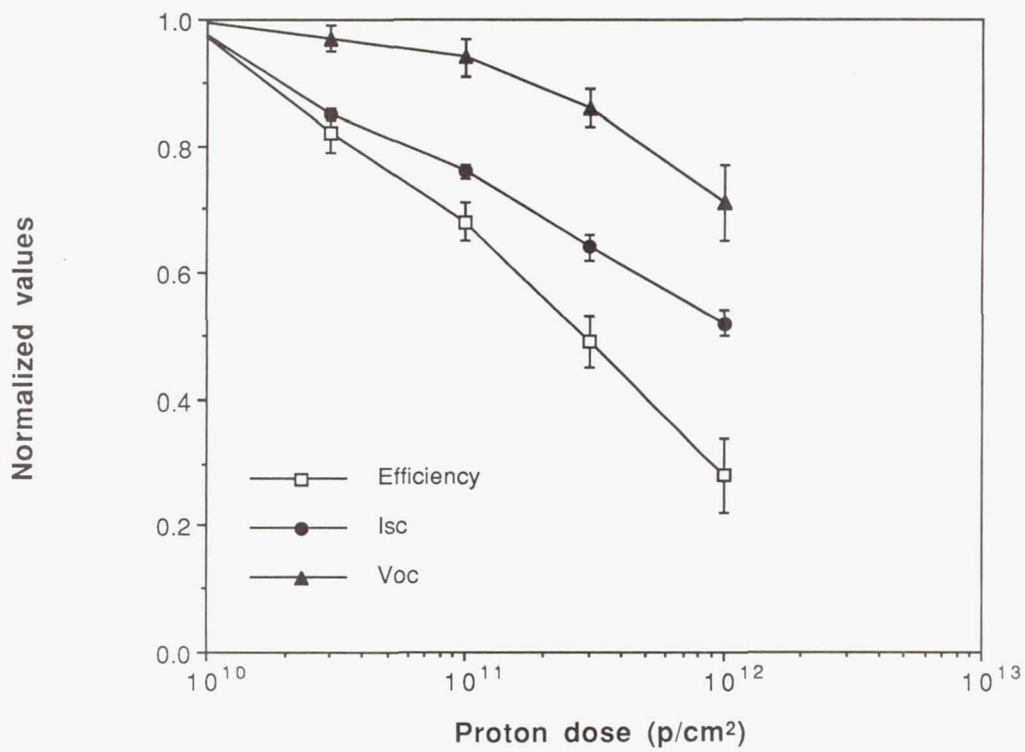


Figure 3. Normalized efficiency, short-circuit current and open circuit voltage for GaSb cells during 1 MeV proton irradiation.

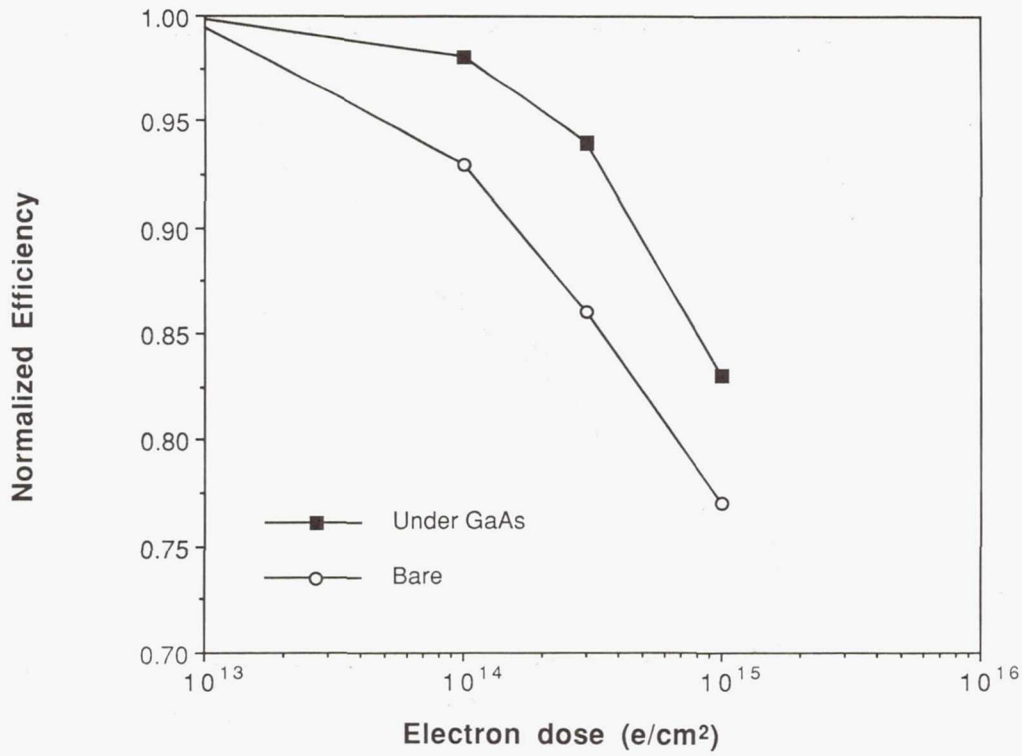


Figure 4. The efficiency degradation of GaSb cells exposed to 1 MeV electrons. The data is averaged and normalized to the beginning of life values, and compares bare GaSb cells with those in a tandem assembly.

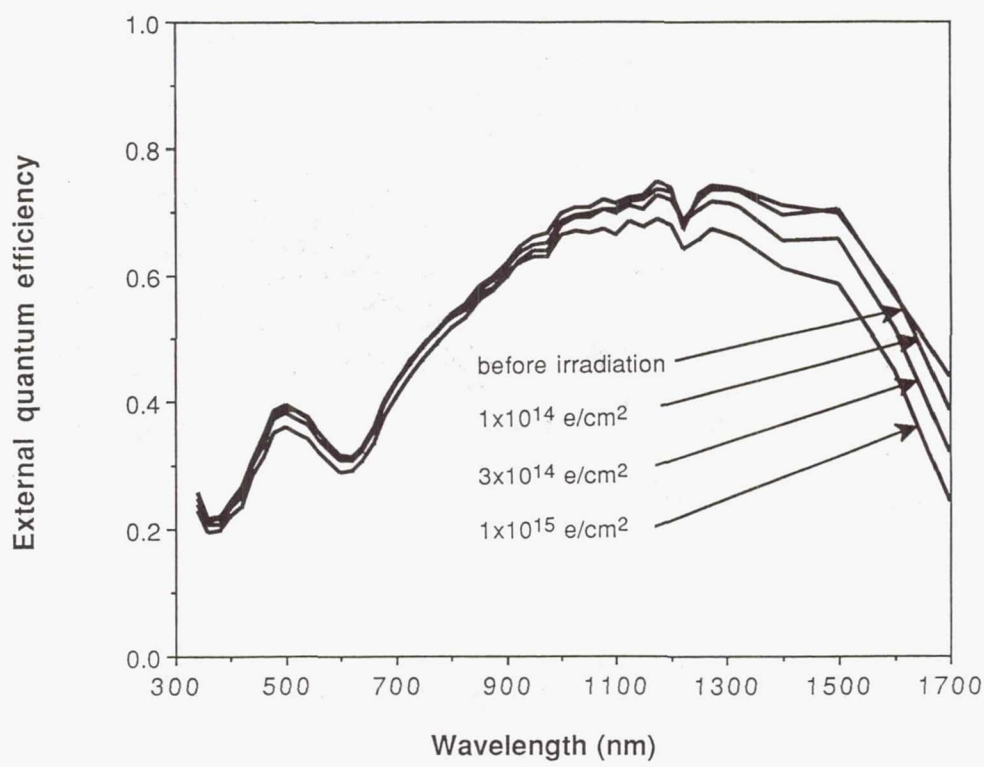


Figure 5. The spectral response curves for a GaSb cell as a function of 1 MeV electron exposure.

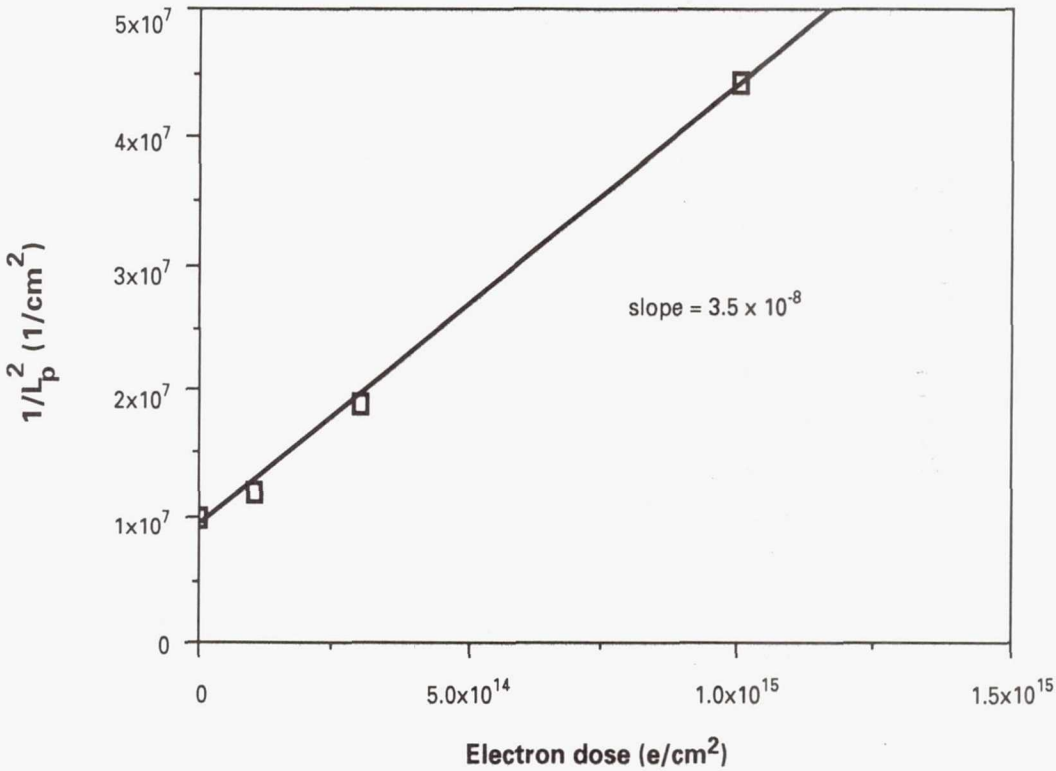


Figure 6. The calculation of the diffusion length damage coefficient from the slope of $1/Lp^2$ vs. the electron dose.

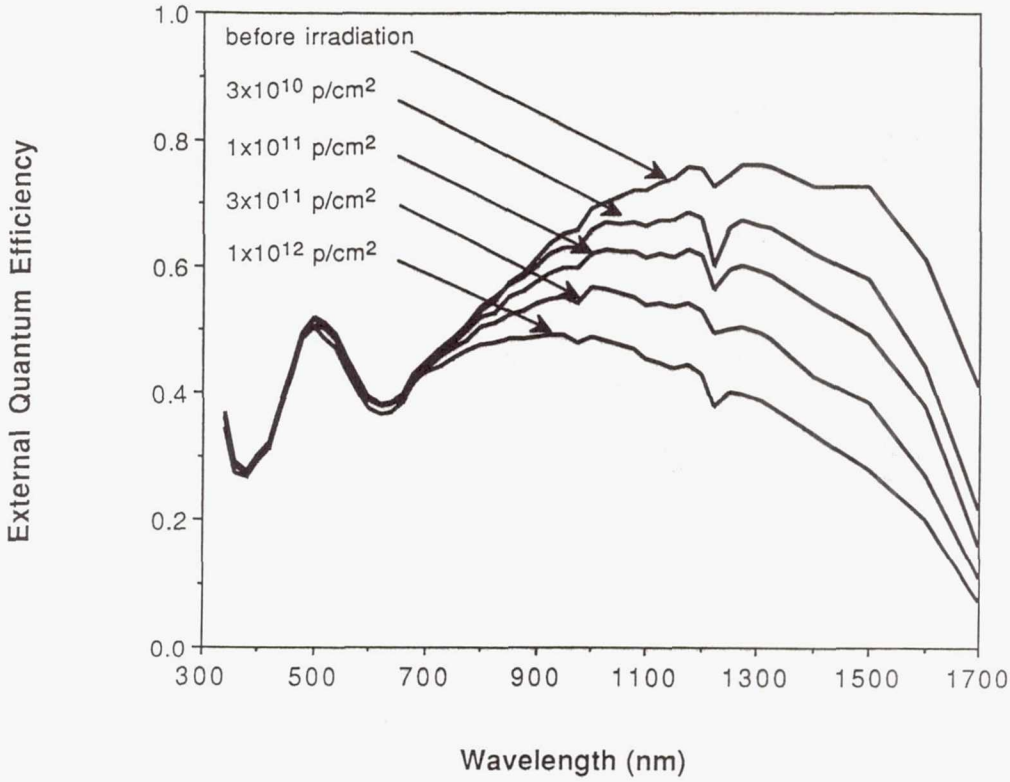


Figure 7. The spectral response curves for a GaSb cell as a function of 1 MeV proton exposure.

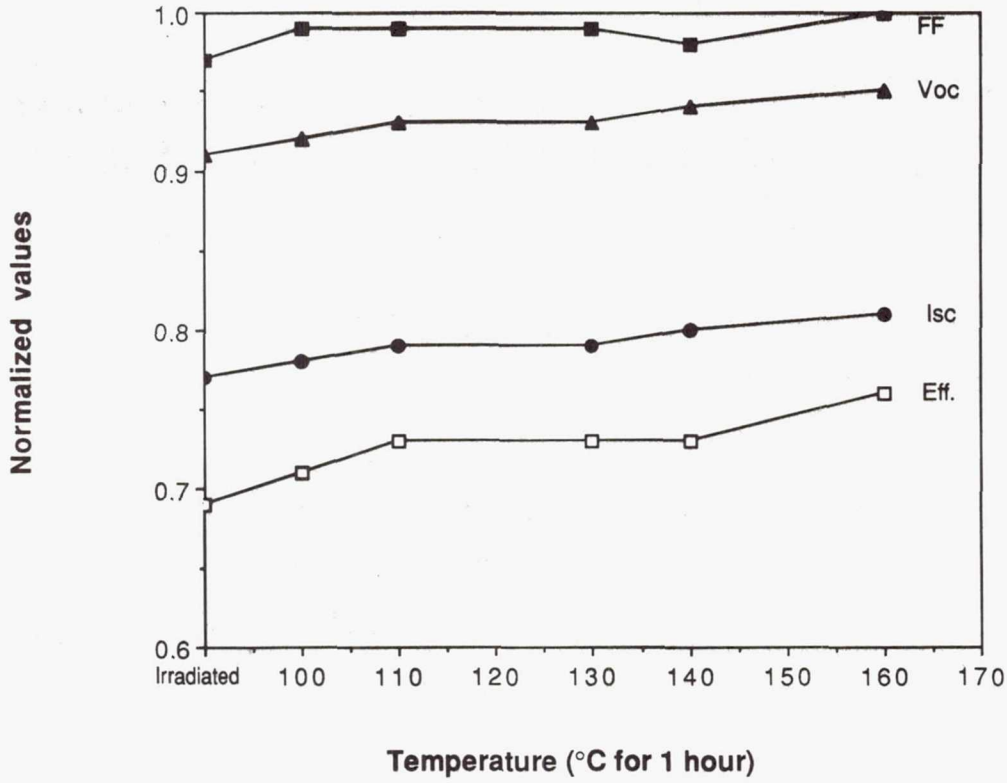


Figure 8. Isochronal annealing (1 hour at each temperature) shows partial recovery of proton-damage GaSb cells at temperatures below 160°C.

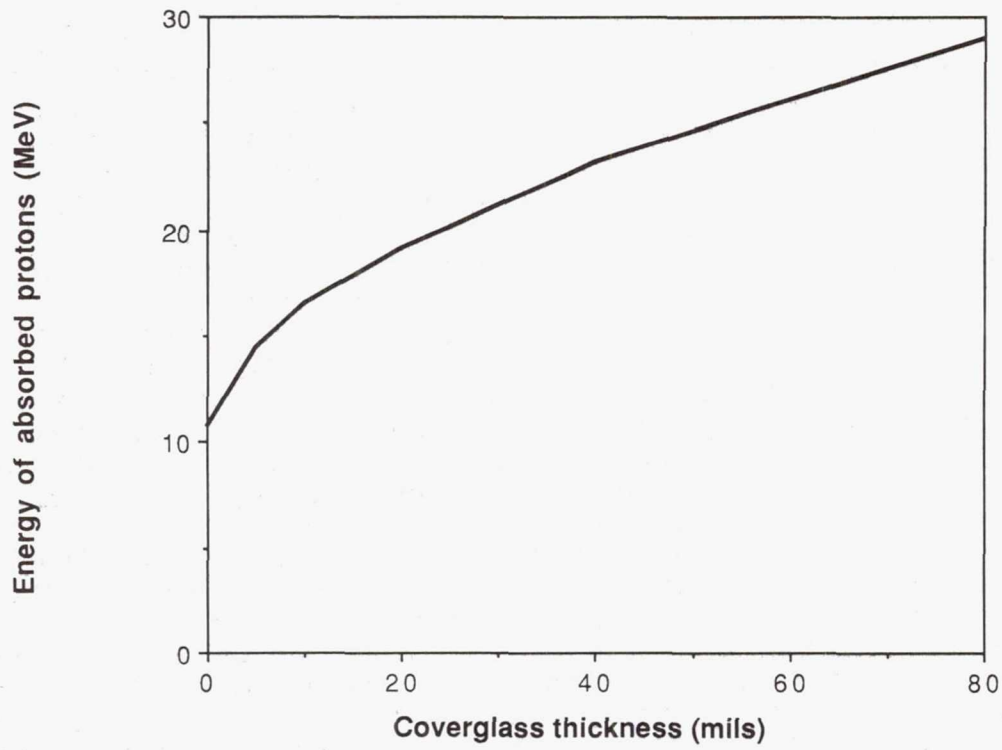


Figure 9. The minimum proton energy required to pass through a coverglass and a 450 µm GaAs cell.

# Temperature Coefficients and Radiation Induced DLTS Spectra of MOCVD Grown $n^+p$ InP Solar Cells

**Robert J. Walters and Richard L. Statler**
SFA Incorporated
Landover, MD 20785

and

**Geoffrey P. Summers**
Naval Research Laboratory
Washington, DC 20375
and
Department of Physics University of Maryland Baltimore County
Baltimore, MD 21228

## Abstract

The effects of temperature and radiation on $n^+p$ InP solar cells and mesa diodes grown by metallorganic chemical vapor deposition (MOCVD) have been studied. Prior to irradiation, the performance of several solar cells as a function of temperature from 90 to 400 K was measured and temperature coefficients of the photovoltaic parameters will be presented. The solar cells and diodes were then electron and proton irradiated, and the radiation induced defects (RID) were characterized by Deep Level Transient Spectroscopy (DLTS) and by I-V measurements on the cells thus providing the most direct evidence available of a relationship between the changes in the solar cell performance with changes in the H4 defect concentration. In contrast to previous work (Yamaguchi, 1990), the DLTS spectra induced by the proton and the electron irradiations were essentially the same. Also, the relative number of defects found as a result of the electron and proton irradiation is shown to be proportional to the calculated non-ionizing energy loss (NIEL) in InP, indicating that the same defect structure was produced in both cases, in agreement with the DLTS results. Minority carrier injection annealing experiments were then performed on the irradiated diodes at 200 K. The results showed that in both the electron and proton irradiated samples, the injection caused a substantial reduction in the major RID labeled H4. However, the H4 defect could not be completely eliminated but instead displayed a non-zero, asymptotic limiting concentration. Furthermore, this residual defect concentration was about 50% greater in the proton than in the electron irradiated diodes. In contrast, thermal annealing of the diodes at 375 K showed no residual defect concentration.

## Introduction

Due to the superior radiation resistance of InP over Si and GaAs (Yamamoto, 1984 and Weinberg, 1985) and its ability to anneal radiation damage at relatively low temperatures and by minority carrier injection (McKeever, 1991 and Walters, 1991), InP has been considered as a space solar cell material since 1984. Progress in developing these cells has been extremely rapid resulting in the production of 4 $cm^2$ cells of over 19% efficiency (air mass zero (AM0), 25 °C) in the U.S. in 1989 (manufactured by the Spire Corp. under an NRL contract) and the launch of the MUSES-A Lunar Orbiter spacecraft powered by 1300 InP solar cells in 1990 (Yamaguchi, 1990). Despite this rapid device development, the effects of temperature and irradiation on InP devices has not been fully studied. The only temperature effects studies are those of Weinberg et al. which produced results which either varied substantially among different InP cells (Weinberg, 1987) or covered only a limited temperature range (Weinberg, 1990). Three proton irradiation studies have been published (Weinberg, 1986; Takamoto, 1990; and Yamaguchi, 1990). However, since they used room temperature I-V measurements to characterize the irradiated solar cells and InP readily anneals under minority carrier injection, the interpretation of their results is not clear. Furthermore, the recent DLTS study of proton irradiated InP diodes (Yamaguchi, 1990) showed that protons in the range 2 to 7 MeV produced a DLTS spectrum significantly different than that produced by 1 MeV electrons which, from a kinematic viewpoint, is quite unexpected.

In this study, high efficiency MOCVD InP solar cells (≈18%) were illuminated with simulated solar light (AM0) in a DLTS cryostat. The cell temperature was varied over the range of 400 to 90 K, I-V curves were measured, and temperature coefficients for the photovoltaic parameters were determined. There was little variation in the measured values over all the cells. The solar cells were then irradiated with 3 MeV protons and 1 MeV electrons along with diodes of identical structure. The RID were characterized by DLTS measurements on both the cells and diodes, and the solar cell degradation was characterized by I-V measurements made at 90 K. At this low temperature, the AM0, 1 sun I-V measurement did not induce minority carrier injection annealing. It is shown that 3 MeV proton irradiation of MOCVD InP produces a DLTS spectrum essentially identical to that of 1 MeV electron irradiated InP. Also, the results show, for the first time, the actual DLTS spectrum corresponding to the changes in the performance of MOCVD grown InP solar cells.

## Experimental Notes

Figures 1a and b show a schematic drawing of the solar cells and diodes, respectively. Both device types were grown by metallorganic chemical vapor deposition (MOCVD) with identical internal structure. The 3 $\mu$m thick base p region was Zn doped to a level of 3 $\times 10^{16}$ $cm^{-3}$, and the $n^+$ region doping level was > $10^{18}$ $cm^{-3}$. The inset of figure 2 is a typical set of pre-irradiation photovoltaic parameters measured at room temperature.

The cells were illuminated through a sapphire window in the DLTS

cryostat by an Oriel 1000 W, Xe arc lamp solar simulator at 1 sun intensity, air mass zero (AM0). The simulator intensity was calibrated by standard cells and was constant to within 0.15 % during the measurements.

DLTS measurements were made using a Bio-Rad DL 4600 spectrometer. For all DLTS scans, a -2 v reverse bias was used which defined a ≈ 0.5 μm depletion region. In the solar cells, hole traps were detected with a 200 ms, 0 v fill pulse while electron traps were detected with a 50 ms, 1.5 v fill pulse. These pulses saturated the DLTS peak heights. In the diodes, the same voltage pulses were used with a 1 ms pulse width (unless stated otherwise).

The 3-MeV proton irradiation was performed at room temperature, in the dark, with a 60 nA current using the Pelletron Accelerator at the Naval Research Laboratory. A Faraday cup was used for dosimetry. The 1 MeV electron irradiation was performed using the Van de Graaff accelerator at NASA Goddard with a current density of 0.2 $\mu A/cm^2$. A Faraday cup and calibrated radiochromatic films were used for dosimetry.

## Results

The first results of this study are the temperature coefficients of the photovoltaic parameters of the solar cells. Prior to irradiation, the solar cell temperature was changed from 90 to 400 K in 25 K steps and the I-V curve was measured at each step (figure 2). From these curves, the value of the short circuit current (Isc), open circuit voltage (Voc), maximum power (Pmax), fill factor (FF), and efficiency (Eff) were determined and plotted vs. temperature (figures 3 (a)and(b)). For each cell measured, the data for each parameter over the entire temperature range could be fit to a straight line to within <5 %. Therefore, the temperature coefficient was determined as the slope of the best fit straight line. The coefficients were then averaged over all of the cells to give the final values (table 1). The errors in table 1 are the standard deviations of the averages over the different cells. The relatively large error for the FF may be due to loose top metalization contacts on some of the cells which introduced a temperature dependent series resistance into the cell contacts.

The solar cells and mesa diodes were then irradiated with 3 MeV protons up to a fluence of 5 $x10^{12}$ $cm^{-2}$. Several other mesa diodes were irradiated with 1 MeV electrons up to a fluence of 3 $x10^{15}$ $cm^{-2}$. Immediately after irradiation, the DLTS hole trap spectrum was measured in each set of devices. The minority carrier traps were not measured until after the radiation damage was characterized to avoid minority carrier injection annealing effects. The DLTS spectra measured in the proton irradiated solar cells was similar to that measured in the proton irradiated diodes (figure 4) (for an example of the spectrum measured in the diodes see Walters, 1991). The spectrum measured in the electron irradiated diodes is shown in figure 5. Comparison of figures 4 and 5 shows that all the defects seen following electron irradiation are seen in the proton irradiated samples. The defect labeled HP1 in the proton irradiated spectrum is detected in electron irradiated samples at higher fluences than used here, and EC was seen in the electron irradiated samples after an annealing stage (private communication from S. Messenger). The measured parameters of the

defects in figure 4 (table 2) match well with values measured in several other studies (McKeever, 1991; Yamaguchi, 1988; and Sibille 1982).

As expected, the defect introduction rate for 3 MeV protons was substantially higher than for 1 MeV electrons- the measured ratio is ≈760. For predictive purposes, it is necessary to determine whether the defect introduction rate is proportional to the calculated NIEL value. The NIEL calculation estimates the average number of vacancy-interstitial pairs initially produced by the irradiation (Burke, 1986). For the energies involved here, the cross sections for both 3 MeV protons and 1 MeV electrons are essentially Rutherford-like and the calculation is relatively straight forward. Similar calculations of the NIEL as function of incident electron and proton energy for Si and GaAs have been discussed in detail previously (Summers, 1988 and references therein). Briefly, the calculation involves a product of the cross section for interaction and the recoil energy, corrected for Lindhard energy partition (Lindhard, 1963). The calculation shows that the ratio of the NIEL for 3 MeV protons to 1 MeV electrons in InP is ≈740. The agreement of this calculated ratio with the measured ratio of introduction rates indicates that the H4 defect introduction rate is directly proportional to the number of defects initially produced by the irradiation. This is a important result for predicting radiation induced degradation in InP devices in general.

To further characterize the radiation damage, I-V measurements were made at 90 K on an irradiated cell (figure 6). The measurement shows that the irradiation reduced the Isc by 54%, the Voc by 2.5%, and the Pmax and Eff by 71%. A DLTS spectrum taken immediately following this measurement was identical to that of figure 4 which insures that no minority carrier injection annealing was induced by the illumination. This is the first data which clearly shows the defect spectrum corresponding to the radiation induced degradation of the solar cell performance before injection annealing.

After the radiation induced defects were measured, minority carrier injection annealing studies were performed on the diodes. Figure 7 shows the results of injecting an electron irradiated InP mesa diode with 6.4 $mA/cm^2$ and a proton irradiated InP mesa diode with 30 $mA/cm^2$ at 200 K. While the sensitivity of the H4 defect to injection is well known (Ando, 1986; McKeever, 1991; and Walters, 1991), figure 7 shows that not all of the H4 defect concentration will anneal under injection at this temperature. In both cases, the H4 defect concentration approaches a non-zero, limiting value, and this residual defect concentration seems to be about 50% larger in the proton irradiated samples than in the electron irradiated samples. However, also depicted in figure 7 is the results of isothermal annealing at 375 K of a proton irradiated diode. Over 5 hours of annealing, this data shows a first order annealing process. The same activation energy was measured for the H4 defect by DLTS before and after the injection annealing. The cause of this annealing behavior and its effect on the long term solar cell performance in a space environment is uncertain and still under investigation.

## Discussion

When measuring the properties of a material, the main concern is

the consistency of the measurement from one sample to the next. The uncertainties of the temperature coefficients presented in table 1 indicate that this is a reliable data set describing the temperature variation of InP solar cell performance over a large temperature range. The magnitude of the coefficients indicate the necessity of considering the operating temperature of the cell when predicting its performance. It is concluded that, given a single measurement at room temperature on a good quality MOCVD $n^+p$ InP cell, these coefficients enable an accurate estimate of the cell performance through the 90-400 K temperature range and will be useful in any modeling study.

To completely characterize a solar cell for space fight, the effects of radiation on the cell performance must be well understood. To this end, this study has shown that the defects produced by 1 MeV electron irradiation of MOCVD InP solar cells are the same as those produced by low energy proton irradiation. Also, since the defects were measured in the actual solar cells, the degradation of the solar cell performance has been clearly associated with the introduction of the major RID labeled H4. Until now, this conclusion was based on circumstantial evidence measured on different samples. Furthermore, this study has suggested a linear dependence of the defect introduction rate on the calculated NIEL value for a given incident particle. Since the NIEL value can be relatively easily calculated for a any given incident particle spectrum, this result would allow the calculation of the damage rate due to an entire spectrum of irradiating particles from a measurement of the damage due to irradiation at a single energy.

Finally, this study has shown that, at 200 K, minority carrier injection annealing is unable to completely eliminate the H4 defect, and the residual defect concentration was about 50% larger in the proton than in the electron irradiated samples. It seems that while there is only a single defect level producing the H4 DLTS peak, there is some portion of the H4 defect concentration which is insensitive to the injection annealing. While the reason for this behavior is still uncertain, it does seem to pose a limiting factor on the long term radiation resistance of InP at low temperatures. However, since the thermal annealing behavior at 375 K, which is near the normal operating temperature of a space solar cell, did not show this behavior, it is expected that, under normal space solar cell operating conditions, the combination of minority carrier injection and thermal annealing of the H4 defect will make InP extremely radiation resistant. This conclusion confirms the results of several previous studies (Yamamoto, 1984 and Weinberg, 1985).

## Conclusions

This study has shown that MOCVD is capable of consistently producing good quality InP solar cells with Eff > 19% which display excellent radiation resistance due to minority carrier injection and thermal annealing. It has also been shown that universal predictions of InP device performance based on measurements on a small group of test samples can be expected to be quite accurate, and that the degradation of an InP device due to any incident particle spectrum should be predictable from a measurement following a single low energy proton irradiation.

## References


Ando, K., M. Yamaguchi, and C. Uemura. 1986 Phys. Rev B. **34**, 15 Nov. 3041-3044

Burke, E.A. 1986 IEEE Trans. on Nuclear Science **NS-33**, No. 6, Dec. 1276-1281

Lindhard, J., V. Nielsen, M. Scharff and P.V. Thomsen. 1963 Mat. Fys. Medd. Dan. Vid. Selsk., **33**, n 10

McKeever, S.W.S, R.J. Walters, S.R. Messenger, and G.P. Summers. 1991 J. Appl. Phys. **69(3)**, 1435-1439, 1 Feb.

Sibille, A. and J.C. Bourgoin. 1982 Appl. Phys. Lett. **41**, 15 Nov.

Summers, G.P., E.A. Burke, M.A. Xapsos, C.J. Dale, P.W. Marshall, and E.L. Peterson. 1988 IEEE Trans. on Nuclear Science **NS-35**, 1221-1226

Takamoto, T., H. Okazaki, H. Takamura, M. Ohmori, M. Ura, and M. Yamaguchi. 1990 IEEE Proc. 2nd International Conf. on InP and Related Materials, 62-65

Walters, R.J. and G.P Summers. 1991 J. Appl. Phys. 1 May

Weinberg, I., C.K. Swartz, and R.E. Hart, Jr. 1985 IEEE 18th Photovoltaic Specialists Conf., 1722-1724

Weinberg, I., C.K. Swartz, R.E. Hart, Jr. and M. Yamaguchi 1986 5th European Symposium on Photovoltaic Generators in Space, 415-420

Weinberg, I., C.K. Swartz, R.E. Hart, Jr. and R.L. Statler, 1987 IEEE 19th Photovoltaic Specialist Conf., 548-557

Weinberg, I., C.K. Swartz, H.B. Curtis, P. Jenkins, and D.J. Brinker. 1990 IEEE Proc. 3rd International Conf. on InP and Related Materials

Yamaguchi, M. and K. Ando, 1988 J. Appl. Phys. **63**, 1 June 5555-5562

Yamaguchi, M., T. Hayashi, A. Ushirokawa, Y. Takahashi, M. Koubata, M. Hasimoto, H. Okazaki, T. Takamoto, M. Ura, M. Ohmori, S. Ikegami, H. Arai, and T. Orii. 1990 IEEE 21st Photovoltaic Specialist Conf.

Yamamoto, A., M. Yamaguchi, C. Uemura. 1984 Appl. Phys. Lett. **44** 15 March 611-613

**TABLE 1**
Temperature coefficients for InP Solar Cells

| $\frac{dIsc}{dT}\ \frac{\mu A}{K}$ | $-\frac{dVoc}{dT}\ \frac{mV}{K}$ | $-\frac{dPmax}{dT}\ \frac{\mu W}{K}$ | $-\frac{dFF}{dK}\ \frac{10^{-4}}{K}$ | $-\frac{dEff}{dK}\ \frac{10^{-2}\%}{K}$ |
|---|---|---|---|---|
| 7.81 ± 0.68 | 1.939 ± .051 | 10.45 ± .85 | 5.3 ± 1.3 | 3.07±.25 |

**TABLE 2**
Parameters of Defects Measured in Irradiated
MOCVD Grown $n^+p$ InP Solar Cells and Diodes by DLTS

| | HP1 | H2 | H3 | H4 | H5 | H7 | EA | EB | EC |
|---|---|---|---|---|---|---|---|---|---|
| $E_a$ (eV) | .15 | .20 | .30 | .37 | .54 | .61 | .26 | .74 | .16 |
| $\sigma_\infty$ $x10^{15}$ $cm^{-2}$ | .048 | .011 | .66 | .14 | 6.0 | 5.3 | 30 | 500 | 2.0 |

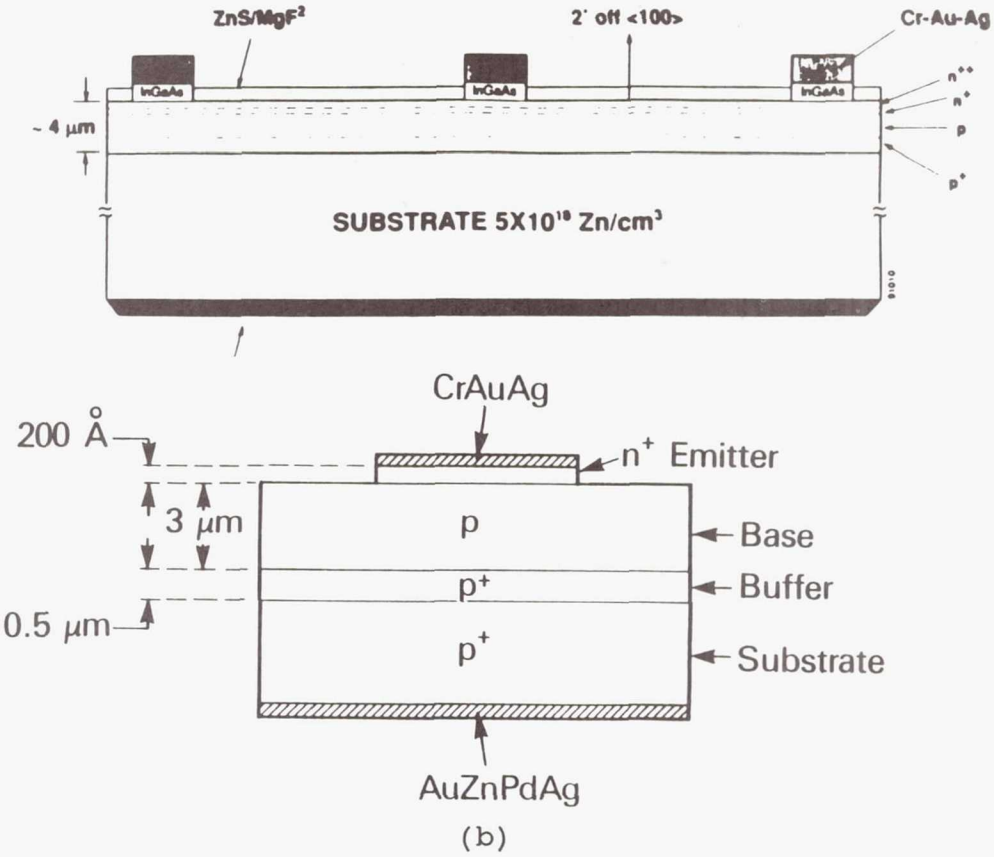


(b)

Figure 1. Schematic drawings of the (a) solar cells and (b) mesa diodes

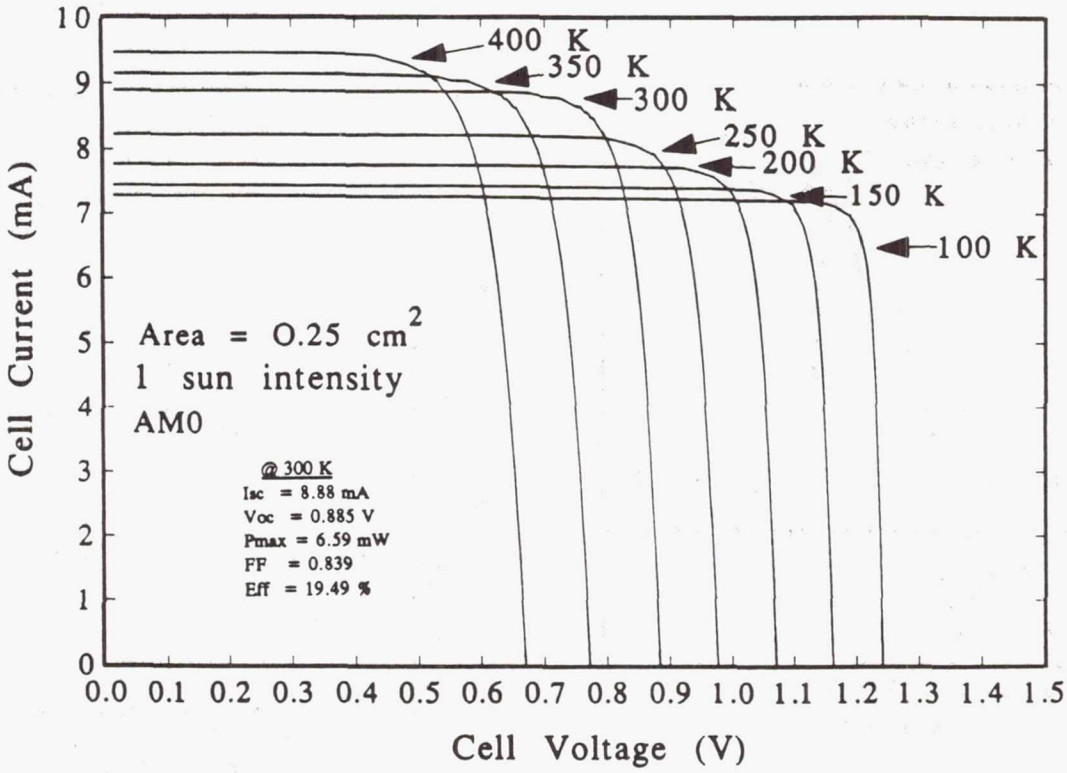


Figure 2. A typical set of I-V curves measured vs. temperature from 400 to 90 K

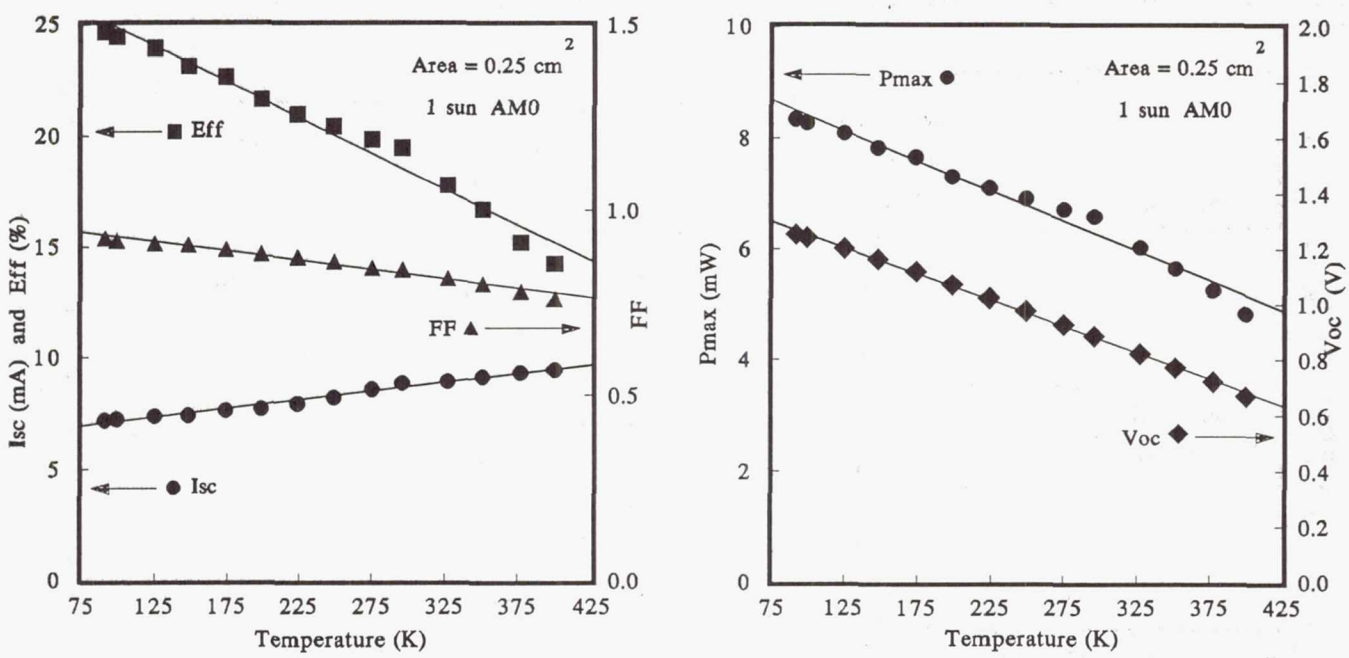


(a) (b)

Figure 3. The plots of the photovoltaic parameters gained from the above I-V curves vs. temperature.

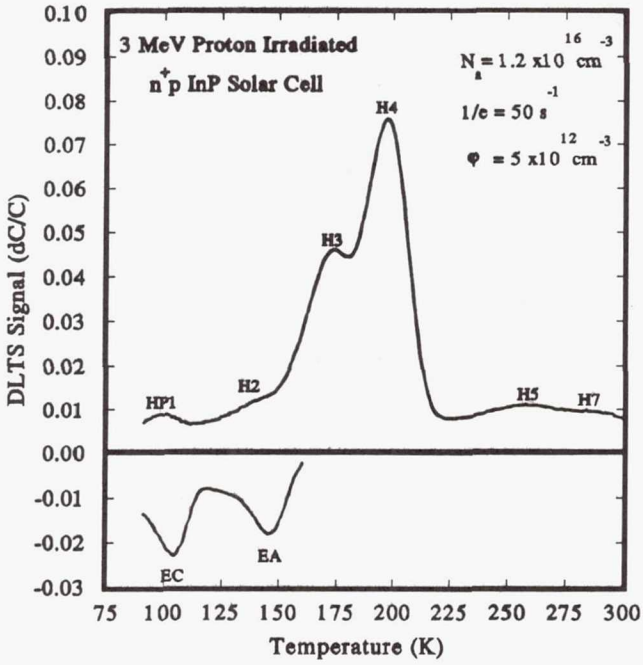


Figure 4. Typical DLTS spectrum of a proton irradiated InP solar cell

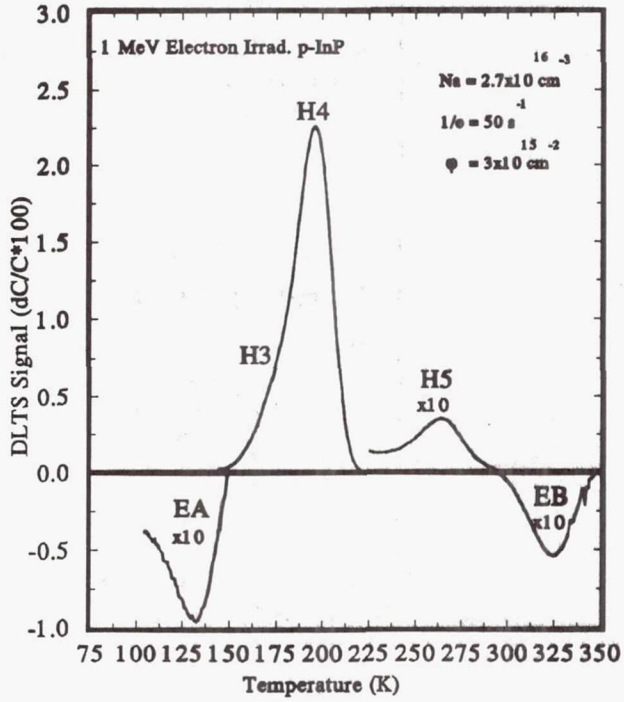


Figure 5. Typical DLTS spectrum of an electron irradiated InP diode.

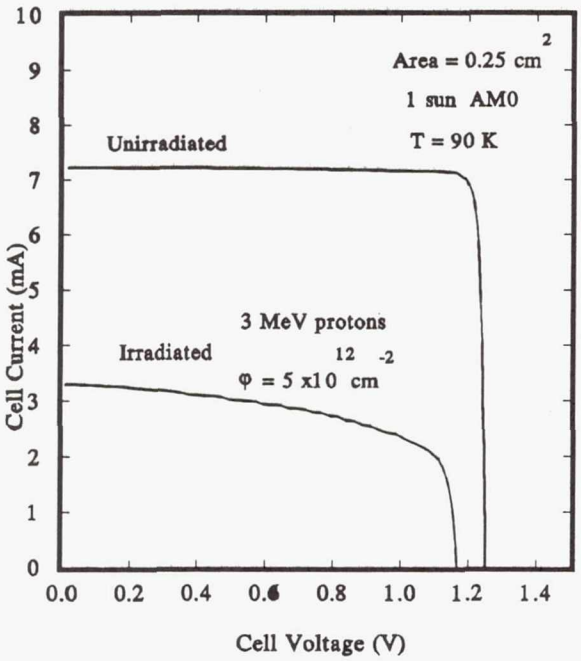


Figure 6. Typical I-V measurements at 90 K before and after proton irradiation

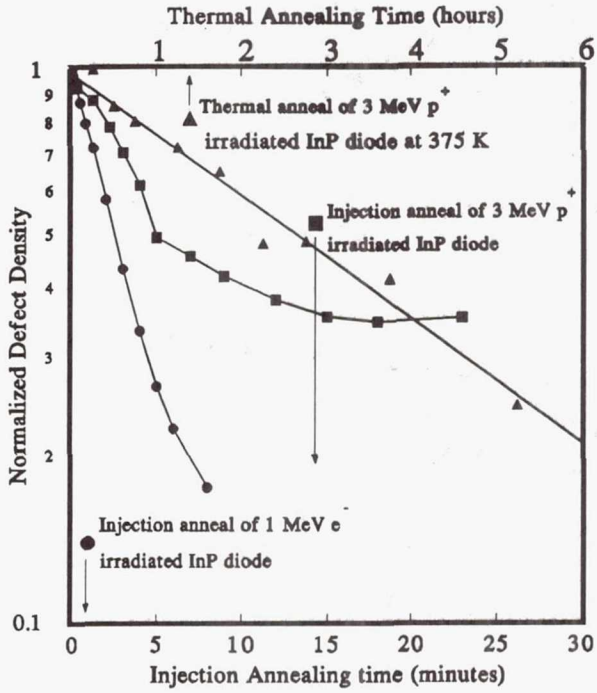


Figure 7. Comparison of the annealing behavior of the H4 defect

# ANNEALING CHARACTERISTICS OF AMORPHOUS SILICON ALLOY SOLAR CELLS IRRADIATED WITH 1.00 MeV PROTONS*

Salman S. Abdulaziz and James R. Woodyard

Institute for Manufacturing Research
and
Department of Electrical and Computer Engineering
Wayne State University
Detroit, MI 48202

## ABSTRACT

a-Si:H and a-$Si_x$,$Ge_{(1-x)}$:H solar cells were irradiated with 1.00 MeV proton fluences in the range of 1.00E14 to 1.25E15 $cm^{-2}$. Annealing of the short-circuit current density was studied at 0, 22, 50, 100 and 150 °C. Annealing times ranged from an hour to several days. The measurements confirmed that annealing occurs at 0 °C and the initial characteristics of the cells are restored by annealing at 200 °C. The rate of annealing does not appear to follow a simple nth order reaction rate model. Calculations of the short-circuit current density using quantum efficiency measurements and the standard AM1.5 global spectrum compare favorably with measured values. It is proposed that the degradation in $J_{sc}$ with irradiation is due to carrier recombination through the fraction of $D^0$ states bounded by the quasi-Fermi energies. The time dependence of the rate of annealing of $J_{sc}$ does appear to be consistent with the interpretation that there is a thermally-activated dispersive transport mechanism which leads to the passivation of the irradiation-induced defects.

## INTRODUCTION

This work continues our study of 1.00 MeV proton irradiation of plasma enhanced chemical vapor deposited hydrogenated amorphous silicon (a-Si:H) and hydrogenated amorphous silicon-germanium (a-$Si_x$,$Ge_{(1-x)}$:H) solar cells (1-3). The radiation resistance was evaluated using current-voltage (I-V) and quantum efficiency (QE) measurements. Earlier work shows that a-Si:H and a-$Si_x$,$Ge_{(1-x)}$:H solar cells irradiated with 1.00 MeV protons degrade mainly due to the decrease in the short-circuit current ($I_{sc}$) and the fill factor (FF) (1-4). The most recent work shows that a-Si:H solar cells have better radiation resistance than a-$Si_x$,$Ge_{(1-x)}$:H cells (3). However, earlier investigations suggest a-Si:H cells have poorer radiation resistance when compared to a-$Si_x$,$Ge_{(1-x)}$:H cells (4). The irradiated a-Si:H and a-$Si_x$,$Ge_{(1-x)}$:H solar cells regained their original I-V characteristics after a one hour anneal at 200 °C (1,2); some of the cells had improved I-V characteristics as compared with the pre-irradiated values (1). On the other hand,

annealing a-Si:H cells for one hour at 200 °C restored the QE to only 80 % of the pre-irradiated values, while others showed complete recovery; QE was measured without a D.C. light bias (2).

Subsequent measurements under a D.C. light bias corresponding to the AM1.5 global spectrum showed that QE was restored to pre-irradiated values for all cells (3). QE of a-$Si_x$,$Ge_{(1-x)}$:H cells was measured only under D.C. light bias, and showed complete recovery when annealed at 200 °C for one hour (3). It was found that QE depends on the light bias; $I_{sc}$ must be significantly larger than the dark current in order for QE to be independent of light bias (2,3).

The fact that QE and I-V characteristics of both a-Si:H and a-$Si_x$,$Ge_{(1-x)}$:H cells were restored to pre-irradiated values following a one hour anneal at 200 °C is an indication that 1.00 MeV protons do not produce intermixing of doped and intrinsic layers. The nature of the defects is not clear, although, earlier work suggests the defects are introduced in the intrinsic layer (5). The improved radiation resistance of a-Si alloy cells, as compared to crystalline silicon (x-Si), appears to be due to the fact that the active material is fabricated from thin films. The range of 1.00 MeV protons in a-Si alloy and x-Si materials is of the order of 10 microns. Since a-Si alloy cells are about 0.5 microns thick, the energy deposited in the active layers is considerably smaller than the energy deposited in x-Si cells. Stopping power calculations show the thinner the active layer of a cell, the lower the energy deposited in the cell by 1.00 MeV protons, and the fewer the number of defects produced by nuclear displacements (5); the authors propose that nuclear displacements produce defects which are optically and electrically active.

The purpose of this work is to investigate the annealing behavior of a-Si:H and a-$Si_x$,$Ge_{(1-x)}$:H solar cells irradiated with 1.00 MeV proton fluences in the 1.00E14 to 1.25E15 $cm^{-2}$ range.

## EXPERIMENTAL

Two sets of solar cells were employed in this study, a-Si:H and a-$Si_x$,$Ge_{(1-x)}$:H. The solar cells were fabricated in a Plasma Enhanced Vapor Deposition (PECVD) system. The structure of each solar cell is surface/grid/ITO/$p^+$/i/$n^+$/stainless steel substrate with an active cell area of 1.0 $cm^2$; ITO serves as the top electrical contact and anti-reflection coating. The a-Si:H solar cells are identified as cells C2, C3, C5, D5, N3, N5, and N6; N5 and N6 have no electrical grid,instead electrical connection was made using silver paint. The a-$Si_x$,$Ge_{(1-x)}$:H cells are identified as cells A1, A2, A3, B4, B5, and B6. The i-layer thicknesses of the a-Si:H and a-$Si_x$,$Ge_{(1-x)}$:H cells are estimated to be between 350-400 and 280-320 nm, respectively. The Ge composition in the a-$Si_x$,$Ge_{(1-x)}$:H cell is estimated to be about 20-30%.

Prior to irradiation each cell was annealed in a 1E-6 Torr vacuum for three hours at 200 °C; the I-V characteristics of the cells were measured at an ambient temperature of about 22 °C both in the dark and under illumination. The illumination source was an ELH lamp with a heat-absorbing filter. The illumination intensity was set to produce an $I_{sc}$ of 20.0 mA in a calibrated crystal silicon

solar cell which corresponded to the $I_{sc}$ produced by an AM1.5 global simulator. The calibration procedure was utilized prior to each measurement. The solar cell efficiencies are about 10% under AM1.5 global illumination. Because of the spectral mismatch between the AM1.5 global spectrum and the ELH lamp used in this investigation, the cell efficiencies will not be discussed; only changes in $I_{sc}$, FF and open-circuit voltage ($V_{oc}$) will be discussed. The samples were irradiated with a uniform 1.00 MeV proton beam of 1.0 $cm^2$ area in a vacuum measuring less than 1E-6 Torr; the beam current was about 50 nanoamperes and the fluences ranged from 1.00E14 to 1.25E15 $cm^{-2}$. The irradiations took place in the dark and at an ambient temperature of about 22 °C; thermal annealing due to the power deposited by the beam in the samples has been shown to be negligible. The samples were stored at 0 °C following irradiation in order to minimize annealing effects (1). The I-V measurements were repeated under the same conditions as before irradiation.

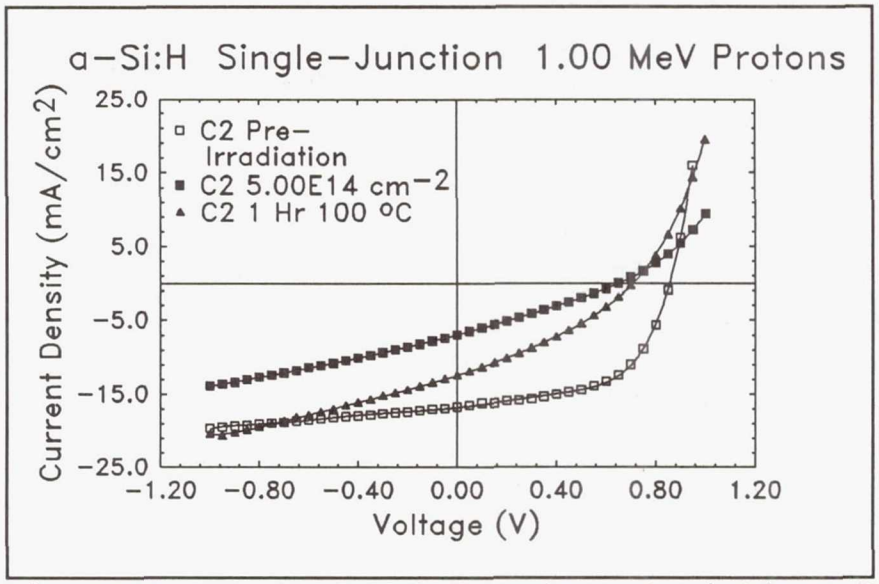


**Figure 1.** AM1.5 global J-V characteristics of a-Si:H solar cell C2 irradiated with a 1.00 MeV proton fluence of 5.00E14 $cm^{-2}$ and annealed for one hour at 100 °C.

The I-V measurements of the a-Si:H solar cells N3, N5 and N6 were inadvertently measured under a lower illumination than AM1.5 global. A calibration error resulted in a $J_{sc}$ of 7.16 $mA/cm^2$ in-

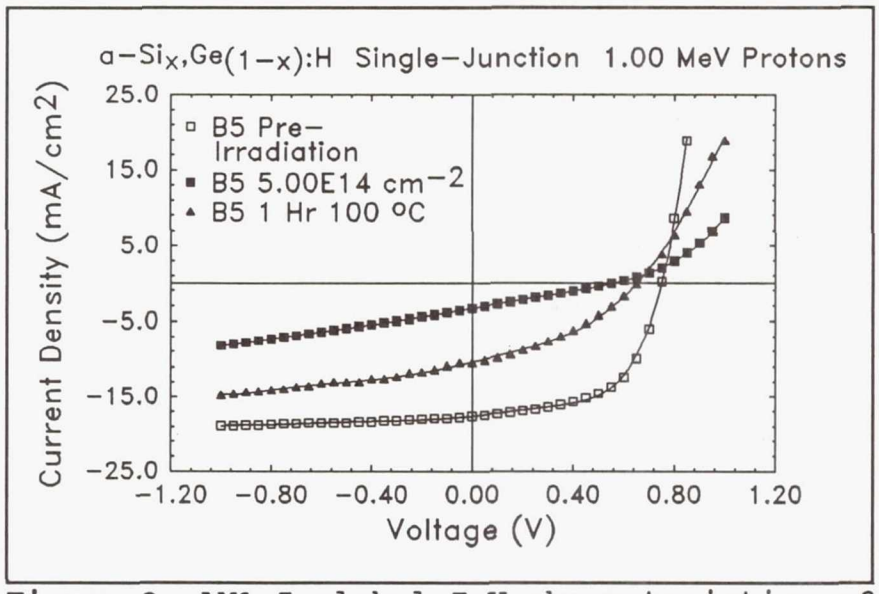


**Figure 2.** AM1.5 global J-V characteristics of a-$Si_x$,$Ge_{(1-x)}$:H solar cell irradiated with 1.00 MeV proton to a fluence of 5.00E14 $cm^{-2}$ and annealed one hour at 100 °C.

stead of 17.0 mA/-cm$^2$. Since the cells had already been annealed, it was not possible to repeat the I-V characteristics. $J_{sc}$ for the cells was corrected using a multiplicative factor of 2.37, the ratio of $J_{sc}$ under AM1.5 global illumination to $J_{sc}$ under the erroneous low level illumination. Supporting measurements were made to insure that the correction did not influence the shape of the I-V curves.

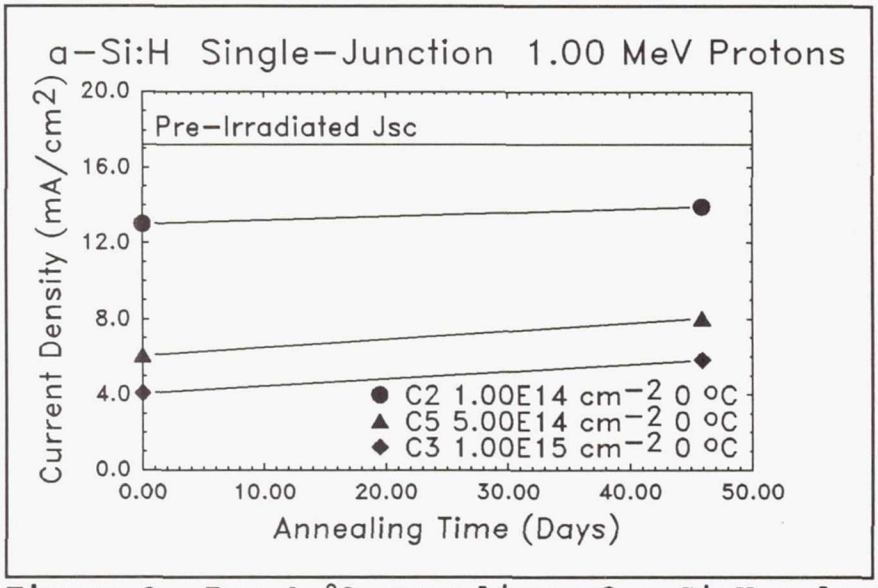


**Figure 3.** Jsc 0 °C annealing of a-Si:H solar cells irradiated with 1.00 MeV proton to fluences of 1.00E14, 5.00E14 and 1.00E15 cm$^{-2}$.

## RESULTS

Figure 1 shows the effect of 1.00 MeV protons with a fluence of 5.00E14 cm$^{-2}$ on the I-V characteristic of a-Si:H cell C2. Since the cells have area of 1.0 cm$^2$, the ordinate corresponds to the current density and the graphs represent the J-V characteristics. The solid lines used to fit the data were calculated using a seventh order regression. Pre-irradiated short-circuit current density ($J_{sc}$), $V_{oc}$ and FF degraded following irradiation from 16.7 mA/cm$^2$, 0.86 V, and 0.56 to 6.94 mA/cm$^2$, 0.62 V, and 0.29, respectively. A one-hour anneal at 100 °C resulted in $J_{sc}$, $V_{oc}$ and FF being restored to 12.4 mA/cm$^2$, 0.72

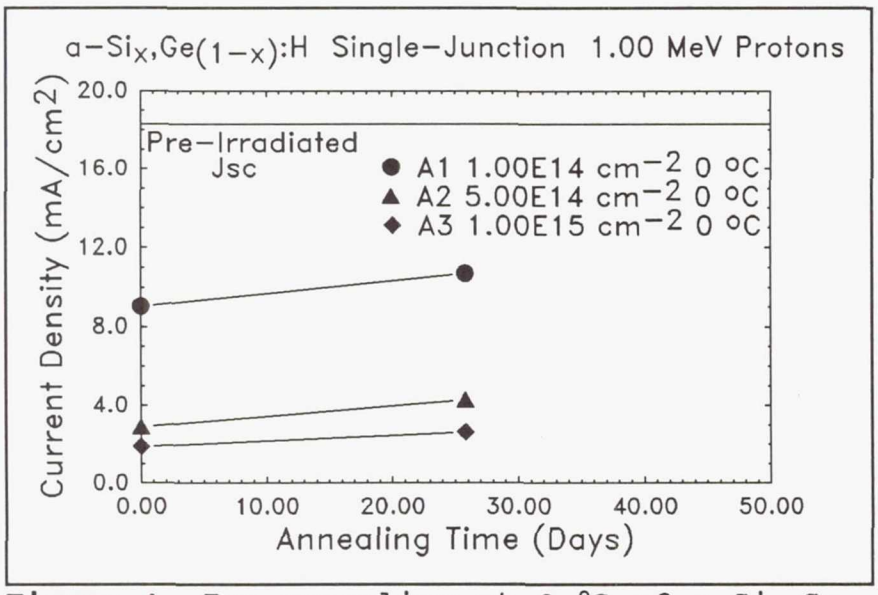


**Figure 4.** Jsc annealing at 0 °C of a-$Si_x$,$Ge_{(1-x)}$:H solar cells irradiated with 1.00E14, 5.00E14 and 1.00E15 cm$^{-2}$ 1.00 MeV Protons.

V, and 0.32, respectively.

The degradation in the J-V characteristic of a-$Si_x$,$Ge_{(1-x)}$:H cell B5 by a 1.00 MeV proton fluence of 5.00E14 $cm^{-2}$ is shown in figure 2. The pre-irradiated $J_{sc}$, $V_{oc}$ and FF were 17.3 $mA/cm^2$, 0.73 V and 0.57, respectively. The irradiation degraded the $J_{sc}$, $V_{oc}$ and FF to 3.35 $mA/cm^2$, 0.57 V and 0.26, respectively. $J_{sc}$, $V_{oc}$ and FF increased to 10.1 $mA/cm^2$, 0.67 V and 0.37, respectively, following a one-hour anneal at 100 °C.

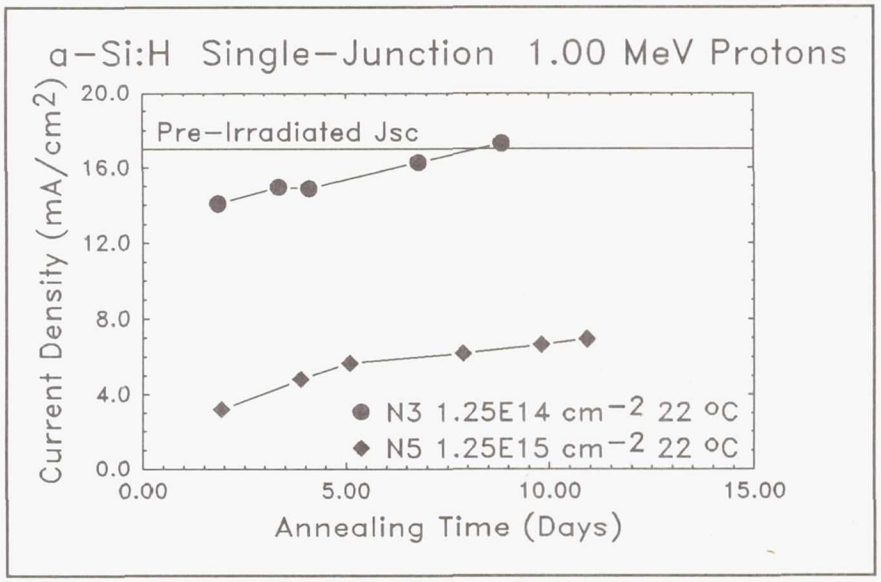


**Figure 5.** Jsc 22 °C annealing of a-Si:H solar cells irradiated with 1.00 MeV proton to fluences of 1.25E14 and 1.25E15 $cm^{-2}$.

Figure 3 shows the annealing of $J_{sc}$ at 0 °C for a-Si:H cells C2, C5 and C3 following 1.00 MeV proton irradiation with fluences of 1.00E14, 5.00E14 and 1.00E15 $cm^{-2}$, respectively. Figures 1 and 2 show $J_{sc}$ is negative; figures 3 through 8 plot the absolute value of the short-circuit current density as a function of time, $J_{sc}(t)$. The first $J_{sc}$ measurements were taken on the first day following irradiation of the samples. Straight line segments are employed to connect the data points in order to make it easier to follow the trend of the data. Figure 3 clearly shows that annealing of $J_{sc}(t)$ at 0 °C occurs for the three cells during the 45.9 days following irradiation. The effect of 0 °C annealing on the $J_{sc}$-(t) of a-$Si_x$,$Ge_{(1-x)}$:H cells A1, A2 and A3 is show in figure 4. Again, it is clear that during the 25.8 days following irradiation, 0 °C annealing occurs.

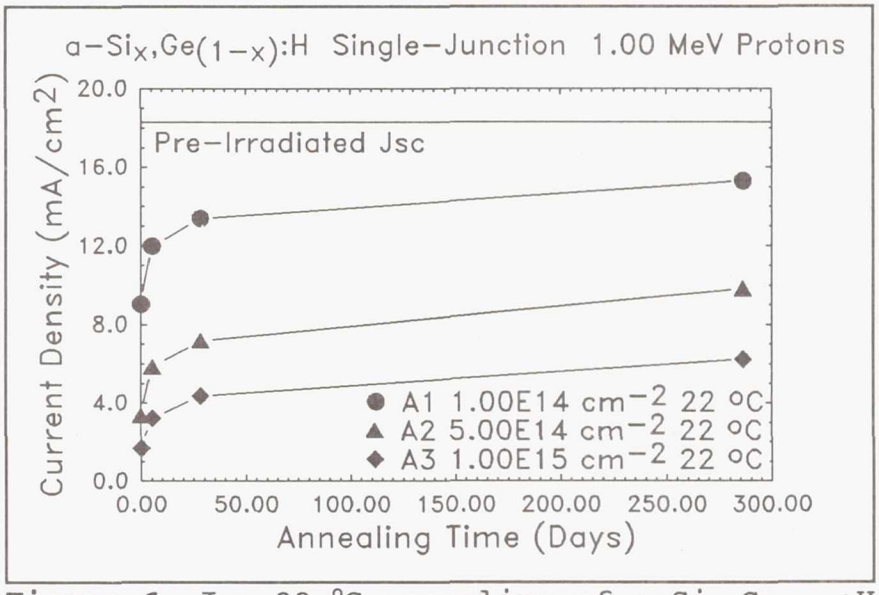


**Figure 6.** Jsc 22 °C annealing of a-$Si_x$,$Ge_{(1-x)}$:H solar cells irradiated with 1.00 MeV proton to fluences of 1.00E14, 5.00E14 and 1.00E15 $cm^{-2}$.

Figure 5 shows the annealing of $J_{sc}$ at 22 °C (room temperature) for a-Si:H cells N3 and N5 following 1.00 MeV proton irradiation with fluences of 1.25E14 and 1.2-5E15 $cm^{-2}$, respectively. The first $J_{sc}$ measurements were taken 1.83 days after irradiating the samples. Annealing cell N3 at 22 °C for 8.83 days resulted in $J_{sc}$ increasing from 14.1 to 17.3 $mA/cm^2$. The corresponding data for cell N5, annealed for 10.92 days, ranged from 3.2 to 6.9 $mA/cm^2$.

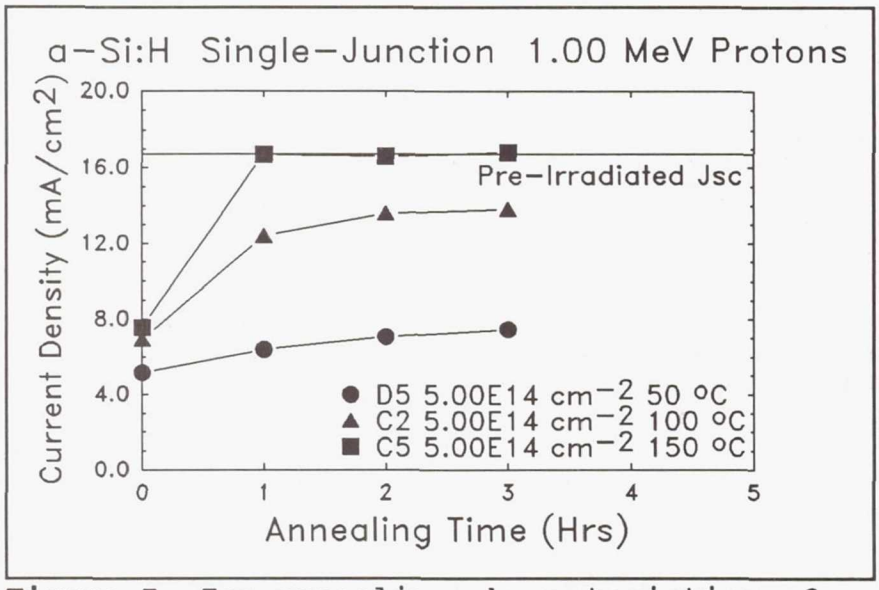


**Figure 7.** Jsc annealing characteristics of a-Si:H cells at 50, 100 and 150 °C following 5.00E14 $cm^{-2}$ 1.00 MeV proton irradiation.

The effect of annealing a-$Si_x$,$Ge_{(1-x)}$:H cells A1, A2 and A3 at 22 °C is show in figure 6. Irradiation with 1.00E14, 5.00E14 and 1.00E15 $cm^{-2}$ fluences of 1.00 MeV protons degraded $J_{sc}$ to 9.0, 3.4 and 1.7 $mA/cm^2$, respectively. Annealing cell A1 at 22 °C for 286 days resulted in $J_{sc}$ increasing to 15.3 $mA/cm^2$. Annealing cells A2 and A3 resulted in the increase of $J_{sc}$ to 9.8 and 6.3 $mA/cm^2$, respectively.

Figure 7 shows $J_{sc}(t)$ at various annealing temperatures for a-Si:H cells D5, C2 and C5 following irradiation with a 1.00 MeV proton fluence of 5.00E14 $cm^{-2}$. The post-irradiated $J_{sc}$ values of cells D5, C2 and C5 were 5.16, 6.94 and 7.55 $mA/cm^2$, respectively. Cells D5, C2 and C5 were isochronally annealed for three one-hour intervals at 50, 100 and 150 °C, respectively. The measurements show that $J_{sc}$ for cells

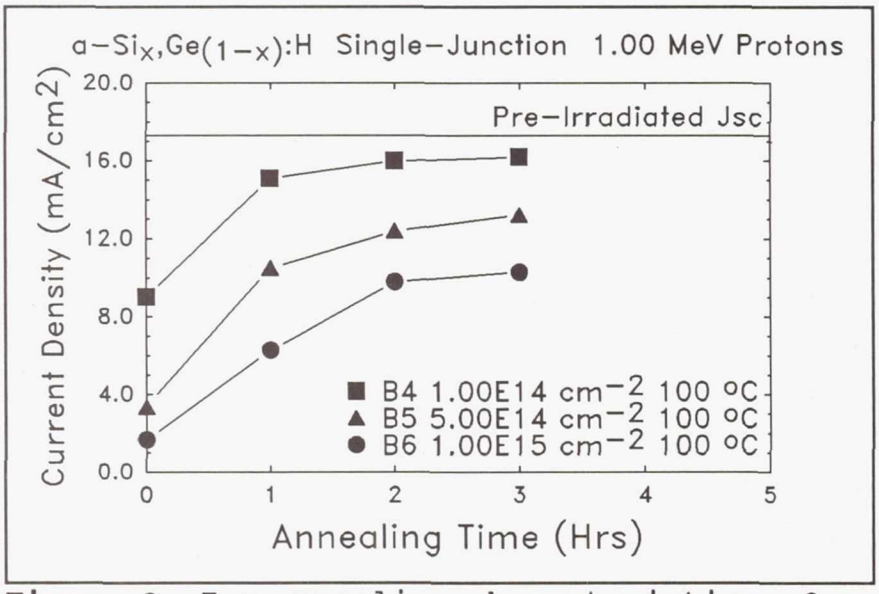


**Figure 8.** Jsc annealing characteristics of a-$Si_x$,$Ge_{(1-x)}$:H cells 100 °C following 1.00E14, 5.00E14 and 1.00E15 $cm^{-2}$ 1.00 MeV proton irradiation.

D5, C2 and C5 increased from the post-irradiated values to 7.5, 13.8 and 16.8 mA/cm$^2$, respectively, following the third one-hour anneal.

The annealing of $J_{sc}$ at 100 °C of a-$Si_x$,$Ge_{(1-x)}$:H cells B4, B5 and B6 is shown in figure 8. The post-irradiated values of $J_{sc}$ following 1.00E14, 5.00E14 and 1.00E15 cm$^{-2}$ fluences of 1.00 MeV protons were 9.0, 3.4 and 1.7 mA/cm$^2$ for cells B4, B5 and B6, respectively. The cells were annealed for three one-hour intervals at 100 °C. Following the anneals, $J_{sc}$ of cells B4, B5 and B6 increased to 16.2, 13.2 and 10.3, respectively.

QE measurements show the same behavior with fluence as we reported earlier (3). The short-circuit current density was calculated using a convolution of the measured QE and a standard AM1.5 global spectrum. A comparison of the calculated short-circuit current density, $J_{sc-cal}$, with the measured $J_{sc}$ is shown in table I; the error in the comparison is of the order of 10%. These results are characteristic of our analyses for several cells under different conditions including various stages of annealing. We find that convoluting QE with a standard AM0 spectrum, predicts the AM1.5 global power density should be multiplied by 1.28 in order to obtain the AM0 power density for these cells.

**Table I.** $J_{sc}$ (measured) and $J_{sc-cal}$ (calculated) in mA/cm$^2$ for a-Si:H cell C3 and a-$Si_x$,$Ge_{(1-x)}$:H cell A3 under AM1.5 global conditions. PRE=pre-irradiated, POST=post-irradiated with 1.00 MeV proton fluence 1.00E15 cm$^{-2}$, and %DIFF=percentage difference between $J_{sc}$ and $J_{sc-cal}$.

| | a-Si:H | | a-$Si_x$,$Ge_{(1-x)}$:H | |
|---|---|---|---|---|
| | PRE | POST | PRE | POST |
| $J_{sc}$ | 16.7 | 4.08 | 18.3 | 1.89 |
| $J_{sc-cal}$ | 15.1 | 4.26 | 17.8 | 2.17 |
| %DIFF | 9.6 | 4.4 | 2.7 | 15 |

## DISCUSSION

The results show that, qualitatively, $J_{sc}$ of both a-Si:H and a-$Si_x$,$Ge_{(1-x)}$:H solar cells anneal in a similar manner. However, the radiation resistance of a-Si:H cells is better than that of the a-$Si_x$,$Ge_{(1-x)}$:H cells, and quantitatively, the details are different. Both a-Si:H and a-$Si_x$,$Ge_{(1-x)}$:H solar cells exhibit annealing in the temperature range from 0 through 150 °C. The annealing rate of $J_{sc}$ is dependent upon the 1.00 MeV fluence and the annealing temperature. The larger the fluence and the lower the annealing temperature, the smaller the annealing rate of $J_{sc}$. For the annealing temperature range studied, the rate of annealing in $J_{sc}(t)$ is initially faster, and slows as the annealing time increases; this feature is common to both a-Si:H and a-$Si_x$,$Ge_{(1-x)}$:H cells. Our attempts to characterize the annealing of $J_{sc}$ with nth order reaction rate kinetics have not been successful. We plan on pursuing the annealing kinetics with the aid of a numerical device

model in an effort to understand the defect passivation mechanism.

The similarity of the annealing characteristics of $J_{sc}(t)$ in both a-Si:H and a-$Si_x$,$Ge_{(1-x)}$:H solar cells suggests that hydrogen plays a role in the passivation of $D^o$ defects; we do not have any direct evidence to support this conjecture. Additionally, we are unable to confirm the hydrogen glass model proposed by Kakalious and Jackson (10). We quenched our cells from 200 to 45 °C in times as short as 2.0 minutes; no glass-like metastable effects have been observed in light and dark I-V characteristics, nor in measurements of the dark conductivity activation energy. However, the time dependence of the rate of annealing of $J_{sc}$ does appear to be consistent with the interpretation that there is a thermally-activated dispersive transport mechanism which leads to the passivation of the irradiation-induced defects.

The difference between $J_{sc}$ and $J_{sc-cal}$ is about 10%. We believe that this difference is due to the experimental technique employed. The cells were illuminated with an ELH lamp which only approximates the AM1.5 global spectrum; the difference in the spectra will introduce error in the comparison. Other sources of error must also be investigated. Accurate QE measurements are necessary in order to investigate the details of carrier transport. We remain puzzled by our earlier observations that the I-V characteristics of some cells improved following irradiation and annealing at 200 °C (1). While we do not have QE measurements for the cells, the shapes of the I-V curves suggest that the surface recombination velocities at the interfaces between the $p^+$-i-$n^+$ layers are altered by irradiation and annealing. QE measurements should enable us to shed light on the role of surface recombination velocities in these cells.

The 1.00 MeV proton fluence has been correlated with irradiation-induced defects and a sub-band-gap density of states function (DOSF); a peak in the DOSF located about 1.35 eV below the conduction-band edge was proposed (6). Recent device modelling work by Schumm and Bauer suggests that the peak is due to the neutral dangling bond ($D^o$); they show that the high level of optical injection under AM1.5 global illumination suppresses the $D^-$ and $D^+$ peaks in the DOSF, and that the $D^o$ state dominates (7). The modelling work of Hack and Shur suggests that the electric field in the intrinsic layer under high injection conditions is somewhat constant (8). If this is the case in our cells, then the density of the $D^o$ states will be fairly uniform throughout the intrinsic layer. Taylor and Simmons have shown that only the states between the quasi-Fermi levels are important in carrier recombination (9). We propose that the degradation in $J_{sc}$ with irradiation is due to carrier recombination through the fraction of $D^o$ states bounded by the quasi-Fermi energies.

## CONCLUSION

We have shown that a-Si:H and a-$Si_x$,$Ge_{(1-x)}$:H solar cells anneal qualitatively in the same fashion after irradiation with 1.00 MeV proton fluences ranging between 1.00E14 and 1.25E15 $cm^{-2}$. Annealing at temperatures as low as 0 °C was observed for both types of cells

for the first time. The rate of annealing does not appear to follow a simple nth order reaction rate model. Calculations of the short-circuit current density using quantum efficiency measurements and the standard AM1.5 global spectrum compare favorably with measured values. It is proposed that the degradation in $J_{sc}$ with irradiation is due to carrier recombination through the fraction of $D^0$ states bounded by the quasi-Fermi energies. The time dependence of the rate of annealing of $J_{sc}$ does appear to be consistent with the interpretation that there is a thermally-activated dispersive transport mechanism which leads to the passivation of the irradiation-induced defects.

## REFERENCES

* This work was supported under NASA contract NAG 3-833 and the Wayne State University Institute for Manufacturing Research.

1. J. S. Payson, S. Abdulaziz, Y. Li, and J. R. Woodyard, Space Photovoltaic Research and Technology Conference, 1989 NASA Conference Publication 3107, 389 (1991).
2. J. Scott Payson, Salman Abdulaziz, Yang Li, and James. R. Woodyard in Amorphous Silicon Technology-1990, edited by P.C. Taylor, M.J. Thompson, P.G. LeComber, Y. Hamakawa and A. Madan (Mater. Res. Soc. Symp. Proc. **192**, Pittsburgh, PA, 1990) pp. 63-68.
3. Salman Abdulaziz, J. Scott Payson, Yang Li and James. R. Woodyard, Proc. of the 21st IEEE Photovoltaic Specialists Conference, 1510 (1990).
4. Joseph J. Hanak, Art Myatt, Prem Nath, and James R. Woodyard, Proc. of the 18th IEEE Photovoltaic Specialists Conference, 1718 (1985).
5. James R. Woodyard and J. J. Hanak in Amorphous Silicon Semiconductors-Pure and Hydrogenated, edited by A. Madan, M. Thompson, D. Adler and Y. Hamakawa (Mater. Res. Soc. Symp. Proc. **95**, Pittsburgh, PA, 1987) pp. 533-538.
6. J. Scott Payson, Yang Li and J. R. Woodyard in Amorphous Silicon Technology-1989, edited by A. Madan, M. Thompson, P.C. Taylor, Y. Hamakawa and P.G. LeComber, Y. Hamakawa and A. Madan (Mater. Res. Soc. Symp. Proc. **149**, Pittsburgh, PA, 1987) pp. 321-326.
7. G. Schumm and G. H. Bauer in Amorphous Silicon Technology-1990, edited by P.C. Taylor, M.J. Thompson, P.G. LeComber, Y. Hamakawa and A. Madan (Mater. Res. Soc. Symp. Proc. **192**, Pittsburgh, PA, 1990) pp. 189-194.
8. M. Hack and M. Shur, J. Appl. Phys **58** 997 (1985).
9. G. W. Taylor and J. G. Simmons, J. Non-Cry. Sol. **8-10** 940 (1972).
10. James Kakalios and Warren B. Jackson in Amorphous Silicon and Related Materials edited by Hellmut Fritzsche (World Scientific Publishing Company, 1988) p. 207.

# THE ADVANCED SOLAR CELL ORBITAL TEST

D.C. Marvin
The Aerospace Corporation
Los Angeles, CA 90245

and

M. Gates
Boeing Aerospace and Electronics Division
Seattle, WA 98124

The motivation for advanced solar cell flight experiments is discussed and the ASCOT flight experiment is described. Details of the types of solar cells included in the test and the kinds of data to be collected are given.

## INTRODUCTION

During the past 30 years, silicon solar cells have provided power for virtually the entire range of satellite missions. The requirements for these missions have included electrical power loads as high as several kilowatts and radiation fluences high enough to require the use of thick coverglasses. Nonetheless,it is only recently that the need for advanced solar cells has become sufficiently compelling that many Air Force programs are seriously considering their use.

The primary characteristics of advanced cells which are of interest include increased areal power density ($W/m^2$), specific power density (W/kg), and reduced degradation at end of life. Increased areal power density allows more power to be obtained from an existing array area, so that the same launch vehicle shroud can accommodate the spacecraft and no redesign of the solar array structure is needed. Increased specific power allows more power to be obtained without increasing the vehicle weight beyond an existing launch capability, or the same amount of power to be obtained at a lower weight, thus allowing additional payload. Reduced degradation allows mission extension or flight in very high radiation orbits There are many programs which are considering advanced solar cells for one or more of these reasons.

One reason for the limited acceptance of new solar cell technologies is the lack of proven on-orbit performance. Spacecraft customers and contractors are acutely aware of the consequences of power subsystem failure, and therefore use a conservative approach to new technologies. Clearly a successful flight demonstration is the most convincing evidence of the readiness of a new technology for application. The lack of on-orbit failures and the observation of the expected level of performance is persuasive to potential users.

The importance of a flight demonstration goes beyond the observation of expected performance. The quantitative behavior of solar cells in the actual space environment can also be used to validate the ground test models and procedures used for design and analysis of advanced cells. The most important of these ground tests is the radiation degradation analysis. In these tests, a few sample solar cells are irradiated with 1 MeV electrons and low energy protons. Typically the dose rate in these exposures is such that the cell receives a year's fluence in an hour

or so. In addition the flux is often unidirectional, rather than omnidirectional as the space environment is. Finally, each solar cell is irradiated with only a single particle type and energy, rather than with the true orbital spectrum. All of these limitations may give rise to inaccuracies in the prediction of solar cell performance.

In order to use the information from these tests to predict the on-orbit performance of cells, the equivalent fluence concept is invoked. In this theory, 1 MeV electrons are chosen as a reference particle. The fluence of 1 MeV electrons which cause the same degradation as a test particle is referred to as the damage equivalence for that particle. This equivalence is established by experiment for a variety of electron and proton energies. Based on this information, the degradation due to an arbitrary space spectrum can, in principle, be computed. The validity of the equivalent fluence concept has been verified for silicon solar cells through many years of comparison between flight and ground test data. It has not been well established for any of the advanced materials.

## THE ASCOT FLIGHT EXPERIMENT

The purpose of ASCOT is to flight test six advanced solar cell types in a high radiation, proton dominated space environment. Although the details of the host spacecraft, its orbit, and its launch date are proprietary, most of the significant details can be presented. One year in the ASCOT orbit results in a 1 MeV electron equivalent fluence of $1.5E15/cm^2$ into a silicon solar cell fitted with a 6 mil cover. This is about the same dose as accumulates in 50 years in a geosynchronous orbit. This orbit is therefore especially good for flight testing of hardened solar cells, because it accumulates radiation in a very short time. The experiment is designed to survive for at least three years. On-board dosimeters will provide an accurate measure of the actual flight environment.

The experiment consists of twenty four modules. Since there are six solar cell types, there are four identical modules populated with each cell type. Each module consists of a series string of five identical solar cells. A schematic of a typical 3x6 inch module assembly is shown in Figure 1. The cells are electrically isolated from the aluminum plate with a dielectric, and wired in series with silver mesh interconnects. Each module has a dedicated thermistor mounted directly under the cell string. The modules are designed to maintain a preselected temperature which corresponds to the expected operating temperature of the specific solar cell type when installed on a rigid panel array. Accomplishing this requires the judicious use of optical solar reflectors (OSR) because the flight experiment never experiences sun angles less than 45 degrees from normal. The OSR covers a fraction of the total module area which produces the desired temperature. In addition, the design is required to maintain a temperature gradient across a given module of less than 1°C.

The concept of the experiment is to measure 33 points along the IV curve of each module under known conditions of illumination and temperature. This is accomplished by using a programmable current sink, which is controlled with a Read Only Memory (ROM) system. The ROM is programmed before launch with the characteristics of each cell type, so that the spacing of the measurement points gives good definition to the IV curve both at the beginning and end of the 3 year mission. Analysis predicts that the accuracy of the voltage measurements will be approximately 0.5% of full scale. The use of a current sink, as opposed to a current generator, ensures that the cell strings cannot be reverse biased into failure under unexpected conditions. The telemetry system scans the 33 points in all 24 modules in approximately 5 minutes, so that the environmental conditions are not expected to change significantly. In order to minimize the telemetry requirements, only the voltage component of the IV curve is down-linked. The current sink values and calibration signals are interspersed in the voltage data.

The solar cell types included in the ASCOT experiment are listed in the following table. All cell sizes are 2x2 cm and are fitted with 12 mil coverglasses. The BOL and EOL efficiencies are given, where EOL is defined as 10 years with a 12 mil cover in the ASCOT orbit. The application column indicates the principal benefit of the cell type.

Table 1: Beginning and end of life efficiencies for solar cells in the ASCOT flight experiment.

| Cell type | BOL (28°C) | EOL (28°C) | Application |
|---|---|---|---|
| 8 mil Si | 12% | 7.3% | Reference |
| 2 mil Si | 13.5% | 7.4% | Low cost |
| GaAs/Ge | 18.5% | 10.2% | Improved efficiency |
| GaAs/Ge thin emit | 18.5% | 11.8% | Hardened |
| AlGaAs | 17% | 11.1% | Tandem component |
| GaAs/CIS | 22% | 14.1% | High efficiency |

Note: The GaAs and CIS cells are measured independently.

The silicon cells were purchased from Applied Solar Energy Corporation (ASEC). The 8 mil cells are BSR type, while the 2 mil cells are BSF/R. The standard GaAs/Ge cells were purchased from Spectrolab, Inc. Thin (0.25um) emitter GaAs/Ge cells were grown by Research Triangle Institute, contacted and interconnected by ASEC, and provided at no cost. The homojunction AlGaAs cells were also prepared by RTI and ASEC, but provided courtesy of Mr. Steven Cloyd of WRDC who funded the development effort which produced these cells. The GaAs/CIS cells were purchased from Boeing.

## CONCLUSIONS

ASCOT will be the first flight test of recently developed solar cells intended for high radiation environments. The orbit will expose the cells to a sufficiently high radiation dose that useful degradation data will be obtained in the first year. This data will guide future development of concepts such as thin emitter cells, AlGaAs cells, and tandem cells. In addition, the radiation ground test procedures for advanced materials will be verified.

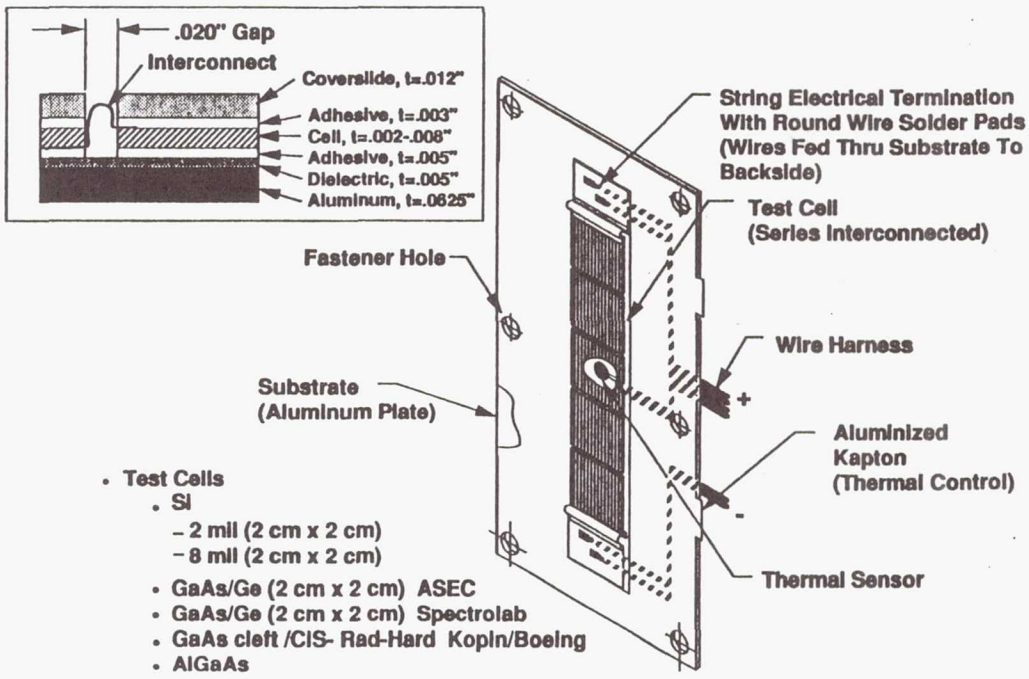

# LOW EARTH ORBITAL ATOMIC OXYGEN, MICROMETEOROID, AND DEBRIS INTERACTIONS WITH PHOTOVOLTAIC ARRAYS

Bruce A. Banks, Sharon K. Rutledge, and Kim K. de Groh
NASA Lewis Research Center
Cleveland, Ohio

## SUMMARY

Polyimide Kapton solar array blankets can be protected from atomic oxygen in low earth orbit if $SiO_X$ thin film coatings are applied to their surfaces. The useful lifetime of a blanket protected in this manner strongly depends upon the number and size of defects in the protective coatings. Atomic oxygen degradation is dominated by undercutting at defects in protective coatings caused by substrate roughness and processing rather than micrometeoroid or debris impacts. This is due to the low flux of debris and micrometeoroid impact particles of significant size. Recent findings from the Long Duration Exposure Facility (LDEF) and ground-based studies show that interactions between atomic oxygen and silicones may cause crazing and contamination problems which may lead to solar array degradation.

## INTRODUCTION

Atomic oxygen is formed in the low-earth-orbital (LEO) environment through photodissociation of $O_2$ by solar photons having wavelengths shorter than 2430Å. Because of the low probability of atomic oxygen interaction with neighboring atoms or molecules, it remains atomic in its 3p ground state rather than re-associating. Spacecraft such as Space Station Freedom (SSF), will collide with this LEO atomic oxygen atmosphere with impingement energies of 4.5 ± 1 eV (ref. 1.). As a result of this atomic oxygen bombardment, oxidation of unprotected polyimide Kapton, which is a structural support member for the solar array, would result in unacceptably low durability of the solar array blanket. No suitable materials have been found to date as replacements for solar array blankets which possess both the desirable properties of polyimide Kapton and have acceptable durability to atomic oxygen. Metal oxide protective coatings such as $SiO_X$, and other metal oxides including fluoropolymer filled metal oxides (for improved strain to failure) have been identified as suitable materials to provide atomic oxygen protection to underlying polyimide Kapton (ref. 2-4). The durability of $SiO_X$-protected Kapton depends strongly upon the number and size of defects in the coating which allow atomic oxygen to react with the underlying polyimide Kapton.

Other materials used in the fabrication of flexible solar arrays such as silicones react with atomic oxygen to develop an $SiO_2$ protective surface layer; however, crazing of the surface and deposition on adjoining surfaces from the silicone present durability and contamination concerns.

## ATOMIC OXYGEN

### Low Earth Orbital Environment

The characteristics of the LEO atomic oxygen environment which significantly influence the rate of oxidation of exposed polymeric materials are the energy, flux, and angle of attack of the impinging atomic oxygen. The full-width-at-half-maximum energy spread of approximately 2 eV for a mean ram energy of 4.5 eV (at altitudes of 400 kilometers) is the result of both the Maxwell Boltzman distribution of hot (approximately 1000 K) atomic oxygen and the spacecraft orbital inclination with respect to the earth's atmospheric rotation direction (ref. 1). The atomic oxygen fluence is strongly dependent on the altitude, solar activity, and time of day with respect to solar noon. Table I lists the atomic oxygen durability requirements for SSF surfaces. These requirements

represent worst case scenarios with a high atomic oxygen fluence to assure 15 year solar array durability (ref. 5). Atomic oxygen fluence to surfaces which are not perpendicular to the ram direction is approximately proportional to the cosine of the angle of attack as shown in Figure 1 (for 400 km altitude) for angles below 80°. Beyond 80° the arriving fluence is significantly elevated above a cosine dependence because the high temperature Maxwell Boltzman distribution contributes impinging velocity vectors which can be at various angles with respect to the ram direction. In addition, the earth's atmospheric co-rotation produces a sinusoidally varying velocity vector orientation because of the typical orbital inclination of 28.5°. The total consequence of the various velocity vector contributors is that surfaces 90° to the orbital ram direction are exposed to fluences which are 4.1% of the ram fluence as shown in Figure 1 (ref. 6).

## Interactions with Array Materials

Atomic oxygen protection of the SSF Kapton solar array blankets is to be achieved by RF magnetron sputter-deposited 1300Å-thick coatings of $SiO_X$ (where X is between 1.9 and 2.0) applied to each side of two sheets of 0.00254 cm thick Kapton H sheets which are clad together with a silicone adhesive (McGahn Nusil CV-2502) containing a fiberglass scrim (Figure 2). The purpose of the fiberglass scrim in the silicone adhesive is to provide structural integrity to the clad Kapton blanket through load transference even after significant atomic oxygen degradation. Degradation of the solar array blanket by atomic oxygen occurs chiefly at defects in the $SiO_X$-protective coatings. Such defects are typically pin windows or scratches in the protective coating which allow atomic oxygen to attack the underlying Kapton material. Defects can arise as a result of the initial uncoated Kapton roughness or surface irregularities, contamination, abrasion during $SiO_X$ sputter deposition, flexure or abrasion during flexible circuit processing, or from micrometeoroid and debris impact in space. Such coatings have been found to possess approximately 1000 defects per $cm^2$. The atomic oxygen durability of the protective coatings can be assessed using RF plasma discharges in air or oxygen to simulate LEO atomic oxygen degradation. Figure 3 shows the percent mass remaining of $SiO_X$-coated Kapton as a function of effective atomic oxygen fluence in an asher operated with air. Some of the coatings have total defect areas which are so large that they cannot survive the desired SSF 15-year fluence requirement of $4.85 \times 10^{22}$ atoms/$cm^2$ for the average of solar and antisolar facing surfaces of the array. Differences in the rate of mass loss in test coupons appears to be strongly dependent on the number and size of atomic oxygen defects in the protective coatings. Figure 4a is a scanning electron micrograph of a $SiO_X$-protected Kapton surface after atomic oxygen exposure to an effective fluence of $1 \times 10^{21}$ atoms/$cm^2$ in an RF plasma asher. Figure 4b shows the same location after tape was used to remove the $SiO_X$ coating. As can be seen in Figure 4b, atomic oxygen undercutting at the site of pin windows and scratches is clearly evident even in places where little evidence of atomic oxygen undercutting can be seen in Figure 4a. If the applied protective coating is free from residual stress, undercutting of the coating can occur without the coating tearing. If sufficient stress exists to cause the coating to tear when undercut, significantly more atomic oxygen will be allowed to enter the defect causing accelerated damage to the underlying Kapton. The shape of the undercut cavities below pin windows is highly dependent upon the directional characteristics of the atomic oxygen arrival. Figure 5 illustrates the initial shape of atomic oxygen undercutting resulting from isotropic RF plasma atomic oxygen arrival, directed beam or fixed ram atomic oxygen arrival, and sweeping ram arrival. Functional solar arrays will be exposed to sweeping ram atomic oxygen arrival, which should produce an initial atomic oxygen undercut geometry which is elongated in shape. As the atomic oxygen oxidizes all the way through the Kapton to the $SiO_X$ coating on the opposite side of the sheet, significantly more scattering of the atomic oxygen will occur, which should be more closely replicated by the plasma asher environment than by fixed arrival direction exposures. Thus with time, undercutting patterns at pin window defect sites should evolve to nearly circular symmetry.

Evidence of atomic oxygen undercutting in space, even for ram atomic oxygen arrival, can be seen from the results of aluminized Kapton multilayer insulation exposed on the LDEF spacecraft. Figure 6 shows aluminized Kapton from the LDEF spacecraft which was exposed to an estimated fluence of $5.77 \times 10^{21}$ atoms/$cm^2$, both prior to (Fig 6a) and after (Fig 6b) removal of the aluminum coating. Projections of durability of solar array material exposed to sweeping atomic oxygen arrival conditions as anticipated by SSF may be accomplished

from ground based plasma asher and directed beam simulations as well as with in-space directed ram exposure experiments such as the LDEF spacecraft. By comparison of ground and space based data, Monte Carlo models can be created and used to project performance of arrays in space (ref. 7).

Silicone adhesives are used extensively in the construction of the SSF solar array, as shown in Figure 2. Portions of the silicone (Dow Corning 93-500) adhesives used to attach the cover glass to the solar cells will be exposed to atomic oxygen attack. If significant degradation of the Kapton circuit carrier sheet or Kapton overlay sheet occurs, then exposure of the cladding silicone adhesive (McGahn Nusil CV-2502) may occur. In addition, silicones are used for thermal control of solar array diode surfaces. Although silicones tend to develop $SiO_2$-protective outer layers, high fluence atomic oxygen exposure tends to cause silicones to develop tensile stresses in the near surface layers, causing crazing, which can extend deep into the silicone bulk. As such crazing advances, secondary branch cracks also develop. Figure 7 is a scanning electron micrograph of silicone adhesive (from Kapton adhesive tape) exposed on the LDEF spacecraft to an estimated fluence of $4.92 \times 10^{21}$ atoms/cm$^2$. In addition to crazing, silicones eject polymeric fragments during atomic oxygen attack which contaminate adjoining surfaces. This contaminant layer develops as a brown coating where further atomic oxygen bombards the contaminated surfaces. Figure 8 is a photograph of a portion of the Solar-Array-Materials Passive LDEF experiment (A0171) which contained samples of silicones (ref. 8). To the immediate right side of the light-colored silicone samples in the center of the photograph are clear regions followed by dark deposits (further to the right) where atomic oxygen impingement occurred. Similar dark contaminant layers have been observed in ground plasma asher tests. This LDEF experiment was located on row A8 which had atomic oxygen arriving from 38° to the left of the surface normal. Figure 9 illustrates the transference and observed dark contamination which results from further atomic oxygen bombardment of the ejected silicone polymeric fragments. Little is known about the surface mobility of the atomic oxygen ejected silicone molecular fragments; however, extensive silicone contamination has been observed on LDEF surfaces. The role of ultraviolet solar illumination on contamination issues is not fully clear, based on LDEF and plasma asher results to date. If ejected silicone polymeric fragments can transport themselves to the front surface of solar cell cover glasses then atomic oxygen darkening could degrade solar array output through darkening around the perimeter of each cell. Figure 10 illustrates how atomic oxygen might reach the silicone cover glass adhesive allowing ejected silicone contaminants to redeposit on adjoining surfaces.

## MICROMETEOROIDS AND DEBRIS

The flux of particles of a given diameter and smaller that arrive on surfaces characteristic of the SSF orbital environment is shown in Figure 11 (ref. 9). The flux of micrometeoroid particles is surpassed by debris particles for particles of diameter less than $10^{-3}$ cm. Large diameter particles can create large defects in the protective coatings on solar array blankets. However, the flux of large particles is not sufficient to contribute to substantial oxidative solar array mass loss from subsequent atomic oxygen attack. Smaller particles, though more frequent in number, produce crater areas which are negligibly small for particles below $10^{-5}$ cm in diameter (ref. 9). The fractional mass loss, $\Delta M/M$, of the SSF solar array blanket, due to atomic oxygen attack at debris-caused defect sites, can be shown to be approximated by:

$$\frac{\Delta M}{M} = \frac{\pi k}{2y}\left(\frac{R^2 d^2}{4} - x^2\right) d^{-2.5} f E t^2$$

where: $k$ = constant = $2.82 \times 10^{-17} (cm)^{0.5}/sec$ (ref 9)
$R$ = ratio of crater to debris particle diameter
$d$ = debris particle diameter, cm
$x$ = $SiO_X$ protective coating thickness, cm
$f$ = atomic oxygen flux, atoms/$cm^2$/sec
$E$ = Kapton atomic oxygen erosion yield, $cm^3$/atom
$t$ = mission duration , sec
$y$ = Kapton thickness, cm

For $R = 5$ (ref. 10), $x = 1.3 \times 10^{-5}$ cm (1300Å), $f = 1.14 \times 10^{14}$ atom/$cm^2$/sec (ref. 5), $E = 3.0 \times 10^{-24}$ $cm^3$/atom (ref. 1), $t = 4.73 \times 10^8$ sec (15 yrs.), and $y = 0.00254$ cm;

The mass loss of the antisolar facing Kapton overlay is calculated to be only 0.2% of the initial mass after 15 years in low earth orbit. If one assumes that the debris-caused atomic oxygen defects have extensive atomic oxygen undercutting, then the atomic oxygen reaction probability may be near 1 due to multiple scattering, producing erosion yields near $2.2 \times 10^{-23} cm^3$/atom. Even with such an assumption, the percent mass loss of the Kapton overlay would still represent only 1.4% of the initial blanket mass. Although debris particles ($\geq 10^{-5}$ cm in diameter) appear to be the largest contributor to the number of defects (approximately 3000/$cm^2$/yr), the area of damage caused by these particles is far less than the area of pin windows and scratches (approximately 1000 defects/$cm^2$) resulting from the Kapton roughness, deposition of the coating, and from flexible circuit processing. Because the micrometeoroid flux is significantly below the debris flux for $10^{-5}$ to $10^{-4}$ cm diameter particles, micrometeoroids do not represent a life-limiting hazard to the atomic oxygen durability of solar array blankets. Results of micrometeoroid or debris particle impacts on $SiO_X$-protective coatings has been witnessed on the LDEF spacecraft as show in Figure 12. As can be seen from Figure 12, cracking of the glass coating is limited to the vicinity of the impact site, even for this rather large diameter crater.

## CONCLUSIONS

Atomic oxygen protective coatings, such as sputter deposited $SiO_X$, are inherently durable to low-earth-orbital atomic oxygen attack. Defects in these coatings caused as a result of surface roughness, coating deposition, processing, or micrometeoroid and debris impact will allow atomic oxygen to attack the underlying polyimide Kapton material. The atomic oxygen durability of current $SiO_X$-deposited coatings indicates that initial roughness, coating deposition, and processing-caused defects dominate the atomic oxygen degradation processes. Micrometeoroid and debris impacts do not constitute a threat to the atomic oxygen durability of solar array blankets. Potential atomic oxygen interaction with silicones must be considered to determine whether or not crazing and contamination associated with atomic oxygen interactions will cause solar array degradation.

## REFERENCES


1. Banks, Bruce A., Rutledge, Sharon K., Auer, Bruce A., and DiFilippo, Frank, "Atomic Oxygen Undercutting of Defects on $SiO_2$ Protected Polyimide Solar Array Blankets," Proceedings of the Materials Degradation in Low Earth Orbit Symposium of the 119th TMS Annual Meeting and Exhibit, Anaheim, CA, February 18-22, 1990.

2. Banks, Bruce A., Mirtich, Michael J., Rutledge, Sharon K., and Nahra, Henry K., "Protection of Solar Array Blankets from Attack by Low Earth Orbital Atomic Oxygen," Proceedings of the 18th IEEE Photovoltaic Specialist Conference, October 21-25, 1985, Las Vegas, NV.

3. Banks, Bruce, A., Mirtich, Michael J., Sovey, James S., Nahra, Henry K., and Rutledge, Sharon K., "Flexible Fluoropolymer Filled $SiO_2$ Protective Coatings," Presented at the Technology 2000 Conference, Washington, D.C., November 27-28, 1990.

4. Rutledge, Sharon K. and Mihelcic, Judith A., "Undercutting of Defects in Thin Film Protective Coatings on Polymer Surfaces Exposed to Atomic Oxygen," NASA TM 101986, Presented at the 16th International Conference on Metallurgical Coatings, American Vacuum Society, San Diego, CA, April 17-21, 1989.

5. Rockwell International Corporation SSF document RC1800, section 3.2.5.1.1.3 atomic oxygen, January 10, 1991.

6. Bourassa, Roger J. and Gillis, James R., "Data Summary: Atomic Oxygen Flux and Fluence Calculation for Long Duration Exposure Facility (LDEF), NAS1-18224, task 12, LDEF Materials Data Analysis, Boeing Defense and Space Group, Seattle, WA, August 13, 1990.

7. Banks, Bruce A., Auer, Bruce M., Rutledge, Sharon K. and Hill, Carol M., "Atomic Oxygen Interaction with Solar Array Blankets at Protective Coating Defect Sites," Presented at the 4th Annual Workshop on Space Operations, Automation and Robotics (SOAR 90), Albuquerque, NM, June 26-28, 1990.

8. Clark, Linwood, Kinard, William, Carter, David, Jones, James Jr., "The Long Duration Exposure Facility (LDEF) Mission One Experiments," NASA SP-4731984.

9. Space Station Program Natural Environment Definition for Design, Change request SSP-30425, January, 1991.

10. Carey, W. C., McDonnell, J., and Dixon, D. "An Empirical Penetration Equation for Thin Metallic Films Used in Capture Cell Techniques" in Properties and Interactions of Interplanetary Dust, pp. 131-136, published by D. Reidel Publishing Co., 1985.

TABLE I. - ATOMIC OXYGEN DURABILITY REQUIREMENTS FOR THE SSF PHOTOVOLTAIC ARRAY

| Surface | Atomic Oxygen Flux, atoms/cm$^2$ sec | Atomic Oxygen 15 year Fluence, atoms/cm$^2$ |
|---|---|---|
| Ram Facing | $3.6 \times 10^{14}$ | $1.7 \times 10^{23}$ |
| Solar Facing | $9.1 \times 10^{13}$ | $4.31 \times 10^{22}$ |
| Anti-Solar Facing | $1.14 \times 10^{14}$ | $5.40 \times 10^{22}$ |
| Average of Solar and Anti-Solar Facing | $1.02 \times 10^{14}$ | $4.85 \times 10^{22}$ |

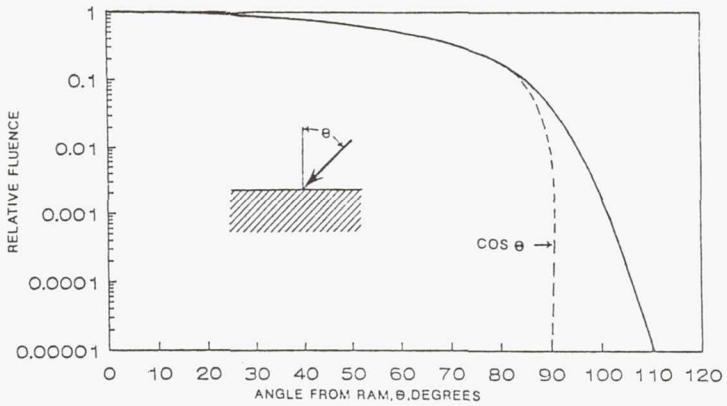


Figure 1: Atomic oxygen fluence dependence on arrival angle.

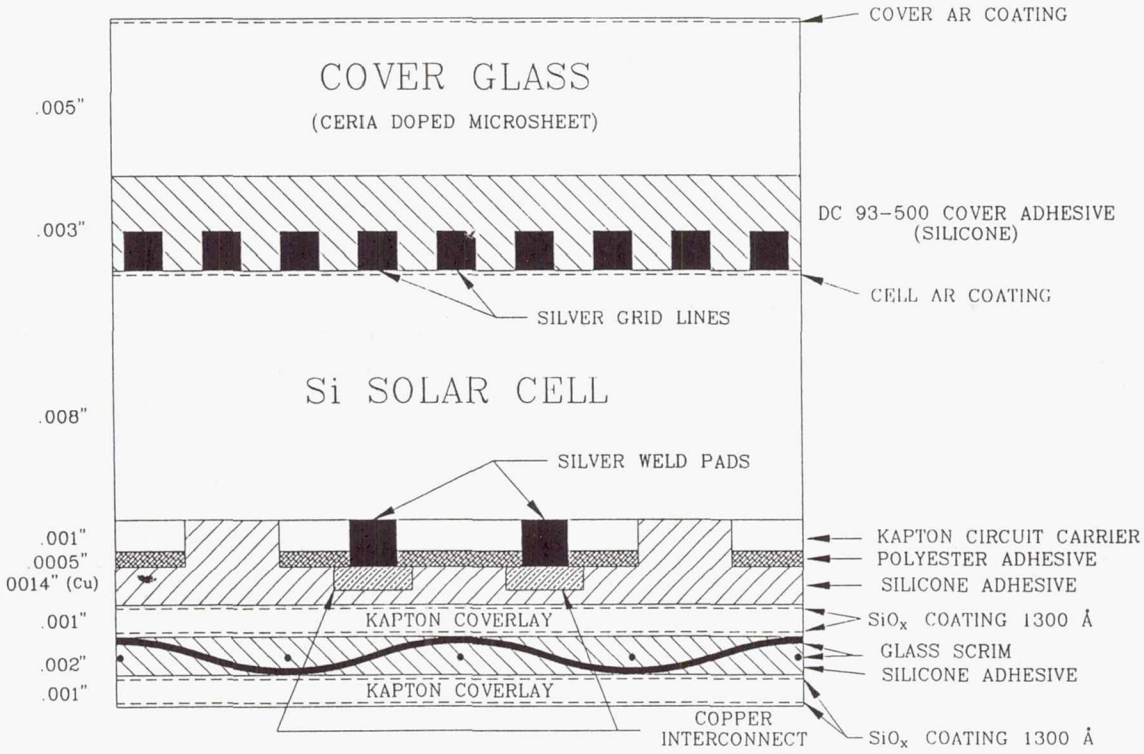


Figure 2: SSF solar array blanket cross section.

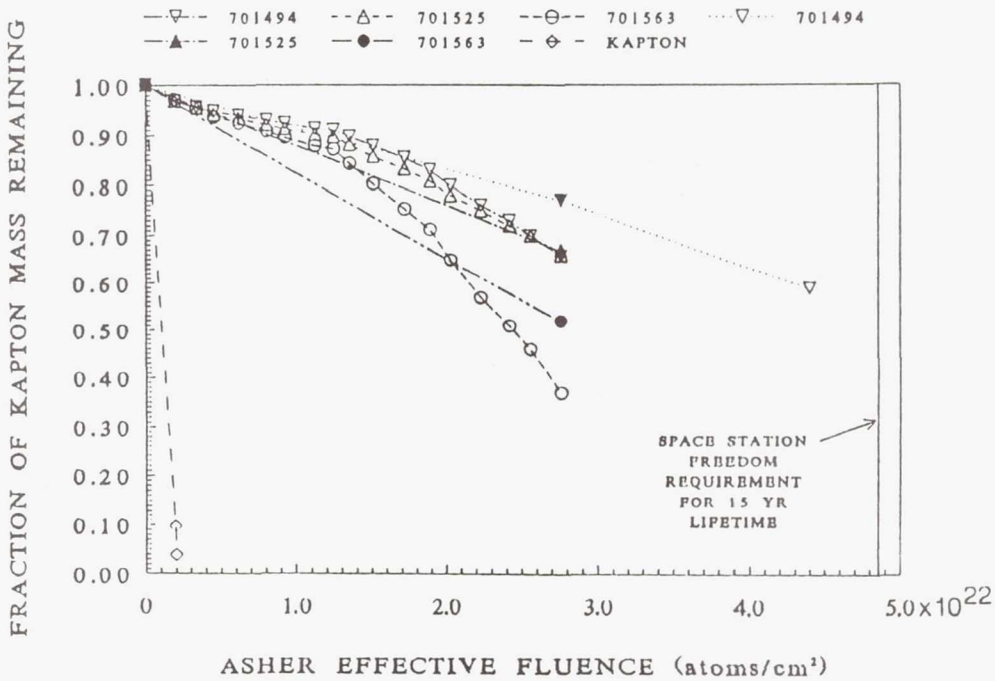


Figure 3: Mass loss for $SiO_X$ (1300Å) coated Kapton exposed to atomic oxygen in a plasma asher.

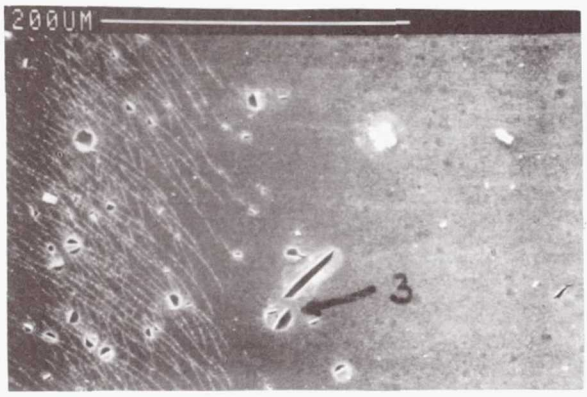


a: Prior to removal of the $SiO_X$ coating.

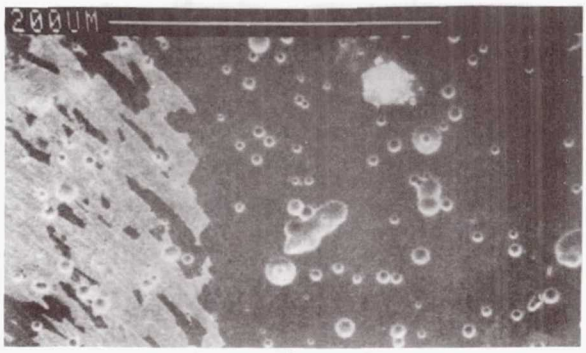


b: After removal of the $SiO_X$ coating.

Figure 4: $SiO_X$ (590Å) coated Kapton after exposure in a plasma asher to an atomic oxygen fluence of $1 \times 10^{21}$ atoms/$cm^2$.

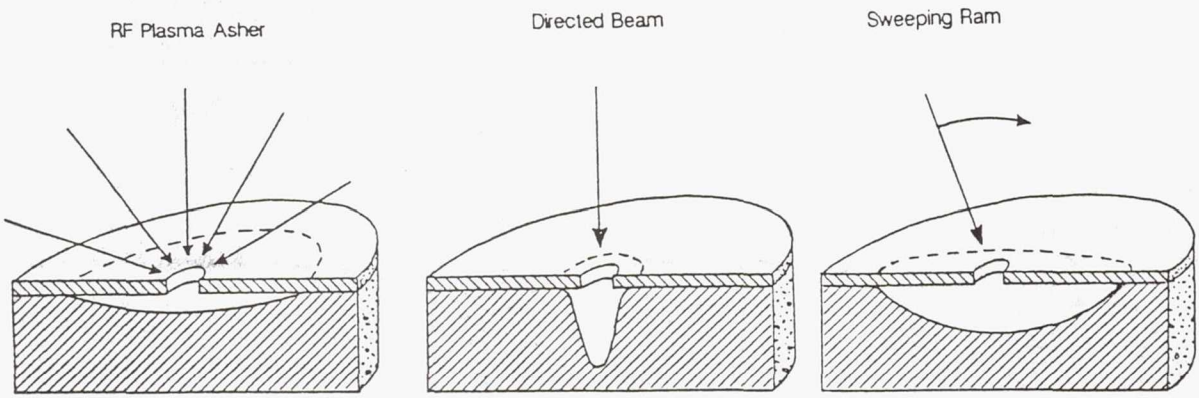


Figure 5: Atomic oxygen undercutting profiles for various directions of atomic oxygen arrival.

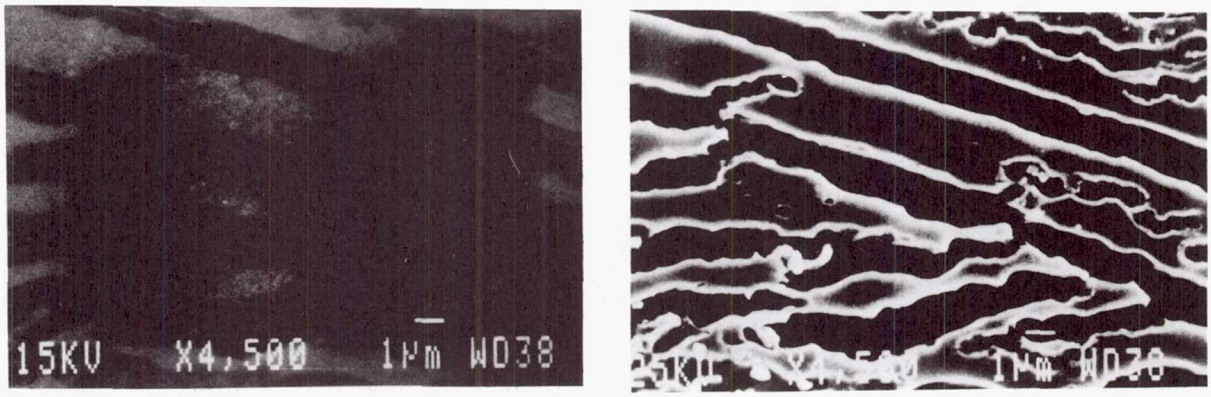


a: Prior to removal of the aluminum coating.

b: After chemical removal of the aluminum coating.

Figure 6: LDEF aluminized Kapton multilayer insulation at crack sites in the aluminization after exposure to a LEO atomic oxygen fluence of $5.77 \times 10^{21}$ atoms/cm$^2$.

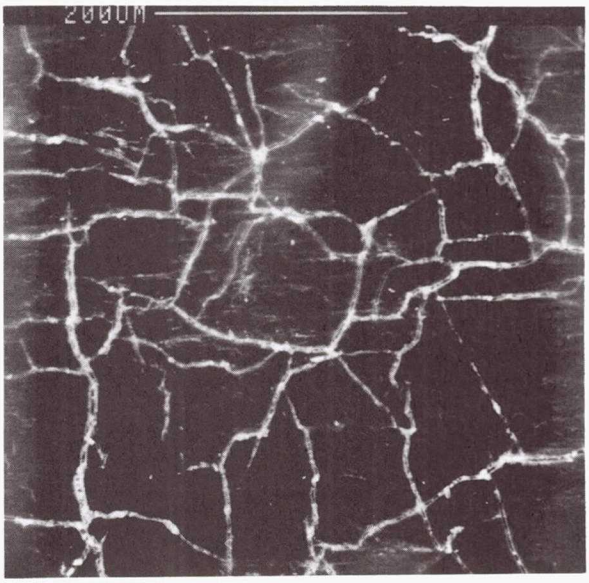


Figure 7: Silicone adhesive after LDEF exposure to an estimated fluence of $4.92 \times 10^{21}$ atoms/cm$^2$.

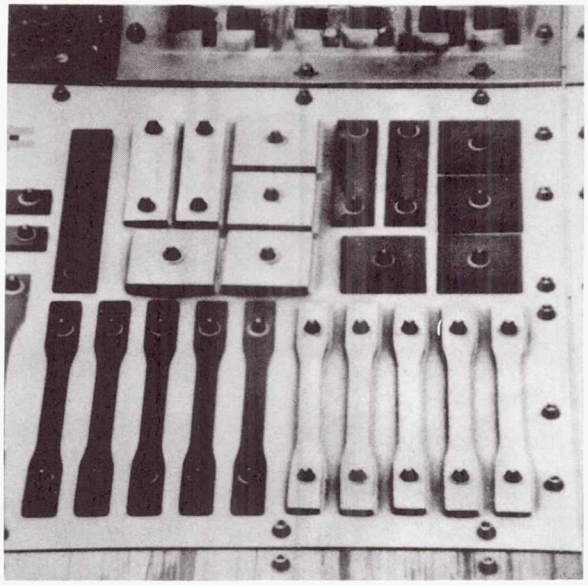

Figure 8: Photograph of LDEF silicone contamination resulting from atomic oxygen interactions with silicones.

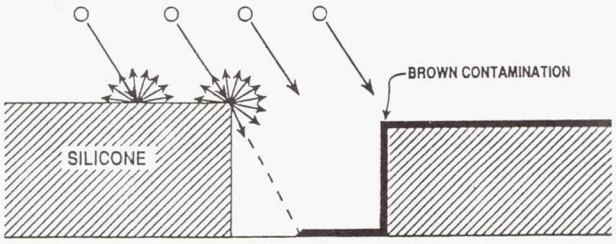


Figure 9: Atomic oxygen interactions with silicones which could produce brown contamination coatings as observed on the LDEF spacecraft.

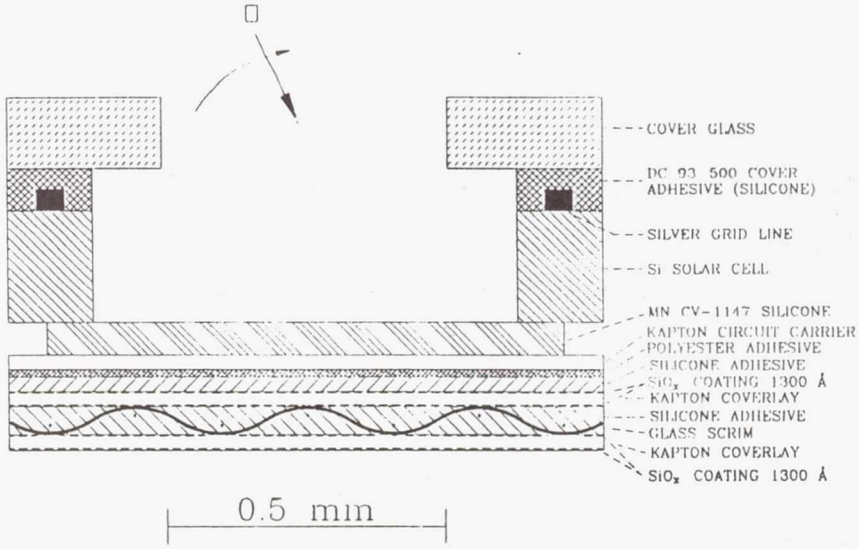


Figure 10: SSF solar array blanket cross section at the gaps between solar cells showing line of site arrival between atomic oxygen and silicone adhesive.

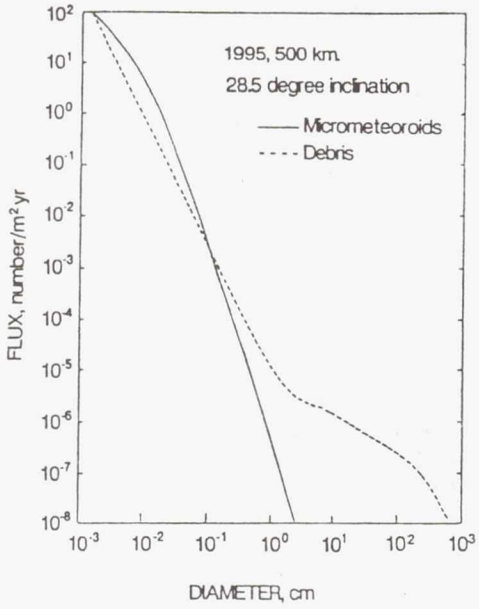


Figure 11: Micrometeoroid and debris flux for particles of equal to or smaller than a given diameter (ref. 9).

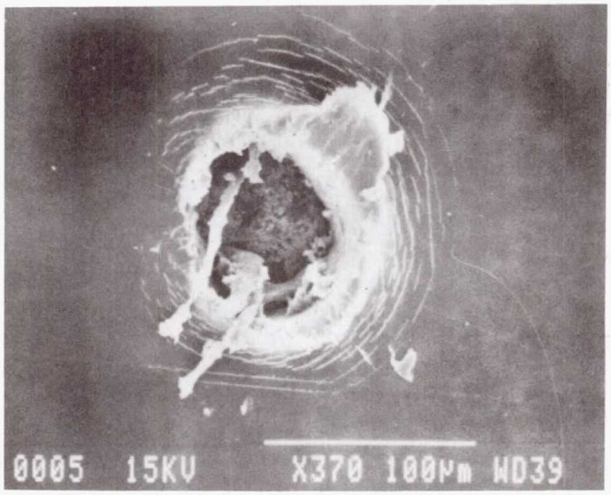


Figure 12: Debris or micrometeoroid impact site on a Kapton sample coated with 650Å of $SiO_2$ from the LDEF Ion Beam Textured and Coated Surfaces Experiment located at 6E.

# The Space Radiation Environment for Electronics

E. G. STASSINOPOULOS AND JAMES P. RAYMOND, FELLOW, IEEE

*Invited Paper*

*The earth's space radiation environment is described in terms of charged particles as relevant to effects on spacecraft electronics. The nature and magnitude of the trapped and transiting environments are described in terms of spatial distribution and temporal variation. The internal radiation environment of the spacecraft is described in terms of shielding the high-energy particles of the free-field environment. Exposure levels are presented in terms of ionizing radiation dose and particle fluence for comparison to electronic component susceptibility.*

## Introduction

The space radiation environment can have serious effects on spacecraft electronics. In this paper, the earth's space radiation environment is described in terms of trapped and nontrapped charged particles as relevant to effects on internal electronics. The nature and magnitude of the spatial distribution and temporal variation in the trapped radiation environment are presented. Transiting cosmic rays of galactic and solar origin are described, and their interaction with the earth's magnetic field is considered. In terms of spacecraft electronics, accumulated damage from electron and proton exposure will limit system endurance. Transient effects from individual high-energy protons or cosmic rays can disrupt system operation, perhaps irreversibly.

The internal radiation environment is described in terms of shielding the high-energy electrons, protons, and cosmic rays of the external environment. Exposure levels are presented in terms of ionizing radiation dose and particle fluence for comparison to electronic component damage susceptibility. Transient effects are presented in terms of particle flux for assessment of the potential frequency or probability of critical effects in the electronics. Of particular importance are the limits in shielding effectiveness for high-energy electrons, protons, and cosmic rays.

The interactions between the space radiation environment and the spacecraft electronics include those at the external surfaces as well as in the internal electronics. Important effects at the external surfaces include degradation of solar cells and charging of dielectric material, which can result in transient-producing arc-discharges. For these external effects the characterization of the free-field electron and proton environments as a function of particle energy and time are important. The internal spacecraft radiation environment is defined by particle transport through the spacecraft structure and, when necessary, shielding added to protect sensitive electronic pieceparts. Important effects on the internal electronics are performance degradation resulting from energy deposition by accumulated ionization in the semiconductor materials; accumulated atomic displacement damage in the crystal semiconductors by high-energy protons; and transient effects resulting from the ionization tracks from the interaction of a single cosmic ray or high-energy proton. Therefore, of particular interest for effects on the internal electronics are the total electron and proton exposure (i.e., fluence) and time-dependent rate of high-energy protons and cosmic rays (i.e., flux).

Manuscript received May 31, 1988; revised July 21, 1988.

E. G. Stassinopoulos is with the NASA Goddard Space Flight Center, Greenbelt, MD 20771, USA.

J. P. Raymond is with Mission Research Corporation, San Diego, CA 92123, USA.

IEEE Log Number 8824355.

## I. The Trapped Radiation Environment

The earth's natural radiation environment consists of electrons, protons, and heavy ions: a) trapped by the earth's magnetic field, or b) transiting through the domains of the earth's artificial satellites. As the earth sweeps through the solar wind, a geomagnetic cavity is formed by the earth's magnetic field, as shown in Fig. 1, which defines the magnetosphere. The cavity is hemispherical on the sun side, with a boundary at approximately 10–12 earth radii ($R_e$ = 6380 km). On the night side, it is cylindrical, approximately 40 $R_e$ in diameter. Because of the sweeping action of the solar wind, it extends over several hundred $R_e$ in the antisolar direction. The main particle trapping region, of specific interest in this paper, is the crosshatched area labeled plasmasphere.

The total magnetic field of the magnetosphere is defined in terms of two interacting and superimposed sources of internal and external origin. The internal field of the earth is thought to be caused by convective motion in the molten nickel-iron core of the planet, and by a residual permanent

©1988 IEEE. Reprinted, with permission, from Proceedings of the IEEE; vol. 76, no. 11, pp. 1423 to 1442; Nov. 1988.

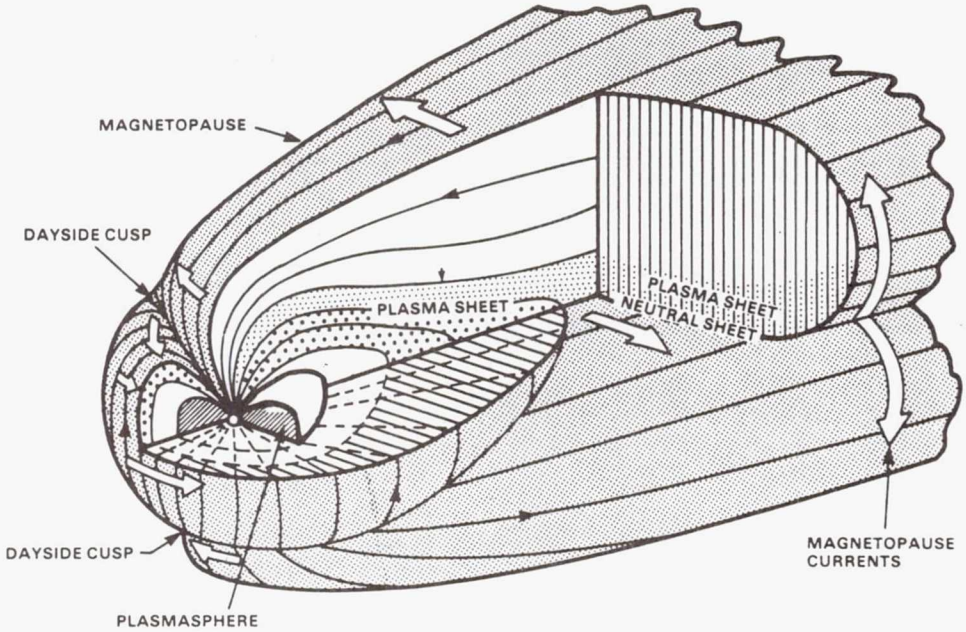


**Fig. 1.** Geomagnetic cavity.

magnetism in the earth's crust. The external field is comprised of the sum-total effect of currents and fields set up in the magnetosphere by the solar wind. The internal field component of the earth's magnetic field exhibits gradual changes with time, characterized as secular variations [1], [2]. These temporal effects are also observed in the shrinking value of the earth's dipole moment, and the drift in the location of the boreal (north) and austral (south) magnetic poles.

Superimposed on these slow internal changes are cyclic variations in the external field, whose magnitudes depend on the degree of perturbation experienced by the magnetosphere. Specifically, strong perturbations of the geomagnetic field are present in the outer magnetosphere, and depend on local time (diurnal effects), season (tilt effects), and solar wind conditions (including solar flares) [3]. All of these affect the magnetospheric current systems, which in turn modify the local field values.

A characteristic of the geomagnetic field, of particular significance to space radiation effects in electronics, is the Brazilian or South Atlantic Anomaly (SAA). This is primarily the result of the offset of the dipole term of the geomagnetic field by approximately 11° from the earth's axis of rotation, and displacement of about 500 km toward the Western Pacific. The effect is an apparent depression of the magnetic field over the coast of Brazil. There, the Van Allen belts reach lower altitudes, extending down into the atmosphere. The SAA is responsible for most of the trapped radiation received in low earth orbits (LEO). In contrast, on the opposite side of the globe, the Southeast-Asian Anomaly displays correspondingly stronger field values, and the trapped particle belts are located at higher altitudes.

### *A. Trapped Radiation Domains*

The earth's magnetic field, above the dense atmosphere, is populated with trapped electrons, protons, and small amounts of low energy heavy ions. These particles gyrate around and bounce along magnetic field lines, and are reflected back and forth between pairs of conjugate mirror points (i.e., regions of maximum magnetic field strength along their trajectories) in opposite hemispheres. At the same time, because of their charge, electrons drift eastward around the earth, while protons and heavy ions drift westward. Fig. 2 [4] illustrates the spiral, bounce, and drift motion of the trapped particles.

The magnetosphere can be divided into five domains for particle species populating or visiting, as shown in Fig. 3. The strong dependence of trapped particle fluxes on altitude and latitude is expressed in terms of the McIlwain $L$ parameter [5], where $L$ is a dimensionless ratio of the earth's radius, approximately equal to the geocentric distance of a field line in the geomagnetic equator. Also shown in Fig. 3 are the domains mapped by using the dipole field equation

$$R = L \cos^2 \Lambda$$

(or $R - \Lambda$ space). $R$ is defined as the radial distance, and $\Lambda$ is defined as the invariant latitude. It should be noted that the representation using $L$ becomes increasingly invalid for equatorial distances greater than four times $R_e$ because of the more complex particle motion in the geomagnetic field, and the distortion of the geomagnetic cavity by solar wind interaction effects.

The indicated domain boundaries should be considered only transitions, not actual lines. These boundaries are assumed for modeling purposes and, additionally, are used here for a qualitative picture of the charged particle distribution. "Real" boundaries are diffused areas, varying with particle energy, and fluctuating in position due to magnetic perturbations, local time effects, solar cycle variations (minimum and maximum activity phases), and individual solar events.

*1) Electrons:* Energetic Van Allen belt electrons are distinguished into "inner zone" and "outer zone" popula-

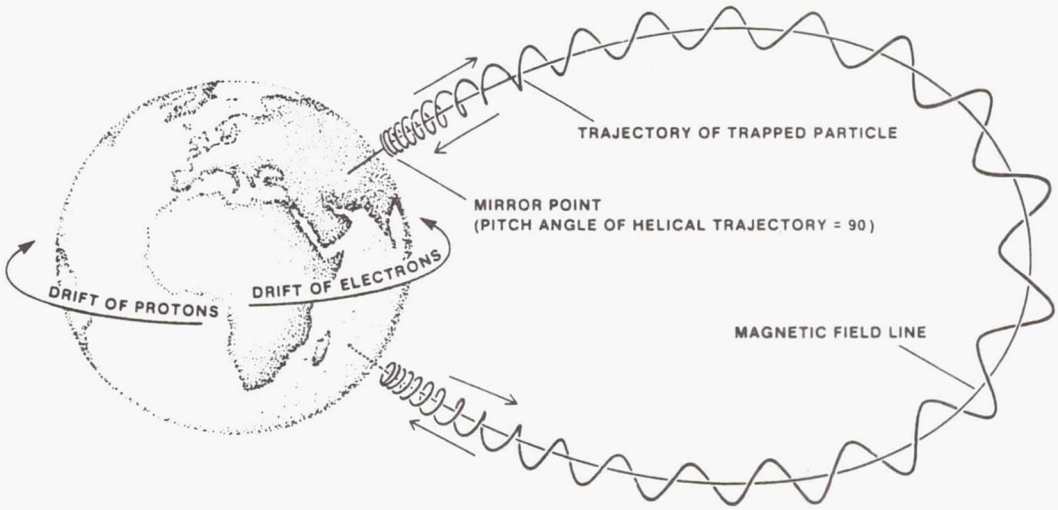


**Fig. 2.** Motions of trapped particles.

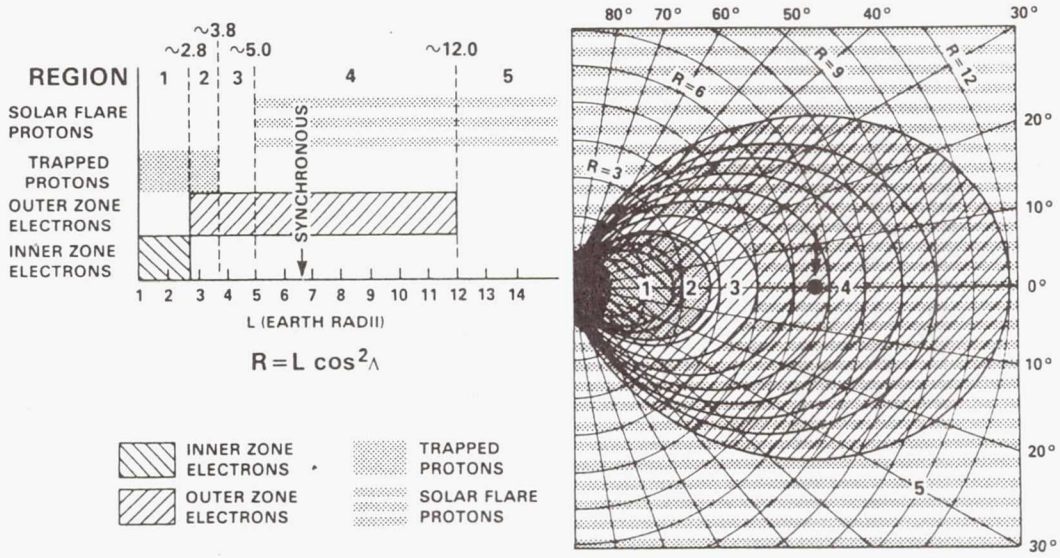


**Fig. 3.** Charged particle distribution in the magnetosphere.

tions. The volume of space occupied by the "inner zone" extends at the equator to about 2.4 $R_e$. These domains are indicated, respectively, by regions 1, and 2-3-4 in Fig. 3. The $L = 2.8$ line is used to separate the inner and outer zone domains, while the termination of the outer zone at $L = 12$ is intended only to delineate the maximum outward extent of stable, or pseudo-electron trapping. The region between $L = 2.5$ and 2.8 is called the "slot." During magnetospherically quiet times, its electron density is very low. However, during magnetic storms, the electron flux in the "slot" may increase by several orders of magnitude.

The inner zone electrons are less severe compared to the outer zone electrons. Specifically, the outer zone has peak fluxes exceeding those of the inner zone by about an order of magnitude. Also, the outer zone spectra extend to much higher energies (~7 MeV) than the inner zone spectra (<5 MeV). In this paper, we will present a detailed description of both the external and internal radiation environments for low earth orbits (i.e., LEO) in the inner zone, and for geostationary orbits (i.e., GEO) within the outer zone.

*2) Protons:* Protons with energies greater than 10 MeV populate regions 1 and 2 with an approximate trapping boundary placed at $L = 3.8$ as shown Fig. 3. In contrast to the electrons, the energetic trapped protons ($E > 1$ MeV) occupy a volume of space which varies inversely and monotonically with their energy as shown in Fig. 4. Consequently, these particles cannot be assigned to "inner" and "outer" zones. Fig. 5 shows the proton flux intensities as a function of radial distance and energy. In low earth orbits, the most intense and penetrating radiation is encountered in the form of protons in the South Atlantic Anomaly (SAA).

### *B. Models*

Available radiation measurements from space form the basis for models of the trapped electron and proton envi-

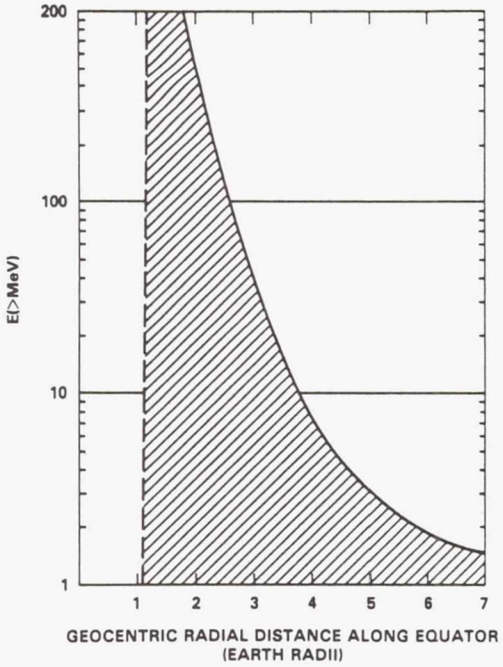


**Fig. 4.** Trapped proton population as a function of energy.

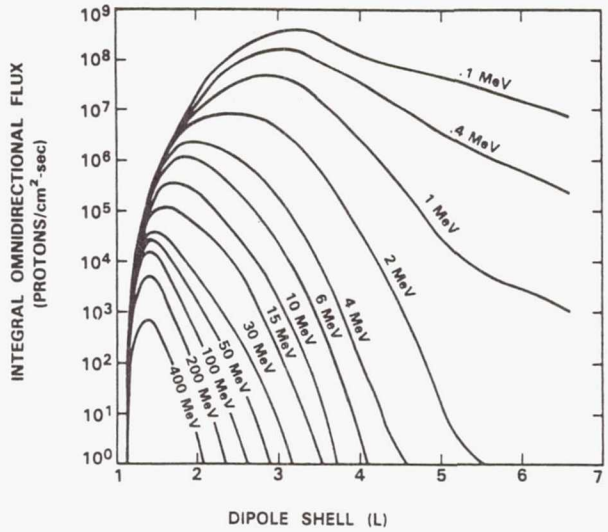


**Fig. 5.** Equatorial radial profiles for proton fluxes.

ronment. These models have been developed by the U.S. National Space Science Data Center (NSSDC) at NASA's Goddard Space Flight Center. All models are constructed with several dozen data sets from a corresponding number of satellites, providing a wide spatial and a long temporal coverage.

The most recent of these models, AP8 for protons [6] and AE8 for electrons [7], permit long term average predictions of trapped particle fluxes encountered in any orbit, and currently constitute the best estimates for the trapped radiation belts. However, statistics associated with randon fluctuations and short-term cyclical variations have been averaged out. The solar cycle dependence is reflected by the average conditions for the solar minimum and solar maximum activity phases of the 11-year cycle.

The predictions of these models for low earth orbit missions are presented in Tables 1 and 2 and Figs. 6 and 7. Table 1 presents the averaged orbit integrated fluxes for protons as a function of energy, parametrically for orbital inclinations of 28.5°, 60°, and 90°, all for both 300 km and 500 km circular orbit altitudes. Table 2 presents comparable data for the trapped electron environment. Fig. 6 gives the integral proton spectra for a circular 500 km, 60° inclination

**Table 1** Trapped Proton Fluxes, LEO, Solar Minimum

| E(>MEV) | 300 KM INCLINATION | | | 500 KM INCLINATION | | |
|---|---|---|---|---|---|---|
| | 28.5 DEG | 60 DEG | 90 DEG | 28.5 DEG | 60 DEG | 90 DEG |
| 0.04 | 5.420E+05 | 3.038E+08 | 1.509E+08 | 6.730E+06 | 9.595E+08 | 5.013E+08 |
| 0.07 | 5.399E+05 | 2.577E+08 | 1.297E+08 | 6.714E+06 | 7.947E+08 | 4.176E+08 |
| 0.10 | 5.379E+05 | 2.198E+08 | 1.121E+08 | 6.699E+06 | 6.620E+08 | 3.512E+08 |
| 0.50 | 5.202E+05 | 5.145E+07 | 3.055E+07 | 6.550E+06 | 1.329E+08 | 8.003E+07 |
| 1.00 | 5.028E+05 | 2.056E+07 | 1.386E+07 | 6.411E+06 | 5.126E+07 | 3.384E+07 |
| 2.00 | 4.945E+05 | 8.707E+06 | 6.445E+06 | 6.305E+06 | 2.246E+07 | 1.598E+07 |
| 3.00 | 4.890E+05 | 5.687E+06 | 4.265E+06 | 6.208E+06 | 1.539E+07 | 1.124E+07 |
| 4.00 | 4.835E+05 | 3.895E+06 | 2.949E+06 | 6.113E+06 | 1.123E+07 | 8.390E+06 |
| 5.00 | 4.781E+05 | 2.792E+06 | 2.129E+06 | 6.020E+06 | 8.679E+06 | 6.606E+06 |
| 6.00 | 4.728E+05 | 2.092E+06 | 1.606E+06 | 5.929E+06 | 7.054E+06 | 5.453E+06 |
| 8.00 | 4.613E+05 | 1.535E+06 | 1.184E+06 | 5.739E+06 | 5.663E+06 | 4.448E+06 |
| 10.00 | 4.501E+05 | 1.191E+06 | 9.242E+05 | 5.556E+06 | 4.774E+06 | 3.795E+06 |
| 15.00 | 4.348E+05 | 9.010E+05 | 7.073E+05 | 5.234E+06 | 3.947E+06 | 3.169E+06 |
| 20.00 | 4.203E+05 | 7.359E+05 | 5.827E+05 | 4.936E+06 | 3.422E+06 | 2.760E+06 |
| 25.00 | 4.064E+05 | 6.609E+05 | 5.241E+05 | 4.720E+06 | 3.169E+06 | 2.556E+06 |
| 30.00 | 3.930E+05 | 6.026E+05 | 4.779E+05 | 4.517E+06 | 2.958E+06 | 2.384E+06 |
| 35.00 | 3.770E+05 | 5.588E+05 | 4.433E+05 | 4.313E+06 | 2.780E+06 | 2.248E+06 |
| 40.00 | 3.616E+05 | 5.201E+05 | 4.129E+05 | 4.119E+06 | 2.617E+06 | 2.123E+06 |
| 45.00 | 3.470E+05 | 4.857E+05 | 3.857E+05 | 3.935E+06 | 2.468E+06 | 2.009E+06 |
| 50.00 | 3.331E+05 | 4.548E+05 | 3.613E+05 | 3.761E+06 | 2.330E+06 | 1.902E+06 |
| 60.00 | 2.999E+05 | 3.917E+05 | 3.118E+05 | 3.382E+06 | 2.055E+06 | 1.681E+06 |
| 80.00 | 2.441E+05 | 2.959E+05 | 2.363E+05 | 2.748E+06 | 1.613E+06 | 1.324E+06 |
| 100.00 | 1.997E+05 | 2.276E+05 | 1.823E+05 | 2.243E+06 | 1.279E+06 | 1.053E+06 |
| 150.00 | 1.018E+05 | 1.055E+05 | 8.646E+04 | 1.279E+06 | 6.951E+05 | 5.742E+05 |
| 200.00 | 5.303E+04 | 5.103E+04 | 4.278E+04 | 7.439E+05 | 3.896E+05 | 3.226E+05 |
| 250.00 | 2.684E+04 | 2.526E+04 | 2.144E+04 | 4.334E+05 | 2.246E+05 | 1.856E+05 |
| 300.00 | 1.377E+04 | 1.281E+04 | 1.100E+04 | 2.547E+05 | 1.313E+05 | 1.082E+05 |
| 350.00 | 6.940E+03 | 6.559E+03 | 5.680E+03 | 1.506E+05 | 7.733E+04 | 6.359E+04 |
| 400.00 | 3.219E+03 | 3.139E+03 | 2.714E+03 | 8.914E+04 | 4.594E+04 | 3.753E+04 |
| 500.00 | 4.961E+02 | 7.257E+02 | 5.937E+02 | 3.108E+04 | 1.618E+04 | 1.328E+04 |

**Table 2** Trapped Electron Fluxes, LEO, Solar Minimum

| E(>MEV) | 300 KM INCLINATION 28.5 DEG | 300 KM INCLINATION 60 DEG | 300 KM INCLINATION 90 DEG | 500 KM INCLINATION 28.5 DEG | 500 KM INCLINATION 60 DEG | 500 KM INCLINATION 90 DEG |
|---|---|---|---|---|---|---|
| 0.04 | 2.973E+08 | 3.203E+09 | 2.971E+09 | 5.153E+09 | 9.171E+09 | 7.876E+09 |
| 0.07 | 2.351E+08 | 2.391E+09 | 2.257E+09 | 4.082E+09 | 7.007E+09 | 6.066E+09 |
| 0.10 | 1.861E+08 | 1.795E+09 | 1.730E+09 | 3.236E+09 | 5.382E+09 | 4.712E+09 |
| 0.20 | 5.629E+07 | 6.779E+08 | 7.424E+08 | 9.975E+08 | 1.908E+09 | 1.816E+09 |
| 0.30 | 2.227E+07 | 3.631E+08 | 4.262E+08 | 3.969E+08 | 9.484E+08 | 9.514E+08 |
| 0.40 | 1.144E+07 | 2.384E+08 | 2.849E+08 | 2.017E+08 | 5.895E+08 | 6.029E+08 |
| 0.50 | 5.897E+06 | 1.616E+08 | 1.950E+08 | 1.030E+08 | 3.807E+08 | 3.944E+08 |
| 0.60 | 3.985E+06 | 1.283E+08 | 1.526E+08 | 6.850E+07 | 2.917E+08 | 3.007E+08 |
| 0.70 | 2.701E+06 | 1.027E+08 | 1.204E+08 | 4.574E+07 | 2.258E+08 | 2.315E+08 |
| 0.80 | 1.948E+06 | 8.399E+07 | 9.744E+07 | 3.268E+07 | 1.813E+08 | 1.845E+08 |
| 0.90 | 1.494E+06 | 7.001E+07 | 8.051E+07 | 2.494E+07 | 1.504E+08 | 1.515E+08 |
| 1.00 | 1.147E+06 | 5.850E+07 | 6.669E+07 | 1.904E+07 | 1.252E+08 | 1.248E+08 |
| 1.25 | 7.213E+05 | 3.857E+07 | 4.262E+07 | 1.179E+07 | 8.119E+07 | 7.931E+07 |
| 1.50 | 4.549E+05 | 2.554E+07 | 2.742E+07 | 7.310E+06 | 5.292E+07 | 5.076E+07 |
| 1.75 | 3.051E+05 | 1.747E+07 | 1.828E+07 | 4.870E+06 | 3.561E+07 | 3.371E+07 |
| 2.00 | 2.053E+05 | 1.199E+07 | 1.224E+07 | 3.250E+06 | 2.407E+07 | 2.250E+07 |
| 2.25 | 1.392E+05 | 8.275E+06 | 8.289E+06 | 2.194E+06 | 1.644E+07 | 1.516E+07 |
| 2.50 | 9.419E+04 | 5.725E+06 | 5.637E+06 | 1.484E+06 | 1.127E+07 | 1.026E+07 |
| 2.75 | 3.788E+04 | 3.899E+06 | 3.751E+06 | 5.934E+05 | 7.373E+06 | 6.610E+06 |
| 3.00 | 1.521E+04 | 2.695E+06 | 2.529E+06 | 2.405E+05 | 4.956E+06 | 4.361E+06 |
| 3.25 | 4.850E+03 | 1.856E+06 | 1.695E+06 | 7.591E+04 | 3.324E+06 | 2.862E+06 |
| 3.50 | 1.357E+03 | 1.292E+06 | 1.148E+06 | 2.394E+04 | 2.274E+06 | 1.914E+06 |
| 3.75 | 3.874E+02 | 8.495E+05 | 7.316E+05 | 7.263E+03 | 1.474E+06 | 1.206E+06 |
| 4.00 | 0.000E+00 | 5.650E+05 | 4.726E+05 | 8.860E+02 | 9.693E+05 | 7.712E+05 |
| 4.50 | 0.000E+00 | 2.066E+05 | 1.643E+05 | 0.000E+00 | 3.493E+05 | 2.633E+05 |
| 5.00 | 0.000E+00 | 6.828E+04 | 5.129E+04 | 0.000E+00 | 1.143E+05 | 7.979E+04 |
| 5.50 | 0.000E+00 | 1.572E+04 | 1.188E+04 | 0.000E+00 | 2.659E+04 | 1.751E+04 |
| 6.00 | 0.000E+00 | 2.858E+03 | 1.970E+03 | 0.000E+00 | 3.923E+03 | 2.470E+03 |
| 6.50 | 0.000E+00 | 0.000E+00 | 0.000E+00 | 0.000E+00 | 1.235E+02 | 6.052E+01 |
| 7.00 | 0.000E+00 | 0.000E+00 | 0.000E+00 | 0.000E+00 | 0.000E+00 | 0.000E+00 |

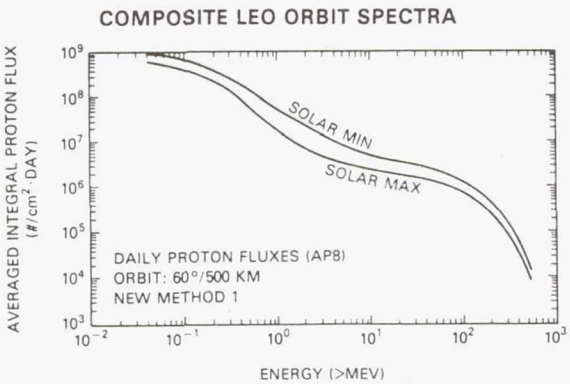


**Fig. 6.** Low earth orbit (LEO) proton fluxes.

orbit, for both solar minimum and solar maximum conditions. The relative hardness of the LEO proton spectrum should be noted. Between 50 and 500 MeV the proton flux decreases only by a factor of 4. Fig. 7 presents the comparable data for the trapped electron environment.

It should be noted that the model in the low altitude regime (< 1000 km), that is, in the atmospheric cutoff region, must be related to the correct geomagnetic field strength. If used with current or projected (i.e., future) field strength values, the predicted fluxes will be too high by factors ranging from approximately 2 (at 800–1000 km) to approximately 50 (at 200–500 km). This is the result of the geomagnetic field changing with time. In this process, the dipole moment is decreasing, pulling heavily populated field lines down into the denser regions of the atmosphere, where there occur

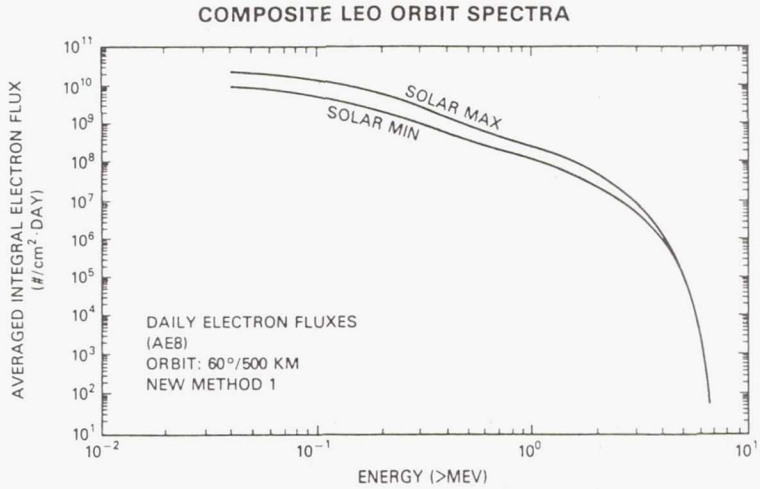


**Fig. 7.** Low earth orbit (LEO) electron fluxes.

significant particle losses (mostly due to coulomb scattering), which are not represented in the model.

The geosynchronous integral electron spectrum, obtained from the AE8-MAX model, is given in Table 3 and is plotted in Fig. 8. Worst and best cases are shown, corresponding to "parking" longitudes at 160° W ($L = 7.0$), and 70° W ($L = 6.6$), respectively. The flux ratio between the worst and best cases is about 1.8 for electron energies greater than 1 MeV, and 2.3 for electron energies greater than 2 MeV.

The proton spectrum at GEO, in contrast to that of LEO, is very soft and, essentially, is depleted for protons of energies greater than 1.75 MeV. Thus, trapped protons in GEO are stopped by very small material thicknesses (approximately 0.05 mm of aluminum), and are not of concern to the internal electronics.

**Table 3** Geostationary Electron Fluxes

| E(>MEV) | 70 DEG W | 160 DEG W |
|---|---|---|
| 0.04 | 3.775E+07 | 4.643E+07 |
| 0.07 | 3.023E+07 | 3.847E+07 |
| 0.10 | 2.421E+07 | 3.188E+07 |
| 0.20 | 1.145E+07 | 1.587E+07 |
| 0.30 | 5.944E+06 | 8.575E+06 |
| 0.40 | 3.383E+06 | 5.044E+06 |
| 0.50 | 1.925E+06 | 2.967E+06 |
| 0.60 | 1.224E+06 | 2.048E+06 |
| 0.70 | 7.788E+05 | 1.414E+06 |
| 0.80 | 5.290E+05 | 9.879E+05 |
| 0.90 | 3.838E+05 | 6.983E+05 |
| 1.00 | 2.784E+05 | 4.935E+05 |
| 1.25 | 1.338E+05 | 2.475E+05 |
| 1.50 | 6.435E+04 | 1.242E+05 |
| 1.75 | 3.497E+04 | 7.171E+04 |
| 2.00 | 1.900E+04 | 4.142E+04 |
| 2.25 | 9.313E+03 | 2.128E+04 |
| 2.50 | 4.653E+03 | 1.093E+04 |
| 2.75 | 2.816E+03 | 6.494E+03 |
| 3.00 | 1.737E+03 | 3.858E+03 |
| 3.25 | 1.118E+03 | 2.484E+03 |
| 3.50 | 7.196E+02 | 1.600E+03 |
| 3.75 | 4.260E+02 | 8.527E+02 |
| 4.00 | 2.522E+02 | 4.546E+02 |
| 4.50 | 6.825E+01 | 1.187E+02 |
| 5.00 | 1.673E+00 | 4.519E+00 |
| 5.50 | 0.000E+00 | 0.000E+00 |
| 6.00 | 0.000E+00 | 0.000E+00 |
| 6.50 | 0.000E+00 | 0.000E+00 |
| 7.00 | 0.000E+00 | 0.000E+00 |

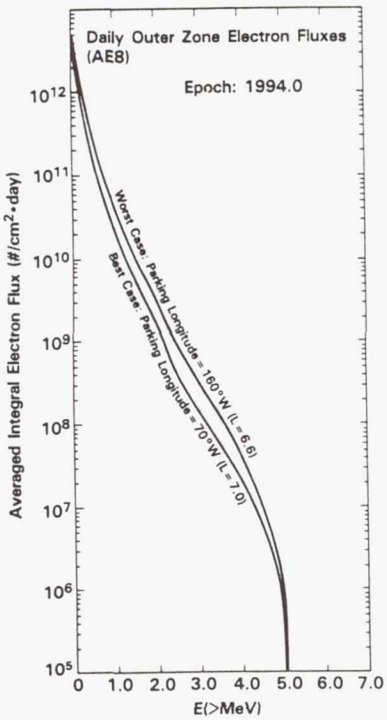


**Fig. 8.** Geostationary electron spectra.

### C. *Variations*

The trapped particle fluxes respond to changes in the geomagnetic field induced by solar activity, and, therefore, exhibit a strong dynamic behavior, especially in the outer belts. Satellite measurements in geosynchronous (GEO) equatorial orbits have revealed a complicated temporal pattern consisting of a superposition of several cyclical variations in conjunction with sporadic fluctuations [8]–[10]. The main periodic variations include a diurnal cycle, which in GEO is characterized by order-of-magnitude electron flux changes [8], and the 11-year solar activity cycle.

Sporadic magnetic storms in GEO can produce a modulation of the electron flux above 50 keV by an order of magnitude within a period of less than 10 minutes [9], and with a corresponding decay in days. Substorms, which are a common feature of the midnight to dawn sector of a GEO orbit, result in the injection of electrons with energies between 50 and 150 keV from the magnetospheric tail region. The electron flux above 200 keV remains constant, or actually decreases. The short term variations in electron flux in the outer belt, including local time variations, are particularly critical in the assessment of spacecraft charging effects. For the internal electronics, the principal effect of the electron exposure is ionization damage, which accumulates slowly over the life of the mission.

Another important solar-activity-induced modulation of the trapped particle population, particularly of protons, occurs in the low altitude regime of the magnetosphere. Here, during the active phase of the solar cycle, the increased energy output from the sun causes the atmosphere to expand, thereby raising the density of the atmospheric constituents normally encountered at heights between 200 and 1000 km. This increase in atmospheric density depletes, through coulomb scattering, the populations of those trapped particles that have their mirror points at these low altitudes, with significant effects on the radiation exposure of satellites orbiting in that domain.

The solar cycle variations observed in some areas of the trapped particle domain are functions of energy and magnetic parameter $L$. They generally have opposite effects on each particle specie, particularly in the low altitude regime:

| | Solar Min | Solar Max |
|---|---|---|
| Electron Intensities | lower | higher |
| Proton Intensities | higher | lower |

No solar cycle changes of consequence have been measured in the heart of the proton trapping domain. No significant long term variations, within current models, occur in the electron populations at geostationary altitudes. However, in the atmospheric cutoff regions, electron and proton variations may range up to a factor of 5.

*D. Flux-Free Time*

As mentioned previously, the South Atlantic Anomaly (SAA) is a region of trapped particle radiation close to the earth. Hence, for low altitude, low inclination orbits, the SAA is the most important factor in determining the level of radiation exposure of spacecraft. For low earth orbits (LEO) with higher inclinations (>35°, the protrusions of the outer zone electron belts (the electron "horns") in the mid-latitude regions must also be considered. Of particular importance is the temporal distribution of the proton exposure, which determines the maximum rate of potential proton-induced single-event upsets in the electronics, as well as the periods in which no upsets will be observed.

The intermittent exposure of LEO satellites to the trapped Van Allen belt radiation is illustrated for electrons in Fig. 9 for a circular 900 km, 99° inclination orbit during its worst pass through the SAA. Note in Fig. 9 that even in a worst case pass, there are time periods during which instantaneous electron fluxes above 0.5 MeV are below 1 particle per square centimeter per second. The same is true for protons above 5 MeV. These time periods are the "flux free time" (FFT) intervals. They may occur over short orbit segments (partial FFT per period), or over the entire length of a revolution (total FFT per period). In terms of geomagnetic geometry, the FFTs establish the duration for which the trajectory lies outside the trapping domain of the corresponding particle species, evaluated at the given energies. Or, conversely, they are a measure of the degree to which the trajectory is exposed to the charged particle trapping domains.

The number of consecutive flux-free orbits of circular trajectories is primarily a function of altitude and inclination and, to a lesser degree, a function of particle energy. Generally, higher energies will yield longer FFTs because the more energetic particles occupy a smaller volume of space, particularly in the case of protons. For an orbit configuration similar to the one illustrated in Fig. 9, and for protons with energies greater than 5 MeV, or electrons of energy greater than 0.5 MeV, there are no completely flux-free orbits. The total FFT is entirely composed of contributions from partially exposed revolutions. In terms of the solar cycle, it can be summarized in percent of total mission duration as:

| | Protons | Electrons |
|---|---|---|
| | ($E$ > 5 MeV) | ($E$ > 0.5 MeV) |
| Solar Minimum | 81% | 33% |
| Solar Maximum | 83% | 53% |

For a 500 km, 30° inclination LEO, the FFT includes six completely flux free orbits per day, that is, orbits which do not pass through the SAA or the electron "horn" regions. In this case, the FFT can be summarized in percent of total mission duration as:

| | Protons | Electrons |
|---|---|---|
| | ($E$ > 5 MeV) | ($E$ > 0.5 MeV) |
| Solar Minimum | 90% | 89% |
| Solar Maximum | 92% | 88% |

In terms of the spacecraft electronics, the fluxes of the electron and proton environments are important in the total ionizing radiation induced damage, and the proton flux and flux-free-time are important in the potential rate of proton-induced transient upsets.

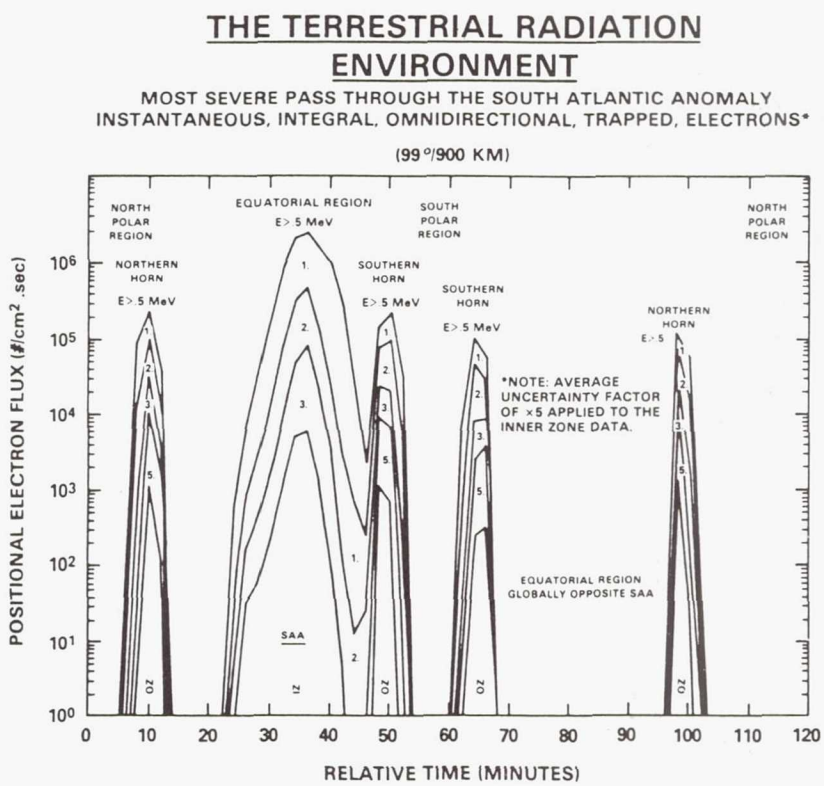


**Fig. 9.** Positional electron flux profile.

*E. Artificial Enhancement*

A severe hazard for space missions could be introduced by a high altitude nuclear explosion. Such an effect would result in the injection into the magnetosphere of energetic electrons from the beta decay of fission fragments. Subsequent trapping of the electrons in the magnetic field [11] could produce an enhancement of the electron population by many orders of magnitude.

The principal hazard would be to missions in low earth orbits, mainly because of an expected very stable trapping with lifetimes up to eight years [11]. Fig. 10 shows the isochronal contours for the trapped electrons resulting from the STARFISH exoatmospheric nuclear explosion of July 1962 over Johnston Island in the Pacific. However, depending on the location of the explosion, the injection could also produce a temporary large enhancement of the electron environment at geostationary orbits. At GEO, the trapping would be less stable, with exponential decay periods of between 10 and 20 days. The apparent longevity, or conversely, the decay rate, of such fission electrons depends to a large extent on the injection latitude and altitude; that is, it is a function of the magnetic dipole shell parameter $L$ and, to a lesser degree, of magnetic field strength [12].

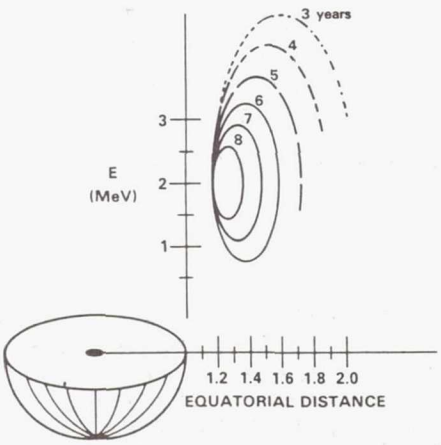


**Fig. 10.** Isochronal contours for STARFISH electron longevity.

For the internal electronics, it is important to note that both the total ionizing exposure level and exposure dose rate are substantially increased by the artificially enhanced environment.

## II. Trapped Radiation Transport, Shielding, and Doses

*A. Emerging Radiation*

In interacting with spacecraft materials, the electrons and protons of the trapped radiation belts are modified in intensity by shielding, and modified in character through the production of secondary radiation. The secondary radiation can extend the penetration of the primary radiation and lead to an increase in dose deposition over that of the attenuated incident radiation. The most significant secondary radiation is the bremsstrahlung, or "braking radiation," produced in the deceleration of electrons penetrating the spacecraft. This is a continuous X-ray spectrum emitted roughly in the direction of electron penetration. The mean X-ray energy is about one-third that of the initial electron energy. The bremsstrahlung intensity depends linearly on the atomic number of the spacecraft material and on the square of the initial electron energy. Bremsstrahlung from energetic electrons populating the radiation belts is very penetrating, and thus difficult to attenuate, especially with the low-atomic number materials popular on spacecraft (e.g., aluminum). On the other hand, these low-atomic number materials tend to produce less bremsstrahlung.

*1) Electrons and Bremsstrahlung:* To illustrate, Figs. 11 and 12 show the emerging electron and bremsstrahlung spectra behind spherical aluminum shielding for the incident environment of a 500 km circular orbit of 60° inclination. As the curves of Fig. 11 clearly indicate, the trapped electrons are very effectively attenuated by the aluminum

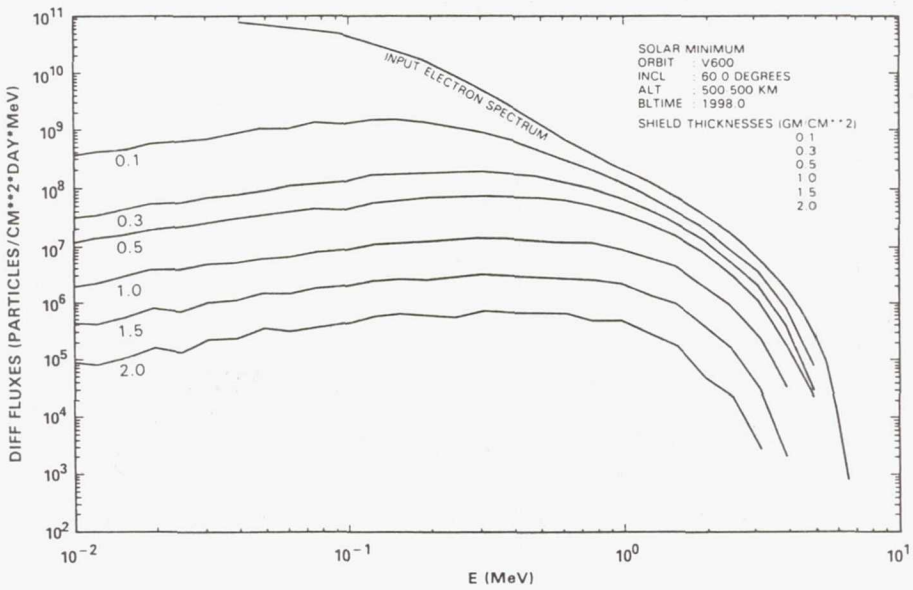


**Fig. 11.** Emerging electron spectra behind spherical aluminum shields.

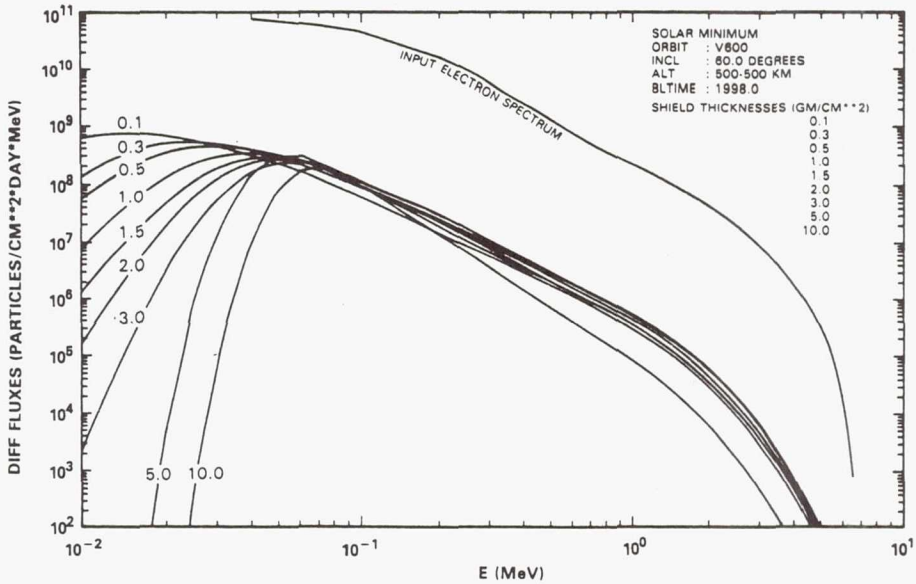


**Fig. 12.** Emerging bremsstrahlung spectra behind spherical aluminum shields.

shield, and are nearly all stopped by thickness greater than 2 grams per square centimeter, even at the highest electron energies. However, as shown in Fig. 12, the bremsstrahlung flux levels for energies above 40 keV are not significantly affected by any of the aluminum shields from 0.1 to 10 grams per square centimeter. It is important to note, however, that above 100 keV, the photon fluxes are, on the average, over three orders of magnitude lower than the incident electron flux at corresponding energy levels.

*2) Trapped Protons:* Transport of the trapped protons is illustrated in Fig. 13, which shows the emerging proton spectra behind spherical aluminum shields for the 500 km circular, 60° inclination orbit. As shown, the aluminum shielding is very effective for the low energy protons, but ineffective for the high energy (greater than 30 MeV) protons. The shielding effectiveness of the low proton energies is important in reducing the ionizing energy deposition in the internal electronics. On the other hand, the "hardening" of the proton spectra provides little help in reducing potential proton-induced single-event upsets.

*3) Variables Affecting Dose Evaluations:* Obtaining estimates of the dose on a given component of the internal electronics in a spacecraft is a complex process involving several variables that directly affect the results. These variables include: 1) primary environment definition, 2) description of the input spectra, and 3) contributions from secondary particles and photons.

Four areas stand out that are of particular concern to shielding and transport evaluations. These are completely independent from, and unrelated to, the definition of the

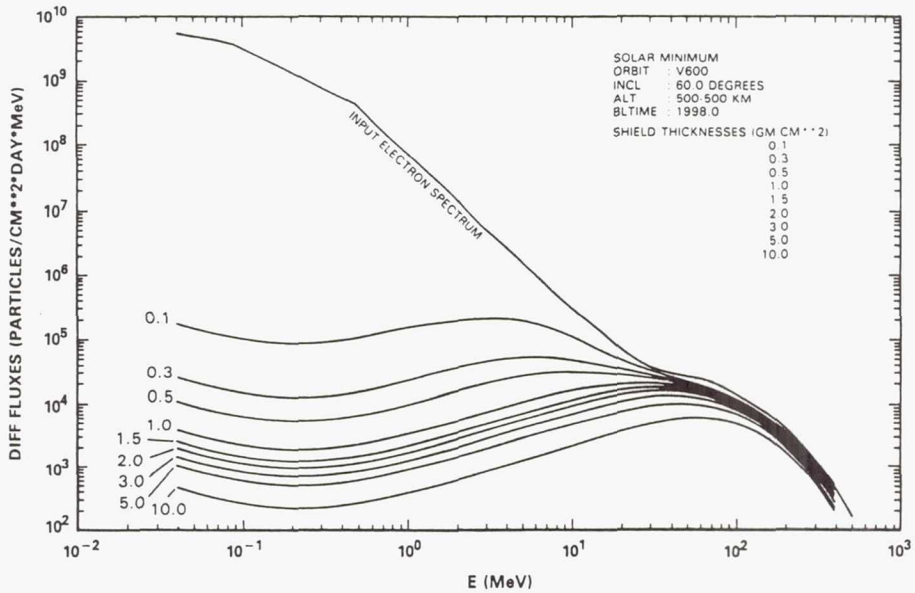


**Fig. 13.** Emerging trapped proton spectra behind spherical aluminum shields.

spacecraft-encountered radiation environment. The areas are: 1) shield geometry and shielding analysis technique, b) shield material composition, c) target (i.e., component) composition (e.g., package, passivation, metalization and semiconductor of a complex microcircuit), and d) dose units. Each of these, as shown in Table 4, offers a multiplicity

**Table 4** Areas of Concern for Shielding and Transport Evaluation

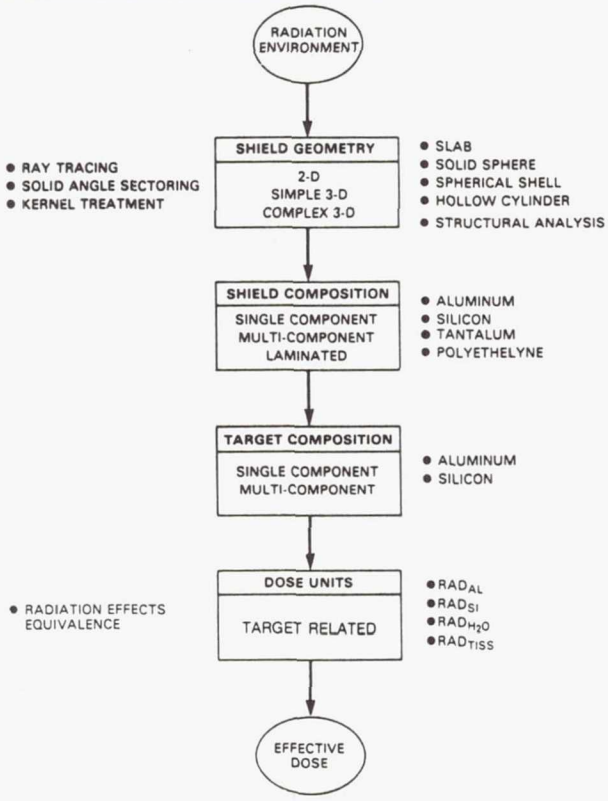


of choices and conditions that need to be clearly identified and defined whenever calculations are performed and results presented. Otherwise, the comparison of dose data compiled by several independent sources, although derived from the same spacecraft surface incident spectrum, becomes meaningless and futile. In such cases, disagreements by factors up to 20 have been known to occur.

Energy deposition in the internal electronics is measured in units of rads (material). A rad (radiation absorbed dose) is defined as 100 ergs of energy deposition per gram of absorber material, without reference to the nature of the energy deposition. The MKS equivalent of the rad is the Gray, which is defined as the energy deposition of 1 Joule in one kg of material (e.g., 100 rad(Al) = 1 Gy(Al)). For electron exposure, the energy deposition is almost all by ionization. For proton exposure, the energy deposition includes both ionization and atomic displacements.

The calculation of radiation penetration and dose deposition, in principle, is well understood (with the possible exception of intra-nuclear cascades), and usually can be carried out to adequate accuracy with a variety of available radiation transport codes. Analysis of the internal secondary radiation environment in specific spacecraft, while complex, is possible, and has been performed using ray tracing techniques, solid angle sectoring, and Monte Carlo modeling [13].

Generally, space radiation transport and dose calculations use idealized shielding configurations such as solid or hollow spheres, semi-infinite slabs, and cylinders, usually with aluminum as a reference material. The use of the idealized configurations readily permits parametric analysis of dose attenuation, exploration of the consequences of environmental uncertainties, and identification of the shielding required for a given spacecraft. In comparing results from different geometries, it should be noted that for omnidirectional isotropic flux incidence, spherical shields yield dose results roughly 2 to 6 times higher than $4\pi$ exposure of slab shields with centered dose points. Cylindrical shields yield intermediate results between the spherical and slab configurations. The differences in configurations, however, also depend on particle species, energy spectrum, shield thickness, and (particularly) target composition.

### *B. Ionizing Radiation Dose*

To illustrate the ionizing dose exposure, daily dose values for low earth orbits (LEO) and geostationary orbits (GEO) are presented in Tables 5 through 7 and Figs. 14 through 16. The materially attenuated doses and fluxes presented were calculated with state-of-the-art transport codes [13], [14].

Tables 5 through 7 present the calculated daily doses for LEO at 500 km altitudes and inclinations of 28.5, 60, and 90 degrees for solar minimum conditions based on the trapped electron and proton models. Daily silicon doses in LEO at 500 km altitude and 30° inclination for solar minimum and maximum, are shown in Fig. 14 for a two-sides exposure of aluminum slab shields and for a solid spherical shield, as an average over 15 orbits. The electron dose includes the bremsstrahlung contribution.

As discussed previously, the South Atlantic Anomaly (SAA) is the primary contributor to the doses accumulated by spacecraft in LEO. Fig. 15 shows contours of total dose for an attitude of 500 km for a spherical shield thickness of 2 grams per square centimeter of aluminum. Superimposed on the world maps are the worst case passes through the SAA for 28.5, 57, and 90 degree inclination orbits. As mentioned previously, for low inclination orbits (<45°), there are periods when complete revolutions are in flux free time. These time periods are especially important when considering extra-vehicular-activities (EVAs).

The corresponding electron-plus-bremsstrahlung daily dose for an aluminum shield of solid sphere geometry in GEO at the parking longitude, with the lowest average flux (70° W), is illustrated in Fig. 16 in the form of a dose-depth curve. For the parking longitude with the large average flux (160° W), the dose behind a 2 gram per square centimeter shielding thickness is a factor of about 1.7 higher, regardless of geometry.

### *C. Permanent Damage Susceptibility of Electronics*

The basic permanent damage mechanisms in semiconductor devices exposed to high-energy electrons and protons are accumulated ionization effects and atomic displacements in bulk semiconductors. Energy deposition

**Table 5** Daily Dose, 28.5 Degrees/500 km, Solar Minimum

| S GM/SQCM | T MM | T MILS | ELEC RADS-AL | BREM RADS-AL | PROTON RADS-AL | TOTAL RADS-AL |
|---|---|---|---|---|---|---|
| 0.01 | 0.04 | 1.00 | 2.494E+02 | 9.518E-02 | 1.805E+00 | 2.513E+02 |
| 0.02 | 0.07 | 3.00 | 1.417E+02 | 6.745E-02 | 1.629E+00 | 1.434E+02 |
| 0.03 | 0.11 | 4.00 | 8.896E+01 | 5.151E-02 | 1.540E+00 | 9.055E+01 |
| 0.04 | 0.15 | 6.00 | 6.008E+01 | 4.162E-02 | 1.472E+00 | 6.160E+01 |
| 0.05 | 0.19 | 7.00 | 4.266E+01 | 3.479E-02 | 1.411E+00 | 4.410E+01 |
| 0.06 | 0.22 | 9.00 | 3.142E+01 | 2.959E-02 | 1.373E+00 | 3.283E+01 |
| 0.07 | 0.26 | 10.00 | 2.387E+01 | 2.552E-02 | 1.334E+00 | 2.523E+01 |
| 0.08 | 0.30 | 12.00 | 1.859E+01 | 2.227E-02 | 1.300E+00 | 1.991E+01 |
| 0.09 | 0.33 | 13.00 | 1.477E+01 | 1.967E-02 | 1.268E+00 | 1.606E+01 |
| 0.10 | 0.37 | 15.00 | 1.195E+01 | 1.753E-02 | 1.236E+00 | 1.320E+01 |
| 0.20 | 0.74 | 29.00 | 2.781E+00 | 8.622E-03 | 1.032E+00 | 3.821E+00 |
| 0.30 | 1.11 | 44.00 | 1.191E+00 | 5.951E-03 | 9.200E-01 | 2.117E+00 |
| 0.40 | 1.48 | 58.00 | 6.660E-01 | 4.589E-03 | 8.468E-01 | 1.517E+00 |
| 0.50 | 1.85 | 73.00 | 4.268E-01 | 3.742E-03 | 7.885E-01 | 1.219E+00 |
| 0.60 | 2.22 | 87.00 | 2.915E-01 | 3.170E-03 | 7.501E-01 | 1.045E+00 |
| 0.80 | 2.96 | 117.00 | 1.497E-01 | 2.451E-03 | 6.962E-01 | 8.483E-01 |
| 1.00 | 3.70 | 146.00 | 7.871E-02 | 2.012E-03 | 6.534E-01 | 7.341E-01 |
| 1.25 | 4.63 | 182.00 | 2.860E-02 | 1.654E-03 | 6.189E-01 | 6.492E-01 |
| 1.50 | 5.56 | 219.00 | 6.463E-03 | 1.412E-03 | 5.844E-01 | 5.923E-01 |
| 1.75 | 6.48 | 255.00 | 1.053E-03 | 1.238E-03 | 5.595E-01 | 5.617E-01 |
| 2.00 | 7.41 | 292.00 | 1.032E-04 | 1.105E-03 | 5.386E-01 | 5.398E-01 |
| 2.50 | 9.26 | 365.00 | 0.000E+00 | 9.225E-04 | 5.008E-01 | 5.017E-01 |
| 3.00 | 11.11 | 437.00 | 0.000E+00 | 8.022E-04 | 4.704E-01 | 4.712E-01 |
| 3.50 | 12.96 | 510.00 | 0.000E+00 | 7.156E-04 | 4.386E-01 | 4.393E-01 |
| 4.00 | 14.81 | 583.00 | 0.000E+00 | 6.485E-04 | 4.140E-01 | 4.146E-01 |
| 4.50 | 16.67 | 656.00 | 0.000E+00 | 5.942E-04 | 3.923E-01 | 3.929E-01 |
| 5.00 | 18.52 | 729.00 | 0.000E+00 | 5.490E-04 | 3.710E-01 | 3.715E-01 |
| 6.00 | 22.22 | 875.00 | 0.000E+00 | 4.770E-04 | 3.345E-01 | 3.350E-01 |
| 8.00 | 29.63 | 1167.00 | 0.000E+00 | 3.795E-04 | 2.797E-01 | 2.801E-01 |
| 10.00 | 37.04 | 1458.00 | 0.000E+00 | 3.118E-04 | 2.381E-01 | 2.384E-01 |

**Table 6** Daily Dose, 60 Degrees/500 km, Solar Minimum

| S GM/SQCM | T MM | T MILS | ELEC RADS-AL | BREM RADS-AL | PROTON RADS-AL | TOTAL RADS-AL |
|---|---|---|---|---|---|---|
| 0.01 | 0.04 | 1.00 | 4.304E+02 | 1.679E-01 | 6.493E+01 | 4.955E+02 |
| 0.02 | 0.07 | 3.00 | 2.406E+02 | 1.187E-01 | 2.498E+01 | 2.657E+02 |
| 0.03 | 0.11 | 4.00 | 1.539E+02 | 9.230E-02 | 1.545E+01 | 1.694E+02 |
| 0.04 | 0.15 | 6.00 | 1.076E+02 | 7.633E-02 | 1.071E+01 | 1.184E+02 |
| 0.05 | 0.19 | 7.00 | 7.992E+01 | 6.540E-02 | 7.814E+00 | 8.780E+01 |
| 0.06 | 0.22 | 9.00 | 6.208E+01 | 5.710E-02 | 6.268E+00 | 6.841E+01 |
| 0.07 | 0.26 | 10.00 | 4.989E+01 | 5.060E-02 | 5.159E+00 | 5.510E+01 |
| 0.08 | 0.30 | 12.00 | 4.115E+01 | 4.537E-02 | 4.395E+00 | 4.559E+01 |
| 0.09 | 0.33 | 13.00 | 3.468E+01 | 4.110E-02 | 3.844E+00 | 3.857E+01 |
| 0.10 | 0.37 | 15.00 | 2.967E+01 | 3.756E-02 | 3.389E+00 | 3.310E+01 |
| 0.20 | 0.74 | 29.00 | 1.090E+01 | 2.170E-02 | 1.675E+00 | 1.260E+01 |
| 0.30 | 1.11 | 44.00 | 6.208E+00 | 1.625E-02 | 1.164E+00 | 7.389E+00 |
| 0.40 | 1.48 | 58.00 | 4.088E+00 | 1.316E-02 | 9.099E-01 | 5.011E+00 |
| 0.50 | 1.85 | 73.00 | 2.833E+00 | 1.104E-02 | 7.575E-01 | 3.601E+00 |
| 0.60 | 2.22 | 87.00 | 2.008E+00 | 9.501E-03 | 6.737E-01 | 2.691E+00 |
| 0.80 | 2.96 | 117.00 | 1.056E+00 | 7.438E-03 | 5.723E-01 | 1.636E+00 |
| 1.00 | 3.70 | 146.00 | 5.778E-01 | 6.156E-03 | 5.052E-01 | 1.089E+00 |
| 1.25 | 4.63 | 182.00 | 2.756E-01 | 5.123E-03 | 4.589E-01 | 7.396E-01 |
| 1.50 | 5.56 | 219.00 | 1.309E-01 | 4.425E-03 | 4.216E-01 | 5.570E-01 |
| 1.75 | 6.48 | 255.00 | 6.178E-02 | 3.921E-03 | 3.964E-01 | 4.621E-01 |
| 2.00 | 7.41 | 292.00 | 2.811E-02 | 3.540E-03 | 3.764E-01 | 4.081E-01 |
| 2.50 | 9.26 | 365.00 | 4.293E-03 | 3.016E-03 | 3.411E-01 | 3.484E-01 |
| 3.00 | 11.11 | 437.00 | 4.175E-04 | 2.677E-03 | 3.140E-01 | 3.171E-01 |
| 3.50 | 12.96 | 510.00 | 8.088E-06 | 2.436E-03 | 2.882E-01 | 2.907E-01 |
| 4.00 | 14.81 | 583.00 | 0.000E+00 | 2.251E-03 | 2.689E-01 | 2.711E-01 |
| 4.50 | 16.67 | 656.00 | 0.000E+00 | 2.099E-03 | 2.524E-01 | 2.545E-01 |
| 5.00 | 18.52 | 729.00 | 0.000E+00 | 1.970E-03 | 2.364E-01 | 2.384E-01 |
| 6.00 | 22.22 | 875.00 | 0.000E+00 | 1.756E-03 | 2.098E-01 | 2.116E-01 |
| 8.00 | 29.63 | 1167.00 | 0.000E+00 | 1.453E-03 | 1.706E-01 | 1.721E-01 |
| 10.00 | 37.04 | 1458.00 | 0.000E+00 | 1.233E-03 | 1.421E-01 | 1.433E-01 |

from electrons and protons includes both ionization and nonionization. Effects of electron exposure in virtually all modern microcircuits are dominated by accumulated ionization. Definition of the internal ionizing radiation environment in terms of rads(Si) is generally adequate. Failure levels resulting from accumulated ionization can be as low as approximately 1000 rads(Si) for very sensitive unhardened microcircuits to greater than 10 Megarads(Si) for hardened microcircuits [15].

Effects of proton exposure over the energy range of interest in the space environment include both ionization and atomic displacement damage [16]. Failure levels resulting from proton-induced displacement damage can be as low as 1E10 p/cm$^2$ for very sensitive bipolar analog microcircuits or power transistors. In general, however, effects of proton exposure on the internal electronics are dominated by the ionizing energy deposition [15]. Definition of the proton environment for the internal electronics should include

**Table 7** Daily Dose, 90 Degrees/500 km, Solar Minimum

| S GM/SQCM | T MM | T MILS | ELEC RADS-AL | BREM RADS-AL | PROTON RADS-AL | TOTAL RADS-AL |
|---|---|---|---|---|---|---|
| 0.01 | 0.04 | 1.00 | 3.693E+02 | 1.449E-01 | 4.279E+01 | 4.123E+02 |
| 0.02 | 0.07 | 3.00 | 2.123E+02 | 1.049E-01 | 1.725E+01 | 2.297E+02 |
| 0.03 | 0.11 | 4.00 | 1.395E+02 | 8.307E-02 | 1.090E+01 | 1.504E+02 |
| 0.04 | 0.15 | 6.00 | 9.986E+01 | 6.959E-02 | 7.660E+00 | 1.076E+02 |
| 0.05 | 0.19 | 7.00 | 7.573E+01 | 6.027E-02 | 5.652E+00 | 8.144E+01 |
| 0.06 | 0.22 | 9.00 | 5.986E+01 | 5.315E-02 | 4.573E+00 | 6.449E+01 |
| 0.07 | 0.26 | 10.00 | 4.885E+01 | 4.748E-02 | 3.789E+00 | 5.269E+01 |
| 0.08 | 0.30 | 12.00 | 4.079E+01 | 4.288E-02 | 3.247E+00 | 4.408E+01 |
| 0.09 | 0.33 | 13.00 | 3.471E+01 | 3.907E-02 | 2.855E+00 | 3.761E+01 |
| 0.10 | 0.37 | 15.00 | 2.997E+01 | 3.586E-02 | 2.529E+00 | 3.254E+01 |
| 0.20 | 0.74 | 29.00 | 1.127E+01 | 2.103E-02 | 1.287E+00 | 1.258E+01 |
| 0.30 | 1.11 | 44.00 | 6.340E+00 | 1.573E-02 | 9.079E-01 | 7.263E+00 |
| 0.40 | 1.48 | 58.00 | 4.096E+00 | 1.270E-02 | 7.170E-01 | 4.826E+00 |
| 0.50 | 1.85 | 73.00 | 2.789E+00 | 1.062E-02 | 6.008E-01 | 3.400E+00 |
| 0.60 | 2.22 | 87.00 | 1.948E+00 | 9.110E-03 | 5.356E-01 | 2.493E+00 |
| 0.80 | 2.96 | 117.00 | 1.001E+00 | 7.104E-03 | 4.559E-01 | 1.464E+00 |
| 1.00 | 3.70 | 146.00 | 5.370E-01 | 5.874E-03 | 4.019E-01 | 9.448E-01 |
| 1.25 | 4.63 | 182.00 | 2.496E-01 | 4.890E-03 | 3.644E-01 | 6.189E-01 |
| 1.50 | 5.56 | 219.00 | 1.148E-01 | 4.227E-03 | 3.351E-01 | 4.541E-01 |
| 1.75 | 6.48 | 255.00 | 5.203E-02 | 3.751E-03 | 3.153E-01 | 3.711E-01 |
| 2.00 | 7.41 | 292.00 | 2.264E-02 | 3.392E-03 | 3.003E-01 | 3.263E-01 |
| 2.50 | 9.26 | 365.00 | 3.159E-03 | 2.896E-03 | 2.740E-01 | 2.800E-01 |
| 3.00 | 11.11 | 437.00 | 2.841E-04 | 2.573E-03 | 2.538E-01 | 2.567E-01 |
| 3.50 | 12.96 | 510.00 | 4.912E-06 | 2.344E-03 | 2.340E-01 | 2.363E-01 |
| 4.00 | 14.81 | 583.00 | 0.000E+00 | 2.168E-03 | 2.187E-01 | 2.209E-01 |
| 4.50 | 16.67 | 656.00 | 0.000E+00 | 2.022E-03 | 2.056E-01 | 2.076E-01 |
| 5.00 | 18.52 | 729.00 | 0.000E+00 | 1.899E-03 | 1.927E-01 | 1.946E-01 |
| 6.00 | 22.22 | 875.00 | 0.000E+00 | 1.694E-03 | 1.713E-01 | 1.730E-01 |
| 8.00 | 29.63 | 1167.00 | 0.000E+00 | 1.402E-03 | 1.396E-01 | 1.410E-01 |
| 10.00 | 37.04 | 1458.00 | 0.000E+00 | 1.191E-03 | 1.165E-01 | 1.177E-01 |

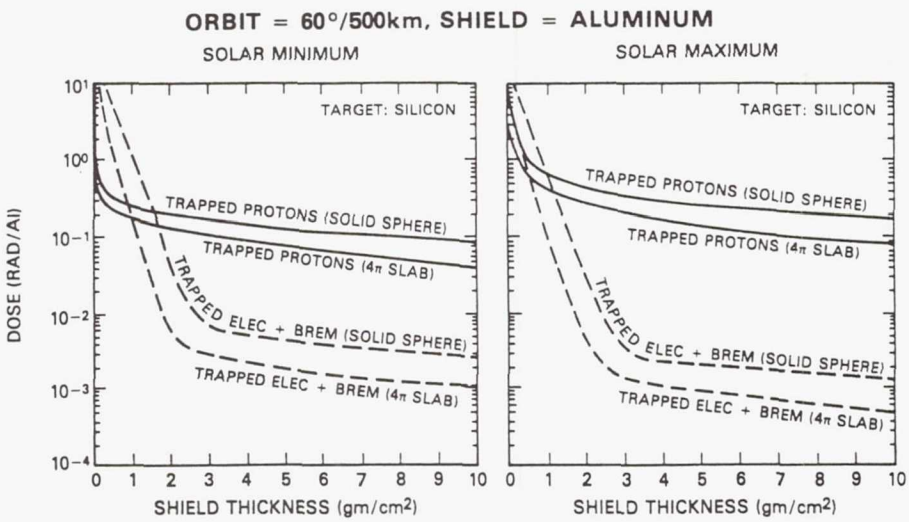


**Fig. 14.** Daily dose for low earth orbits.

both the proton-induced energy deposition (in rads(Si)), and the internal proton fluence and energy spectra for accurate characterization.

*D. Single Event Susceptibility of Electronics*

The high energy protons of the trapped space radiation environment can cause single event effects in modern semiconductor electronics. The proton energy threshold for these effects is approximately 10 MeV, with the cross section for nuclear reactions increasing substantially at 30 MeV and above [16]. Typically, a nuclear reaction resulting in a single event occurs on the order of once for every 100 000 protons. In terms of microcircuit susceptibility, for a 60° orbit, the maximum proton-induced upset rate occurs in the heart of the proton trapping domain of the radiation belts at an altitude of approximately 2600 km. It has been estimated that for electronics with "typical" shielding, the single event upset rate could be as high as 0.1 upsets/bit-day for very susceptible microcircuit technologies, decreasing by at least five orders of magnitude for less susceptible microcircuit technologies [17].

At low altitudes, low inclination orbits, the proton-induced single event upset rate is determined by passages through the South Atlantic Anomaly. During the flux-free times, the electronics will be free of single event upsets from trapped protons. The confinement of proton-induced upsets to passages through the SAA may be either an advantage or handicap to overall satellite system hardening.

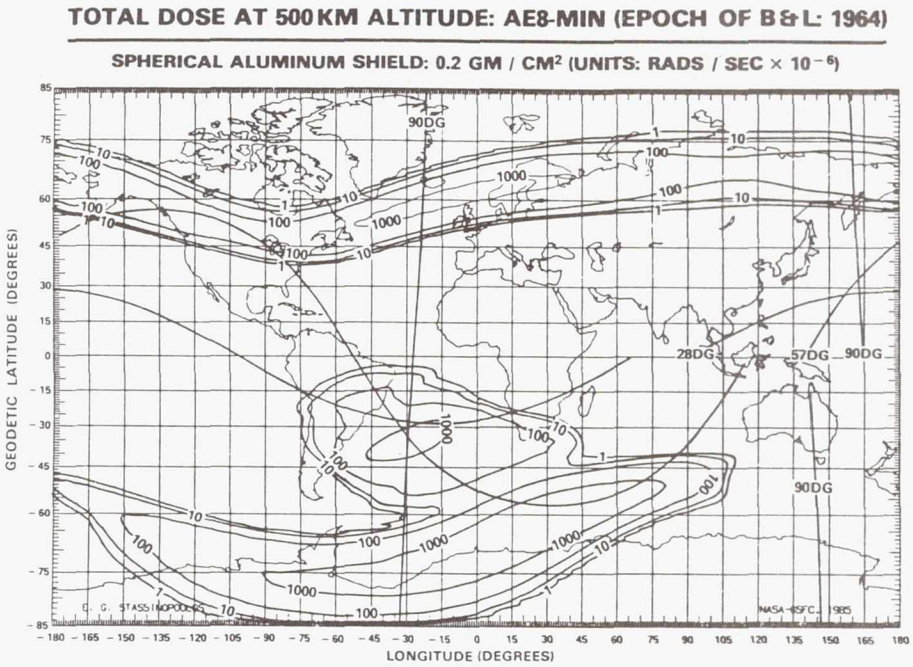


Fig. 15. World map contours of total dose: shield thickness = 0.2 gm/cm$^2$.

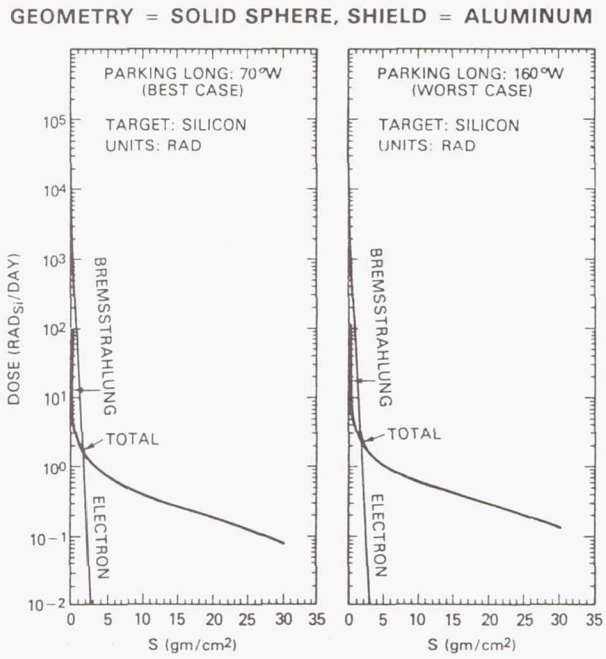


Fig. 16. Daily electron doses for geostationary orbits.

## III. Transiting Radiation

The transiting radiation of the space radiation environment is composed of a solar contribution and a galactic contribution. Each is composed of high energy protons and heavy ions. In terms of the spacecraft electronics, the dominant effects are those associated with the ionization tracks of single particles, as well as the effects of total accumulated ionization. As with the trapped radiation environment, we will first present the external environment, then the internal environment, and finally comment on the effects in the spacecraft electronics.

### A. Solar Cosmic Rays

*1) Solar Flare Protons:* Disturbed regions on the sun sporadically emit bursts of energetic charged particles into interplanetary space. These solar energetic particle (SEP) events (usually occurring in association with solar flares) are composed primarily of protons, with a minor constituent of alpha particles (5–10 percent), heavy ions, and electrons. The emission of protons from the SEP event can last as long as several days.

The time history of energetic solar flare particles as they arrive at the earth after the occurrence of the parent flare has several important characteristics. First, the particles arrive in tens of minutes to several hours (depending on their energy and point of origin on the sun); second, they peak within two hours to one day; and third, they decay within a few days to one week. It is important to note that the most energetic protons arrive at the earth in about 10–30 minutes.

SEP event phenomenology distinguishes between ordinary (OR) events and anomalously-large (AL) events. AL events are quite rare. Fig. 17 shows the energetic solar flare proton events since 1956. As shown, three AL events occurred during the 19th solar cycle, one during the 20th cycle, and none in the 21st cycle [18]. They occur mostly near the first and last year of the solar maximum phase. The prediction of AL events was initially based on an empirical model [3], and later on a probabilistic treatment involving modified Poisson statistics [19]. A simple statistical predictive model for solar flares is provided by SOLPRO [20], which is based exclusively on satellite spectral measurements covering nearly the entire 20th solar cycle. This model predicts, for a given mission duration and a specified confidence

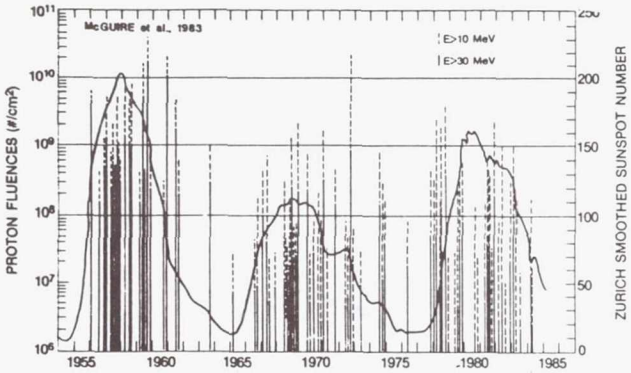


**Fig. 17.** Solar flare proton events for solar cycles 19, 20, and 21.

level, the mission integrated proton fluence spectrum from OR events, and the number of AL events to be expected with their event-integrated fluence spectra. In terms of proton fluence, since AL events are rare, small-sample statistics are the only appropriate prediction technique. Thus, for spacecraft of mission durations greater than one year, OR event fluences are not significant, because probability theory predicts the occurrence of at least one AL event, even for a confidence level as low as 80 percent.

*2) Solar Heavy Ions:* For ordinary solar flare events, the relative abundance of the helium ions in the emitted particle fluxes is usually between 5 and 10 percent, while the fluxes of heavier ions are very small, and significantly below the galactic background. However, during major solar events, the abundance of some heavy ions may increase rapidly by three or four orders of magnitude above the galactic background, for periods of several hours to days. The increased flux of the heavy ions can have serious consequences in terms of an increased frequency of single event effects within the spacecraft electronics.

### *B. Galactic Cosmic Rays*

The region outside the solar system in the outer part of the galaxy is believed to be filled uniformly with cosmic rays. These consist of about 85 percent protons, about 14 percent alpha particles, and about 1 percent heavier nuclei. The galactic cosmic rays range in energy to above 10 GeV per nucleon. Fig. 18 shows the spectral distributions for hydrogen, helium, carbon, and oxygen ions. The differential energy spectra of the cosmic rays near the earth tend to peak around 1 GeV/nucleon. Toward lower energies, the spectral shape is depressed by interactions with the solar wind and the interplanetary magnetic field. This reduction in flux becomes more pronounced during the active phase of the solar cycle. The total flux of cosmic ray particles seen outside the magnetosphere at the distance of the earth from the sun (i.e., 1 AU) is approximately 4 per square-centimeter per second (primarily composed of protons). For all practical purposes, the cosmic ray flux can be considered as omnidirectional, except for very low altitude orbits, where the solid angle subtended by the earth defines a region free from these particles. Fig. 19 shows the relative abundances of the galactic cosmic ray ions. A model for these particles is available [21].

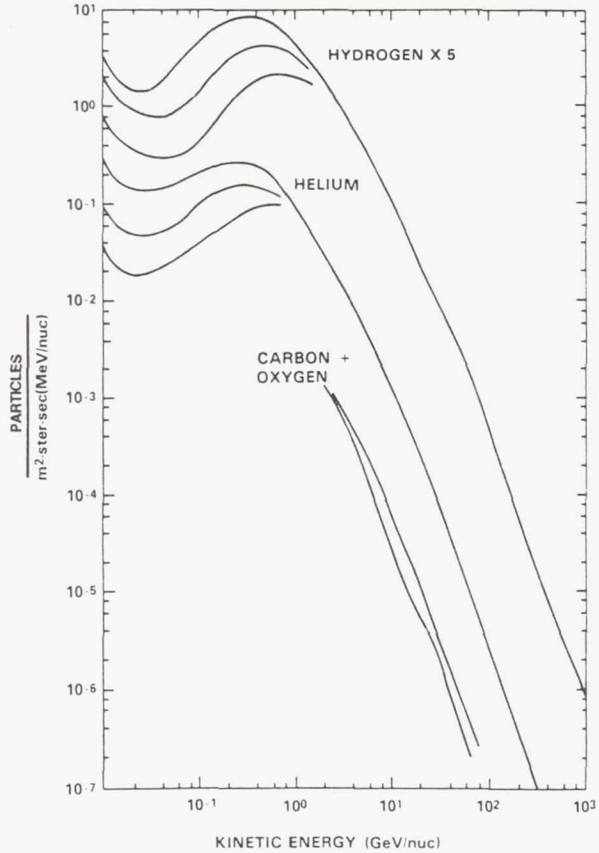


**Fig. 18.** Cosmic ray spectral distributions.

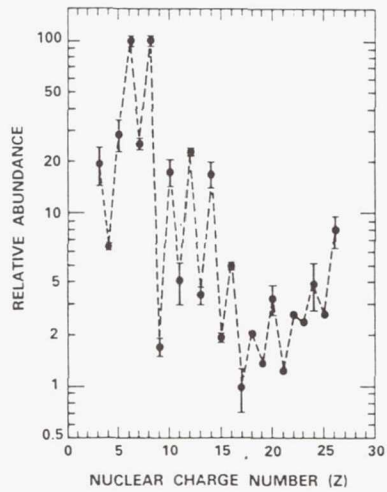


**Fig. 19.** *Relative abundance of nuclei in the galactic cosmic radiation.*

### *C. Geomagnetic Shielding*

Low altitude and latitude earth orbits are essentially shielded from solar or galactic cosmic rays by the geomagnetic field up to inclinations of about 45°. The earth's field acts as an energy filter preventing particles with less than given momentum values from penetrating to certain altitude-latitude combinations. Figs. 20 and 21 show the total ion energy required to penetrate the magnetosphere in

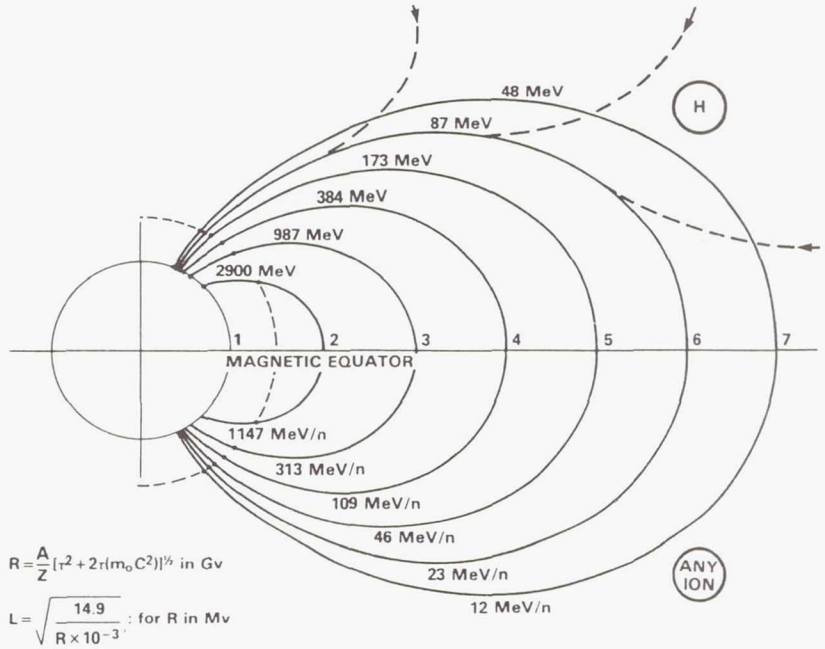


**Fig. 20.** Total energy required to penetrate the magnetosphere.

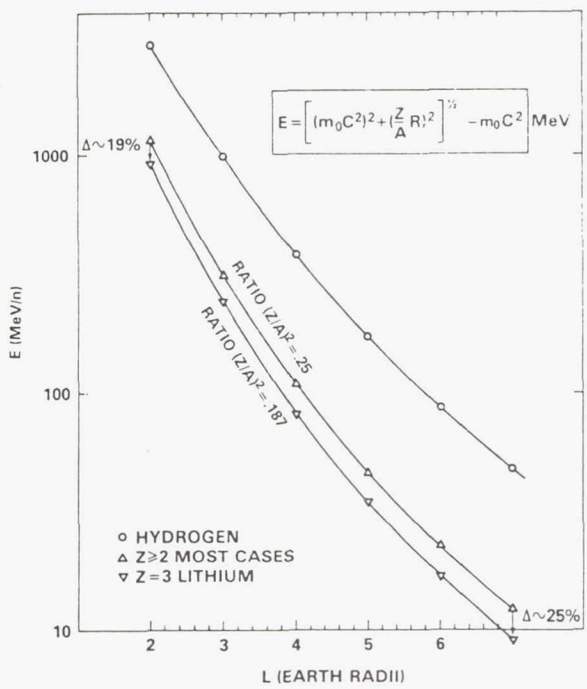


**Fig. 21.** Total energy required to penetrate the magnetosphere.

terms of the dipole parameter *L*. Table 8 and Fig. 22 show the effects of geomagnetic shielding on solar flare protons for high inclination (greater than 60°) low earth orbits. Fig. 23 shows the effect of shielding on cosmic ray silicon atoms for low earth orbits. Fig. 24 shows the magnetospheric attenuation dependence of the galactic cosmic ray iron spectrum on energy and *L*.

For geostationary orbits, magnetic shielding is relatively ineffective, and such orbits will be exposed to galactic

**Table 8** Solar Flare Proton Fluences, 1 AL, Altitude = 500 km

| ENERGY (>MEV) | 1 AL UNATTEN #/SQCM*EVENT | 28.5 DEG #/SQCM*EVENT | 60 DEG #/SQCM*EVENT | 90 DEG #/SQCM*EVENT |
|---|---|---|---|---|
| 10.0 | 1.680E+10 | 0 | 5.314E+08 | 3.837E+09 |
| 20.0 | 1.152E+10 | - | 4.429E+08 | 2.761E+09 |
| 30.0 | 7.900E+09 | - | 3.502E+08 | 1.960E+09 |
| 40.0 | 5.417E+09 | - | 2.654E+08 | 1.386E+09 |
| 50.0 | 3.714E+09 | - | 1.996E+08 | 9.735E+08 |
| 60.0 | 2.547E+09 | - | 1.461E+08 | 6.819E+08 |
| 70.0 | 1.746E+09 | - | 1.062E+08 | 4.762E+08 |
| 80.0 | 1.197E+09 | - | 7.717E+07 | 3.322E+08 |
| 90.0 | 8.210E+08 | - | 5.516E+07 | 2.316E+08 |
| 100.0 | 5.629E+08 | - | 3.903E+07 | 1.608E+08 |
| 110.0 | 3.860E+08 | - | 2.762E+07 | 1.117E+08 |
| 120.0 | 2.646E+08 | - | 1.976E+07 | 7.766E+07 |
| 130.0 | 1.815E+08 | - | 1.417E+07 | 5.389E+07 |
| 140.0 | 1.244E+08 | - | 1.011E+07 | 3.723E+07 |
| 150.0 | 8.531E+07 | - | 7.225E+06 | 2.571E+07 |
| 160.0 | 5.850E+07 | - | 5.177E+06 | 1.779E+07 |
| 170.0 | 4.011E+07 | - | 3.696E+06 | 1.231E+07 |
| 180.0 | 2.750E+07 | - | 2.610E+06 | 8.508E+06 |
| 190.0 | 1.886E+07 | - | 1.827E+06 | 5.874E+06 |
| 200.0 | 1.293E+07 | 0 | 1.276E+06 | 4.056E+06 |

cosmic ray hydrogen of energies above approximately 60 MeV, and heavier ions above 15 MeV per nucleon. This is illustrated in Table 9 for energetic solar flare protons, and is independent of parking longitude.

Geomagnetic shielding effects on geocentric missions are usually evaluated with simple rigidity considerations, for economy reasons, and because of substantial diurnal variations in the cutoff latitudes associated with geomagnetic tail effects (2–4 degrees), and storm-induced changes (>4 degrees).

## IV. Transiting Radiation Transport, Shielding, and Energy Deposition

### *A. Emerging Radiation Spectra*

*1) Solar Flare Protons:* Considerations in the transport of solar flare protons are similar to those previously discussed

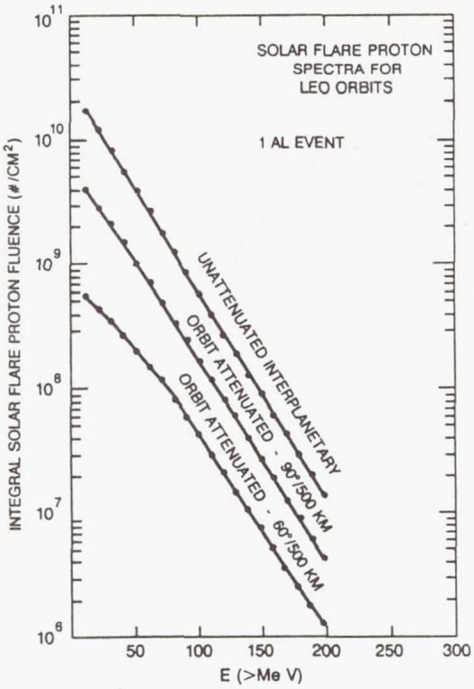


**Fig. 22.** Magnetospheric attenuation of solar flare protons for LEO.

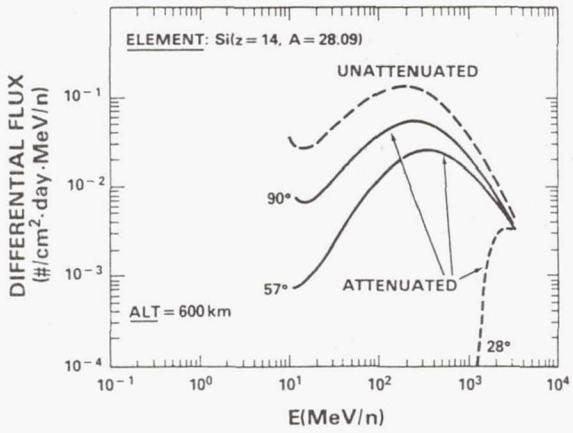


**Fig. 23.** Magnetospheric attenuation of cosmic rays for LEO.

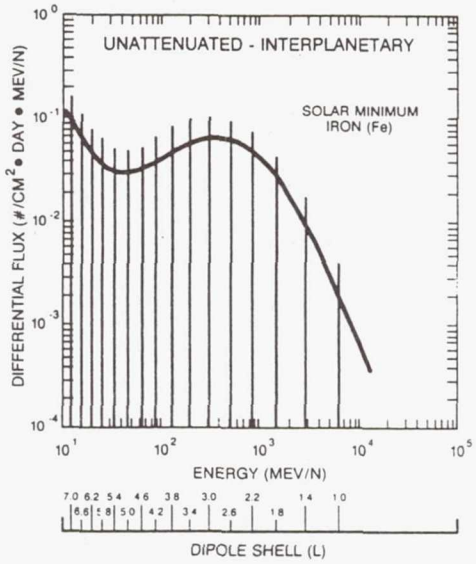


**Fig. 24.** Dependence of the attenuation of galactic cosmic rays on energy and *L*.

**Table 9** Solar Flare Proton Fluences, 1 AL, GEO

| ENERGY (>MEV) | 1 AL UNATTEN #/SQCM*EVENT | ENERGY (>MEV) | 1 AL 160 W #/SQCM*EVENT | ENERGY (>MEV) | 1 AL 70 W #/SQCM*EVENT |
|---|---|---|---|---|---|
| 10.0 | 1.680E+10 | NOT ACCESSIBLE | | NOT ACCESSIBLE | |
| 20.0 | 1.152E+10 | | 0 | | 0 |
| 30.0 | 7.900E+09 | | 0 | | 0 |
| 40.0 | 5.417E+09 | 48.1 | 3.990E+09 | | 0 |
| 50.0 | 3.714E+09 | 50.0 | 3.714E+09 | | 0 |
| 60.0 | 2.547E+09 | 60.0 | 2.547E+09 | 60.4 | 2.509E+09 |
| 70.0 | 1.746E+09 | 70.0 | 1.746E+09 | 70.0 | 1.746E+09 |
| 80.0 | 1.197E+09 | 80.0 | 1.197E+09 | 80.0 | 1.197E+09 |
| 90.0 | 8.210E+08 | 90.0 | 8.210E+08 | 90.0 | 8.210E+08 |
| 100.0 | 5.629E+08 | 100.0 | 5.629E+08 | 100.0 | 5.629E+08 |
| 110.0 | 3.860E+08 | 110.0 | 3.860E+08 | 110.0 | 3.860E+08 |
| 120.0 | 2.646E+08 | 120.0 | 2.646E+08 | 120.0 | 2.646E+08 |
| 130.0 | 1.815E+08 | 130.0 | 1.815E+08 | 130.0 | 1.815E+08 |
| 140.0 | 1.244E+08 | 140.0 | 1.244E+08 | 140.0 | 1.244E+08 |
| 150.0 | 8.531E+07 | 150.0 | 8.531E+07 | 150.0 | 8.531E+07 |
| 160.0 | 5.850E+07 | 160.0 | 5.850E+07 | 160.0 | 5.850E+07 |
| 170.0 | 4.011E+07 | 170.0 | 4.011E+07 | 170.0 | 4.011E+07 |
| 180.0 | 2.750E+07 | 180.0 | 2.750E+07 | 180.0 | 2.750E+07 |
| 190.0 | 1.886E+07 | 190.0 | 1.886E+07 | 190.0 | 1.886E+07 |
| 200.0 | 1.293E+07 | 200.0 | 1.293E+07 | 200.0 | 1.293E+07 |

for the trapped protons. The materially attenuated emerging spectra reflect the shielding effect on the distribution of the solar flare protons, as shown in Fig. 25. The proton fluxes in the 0.1 to 10 MeV range emerging behind spherical aluminum shields of thickness ranges from 0.3 to 5 grams/cm$^2$ are substantial. Particularly relevant to single particle event effects in the electronics is the Linear Energy Transfer (LET) in silicon, defined as the energy deposition per unit length in the active region of the semiconductor device. The LET spectrum for one AL event is shown in Fig. 26 for the interplanetary solar flare proton spectrum not attenuated by the magnetosphere, emerging from spherical aluminum shields of two thicknesses. Stopping powers ($dE/dx$) were calculated from the classical equation [22]. The Bethe formula is accurate to about 20 percent at a few MeV per nucleon [23]. The error decreases at higher energies, where the assumptions of the Bethe formulation are increasingly valid. At energies below a few MeV per nucleon, the error increases due to unmodeled details of the energy loss mechanisms.

In general, the ionization loss of a single proton is insufficient to cause a single event effect in a semiconductor device. Observed single event effects from proton exposures are the result of the energy deposition of particles produced by nuclear interactions by the incident proton with the target nucleus. The proton threshold energy for these nuclear interactions is approximately 30 MeV [17].

*2) Galactic Cosmic Rays:* Fig. 27 shows the unattenuated interplanetary spectra for silicon cosmic ray ions, the magnetospherically attenuated orbit-integrated spectra incident on the surface of the spacecraft, and the shielded spectra of emerging particles behind selected thicknesses of spherical aluminum geometries for an orbit of 57° inclination and 600 km altitude. Differential particle fluxes are shown referenced to the left ordinate. Also shown in Fig. 27 is the Linear Energy Transfer (LET) spectrum of the silicon

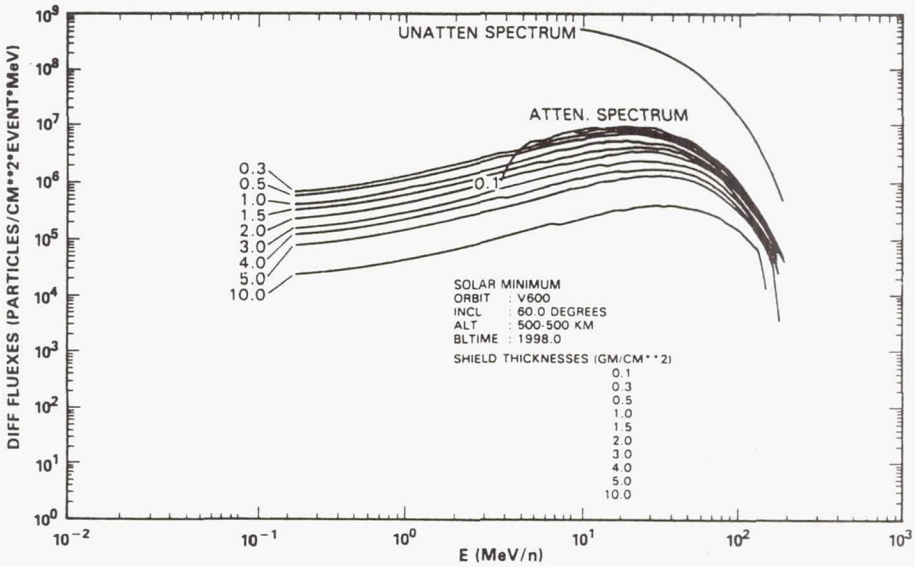


**Fig. 25.** Emerging solar flare proton spectra, given for 1 AL event, behind spherical aluminum shields.

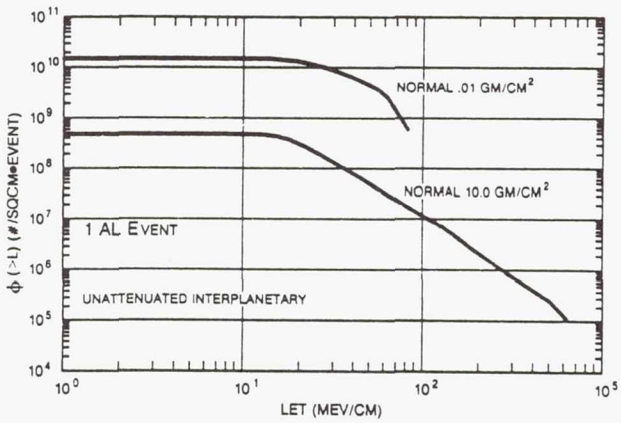


**Fig. 26.** Integral LET spectra for solar flare protons behind spherical aluminum shields.

ion as a function of energy, referenced to the right ordinate. The LET spectrum is important in defining the energy deposited by a single particle, and subsequent single event effects in the spacecraft electronics.

In passing through shielding material, nuclear reactions are induced by heavy ions with energies above an effective threshold of a few MeV/nucleon. These nuclear reactions provide a source of secondary radiation, both prompt and delayed. Above several hundred MeV/nucleon, nuclear reactions surpass atomic ionization as the main attenuation mechanism in material. At higher energies, the interaction of the incident particle tends to occur primarily with individual nucleons in the target nucleus, and can lead to the ejection of several energetic protons and neutrons. This "spallation" process leaves the product nucleus highly excited, with de-excitation occurring through the "evaporation" of additional nucleons and the emission of gamma

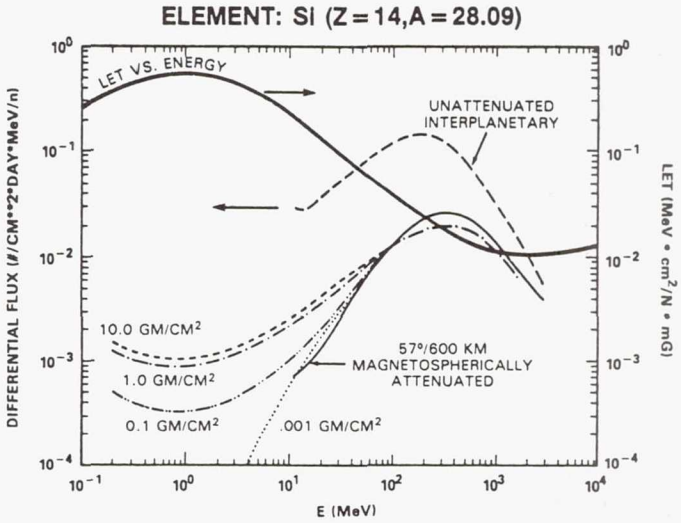


**Fig. 27.** Galactic cosmic ray spectra (solar min.) emerging behind spherical aluminum shields.

rays. For 400 MeV protons incident on aluminum, the average total nuclear emission is 4.8, including 2.8 spallation nucleons with an average energy of 120 MeV [24]. The process can generate a rich variety of residual nuclei, especially in heavier elements, as a result of the multiplicity of statistically possible reaction paths (i.e., the specific number of protons and neutrons emitted). These product nuclei frequently are radioisotopes decaying by beta-ray emission with a variety of lifetimes.

Several important features are illustrated by the curve of Fig. 28. First, there is substantial attenuation by the earth's magnetic field of all particles in the energy range of 10–10 000 MeV per nucleon. Second, there is an insignificant effect of material shielding in the energy range from about 90 to 10 000 MeV. Note that there is no substantial decrease in flux even for aluminum shielding of 10 grams/cm$^2$ (approximately 1.5 inches). Third, there is an unavoidable shield side effect of a significant increase in the low energy (0.8–50 MeV/nucleon) high-LET fluxes for shield thickness greater than 0.1 gram/cm$^2$ of aluminum. With increasing shield thicknesses, the population of high energy ions decreases slightly, but with a resultant increase in the low energy (0.8–50 MeV/nuclear) ions. Since the LET increases with decreasing energy in this range (heavy solid curve) the presence of the shield actually increases the severity of the environment to the internal electronics.

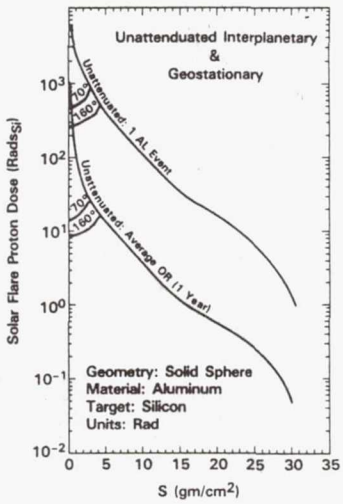


Fig. 28. Solar flare proton dose.

### B. *Ionizing Radiation Dose*

In general, the ionizing radiation dose from the transiting radiation environment is not significant compared to that of the trapped radiation environment. Particle fluxes from energetic solar flares are heavily attenuated by the geomagnetic field, which prevents their penetration to low orbital altitudes and inclinations. For a 500 km, 30° inclination orbit, the attenuation is nearly total. In a 500 km, 57° inclination orbit, some penetration occurs. In contrast, a polar orbit experiences a substantial degree of exposure at any altitude.

In GEO, the geomagnetic shielding is relatively ineffective. Even so, the average yearly dose from ordinary (OR) events behind a 2 gram/cm$^2$ spherical aluminum shield is quite small, approximately 18 rads(Si)/year. In comparison,

**Table 10** Solar Flare Shielded Dose, 1 AL, GEO

| | MAGNETOSPHERICALLY UNATTENUATED | | MAGNETOSPHERICALLY ATTENUATED TO 70DEG W | | MAGNETOSPHERICALLY ATTENUATED TO 160DEG W | |
|---|---|---|---|---|---|---|
| S (GM/SQCM) | SLAB(4PI) (RADS-SI) | SOLID SPHERE (RADS-SI) | SLAB(4PI) (RADS-SI) | SOLID SPHERE (RADS-SI) | SLAB(4PI) (RADS-SI) | SOLID SPHERE (RADS-SI) |
| 0.01 | 4.690E+03 | 4.597E+03 | 4.796E+02 | 4.782E+02 | 2.680E+02 | 2.675E+02 |
| 0.02 | 4.762E+03 | 4.645E+03 | 4.810E+02 | 4.781E+02 | 2.686E+02 | 2.674E+02 |
| 0.03 | 4.812E+03 | 4.688E+03 | 4.824E+02 | 4.782E+02 | 2.692E+02 | 2.675E+02 |
| 0.04 | 4.846E+03 | 4.737E+03 | 4.838E+02 | 4.784E+02 | 2.696E+02 | 2.675E+02 |
| 0.05 | 4.868E+03 | 4.788E+03 | 4.850E+02 | 4.786E+02 | 2.702E+02 | 2.676E+02 |
| 0.06 | 4.878E+03 | 4.850E+03 | 4.862E+02 | 4.788E+02 | 2.708E+02 | 2.676E+02 |
| 0.08 | 4.872E+03 | 4.950E+03 | 4.886E+02 | 4.794E+02 | 2.718E+02 | 2.678E+02 |
| 0.10 | 4.828E+03 | 5.221E+03 | 4.910E+02 | 4.802E+02 | 2.728E+02 | 2.680E+02 |
| 0.20 | 4.004E+03 | 5.875E+03 | 5.000E+02 | 4.849E+02 | 2.768E+02 | 2.696E+02 |
| 0.30 | 3.202E+03 | 5.117E+03 | 5.062E+02 | 4.902E+02 | 2.802E+02 | 2.716E+02 |
| 0.40 | 2.680E+03 | 4.429E+03 | 5.110E+02 | 4.950E+02 | 2.826E+02 | 2.737E+02 |
| 0.50 | 2.298E+03 | 3.957E+03 | 5.144E+02 | 4.998E+02 | 2.846E+02 | 2.758E+02 |
| 0.60 | 2.004E+03 | 3.553E+03 | 5.168E+02 | 5.051E+02 | 2.862E+02 | 2.776E+02 |
| 0.70 | 1.774E+03 | 3.216E+03 | 5.182E+02 | 5.108E+02 | 2.874E+02 | 2.794E+02 |
| 0.80 | 1.587E+03 | 2.966E+03 | 5.190E+02 | 5.168E+02 | 2.884E+02 | 2.814E+02 |
| 0.90 | 1.428E+03 | 2.727E+03 | 5.188E+02 | 5.232E+02 | 2.892E+02 | 2.836E+02 |
| 1.00 | 1.296E+03 | 2.512E+03 | 5.180E+02 | 5.297E+02 | 2.898E+02 | 2.860E+02 |
| 1.25 | 1.038E+03 | 2.134E+03 | 5.130E+02 | 5.488E+02 | 2.900E+02 | 2.921E+02 |
| 1.50 | 8.504E+02 | 1.795E+03 | 5.038E+02 | 5.690E+02 | 2.890E+02 | 2.988E+02 |
| 1.75 | 7.120E+02 | 1.592E+03 | 4.908E+02 | 6.002E+02 | 2.868E+02 | 3.061E+02 |
| 2.00 | 5.978E+02 | 1.402E+03 | 4.736E+02 | 6.153E+02 | 2.834E+02 | 3.144E+02 |
| 2.50 | 4.430E+02 | 1.037E+03 | 4.244E+02 | 7.829E+02 | 2.736E+02 | 3.334E+02 |
| 3.00 | 3.424E+02 | 8.769E+02 | 3.406E+02 | 8.544E+02 | 2.592E+02 | 3.626E+02 |
| 3.50 | 2.654E+02 | 7.021E+02 | 2.654E+02 | 6.989E+02 | 2.394E+02 | 3.929E+02 |
| 4.00 | 2.136E+02 | 5.719E+02 | 2.136E+02 | 5.725E+02 | 2.118E+02 | 4.972E+02 |
| 4.50 | 1.733E+02 | 4.956E+02 | 1.733E+02 | 4.954E+02 | 1.733E+02 | 5.004E+02 |
| 5.00 | 1.418E+02 | 4.160E+02 | 1.418E+02 | 4.161E+02 | 1.418E+02 | 4.147E+02 |
| 6.00 | 9.860E+01 | 3.047E+02 | 9.860E+01 | 3.047E+02 | 9.860E+01 | 3.050E+02 |
| 8.00 | 5.120E+01 | 1.759E+02 | 5.120E+01 | 1.759E+02 | 5.120E+01 | 1.759E+02 |
| 10.00 | 2.870E+01 | 1.094E+02 | 2.870E+01 | 1.094E+02 | 2.870E+01 | 1.094E+02 |
| 15.00 | 7.984E+00 | 3.464E+01 | 7.984E+00 | 3.464E+01 | 7.984E+00 | 3.464E+01 |
| 20.00 | 2.558E+00 | 1.580E+01 | 2.558E+00 | 1.580E+01 | 2.558E+00 | 1.580E+01 |
| 30.00 | 1.104E-01 | 1.250E+00 | 1.104E-01 | 1.250E+00 | 1.104E-01 | 1.250E+00 |

the event-integrated dose from an anomalously large (AL) flare at parking longitude of 70° W would be approximately 600 rads(Si)/event for the same shield and target as shown in Fig. 28 and Table 10. Tripling the shield thickness to 6 grams/cm$^2$ would result in 300 rads/event.

### C. Single Event Susceptibility of Electronics

Single event upset effects in electronics from the transiting space radiation environment may be the result of either the energetic solar flare protons or cosmic rays. The nature of trapped proton-induced single event effects has been discussed previously. In general, the single event upset rate due to transiting protons is small compared to that due to cosmic rays, except for the occurrence of an AL. To cover the occurrence of an AL during the spacecraft mission, both the expected duration and fluence of the AL must be considered in the electronics design.

For the cosmic ray component of the transiting space radiation environment, the definition of the LET spectrum of the internal radiation environment is a fundamental basis for characterization of component susceptibility. Observed effects from single heavy high energy ions include memory bit upset, microprocessor errors, CMOS latchup and burnout in power MOSFETs, and electrically-erasable PROMs [25], [26]. The probability of latchup or burnout is much less than that of memory bit upset or logic errors, but the consequences to system operation may be much more severe.

Generally, cosmic-ray-induced single event effects dominate proton-induced single event effects both at altitudes below 1000 km and above 4000 km for 60° circular orbits. For orbits of lower inclinations, the cosmic rays are shielded by the earth's magnetic field, causing the cosmic ray upset level to decrease compared to the proton upset rate. On the other hand, for orbits of higher inclinations, the relative upset rate of the cosmic rays increases. The variations in the spacecraft orbit, space radiation environment, and device susceptibility should be considered in estimating specific cosmic ray/proton upset levels in support of spacecraft electronics design. The specification of the internal electronics environment should include the time-dependent proton flux and energy spectrum, the cosmic ray LET spectrum, and the cosmic ray spectrum by particle species and energy spectrum. The actual cosmic ray spectrum can be a valuable supplement to the LET spectrum in those cases where more detail is necessary to support experimental characterization in ground-based laboratory facilities.

## Conclusion

The richly diverse earth space radiation environment has been described in terms of its nature and variations with respect to the susceptibility of spacecraft electronics. The constraints of space radiation effects on spacecraft electronics design can be significant, but with careful component selection, shielding, and design, systems can be realized that are both of high performance and long endurance.

This paper has specifically addressed the earth radiation environment, but our planet is not alone in its magnetic field and trapped radiation belts. Jupiter, to be explored by the Galileo spacecraft, has a trapped radiation environment much more severe than that of the earth. Even in transit to the outer planets and beyond, the galactic cosmic rays must be considered in their effects on the electronics. As our knowledge of the space radiation environments and radiation effects of electronics grows, the electronics technology itself evolves. The combination will be both exciting and challenging for many years to come.

## References


[1] D. R. Barraclough, R. M. Harwood, B. R. Leaton, and S. R. C. Malin, "A model of the geomagnetic field at epoch 1975," *Geophys. J. R. Astron. Soc.*, vol. 43, p. 645, 1975.

[2] IAGA Division I, Working Group 1, "International geomagnetic reference field, revision 1985," EOS, vol. 67, pp. 523–524, June 1986.

[3] E. G. Stassinopoulos and J. H. King, "Empirical solar proton model for orbiting spacecraft applications," *IEEE Trans. Aerosp. Electron. Syst.*, vol. AES-10, no. 4, July 1974.

[4] W. N. Spjeldvik and P. L. Rothwell, "The earth's radiation belts," Rep. AFGL-TR-83-0240, Air Force Geophysics Laboratory, Hanscom AFB, MA, Sept. 29, 1983.

[5] C. E. McIlwain, "Coordinates for mapping the distribution of magnetically trapped particles," *J. Geophys. Res.*, vol. 66, no. 11, pp. 3681–3691, 1961.

[6] D. M. Sawyer and J. I. Vette, "AP8 trapped proton environment for solar maximum and solar minimum," Rep. NSSDC 76-06, National Space Science Data Center, Greenbelt, MD, Dec., 1976.

[7] "AE8 trapped electron model," to be published by the National Space Science Data Center, NASA-Goddard Space Flight Center.

[8] L. J. Lanzerotti, C. S. Roberts, and W. L. Brown, "Temporal variations in the electron flux at synchronous altitude," *J. Geophys. Res.*, vol. 72, no. 23, pp. 5893–5902, Dec. 1967.

[9] R. P. Lin and K. A. Anderson, "Periodic modulation of the energetic electron fluxes in the distant radiation zone," *J. Geophys. Res.*, vol. 71, no. 7, pp. 1827–1835; Apr. 1966.

[10] B. J. O'Brein, "A large diurnal variation of the geomagnetically trapped radiation," *J. Geophys. Res.*, vol. 68, no. 4, pp. 989–995; Feb. 1963.

[11] M. J. Teague and E. G. Stassinopoulos, "A model of the Starfish flux in the inner radiation zone," NASA/GSFC Rep. X-601-72-487, Dec. 1972.

[12] E. G. Stassinopoulos and P. Verzariu, "General formula of decay lifetimes of Starfish electrons," *J. Geophys. Res.*, vol. 76, no. 7, pp. 1841–1844, Mar. 1971.

[13] T. M. Jordan, "Adjoint Monte Carlo electron shielding calculations," *ANS Trans.*, vol. 41, June 1982.

[14] S. Seltzer, "SHIELDOSE: A computer code for space shielding radiation dose calculations," U.S. Dep. Commerce, National Bureau of Standards, NBS Technical Note 1116, May 1980.

[15] J. P. Raymond and E. L. Petersen, "Comparison of neutron, proton, and gamma ray effects in semiconductor devices," *IEEE Trans. Nuclear Sci.*, vol. NS-34, no. 6, pp. 1622–1628, Dec. 1987.

[16] E. L. Petersen, "Soft errors due to protons in the radiation belt," *IEEE Trans. Nuclear Sci.*, vol. NS-28, no. 6, pp. 3981–3986; Dec. 1981.

[17] W. L. Bendel and E. L. Petersen, "Proton upsets in orbit," *IEEE Trans. Nuclear Sci.*, vol. NS-30, no. 6, pp. 4481–4485, Dec. 1983.

[18] J. N. Goswami, R. E. McGuire, R. C. Reddy, D. Lai, and R. Jha, "Solar flare protons and alpha particles during the last three solar cycles," submitted to *J. Geophys. R.* (Los Alamos Preprint LA-UR-87-1176).

[19] J. H. King, "Solar proton fluences for 1977–1983 space missions," *J. Spacecraft and Rockets*, vol. 11, pp. 401–408, 1974.

[20] E. G. Stassinopoulos, "SOLPRO: A computer code to calculate probabilistic energetic solar proton fluences," NSSDC Rep. no. 75-11, National Space Science Data Center, Greenbelt, MD, Apr. 1975.

[21] J. H. Adams, R. Silberg, and C. H. Tszo, "Cosmic ray effects on microelectronics, Part I: The near-earth particle environment," Naval Research Laboratory, NRL Mem. Rep. 4506, Aug. 1981.

[22] H. Bethe, "Theory of the passage of fast corpuscular rays through matter," *Ann. Physik*, Ser. 5, pp. 5–325; 1920.

[23] U. Littmark and J. F. Ziegler, *Handbook of Range Distributions for Energetic Ions in all Elements*. New York, NY: Pergamon Press, 1980.
[24] J. W. Haffner, *Radiation and Shielding in Space*. New York, NY: Academic Press, 1967.
[25] D. K. Nichols, L. S. Smith, W. E. Price, R. Koga, and W. A. Kolasinski, "Recent trends in parts SEU susceptibility from heavy ions," *IEEE Trans. Nuclear Sci.*, vol. NS-34, no. 6, pp. 1332–1337, Dec. 1987.
[26] A. E. Waskiewicz, J. W. Groniger, V. H. Strahan, and D. M. Long, "Burnout of power MOS transistors with heavy ions of Californium-252," *IEEE Trans. Nuclear Sci.*, vol. NS-33, no. 6, pp. 1710–1713, Dec. 1986.

of radiation effects in electronic devices; modeling of physical processes in the earth's magnetosphere and in interplanetary space; large-scale data analysis and correlation; space-borne and laboratory scientific and engineering experiments; dosimetry research and applications; etc. He has published over 100 papers and articles in scientific, technical, and engineering journals, books, and official NASA publications.

# LEO SPACE PLASMA INTERACTIONS

Dr. Dale C. Ferguson
NASA Lewis Research Center
Cleveland, Ohio

Photovoltaic arrays interact with the low Earth orbit (LEO) space plasma in two fundamentally different ways. One way is the steady collection of current from the plasma onto exposed conductors or semiconductors. The relative currents collected by different parts of the array will then determine the floating potential of the spacecraft. In addition, these steady state collected currents may lead to sputtering or heating of the array by the ions or electrons collected, respectively. The second type of interaction is a short timescale arc into the space plasma, which may deplete the array and/or spacecraft of stored charge, damage solar cells, and produce EMI. Such arcs only occur at high negative potentials relative to the space plasma potential, and depend on the steady state ion currents being collected. New high voltage solar arrays being incorporated into advanced spacecraft and space platforms may be endangered by these plasma interactions. Recent advances in laboratory testing and current collection modeling promise the capability of controlling, and perhaps even using, these space plasma interactions to enable design of reliable high voltage space power systems. Some of the new results may have an impact on solar cell spacing and/or coverslide designs. Planned space flight experiments are necessary to confirm our models of high voltage solar array plasma interactions. Finally, computerized, integrated plasma interactions design tools are being constructed to place plasma interactions models into the hands of the spacecraft designer.

## INTRODUCTION

The standard power source for space applications continues to be photovoltaic arrays. Standard space arrays have used low voltages, such as 28 V, and have had minimal interactions with the ionized plasma of the earth's upper atmosphere. With no exposed high voltages, such systems will come to an equilibrium potential not far from the potential of the surrounding plasma. However, with the advent of large space power systems, and the necessity of large distributed areas for array photon collection, there has come a desire for high efficiency power transmission. To electrical power system designers, this implies high voltage systems, because the distribution losses go up as the square of the necessary current. With high voltage systems, the same amount of power may be distributed at lower current levels, and concomitant higher efficiencies.

Modern large solar array designs for high power space applications typically use end-to-end voltages of 160 to 200 V (eg. Space Station Freedom [SSF] and Advanced Photovoltaic Solar Array [APSA]). With such high distributed voltages, some parts of the array must be at relatively high potentials, with respect to the ambient plasma potential. Ground tests and theories concur that solar arrays at high potentials will interact with the surrounding plasma in two fundamentally different ways. Firstly, they will collect steady currents from the plasma onto exposed conductors (such as cell interconnects) or semiconductors (such as cell edges).

These currents will act as a drain on the power system, and for that reason are sometimes called parasitic currents. High potentials will pull in larger parasitic currents than the low potentials on solar arrays flown to date. The absence of a hard electrical ground in the space plasma will require that the power system, and solar arrays, will take on potentials (called floating potentials) such that electron currents collected by the more positive parts of the system will be balanced by the ions collected by the negative areas. In general, only connected electrical conductors must obey a "global" current balance condition. Insulators and isolated conductors exposed to the plasma will locally balance the electron and ion currents to their surfaces, resulting in a slightly negative surface potential. This potential is necessary to repel enough of the fast-moving electrons to restrict the electron current to match the slow-moving ion current collected at small negative potentials.

When applied globally to a space power system, the current balance condition requires that for unimpeded electron and ion current collection, the entire system will float with about 95% of its area negative, and about 5% positive of the plasma potential. For a 160 V solar array hooked to an insulated structure, this means that the most negative end of the array will be at about 152 V negative of the plasma potential, and the positive end at only 8 V positive. High negative potentials relative to the surrounding plasma may lead to undesirable interactions, among them sputtering and arcing into the plasma.

If parts of the solar array are forced to be at high positive potentials relative to the surrounding plasma, other undesirable effects may occur. At potentials above about 100 V positive of the plasma, solar cells and arrays may collect anomalously high currents, tantamount to the currents one might expect if the insulating surfaces were collecting current as well as the conducting or semiconducting surfaces. This effect is called "snapover", from the belief that it is caused by the high surface potentials on the conductors "snapping over", because of secondary electron effects, onto the surfaces of the adjacent insulators. It might lead to unacceptably high parasitic current power losses. One other possible undesirable effect might be localized heating due to snapover currents onto small exposed areas, which could lead to pyrolysis of Kapton® surrounding the exposed conductor.

Ion current collection by conducting surfaces at high negative potentials is implicated in the second fundamental type of environmental interactions. The interaction of interest here is arcing from surfaces to the space plasma (or to other spacecraft surfaces). These transient arcs may discharge the entire electrically connected surface of the spacecraft or array, and are therefore potentially destructive of solar cells and/or array current traces. Solar array arcs into the plasma occur where conductors or semiconductors collecting ion current from the plasma are adjacent to insulating materials, such as coverslides or Kapton®. They are very short (microsecond) localized transients, emitting heat, radio frequency interference, light, and a very dense localized plasma, and causing a rapid positive swing of all spacecraft potentials. There seems to be a threshold voltage for solar array plasma arcing, at around -230 V, although it may vary with materials used.

The advantages of using high end-to-end voltages on space photovoltaic power systems must be weighed against the risks of damage due to plasma interactions. There exist possibilities of tailoring the system plasma interactions so that they may be ameliorated, or in

some instances even used to control vehicle potentials. An understanding of the phenomena is necessary in order to explore these possibilities.

## STEADY STATE CURRENT COLLECTION

Figures 1 and 2 show the current collection behavior of a typical solar array immersed in the space plasma, when its conductors (or semiconductors) are at a potential V relative to the plasma potential (Stevens and Stillwell, 1989). It may be seen that for electron current collection, there is a region of depressed plasma current collection for low potentials (less than about 100 V). This is because the insulating surfaces which surround the exposed conductors have a slightly negative potential, to be able to locally repel fast-moving electrons to allow the slower ions to balance current locally. These potentials, typically three to five times the plasma electron temperature (that is, 0.3 to 1.0 volts), extend into the region of space above the conductor, and may partially choke off the electron current to the conductor, depending on the exact geometry. Above about 100-200 V, there is a transition to anomalously high electron current, corresponding to the snapover phenomenon mentioned in the introduction. Here, it almost seems like the entire coverslide surface has become a conductor, for the purposes of electron collection. Although there is disagreement about the mechanism of the snapover phenomenon (Gabriel *et al*, 1983, Thiemann and Schunk, 1990), it may be due to charging of the adjacent insulators by secondary electron emission, where emitted electrons hop across the insulator until reaching the conducting surface, or perhaps by other surface conduction processes.

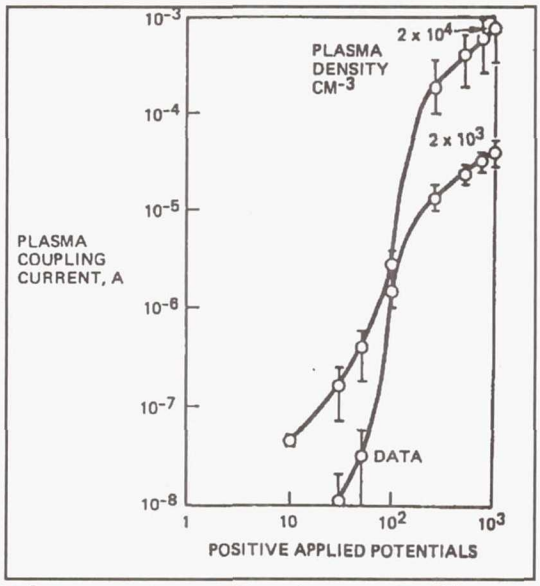


**Figure 1.** Electron Collection

By way of contrast, notice the extremely small ion collection currents at the same plasma densities and potentials negative of the plasma. Here the ion collection currents appear to be approximately linear with voltage up to the voltage range where arcing typically occurs. The great differences in the size and effects of electron and ion currents is due primarily to the difference in the ion and electron mass, which is a factor of 1836 even for the lightest positive ion, hydrogen. In low Earth orbit (LEO), most of the ions are atomic oxygen, sixteen times more massive still. Spacecraft speeds are typically much less than electron thermal speeds, so that the electrons are collected from all directions, at the thermal flux as modified by local potentials. However, the positive ions move much slower than the spacecraft,

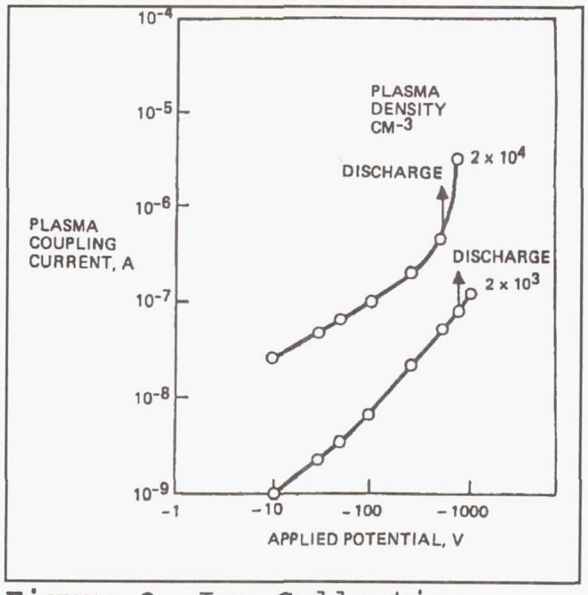


**Figure 2.** Ion Collection

and so their flux is the ram flux, again modified by local potentials. Current collection in the wake of a large structure or array is complicated by the supersonic wake, depleted of ions, and also depleted of electrons by small space charge built up from the absence of ions. Electron and ion current densities may be orders of magnitude lower in spacecraft or array wakes than in the undisturbed plasma.

By balancing electron and ion currents collected by the entire structure and arrays, one may determine the spacecraft floating potential. Simple models balancing the electron and ion currents to an array yield about a 95% negative floating fraction. It is reasonable, therefore, in the absence of very large ion collecting areas on the spacecraft, to assume that the array floats wholly negative, its most positive part at 0 volts relative to the plasma. This will be modified by vxB potentials due to the spacecraft motion through the ionosphere, and by changes in the relative conducting areas for electron and ion current collection. However, it does show that for steady state conditions, a distributed voltage in contact with the space plasma will be more liable to ion-collection problems than those due to electron collection. Paramount under these problems are sputtering, dielectric breakdown, and arcing to or through the space plasma. I will treat dielectric breakdown and arcing to the space plasma in the next section on transient events.

Sputtering is the physical removal of material from a surface by impact of incoming atoms or ions. Sputtered material may be redeposited on other surfaces, contaminating those surfaces with a thin film coating. Sputtering at negative potentials starts occurring when exposed conductors are at the sputtering threshold below the plasma potential. For most materials, this is between 10 and 30 volts. Sputtering yields are, however, small for energies less than about 100 electron volts, so sputtering only becomes a serious problem for negative potentials greater than this. Near holes in insulating coatings, the sputtering ions will be focussed to fluxes perhaps 17 times their undisturbed flux, exacerbating the problem. See Figure 3 (courtesy of Joel Herr, Sverdrup Technology, Inc.). All previous space power systems have generated end-to-end voltages much less than about 100 volts, so sputtering was not considered in their design. However, for Space Station Freedom, it has been estimated that sputtering may produce a loss of (or contamination of) about 0.4 mils of material per year (Ferguson *et al*, 1990). Atomic oxygen protective coatings are typically much thinner than this, and one might expect that if they were sputtered (as, for instance near the edges of solar cells), their lifetime would be much less than one year. Even coatings as thick as 5 mils might be eroded away during the lifetime of SSF. Sputtering problems are especially severe on rapidly switched components, because all of their insulating surfaces directly above conductors will spend most of the time at very negative potentials, as the plasma ions find it impossible to react quickly enough to neutralize the surfaces. Sputter coating may be a particularly difficult problem for solar cell coverslides, for their anti-reflective coatings may lose their efficiency if covered with transparent sputter effluent, or lose transparency altogether if coated with an opaque sputter product.

Electron collection problems are likely to become important only if the most negative end of the array is somehow elevated to a potential near the plasma potential. This may occur on negatively grounded arrays through thruster firings or other effluent dumps from the spacecraft, during arcs, or through purposeful increase of ion collection or decrease of electron

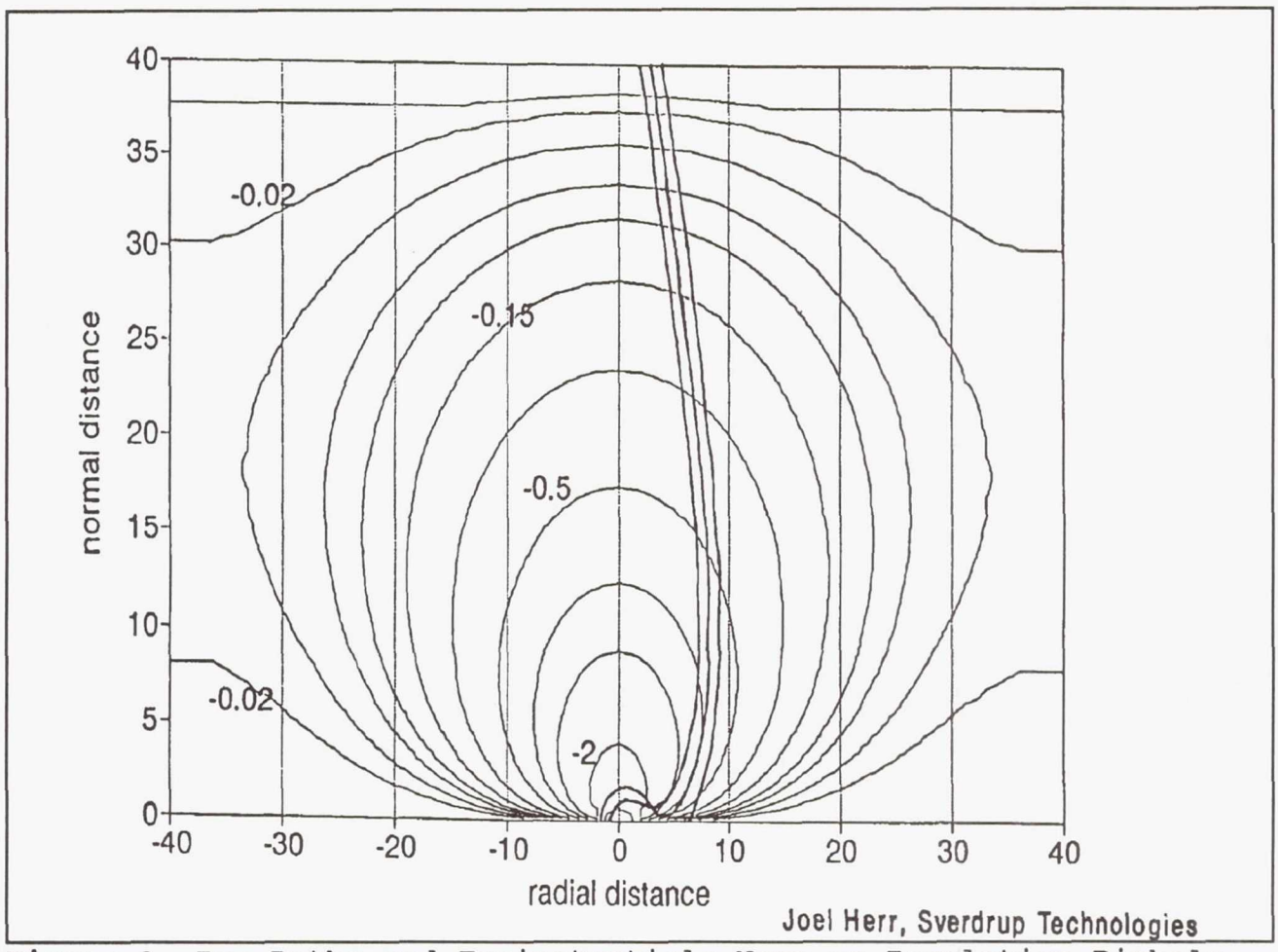


**Figure 3.** Ion Paths and Equipotentials Near an Insulation Pinhole

current collection. These mechanisms may decrease the relative electron to ion collection current ratio, and push the spacecraft potential more positive. It is estimated that under thruster firings on the negatively grounded SSF, the arrays may collect 10 amps of current or more (Ferguson *et al*, 1990). This current drain will show up as a 1.6 kW parasitic loss in the power system. More importantly, however, large temperature increases may occur in thin power system traces, leading to pyrolysis (charring) of Kapton® or melting of copper or aluminum (as recently found by T. Morton, Sverdrup Technology, Inc.). This is only likely to occur if all of the following conditions are met:

1. The current-carrying trace is thin and covered with a poor heat conductor.
2. A hole large enough to prevent current chokeoff (about 60 mils, Chock, LeRC) but small enough to collect high snapover currents exists in the insulator covering.
3. The conductive trace is exposed to a high density LEO plasma in the ram direction.
4. The trace is above +100 V with respect to the LEO plasma.
5. All above conditions obtain for several seconds (perhaps 10 seconds).

Kapton® pyrolysis was seen to occur on a test panel-pair of SSF arrays in a vacuum chamber at +450 volts (Felder, 1990). The charred area did not spread from the vicinity of the trace,

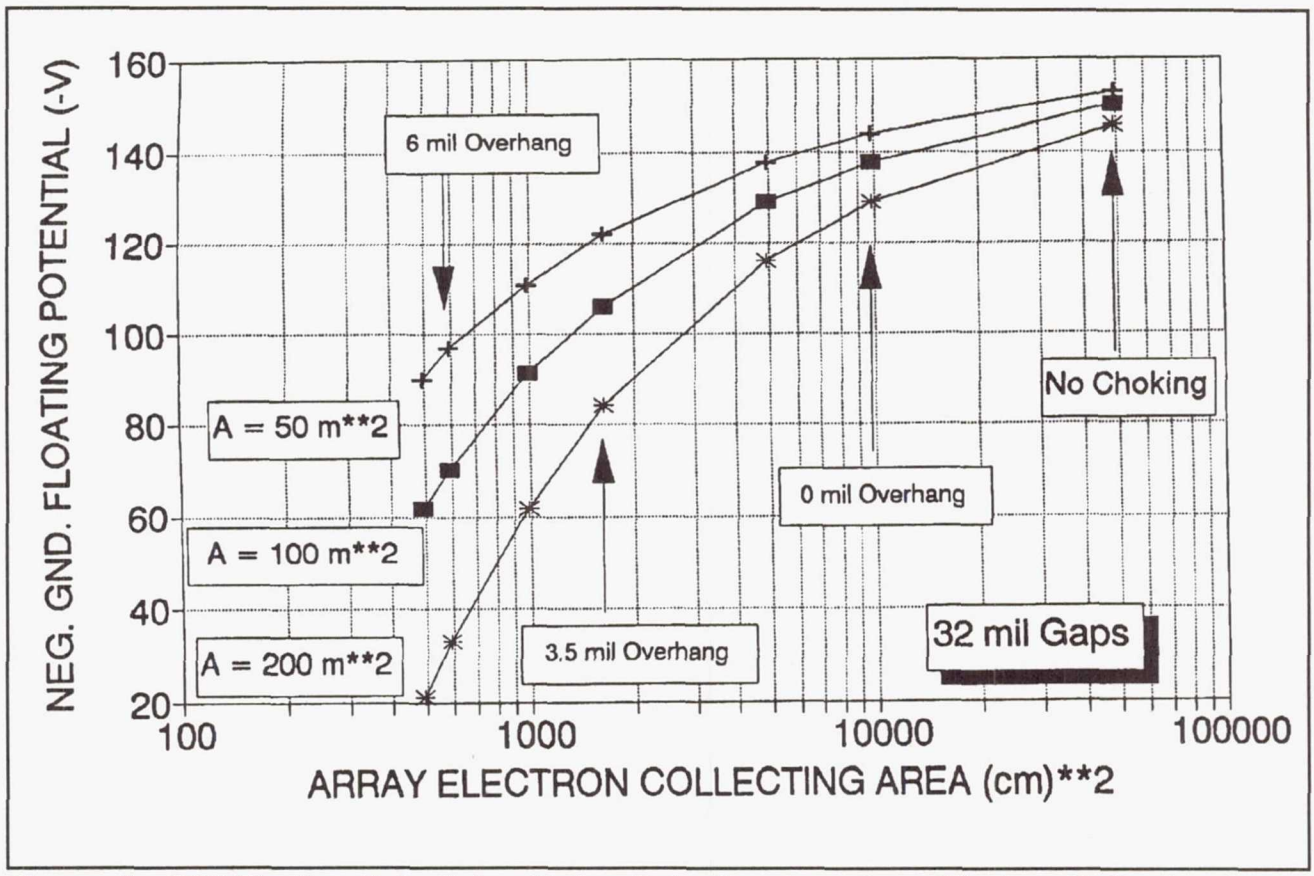


**Figure 4**. SSF Floating Potentials with Ion Collecting Area A vs. Electron Collecting Area

but did significantly increase the effective electron current collecting area of the array until it was repaired with a Kapton® patch. In the tank tests, the array was artificially biased to high potentials under dark conditions. It is not known whether arc-tracking of the pyrolysis might occur when current-carrying traces undergo pyrolysis in daylight. In space, holes for pyrolysis might be created by sputter or atomic oxygen enlargement of debris impact holes, or other array blanket defects.

It is possible to change the current-collection characteristics of solar cells and arrays through design practices. It has been found by modeling SSF array current collection with 3-D computer codes (NASCAP/LEO, R. Chock, LeRC) that the narrow spacing of the cells acts very well to choke off electron current collection in ground tests, and is predicted to do so somewhat under space conditions. Chock has shown that it may be possible to increase the overhangs of solar cell coverslides beyond the cell edges, and to decrease the gaps between solar cells, to produce an array which collects electrons no more efficiently than ions, and thereby to significantly influence the floating potential behavior of large space arrays. Figure 4 shows these results. The manufacturing feasibility of these solutions is now being evaluated by major solar cell manufacturers. Caulking the gaps between cells, or painting the edges of cells, on the most positive segments of solar arrays may be alternative methods of decreasing array electron collection and producing a more 50%-50% distribution of array potentials.

## TRANSIENT EVENTS

Classical solar array arcing to the plasma is well documented in both ground test and space flight conditions (eg. Snyder, 1984, Grier, 1983). Figure 5 (Ferguson, 1986) shows the voltage dependence of the sporadic arc rate for 2x2 cm and 2x4 cm standard silicon solar cells on the ground and in space. The same threshold seems to apply to all available data, about -230 V. Somewhat disturbing is the tendency of the space results to lie above the ground test results at all voltages above the threshold. The cause for this effect is not known. SSF solar arrays arced into the plasma during tank tests at voltages of -205 V (Nahra *et al*, 1990). Whether this is the threshold voltage for them is not yet known, since accurate rate vs. voltage data were not obtained. Theories predict that the threshold voltage should be a function of the conducting material exposed to the plasma, and there are some supportive test data, but the predictive ability of the existing theories is just now being explored (eg. Hastings *et al*, 1990).

The arc rate for 2x2 standard cells depends linearly on the ion current collected and as a steep power-law of the voltage (at voltages above threshold). The arcs occur (usually) directly into the plasma, rather than to adjacent conductors. There seems to be no strong dependence of arc rate on number of possible arc sites (number of cells), and this has been interpreted as a reset phenomenon occurring after each arc. In both ground and space testing, the arc rate has decreased to a constant level on a timescale of hours after immersion into the vacuum. It has been found (Upschulte *et al*, this conference) that this is most likely due to outgassing of solar cell adhesives, and a significant reduction in arc rate has been achieved by modifying solar cell coverslide adhesion and cleaning techniques. Increas-

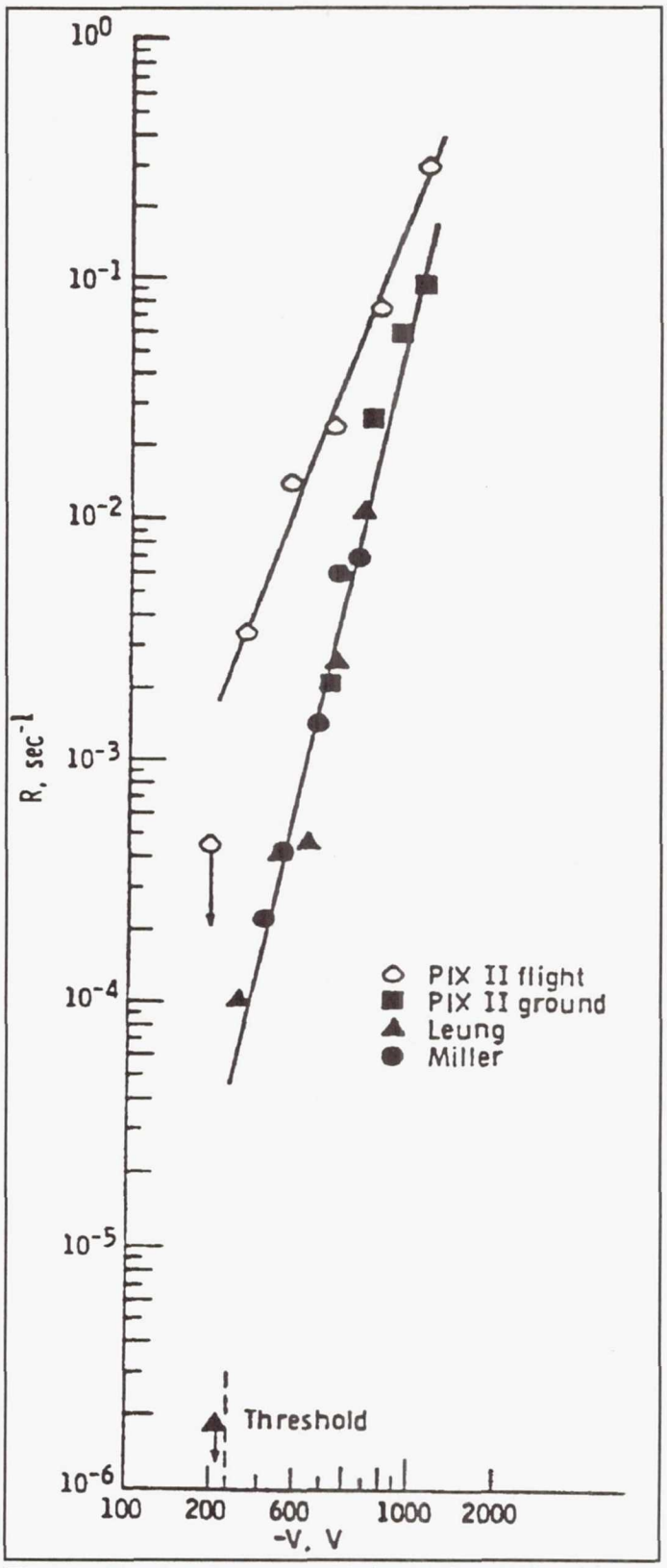


**Figure 5.** Arc Rate vs. Voltage for LEO Ram Conditions

ing the solar cell coverslide overhangs may decrease the arc rate by decreasing local ion current collection. There is some evidence (Chock, LeRC) that arc sites on the SSF array in ground tests preferentially occurred where coverslide overhangs were small or nonexistent. It is doubtful that such techniques will change the arcing threshold.

Arcs similar to classical solar cell arcs may occur on spacecraft surfaces with an insufficient dielectric strength covering over the conducting material. Anodized aluminum surfaces have been seen in ground tests to arc into the plasma at potentials as small as -80 V. While not directly of concern to spacecraft solar array operations, large negative potentials on spacecraft may be the result of the spacecraft electrical power grounding scheme, the end-to-end voltage on the arrays, and the relative electron and ion current collection characteristics of the solar arrays. They may therefore be controlled by changing the array floating potentials through coverslide and gap specifications, as well as by a proper grounding scheme and properly chosen coatings. Arcs of all types seem to discharge the entire connected capacitance of the power system where they occur, and are therefore powerful current transfer events.

Figure 6 shows new laboratory results of arc strength versus connected capacitance in the system (Snyder, LeRC). For large capacitances, as on very large solar array panels or on large anodized spacecraft structure panels, peak arc currents may extend to thousands of amps. The limiting mechanism for peak arc currents has not yet been found. It is believed

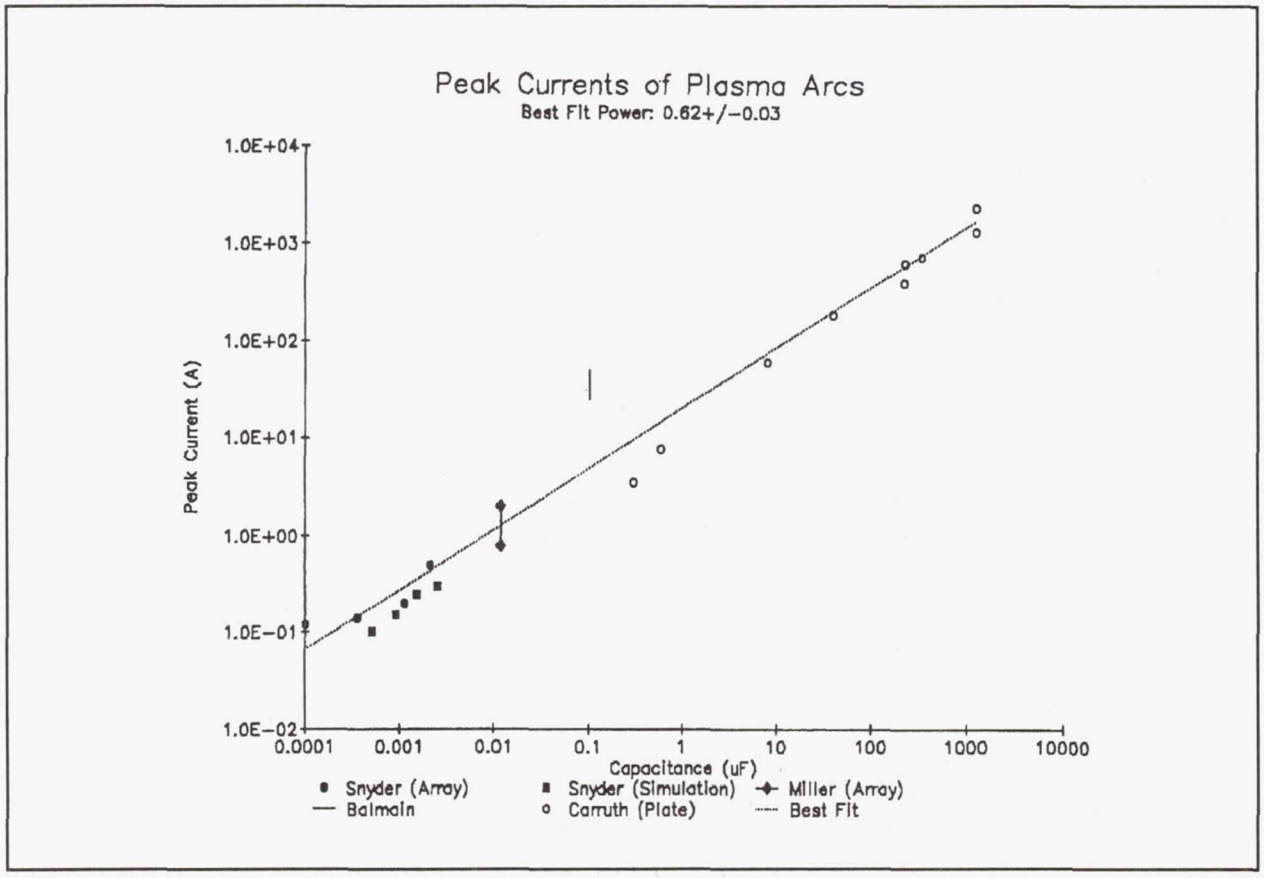


**Figure 6**. Peak Arc Currents vs. Connected Capacitance

that large arcs produce a local plasma of such density that sufficient charge carriers exist for thousand amp arcs. Large arcs may locally disrupt the surface, interrupt power for a short time, produce prompt contamination, and generate copious amounts of electromagnetic interference (EMI). Figure 7 shows EMI produced by laboratory tests of small solar arrays of a given capacitance in a plasma (Leung, 1985). It is desirable to limit the potential of spacecraft systems and arrays with respect to the plasma in order to prevent arcs, or to at least limit the amount of connected capacitance available to potential arc sites.

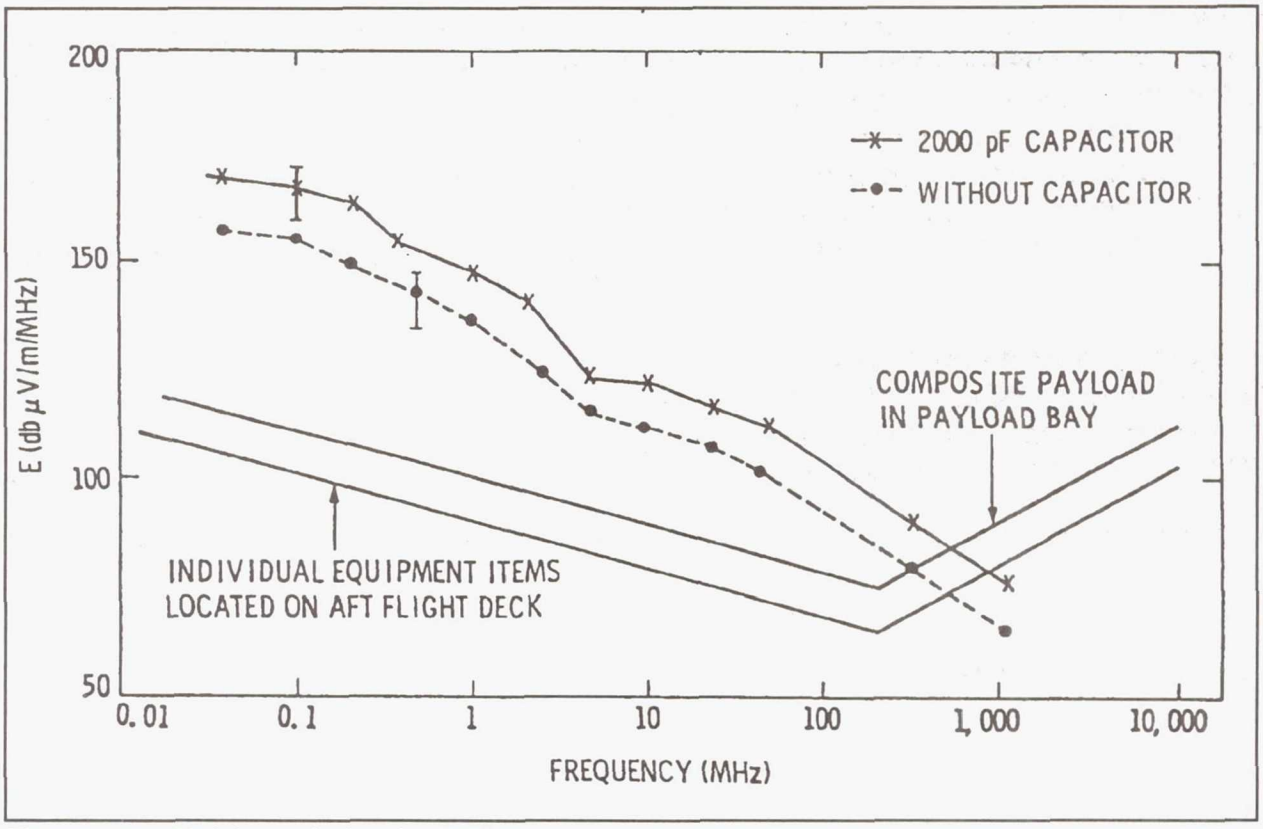


**Figure 7**. EMI from Solar Array Arcs

## SPACE FLIGHT EXPERIMENTS

Several space flight experiments to test the various results and conclusions summarized in this paper are in preparation. I am Principal Investigator on the Solar Array Module Plasma Interaction Experiment (SAMPIE) to fly on Shuttle in 1993. It will investigate arcing thresholds for various materials and configurations, serve as a demonstration flight for the SSF and APSA cells, and investigate arcing and current collection characteristics of several solar cell types and proposed configurations. In addition, it will look for dielectric breakdown on anodized aluminum samples. By using a biased guard ring, we will attempt to simulate the effects of the presence of a large surrounding array on solar cell current collection. SAMPIE has been approved for Phase C/D development, and will incorporate much of worth from the old defunct VOLT flight experiment. SAMPIE will use the large collecting area of the Shuttle main engine nozzles to keep the spacecraft potentials from being pushed far negative when the

small (1000 $cm^2$) SAMPIE modules are biased to high positive potentials. (That this statement had to be made shows the extreme tendency for negative potentials to predominate). It is believed that real arcing thresholds and valuable space data on other interactions will be obtained from this experiment.

PASP+ is an orbital experiment designed by the Geophysics Laboratory and funded by the Department of Defense. It will look at arcing thresholds and radiation degradation on a variety of solar array types (many of which are of interest mainly to the military). PASP+ will be placed in a highly elliptical polar orbit by a Pegasus launch vehicle, and has a desired lifetime of months to years. NASCAP/LEO modeling (Chock, LeRC) has shown that potentials on PASP+ may be controlled by an electron emitter capable of emitting about 20 mA of current. Power for the experiment will come from operating solar panels of a conventional type. PASP+ is expected to be launched near the end of 1992.

The High Voltage Solar Array experiment (HVSA) is a Japanese satellite, to be launched by a Japanese expendable launch vehicle. It will bias large solar arrays up to various high potentials with respect to the LEO plasma. It is unclear to this author what technique will be used to prevent the vehicle from charging to high negative potentials when the arrays are biased positive. HVSA may fly in 1992.

Other flight opportunities in the near future include SPEAR-3 (for Space Power Experiments Aboard Rockets), an SDIO experiment to investigate very high voltage interactions with space power systems, but which will include some area for solar array tests, and possibly SEDS-2, an orbital experiment which may derive high voltages from an electrodynamic tether.

All of these flight experiments are important to give us more information on the behavior of space photovoltaic plasma interactions, so that our design ideas for preventing arcing and controlling spacecraft electrical potentials may be proven in the space environment.

## COMPUTERIZED DESIGN TOOLS

Along with the possibility of designing space power systems to interact compatibly with, or to take advantage of, their space environment must come tools to enable the spacecraft and space photovoltaic designers to benefit from this new knowledge. At present, there are many large 3-D codes which allow detailed designs to be checked out in a computer-simulated space environment. Among these are NASCAP/LEO (a LEO charging and current collection code, see Mandell *et al*, 1990), POLAR (a polar orbit ram/wake charging code), MOLFLUX (a contamination code), and others. However, these codes are more useful for checking out detailed designs or exploring scientific concepts than for from-the-ground-up spacecraft design. In order to make engineering for spacecraft environmental interactions easier, a new generation of codes is being developed, with adequate scientific approximations and real-time operation, to enable the designer to sit down at his PC and have a good design in a short period of time. The first of these codes, called EPSAT (for Environment Power System Analysis Tool, see Jongeward *et al*, 1990), was funded by SDIO, and is now in beta testing. It runs in real-time on a high-end PC, and allows preliminary analysis and design tradeoffs for a

variety of space plasma and system-produced environmental interactions. In EPSAT, space environmental interactions of all major spacecraft systems may be considered in a self-consistent and integrated way. A spinoff of EPSAT, oriented more toward SSF than SDIO systems, is being funded by SSF, and is called Environments WorkBench (EWB). It is expected that this and other codes will bring space plasma and other space environmental interactions out of the experimental stage so that they may be considered by every spacecraft and space photovoltaic designer.

## REFERENCES


Felder, M.C. (1990). "PV Plasma Interaction Test: Preliminary Results and Status," Final Report of the Joint Workshop on Evaluation of Impacts of Space Station Freedom Grounding Configurations, Ferguson, Snyder, and Carruth, eds., NASA LeRC, August 21, 1990.

Ferguson, D.C. (1986). "The Voltage Threshold for Arcing for Solar Cells in LEO - Flight and Ground Test Results," NASA TM-87259.

Ferguson, D.C., Snyder, D.B., and Carruth, R. (1990). Final Report of the Joint Workshop on Evaluation of Impacts of Space Station Freedom Grounding Configurations, NASA LeRC, August 21, 1990.

Gabriel, S.B., Garner, C.E., and Kitamura, S. (1983). "Experimental Measurements of the Plasma Sheath Around Pinhole Defects in a Simulated High-Voltage Solar Array," AIAA Paper 83-0311.

Grier, N.T. (1983). "Plasma Interaction Experiment II: Laboratory and Flight Results," in NASA CP-2359, p. 333, 1985.

Hastings, D.E., Weyl, G., and Kaufman, D. (1990). "Threshold Voltage for Arcing on Negatively Biased Solar Arrays," J. Spacecraft and Rockets, *27*, p. 539.

Jongeward, G.A., Kuharski, R.A., Kennedy, E., Wilcox, K.G., Stevens, N.J., Putnam, R.M., and Roche, J.C. (1990). "The Environment Power System Analysis Tool Development Program," in NASA CP-3089, p. 352.

Leung, P. (1985). "Characterization of EMI Generated by the Discharge of a 'VOLT' Solar Array - Final Report," JPL Document D-2644, September, 1985.

Mandell, M.J., Katz, I., Davis, V.A., and Kuharski, R.A. (1990). "NASCAP/LEO Calculations of Current Collection," in NASA CP-3089, p. 334.

Nahra, H.K., Felder, M.C., Sater, B.L., and Staskus, J.V. (1990). "The Space Station Photovoltaic Panels Plasma Interaction Test Program: Test Plan and Results," NASA TM-102474.

Snyder, D.B. (1984). "Characteristics of Arc Currents on a Negatively Biased Solar Cell Array in a Plasma," NASA TM-86887.

Stevens, N.J., and Stillwell, R.P. (1989). "Discharge Transient Coupling in Large Space Power Systems," in NASA CP-3059, p. 383.

Thiemann, H., and Schunk, R.W. (1990). "Particle in Cell Simulations of Sheath Formation Around Biased Interconnectors in a Low-Earth-Orbit Plasma," J. Spacecraft and Rockets, *27*, p. 554.


® Kapton is a registered trademark of Dupont de Nemours, Inc.

# THIN FILM CELL DEVELOPMENT WORKSHOP REPORT

James R. Woodyard

Institute for Manufacturing Research
and
Department of Electrical and Computer Engineering
Wayne State University, Detroit, MI 48202

## INTRODUCTION

The workshop was co-chaired by Vijay K. Kapur and James R. Woodyard, and attended by a number of people, some of whom drifted in and out during the two hour session. Sixteen people signed the attendance sheet which was circulated during the workshop. Seven questions were presented for discussion to the workshop co-chairs prior to the workshop by the SPRAT XI Conference organizers. The questions are enumerated below as Q1 through Q7. The questions were reviewed by the workshop attendees at the beginning of the workshop and an additional three questions were added; these are listed below as Q8-Q9.

As the workshop progressed, it became apparent that attendees had different views on the reasons thin-film cells are attractive for space applications. Towards the end of the workshop, the author took the liberty of posing a survey question in an effort to give attendees the opportunity to express their views on the topics discussed during the workshop. Eleven attendees submitted written responses to the questionnaire. Considering that responding to the survey question was at the expense of attending the happy hour, eleven responses is considered respectable. The responses were summarized by the author and are tabulated below in the section: SURVEY QUESTION.

The issue of using thin-film cells in orbits ranging from LEO to GEO was debated during the workshop and in the halls following the workshop, and during the workshop summary presentation. The author has taken the liberty to present another point of view on this matter considering AP8MIN and AE8MAX calculations; these comments are presented below in the section entitled: RADIATION AND EARTH ORBITS.

Three written communications were received following the workshop. The communications have been included in the development of the report.

The author assumes full responsibility for the contents of the workshop report.

## Q1: WHAT ARE POTENTIAL THIN-FILM CELLS?

Cells made from CdTe, CIS and a-Si alloys were stated as potential thin-film cells. Each of the mentioned cell types involve a technology which is implied in stating the material.

Q2: WHAT UNIQUE PERFORMANCE CAPABILITIES DO THIN-FILM CELLS OFFER?

Thin-film cells offer the potential for high specific power density, low cost, flexible arrays, monolithic structures and high EOL.

Specific power densities in excess of 200 W/kg have already been achieved; two papers presented at the conference projected specific power densities in the 500-700 W/kg range. There are applications where high specific power is necessary in order to carry out missions.

Low cost is expected because monolithic structures offer the potential for using automated fabrication technologies; there is also the potential of employing the technology developed for terrestrial applications of thin-film cells.

Flexible arrays have already been demonstrated; the capability makes it possible to use thin-film cell-based arrays for auxiliary space power applications. Flexible arrays may be transported in a canister and deployed upon demand.

Monolithic structures, in addition to offering the potential for low cost, may reduce interconnect problems. It was felt that the integrated nature of monolithic structures offer the potential for including the interconnects in the structure during the device fabrication; the problem of failure of interconnects during temperature cycling should be reduced.

High EOL, relative to thick crystalline cells, is possible because of the higher demonstrated radiation resistance of thin-film cells. Both CIS and a-Si alloys have demonstrated radiation resistances at least 50 times better than crystalline silicon. Thin-film cells may be used without coverglasses which requires an understanding of defect production by particles with energies as low as about 50 keV.

Q3: WHAT ARE THE KEY R&D ISSUES?

The key R&D issues are efficiency, stability and thermal cycling, and the effects of plasma discharges.

Efficiencies of research thin-film cells have been reported which are in excess of 10%. Manufactured large area cells have efficiencies which lag the research cells; research must be done to close the gap. Research is currently funded for terrestrial applications of thin-film cells; it is directed at improving cell efficiencies. The technology developed for terrestrial applications of thin-film cells will result in cells more attractive for space applications.

Stability of cell efficiency is necessary in order for engineers to design arrays for space applications. The effect of the environment and AMO illumination on cell efficiency must be understood. While the optical-induced instability of a-Si alloy cells (Staebler-Wronski effect) is well known, the effect of temperature cycling and AMO illumination on thin-film arrays in a space environment need to be investigated. Mention was also made that we should not overlook the effect of the harsh high-humidity environment of pre-launch.

Thermal cycling of arrays with monolithic structures is a new research area. Concern was expressed that we need to develop experience with monolithic structures to determine their stability in a space environment.

The effect of plasma discharges on thin-film cells needs to be investigated. Blanket arrays are susceptible to discharges on both sides. The role of encapsulants in protecting the blankets needs to be investigated.

Q4: WHAT ARE THE MANUFACTURABILITY ISSUES?

The manufacturability issues are size, integration, cost, flexibility and yield. These issues are common to terrestrial applications; there are a number of both private and public programs addressing these issues. While the details of arrays designed for space applications are different, both the terrestrial and space applications share manufacturability issues. It is clear that the cell engineers must look to the manufacturing engineers to delineate manufacturing problems, and to consider the problems in selecting materials and fabrication technologies for cells.

Q5: CAN THIN-FILM CELLS FOR SPACE APPLICATIONS BE LOW COST?

Yes, if the space technology feeds off the terrestrial programs. Manufacturers of thin-film cell arrays are meeting terrestrial photovoltaic needs. The thin-film photovoltaic technology has developed to the point it is because of the technological developments accomplished by the terrestrial programs. If these programs continue to develop the technology, the thin-film cell will be well positioned to meet cost and efficiency requirements for a space mission that would not be possible otherwise. The attendees speculated on cost verses volume for thin-film cells. Three projections were presented. The first cost projection was based on delivering 200 W arrays; a cost range of 500 $/W for one array to 100 $/W for a quantity of more than 1000 arrays. The second projection was 200 $/W for a 5-10 kW market and 15 $/W for a 5-10 MW market. The third estimate was given for a specific space application requiring 6450 W; the cost was estimated to be 1/5 the cost of crystalline silicon.

Q6: WHAT IS (AND IS NOT) KNOWN ABOUT RADIATION DAMAGE IN THIN-FILM CELLS? WHAT IS EXPECTED?

Research literature contains encouraging radiation resistance results. The workshop attendees view these results as preliminary and indicated that more works needs to be done. Research shows radiation resistances for thin-film cells at least 100 times better than crystalline silicon. However, the defect generation mechanisms are not well understood and should be the subject of future research. Research must consider particle energies down to about 50 keV because of the interest in using thin-film cells without

coverglasses in applications ranging from LEO to deep space. Results have been reported with particle energies in the 0.20 to 2.00 MeV range.

Q7: ARE THIN-FILM CELLS USEFUL IF THEY ARE NOT ON FLEXIBLE LIGHT-WEIGHT SUBSTRATES?

Yes, if the application involves a high radiation environment. It was felt that the documented high radiation resistance of thin-film cells makes them attractive for missions with high radiation environments. The monolithic structure of thin-film cells poses some possible advantages over thick crystalline cells, namely, stable interconnects and lower costs; these advantages could make thin-film cells attractive even if they are not on light-weight substrates.

Q8: HAVE THIN-FILM CELLS BEEN FLOWN, AND IF SO, WHAT ARE THE RESULTS?

CIS and a-Si alloy thin-film cells are in orbit on the LIPS-III satellite which was launched in the spring of 1987 into a 1100 km orbit with a 60° inclination. Raw data were transmitted to the providers of the cells during the SPRAT XI Conference by J. Severns, coordinator of the experiments.

The CIS cells were provided by Boeing Aerospace and Electronics. It was reported that the cells functioned with "no noticeable" degradation until an open-circuit condition developed after two and one-half years in space.

a-Si alloy cells were provided by Solarex and Sovonics. The Solarex cells are single-junction cells with a 300 micron coverglass and continue to function after four years in space. The outputs of the cells have degraded somewhat; it is speculated that the degradation is due to the Staebler-Wronski effect. The Sovonics cells have an ethylene vinyl acetate (EVA) encapsulant. It was reported that the degradation in the outputs of the cells suggests the EVA has deteriorated.

The workshop attendees strongly recommend that the results of the LIPS-III thin-film cell experiments be published as soon as possible. In the event that analysis of the data prior to publication is not possible, the data should be published in raw form; the details of the structures of the various cells and the space environment should also be published. At the very least, the data should be made available to parties with space applications for thin-film cells.

Q9: WHAT IS THE BEST WAY FOR THIN-FILM CELLS TO BE SPACE QUALIFIED?

The attendees were not able to come up with a procedure to space qualify thin-film cells. It was pointed out that materials have been used in thin-film cells without regard to the body of

information on materials approved for space. It would make sense for engineers to have access to resources listing materials approved for space. The terrestrial use of thin-film cells is driving the development of the technology; it appears that engineers interested in space applications do not have easy access to approved materials lists. Workshop attendees indicated that NASA sites have approved space materials lists and a Solar Cell Array Handbook has also been published which deals with space materials issues.

The issue of using space flight as a way of space qualifying cells was discussed. Those interested in this route were encouraged to contact program officers, but to be aware that they balance risk against program success in rather conservative surroundings.

## SURVEY QUESTION

The workshop attendees were requested to respond to the following question in two or three sentences: Do you think thin-film photovoltaic devices will be useful for space applications. The responses were reviewed with an eye towards the reasons given to justify the response. Eleven written responses were received; all respondees indicated that they believed that thin-film photovoltaic devices will be useful for space applications. The number of respondees for each reason is listed in table 1. Note that most respondees gave more than one reason to justify a response.

**Table 1.** Number of Respondees Citing a Reason for an Affirmative Response to the Questionnaire.

| NUMBER | REASON FOR AN AFFIRMATIVE RESPONSE |
|---|---|
| 10 | Good Radiation Resistance |
| 7 | Low Cost |
| 6 | Monolithic Structure |
| 4 | Flexible Substrate |
| 2 | Light Weight |
| 1 | If R&D Is Carried Out |
| 1 | If Manufacturing Technology Is Developed |
| 1 | High Specific Power |
| 1 | Auxiliary Power Unit For A Concentrator Power Unit |

## RADIATION AND EARTH ORBITS.

It became clear during the SPRAT XI Conference that the radiation resistance of thin-film cells makes them attractive for space applications. Indeed, the survey question shows this is the case. However, it was not clear that the dependence of the radiation environment on altitude was known. The author requested Mark Kruer, TRW Space & Technology Group, to provide some typical

integrated fluences for protons and electrons as a function of altitude. The energies covered 0.10 to 200 MeV for protons, and 0.05 to 10 MeV for electrons. The AP8MIN model was used for protons and the AE8MAX model for electrons. The AP8MIN model results are questionable below 0.60 MeV. The results do not consider the direct radiation from solar flares. The results are show in table 2; appreciation is expressed to Mark Kruer and his group at TRW for providing the calculations.

**Table 2.** Ten Year Integrated Fluxes At Various Altitudes

| Height (km) | Inclination (degrees) | Integrated Flux Proton ($cm^{-2}$) | Integrated Flux Electrons ($cm^{-2}$) |
|---|---|---|---|
| 200 | 28.5 | 1.2E11 | 4.3E8 |
| 200 | 90 | 8.8E9 | 7.4E12 |
| 1,000 | 30 | 3.8E11 | 5.7E14 |
| 35,790 | | 2.8E15 | 1.7E16 |

Table 2 shows that while the integrated fluxes at 200 km for a ten-year period are less than 1E13 $cm^{-2}$ for the two inclinations considered, the radiation in LEO must be considered in the design of an array. The effect of solar flares and man-made radiation must also be considered. The differential flux is, in general, higher at lower energies. If the thin-film cells are flown without coverglasses, the effect of the lower energy particles on the stability of the cells must be understood.

Since the efficiencies of thin-film cells are lower than crystalline cells, arrays made using thin-film cells will have a larger area and increased atmospheric drag. While atmospheric drag is a problem in LEO, there are LEO applications where the use of highly radiation resistant, light-weight and low-cost arrays made from thin-film cells are attractive. It remains for the thin-film cell technology to develop to the level where the cells meet the array designer's requirements.

## CONCLUSION

The Thin-Film Development Workshop provided an opportunity for those interested in the space applications of thin-film cells to debate several topics. The meeting time of the workshop was not adequate to pursue all the topics of interests to the attendees. The unique characteristics of thin-film cells and a number of issues were covered during the discussions. It is clear that there is a great deal of interest in thin-film cells; both manufacturers and space engineers have programs underway to produce arrays for space testing. Workshop attendees see space qualification as a problem; advice on the resources available and procedures to achieve space qualification are needed. It would be highly desirable for the results of the LIPS-III experiment on thin-film cells to be made available.

# III-V CELL DEVELOPMENT WORKSHOP

R.W. Statler
Naval Research Labs
Washington, DC

and

R.P. Gale
Kopin Corporation
Tauton, Massachusetts

- DEVELOPING A GOAL FOR MEANINGFUL DISCUSSION
  - WHY CONSIDER III-V CELLS AT ALL ?
  - WHAT IS THE EXISTING SPACE MISSION NEED FOR III-V CELLS ?
  - WHY SO MANY R&D APPROACHES TO III-V'S ?
- SYSTEMS PEOPLE STATED THERE ARE PROGRAMS NEEDING INCREASED EOL SPECIFIC POWER (W/kg) NOT NOW COMPATIBLE WITH Si CELLS
- COMMERCIAL COMSTAT EOL POWER REQUIREMENTS ARE ALSO PUSHING THE ENVELOPE OF EXISTING SOLAR ARRAY CAPABILITY
- DOE MANAGEMENT PHILOSOPHY REWARDS HIGHEST EFFICIENCY NUMBERS FOR SOLAR CELLS
  - PRACTICAL APPLICATION IS SECONDARY (MARKETABILITY, MANUFACTURABILITY)
- DOD CONTRACTS OFTEN DEFINE CELL EFFICIENCY PERFORMANCE FOLLOWING SPECIFIC RADIATION AND THREAT LEVELS

# PRACTICAL TALK

HOW DOES A SPECIFIC III-V TECHNOLOGY ARRIVE AT PLATEAU OF PRODUCTION OR A MAN TECH PROGRAM ?

- NOT AN EASY OR QUICK PATH - GaAs/Ge MAY HAVE TAKEN 20 YEARS FROM EARLY EFFORTS
- A NEW CELL MUST GUARANTEE SIGNIFICANT IMPROVEMENT TO MEET PERCEIVED MISSION REQUIREMENTS
  - PROBABLY WOULD HAVE AN EOL EFFICIENCY GREATER THAN GaAs/Ge OF (a. 25%, b. 50%, or c. all of the above) TO BECOME INTERESTING ENOUGH TO SPEND $5M +.
- HOW DO YOU JUSTIFY A NEW CELL MAN TECH THRUST ?
  - WHAT DO SYSTEMS PEOPLE LOOK FOR ?

# HOW SYSTEMS PEOPLE RESPOND

- GIVE ME EOL SPECIFIC POWER (W/kg) NUMBERS BECAUSE BOL EFFICIENCY IS PRACTICALLY MEANINGLESS WHEN DESIGNING ARRAY FOR A TOTAL MISSION
- GIVE ME LOW COSTS BECAUSE THIS IS A MAIN DRIVER FOR TECHNOLOGY SELECTION
  - STATED BY SDIO, JPL, AND SSD
  - I KNOW IT WILL COST MORE THAN Si SO THE EOL PERFORMANCE HAS TO BE WORTH IT!
- GIVE ME RELIABILITY ON ORBIT EQUAL TO OR BETTER THAN Si

- SPECIAL MISSION REQUIREMENTS

  - WILL THIS CELL BE SURVIVABLE TO PARTICULAR THREATS

  - TRADE OFFS TO CONSIDER A MORE COSTLY CELL WHICH WILL REDUCE ARRAY SIZE, THEREBY SAVING ONBOARD FUEL WEIGHT

  - TOTAL POWER SYSTEM WEIGHT IS ~1/3 SPACECRAFT WEIGHT A POUND SAVED ON ARRAY GIVES MORE PAYLOAD, ETC.

  - ELECTROPROPULSION SYSTEM REQUIREMENT: 60 - 90 kW AND $2 \times 10^{16}$ 1 MeV $E/cm^2$ FLUENCE - CAN AFFORD TO PAY EXTRA

## SYSTEMS PEOPLE HAD MUCH MORE TO ADD

- IF THE NEW CELL COST IS TOO MUCH, THE MISSION WILL SUDDENLY LOSES ITS IMPORTANCE

  - WILL BE CANCELED OR MODIFIED

- **THE REAL WORLD**

  - PROGRAM OFFICES ARE VERY OPEN TO NEW TECHNOLOGY ...

  - BUT ... POWER SYSTEMS ARE OF LOWER PRIORITY THAN PAYLOAD OR ATTITUDE CONTROL, FOR EXAMPLE

  - BUT ... IF THE NEW POWER SYSTEM IS A BIG WEIGHT SAVER IT CAN GET ATTENTION

  - THE PROGRAM OFFICE HAS AN INPUT FOR WHO GETS THE MAN TECH PROGRAM, WHICH FOLLOWS PROGRESSIVE DEVELOPMENT AND CONFIRMATION OF CELL PERFORMANCE THROUGH FLIGHT DEMONSTRATIONS

  - A REAL TURNOFF FOR PROGRAM OFFICE IS THE HIGH UPFRONT COST OF CELL R&D AND EARLY PRODUCTION COSTS

# LIFE CYCLE COSTS

- LIFE CYCLE COSTS FOR THE OVERALL SPACE MISSION CAN VINDICATE A HIGHER CELL COST IN CERTAIN CASES

- A POST WORKSHOP COMMENT TO THE CHAIRMEN -

  LIFE CYCLE COST ANALYSIS IS STARTING INDUSTRY IN EARLY R&D STAGES TO ELIMINATE LESS FAVORABLE PROJECTS AND FUND A FEW GOOD ONES AT HIGHER LEVELS

  - WHO WOULD IMPLEMENT SUCH A PLAN IN III-V's ?

# SUMMARY OF HOW MAN TECH PROGRAM GETS ACCEPTED

1. THE CELL MUST HAVE HIGH MARKS IN A SYSTEM ANALYSIS
2. CELL DEVELOPMENT WILL BE DONE AT R&D LEVEL, AND NOT PRESCRIBED BY SYSTEM REQUIREMENTS, USUALLY
3. CELL MUST HAVE PASSED SPACE QUALIFICATION, FLIGHT DEMONSTRATIONS, RELIABILITY, GOOD END OF LIFE EFFICIENCY, AND PROBABLY LOOK LIKE A TWO-TERMINAL DEVICE
4. ADVANCED DEVELOPMENT PHASE IS UNDERTAKEN, SHOWING A COST ADVANTAGE TO SPECIFIC MISSION PLANNERS AND BE AS RISK FREE AS PRESENTLY USED CELLS
5. COMMERCIAL MANUFACTURING COSTS MUST BE CONSIDERED IN COSTING OUT THE NEW DEVICE

## SOME SPECIFIC THOUGHTS ON NEW TECHNOLOGIES

- NEED A NATIONAL OR WORLD WIDE SUPPORTING MATERIAL CAPABILITY FOR NEW MATERIALS, SUCH AS IN ?
- GaAs CELL COSTS WERE VERY HIGH UNTIL THE HETEROEPITAXIAL GaAs/Ge WAS DEVELOPED
- 400,000 2 X 4 cm GaAs/Ge HAVE BEEN PRODUCED IN FLIGHT PROGRAMS CAPABILITY FOR NEW MATERIALS, SUCH AS IN ?
  - COST IS GENERALLY TOO HIGH FOR MOST MISSIONS
- InP - LATTICE CELLS WILL HAVE TO BE GROWN ON Si TO RECEIVE SERIOUS ATTENTION, ULTIMATELY

## CONCENTRATOR ARRAYS

- CONCENTRATOR ARRAYS MAKE SOME SYSTEM PLANNERS NERVOUS
  - SPACECRAFT HAVE BEEN KNOWN TO SUDDENLY LOSE ATTITUDE CONTROL
  - GROUND COMMANDS OVER MANY HOURS ARE NEEDED TO RESTORE
  - THE BATTERIES COULD COMPLETELY DISCHARGE IF ONLY CONCENTRATOR PV WAS ONBOARD
- SDIO SUPER POWER SYSTEM HAS AUTONOMOUS CONTROL
  - WILL CORRECT QUICKLY ATTITUDE CONTROL FAILURE
  - THIS DEGREE OF AUTONOMY MAY NOT BE APPROPRIATE FOR SMALLER POWER MISSIONS
- CONCENTRATOR ARRAY HAS MORE EOL SPECIFIC POWER THAN APSA

# SUMMARY

WE HAD A VERY GOOD EXCHANGE OF INFORMATION AND IDEAS. THE COMMENTS FROM SYSTEM-TYPE PEOPLE WERE ESPECIALLY ENLIGHTENING TO SOME R&D PEOPLE, WHO MAY HAVE GOTTEN NEW INSIGHT INTO THE REAL WORLD OF PV USERS.

ALTHOUGH WE DIDN'T DISCUSS THE MERITS OF SPECIFIC III-V TECHNOLOGIES, WE GOT AN APPRECIATION FOR THE DIVERSE CONTRIBUTIONS AND PERSPECTIVES OF THOSE WHO CONSTITUTE THE PV SPECIALIST COMMUNITY.

# Workshop Summary
# Space Environmental Effects

A. Meulenberg
*COMSAT Laboratories*
*Clarksburg, Md 20871*

B. E. Anspaugh
*Jet Propulsion Laboratory*
*California Institute of Technology*
*Pasadena, CA 91109*

This report summarizes the workshop held on Space Environmental Effects that was held as a part of SPRAT XI. Approximately 30 people attended the workshop. The underlying concern of this group was related to the question of how well do laboratory tests correlate with actual experience in space. The discussion ranged over topics pertaining to tests involving radiation, atomic oxygen, high voltage plasmas, contamination in LEO, and new environmental effects that may have to be considered on arrays used for planetary surface power systems.

## Most Important Concerns

There is always a concern over radiation testing. Although the 1 MeV equivalent electron fluence concept together with its related damage coefficients has been in use for several years for predicting the behavior of silicon solar cell arrays, there is still controversy as to how accurate these predictions are. It has always been difficult to check the accuracy of prediction vs experience for several reasons. First, most predictions involve using the published models of the trapped van Allen belts, and these models may only be accurate to within an order of magnitude. Indeed, it may be effectively argued that it is not worth the expenditure of a great deal of effort in deriving extremely accurate damage coefficients, since the models of the radiation belts, or perhaps the radiation belts themselves, are so uncertain. Second, it is often difficult to get data on the short circuit current or maximum power on spacecraft arrays because this data is not available in pure form. Rather, it is usually derived indirectly from other data that is telemetered. Third, there may be other effects which also degrade panel performance that cannot be separated from the radiation effects. They include the effect of uv degradation of coverglasses and/or adhesives, the effect of high panel temperatures which may anneal the panel, the effect of contamination which may arise from outgassing of spacecraft components, rocket plumes, products of atomic oxygen erosion, etc. Fourth, the data available from solar cell flight experiments is usually plagued by one or more of the above effects and the data may be misleading.

In spite of the concerns, real or imagined, the damage coefficient/1 MeV equivalent fluence concept appears to be useful. It is relatively easy to apply and the software for its use is widely distributed so that different panel designers can compute radiation degradation in the same way. Radiation experiments sufficient to allow the computation of a new set of damage coefficients for GaAs/Ge cells have been recently completed at JPL, and these data will be disseminated in the near future.

There are other areas of concern having to do with applying laboratory radiation damage tests to spacecraft panels. One example is a rate effect problem. Do the low flux rates actually seen in space

allow time for self annealing that is not seen in accelerated ground tests? All ground testing is done at accelerated rates. Some attempts have been made to see whether there is a rate effect problem. For example, recent rate tests at JPL using electrons incident on GaAs/Ge cells used two different flux rates differing by a factor of 80. No difference in the cell output was observed, but the "slow" irradiation only lasted a total of 24 hours, much less than the exposure time would be in space for most orbits. Rate tests using protons have not been done to our knowledge. Since one could legitimately expect any possible rate effect to be dependent on the incident particle type, and possibly its energy, a great deal of additional testing will be necessary to effectively address this problem. Rate effects may be process and contamination dependent (LPE vs MOCVD for example) because the impurities introduced during processing may influence the types of radiation defects produced.

Other areas of concern discussed had to do with bias, illumination, and cell loading during ground test radiation experiments. It is not believed that GaAs or Silicon cells are affected by illumination or loading, but the radiation degradation of InP cells is known to be dependent on illumination, so a cautionary flag is raised for those who will be irradiating cells made from new materials.

The irradiation of solar cell areas which are incompletely protected by their coverglasses. These areas are usually near the busbar, but they may also occur when a coverglass develops a crack during panel assembly. In silicon cells, such exposed areas near the busbar have been found to be especially vulnerable to low energy protons. Some preliminary data indicates that the busbar area of GaAs cells are also vulnerable to low energy protons and the busbar itself should have enough thickness to stop most of the low energy protons expected for its particular environment. Cracks in coverglasses do not seem to present a serious problem if the coverglass adhesive at the bottom of the crack is intact (this is usually the case). Another related area of concern is the edge of the solar cell which may not be shielded to obliquely incident radiation. There is very little data dealing with irradiated solar cell edges.

The effect of atomic oxygen on solar panels in LEO is of great concern. The interconnects and flexible substrates are particularly vulnerable, and methods of protecting these items are under development. For instance a coating of $SiO_x$ has been developed for protecting kapton substrates and gold plating on interconnects seems to give some protection. Adequate ground tests need to be developed for proving these developments. Testing by chemical methods may be a possibility, but there must be a correlation between the tests used and actual experience in space.

The development of high voltage arrays is seen to be very desirable in some cases. The decrease in conductor size allowed will provide a significant decrease in array mass in very large arrays. The high voltages bring forth problems with arcing caused by the interaction of the solar arrays with the space plasma. The experience of the workshop participants seemed to indicate that arcing was probably not a hazard to silicon solar cells, but GaAs cells could be a problem due to their greater susceptibility to reverse bias (GaAs/Ge cells do not seem to show this increased susceptibility). There is also a definite hazard to the spacecraft electronics. Here again, the question is raised as to the effectiveness of ground testing. Tests are typically made with monoenergetic particles normally incident. Correlation with such tests with in-flight experience is minimal. Well designed, fully instrumented flight experiments need to be flown.

A rather interesting discussion developed around the requirements specified in Qualification Testing of solar panel components. Many of these tests are performed to certain levels because "that's the way its always been done." These test levels are not likely to change unless they are driven by costs. That is, if a new solar cell design cannot pass an exceptionally high test level, and an expensive development program would have to be launched to develop a cell which could pass the test, a project manager may modify the levels to reflect a more realistic test. Tests applied to new materials may not

be appropriate, but may be borrowed from tests on other materials. New tests may have to be developed for new materials. For example, the greater susceptibility of GaAs solar cells to reverse bias conditions has prompted the requirement that these cells pass certain reverse bias stress tests. Such tests were not necessary for silicon cells. There is always a desire to develop a set of uniform test standards to apply to all spacecraft and their components. But these tests are necessarily mission dependent, driven by the particular environment to be experienced by that mission, and the dream of uniform test standards is doomed to remain but a dream.

**Array Lifetimes and Operation in the Van Allen Belts**

Desirable array lifetimes vary greatly with the mission. Communications satellites operating at GEO need to have lifetimes of 15 years or greater. But an array lifetime of 20 years for SpaceLab in LEO is desirable. However the lifetime of the spacecraft is not usually controlled by the lifetime of the solar arrays. Other elements usually give up first, for example the batteries, station keeping fuel, etc. Array contamination may be a concern for long duration missions. Possible contamination sources noted were products arising from atomic oxygen sputtering, chemical reaction products, and contamination products from electrostatic discharges which may collect on the arrays.

The question of can arrays operate in the van Allen belts can be answered by "yes, they can." Arrays are suitable power sources for most areas in the van Allen belts, but there are certainly some areas where most present-day arrays cannot stay for more than a few days or even hours without losing a significant amount of their power. But arrays can be designed to operate even in the most intense region of the belts for limited periods of time. Such arrays are likely to laden with a large mass of shielding, both front and rear, for the solar cells.

Lightweight array designs are currently under evaluation for the purpose of producing power for ion propulsion engines. These spacecraft are expected to start at LEO and spiral up through the van Allen belts over a period of 100-200 days. It is typical for these arrays, based on conventional thin crystalline silicon cells, to lose $\approx 70\%$ of their power after one trip. Future arrays for operating in these intense radiation environments may use thin film solar cells made of (hopefully) radiation resistant materials such as amorphous silicon, copper indium diselenide, indium phosphide, cadmium telluride, etc. Other solutions are in-orbit annealing and the use of concentrator arrays, where self-shielding would help.

**Approaches to Shielding**

The workshop participants did not hold a great deal of hope for new shielding methods. The use of integral covers, whether deposited by electrostatic bonding or sputtering, could enable the solar array to operate at high temperatures for annealing purposes. Boeing has developed an integral coverglass/solar cell system that can operate at 500°C for $\approx 60$ seconds. The next step is to develop a method of raising the spacecraft solar panels to that temperature in a practical manner.

**Planetary Surface Power Systems**

Damage to solar arrays from dust accretion and scratches from cleaning and/or wind blown objects was mentioned. Earth experience is useful but may be benign compared to other surface

environments. High voltage arrays in Mars' low density atmosphere might experience Paschen breakdown. Likewise, "plasma puffs" in space or Lunar environments (from venting, propellants, etc.) could precipitate discharges.

## Conclusion

The discussions in the Space Environmental Effects Workshop were spirited and useful. Of particular importance was the participation by array people who introduced a "reality factor" and raised some pointed questions. The broad representation of the solar cell community in these workshops assures both continuity and vitality. While many of the questions raised in the workshop were not answered, the discussions indicated that people were addressing most of the problems and that answers were available.

# JOURNEY INTO TOMORROW - NASA's FUTURE SPACE POWER REQUIREMENTS

Gary L. Bennett
National Aeronautics and Space Administration
Washington, D. C.

With the President's Space Exploration Initiative (SEI) of returning to the Moon and then going to Mars, NASA will need to develop a number of enabling technologies, chief among them being power for spacecraft and surface bases. The SEI power technology program will build upon ongoing efforts in the areas of advanced photovoltaics, energy storage, power management, nuclear power, and higher conversion efficiency systems.

## INTRODUCTION

The Office of Aeronautics, Exploration and Technology (OAET) of the National Aeronautics and Space Administration (NASA) sponsors the agency's basic technology programs in aeronautics and space research, including space energy conversion research and technology (R&T). The principal objective of the space energy conversion R&T program is to provide the technology base to meet the power system requirements for future space missions, including growth Space Station, Earth orbiting spacecraft, lunar and planetary bases, and solar system exploration. The space power program is included in three separate but interrelated parts of the space R&T program: R&T Base, Civil Space Technology Initiative (CSTI) and the Exploration Technology Program (ETP). The power program is divided as follows among the three technology programs (Bennett 1991a):

<u>R&T Base</u>

Photovoltaic Energy Conversion
Chemical Energy Conversion
Thermal Energy Conversion
Power Management
Thermal Management

<u>Civil Space Technology Initiative</u>

High Capacity Power

<u>Exploration Technology Program</u>

Surface Solar Power
SP-100 Space Nuclear Reactor Power System

Recent studies of spacecraft such as the Tracking and Data Relay Satellite System (TDRSS) and the Earth Observing System (EOS) (see Figure 1) have shown that the electric power system (EPS) can be on the order of 25% of the mass of the spacecraft, with the EPS mass almost evenly divided between the source (photovoltaics), storage, and power management and distribution (PMAD) (see Figure 2). Thus, there is an incentive to reduce the mass of the EPS since a factor of two reduction in the mass of the EPS could translate into a factor of two increase in the mass fraction allocated to the payload (or more power could be produced for the same mass fraction) (Brandhorst 1991 and Kenny et al. 1990). Reducing mass is crucial to the eventual exploration of the Moon and Mars because the mass that must be launched into low-Earth orbit (LEO) directly affects the cost of mission operations (Mankins and Buoni 1990).

## SPACE EXPLORATION INITIATIVE

Power has been given an even bigger boost by the new national space policy which includes the goal of expanding human presence and activity beyond Earth orbit into the solar system (White House 1989). Clearly with the national goal of moving outward in space and the ever increasing demands of more sophisticated spacecraft, power becomes a very critical technology - and for the inner solar system that generally means solar-based power.

In implementing the national space policy the President has called for the completion of Space Station Freedom (SSF), the return to the Moon (this time to stay), and manned missions to Mars as part of a new Space Exploration Initiative (SEI). As Arnold D. Aldrich, NASA's Associate Administrator for Aeronautics, Exploration and Technology stated in a speech on the SEI in Huntsville, Alabama on 26 September 1990:

"The essence of SEI is not a future program plan nor a current political agenda. The essence is simply an idea: that men and women will return to the Moon and then will explore the planet Mars. Startling in its simplicity, profound in its consequence, the idea of SEI is so powerful given the reach of our space technology capability, that it cannot be ignored. It is an idea whose time has arrived."

Basically what SEI is is a long-term goal or strategic horizon or "vision" for the civil space program that can be used to guide the space program and to provide a basis for measuring progress in the space program.

The reasons for going to the Moon first include its nearness and partial gravity which allows humans to learn to build, to live, and to work on a new planetary surface that is close enough to Earth (~3 days) for emergency returns. In addition the Moon offers the potential for new science opportunities including a location for astronomical observatories. Overall, the Moon provides an evolutionary approach to expanding human presence and activity.

The reasons for going to Mars are many, including:

- To fulfill the human imperative to explore
- To increase knowledge of the solar system, the galaxies, and life itself
- To bind nations together in a peaceful, common endeavor
- To improve the quality of life
- To strengthen our country's competitive economic position

Figure 3 provides an overview of the Space Exploration Initiative by placing it in context of previous studies and the near-term planning and study activities which must precede any decision to go back to the Moon or to go to Mars. Within the philosophy of SEI is the idea of doing mission studies and technology development before a decision is made on the architecture to be used for the lunar/Mars initiative. No technology selections have been made yet. To complement Figure 3, Figure 4 shows selected recent SEI milestones and illustrates the recent history and progress of the SEI program.

One of the recent activities related to SEI has been the Synthesis Group evolution of alternative architectures for the lunar/Mars missions. Basically, the Synthesis Group, which is an outgrowth of the Vice President's request that a wide net be cast for innovative ideas, has developed four architectures. Their work has noted that a key to the successful achievement of the goals of SEI is plentiful power at a reasonable cost. Power will be needed for spacecraft, for planetary bases on the Moon and Mars, for mobile surface vehicles, and for propulsion (such as electric propulsion) (Buden et al. 1991). This conclusion is in concert with other studies on SEI (NASA 1989 and NRC 1990).

The Synthesis Group has concluded that multiple power units and types will be needed to meet the wide range of requirements for the different mission phases. The preference of the Synthesis Group is for modular units to minimize the need for assembly in space and to provide redundancy and a growth capability. The Synthesis Group has recognized that power development will be a continuing effort with product improvements introduced as model or block changes. One obvious but very important conclusion is that emergency life support power systems that are highly reliable (>0.995) will be needed to back up other life support power systems. One of the key challenges will be providing power during the long (14-Earth-day) lunar night. Some of the possible power requirements identified by the Synthesis Group include (Buden et al. 1991):

| | |
|---|---|
| Surface Vehicles | <10 kWe to <100 kWe |
| Piloted spacecraft | ~5 kWe to ~50 kWe |
| Mars Cargo Vehicle | ~10 kWe |
| Lunar/Mars Habitats | ~30 kWe to ~100 kWe |
| Lunar Settlement | ~1 MWe or more |
| Mars Cargo Vehicle (Electric Propulsion) | ~10 MWe |
| Piloted Mars Vehicle (Electric Propulsion) | ≤100 MWe |

Figure 5 taken from NASA's 90-day study of SEI shows the lunar surface power system options and how the power system might evolve. Clearly the initial installations will be powered by photovoltaic arrays with chemical energy storage. As power demands rise, nuclear power (i.e., nuclear reactors) will be the logical choice because of their ability to operate through the long lunar night. Figure 6 compares the total system mass for a photovoltaic array/regenerative fuel cell (RFC) system and a nuclear reactor power system for the provision of 100 kWe continuously through the lunar day and night. Figure 7 shows a possible lunar outpost arrangement. Regardless of how the power system evolves there will be a clear need for solar-based power either initially as the base is established or later as backup to the nuclear reactor power system (NASA 1989).

## EXPLORATION TECHNOLOGY PROGRAM

In recognition of the need to develop technologies in several areas before proceeding with a specific architecture NASA has established the Exploration Technology Program. This program along with human support (life sciences research), the national launch system (heavy-lift launch vehicle), robotic missions, and Space Station Freedom are prerequisites for human exploration of the Moon and Mars.

The Exploration Technology Program has been established (1) to increase reliability and reduce risk; (2) to reduce developmental and operational costs; and (3) to enable new and innovative capabilities in the areas of

- Space Transportation
- In-space Operations
- Surface Operations
- Human Support
- Lunar and Mars Science
- Nuclear Propulsion
- Information Systems and Automation

Figure 8 shows the structure of the SEI technology and advanced development programs. Note that power is involved in several programs (Mankins and Buoni 1990).

Within the Surface Operations area is the Surface Solar Power Program whose objective is to develop solar-based power technology to a level of readiness sufficient to enable or enhance extraterrestrial surface missions. The objective is planned to be achieved through advancing the technologies of energy storage by means of regenerative fuel cells, power generation by means of photovoltaic arrays and advanced, low mass reliable electrical and thermal power management subsystems. The goal is to achieve a solar-based surface power system design based on advanced technologies in these four subsystems that has a reliable life in excess of 40,000 hours at a specific power of 3 We/kg for lunar applications and 8 We/kg for Martian applications. The emphasis will be on higher efficiency, lighter weight solar arrays with a goal of 300 We/kg; high energy density chemical energy storage systems with a goal of 1000 We-h/kg; and automated, smart, fault-tolerant PMAD subsystems (≤55 kg/kWe) (Bennett 1991b).

Also within the Surface Operations area is the SP-100 Space Nuclear Reactor Power System Program whose objective is to develop and validate the technology for space nuclear reactor power systems that can produce tens to hundreds of kilowatts of electric power and be capable of seven years of operational life at full power. The SP-100 program is a joint endeavor of NASA, the Department of Energy (DOE) and the Strategic Defense Initiative Organization (SDIO). Under the SP-100 program a generic 100-kWe space reactor power system is being designed. The reactor concept will be scalable from 10 kWe to 1000 kWe. SP-100 provides a technology base for nuclear electric propulsion (NEP) missions to the outer planets, surface power and spacecraft power (Pluta et al. 1989).

One very important area requiring power is the Mars transportation system. Figure 9 shows the various Mars transportation options. All of these spacecraft are going to require power for the ~400-day to ~1000-day round-trip missions to Mars. One of the options, solar electric propulsion (SEP), is very dependent on having very light-weight and very low cost space solar arrays.

## ROBOTIC MISSIONS

As part of SEI there will be a number of precursor robotic missions which will advance our scientific understanding and develop the basis for human science exploration. These robotic explorers will determine suitable/desirable landing and outpost sites as well as providing design data for human mission elements and demonstrating the technologies and operational concepts for the follow-on human missions. Consequently these robotic missions are integral to the SEI and they represent opportunities and challenges for spacecraft power system designers. For the Moon the emphasis will be on selecting the landing/outpost site. The principal lunar robotic mission is planned to be the planned Lunar Observer which will study the Moon from a 100-km polar orbit.

For Mars the emphasis will be on science and ensuring the success of the follow-on human missions. Some of the candidate Mars robotic missions include: Mars Observer, Site Reconnaissance Orbiter, Mars Landers, and Mars Sample Return/Rovers. The Mars Observer is currently being prepared for a 1992 launch. Figure 10 shows one possible Mars robotic rover concept. While this particular rover has radioisotope thermoelectric generators (RTGs) for power, studies at NASA's Lewis Research Center (LeRC) have shown that solar-powered rovers can be operated on Mars (Appelbaum and Flood 1989).

Figure 11 shows the initial listing of missions developed by NASA's Office of Space Science and Applications ((OSSA). Currently NASA/OSSA is preparing a long-range strategic plan for missions involving astrophysics, solar system exploration, Earth science, space physics, communications, life science and microgravity research. Two of the key technologies identified by NASA/OSSA that are of interest to the Space Photovoltaic Research and Technology (SPRAT) Conference are solar arrays and solar cells. In addition there is a need for radiation hard parts and detectors. Clearly radiation-resistant solar cells mounted on light-weight arrays would be of great benefit to the space science community.

## NEAR-TERM ACTIVITIES

Currently NASA is responding to the *Report of the Advisory Committee on the Future of the U. S. Space Program* which supports the eventual lunar/Mars missions and advocates increased support for technology development (Advisory Committee 1991). NASA will take the results of the Synthesis Group study and integrate them into the overall planning for SEI, which includes defining and executing an SEI preparatory program that includes meaningful technical analyses. In carrying out the SEI program NASA will be working closely with other Federal agencies including the Department of Defense and the Department of Energy. Basically NASA will be nurturing the concept and developing program options for the eventual national decisions.

## CONCLUSION

NASA's future space programs will be heavily dependent upon power. As a consequence the space power community should look upon the requirements of the civil space program as an exciting technical challenge to advance the state of the art through developing electric power systems with higher efficiencies, reduced masses, improved reliability, longer lifetimes and reduced costs.

## REFERENCES


Advisory Committee (1991) *Report of the Advisory Committee On the Future of the U.S. Space Program*, December 1990, available from the Superintendent of Documents, U.S. Government Printing Office, Washington, D.C.

Appelbaum, J. and D. J. Flood (1989) "Photovoltaic Power System Operation in the Mars Environment" in *Proceedings of the 24th Intersociety Energy Conversion Engineering Conference*, held in Crystal City, Virginia, 6-11 August 1989.

Bennett, G. L. (1991a) "The OAST Space Power Program", in *Space Photovoltaic Research and Technology - 1989*, NASA Conference Publication 3107, published in 1991; Proceedings of a conference held at NASA Lewis Research Center, Cleveland, Ohio, 7-9 November 1989.

Bennett, G. L. (1991b) "Powering the Space Exploration Initiative: NASA Future Space Power Requirements and Issues", to be published in *Proceedings of the 26th Intersociety Energy Conversion Engineering Conference*, to be held in Boston, Massachusetts, 3-9 August 1991.

Brandhorst, Jr., H. W. (1991) "Key Issues in Space Nuclear Power Challenges for the Future", *Proceedings of the 8th Symposium on Space Nuclear Power Systems*, CONF-910116, held in Albuquerque, New Mexico, 6-10 January 1991.

Buden, D., D. Bartine, S. Harrison, J. Foreman, and K. Biringer (1991) "The Stafford Commission Synthesis Group Evaluation of Power for the Space Exploration Initiative", to be published in *Proceedings of the 26th Intersociety Energy Conversion Engineering Conference*, to be held in Boston, Massachusetts, 3-9 August 1991.

Kenny, B., R. C. Cull, and M. D. Kankam (1990) "An Analysis of Space Power System Masses", *Proceedings of the 25th Intersociety Energy Conversion Engineering Conference*, held in Reno, Nevada, 12-17 August 1990.

Mankins, J. C. and C. M. Buoni (1990) "Technology and Mars Exploration", AIAA paper 90-3797 presented at the AIAA Space Programs and Technologies Conference, held in Huntsville, Alabama, 25-28 September 1990.

National Aeronautics and Space Administration (1989) *Report of the 90-Day Study on Human Exploration of the Moon and Mars*, NASA, Washington, D. C., November 1989.

National Research Council (1990) *A Review of NASA's 90-Day Study and Alternatives*, National Research Council, National Academy Press, Washington, D.C.

Pluta, P. R., M. A. Smith, and D. N. Matteo (1989) "SP-100, A Flexible Technology for Space Power from 10s to 100s of kWe", paper number 899287 in *Proceedings of the 24th Intersociety Energy Conversion Engineering Conference*, held in Crystal City, Virginia, 6-11 August 1989.

White House (1989) *Fact Sheet, U.S. National Space Policy*, Washington, D.C., 2 November 1989.

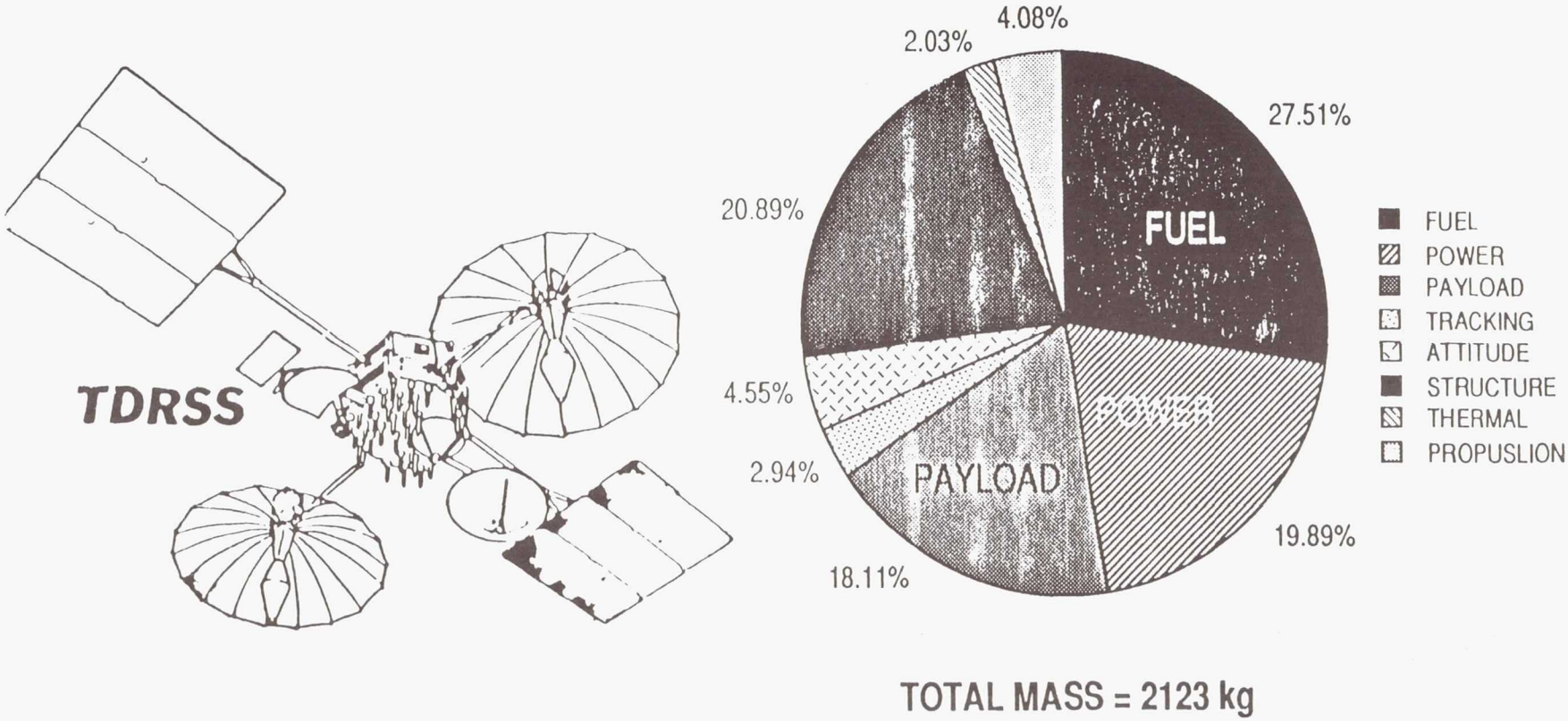


**Figure 1. Distribution of the Wet Mass of the Tracking and Data Relay Satellite System (TDRSS).**

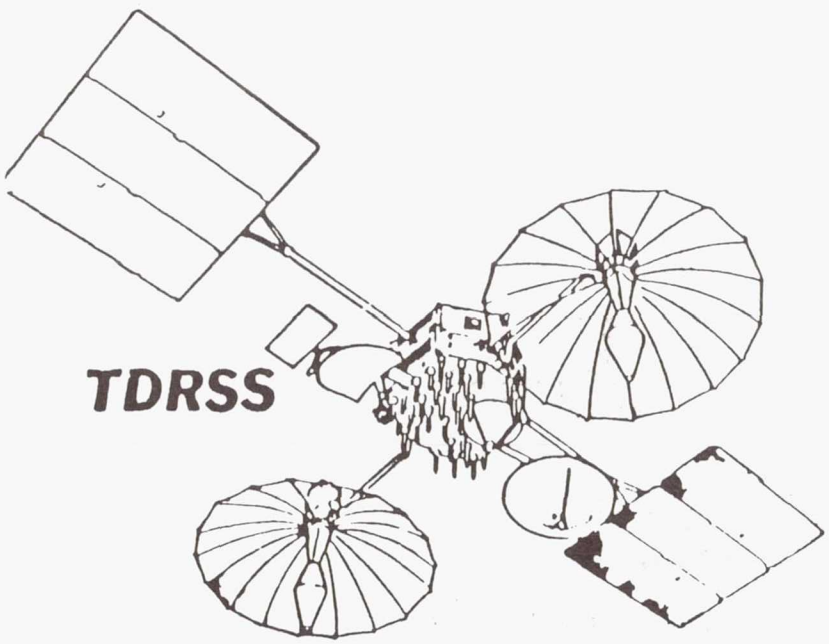


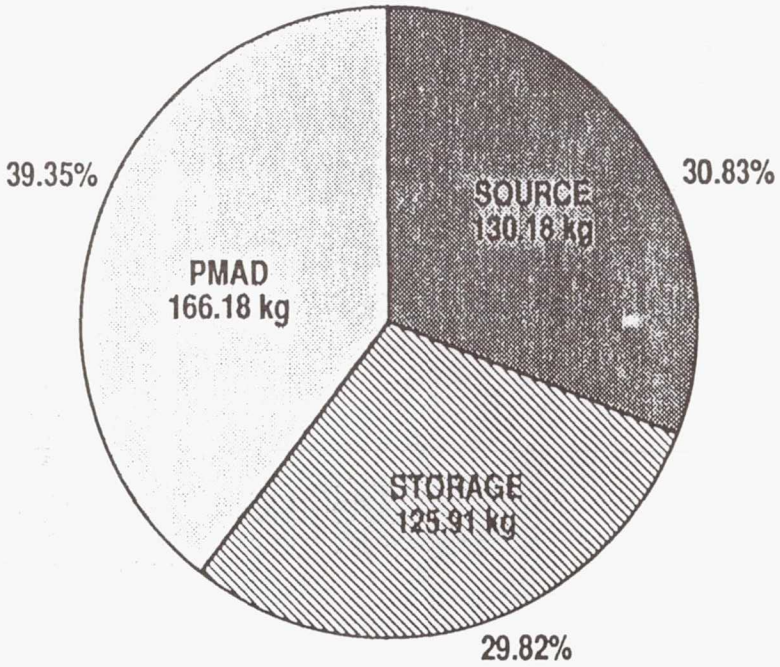


TOTAL EPS MASS = 422kg

Figure 2. Distribution of the Masses of the Subsystems of the Electric Power System (EPS) of the Tracking and Data Relay Satellite System (TDRSS).

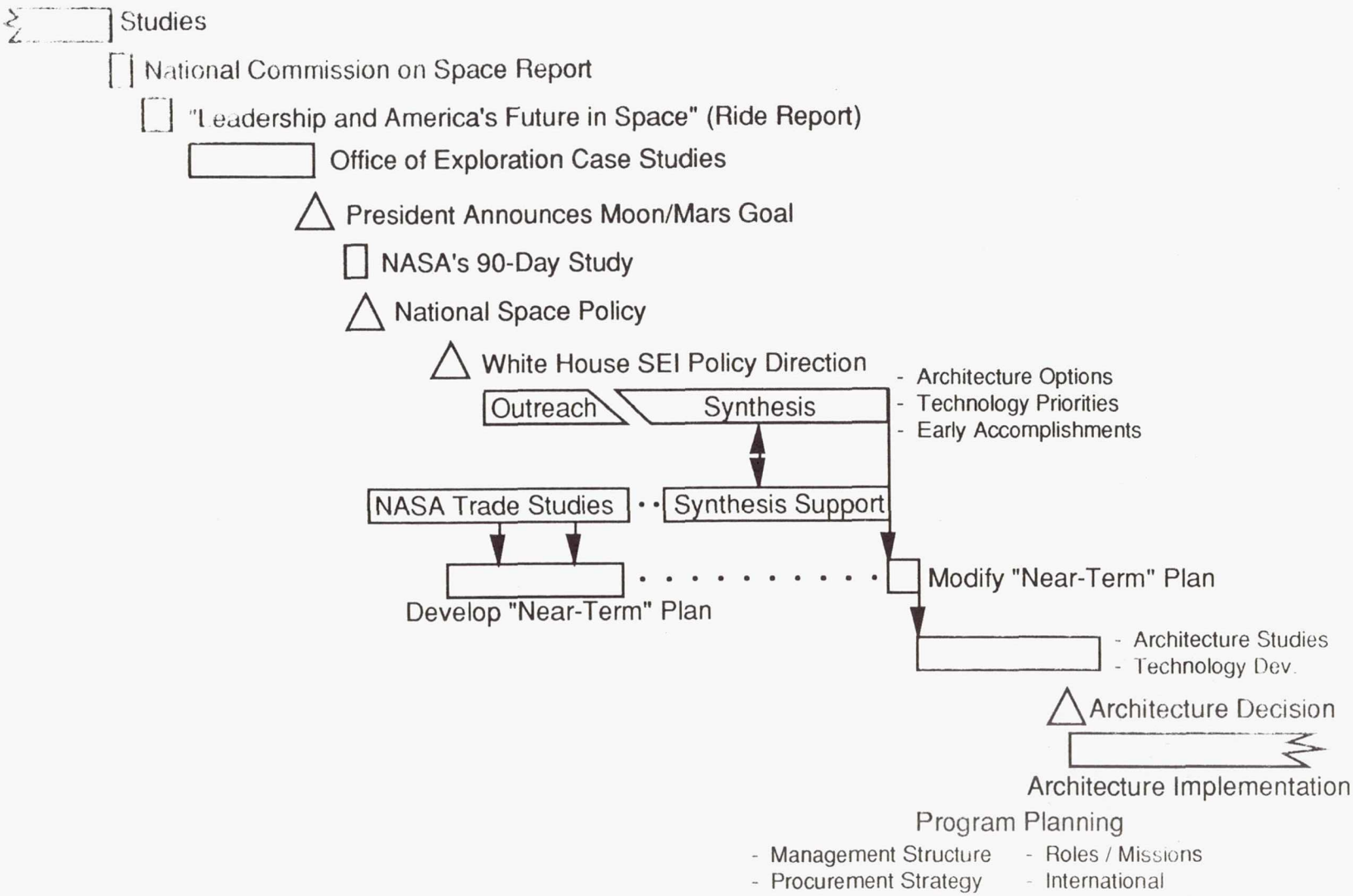


**Figure 3. Overview of the Space Exploration Initiative (SEI).**

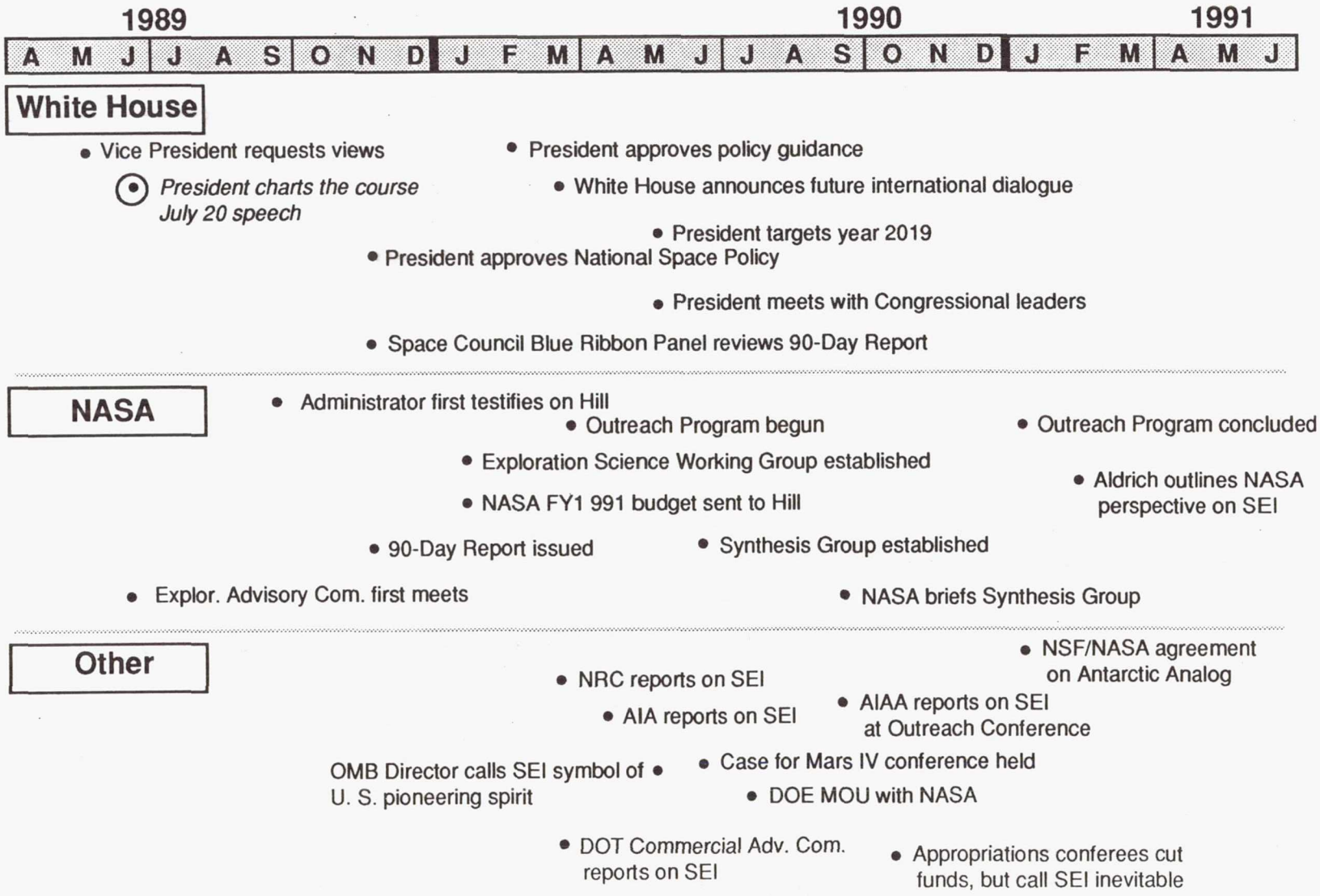


**Figure 4. Selected Milestones for the Space Exploration Initiative (SEI).**

# Lunar Surface Power System Options

**Strategy: Early Outpost Power Needs → Later Outpost Power Needs**

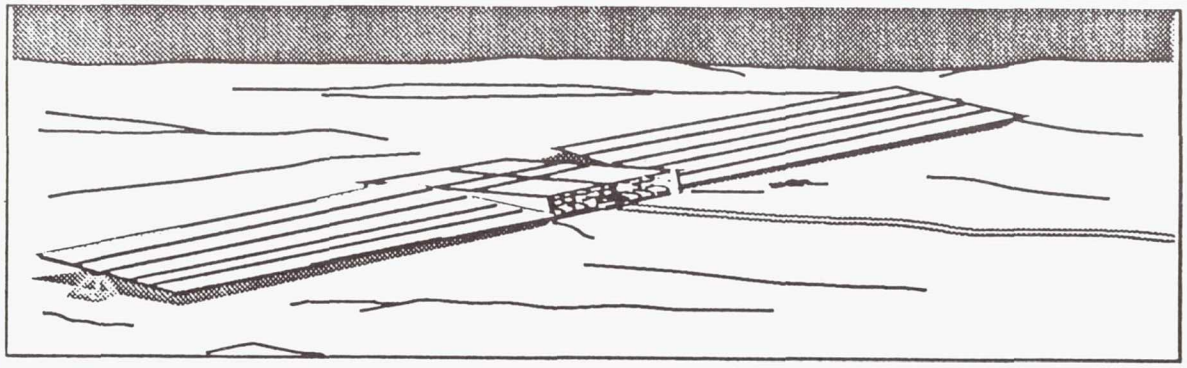

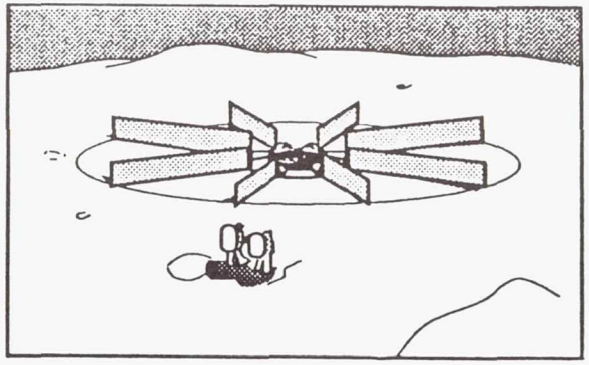

- **Power Generation**
  - Photovoltaic Arrays or Solar Dynamic Modules
    - Low-Moderate Mass/kW
    - Near Term Development
    - Can Be Located Near Outpost
    - Ease of Deployment
    - Daytime Power Only
    - Power Storage Required
    - Moderate Spares
    - Moderate Crew Support
- **Power Storage**
  - Batteries
    - Near Term Development
    - High Initial Mass/kW
    - Short Lived Systems
  - Regenerative Fuel Cells
    - Longer Term Development
    - Moderate Mass/kW
    - Short Lived Systems
    - High Spares/Resupply
- **Nuclear Power**
  - Continuous Day/Night Power
  - No Power Storage Required
  - Low Initial Mass/kW
  - Lowest Spares/Resupply
  - Long Life Systems
  - Minimum Crew Support
  - Longer Term Development
  - Must Be Remote to Outpost
  - Radiation Shielding
  - Political

Figure 5. Options for the Lunar Surface Power System.

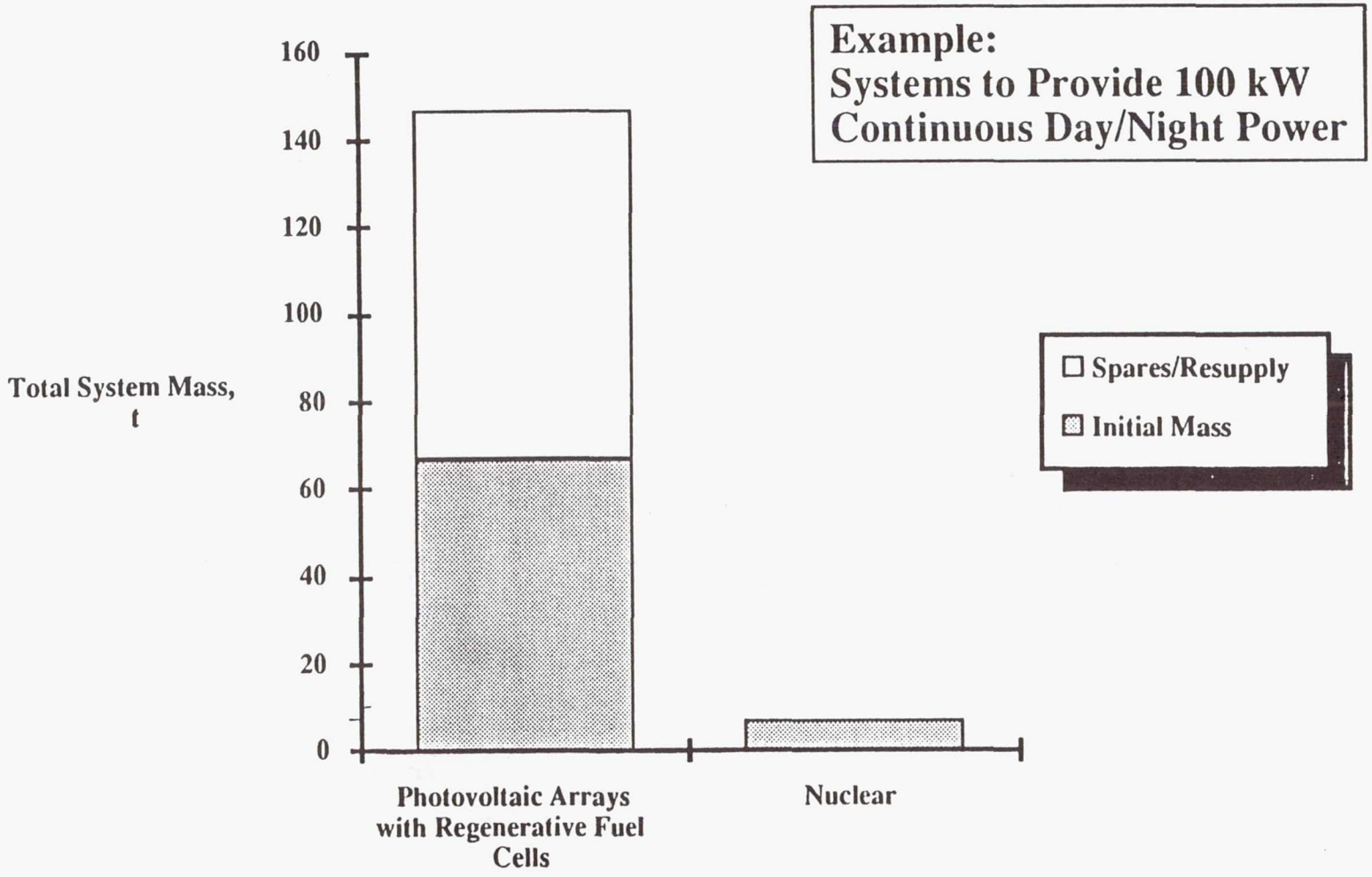


Figure 6. Comparison of the Masses for Two Lunar Surface Power System Options (assuming a 10-year life).

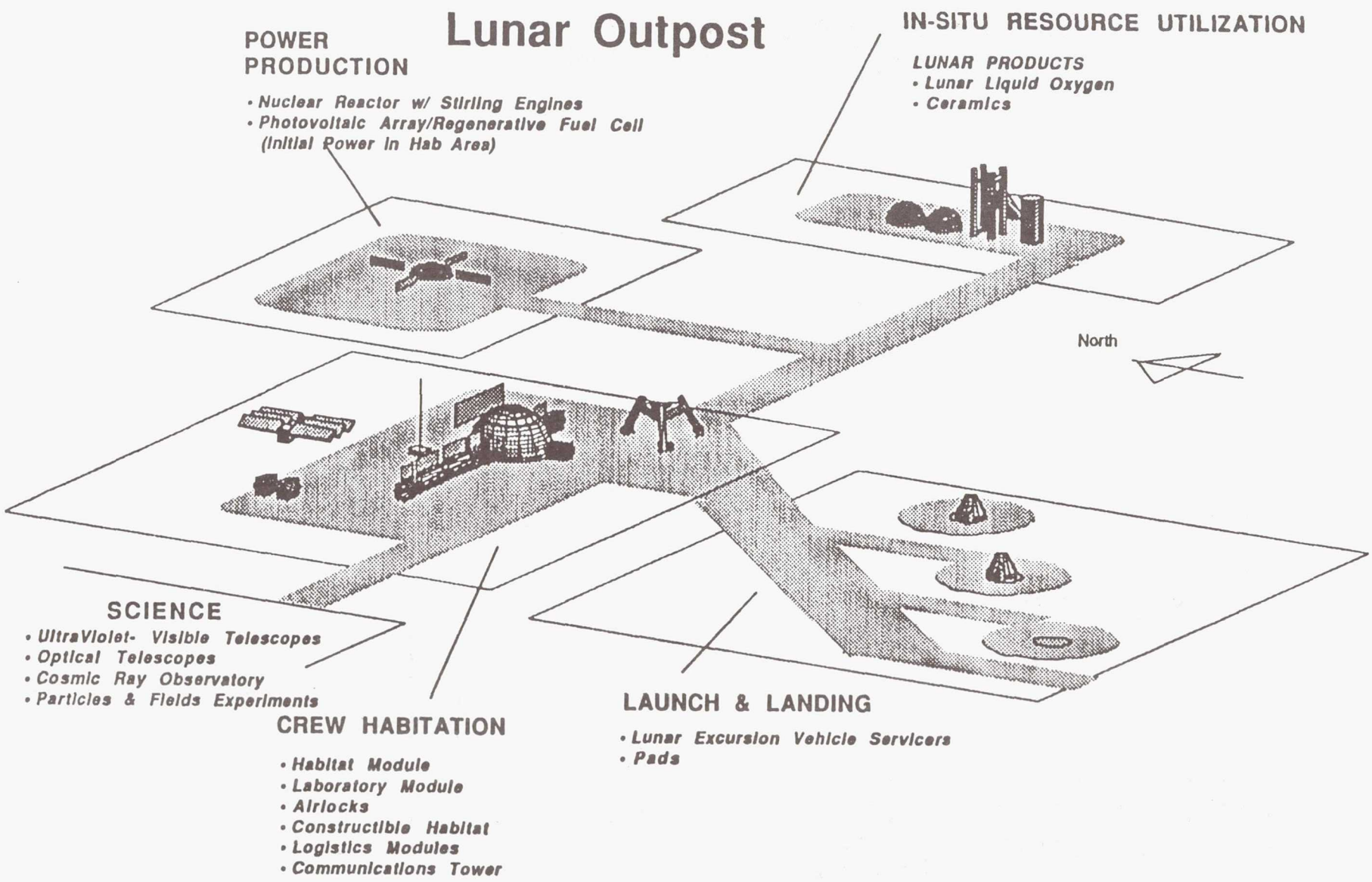


Figure 7. A Possible Layout for the Lunar Outpost.

**SPACE TRANSPORTATION**

- Aerobraking
- Space-based chemical engines
- Autonomous landing
- Auton. rendezvous and docking
- Vehicle structures and cryogenic tankage

**IN-SPACE OPERATIONS**

- Cryogenic fluid systems
- Assembly and construction
- Vehicle servicing and processing

**SURFACE OPERATIONS**

- Space nuclear power
- In situ resource utilization
- Planetary rovers
- Solar power
- Robotics and construction

**LUNAR/MARS SCIENCE**

- Sample acquisition, analysis, and preservation
- Planetary orbiters and landers
- Astrophysical observatories

**INFO SYSTEMS & AUTOM.**

- High-rate communications
- Remote surface science operations
- Planetary photonics
- Exploration data systems

**NUCLEAR PROPULSION**

- Nuclear thermal propulsion
- Nuclear electric propulsion

**Figure 8. Organization of the Space Exploration Initiative Technology and Advanced Development Programs.**

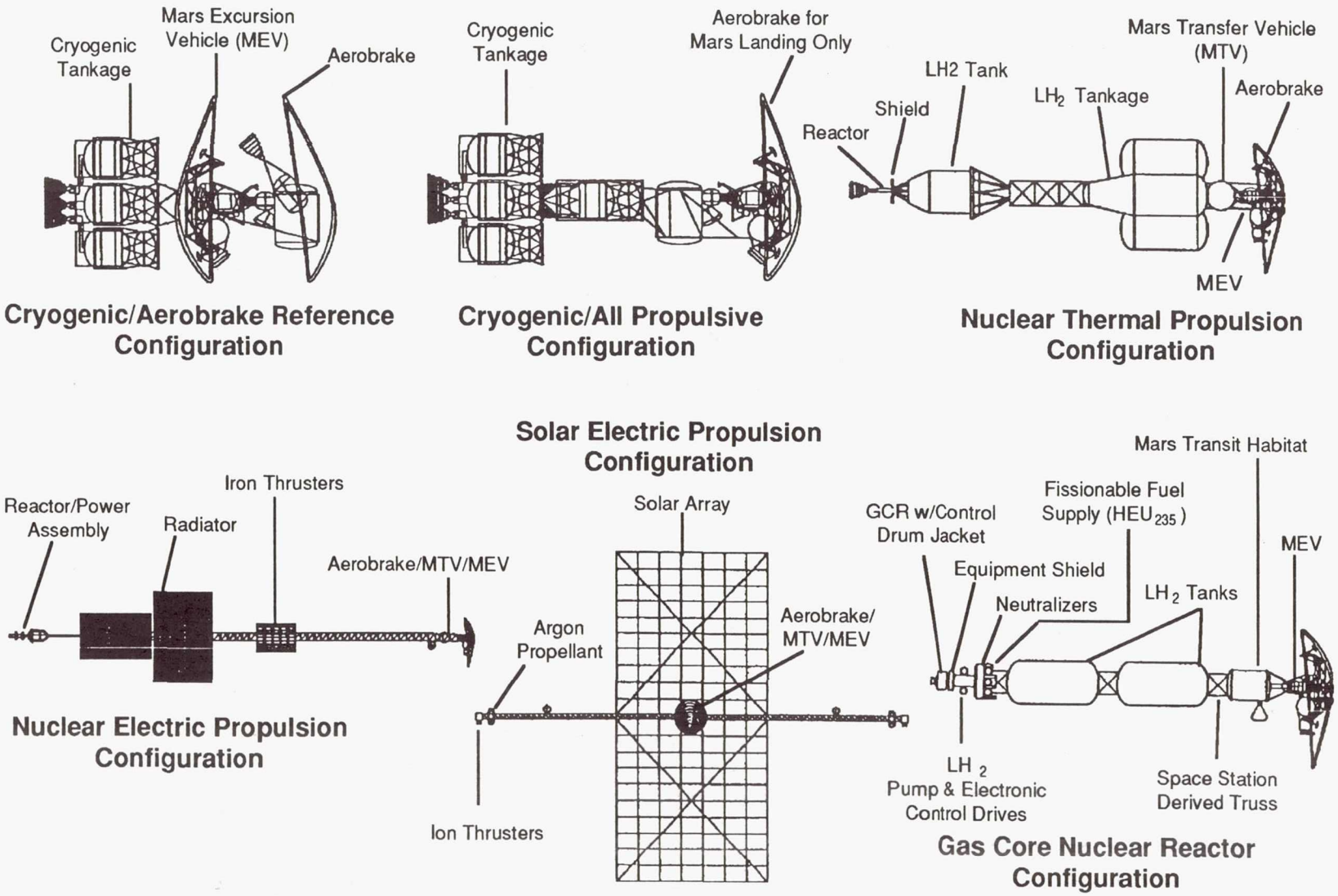


**Figure 9. Concepts for Mars Transportation Vehicles.**

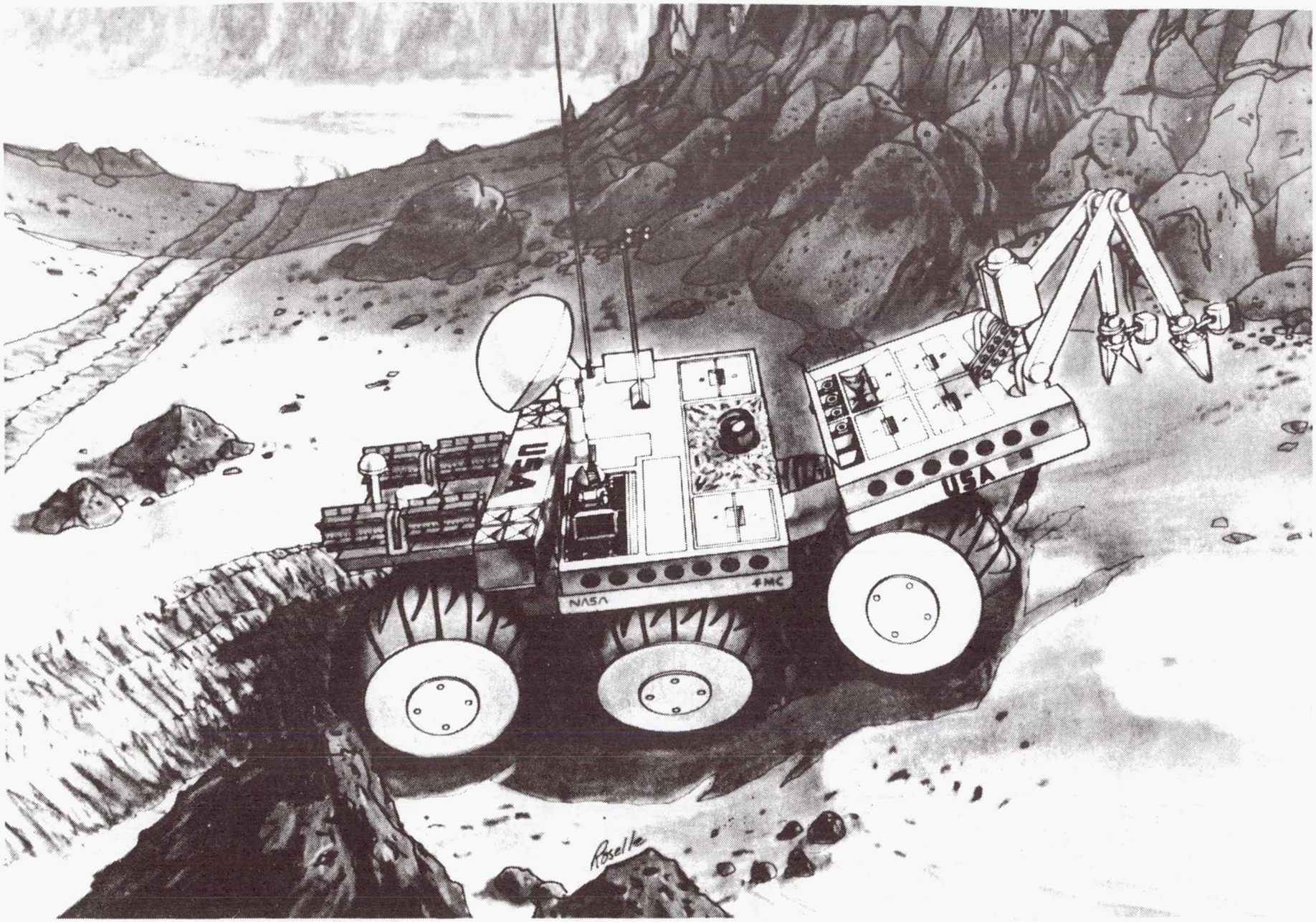


Figure 10. Concept for a Mars Robotic Rover.

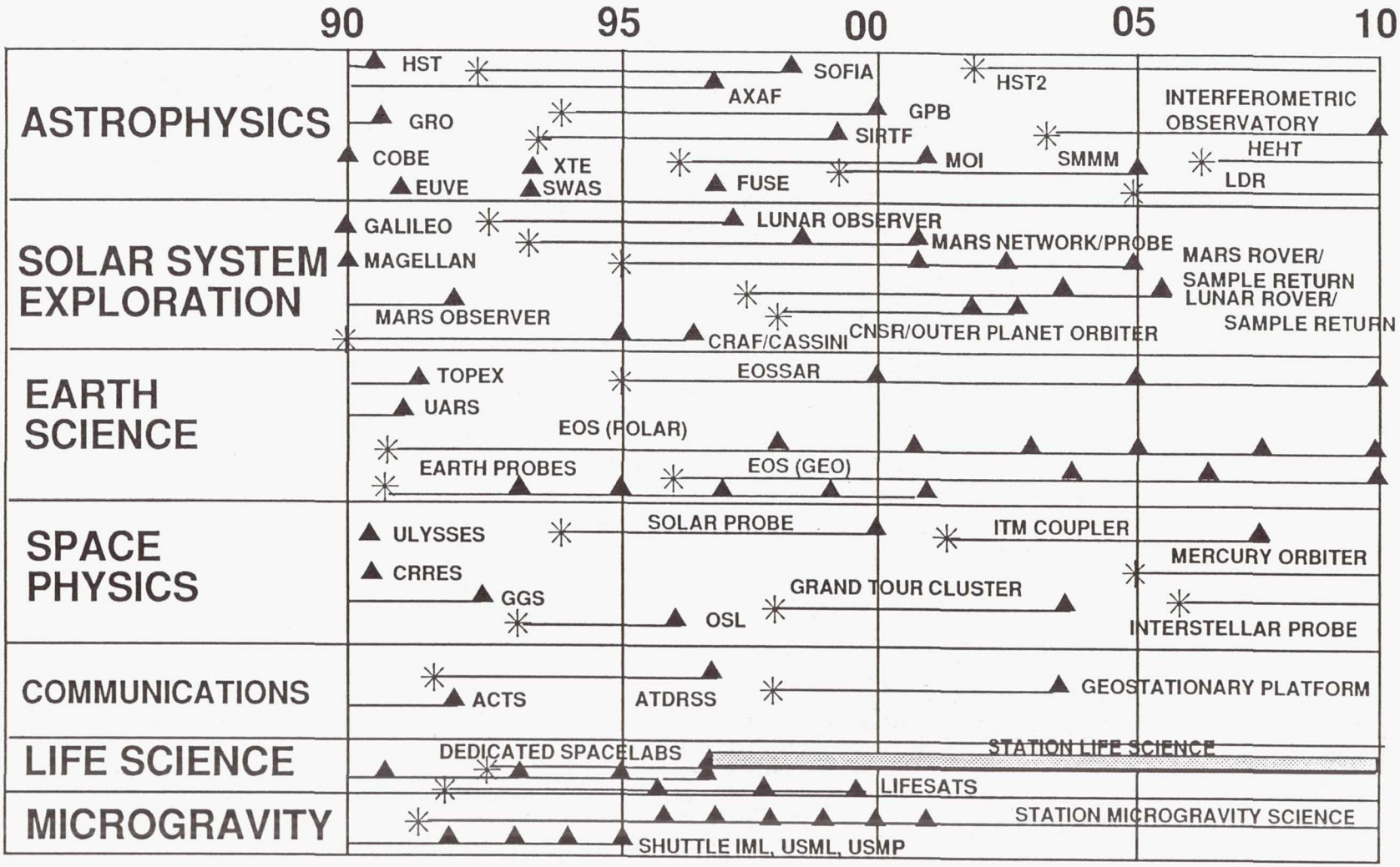


**Figure 11. Preliminary Mission Model for NASA Space Science Missions.**

# THE SURVIVABLE POWER SUBSYSTEM DEMONSTRATION PROGRAM (SUPER)

JACK W. GEIS
WL/POOX-1
(513) 255-4450

## OVERVIEW

- OBJECTIVE
- BACKGROUND
- OVERVIEW OF DESIGN FEATURES
- LOW POWER INITIATIVE
- CONCLUSIONS

## SUPER PROGRAM OBJECTIVE

DEVELOP AND DEMONSTRATE A POWER SUBSYSTEM WHICH WILL SURVIVE POTENTIAL MILITARY THREATS AND BE PRACTICAL ENOUGH THAT SATELLITE PROGRAMS WILL USE IT

## SUPER REQUIREMENTS

SURVIVABILITY

PRACTICALITY

- WEIGHT
- PRODUCTION COST
- RELIABILITY
- SUPPORTABILITY
- LAUNCH ENVIRONMENTS
- SAFETY
- ORBITAL FLEXIBILITY
- PACKAGING FLEXIBILITY
- SCALEABILITY

## TECHNOLOGY BREAKTHROUGHS

CONCENTRATOR ELEMENT WEIGHT

SOLAR CELL EFFICIENCY, TEMPERATURE THRESHOLD

POWER SUBSYSTEM AUTONOMY

FULL SCALE CONCENTRATOR ARRAY POINTING AND TRACKING DESIGN

MULTIPLE DEPLOYMENT AND RETRACTION ARRAY

LARGE C-C STRUCTURAL PART PRODUCTION

GaAs BYPASS DIODES

LOW LOSS BATTERY BYPASS CIRCUIT

# THE SUPER HORSE RACE

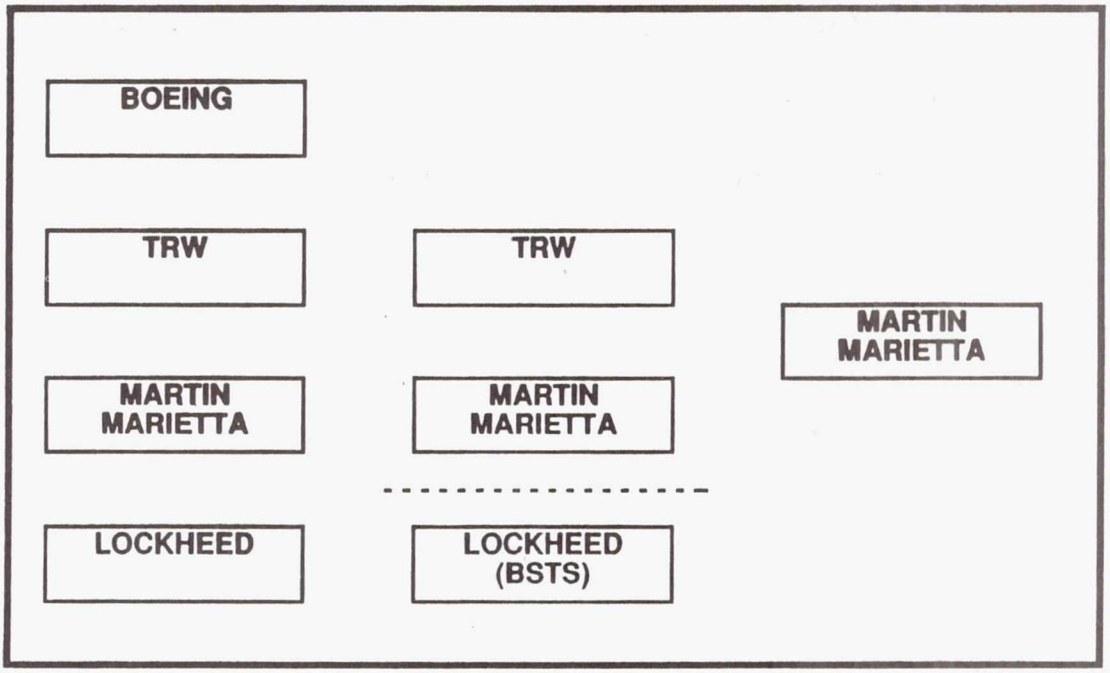


| PHASE I<br>CONCEPTUAL DESIGN | PHASE II<br>PRELIM DESIGN | PHASE III/IV<br>CRITICAL DESIGN, FAB & TEST<br>LAUNCH & SUPPORT |
|---|---|---|

## OVERVIEW OF DESIGN FEATURES

- MARTIN MARIETTA CONCENTRATOR APPROACH (GENERIC SUPER INTEGRATED SUBSYSTEM)

## OVERVIEW OF DESIGN FEATURES (PDR GENERIC APPROACH)

- INTEGRATED POWER SUBSYSTEM
  - SOLAR ARRAY
  - DEPLOYMENT, RETRACTION, AND TRACKING MECHANISMS
  - POWER MANAGEMENT AND DISTRIBUTION
  - THERMAL MANAGMENT
- SURVIVABLE
  - ENABLING TECHNOLOGY:
    PRE-SUPER STATE-OF-THE-ART SOLAR SYSTEMS COULD NOT SURVIVE
  - ACTIVE AND PASSIVE FEATURES
- MODULAR AND SCALEABLE THROUGHOUT 2KW - 40KW USER RANGE

## SUPER
## KEY ASSEMBLIES

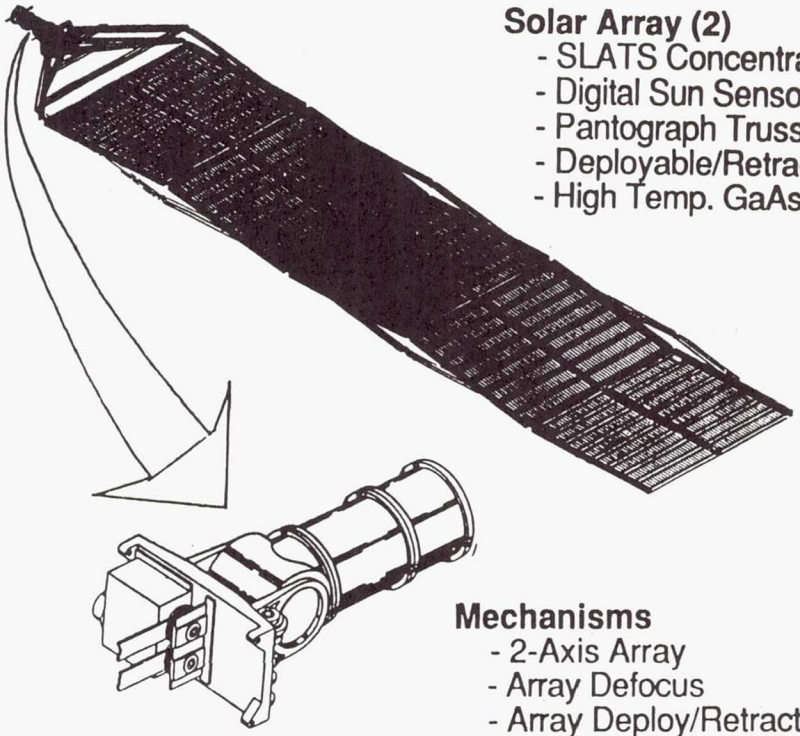

**Solar Array (2)**
- SLATS Concentrator
- Digital Sun Sensors
- Pantograph Truss
- Deployable/Retractable
- High Temp. GaAs Cells

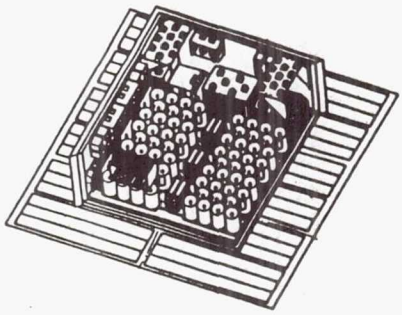

**Modular Power Assembly (2)**
- 50 AH IPV NiH2 Cells
- Individual Battery Maintenance
- Shunt Regulated Array
- Processor Control
- WCHP Thermal Management
- Multi-Threat Shield

**Mechanisms**
- 2-Axis Array
- Array Defocus
- Array Deploy/Retract
- Slip Ring Power Transfer
- Launch Retention

# CONCENTRATOR ELEMENT DESIGN

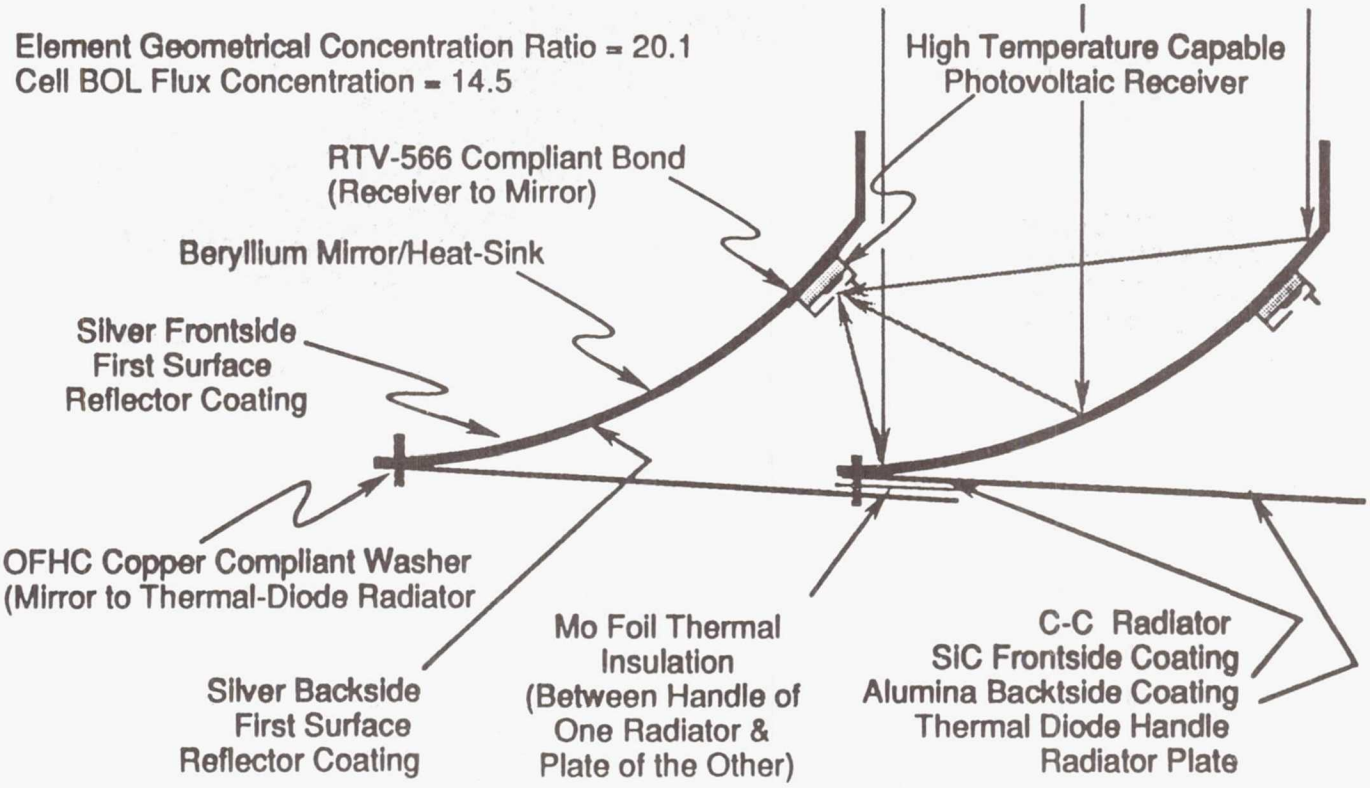

# SOLAR ARRAY

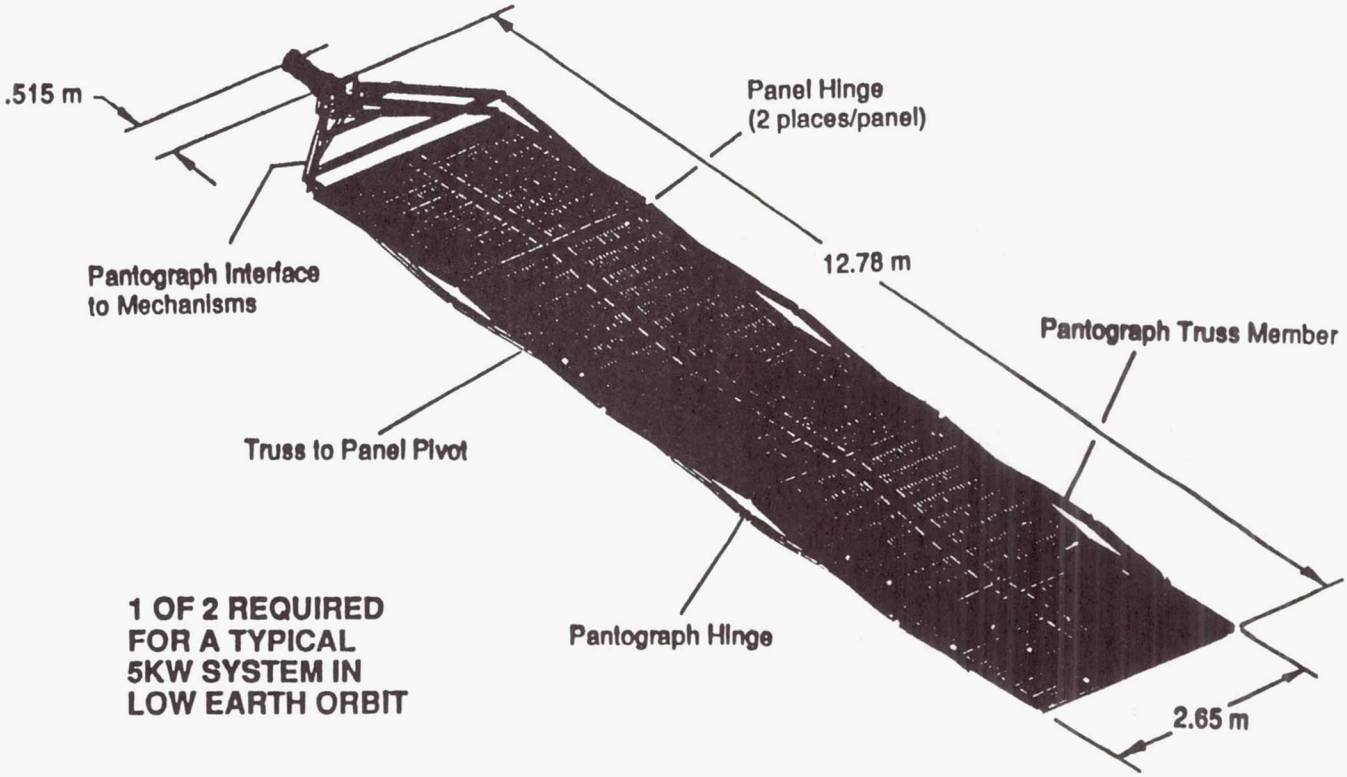


# MECHANISMS

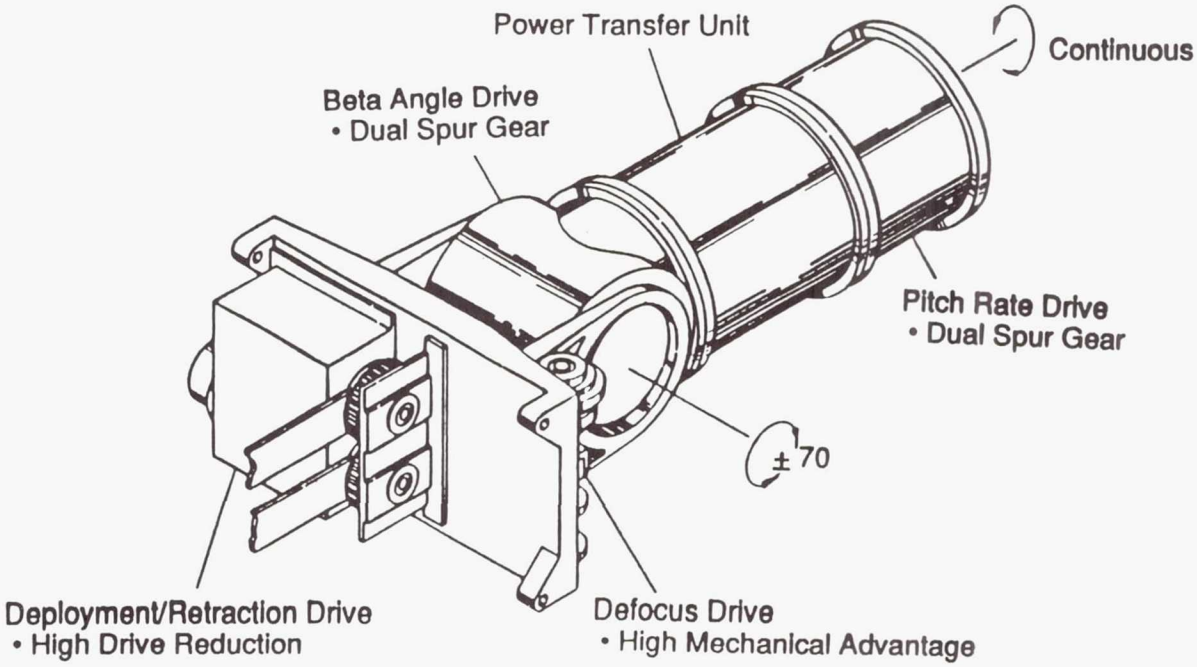

## POWER MANAGEMENT AND DISTRIBUTION - OVERVIEW

### KEY FEATURES

- PROVIDES 100% UNINTERRUPTED POWER DURING AND AFTER THREATS OR SINGLE FAULTS
- UTILIZES A SHUNT CONTROL DIRECT ENERGY TRANSFER SYSTEM
- POWER BUS VOLTAGE 28 VDC (+ 6 VDC, - 4 VDC) (HIGH VOLTAGE CAPABILITY WITH SIMPLE REVISED CIRCUITRY)
- PROVIDES INDIVIDUAL BATTERY CHARGE CONTROL TO EXTEND BATTERY LIFE
- USES A STANDARD 1553B REDUNDANT COMMUNICATION BUS AND ADA SOFTWARE
- CONTROLS FOR AUTONOMOUS SOLAR ARRAY TRACKING AND POINTING
- INTEGRAL THERMAL MANAGEMENT

# TYPICAL MODULAR POWER ASSEMBLY

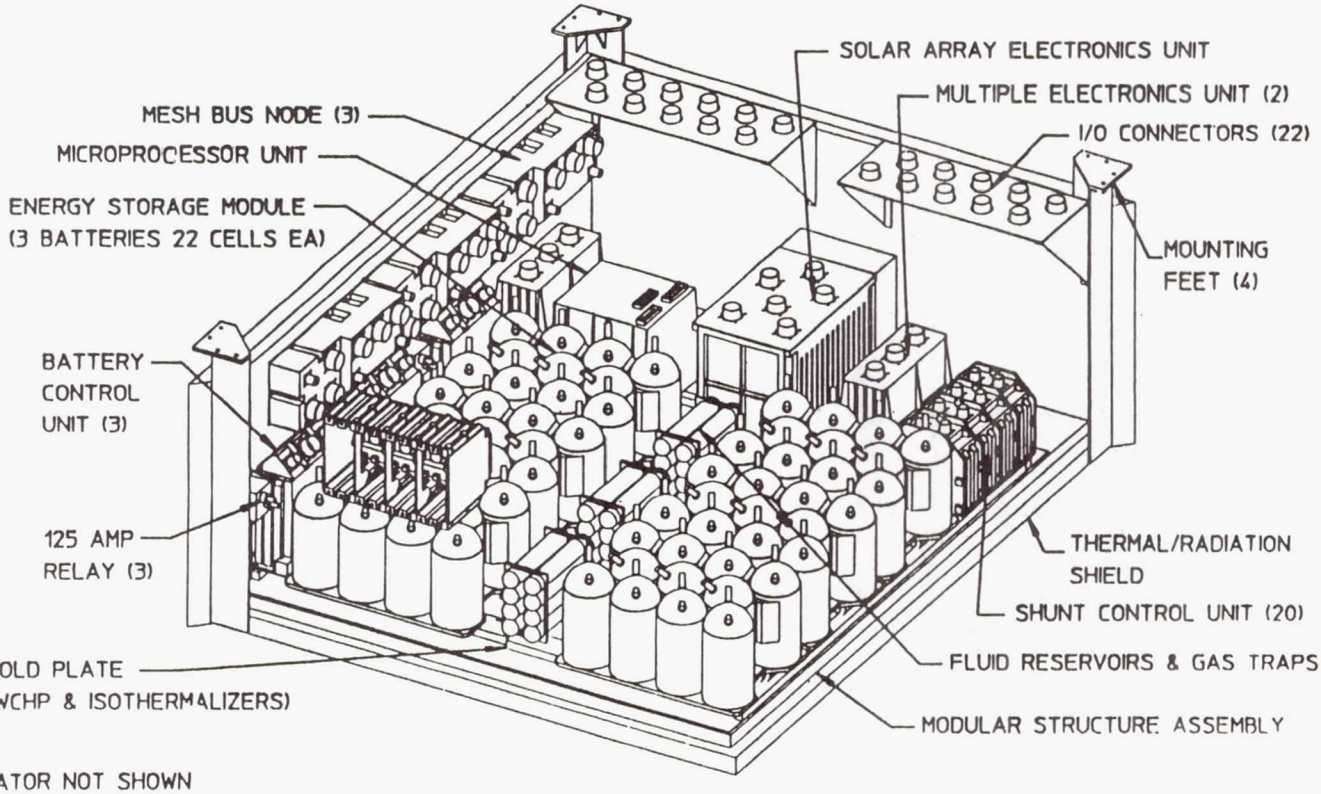


RADIATOR NOT SHOWN
TOTAL QUANTITIES MAY NOT BE SHOWN FOR CLARITY

# SUN SENSOR DESIGN

**2-AXIS ANALOG SUN SENSOR**

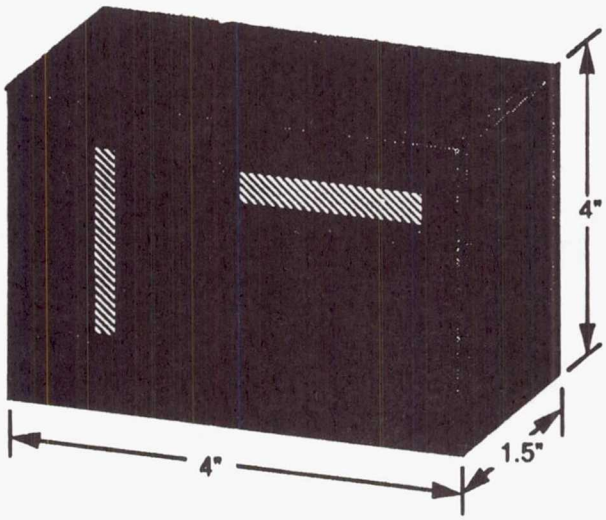


INSULATION OVER AL HOUSING

OPTICAL

**OPTICAL PATH**

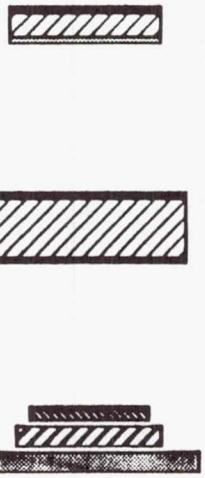

LASER FILTER
SUBSTRATE
UV BLOCKING FILTER

CR/SIOX MULTILAYER WITH SLIT
SIO2
CR/SIOX MULTILAYER WITH CODE

PHOTO CELL
PRINTED CIRCUIT EPOXY SUBSTRATE
AL REAR COVER

# MODULARITY: SOLAR PANELS

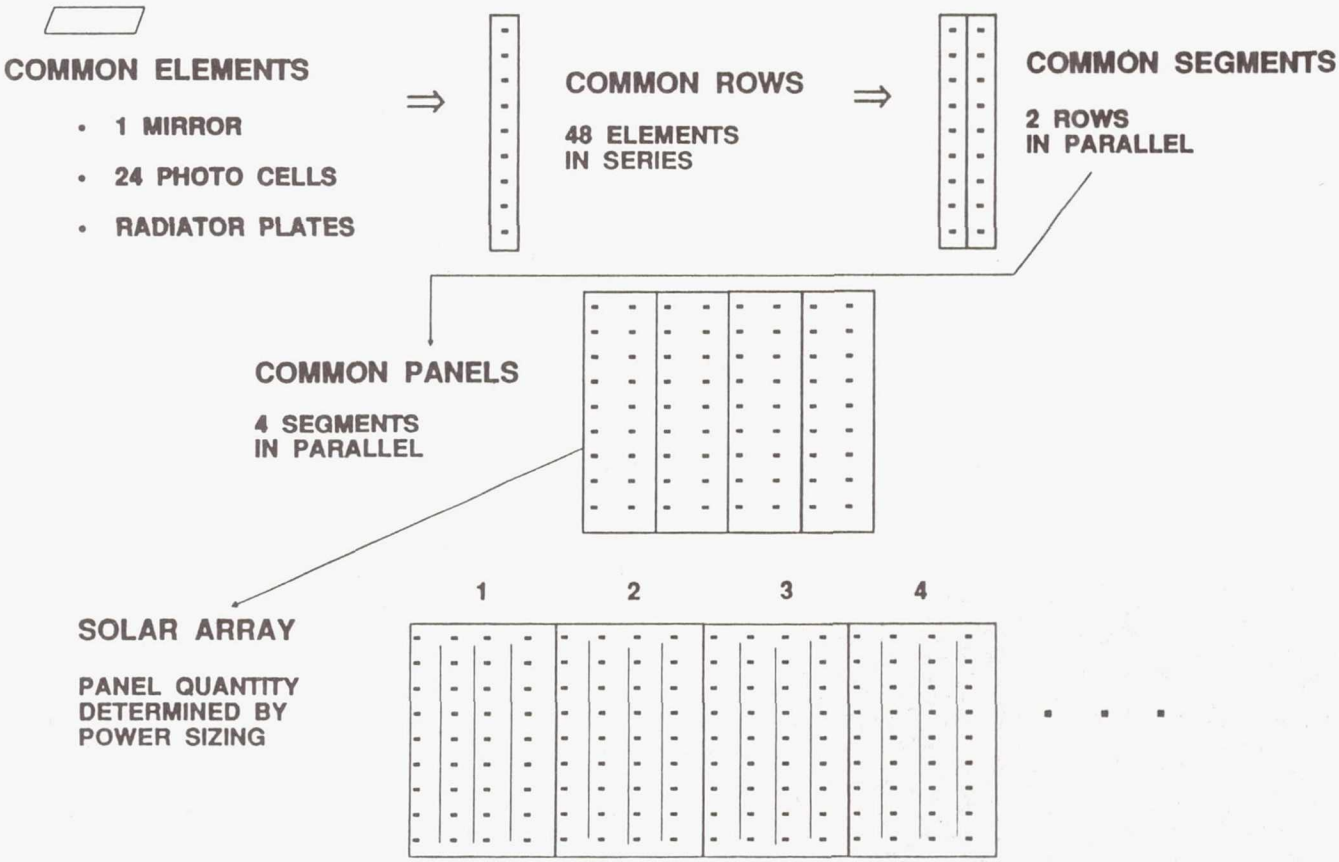


# SUPER SURVIVABILITY

REQUIRES HARDNESS & ABILITY TO WITHSTAND ACTIVE COUNTER MEASURES

AS WELL AS THE NATURAL ENVIRONMENT

- ORBITAL DEBRIS
- ATOMIC OXYGEN
- VAN ALLEN BELTS
- SOLAR ACTIVITY

# MPA THERMAL MANAGEMENT FEATURES

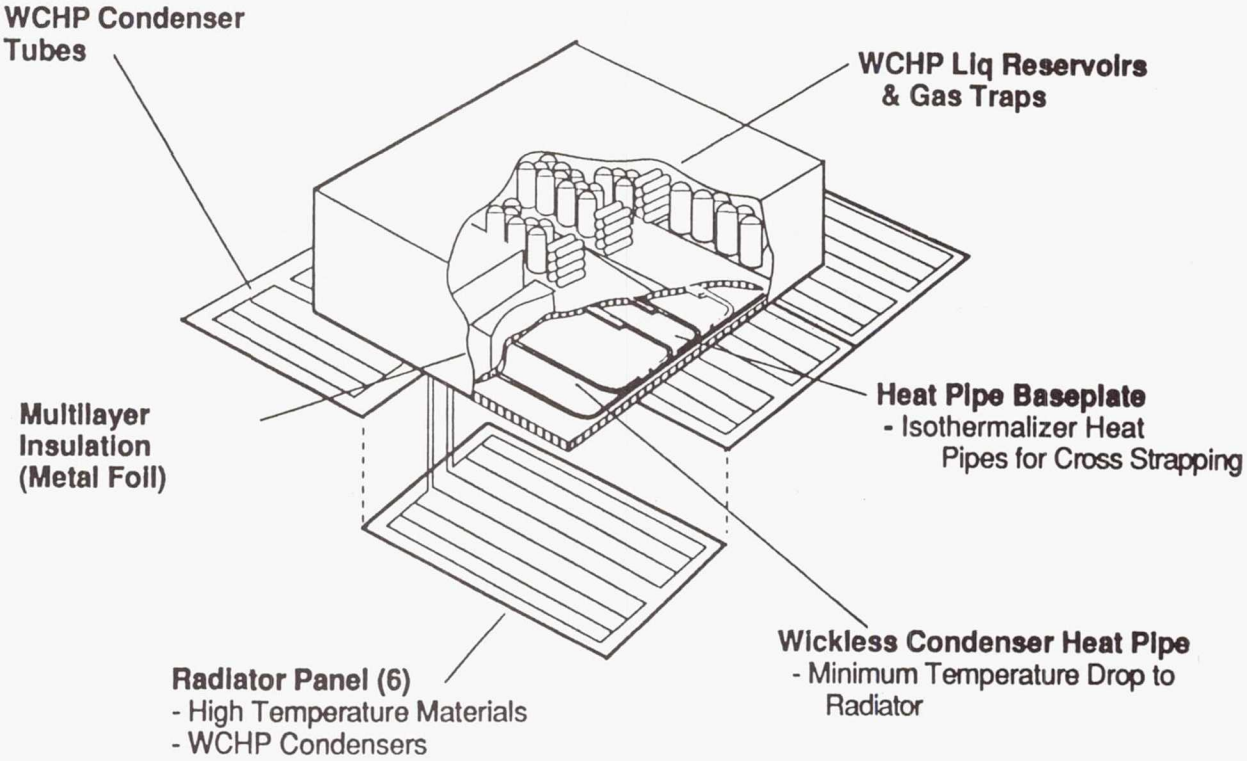


# SURVIVABILITY YIELDS DURABILITY

SUPER'S SURVIVABILITY BENEFITS USERS WHO DON'T DEAL WITH HOSTILE THREATS

- SURVIVABILITY FEATURES PROVIDE ROBUST DURABILITY AGAINST DEGRADATION FROM NATURAL ENVIRONMENT
- LESS THAN 1/3 THE DEGRADATION RATE OF A CONVENTIONAL PLANAR ARRAY

# LOW POWER INITIATIVE

- WHY
  - LOGICAL EXTENSION OF WORK ALREADY DONE
  - SIGNIFICANTLY MORE POTENTIAL USERS AT LOWER POWER LEVELS
    - 0.5KW - 3KW INSTEAD OF 2 - 40 KW
  - DEMONSTRATE COMPATIBILITY WITH LATEST SDI ARCHITECTURE
  - IMPROVED FLIGHT DEMO OPPORTUNITIES —> P91-B

# PHASES III & IV

PHASE III

- CRITICAL DESIGN (CRITICAL DESIGN REVIEW NOV 92)
- FABRICATION (START MAY 92)
- TEST & QUALIFICATION (COMPLETION 2ND QUARTER FY94)
- DELIVERY OF FLIGHT HARDWARE (3RD QUARTER FY94)

PHASE IV

- SUPPORT FOR SPACECRAFT INTEGRATION
- LAUNCH SUPPORT (LAUNCH 4TH QUARTER FY95)
- SUPPORT FOR ON-ORBIT OPERATIONS (3 YEARS)

# CONCLUSION

- SUPER PROGRAM DEMONSTRATES A PRACTICAL GENERIC INTEGRATED SURVIVABLE (DURABLE) POWER SYSTEM
- QUALIFIED SUPER COMPONENTS AND ASSEMBLIES WILL BE AVAILABLE FOR USERS WHO DON'T NEED A TOTAL INTEGRATED POWER SUBSYSTEM

# SUPER

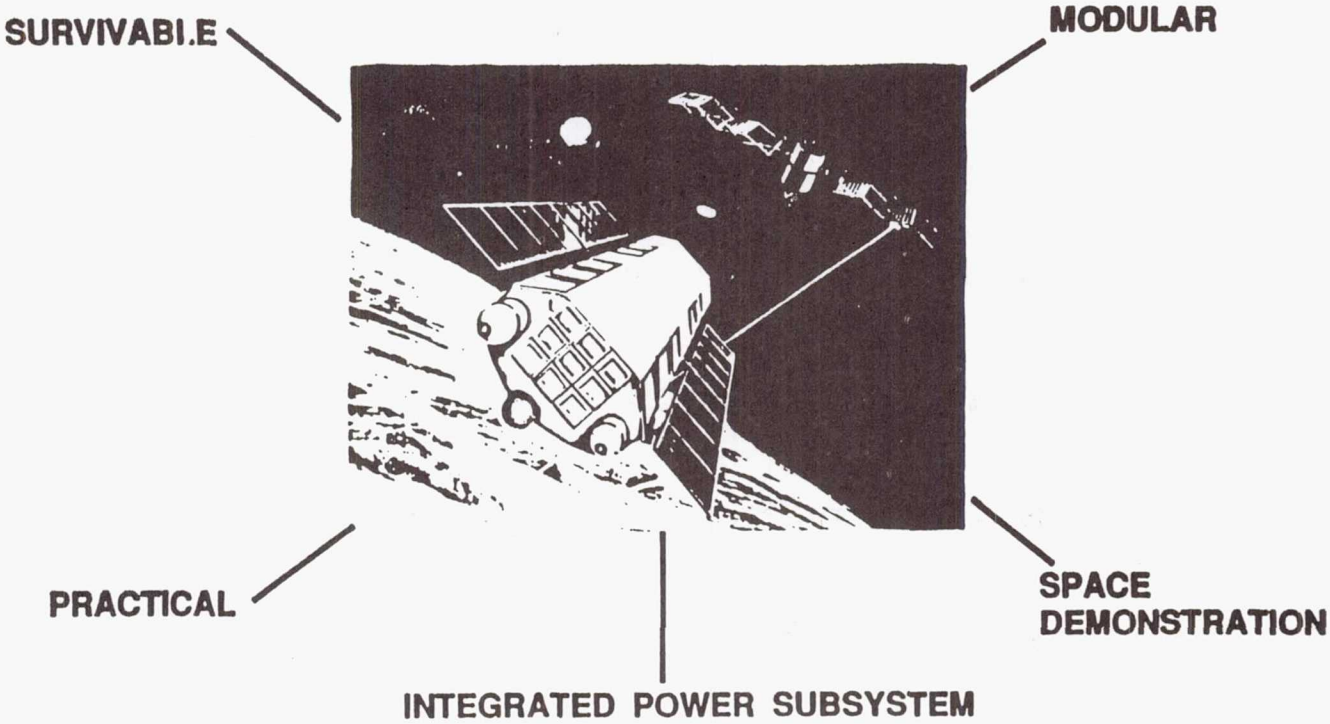

# OVERVIEW

# AIR FORCE AND SDIO

# PHOTOVOLTAICS

Lt. WILLIAM T. COOLEY
WL/POOC-2
WRIGHT-PATTERSON AFB, OH
PH: (513) 255-6235

# OUTLINE

- INTRODUCTORY REMARKS
- BACKGROUND...STATE OF THE ART
- NEW START OBJECTIVES
- POSSIBLE TECHNOLOGIES (NO CONTRACTS YET)
- OTHER ONGOING WORK

# AIR FORCE/SDIO PHOTOVOLTAICS INTRODUCTORY REMARKS

- SDI ARCHITECTURE
  - NEW SYSTEMS
  - NEW PHILOSOPHY
  - TECHNOLOGY IMPLICATIONS
- PHOTOVOLTAICS PROGRAM DRAMATICALLY REDUCED
  - CONTRACT TERMINATIONS
  - NEW PHILOSOPHY TO MEET NEEDS

# STATE OF THE ART PHOTOVOLTAICS

| CELL DESIGN | FEATURES | ACHIEVED BOL EFF % | CONTRACTOR |
|---|---|---|---|
| GaAs/Ge | 4 x 4cm 3.5 mil WA | 18 | ASEC |
| GaAs/Ge | 4 x 4cm x 4.0 mil WT | 18.5 | SPECTROLAB |
| AlGaAs/GaAs | 2 x 2cm x 8 mil (Rad Resistant) | 18 | RTI/ASEC |
| AlGaAs/GaAs | Single Junction | 19 | RTI/ASEC |
| AlGaAs/GaAs/InGaAs | 3 Junction Concentrator | 23 (100x) | VARIAN |
| GaAs | 1 x 0.4 cm 8 mil | 22 (15x) | SPECTROLAB |
| GaAs/Ge | 2 Junction | 24.0 (100x) | SPIRE |
| InP/GaInAsP | 2 Junction on InP Substrate | 15.0 | ARIZONA STATE |
| GaAs + CuInSe | Mechanical Stack | 23.1 | BOEING |

# PROGRAM JUSTIFICATION
# TOP-LEVEL DIRECTION FOR SPACE

## AF Puts Brakes On Upgrades To Space Systems

By VINCENT KIERNAN
Space News Staff Writer

WASHINGTON — Donald Rice, secretary of the U.S. Air Force, has approved a set of planning guidelines that call on the service to avoid costly improvements in its space systems, in an effort to cope with expected tight defense budgets and geopolitical shifts of the 1990s.

Rice has embraced the conclusions of a service-wide study, called the Space Investment Strategy, which mandates that the service slash the "cradle-to-grave" cost of its space systems, an Air Force official said. Also, it calls for placing increased emphasis on technological advances that could make military space systems cheaper to build and operate.

The study was conducted under the auspices of Richard McCormick, deputy assistant secretary of the Air Force for space plans and policy, but included representatives from throughout the service, including the Air Force Space Systems Division, Los Angeles, and Air Force Space Command, Peterson Air Force Base, Colo.

Retired Gen. Larry Welch, former Air Force chief of staff, also approved the conclusions of the study before his recent retirement, said one Air Force official involved in the project.

The study builds on an earlier review of Air Force space efforts, called the Space Road Map, the official said. The intent was to produce a set of principles to guide the Air Force's budgetary decisions, but those studies did not make detailed recommendations about specific programs, he said. The effort's conclusions were presented in a series of briefings; no written report was produced, the official said.

"These reviews have led to a much crisper acquisition strategy for Air Force space efforts as we move into the 21st century," said Martin Faga, U.S. assistant secretary of the Air Force for space.

However, despite the study's conclusion that fiscal restraint will be required in military space programs, the Air Force and U.S. Defense Department clearly an-

See AIR FORCE, Page 20

- SPACE NEWS, 13-19 AUGUST 1990
- DONALD RICE, SECRETARY OF AF APPROVES "SPACE INVESTMENT STRATEGY'
- ...SLASH "CRADLE-TO-GRAVE" COSTS
- ...."INCREASED EMPHASIS ON TECHNOLOGICAL ADVANCES THAT COULD MAKE MILITARY SPACE SYSTEMS CHEAPER TO BUILD AND OPERATE"

# FY91 NEW START PHOTOVOLTAIC OBJECTIVES

- PER PRDA NO 91-01-PKRN
  - MINIMUM 23 PERCENT EFFICIENCY WITH GOAL OF 30 PERCENT
  - MINIMIZE COST (MEASURED IN $/WATT AT EOL)
  - LOW RADIATION DEGRADATION
  - NEGLIGIBLE DEGRADATION WHEN SUBJECTED TO HIGH TEMPFRATURES
  - MODULAR SPECIFIC POWER > 80 W/Kg FOR DEFINED SUBSTRATE
  - EASY INTEGRATION INTO CURRENT PLANAR ARRAY CONFIGURATIONS

# AlGaAs (or GaInAsP) on Si MECHANICAL STACK CONFIGURATION

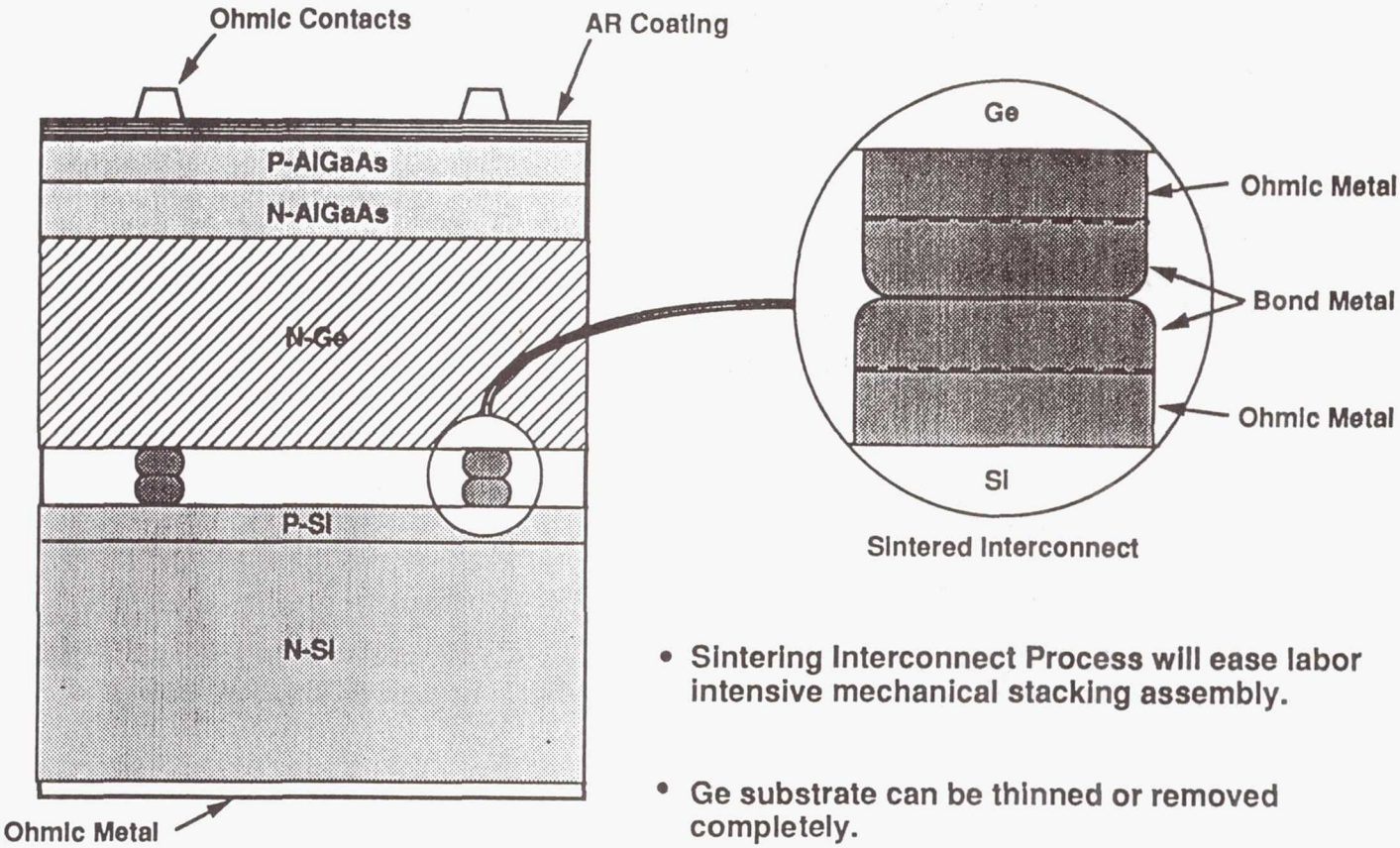


- Sintering Interconnect Process will ease labor intensive mechanical stacking assembly.
- Ge substrate can be thinned or removed completely.

# $GaInP_2$ /GaAs+Ge CONFIGURATION

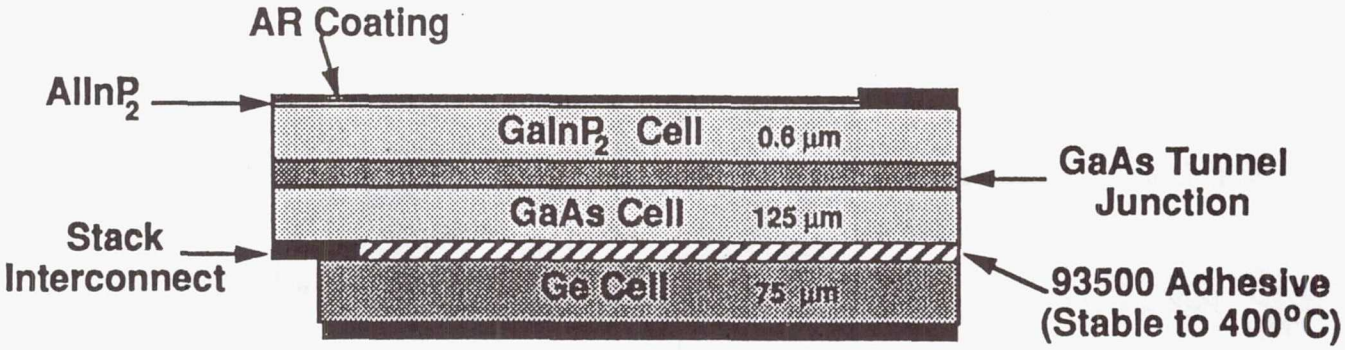


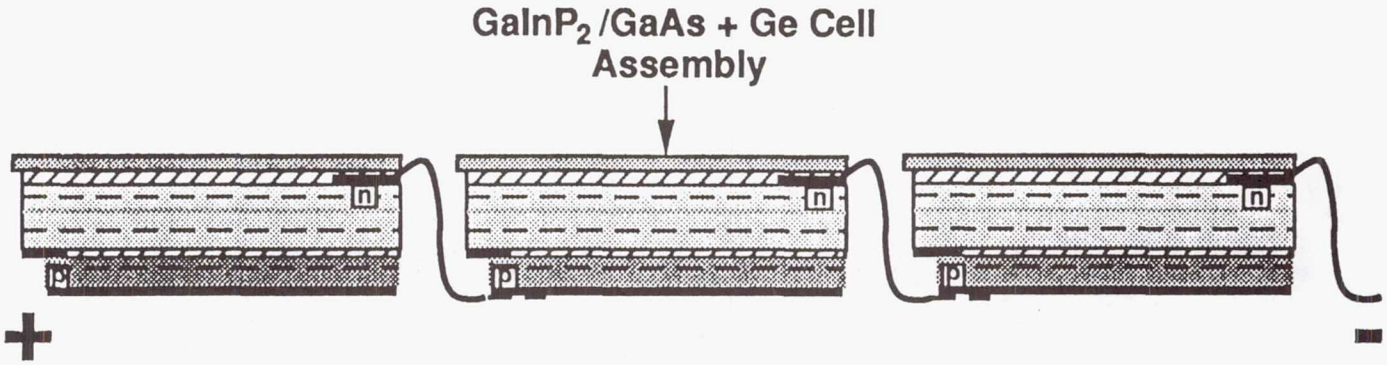


- 2 TERMINAL DEVICE
- "PLUG IN" TO EXISTING ARRAY CONFIGURATIONS

# GaInP/GaAs+Ge
# I-V CHARACTERISTICS

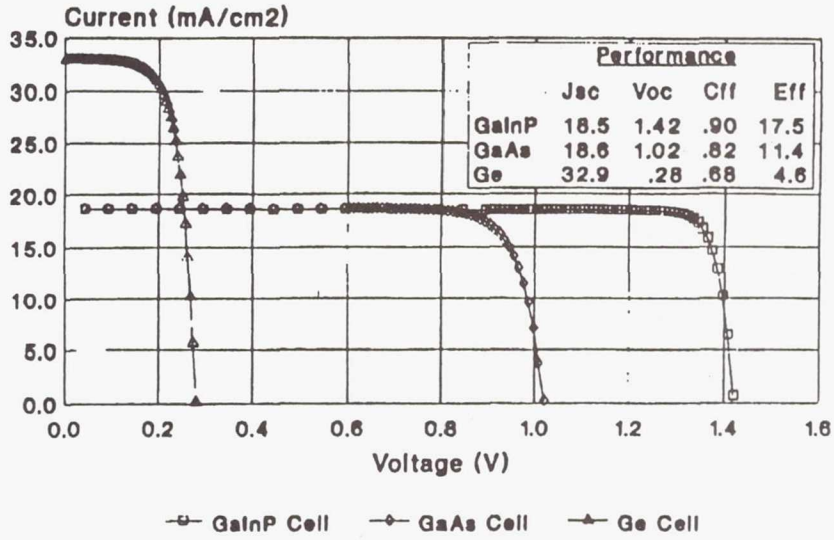


## BOL

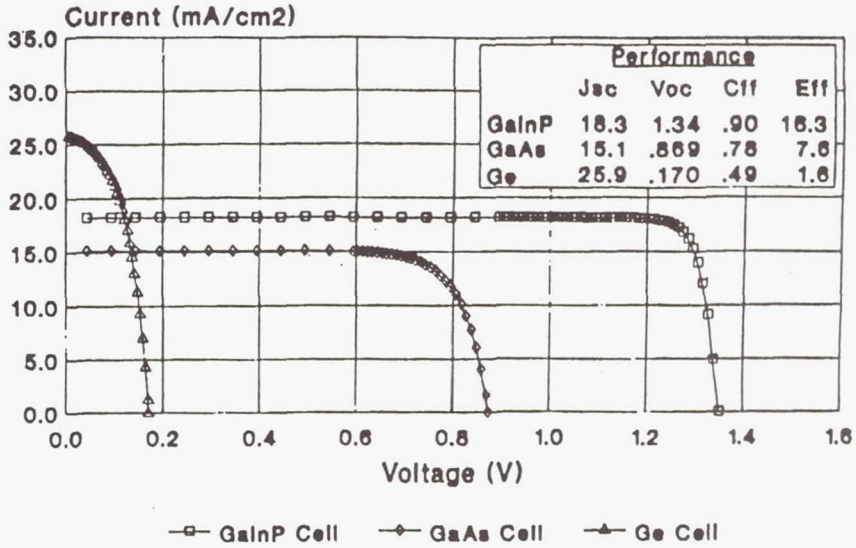


## EOL

$10^{15}$ 1MeV electrons/cm2

# AlGaInP/GaAs/Ge MONOLITHIC CONFIGURATION

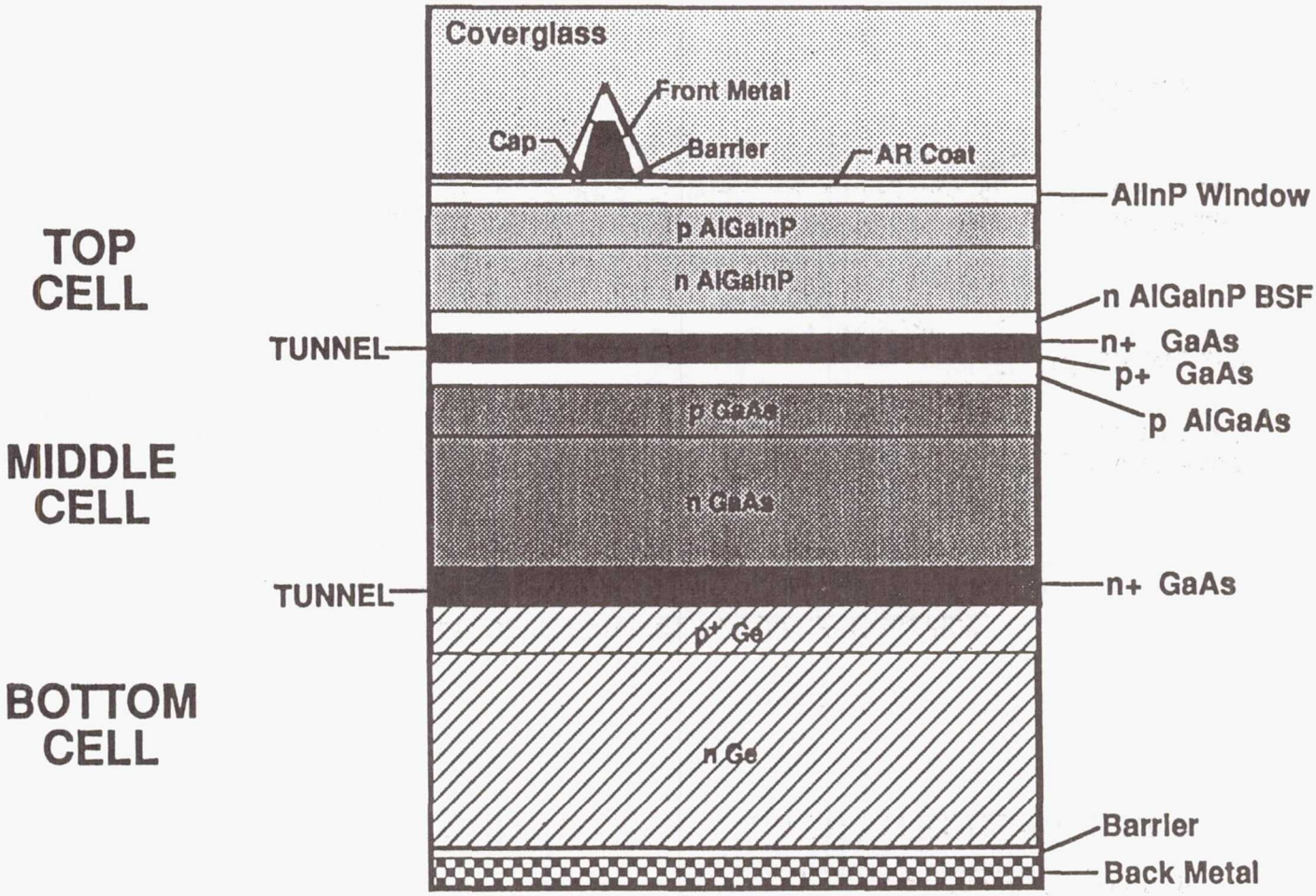

# GaAs/ZnSe/Si CONFIGURATION

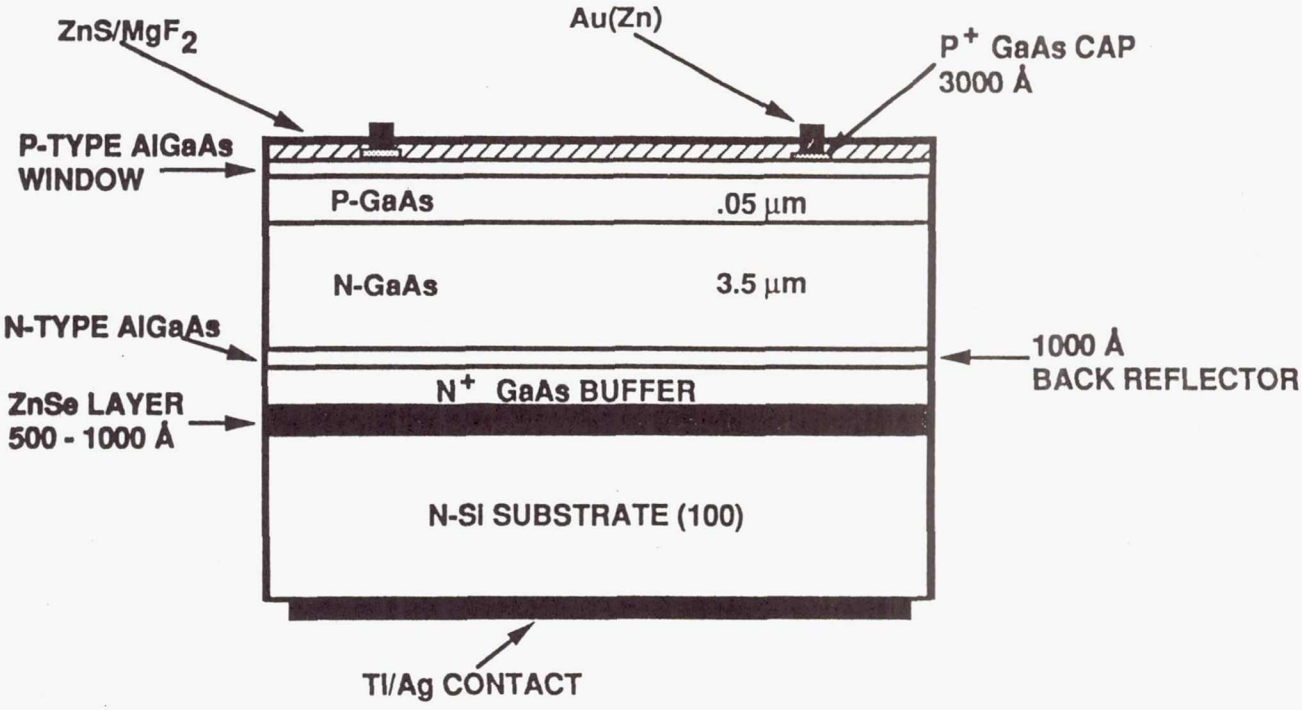


- ZnSe LATTICE MATCHED TO WITHIN 0.24% OF GaAs
- LOW DEFECT SINGLE CRYSTAL ZnSe HAS BEEN GROWN ON Si

☆U.S. GOVERNMENT PRINTING OFFICE:1991 -527 -064/46006

NASA
National Aeronautics and Space Administration

# Report Documentation Page

| | | |
|---|---|---|
| 1. Report No. NASA CP-3121 | 2. Government Accession No. | 3. Recipient's Catalog No. |
| 4. Title and Subtitle SPACE PHOTOVOLTAIC RESEARCH AND TECHNOLOGY—1991 | | 5. Report Date August 1991 |
| | | 6. Performing Organization Code |
| 7. Author(s) | | 8. Performing Organization Report No. E-6161 |
| | | 10. Work Unit No. 506-41-11 |
| 9. Performing Organization Name and Address National Aeronautics and Space Administration Lewis Research Center Cleveland, Ohio 44135-3191 | | 11. Contract or Grant No. |
| | | 13. Type of Report and Period Covered Conference Publication |
| 12. Sponsoring Agency Name and Address National Aeronautics and Space Administration Washington, D.C. 20546-0001 | | 14. Sponsoring Agency Code |

15. Supplementary Notes

Responsible person, Dennis Flood, Lewis Research Center, (216) 433-2303.

16. Abstract

The Eleventh Space Photovoltaic Research and Technology conference was held at NASA Lewis Research Center from May 7 to 9, 1991. The papers and workshop summaries presented in this volume report remarkable progress on a wide variety of approaches in space photovoltaics, for both near and far term applications. Papers were presented in a variety of technical areas, including multijunction cell technology, GaAs and InP cells, system studies, cell and array development, and photovoltaics for conversion of laser radiation. Three workshops were held to discuss the following topics:

- Thin Film Cell Development
- III-V Cell Development
- Space Environmental Effects

| | |
|---|---|
| 17. Key Words (Suggested by Author(s)) Space power Photovoltaic cells Solar cells Solar arrays | 18. Distribution Statement Unclassified—Unlimited Subject Category 20 |

| | | | |
|---|---|---|---|
| 19. Security Classif. (of this report) Unclassified | 20. Security Classif. (of this page) Unclassified | 21. No. of pages 467 | 22. Price* A20 |

NASA FORM 1626 OCT 86

*For sale by the National Technical Information Service, Springfield, Virginia 22161